MAX-PLANCK-INSTITUT
FÜR POLYMERFORSCHUNG

JOHANNES GUTENBERG
UNIVERSITÄT MAINZ

SYNTHESIS OF AMPHIPHILIC POLYPHENYLENE DENDRIMER CONJUGATES AND THEIR IMPACT IN BIORECOGNITION

Dissertation

zur Erlangung des Grades

„Doktor der Naturwissenschaften“

im Promotionsfach Chemie

am Fachbereich

Chemie, Pharmazie, Geographie und Geowissenschaften

der Johannes Gutenberg-Universität Mainz

Jessica Wagner

geb. in Flörsheim am Main

Mainz, Mai 2020

– D77 –

Mainzer Dissertation

Dekan:

1. Gutachter:
2. Gutachter:

Tag der mündlichen Prüfung: 25.06.2020

Die vorliegende Arbeit wurde in der Zeit von Dezember 2016 bis Mai 2020 am Max-Planck-Institut für Polymerforschung [redacted] angefertigt.

Hiermit versichere ich gemäß § 10 Abs. 3d der Promotionsordnung vom 24.07.2007

Ich habe die jetzt als Dissertation vorgelegte Arbeit selbst angefertigt und alle benutzten Hilfsmittel (Literatur, Apparaturen, Material) in der Arbeit angegeben. Ich habe oder hatte die jetzt als Dissertation vorgelegte Arbeit nicht als Prüfungsarbeit für eine staatliche oder andere wissenschaftliche Prüfung eingereicht. Ich hatte weder die jetzt als Dissertation vorgelegte Arbeit noch Teile davon bei einer anderen Fakultät bzw. einem anderen Fachbereich als Dissertation eingereicht.

Mainz, Mai 2020

Jessica Wagner

Für meine Familie

Acknowledgements

Abstract

Amphiphilic structures with precisely arranged hydrophilic and lipophilic groups are abundant in biological architectures such as at protein surfaces, biological membranes, or self-assembling peptides. Despite their prominence in Nature, it is still challenging to synthetically mimic their sophisticated design with the same structural precision. Among various synthetic macromolecules, dendrimers are monodispersed and spherically structured with dimensions similar to proteins. Due to comparable sizes, shapes, and biomimetic properties such as the potential to accommodate guest molecules, dendrimers are often designated as “artificial proteins”. However, aliphatic dendrimers exhibit random backfolding of their dendritic arms depending on the physiological environment which results in their statistical distribution within the dendrimer volume. This phenomenon impedes the creation of precise peripheral pattern characteristically known for protein surfaces. In contrast, aromatic polyphenylene dendrimers (PPDs) provide shape persistency while maintaining peripheral modification capabilities to allow accurate customization of their surface properties. Therefore, this work aimed to deepen the understanding of the role of precise amphiphilic surface patterns in biorecognition. For this purpose, patchy PPD surfaces were employed which consist of alternating sulfonic acid and *n*-propyl groups.

First, the interaction of patchy PPDs with the common gene delivery vector Adenovirus 5 (Ad5) as well as the alterations in cellular uptake and biodistribution of PPD/Ad5 complexes were studied. Only PPDs with a distinct patchy amphiphilic surface structure bound efficiently to Ad5 and thereby remodeled the virus interface. The corona of PPDs on Ad5 allowed cellular uptake and gene transduction of Ad5 into cells that usually do not express the coxsackie-adenovirus receptor (CAR) on their cellular membrane. Thus, cells that are typically not infected by Ad5 can be addressed if Ad5 is coated by a certain PPD corona. Furthermore, the dendrimer corona transformed the adsorption of blood serum proteins by means of the reduction of antibody and blood coagulation factor X binding, which among others directs Ad5 to the liver. Consequently, altering the biological fate of Ad5 *in vivo* by a patchy dendrimer corona is highly attractive in terms of the reduction of both immune responses and liver sequestration in virus-assisted gene therapy.

To further investigate the biological implications of the dendrimer scaffold and periphery, PPDs with different surface patterns with respect to amphiphilicity and charges were synthesized and adsorbed to liposome nanocarriers. The dendrimer-coating remodeled

the protein corona on PPD-coated nanocarriers dependent on the dendrimer scaffold and periphery. Moreover, the patchy PPD corona reduced binding of opsonization proteins compared to uncoated nanocarriers which are known to ultimately induce unspecific cellular uptake. Conversely, adsorption of proteins was observed which are reported to trigger cell-specific uptake. Thus, by adsorbing PPDs with certain biological patches, the biological fate of liposome nanocarriers in blood plasma can be customized.

Furthermore, since the dendrimer exhibits a symmetrical globular structure, the integration of a second bioactive group to the dendrimer scaffold is hampered without the interruption of the amphiphilic biorecognition motif. To enhance the applicability of PPDs in biomedicine by an additional biological function, the dendrimer structure was desymmetrized to a dendron scaffold which corresponds to one quarter of the entire PPD. The bifunctional dendron was obtained by a multi-step synthesis pathway of a patchy dendron providing a reactive handle at its focal point, thus, enabling the post-modification with a fluorophore and a bio-orthogonal group. Due to the patchy surface, the dendron retained its biorecognition properties in terms of cellular uptake, Ad5 binding and protein adsorption while the focal point of the dendron maintained its accessibility for chemical reactions even *in situ* upon Ad5 binding. The chemical accessibility of a single reactive group at the focal point of the dendron opens up many opportunities to attach targeting groups to ultimately allow binding to specific cells.

To install multiple functions such as the patchy recognition motif, fluorophores, drugs or targeting groups within one molecule, the dendron was bound to streptavidin *via* a D-biotin moiety at its focal point. The dendron conjugates inhibited the fibrillation process of the amyloid-beta (Aβ) peptide, which is responsible for the plaque formation and often recognized in Alzheimer's disease. Furthermore, both dendron and protein-hybrid crossed the blood-brain barrier *in vivo*, which qualifies the usage of dendron conjugates in therapeutic applications and contributes to a better molecular understanding of neuro-degenerative diseases.

By the chemical design of precisely arranged amphiphilic groups at the PPD periphery, biological recognition and processes of nanocarriers can be regulated. Furthermore, the advancement of the structural design to a dendron scaffold enhances the application potential for various indications ranging from genetic disorders to brain diseases. Thus, by employing patchy PPDs, this work significantly contributed to an improved understanding of the importance of defined amphiphilic surface structures in biorecognition.

Zusammenfassung

In der Natur kommen biologische Architekturen vor, deren Struktur durch präzise angeordnete hydrophile und lipophile Muster geprägt ist. Beispiele für diese amphiphilen Strukturen sind Proteinoberflächen, biologische Membranen oder selbstorganisierende Peptide. Obwohl diese Architekturen in der Natur weit verbreitet sind, ist es nach wie vor eine große Herausforderung, dieses anspruchsvolle Design mit der gleichen biologischen Präzision synthetisch zu imitieren. Dendrimere sind synthetische Makromoleküle, die sich durch ihre Monodispersität und kugelförmigen Strukturen auszeichnen. Aufgrund ihrer zu Proteinen vergleichbaren Größe und Form sowie ihrer biomimetischen Eigenschaften, wie beispielsweise dem Einschluss von Gastmolekülen, werden Dendrimere häufig als „künstliche Proteine" bezeichnet. Allerdings weisen aliphatische Dendrimere in Abhängigkeit ihrer physiologischen Umgebung eine unkontrollierte Rückfaltung ihrer dendritischen Arme auf, was zu ihrer statistischen Verteilung innerhalb des Dendrimergerüsts führt. Dieses Phänomen erschwert die präzise Anordnung der peripheren Gruppen, die für Proteine charakteristisch sind. Im Gegensatz dazu zeichnen sich aromatische Polyphenylendendrimere (PPDs) durch ihre Formbeständigkeit aus. Dies ermöglicht die genaue Anpassung der Oberflächeneigenschaften durch die Anbringung von spezifischen peripheren Gruppen. Ziel dieser Arbeit war das Verständnis von präzisen amphiphilen Oberflächenmustern in der biologischen Erkennung zu vertiefen. Hierzu wurden gefleckte PPD-Oberflächen verwendet, die aus alternierenden Sulfonsäure- und *n*-Propylgruppen bestehen.

In einer ersten Studie wurde die Interaktion der gefleckten amphiphilen Dendrimere mit dem klinisch verwendeten Gentransport-Vektor Adenovirus 5 (Ad5) sowie die Veränderungen in der zellulären Aufnahme und der biologischen Verteilung durch die Ad5/PPD-Komplexe untersucht. Ausschließlich PPDs mit einer bestimmten amphiphilen Oberflächenstruktur wiesen eine effiziente Bindung an Ad5 auf und führten somit zu einer Veränderung der Virusoberflächentopologie. Die aus adsorbierten PPD-Molekülen bestehende neue Korona auf der Ad5-Oberfläche veränderte die zahlreichen Wechselwirkungen von Ad5 mit seiner Umgebung. So konnte durch die Dendrimer-Korona eine Aufnahme von Ad5 in Zellen, die den erforderlichen Coxsackie-Adenovirus Rezeptor (CAR) nicht auf ihrer Oberfläche exprimieren, induziert werden. Dies ermöglichte somit eine Gentransduktion in CAR-negativen Zellen. Hierdurch konnte gezeigt werden, dass Zellen, die normalerweise nicht durch Ad5 infiziert werden, nun

aufgrund der Dendrimer-Korona adressiert werden können. Des Weiteren wurde durch die Bildung der PPD-Korona die Adsorption von Blutserumproteinen verändert. Dies konnte durch die Reduzierung der Antikörperanbindung und der Verringerung der Bindung des Blutgerinnungsfaktors X, der Ad5 u.a. zur Leber leitet, gezeigt werden. Eine Beeinflussung der Biodistribution von Ad5 *in vivo* durch eine gefleckte Dendrimer-Korona ist somit sehr attraktiv, da es die Immunantwort und die Ansammlung von Ad5 in der Leber in der virusgestützten Gentherapie verringern könnte.

Um die Auswirkungen des Dendrimergerüsts und der -peripherie auf biologische Strukturen näher zu untersuchen, wurden PPDs mit verschiedenen amphiphilen und geladenen Oberflächenmustern synthetisiert und anschließend an liposomale Nanotransporter gebunden. Die Beschichtung mit den Dendrimeren führte zu einer Veränderung der Protein-Korona abhängig von ihrem Gerüst und ihren peripheren Gruppen. Im Vergleich zu unbeschichteten Nanotransportern verringerte die gefleckte PPD-Korona die Adsorption von Opsoninen, die eine unspezifische Zellaufnahme induzieren können. Im Gegensatz dazu wurde die Adsorption von Proteinen, die eine zellspezifische Aufnahme bewirken können, beobachtet. Demzufolge kann das biologische Schicksal von liposomalen Nanotransportern durch die Verwendung von bestimmten PPD-Oberflächenmustern im Blutplasma gesteuert werden.

Da Dendrimere eine symmetrische kugelförmige Struktur aufweisen, ist die Einbindung einer zweiten biologisch aktiven Gruppe in das Dendrimergerüst, ohne das amphiphile Motiv für die biologische Erkennung zu unterbrechen, erschwert. Um die Anwendbarkeit der PPDs in der Biomedizin durch eine weitere biologische Funktion zu erweitern, wurde die Dendrimerstruktur zu einem Dendron, das einem Viertel des gesamten PPDs entspricht, desymmetrisiert. Das bifunktionelle Dendron wurde durch einen mehrstufigen Syntheseweg eines gefleckten Dendrons erhalten, das durch eine reaktive Gruppe an seinem fokalen Punkt die Postmodifizierung mit einem Fluorophor und einer bioorthogonalen Gruppe ermöglicht. Durch die gefleckte Oberfläche des Dendrons wurde die biologische Erkennungseigenschaft erhalten. Damit war die Möglichkeit zur Zellaufnahme, die Bindung an Ad5 und dessen veränderte Proteinadsorption weiterhin gegeben während der fokale Punkt des Dendrons für chemische Reaktionen zur Verfügung stand. Die Postmodifikation war zudem *in situ* nach der Anbindung an Ad5 realisierbar. Diese Zugänglichkeit der reaktiven Gruppe am fokalen Punkt des Dendrons eröffnet somit die Möglichkeit für eine zielgerichtete Therapie durch *targeting*-Gruppen, um bestimmte Zellen zu adressieren.

Um mehrere Funktionen wie das gefleckte biologische Erkennungsmotiv, Fluorophore, Medikamente oder *targeting*-Gruppen in einem Molekül zu integrieren, wurde das Dendron über eine fokal angebrachte D-Biotin-Gruppe an Streptavidin gebunden. Die Dendron-Konjugate bewirkten eine Hemmung des Fibrillierungsprozesses des Amyloid-beta (Aβ)-Peptids. Diese Assemblierung kann zur Ausbildung von Plaques führen, welche häufig bei der Alzheimer-Krankheit erkannt werden. Des Weiteren, konnten sowohl das Dendron als auch das Dendron-Protein-Hybrid die Blut-Hirn-Schranke *in vivo* überwinden, was den Einsatz von Dendron-Konjugaten in therapeutischen Anwendungen ermöglicht sowie zu einem besseren molekularen Verständnis von neurodegenerativen Krankheiten beiträgt.

Durch das chemische Design von präzise angeordneten amphiphilen Gruppen an der PPD-Peripherie, können somit sowohl die biologische Erkennung als auch biologische Prozesse von Nanotransportern verändert werden. Darüber hinaus weist die Weiterentwicklung des strukturellen Designs zu einem Dendrongerüst ein großes Potential auf, um zukünftig gegebenenfalls genetische Störungen bis hin zu Krankheiten im Gehirn zu adressieren. Auf diese Weise konnte in dieser Arbeit ein signifikanter Beitrag zum Verständnis der biologischen Erkennung von definierten amphiphilen Oberflächenmustern durch die Verwendung von gefleckten PPDs geleistet werden.

Graphical Abstract

3 Patchy Amphiphilic Dendrimers Bind Adenovirus and Control Its Host Interactions and In Vivo Distribution.....45

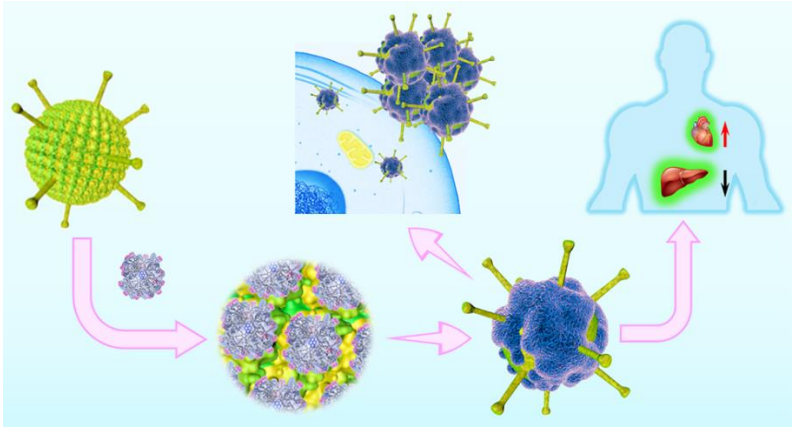

4 Amphiphilic Dendrimers Control Protein Binding and Corona Formation on Liposome Nanocarriers.....81

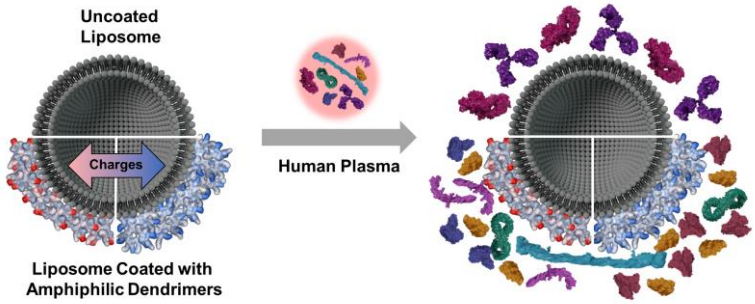

5 Amphiphilic Polyphenylene Dendron Conjugates for Surface Remodeling of Adenovirus 5.....119

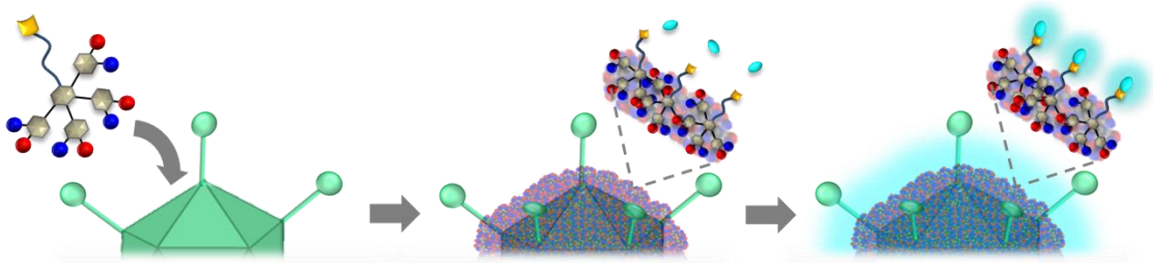

6 Amphiphilic Polyphenylene Dendrimer Conjugates Crossing the Blood-Brain Barrier and Inhibiting Aβ Fibrillation 193

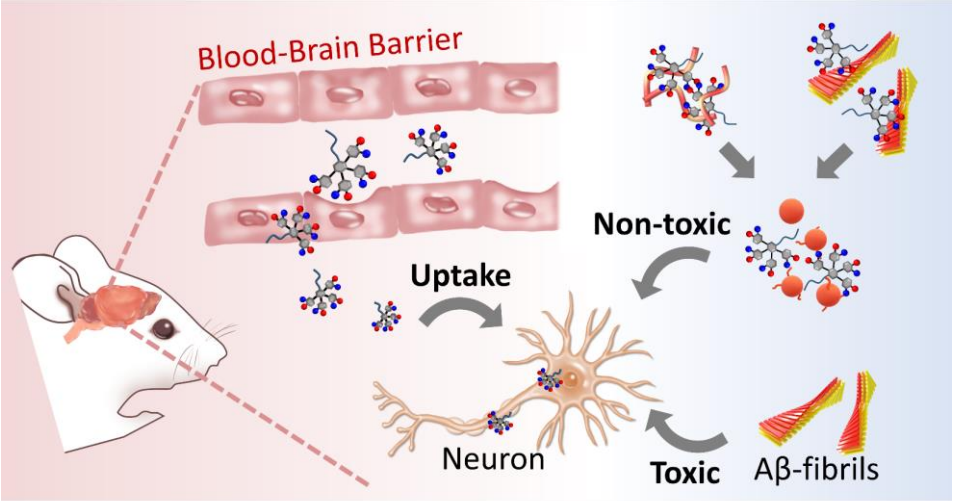

Table of Contents

Abstract ..... **III**

Zusammenfassung ..... **V**

Graphical Abstract ..... **IX**

Table of Contents ..... **XI**

1 Introduction **1**

1.1 Dendritic Architectures – The Development of Dendrimers 2

1.1.1 Architecture and Physicochemical Properties of Dendrimers 3

1.1.2 Synthetic Strategies of Dendrimers – Divergent *versus* Convergent Approach 6

1.2 Structural Design of Dendrimers for the Application in Nanomedicine 8

1.2.1 The Role of Multivalency and Non-Covalent Interactions 8

1.2.2 Relevance of Dendrimers in Neurodegenerative Diseases 11

1.2.3 Dendrimer-Protein Hybrid Materials 13

1.3 Polyphenylene Dendrimers 16

1.3.1 Architecture and Synthesis of Polyphenylene Dendrimers 18

1.3.2 Rational Design of PPDs towards Biomedical Applications 21

1.3.3 Patchy PPDs – The Role of Amphiphilic Surface Patterns 24

1.4 Biological Fate of Nanocarriers in the Blood Stream 26

1.4.1 Biodistribution and Toxicity of Dendrimers 26

1.4.2 Influence of Protein Adsorption on the Biodistribution of Nanocarriers 28

1.5 References 33

2 Motivation and Conceptual Design **41**

3 Patchy Amphiphilic Dendrimers Bind Adenovirus and Control Its Host Interactions and In Vivo Distribution **45**

3.1 Introduction 47

3.2 Results and Discussion 49

3.3 Conclusions 58

3.4 Acknowledgements 59

3.5 Methods 59

3.6 Supporting Information 63

3.7 References 78

4 Amphiphilic Dendrimers Control Protein Binding and Corona Formation on Liposome Nanocarriers 81

4.1 Introduction 82

4.2 Results and Discussion 83

4.3 Conclusion 88

4.4 Acknowledgements 88

4.5 Supporting Information 89

4.6 References 116

5 Amphiphilic Polyphenylene Dendron Conjugates for Surface Remodeling of Adenovirus 5 119

5.1 Introduction 121

5.2 Results and Discussion 124

5.3 Conclusion 133

5.4 Acknowledgements 134

5.5 Supporting Information 135

5.6 References 190

6 Amphiphilic Polyphenylene Dendrimer Conjugates Crossing the Blood-Brain Barrier and Inhibiting Aβ Fibrillation 193

6.1 Introduction 195

6.2 Results and Discussion 197

6.3 Conclusion 210

6.4 Acknowledgements 211

6.5 Materials and Methods 211

6.6 Supporting Information 216

6.7 References 229

7 Summary and Outlook 231

List of Abbreviations 237

List of Figures 241

List of Schemes 243

List of Supporting Figures 244

List of Supporting Tables 248

Appendix 249

List of Publications 249

Conferences and Summer Schools 250

Curriculum Vitae 251

1 Introduction

In recent years, nanotechnology has received an enormously increasing research focus that affects multiple fields of our daily life.[1] Synthetic nanomaterials with dimensional length scales of 1–100 nm became of high interest among others in the development of new medicines as Nature has created complex biological structures such as proteins at a nanoscopic level with a sophisticated design.[2] These macromolecules exhibit many unique features which contribute to their important role in various biological processes within the body such as the binding of ligands for transport or enzymatic processes and interactions with e.g. other proteins, receptors or cells.[3] A better understanding of these mechanisms provides the potential to identify novel treatment strategies for certain diseases as many maladies result from abnormalities in biological processes such as the misfolding of proteins or genetic disorders. Thus, synthetic materials with low nanoscopic dimensions similar to proteins gained a high relevance in the development of new biomedicines which is termed nanomedicine.[4] This field comprises the usage of nanomaterials among others for diagnosis, prevention and treatment of diseases.[1] The structural control of nanomaterials has shown to enable the delivery of drugs to disease sites with the advantage of minimizing side-effects. For this purpose, synthetic nanoscopic transport systems were developed. These so-called nanocarriers range from liposomes, organic polymers and inorganic nanoparticles to dendrimers.[5] For example, the first polyethylene glycol (PEG)-ylated liposome based nano-drug (Doxil®) approved by the Food and Drug Administration (FDA) attracted a lot of attention and fueled the development of nanomedicine as it showed that the blood-circulation time and immunogenicity of small drug molecules can be controlled applying nanocarriers.[6]

However, the biodistribution and toxicity of nanocarriers is dependent on their physicochemical properties (e.g. charge, hydrophobicity, molecular weight and hydrodynamic radius).[7] For medical applications the design of nanocarriers with defined structures, which are known for biological architectures, are crucial. Therefore, structure perfection is an important feature to achieve reproducibility and to understand a certain biorecognition motif which ultimately influences the biological fate. This requirement is often not feasible for the synthesis of traditional polymer-based architectures. To obtain a well-defined nanocarrier platform with high structural precision, dendrimers were developed.[5] The step-wise synthesis of dendrimers enables the adjustment of a distinct

molecular weight, sizes in the low nanometer range as well as a distinct shape, identity and number of surface groups. These features can be compared to the characteristics of proteins, which is attractive for nanomedicine applications despite the higher synthesis efforts of dendrimers compared to polymerization processes.[5, 8] Consequently, this work focuses on the development of dendrimers as protein mimics to contribute to the understanding of precise surface patterns in biorecognition which could ultimately advance nanomedicine research.

1.1 Dendritic Architectures – The Development of Dendrimers

Dendritic architectures are present in biological macro- and microscopic structures ranging from branches and roots in plants to neurons in the nervous system.[9] Inspired by Nature, synthetic branched polymer structures have adopted several different configurations that are broadly divided into mono- and polydisperse frameworks. The latter consists of hyperbranched polymers, dendritic-linear hybrids and dendrigrafts, whereas the monodisperse dendritic structures are represented by dendrimers and dendrons.[10] A schematic overview of dendritic architectures is depicted in Figure 1.1.

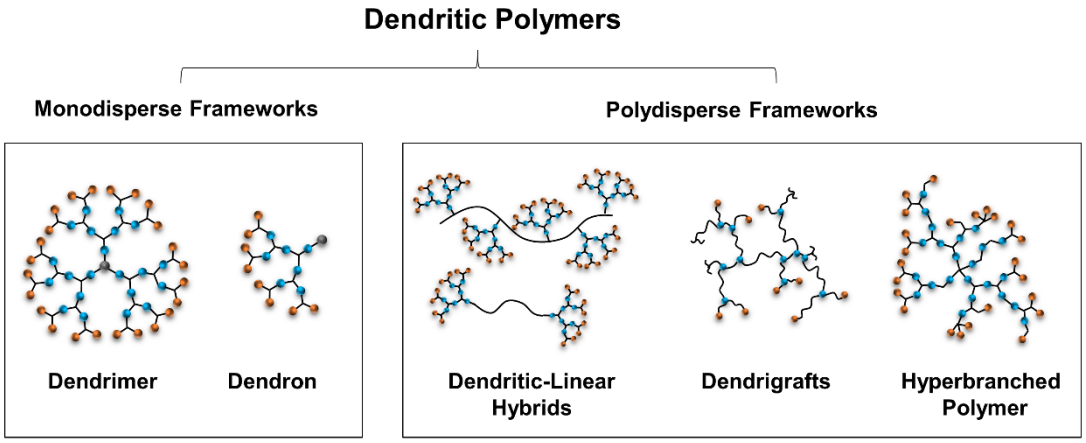

Figure 1.1. Dendritic polymers. Synthetic dendritic structures are divided in monodisperse dendrimers and polydisperse polymers.[10]

Dendrimers are highly branched globular macromolecules which differ from classical polymers due to their monodispersity, well-defined number of terminal groups and nano-size perfection.[11] The term dendrimer, derived from the Greek words *dendron* = tree and *meros* = part, was firstly propagated by Tomalia et al. in 1985.[12] However, the first tree-

like synthetic structures were already described by Vögtle et al. in 1978 and initially designated as "cascade molecules".[13] Based on the design of Vögtle's poly-(propyleneamine) (POPAM), Tomalia et al. prepared poly(amidoamine) (PAMAM) structures which are referred to as "starburst-dendrimers".[14] Independent from these first dendrimers, Newkome et al. developed highly branched structures with terminal hydroxyl groups – the "arborol systems" (Latin: *arbor* = tree).[15] The first arene based dendritic architectures represented the poly(aryl ether) dendrimers by Fréchet and Hawker[16] and the hydrocarbon dendrimers by Miller and Neenan.[17] On this basis, polyphenylene dendrimers were derived by Müllen and co-workers[18] which is described in more detail in chapter 1.3.

1.1.1 Architecture and Physicochemical Properties of Dendrimers

In general, dendrimers consist of a core, a shell and a periphery (Figure 1.2A). Branches emanate in three dimensions from the core which results in a spherical architecture.

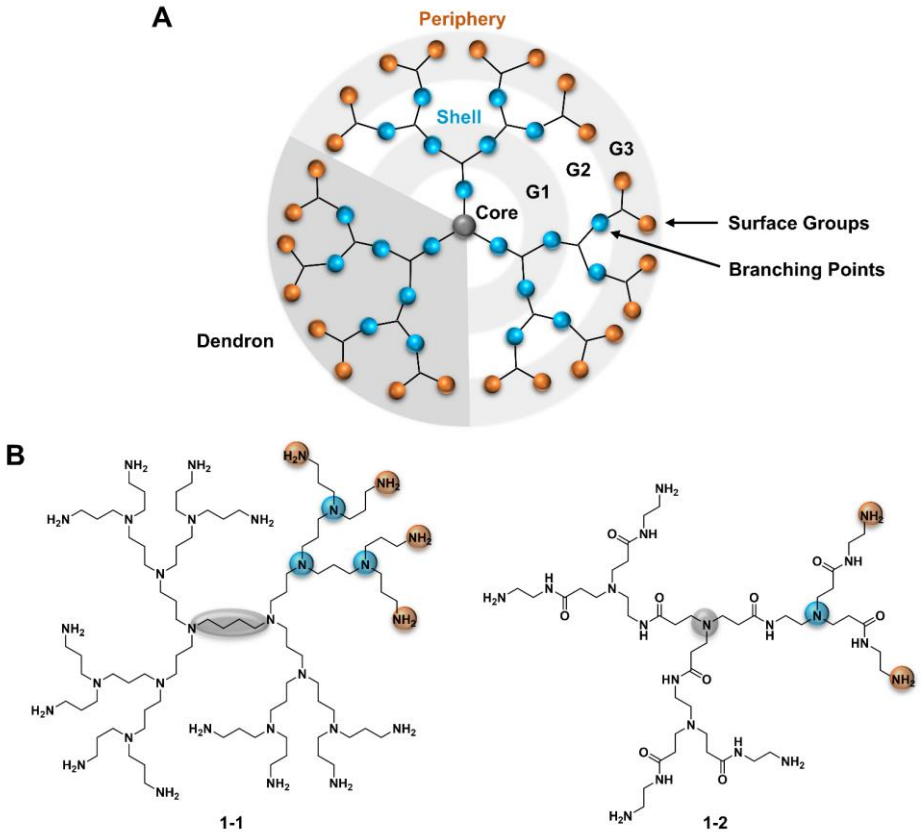

Figure 1.2. Dendrimer scaffold. (**A**) Schematic illustration of a 3rd generation dendrimer and (**B**) chemical structures of 3rd generation POPAM (**1-1**) and 2nd generation PAMAM (**1-2**) dendrimers.

Each segment starting from the central unit is designated as dendron and the degree of branching is enhanced through dendron growth by multiple chemical reactions to achieve the dendrimer shell.[19] Each successive layer of branching points is termed generation (G) and increases the dendrimer diameter e.g. for PAMAM by approximately 1 nm.[20] The stepwise iterative synthesis of dendrimers enables controllable nanoscopic sizes due to the possibility to stop the synthesis at any point (refer to section 1.1.2). This allows the formation of monodisperse structures which is advantageous in comparison to polymerization processes. The dendrimer surface – often referred to as the periphery – is determined by end groups which among others influence the solubility, shape and stability of the dendrimer.[19] In Figure 1.2B, the third generation POPAM **1-1** from Vögtle et al.[13] and second generation PAMAM dendrimer **1-2** from Tomalia et al.[14] are depicted exemplarily for aliphatic dendrimers. The dendritic shell exhibits void spaces, also termed as cavities which are able to include guest molecules.[21] This advantageous property is, for example, used for drug encapsulation (see section 1.2.1).[22, 23]

PAMAM dendrimers of the 3rd up to 5th generation based on an ammonia core have approximately similar dimensions as proteins like insulin (3 nm), cytochrome C (4 nm) and hemoglobulin (5.5 nm). In Figure 1.3, a comparison of dendrimer sizes with those of biological structures, i.e. proteins, a lipid bilayer and deoxyribonucleic acid (DNA), is illustrated. Due to their defined nanoscopic shape, size and spherical architecture, dendrimers exhibit biomimetic properties, which are comparable to those of proteins. Hence, they are often referred to as “artificial proteins”.[20]

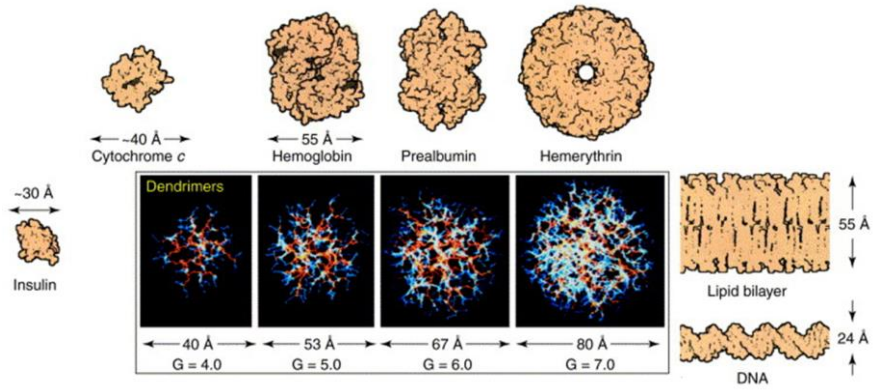

Figure 1.3. Dendrimers as “artificial proteins”. Size comparison of PAMAM dendrimers with biological structures such as proteins, a lipid bilayer and DNA. Adapted from Esfand et al.[20] with permission from Copyright (2001) Elsevier Science Ltd.

As described above, the remarkable feature of dendrimers is their monodispersity. The well-defined architecture and number of surface groups provide information on the

charge, hydrophobicity, molecular weight and hydrodynamic radius of the macromolecules which is advantageous to predict their performance in nanomedicine applications.[7] Nevertheless, the chemical environment including the pH, salt concentration and solvents affect the structure and biological features of dendrimers.[24] Dendrimers such as POPAM **1-1** and PAMAM **1-2** (Figure 1.2B) consist of aliphatic branches that are conformationally flexible and thus, enable backfolding of the dendritic arms into the interior of the dendrimer scaffold. This phenomenon leads to the occupation of the dendrimer cavities as well as a less homogeneous surface and three-dimensional structure.[25, 26] For example, PAMAM dendrimers with terminal amino-groups are positively charged at the surface as well as the tertiary amines in the interior at low pH leading to extended conformations due to the repulsion of the charges. At neutral pH, the surface remains charged and the interior becomes uncharged. In consequence, the dendrons tend to fold back into the interior due to hydrogen bonding. At higher pH ≥ 10, PAMAM becomes uncharged and thus, the repulsion between the surface groups are minimized leading to a compressed globular structure.[26-28] High salt concentrations have a similar effect on dendritic backfolding as observed for increasing the pH.[29] To avoid backfolding and its associated heterogenicity, a shape-persistent dendrimer scaffold is required, which was achieved by Müllen-type polyphenylene dendrimers (PPDs).[18] PPDs consist of a substantially rigid structure which prevents backfolding and allows the synthesis of shape persistent dendrimers[30] and consequently, precise spatial arrangement of surface groups. The chemistry and unique characteristics of PPDs are thoroughly described in chapter 1.3.

Apart from the dendrimer scaffold, the dendrimer generation and the surface chemistry of dendrimers are also important features. As the dendrimer generation increases, the number of reactive groups presented on the surface is multiplied. The so-called multivalency of dendrimers enhances the interaction within its environment compared to a monovalent molecule. Thus, the interaction with biointerfaces such as cells, viruses, proteins or receptors is favored for higher generations. For example, the recognition of a drug (monovalent) with a cellular receptor is enhanced when attached to the dendrimer surface groups (multivalent) through multiple interaction points.[31-33] The impact of the structural dendrimer design for nanomedicine applications is described in chapter 1.2.

1.1.2 Synthetic Strategies of Dendrimers – Divergent *versus* Convergent Approach

In order to obtain monodisperse dendritic structures, two different synthetic approaches were developed – the divergent and convergent approach (Scheme 1.1 and Scheme 1.2 respectively).[34, 35] The synthesis of the POPAM dendrimers developed by Vögtle et al.[13] is based on iterative Michael additions starting from primary monoamines or diamines reacting with acrylonitrile (Step A) followed by the reduction of the nitrile functions (Step B). The obtained terminal amine groups can react in the next Michael addition (Scheme 1.1B). Through multiple repetition of the synthesis steps the first synthetic branched structures were preserved.[13, 19] Based on this strategy, Tomalia et al. described the build-up of PAMAM dendrimers which is, similar to POPAM synthesis, based on a Michael addition on methyl acrylate by ammonia followed by the conversion of the ester functionalities to a primary triamine by adding excess ethylene diamine. Several reaction cycles led to highly branched PAMAM dendrimers.[12] The synthesis described by Vögtle,[13] Tomalia[12] and Newkome et al.[15] follow the divergent route, representing the synthesis from “inwards to the outwards”.[19] As illustrated in Scheme 1.1A, the divergent way starts from a multifunctional core which is coupled to a reactive group of a branching unit (Step A). The branching unit possesses protected functionalities which are activated for the next coupling step (Step B). By multiple repetitions, a high dendrimer generation can be achieved. To furnish a defined surface, an end capping unit is used in the last coupling step.[35]

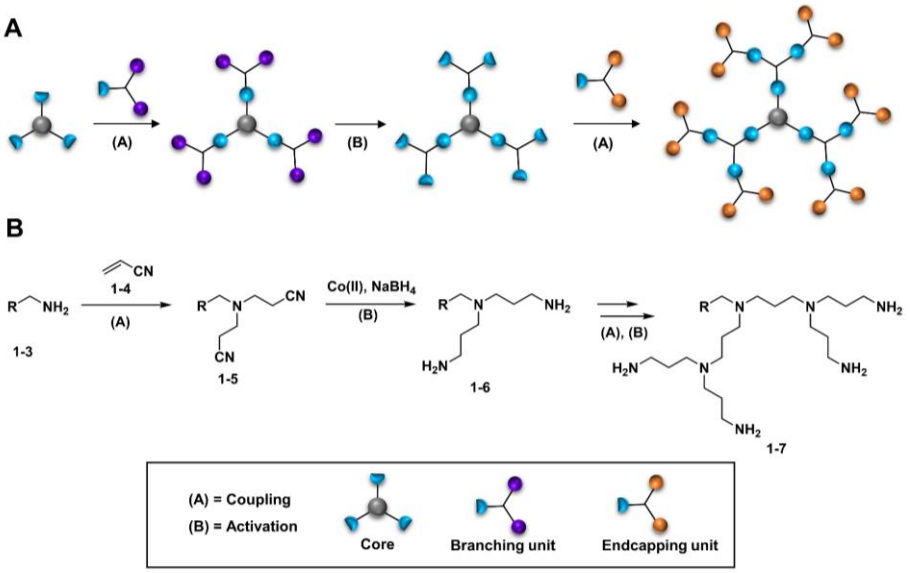

Scheme 1.1. Divergent approach. (**A**) Schematic illustration of the divergent dendrimer synthesis and (**B**) POPAM synthesis according to Vögtle et al.[13]

The main advantage of the divergent synthesis is the possibility to achieve high generation dendrimers by repetitive steps with the possibility of automation, whereas the disadvantage is the exponentially increasing number of branching points which are not always coupled quantitatively even if branching units are added in large excesses. Thus, structural defects of the dendrimers can occur. Due to similar properties of defective to structurally perfect dendrimers they are often difficult to separate.[35]

A second approach towards the synthesis of dendrimers is the convergent way which means that the synthesis occurs from “outwards to inwards” (Scheme 1.2A).[19] For example, the Fréchet poly(aryl ether) dendrimer[16] and arene based hydrocarbon dendrimers reported by Miller and Neenan[17, 36] follow this pathway. In detail, the synthesis proceeds from the periphery to the core by coupling an end group with a branching unit (step A). The branching unit possesses a protected group that can be reacted with the next branching unit upon activation (step B). By this method, dendrons of a desired generation are obtained which are coupled to the core in the final step.[35] The synthesis of a poly(aryl ether) dendrimer is shown in Scheme 1.2B.

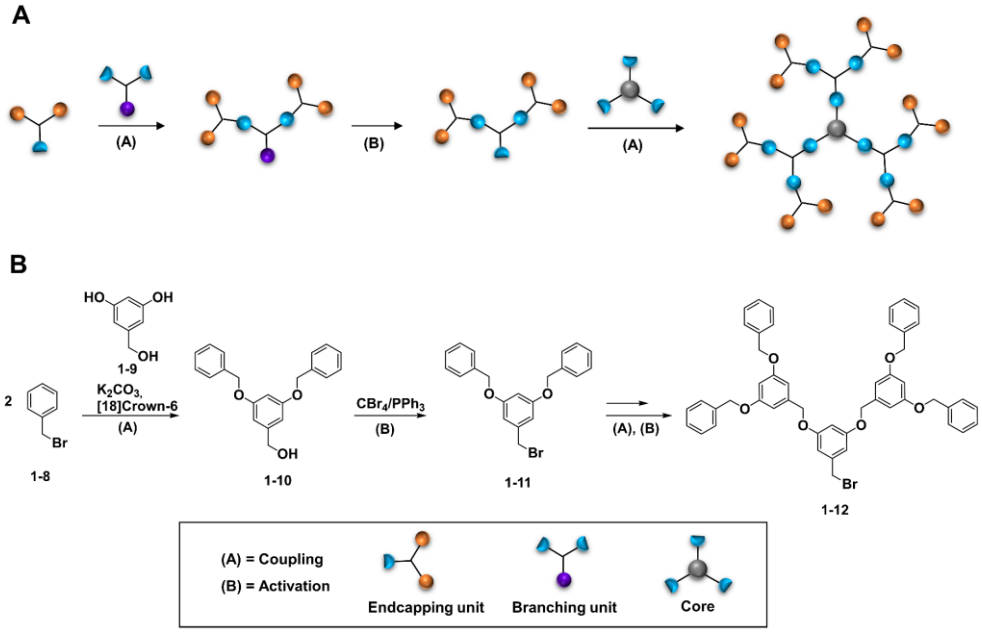

Scheme 1.2. Convergent approach. (**A**) Schematic illustration of convergent dendrimer synthesis and (**B**) synthesis of a Fréchet-type dendrimer.[16]

The advantage of the convergent method compared to the divergent way is the avoidance of structural defects by the employment of a small number of reactive groups. Thus, there is no need to use branching units in excess. However, the main limitation of the convergent synthesis is the steric hindrance which is relevant for the synthesis of

higher generations. Therefore, this method is mainly used for lower-generation dendrimers.[35-37]

1.2 Structural Design of Dendrimers for the Application in Nanomedicine

1.2.1 The Role of Multivalency and Non-Covalent Interactions

Dendrimers emerged as a suitable nanocarrier class for biomedical applications due to their reproducible monodisperse properties which allow highly controlled multivalent surface structures. As described in section 1.1.1, the multivalency is a structural characteristic of dendrimers enhancing their biorecognition through multiple interaction points which is advantageous in drug delivery. During the last two decades, dendrimers with different surface modifications and charged surface motifs were developed in combination with drug molecules, nucleic acids and imaging agents to control their biodistribution and bioavailability, to improve their solubility and efficacy, and to reduce their toxicity.[5, 23, 38, 39]

For cancer therapy approaches, chemotherapeutic drugs such as doxorubicin, methotrexate or paclitaxel were either encapsulated in the dendrimer shell[22, 40, 41] (Figure 1.4A) or ligated covalently to the dendrimer surface (Figure 1.4B).[42, 43] Both strategies show certain advantages and disadvantages. For example, the non-covalent approach may cause leakage of the drug in the blood circulation while the covalent attachment might reduce the efficacy of the drug at the tumor site. The latter approach can be improved by a linker that is cleaved within the microenvironment of tumor cells.[44] Currently, a dendrimer modified with the chemotherapeutic docetaxel (DEP® docetaxel, Starpharma) is in phase II clinical trail.[45] In order to deliver a drug to a specific organ or cell in the body, targeting groups such as folic acid,[46] biotin,[47] targeting peptides[48, 49] or antibodies[50, 51] were conjugated to the dendrimer surface (Figure 1.4B).

In addition to drug delivery, dendrimers are often used in diagnostics and *in vitro* technologies such as immunoassays,[52-55] and DNA microarrays,[56, 57] since the inherent multivalency enhances the detection sensitivity.[58] One example is the Stratus® CS biosensor systems (Dade Behring) traded by Siemens Healthineers which are immunoassays for cardio-diagnostics. The biosensor is based on surface immobilized PAMAMs conjugated to antibodies to detect disease markers in suspected myocardial

ischemia.[59, 60] Furthermore, dendrimers are used as macromolecular Magnetic Resonance Imaging (MRI) agents in order to enhance the effect of the contrast agents by multiple attachment (Figure 1.4B). One commercial dendrimer-based blood pool contrast agent for magnetic resonance angiography is Gadomer-17[61] developed by Bayer Schering AG, which is based on a Denkewalther-type (poly)lysine dendrimer scaffold and Gd-DOTA (gadolinium(III)- 1,4,7,10-tetraazacyclododecane-1,4,7,10-tetraacetic acid) complexes on its surface.[62]

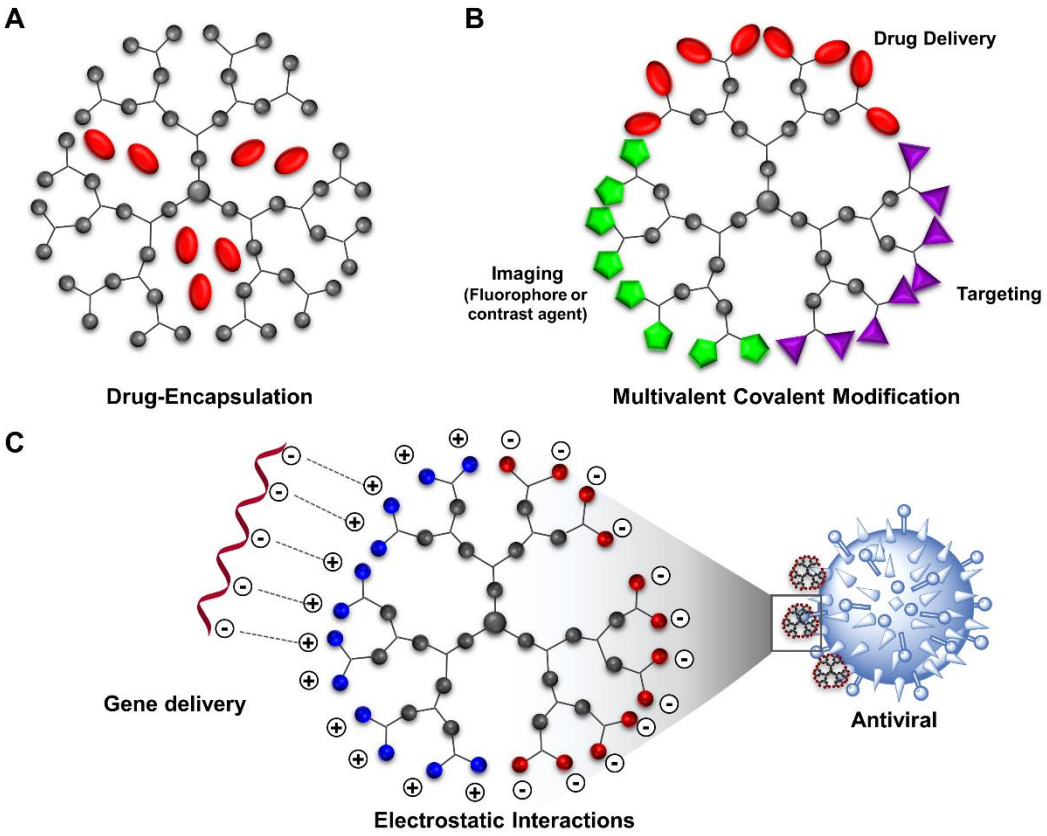

Figure 1.4. Relevance of surface and interior chemistry of dendrimers for pharmaceutical applications. (**A**) Dendrimers for drug delivery applications by either drug encapsulation or (**B**) multivalent modification with drug molecules on the dendrimer surface. The multivalent attachment of fluorophores or contrast agents for imaging and diagnostics or targeting groups on the dendrimer surface also enhances the efficiency of the respective function. (**C**) Electrostatic interactions between charged dendrimer surfaces with biological interfaces such as nucleic acids for gene delivery applications or interactions with viruses as antiviral agents.

Beside covalent modification of the peripheral groups, electrostatic interactions of charged dendrimers with nucleic acids and viruses are used in gene delivery and antiviral treatment respectively (Figure 1.4C).[38] For gene delivery, cationic dendrimers are used to form complexes with the negatively charged nucleic acids and hence, transport the genetic material into the cell. Thus, the dendrimer serves as a vector with similar gene delivery mechanisms known for viruses. The uptake occurs *via* an active endocytosis mechanism and the nucleic acid e.g. DNA must be released from the endosome before

lysosomal activity degrades the dendrimer-DNA complex. Subsequently, the DNA is translocated into the nucleus for transcription into messenger ribonucleic acid (mRNA). The mRNA is transported to the cytosol where it is translated into the desired therapeutic protein.[63] Commercially available PAMAM-dendrimer based *in vitro* gene transfection agents are Superfect® (Qiagen) and Priofect™ (Starpharma).[38, 63, 64]

The control of the multivalent dendrimer surface properties also enables the contrary effect, namely, the inhibition of virus-assisted gene delivery by preventing cellular entrance of the virus particles.[65] Viruses deliver their genome into the host cells by endocytotic pathways which include the interaction between the virus capsid and the receptors on the cellular membrane. In particular, the ionic adhesion between e.g. a cationic virus capsid and the anionic receptor or headgroups on the cellular membrane are involved.[66] The strategies for the application of dendrimers as antivirals are mainly based on negatively charged dendrimers as cell surface mimics to prevent from an infection with e.g. influenza virus, herpes simplex virus (HSV) and human immunodeficiency virus (HIV).[67, 68]

Influenza, a respiratory febrile disease, causes a significant morbitity and mortality worldwide and is either prevented by the usage of vaccines or is treated with antiviral drugs like oseltamivir (neuramidase-inhibitor). Both vaccines and drugs show limitations like reduced efficacy, specificity as well as drug resistance.[69, 70] Influenza virus binds to cellular membrane receptors containing oligosaccharides with sialic acid residues (anionic) *via* its receptor-binding and membrane fusion protein hemagglutinin (HA, cationic).[66, 71] After virus replication, the progeny virions are released from the infected cell *via* enzymatic cleavage of sialic acid residues by the enzyme neuramidase.[72] Due to the development of resistance of influenza viruses to neuramidase inhibitors like oseltamivir, the utilization of dendrimers approaching HA was investigated. Sialic acid surface modified dendrimers based on e.g. PAMAM[73] or carbosilane[74] scaffolds inhibited viral adhesion to the cellular membrane. In addition, a higher valency lead to higher inhibitory effects.[73, 75] Since neuramidase is known to digest sialic acids a carbosilane dendrimer functionalized with a sialic-acid mimicking peptide (Ala-Arg-Leu-Pro-Arg) was developed for HA binding.[76]

Moreover, the effective inhibition of cell adhesion for herpes simplex viruses (HSV-1 and HSV-2) was achieved by a Denkewalter-type poly(lysine) dendrimer (G4),[77] presenting negatively charged naphthalene sulfonic acid groups on its periphery. The safety and

efficacy were successfully tested in several clinical studies and it has been shown to be antiviral and antibacterial. This dendrimer, commercialized as VivaGel® (SPL7013) by Starpharma, is used as sexual/woman's health product on condoms, for treatment and prevention of bacterial vaginosis as well as for prevention of sexually transmitted infections such as HSV-2, HIV and human papillomavirus (HPV) causing cervical cancer.[78]

Therefore, the multivalency of dendrimers by the employment of both covalent modifications and electrostatic interactions presented the opportunity to use dendrimers in nanomedicine. Nevertheless, the applicability of dendrimers is dependent on their ability to cross biological barriers (refer to 1.2.2 and 1.4) and their biodistribution (refer to section 1.4).

1.2.2 Relevance of Dendrimers in Neurodegenerative Diseases

In the past, the behavior of various dendrimers crossing the blood-brain barrier (BBB) was studied for the treatment of neurodegenerative diseases such as Alzheimer's disease (AD).[79] The BBB, also referred to as neurovascular unit (NVU), presents a natural barrier preventing the passage of unwanted substances. The brain capillaries are a complex system and the actual barrier is represented by the brain capillary wall. This is composed of endothelial cells which are in association with pericytes surrounded by a basement membrane and astrocytes. The astrocyte endfeets connect the capillary with the neurons.[80] The endothelial cells are connected by so-called tight junctions which display a paracellular barrier that is hard to overcome. Hence, only small water-soluble molecules enter the brain *via* extracellular pathways. Transcellular diffusion occurs in much higher extend by passive diffusion and receptor-mediated, carrier/transporter-mediated or adsorptive transcytosis. Passive diffusion is only possible for highly lipophilic compounds with a low molecular weight whereas the adsorptive endocytosis is often observed for positively charged components.[81-83] Hence, therapeutics to address brain diseases must comply the requirements for BBB-passage while retaining the desired therapeutic effect. Consequently, the design of these therapeutics is often difficult.

The tunable chemistry of dendrimers enables customizable surface functionalizations for the desired biomedical application as described in section 1.2.1. In principal, dendrimers can access the central nervous system by either active or passive targeting. Passive targeting occurs if molecules preferably accumulate at certain sites which provide a

higher vascular permeability. The so-called enhanced permeability and retention effect (EPR) is initiated by disorders such as tumors. Since the EPR-effect is rather slow and only small amounts reach the brain due to excretion by liver and kidneys, active targeting is considered.[79] The active targeting can be achieved by the attachment of targeting groups such as the protein transferrin or the peptide angiopep-2. These targeting groups interact preferably with overexpressed receptors, i.e. transferrin or low density lipoprotein receptor-related protein 1 (LRP1) respectively, on the cellular membrane of brain capillary endothelial cells.[84, 85]

Alzheimer's disease, which results in dementia, affects millions of people worldwide, but the reason for this disease is still not fully understood. In the brain of AD patients, aggregates, also referred to as senile plaques, are often observed. These plaques can be attributed to the misfolding of the peptide amyloid beta (Aβ) which is produced by the endoproteolytic cleavage of the amyloid precursor protein (APP) by the β- and γ-secretase. The aggregation of Aβ leads to the formation of β-sheets which further assemble into oligomers, fibrils and finally to amyloid plaques in the brain (Figure 1.5).[86] This process, which was reported to induce neurotoxicity and dementia, is called the amyloid cascade hypothesis.[87]

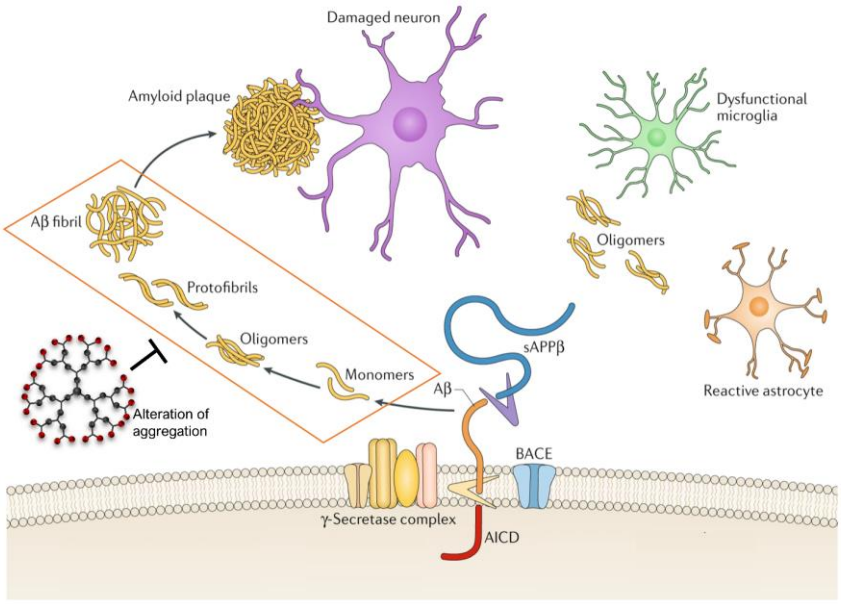

Figure 1.5. Mechanism of amyloid-β (Aβ) aggregation starting from cleavage by the γ-secretase and β-secretase (BACE) into Aβ, the soluble amyloid precursor protein (sAPPβ) and the amyloid precursor protein intracellular domain (AICD). The Aβ monomer aggregate into oligomers, followed by fibril formation and consquently amyloid plaques leading to degeneration of neurons. Dendrimers can alter the aggregation process. Adapted and modified from Panza et al.[88] with permission from Copyright (2019) Springer Nature.

Dendrimers tested for the application as neurotherapeutics in AD are based on e.g. PAMAM,[89-91] poly(propyleneamine),[92, 93] phosphorous[94] or gallic acid-triethylene glycol[95] scaffolds with various dendrimer surface patterns having impact on the fibrillation process of Aβ or inhibition or its toxicity. For example, maltose decorated poly(propyleneamine) dendrimers altered the Aβ-morphologies during aggregation. Both neutral and cationic glycodendrimers crossed the BBB, when administrated intranasally, but cationic dendrimers caused memory loss in wild type mice.[92, 93] Recently, a PAMAM-dendrimer with alternating negative charges (carboxylic acid) and hydrophobic patches demonstrated the alteration of Aβ fibrillation leading to cellular survival. The inhibition was explained by hydrophobic binding-electrostatic repulsion effects between dendrimer and Aβ.[91, 96] Consequently, dendrimers have the potential to be used as nanotherapeutics in neurodegenerative diseases but the combination of BBB transport properties and therapeutic effect needs to be further optimized.

1.2.3 Dendrimer-Protein Hybrid Materials

While dendrimers have been widely used for biomedical applications, the combination of dendrimers with liposomes,[97, 98] nanoparticles[99-102] and proteins[103-106] offers the opportunity for synergistic and multiple effects in the treatment and detection of diseases.[107] Proteins like enzymes,[108] or antibodies[109, 110] have the potential to be used as nanotherapeutics, but their efficacy is often limited by their immunogenicity and instability in the blood stream. Thus, approaches towards the shielding and consequently the enhancement of circulation times in the blood stream of therapeutical proteins were investigated by the formation of protein-polymer hybrid materials.[111] Several PEG modified protein therapeutics were already approved by the FDA.[112]

In principal, the chemical modification of proteins is given by their sophisticated surface structure with specific surface groups. These either enable covalent modifications or interact supramolecularly as e.g. ligand binding sites (Figure 1.6). For the covalent attachment of functionalities to the protein surface the exposed amino acids such as lysine, cysteine, tryptophane and histidine are employed (Figure 1.6A).[113] The ε-amine of lysine reacts with *N*-hydroxysuccinimidyl (NHS) esters, which were among the first reagents used for covalent protein modifications. However, due to the abundance of peripheral lysines, the control over site-selectivity and number of modifications is difficult.[114, 115] A step towards site-selective reactions applying natural amino acids are residual cysteines with low abundance on protein surfaces which can be modified by

their thiol group e.g. in a Michael addition with α,β-unsaturated compounds like maleimides.[116] In order to improve the site-selectivity, proteins can be modified with unnatural amino acids providing azide, alkyne, alkene, cyclooctyne and tetrazole functionalities (Figure 1.6B).[117, 118] The chemical reactions range from copper(I)-catalyzed or strain-promoted azide-alkyne cycloaddition (CuAAC [119, 120] and SPAAC[121]) to photo-click reactions such as thiol-yne reactions[122] or cycloaddition between tetrazole and alkene groups.[123]

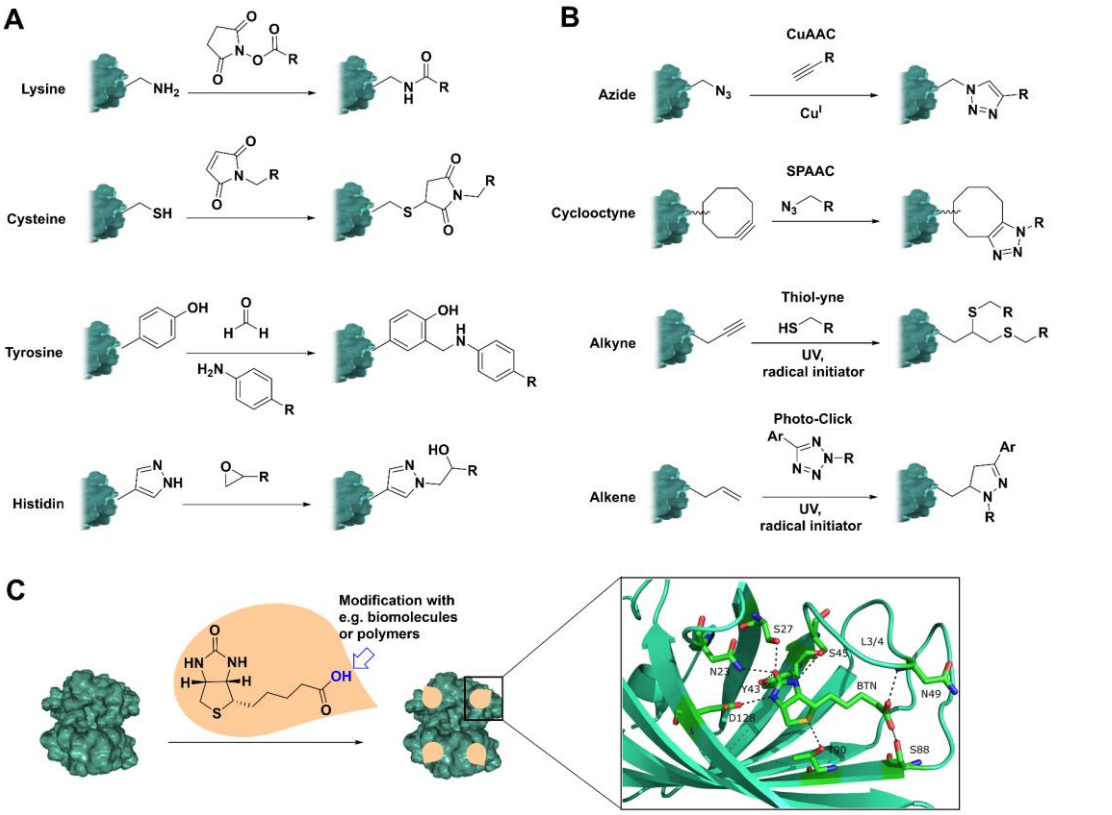

Figure 1.6. Selective chemical protein modifications. (**A**) Protein surface modification applying natural amino acid residues of lysine for NHS-chemistry, cysteine for Michael addition, tyrosine for Mannich reaction[124] and histidine reacting with an epoxide[125] and (**B**) unnatural amino acids with azide, cyclooctyne, alkyne and alkene groups which can be functionalized by either copper(I)-catalyzed or strain-promoted azide-alkyne cycloaddition (CuAAC [119, 120] and SPAAC [121]) or by thiol-yne and tetrazole-alkene photo-click reactions.[122, 123] (**C**) Supramolecular interaction of streptavidin with D-biotin and its D-biotin binding site for the attachment of biotinylated substances. Simulation of the D-biotin-SA interaction is reprinted from Liu et al.[126] (*Sci. Rep.* **2016**, *6*, 27190. DOI: 10.1038/srep27190) licensed under a Creative Commons Attribution (CC BY) license (https://creativecommons.org/licenses/by/4.0/).

Beside covalent protein modification, supramolecular binding *via* bio-orthogonal groups can be achieved by using streptavidin (SA) (Figure 1.6C). SA is a homo-tetrameric protein from the bacterium *Streptomyces avidinii* binding up to four D-biotin molecules. This protein-ligand binding is reported to be one of the strongest interactions with a dissociation constant of $K_d \sim 10^{-14}$ M.[127] As depicted in Figure 1.6C, the D-biotin

backbone binds to SA *via* eight hydrogen bonds with amino acid side chains of SA. The hydrophobic parts are involved in van der Waals interactions.[126, 128] The SA-tetramer is characteristic for its thermal stability (up to 112 °C),[129] stability in a wide pH-range[130] and resistance against denaturing agents.[131, 132] Due to these remarkable properties and high affinity to D-biotin, SA is often used for the immobilization of proteins on surfaces for biosensors[133, 134] or serves as an adapter for attachment of biotinylated polymers[135] and proteins.[136]

Dendrimer-protein hybrids based on covalent binding strategies and supramolecular protein-ligand interactions for nanotherapeutical applications have been developed recently.[104, 105, 137, 138] Different PAMAM-based approaches developed by Weil and co-workers are depicted in Figure 1.7.

One approach towards a covalent protein-dendrimer hybrid material is a human serum albumin (HSA) with PAMAM dendron ligated to its surface. Multiple amine groups of lysines exposed on the surface of HSA were converted to azide residues and ethynyl-PAMAM-dendrons were subsequently attached by CuAAC (Figure 1.7A). The dendronized HSA revealed low cytotoxicity, enhanced cellular uptake compared to native HSA and high loading capacity with the chemotherapeutic doxorubicin leading to cytotoxic activity against cancer cells.[104] When using a PAMAM-dendron with a D-biotin moiety at the focal point, the dendrons were successfully bound to streptavidin (Figure 1.7B). Dendronized SA was successfully transported across the BBB[139] and can be used as multi-domain delivery system for the transport of bioactive proteins i.e. pro-apoptotic cytochrome C, tumor-suppressor p53 or the Rho-inhibitor C3 toxin into cells.[137, 138] This combinatorial concept relies on the self-assembly of biotinylated dendrons and proteins to a SA adaptor core. The dendronization enabled cellular uptake whereas the biological activity of the protein was enhanced.[137] By self-assembly of a pH-responsive dendron-shell onto the surface of active proteolytic enzymes the enzymatic activity was inhibited under physiological conditions (pH 7.4). The enzymatic activity was then restored under acidic conditions (pH 5.0) due to dissassembly of the protein-dendron complex (Figure 1.7C). This system is based on the pH dependent interaction between boronic acid and salicyl hydroxamate. Thus, the dendron-enzyme hybrid was first transported into the cell and subsequently degraded in acidic compartments where the restoration of the proteolytic activity induced cell death.[105] These strategies open up an avenue towards the application of dendrimer-protein hybrid materials in nanomedicine.

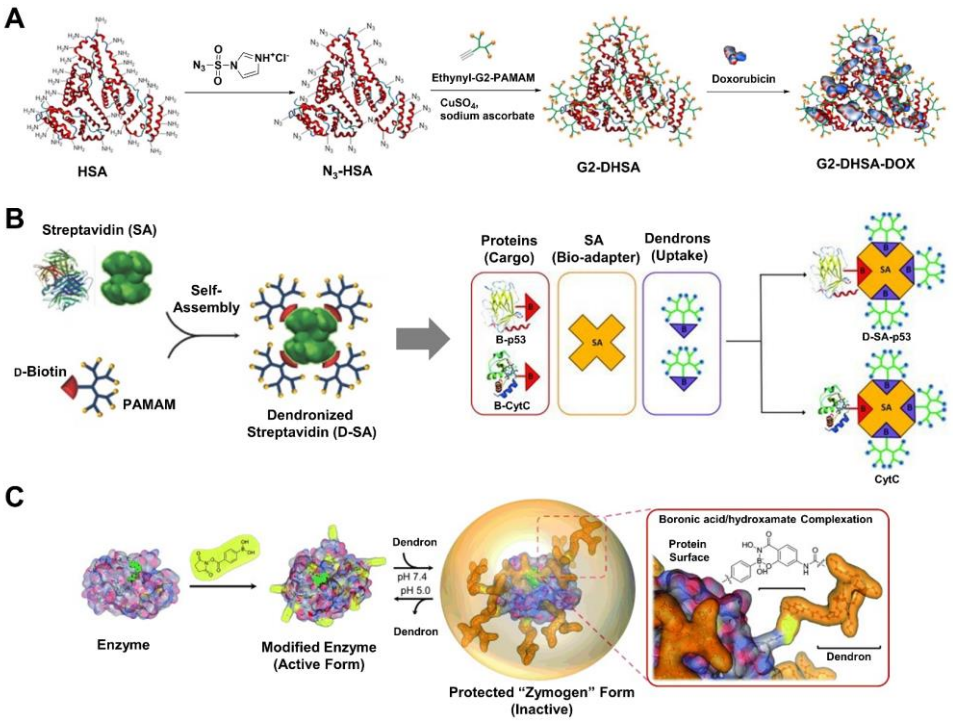

Figure 1.7. Dendrimer-protein hybrid materials. (**A**) HSA-dendron core shell hybrid: Transformation of amines to azides on the HSA surface enabling CuAAC with ethynyl-PAMAM dendrons. This core shell system encapsulates doxorubicin (DOX). Adapted from Kuan et al.[104] with permission from Copyright (2012) American Chemical Society. (**B**) Dendron-SA hybrid: Self-assembly of SA and biotinylated dendrons into dendronized SA and the possibility to use SA as an adapter for a multi-domain delivery system employing PAMAM dendrons for cellular uptake and proteins for bioactivity. Left: Reproduced from Moscariello et al.[139] (*Adv. Sci.* **2018**, *5*, 1700897. DOI: 10.1002/advs.201700897; Copyright (2018) The Authors. Published by WILEY-VCH Verlag GmbH & Co. KGaA, Weinheim) licensed under a Creative Commons Attribution (CC BY) license (https://creativecommons.org/licenses/by/4.0/); right: Reproduced from Ng et al.[137] with permission from Copyright (2013) WILEY-VCH Verlag GmbH & Co. KGaA, Weinheim (**C**) pH responsive dendron-enzyme hybrid: Inactivation of enzymes by attachment of dendrons *via* boronic acid/hydroxamate complexation under physiological pH. At acidic pH, the dendron is released resulting in an reactivation of the enzyme. Reproduced from Ng et al.[105] with permission from Copyright (2014) WILEY-VCH Verlag GmbH & Co. KGaA, Weinheim.

1.3 Polyphenylene Dendrimers

The dendrimers mentioned in the previous sections exhibit flexible aliphatic backbones leading to backfolding of dentritic parts dependent on the physiological environment. Shape persistency of dendrimers is increased by implementation of benzene units to the dendrimer scaffold (Figure 1.8). As described in section 1.1, Miller and Neenan reported the first polyphenylene dendrimers which are synthesized convergently by iterative Suzuki cross-couplings. The divergent approach is not suitable due to the increasing number of coupling reactions at each reaction cycle.[17, 36] In addition, Moore et al. presented the convergent synthesis of phenylacetylene dendrimers with terminal 3,5-di-*tert*-butyl groups to ensure solubility of the polyaromatic dendritic scaffold. Due to limited solubility, the divergent synthesis was hampered.[140] In contrast, Müllen and co-

workers reported the first polyphenylene dendrimer (PPD) that can be synthesized both divergently and convergently by repetitive [4+2] Diels-Alder reactions.[141, 142] Examples for rigid polyaromatic dendrimers by Miller and Neenan, Moore et al. and Müllen et al. are shown in Figure 1.8.

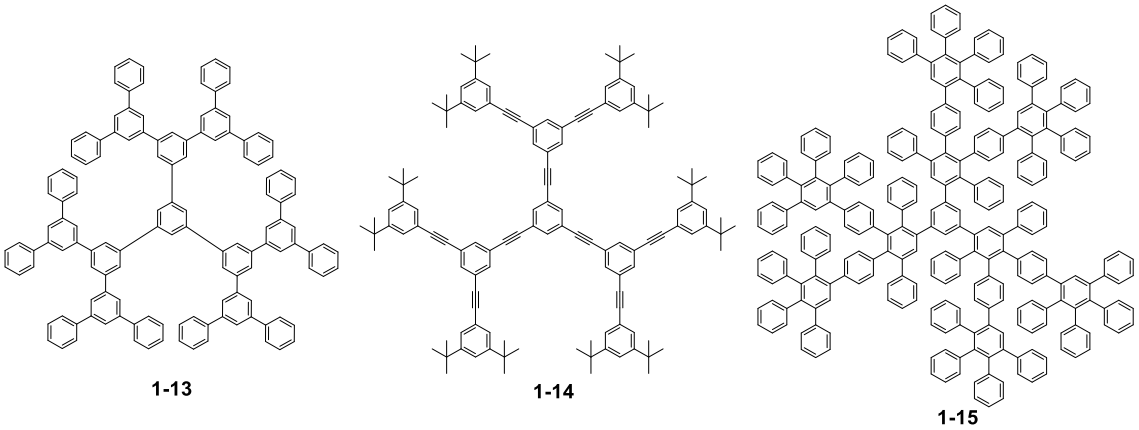

Figure 1.8. Rigid dendrimers with multiple phenylene units. Polyphenylene dendrimers according to Miller and Neenan[17, 36] (**1-13**) and Müllen et al.[141, 142] (**1-15**) and phenylacetylene based dendrimer from Moore et al.[140] (**1-14**).

Initially, the three-dimensional PPDs were used as precursors for flat two-dimensional polyaromatic hydrocarbons (PAH) which were preserved by cyclodehydrogenation (Scheme 1.3). PAHs were some of the first reported synthetic graphene sections.[141, 143] In 2010, Andre Geim and Konstantin Novoselov were awarded the Nobel prize for their research on graphene materials.[144-146]

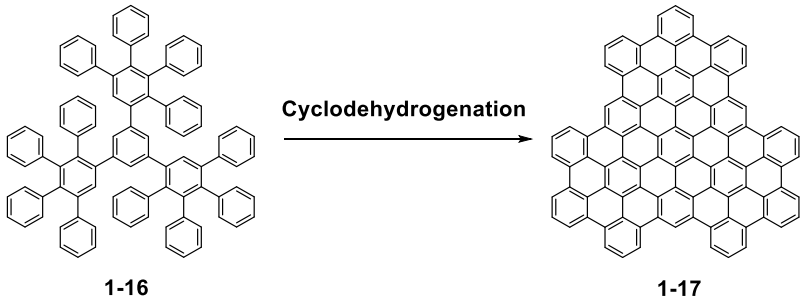

Scheme 1.3. Cyclodehydrogenation of PPD **1-16** to PAH **1-17**.[147]

1.3.1 Architecture and Synthesis of Polyphenylene Dendrimers

Müllen-type polyphenylene dendrimers (PPDs) are characterized by their inherently rigid, monodisperse and highly branched pentabenzene scaffold.[18, 147] As a consequence of their bulky and sterical demanding *para*-substituted benzene architecture shape-persistency is achieved. Thus, in contrast to aliphatic dendrimers, backfolding of dendritic parts is prevented. The PPD cannot collapse into more compact forms which has been experimentally confirmed by small angle neutron scattering (SANS).[30] Hence, the dendrimer exhibits a spatially defined scaffold and the peripheral functions are precisely positioned on the dendrimer surface. This feature is among others attractive for the application of PPDs as protein mimics (refer to section 1.1.1 and 1.3.3). In addition, they are chemically and thermally stable which is desired for further modifications that can be performed either *a priori* or *a posteriori*. Furthermore, the PPD structure is characteristic for its hydrophobic voids that are able to include lipophilic guest molecules.[37]

Both convergent and divergent synthesis of PPDs were developed by Müllen et al.[18, 142] The divergent approach opened up the opportunity to synthesize dendrimers of higher generations and branching compared to the convergent method due to the increasing steric demanding dendrons which mainly hamper their attachment to the core (convergent approach). Therefore, the divergent approach is used more frequently.[37] The divergent PPD synthesis is based on iterative “growth steps”, the [4+2] Diels-Alder cycloadditions, and “activation steps” to deprotect the dendrimer for the next reaction cycle (Scheme 1.4 and section 1.1.2, Scheme 1.1). The synthesis starts from an ethynylated core (**1-18**) whereby the acetylene moiety (dienophile) undergoes a cycloaddition with the branching unit **1-19** (diene). The branching unit consists of a tetraphenylcyclopentadienone (CP) with protected ethynyl-groups which become available for the next growth step upon activation.[18] This reversible pericyclic reaction with inverse electron demand, firstly reported by Dilthey et al., is performed at elevated temperatures above 140 °C. Through the cycloaddition, a norbornadien-7-one intermediate (**1-20**) is formed which further reacts to the highly substituted first generation dendrimer by thermic elimination of the carbon monoxide (CO).[148, 149] The advantage of this cycloaddition is the shift of the equilibrium towards the products due to the irreversible extrusion of CO. Thus, a retro-Diels-Alder reaction is prevented which is important for further growth steps. The activation for the next cycloaddition is performed by deprotecting the tri*iso*propylsilyl (TIPS)-protected ethynyl moieties of the attached branching unit by treatment with tetra-*n*-butylammonium fluoride (TBAF).[18] In the final

step, a CP with a certain functionalization (**1-21**) determining the surface of the dendrimer is used. By repetition of these two crucial reaction steps, PPDs based on a perylenediimide core were achieved up to the ninth generation. These dendrimers exhibit a diameter up to 33 nm and a mass in the megadalton range which were determined by transmission electron microscopy (TEM) and Matrix Assisted Laser Desorption Ionization–Time of Flight (MALDI-TOF) Mass Spectrometry respectively.[150]

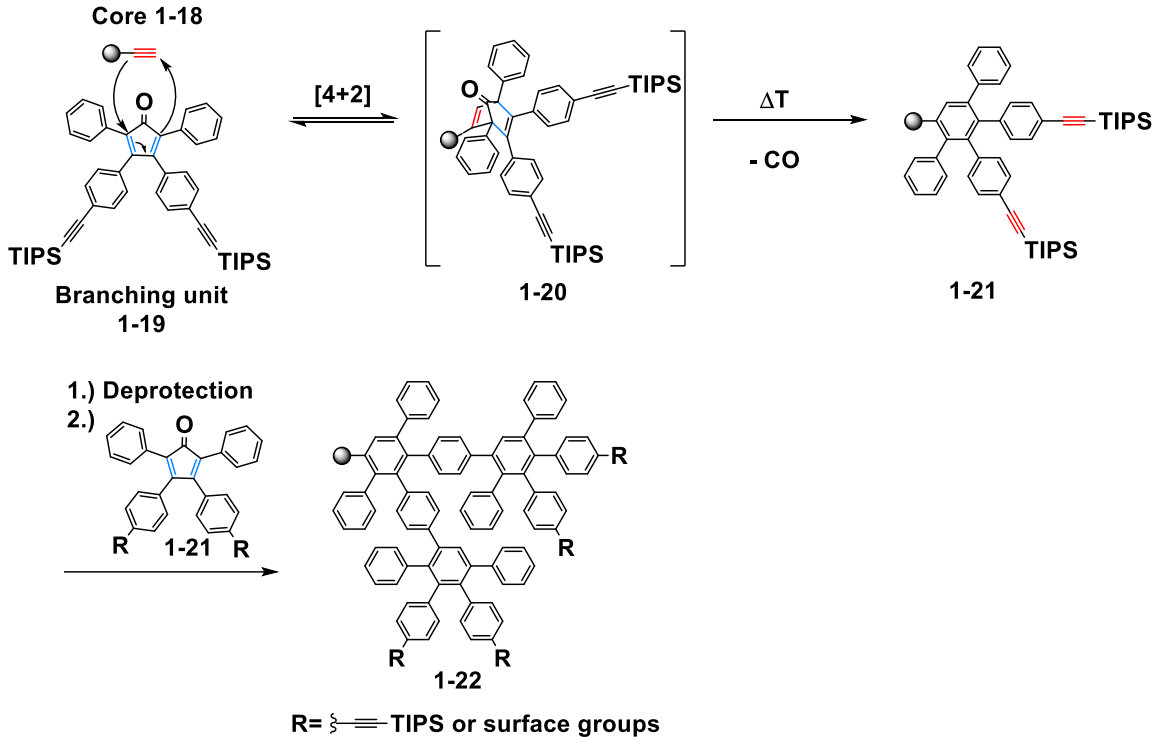

Scheme 1.4. Divergent PPD synthesis. [4+2] Diels-Alder cycloaddition of an ethynylated core (**1-18**) with the AB2 building block (**1-19**) leading to a nobornadien-7-one intermediate (**1-20**)**.** First-generation dendrimer (**1-21**) is achieved after irreversible extrusion of CO. After desilylation and cycloaddtion with a branching unit or surface building block (**1-21**) the next dendrimer generation is obtained (**1-22**).

The geometry of the PPD is determined by the core design defining the number of dendrons and their spatial orientation. In Figure 1.9, a selection of dendrimer cores ranging from a 1,3,5-triethynyl benzene (**1-23**) over a tetraethynylated tetraphenyl methane core (**1-24**) to a hexaethynylated core (**1-25**) are depicted. Tetramethylmethane based dendrimers adopt globular structures due to the tetrahedral orientation of the dendrons emanating from the core whereas PPDs with dendrimer cores **1-23** and **1-25** lead to flatter geometries.[151] Besides defining the orientation of dendritic branches, cores like ethynylated perylene diimide (**1-26**)[152] and pyrene-core (**1-27**)[153] can serve as a fluorescent unit which is among others attractive for imaging in biological applications.[154-156] In addition, asymmetrical dendrimers were synthesized by utilizing a

core with one reactive and one protected site. By this approach it was possible to include two different functions to one macromolecule.[157]

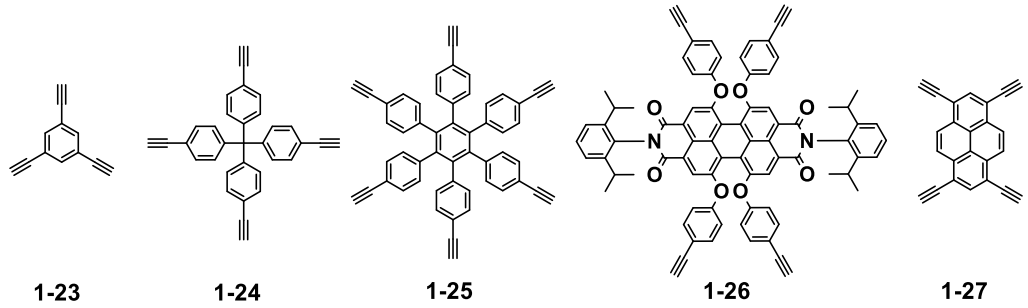

Figure 1.9. Examples of dendrimer cores with different geometries influencing the branching and spatial orientation of dendritic branches.[151-153]

The branching of each dendron is determined by the building blocks, the tetraphenylcyclopentadienones (CPs, "tetracyclones"), with either two (AB2, **1-19**)[141] or four (AB4, **1-28**)[158] tri*iso*propyl (TIPS) protected ethynyl groups (Figure 1.10). The surface can be controlled by the selection of a tetracyclone with the desired end groups (CP **1-29**). The CPs are synthesized by a twofold Knoevenagel condensation between a diphenyl acetone (**1-30**) and a benzil (1,2-diphenylethane-1,2-dione, **1-31**) derivative (Figure 1.10B).[151]

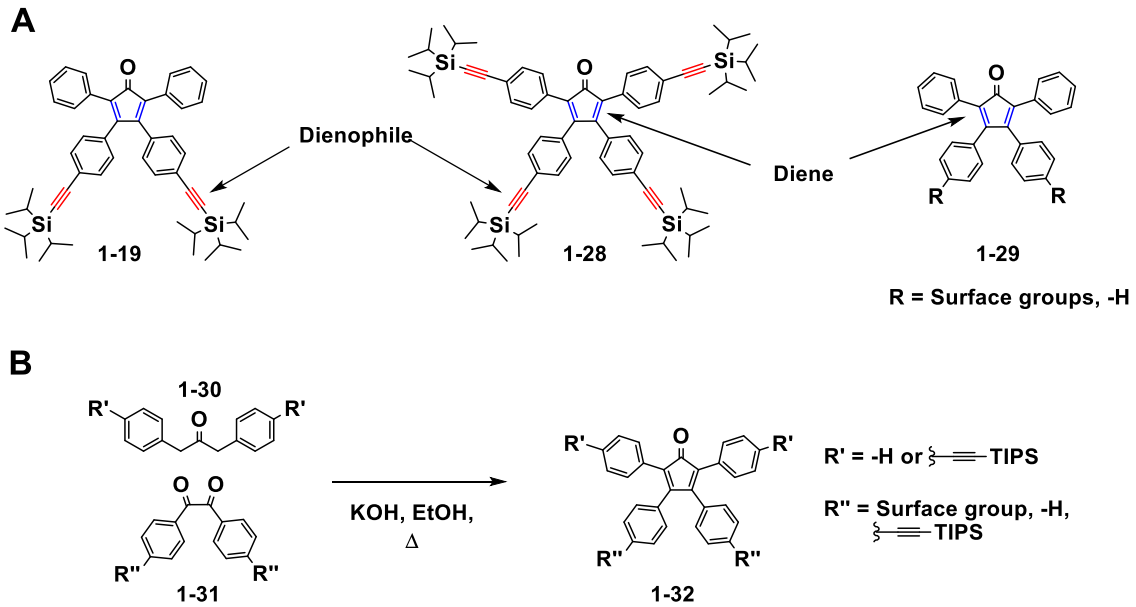

Figure 1.10. Building blocks for PPD synthesis. (**A**) AB2 (**1-19**) and AB4 (**1-28**) serve as branching units and building block **1-29** as end-capping unit introducing the surface groups.[158] (**B**) CPs are synthesized by a twofold Knoevenagel condensation applying e.g. potassium hydroxide (KOH) as base.[151]

1.3.2 Rational Design of PPDs towards Biomedical Applications

In the last two decades, the scaffold and surface structure of PPDs were further modified to control their polarity and interactions with guest molecules. The rational design of PPDs ranges from functionalization of the dendrimer shell for inclusion of guest molecules for the application as sensing materials to drug encapsulation and surface modification for biomedical applications.[147]

One approach towards the use of apolar PPDs in biological applications is the synthesis of a desymmetrized PPD bearing three peripheral perylenemonoimide chromophores and one bioactive group, a D-biotin moiety (Figure 1.11A). To solubilize the hydrophobic PPD scaffold in water, the detergent Tween 20 was added forming a supramolecular complex with the PPD (Figure 1.11B). Despite the addition of a detergent, the fluorescence quantum yield was unaffected under buffer conditions and after addition of serum proteins. This polychromophore-dendrimer-detergent complex was bound to streptavidin *via* the D-biotin anchor group leading to a fluorescent labelling of the protein *via* supramolecular interactions.[159]

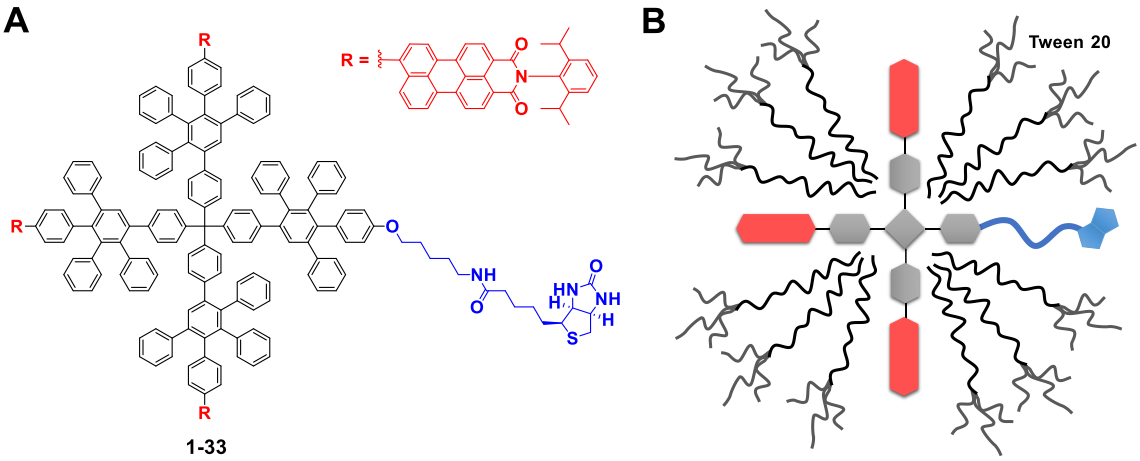

Figure 1.11. PPD as fluorescent probe for bioassays. (**A**) Chemical structure of an asymmetric PPD with three peripheral perylenemonoimide groups and one D-biotin group. (**B**) Schematic illustration of the PPD-detergent complex to solubilize the PPD structure.[159]

To introduce water-solubility to the PPD structure without the use of detergents, the surface of PPDs was modified with polar groups. The surface of PPDs is either introduced *a priori* by the employment of an endcapping unit bearing the desired functionalities or *a posteriori* after dendrimer growth.[37] The prerequisite for an *a priori* functionalization is the thermal stability of the peripheral moiety during the cycloaddition. This approach was used among others for the attachment of chromophores such as

perylenemonoimide for the synthesis of dendritic multichromophores,[160, 161] terthiophene moieties for electrical conductivity[162] or dodecyl-functionalities for the self-assembly into nanorods.[163, 164] Often, the desired surface functionalities are too sensitive or too sterically demanding under the required cycloaddition conditions and thus, need to be attached after PPD synthesis. In addition, structural variability is enhanced.[165, 166] To achieve a hydrophilic dendrimer shell on a hydrophobic PPD scaffold, the post-functionalization with peptides was presented. The surface of first- and second-generation PPDs were modified with short lysine and glutamic acid based hexapeptides by a chemoselective reaction of sulfhydryl groups of a cysteine residue with the peripheral maleimide functionalities of the PPD (Scheme 1.5A).[165]

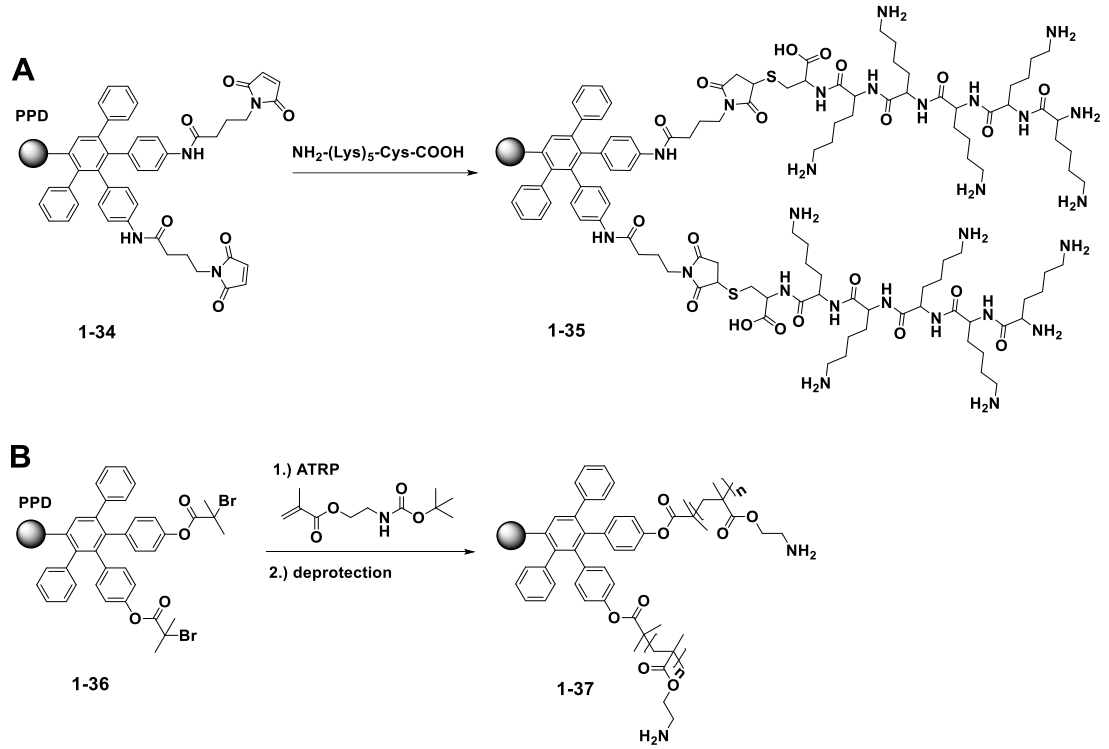

Scheme 1.5. *A posteriori* surface modifications for biological applications. (**A**) Attachment of lysine based hexapeptides to the PPD periphery by thiol-maleimide Michael addition.[165] (**B**) The PPD surface bearing the macroinitiator 2-bromo-2-methylpropionic ester is modified *via* ATRP with amine-containing poly-methacrylates for nucleic acid binding.[166]

Polylysine functionalized PPDs were also obtained by applying α-amino acid *N*-carboxyanhydride (NCA) polymerization (grafting from) or by direct attachment of the peptide *via* amide coupling (grafting to). These dendrimer-peptide conjugates are characterized by their shape-persistency and water-solubility. In addition, by the utilization of an asymmetric dendrimer core two different functional groups were integrated into the dendrimer scaffold.[167] The length of the poly-L-lysine peptide

controlled its self-assembly properties and their secondary structures were influenced by the packing restrictions of the PPD scaffold.[168]

Another approach towards hydrophilic PPD shells is the decoration of PPD surfaces with the macroinitiator 2-bromo-2-methylpropionic ester which is introduced by the endcapping unit. The surface groups were funtionalized *a posteriori* with 2-*tert*-butoxycarbonyl-aminoethyl methacrylate (Boc-AEMA) in an atom transfer radical polymerization (ATRP). As a result, water-soluble core-shell systems consisting of a PPD-based core and a methacrylate polymer shell were achieved (Scheme 1.5B). The polymer shell of these macromolecules – also termed as dendritic star polymers – consists of multiple primary amines introducing water solubility and positive charges to achieve a biological function.[166] The dendritic star polymers bearing a perylene diimide core were used for either staining of the extracellular matrix (ECM) or cellular uptake approaches depending on the polymer length.[169, 170] As also reported for positively charged PAMAM dendrimers[171] (refer to section 1.2.1), the core-shell dendrimer systems showed binding to DNA and RNA fragments which is promising for gene delivery applications.[166, 172] The DNA binding was controlled by the number of amine groups leading to well-defined nanostructures analyzed by atomic force microscopy (AFM).[166] The fluorescent (perylene diimide core) cationic core-shell system demonstrated high gene delivery efficacy and low cytotoxicity in living cells. To genetically control insect pest, the dendrimer was mixed with CHT10-dsRNA.[172] Double-stranded RNA (dsRNA) can be used for gene silencing by sequence specific cleavage of target mRNA.[173] The mid-gut chitinase gene CHT10 of the Asian corn borer, which is one of the most devastating pests of corn, supresses the larval development of insects.[174] By oral administration of dendrimer/CHT10-dsRNA the gene expression was suppressed in larvae leading to impaired growth and finally death whereas larvae fed with exclusive CHT10-dsRNA were less affected. Thus, a first strategy for the control of insect pest by a PPD based gene delivery system was presented.[172] These approaches demonstrated the first steps towards the use of PPDs in biomedical applications.

1.3.3 Patchy PPDs – The Role of Amphiphilic Surface Patterns

As described in section 1.3.1, the shape-persistency of PPDs allows the formation of globular structures without backfolding of the dendritic branches which in turn enables the precise arrangement of surface functionalities. The attachment of e.g. hydrophilic and hydrophobic surface groups could result in unique amphiphilic surface patterns. Furthermore, PPDs consist of a hydrophobic interior. These special characteristics of PPDs can be compared to biomolecules such as proteins which are macromolecules with defined surface patterns determined by their amino acid sequence folding into globular structures. The majority of the hydrophobic amino acids are located in the protein interior and thus, shielded from the surrounded aqueous environment. However, hydrophobic amino acids also appear on the surface, but to a lesser extend than hydrophilic ones.[175-177] These defined surface structures of proteins serve as biorecognition motifs for several interactions within the body such as protein-protein interactions or ligand binding.[3]

In recent years, surface patterned nanocarrier systems have been investigated to elucidate the impact of amphiphilic pattern on biorecognition.[178-180] One example are gold nanoparticles with hydrophilic 11-mercapto-1-undecanesulfonate (red) and hydrophobic 1-octanethiol (white) groups which were proposed to be arranged in stripes and to lead to cellular uptake.[178] However, the existence of stripes on the nanoparticle surface was controversially discussed.[181-184] Different morphologies such as random, mixed, striped, janus or patchy surface pattern were proposed which influence the biological properties of nanocarriers such as cellular uptake (Figure 1.12A).[185] Nevertheless, the coating of nanocarriers does not reflect a truly engineered surface at a definition that is known for proteins.

In order to achieve defined amphiphilic nanocarrier surfaces with resolutions comparable to those of proteins, Stangenberg et al. synthesized a set of tetraphenylene methane based PPDs with amphiphilic surface pattern consisting of alternating sulfonic acid and *n*-propyl groups. By this approach, the peripheral groups of these so-called “patchy” dendrimers are well positioned on the dendrimer surface. The polar sulfonate groups enhanced water-solubility and thus, rendering these dendrimers as promising candidates for biological studies.[186] In comparison to the conformationally flexible peptide and polymer surface modifications (refer to Scheme 1.5), the “patchy” rim allowed a precise surface pattern, which is attractive to study a certain biorecognition motif. In a follow-up

study, PPDs with amphiphilic surface patterns based on a fluorescent pyrene core, which allowed cell imaging, were synthesized (Figure 1.12B). The amphiphilic dendrimers were internalized into human lung cancer cells (A549) and murine brain endothelial cells (bEnd.3) *in vitro* with high cellular viabilities. *In vivo* studies in zebrafish embryos revealed low mortality rates compared to a control group with positively charged PAMAM dendrimers. The dendrimers provide a hydrophobic scaffold which enabled the encapsulation of lipophilic guest molecules such as the fatty acid 16-DOXYL-stearic acid (16-DSA) and the drug doxorubicin (Figure 1.12C). In addition, it was demonstrated that the PPD can sufficiently transport doxorubicin into cells. Thus, their defined three-dimensional structure, distinct surface pattern, hydrophobic interior and size was assessed to be similar to the transport protein human serum albumin (HSA).[156]

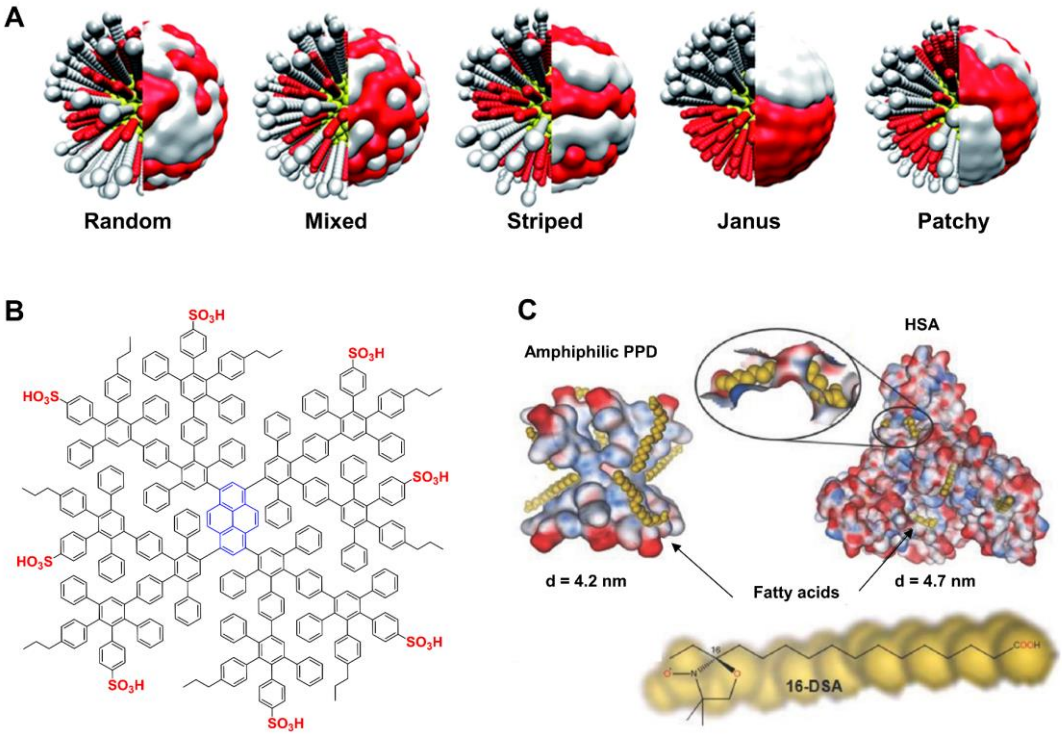

Figure 1.12. Comparison of amphiphilic Au-nanoparticle surfaces with the surface of amphiphilic PPDs and proteins. (**A**) Schematic illustration of different nanoscale morphologies on Au-nanoparticles with hydrophilic 11-mercapto-1-undecanesulfonate (red) and hydrophobic 1-octanethiol (white) groups. Reproduced from Van Lehn et al.[185] with permission from Copyright (2014) The Royal Society of Chemistry. (**B**) Amphiphilic "patchy" PPD with alternating sulfonic acid and *n*-propyl groups on the periphery. (**C**) 3D-model of the amphiphilic PPD with precise surface pattern and the ability to include fatty acids (16-DSA) within its void spaces representing similar properties as HSA. Reproduced from Stangenberg et al.[156] with permission from Copyright (2014) Wiley-VCH Verlag GmbH & Co. KGaA, Weinheim.

To understand the cellular uptake properties of amphiphilic PPDs, the interaction with a lipid monolayer was investigated. X-ray reflectivity measurements showed that the surface monolayer was not disrupted by the dendrimer. In addition, the lipid tails became less ordered upon interaction with the PPD, whereas water molecules got more ordered.

These observations indicated that the negative charges of the dendrimer interacted electrostatically with the positively charged headgroups which kept the dendrimer below the headgroup of the lipid. In addition, no insertion into the lipid monolayer was noticed.[187]

The impact of the peripheral sulfonic acid groups and the ratio of hydrophobic and hydrophilic pattern on the cellular uptake properties and cytotoxicity were further studied by Hammer et al. PPDs with alternating hydrophilic groups, consisting of sulfonic, carboxylic or phosphonic acid groups, and hydrophobic *n*-propyl groups were synthesized. The different polar moieties showed similar cellular uptake properties while retaining high cellular viability. Additionally, the ratio of polar and apolar groups was varied from 1:1 to 2:1 (polar:apolar). The cellular uptake was drastically reduced when increasing the polar groups to 2:1 (polar:apolar). Thus, this study revealed that the chemical identity of the hydrophilic acid moiety is less important than the balance between polar and apolar surface groups towards the interaction with cellular membranes.[188]

Consequently, these patchy PPDs represented the first PPD surface pattern which is promising for further biomedical applications due to cellular uptake properties, low toxicity and protein mimetic characteristics.

1.4 Biological Fate of Nanocarriers in the Blood Stream

1.4.1 Biodistribution and Toxicity of Dendrimers

Dendrimers are used for drug delivery approaches in order to overcome limiting factors such as poor water solubility, low specificity, low concentrations at the target, high affinity to blood plasma proteins and rapid elimination of the drug.[32] For pharmaceutical applications, it is crucial that the dendrimer crosses biological barriers such as cellular membranes or the blood-brain barrier (BBB). In addition the assessment of its biopermeability, biodistribution, toxicity and immunogenicity is essential.[24, 189]

The investigation of more than 130 nanocarrier types, including among others dendrimers, polymers, liposomes and gold colloids resulted in the finding that size, hydrophobicity and surface charges are the main factors affecting the biocompatibility of nanocarriers.[190] Commonly, hydrophobic nanoparticles are rapidly cleared from the

blood stream by the cells of the mononuclear phagocyte system (MPS), also referred to as reticuloendothelial system (RES), which is part of the immune system. Furthermore, the size determines the excretion pathway. Nanocarriers smaller than 8 nm are mostly excreted by the kidneys, whereas larger ones are cleared by or accumulate in the liver.[190, 191] Cationic nanocarriers are more cytotoxic and tend to induce haemolysis and platelet aggregation, which is less prominent for anionic and neutral particles.[192, 193] These tendencies are in line with the observations for dendrimers whose biodistribution and toxicity is mainly determined by their size[194] and surface chemistry[193] (Figure 1.13). For example, smaller PAMAM dendrimers of generation 3 to 4 (G3-4, 3-5 nm) are eliminated by the kidneys whereas PAMAM at generation G5 is excreted by both liver and kidney and G6-9 are eliminated exclusively through the liver.[194, 195] Increase in size (>10 nm) provokes less effective membrane permeability. This includes the renal glomerulus reducing the renal clearance and the enhancement of RES recognition. Consequently, to reduce side effects of dendrimers, lower generations are recommended which are relatively rapidly cleared from the blood stream.[5] Thus, small dendrimers (G2-G3) were suggested for the application as blood pool agents in MRI.[194] Apart from size dependency, dendrimer surfaces are crucial factors in the distribution, excretion and toxicity. Positively charged PAMAM is quickly cleared from the blood circulation whereas the blood retention time of anionic dendrimers is prolonged due to lesser interactions with biological barriers. However, the latter ones tend to accumulate in the liver.[5, 193] Conversely, the modification of the surface with polyethylene glycol enhance the blood circulation time while diminishing the accumulation in the liver.[196] Consequently, by the careful design of dendrimers in terms of size and surface functionalizations, the biological pathway within the body can be controlled and optimized for a particular therapeutic need.

Apart from determining the biodistribution, the surface functionalization has an impact on the toxicity when interacting with biological interfaces in the body. Biological barriers like cellular membranes present negative charges on their surface given by the negatively charged headgroups of the phospholipids.[197] The interaction of cationic dendrimers with those barriers may cause cytotoxicity due to the formation of nanopores which can result in cell lysis. In addition, cationic dendrimers tend to interact with the red blood cells which causes haemolysis.[5, 7, 189, 193] The toxicity of cationic PAMAM dendrimers increases with the generation[198] and induces higher cytotoxicity compared to negatively charged (anionic) or neutral dendrimers. Due to the fact that dendrimers with cationic surfaces lead to higher toxicity both *in vitro* and *in vivo* the modulation of the surface with anionic

or neutral functionalities is favored.[5, 193, 199] The dependency of surface chemistry and size on biodistribution and toxicity is summarized in Figure 1.13.

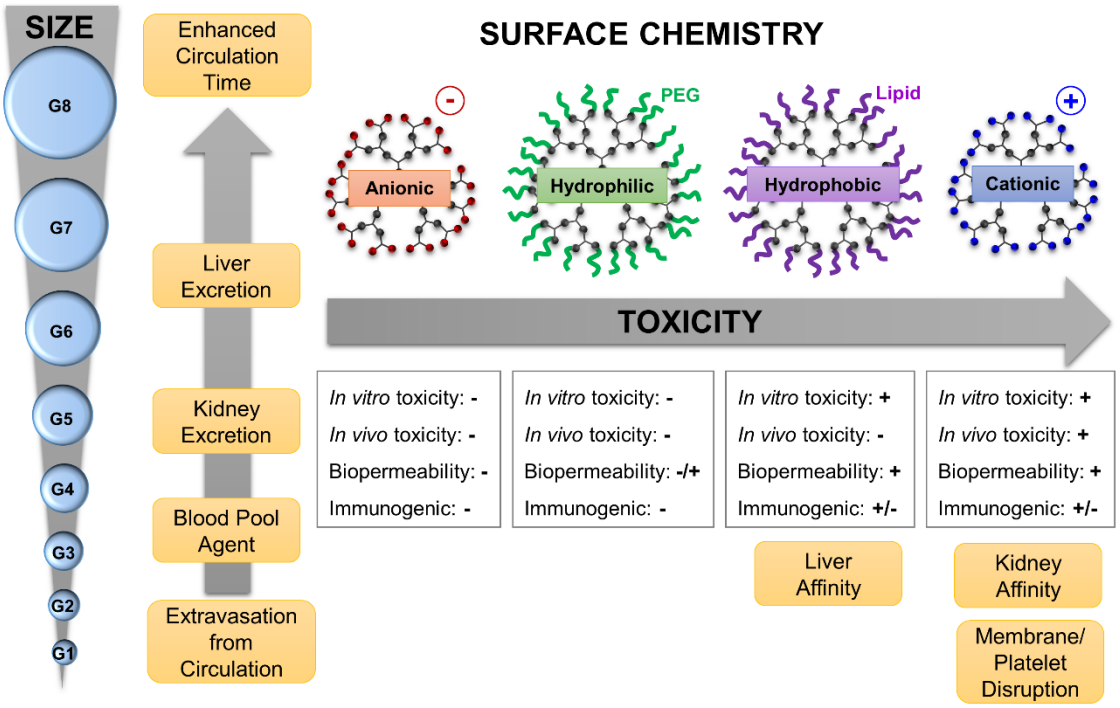

Figure 1.13. Dependency of size (generation G) and surface chemistry of dendrimers on the biodistribution, toxicity, biopermeability and immunogenicity.[5]

1.4.2 Influence of Protein Adsorption on the Biodistribution of Nanocarriers

As described in the previous section, the biodistribution and toxicity of nanocarriers are influenced by many factors including size and surface chemistry. Often, the biological fate of nanocarriers is already affected when exposed to a physiological environment. When entering the blood stream, the adsorption of blood proteins to the surface of the nanomaterial occurs, which results in the so-called protein corona.[200] Already in the 1960s, Vroman postulated the dynamic adsorption of blood proteins to surfaces which is termed “Vroman effect”.[201] In these first studies, the adsorption kinetics and the identity of proteins adsorbed to the surfaces were investigated.[201, 202] In the last two decades, various methods were established to determine the composition of the protein corona. These strategies target the thickness, density, identity and quantity of the protein corona as well as the conformation and affinity of protein adsorption in the blood stream.[200]

The blood is a highly complex fluid containing both cellular and acellular components (Figure 1.14A). The red blood cells (99.1%) are responsible for gas transport whereas

leukocytes and platelets are involved in inflammation and wound healing processes. The acellular part, also referred to as blood plasma, mainly consists of water and only a small percentage (8%) is related to over 1100 plasma proteins.[203, 204] Walkey et al. described the surface properties of nanocarriers such as size, shape and surface chemistry as synthetic identity prior to exposure to biological fluids (Figure 1.14B). The physico-chemical properties of the nanocarrier including the size,[205] hydrophobicity,[206] charge[205, 207] and surface chemistry[208, 209] play a critical role in protein adsorption (Figure 1.14C). The protein adsorption is driven by many interactions such as hydrogen bonding, van der Waals, hydrophobic and electrostatic interactions.[190] The biological identity of the nanocarrier is determined by the size and aggregation in the physiological environment including the protein corona composition (Figure 1.14B).[200] The protein corona around nanocarriers formed in biological fluids such as blood plasma and blood serum (plasma without clotting factors) influences the physiological response[200] by means of cellular uptake, biodistribution, toxicity, aggregation and immunogenicity.[206, 207, 210-214]

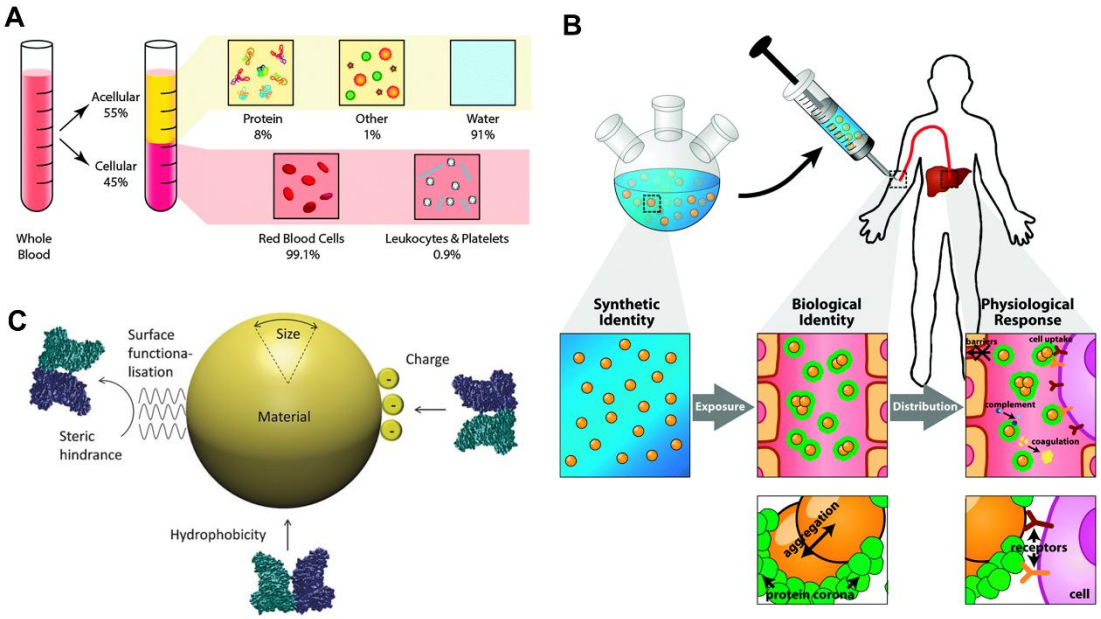

Figure 1.14. Parameters influencing the protein corona formation and biological fate of nanocarriers. (**A**) Blood composition: The blood consists of cellular and acellular (plasma) components. The plasma mainly consists of water and a small percentage comprises a complex mixture of biomolecules and over 1100 proteins. Reproduced from Lazarovits et al.[204] with permission from Copyright (2015) The Royal Society of Chemistry. (**B**) The synthetic identity of a nanocarrier influences its protein corona when exposed to a physiological fluid (biological identity) and consequently its physiological response. Reproduced from Walkey et al.[200] with permission from Copyright (2012) The Royal Society of Chemistry. (**C**) Adsorption of proteins to the nanocarrier surface dependent on material, size, hydrophobicity, charge and surface functionalization. Reproduced from Schöttler et al.[215] with permission from Copyright (2016) WILEY-VCH Verlag GmbH & Co. KGaA, Weinheim.

Nanocarriers are cleared from the blood stream by cells of the MPS as described in the previous section. The elimination of unwanted nanocarriers is triggered by the adsorption of opsonin proteins such as immunoglobulin G (IgG) or complement proteins triggering the uptake into macrophages and monocytes of the MPS.[215, 216] In contrast, there are blood proteins that serve as dysopsonins, e.g. the apolipoprotein clusterin,[209, 214] and proteins that direct selective uptake into specific cells.[207, 217] In general, neutral nanoparticles induce slower opsonization rates than charged nanoparticles.[218] Gessner et al. reported that anionic and cationic nanocarriers bind to proteins with an isoelectric point (pI) < 5.5 and pI > 5.5 respectively. For example, albumin and immunoglobulin G (IgG) bound to strong basic (NH_2) and weak acidic (COO^-) functionalized nanocarriers whereas lipoproteins such as apolipoprotein H adsorbed to strongly acidic (SO_3^-) nanoparticles.[219] For positively charged PAMAM dendrimers, binding of complement proteins was observed which in turn triggered immune responses. In addition, the complement binding increased with higher generations.[220] Polyphosphoester-coated nanocarriers showed enhanced uptake into macrophages when increasing the polymer hydrophobicity. This correlated with decreased clusterin (dysopsonin) binding and enhanced IgG (opsonin), complement and albumin binding.[206] The gold standard to prolong blood-circulation by reduction of non-specific cellular uptake, known as stealth effect, is the covalent attachment of the hydrophilic polymer PEG. For example, PEGylated nanocarriers demonstrated the binding of the apolipoprotein clusterin in blood plasma preventing the nanocarrier from non-specific cellular uptake.[209] Therefore, a careful structural design of nanocarriers including dendrimers is required in order to predict the protein corona formation and consequently its biorecognition (Figure 1.14B and C).

For example, liposomes are widely used for the transport of therapeutic payloads in the field of drug or gene delivery.[221] As already mentioned, the use of liposomes attracted much attention after the first nano-drug Doxil® became FDA-approval in 1995.[6] However, similar to other nanocarriers, their biodistribution is affected by the formation of a protein corona which hampers targeted delivery. Consequently, the rational design of the liposome's synthetic identity to control the protein corona is required.[221] This also applies to viruses such as adenoviruses (Ads) which are used as gene therapy vectors. One of the most common vector is adenovirus 5 (Ad5), which is mainly used in cancer therapy.[222] Ads are unenveloped icosahedral, linear double-stranded DNA (dsDNA) viruses with a size of ~90 nm. The capsid is composed of three major proteins, the hexon, the penton base and its associated fibers.[223] The cellular uptake of Ad5 is directed by

the interaction of the fiber with the coxsackie-adenovirus receptor (CAR) which is expressed on the cell surface (Figure 1.15A). The cellular internalization is facilitated by the interaction of the penton base with integrins. However, CAR is not expressed on every cell in the body and therefore, limits the applicability of Ad5-assisted gene therapy.[224] Furthermore, the adsorption of proteins in the blood stream among others hampers CAR-binding and controls their biodistribution *in vivo.* Predominantly, the binding of antibodies and proteins of the complement system furnishs RES recognition. The clearance of Ad5 from the blood stream by RES recognition or uptake by non-immune cells can potentially provoke immune responses which can eventually result in acute toxicity.[225] The adsorption of blood coagulation factor X, which binds to the hexon capsid protein, can prevent binding of antibodies and complement proteins. In addition, it serves as a bridge receptor for binding to heparane sulfate inducing gene transduction in hepatocytes.[226]

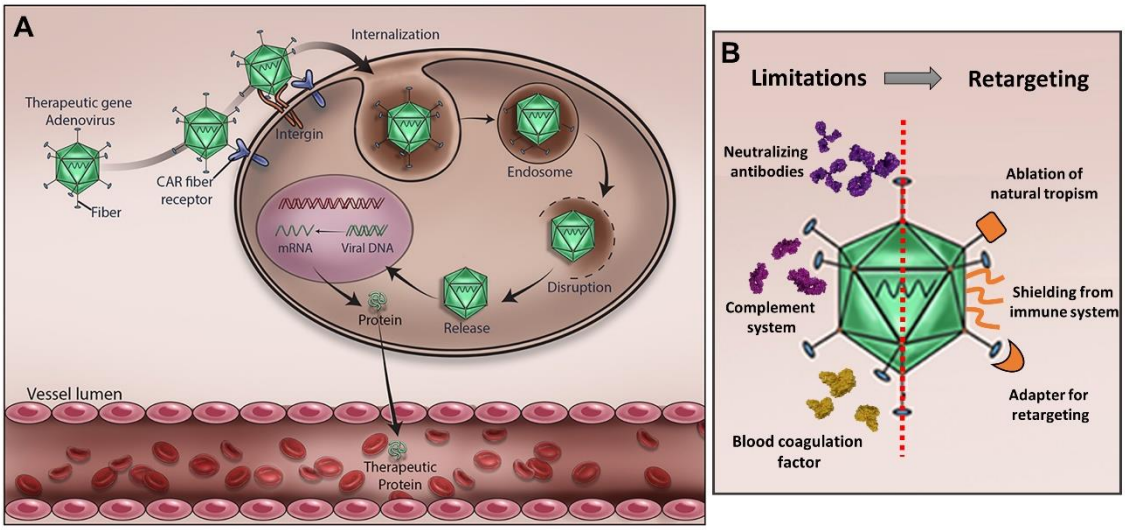

Figure 1.15. Adenovirus-assisted gene therapy. (**A**) Mechanism of gene delivery of therapeutic DNA by Ad and (**B**) Binding of blood proteins such as neutralizing antibodies, complement proteins or blood coagolation factor X, which are crucial in the biodistribution of Ad5, and retargeting strategies. Adapted from Goswami et al.[227] (*Frontiers in Oncology* **2019**, *9*. DOI: 10.3389/FONC.2019.00297) licensed under a Creative Commons Attribution (CC BY) license (https://creativecommons.org/licenses/by/4.0/).

Recently, different strategies were developed to avoid binding of opsonization proteins and factor X binding in order to improve Ad5-assisted gene therapy. Furthermore, approaches towards the development of CAR-independent cellular internalization pathways to address cells that can not be infected naturally by Ad5 were investigated. These strategies range from ablation of the natural tropism, to the attachment of adapter-molecules or shielding of the virus with polymers like polyethylene glycol (Figure 1.15B). The main disadvantage of the attachment of polymers is the inhibition of binding to

cellular receptors and the release of the viral DNA once internalized into the cell. Therefore, targeting groups are often required for such coatings to enable or increase cellular uptake.[222]

Hence, the biological fate of nanocarrier systems and viruses is highly affected by their surface contour. The coating or functionalization of the surface among others influences the protein adsorption which ultimately affects biological responses. However, when using polymer-coatings, the surface pattern on nanocarriers can not be precisely defined as it is known for biological structures such as proteins. Thus, the employment of monodisperse dendrimers with protein-mimicking properties is attractive to further understand interactions of sophisticated surface structures in biological fluids.

1.5 References

[1] S. Soares, J. Sousa, A. Pais, C. Vitorino, *Front. Chem.* **2018**, *6*, 360.

[2] D. A. Tomalia, J. B. Christensen, U. Boas, in *Dendrimers, Dendrons, and Dendritic Polymers: Discovery, Applications, and the Future*, Cambridge University Press, Cambridge, **2012**, pp. 25-112.

[3] B. Alberts, A. Johnson, J. Lewis, M. Raff, K. Roberts, P. Walter, in *Molecular Biology of the Cell, 4th edition*, Garland Science, New York, **2002**, Protein Function. Available from: https://www.ncbi.nlm.nih.gov/books/NBK26911/

[4] Z. Chen, Z. Wang, Z. Gu, *Acc. Chem. Res.* **2019**, *52*, 1255-1264.

[5] R. M. Kannan, E. Nance, S. Kannan, D. A. Tomalia, *J. Intern. Med.* **2014**, *276*, 579-617.

[6] Y. Barenholz, *J. Controlled Release* **2012**, *160*, 117-134.

[7] L. M. Kaminskas, B. J. Boyd, C. J. H. Porter, *Nanomedicine* **2011**, *6*, 1063-1084.

[8] F. U. Din, W. Aman, I. Ullah, O. S. Qureshi, O. Mustapha, S. Shafique, A. Zeb, *Int. J. Nanomed.* **2017**, *12*, 7291-7309.

[9] D. A. Tomalia, *Mater. Today* **2005**, *8*, 34-46.

[10] M. V. Walter, M. Malkoch, *Chem. Soc. Rev.* **2012**, *41*, 4593-4609.

[11] E. Abbasi, S. F. Aval, A. Akbarzadeh, M. Milani, H. T. Nasrabadi, S. W. Joo, Y. Hanifehpour, K. Nejati-Koshki, R. Pashaei-Asl, *Nanoscale Res. Lett.* **2014**, *9*, 247-247.

[12] D. A. Tomalia, H. Baker, J. Dewald, M. Hall, G. Kallos, S. Martin, J. Roeck, J. Ryder, P. Smith, *Polym. J.* **1985**, *17*, 117-132.

[13] E. Buhleier, W. Wehner, F. Vögtle, *Synthesis* **1978**, 155-158.

[14] D. A. Tomalia, H. Baker, J. Dewald, M. Hall, G. Kallos, S. Martin, J. Roeck, J. Ryder, P. Smith, *Macromolecules* **1986**, *19*, 2466-2468.

[15] G. R. Newkome, Z. Yao, G. R. Baker, V. K. Gupta, *J. Org. Chem.* **1985**, *50*, 2003-2004.

[16] C. Hawker, J. M. J. Fréchet, *J. Chem. Soc., Chem. Commun.* **1990**, 1010-1013.

[17] T. M. Miller, T. X. Neenan, *Chem. Mater.* **1990**, *2*, 346-349.

[18] F. Morgenroth, C. Kübel, K. Müllen, *J. Mater. Chem.* **1997**, *7*, 1207-1211.

[19] F. Vögtle, G. Richardt, N. Werner, in *Dendrimer Chemistry*, WILEY-VCH, Weinheim, **2009**, pp. 1-24.

[20] R. Esfand, D. A. Tomalia, *Drug Discov. Today* **2001**, *6*, 427-436.

[21] M. Maciejewski, *J. Macromol. Sci., Chem.* **1982**, *17*, 689-703.

[22] C. Kojima, K. Kono, K. Maruyama, T. Takagishi, *Bioconjugate Chem.* **2000**, *11*, 910-917.

[23] A. R. Menjoge, R. M. Kannan, D. A. Tomalia, *Drug Discov. Today* **2010**, *15*, 171-185.

[24] U. Boas, P. M. H. Heegaard, *Chem. Soc. Rev.* **2004**, *33*, 43-63.

[25] S. Rosenfeldt, N. Dingenouts, M. Ballauff, N. Werner, F. Vögtle, P. Lindner, *Macromolecules* **2002**, *35*, 8098-8105.

[26] P. K. Maiti, T. Çağın, S.-T. Lin, W. A. Goddard, *Macromolecules* **2005**, *38*, 979-991.

[27] I. Lee, B. D. Athey, A. W. Wetzel, W. Meixner, J. R. Baker, *Macromolecules* **2002**, *35*, 4510-4520.

[28] W. Chen, D. A. Tomalia, J. L. Thomas, *Macromolecules* **2000**, *33*, 9169-9172.

[29] P. Welch, M. Muthukumar, *Macromolecules* **1998**, *31*, 5892-5897.

[30] P. Carbone, F. Negri, F. Müller-Plathe, *Macromolecules* **2007**, *40*, 7044-7055.

[31] A. Mulder, J. Huskens, D. N. Reinhoudt, *Org. Biomol. Chem.* **2004**, *2*, 3409-3424.

[32] A. Santos, F. Veiga, A. Figueiras, *Materials* **2019**, *13*, 65.

[33] O. Rolland, C.-O. Turrin, A.-M. Caminade, J.-P. Majoral, *New J. Chem.* **2009**, *33*, 1809-1824.
[34] J. Šebestík, M. Reiniš, J. Ježek, in *Biomedical Applications of Peptide-, Glyco- and Glycopeptide Dendrimers, and Analogous Dendrimeric Structures* (Eds.: J. Sebestik, M. Reinis, J. Jezek), Springer Vienna, Vienna, **2012**, pp. 55-81.
[35] F. Vögtle, G. Richardt, N. Werner, in *Dendrimer Chemistry*, WILEY-VCH, Weinheim, **2009**, pp. 25-48.
[36] T. M. Miller, T. X. Neenan, R. Zayas, H. E. Bair, *J. Am. Chem. Soc.* **1992**, *114*, 1018-1025.
[37] D. Türp, T.-T.-T. Nguyen, M. Baumgarten, K. Müllen, *New J. Chem.* **2012**, *36*, 282-298.
[38] Y. Kim, E. J. Park, D. H. Na, *Arch. Pharmacal Res.* **2018**, *41*, 571-582.
[39] C. C. Lee, J. A. MacKay, J. M. J. Fréchet, F. C. Szoka, *Nat. Biotechnol.* **2005**, *23*, 1517-1526.
[40] W. Ke, Y. Zhao, R. Huang, C. Jiang, Y. Pei, *J. Pharm. Sci.* **2008**, *97*, 2208-2216.
[41] K. K. Bansal, D. Kakde, U. Gupta, N. K. Jain, *J. Nanosci. Nanotechnol.* **2010**, *10*, 8395-8404.
[42] Y.-Y. Jiang, G.-T. Tang, L.-H. Zhang, S.-Y. Kong, S.-J. Zhu, Y.-Y. Pei, *J. Drug Targeting* **2010**, *18*, 389-403.
[43] L. M. Kaminskas, B. D. Kelly, V. M. McLeod, G. Sberna, B. J. Boyd, D. J. Owen, C. J. H. Porter, *Mol. Pharmaceutics* **2011**, *8*, 338-349.
[44] L. M. Kaminskas, V. M. McLeod, C. J. H. Porter, B. J. Boyd, *Mol. Pharmaceutics* **2012**, *9*, 355-373.
[45] Starpharma, Dendrimer Drug Delivery (DEP®), https://starpharma.com/drug_delivery, (accessed: April 2020).
[46] A. Quintana, E. Raczka, L. Piehler, I. Lee, A. Myc, I. Majoros, A. K. Patri, T. Thomas, J. Mulé, J. R. Baker, *Pharm. Res.* **2002**, *19*, 1310-1316.
[47] W. Yang, Y. Cheng, T. Xu, X. Wang, L.-p. Wen, *Eur. J. Med. Chem.* **2009**, *44*, 862-868.
[48] I. Dijkgraaf, A. Y. Rijnders, A. Soede, A. C. Dechesne, G. W. van Esse, A. J. Brouwer, F. H. M. Corstens, O. C. Boerman, D. T. S. Rijkers, R. M. J. Liskamp, *Org. Biomol. Chem.* **2007**, *5*, 935-944.
[49] X. He, C. S. Alves, N. Oliveira, J. Rodrigues, J. Zhu, I. Bányai, H. Tomás, X. Shi, *Colloids Surf., B.* **2015**, *125*, 82-89.
[50] S. L. Mekuria, T. A. Debele, H.-Y. Chou, H.-C. Tsai, *J. Phys. Chem. B* **2016**, *120*, 123-130.
[51] T. P. Thomas, A. K. Patri, A. Myc, M. T. Myaing, J. Y. Ye, T. B. Norris, J. R. Baker, *Biomacromolecules* **2004**, *5*, 2269-2274.
[52] P. Singh, F. Moll, 3rd, S. H. Lin, C. Ferzli, K. S. Yu, R. K. Koski, R. G. Saul, P. Cronin, *Clin. Chem.* **2020**, *40*, 1845-1849.
[53] D. Bhatnagar, I. Kaur, A. Kumar, *Int. J. Biol. Macromol.* **2017**, *95*, 505-510.
[54] S. Zhang, L. Zang, X. Zhang, H. Dai, G. Xu, Q. Zhang, C. Yang, Y. Lin, *Electrochim. Acta* **2016**, *196*, 67-74.
[55] R. Akter, B. Jeong, Y.-M. Lee, J.-S. Choi, M. A. Rahman, *Biosens. Bioelectron.* **2017**, *91*, 637-643.
[56] R. Benters, C. M. Niemeyer, D. Drutschmann, D. Blohm, D. Wöhrle, *Nucleic Acids Res.* **2002**, *30*, e10-e10.
[57] V. Le Berre, E. Trévisiol, A. Dagkessamanskaia, S. Sokol, A.-M. Caminade, J. P. Majoral, B. Meunier, J. François, *Nucleic Acids Res.* **2003**, *31*, e88-e88.
[58] V. Balzani, P. Ceroni, S. Gestermann, C. Kauffmann, M. Gorka, F. Vögtle, *Chem. Commun.* **2000**, 853-854.
[59] P. Singh, F. Moll, 3rd, S. H. Lin, C. Ferzli, K. S. Yu, R. K. Koski, R. G. Saul, P. Cronin, *Clin. Chem.* **1994**, *40*, 1845-1849.

[60] Siemens Healthineers, Stratus® CS 200 Acute Care™ Troponin Analyzer, https://www.siemens-healthineers.com/cardiac/cardiac-systems/stratus-cs-acute-care, (accessed: April 2020).
[61] B. Misselwitz, H. Schmitt-Willich, W. Ebert, T. Frenzel, H.-J. Weinmann, *Magn. Reson. Mater. Phys., Biol. Med.* **2001**, *12*, 128-134.
[62] R. C. Orth, J. Bankson, R. Price, E. F. Jackson, *Magn. Reson. Med.* **2007**, *58*, 705-716.
[63] J. D. Eichman, A. U. Bielinska, J. F. Kukowska-Latallo, J. R. Baker, *Pharm. Sci. Technol. Today* **2000**, *3*, 232-245.
[64] M. X. Tang, C. T. Redemann, F. C. Szoka, *Bioconjugate Chem.* **1996**, *7*, 703-714.
[65] A. R. Borges, C. L. Schengrund, *Curr. Drug Targets: Infect. Disord.* **2005**, *5*, 247-254.
[66] M. Lakadamyali, M. J. Rust, X. Zhuang, *Microbes Infect.* **2004**, *6*, 929-936.
[67] D. Sepúlveda-Crespo, R. Ceña-Díez, J. L. Jiménez, M. Ángeles Muñoz-Fernández, *Med. Res. Rev.* **2017**, *37*, 149-179.
[68] S. C. Günther, J. D. Maier, J. Vetter, N. Podvalnyy, N. Khanzhin, T. Hennet, S. Stertz, *Sci. Rep.* **2020**, *10*, 768.
[69] F. Krammer, P. Palese, *Nat. Rev. Drug Discovery* **2015**, *14*, 167-182.
[70] A. Moscona, *N. Engl. J. Med.* **2005**, *353*, 2633-2636.
[71] J. J. Skehel, D. C. Wiley, *Annu. Rev. Biochem.* **2000**, *69*, 531-569.
[72] P. Gaur, P. Ranjan, S. Sharma, J. R. Patel, J. B. Bowzard, S. K. Rahman, R. Kumari, S. Gangappa, J. M. Katz, N. J. Cox, R. B. Lal, S. Sambhara, S. K. Lal, *J. Biol. Chem.* **2012**, *287*, 15109-15117.
[73] J. D. Reuter, A. Myc, M. M. Hayes, Z. Gan, R. Roy, D. Qin, R. Yin, L. T. Piehler, R. Esfand, D. A. Tomalia, J. R. Baker, *Bioconjugate Chem.* **1999**, *10*, 271-278.
[74] H. Oka, T. Onaga, T. Koyama, C.-T. Guo, Y. Suzuki, Y. Esumi, K. Hatano, D. Terunuma, K. Matsuoka, *Bioorg. Med. Chem.* **2009**, *17*, 5465-5475.
[75] J. J. Landers, Z. Cao, I. Lee, L. T. Piehler, P. P. Myc, A. Myc, T. Hamouda, A. T. Galecki, J. R. Baker, Jr., *J. Infect. Dis.* **2002**, *186*, 1222-1230.
[76] K. Hatano, T. Matsubara, Y. Muramatsu, M. Ezure, T. Koyama, K. Matsuoka, R. Kuriyama, H. Kori, T. Sato, *J. Med. Chem.* **2014**, *57*, 8332-8339.
[77] R. G. Denkewalter, J. Kolc, W. J. Lukasavage, Google Patents, **1981**.
[78] Starpharma, VivaGel®, https://starpharma.com/vivagel, (accessed: March 2020).
[79] V. Leiro, S. Duque Santos, C. D. F. Lopes, A. Paula Pêgo, *Adv. Funct. Mater.* **2018**, *28*, 1700313.
[80] H. C. Helms, N. J. Abbott, M. Burek, R. Cecchelli, P.-O. Couraud, M. A. Deli, C. Förster, H. J. Galla, I. A. Romero, E. V. Shusta, M. J. Stebbins, E. Vandenhaute, B. Weksler, B. Brodin, *J. Cereb. Blood. Flow Metab.* **2016**, *36*, 862-890.
[81] W. A. Banks, *BMC Neurol.* **2009**, *9*, S3.
[82] N. J. Abbott, in *Drug Delivery to the Brain: Physiological Concepts, Methodologies and Approaches* (Eds.: M. Hammarlund-Udenaes, C. M. E. de Lange, G. R. Thorne), Springer New York, New York, NY, **2014**, pp. 3-21.
[83] F. Hervé, N. Ghinea, J.-M. Scherrmann, *AAPS J.* **2008**, *10*, 455-472.
[84] Z. Xu, Y. Wang, Z. Ma, Z. Wang, Y. Wei, X. Jia, *Polym. Chem.* **2016**, *7*, 715-721.
[85] Y. Li, H. He, X. Jia, W.-L. Lu, J. Lou, Y. Wei, *Biomaterials* **2012**, *33*, 3899-3908.
[86] G.-f. Chen, T.-h. Xu, Y. Yan, Y.-r. Zhou, Y. Jiang, K. Melcher, H. E. Xu, *Acta Pharmacol. Sin.* **2017**, *38*, 1205-1235.
[87] J. A. Hardy, G. A. Higgins, *Science* **1992**, *256*, 184.
[88] F. Panza, M. Lozupone, G. Logroscino, B. P. Imbimbo, *Nat. Rev. Neurol.* **2019**, *15*, 73-88.
[89] D. A. Patel, J. E. Henry, T. A. Good, *Brain Res.* **2007**, *1161*, 95-105.

[90] B. Klajnert, M. Cortijo-Arellano, J. Cladera, M. Bryszewska, *Biochem. Biophys. Res. Commun.* **2006**, *345*, 21-28.
[91] Z. Wang, X. Dong, Y. Sun, *Langmuir* **2018**, *34*, 14419-14427.
[92] O. Klementieva, N. Benseny-Cases, A. Gella, D. Appelhans, B. Voit, J. Cladera, *Biomacromolecules* **2011**, *12*, 3903-3909.
[93] O. Klementieva, E. Aso, D. Filippini, N. Benseny-Cases, M. Carmona, S. Juvés, D. Appelhans, J. Cladera, I. Ferrer, *Biomacromolecules* **2013**, *14*, 3570-3580.
[94] T. Wasiak, M. Ionov, K. Nieznanski, H. Nieznanska, O. Klementieva, M. Granell, J. Cladera, J.-P. Majoral, A. M. Caminade, B. Klajnert, *Mol. Pharmaceutics* **2012**, *9*, 458-469.
[95] B. Klajnert, T. Wasiak, M. Ionov, M. Fernandez-Villamarin, A. Sousa-Herves, J. Correa, R. Riguera, E. Fernandez-Megia, *Nanomedicine: NBM* **2012**, *8*, 1372-1378.
[96] Z. Wang, X. Dong, Y. Sun, *Langmuir* **2019**, *35*, 14681-14687.
[97] Y. Liu, Y. Ng, M. R. Toh, G. N. C. Chiu, *J. Controlled Release* **2015**, *220*, 438-446.
[98] R. Maji, C. A. Omolo, N. Agrawal, K. Maduray, D. Hassan, C. Mokhtar, I. Mackhraj, T. Govender, *Mol. Pharmaceutics* **2019**, *16*, 4594-4609.
[99] X. Shi, S. Wang, S. Meshinchi, M. E. Van Antwerp, X. Bi, I. Lee, J. R. Baker Jr., *Small* **2007**, *3*, 1245-1252.
[100] X. Xu, Y. Jian, Y. Li, X. Zhang, Z. Tu, Z. Gu, *ACS Nano* **2014**, *8*, 9255-9264.
[101] A. Jędrzak, B. F. Grześkowiak, E. Coy, J. Wojnarowicz, K. Szutkowski, S. Jurga, T. Jesionowski, R. Mrówczyński, *Colloids Surf., B.* **2019**, *173*, 698-708.
[102] V. Brunetti, L. M. Bouchet, M. C. Strumia, *Nanoscale* **2015**, *7*, 3808-3816.
[103] J. Maly, O. Stanek, J. Frolik, M. Maly, F. Ennen, D. Appelhans, A. Semeradtova, D. Wrobel, M. Stofik, T. Knapova, M. Kuchar, L. C. Stastna, J. Cermak, P. Sebo, P. Maly, *Macromol. Biosci.* **2016**, *16*, 553-566.
[104] S. L. Kuan, B. Stöckle, J. Reichenwallner, D. Y. W. Ng, Y. Wu, M. Doroshenko, K. Koynov, D. Hinderberger, K. Müllen, T. Weil, *Biomacromolecules* **2013**, *14*, 367-376.
[105] D. Y. W. Ng, M. Arzt, Y. Wu, S. L. Kuan, M. Lamla, T. Weil, *Angew. Chem. Int. Ed.* **2014**, *53*, 324-328.
[106] C. Wängler, G. Moldenhauer, M. Eisenhut, U. Haberkorn, W. Mier, *Bioconjugate Chem.* **2008**, *19*, 813-820.
[107] P. Kesharwani, A. Gothwal, A. K. Iyer, K. Jain, M. K. Chourasia, U. Gupta, *Drug Discov. Today* **2018**, *23*, 300-314.
[108] S. S. Kumar, S. Abdulhameed, in *Bioresources and Bioprocess in Biotechnology: Volume 2 : Exploring Potential Biomolecules* (Eds.: S. Sugathan, N. S. Pradeep, S. Abdulhameed), Springer Singapore, Singapore, **2017**, pp. 45-73.
[109] P. J. Carter, *Nat. Rev. Immunol.* **2006**, *6*, 343-357.
[110] P. J. Carter, G. A. Lazar, *Nat. Rev. Drug Discovery* **2018**, *17*, 197-223.
[111] D. S. Pisal, M. P. Kosloski, S. V. Balu-Iyer, *J. Pharm. Sci.* **2010**, *99*, 2557-2575.
[112] J. K. Dozier, M. D. Distefano, *Int. J. Mol. Sci.* **2015**, *16*, 25831-25864.
[113] E. Baslé, N. Joubert, M. Pucheault, *Chem. Biol.* **2010**, *17*, 213-227.
[114] G. W. Anderson, J. E. Zimmerman, F. M. Callahan, *J. Am. Chem. Soc.* **1964**, *86*, 1839-1842.
[115] N. Stephanopoulos, M. B. Francis, *Nat. Chem. Biol.* **2011**, *7*, 876-884.
[116] J. M. Chalker, G. J. L. Bernardes, Y. A. Lin, B. G. Davis, *Chem. Asian J.* **2009**, *4*, 630-640.
[117] K. Lang, J. W. Chin, *Chem. Rev.* **2014**, *114*, 4764-4806.
[118] C. D. Spicer, B. G. Davis, *Nat. Commun.* **2014**, *5*, 4740.
[119] V. V. Rostovtsev, L. G. Green, V. V. Fokin, K. B. Sharpless, *Angew. Chem. Int. Ed.* **2002**, *41*, 2596-2599.

[120] Q. Wang, T. R. Chan, R. Hilgraf, V. V. Fokin, K. B. Sharpless, M. G. Finn, *J. Am. Chem. Soc.* **2003**, *125*, 3192-3193.
[121] N. J. Agard, J. A. Prescher, C. R. Bertozzi, *J. Am. Chem. Soc.* **2004**, *126*, 15046-15047.
[122] M. L. Conte, S. Staderini, A. Marra, M. Sanchez-Navarro, B. G. Davis, A. Dondoni, *Chem. Commun.* **2011**, *47*, 11086-11088.
[123] W. Song, Y. Wang, J. Qu, Q. Lin, *J. Am. Chem. Soc.* **2008**, *130*, 9654-9655.
[124] N. S. Joshi, L. R. Whitaker, M. B. Francis, *J. Am. Chem. Soc.* **2004**, *126*, 15942-15943.
[125] G. Chen, A. Heim, D. Riether, D. Yee, Y. Milgrom, M. A. Gawinowicz, D. Sames, *J. Am. Chem. Soc.* **2003**, *125*, 8130-8133.
[126] F. Liu, J. Z. H. Zhang, Y. Mei, *Sci. Rep.* **2016**, *6*, 27190.
[127] C. M. Dundas, D. Demonte, S. Park, *Appl. Microbiol. Biotechnol.* **2013**, *97*, 9343-9353.
[128] D. E. Hyre, I. Le Trong, E. A. Merritt, J. F. Eccleston, N. M. Green, R. E. Stenkamp, P. S. Stayton, *Protein Sci.* **2006**, *15*, 459-467.
[129] M. n. González, C. E. Argaraña, G. D. Fidelio, *Biomol. Eng.* **1999**, *16*, 67-72.
[130] B. A. Katz, *J. Mol. Biol.* **1997**, *274*, 776-800.
[131] E. A. Bayer, S. Ehrlich-Rogozinski, M. Wilchek, *Electrophoresis* **1996**, *17*, 1319-1324.
[132] G. P. Kurzban, E. A. Bayer, M. Wilchek, P. M. Horowitz, *J. Biol. Chem.* **1991**, *266*, 14470-14477.
[133] J. Wallner, G. Lhota, D. Jeschek, A. Mader, K. Vorauer-Uhl, *J. Pharm. Biomed. Anal.* **2013**, *72*, 150-154.
[134] H. Morgan, D. M. Taylor, *Biosens. Bioelectron.* **1992**, *7*, 405-410.
[135] D. Bontempo, R. C. Li, T. Ly, C. E. Brubaker, H. D. Maynard, *Chem. Commun.* **2005**, 4702-4704.
[136] K. Oohora, S. Burazerovic, A. Onoda, Y. M. Wilson, T. R. Ward, T. Hayashi, *Angew. Chem. Int. Ed.* **2012**, *51*, 3818-3821.
[137] D. Y. W. Ng, J. Fahrer, Y. Wu, K. Eisele, S. L. Kuan, H. Barth, T. Weil, *Adv. Healthcare Mater.* **2013**, *2*, 1620-1629.
[138] S. L. Kuan, C. Förtsch, D. Y. W. Ng, S. Fischer, Y. Tokura, W. Liu, Y. Wu, K. Koynov, H. Barth, T. Weil, *Macromol. Biosci.* **2016**, *16*, 803-810.
[139] P. Moscariello, D. Y. W. Ng, M. Jansen, T. Weil, H. J. Luhmann, J. Hedrich, *Adv. Sci. (Weinheim, Ger.)* **2018**, *5*, 1700897-1700897.
[140] Z. Xu, M. Kahr, K. L. Walker, C. L. Wilkins, J. S. Moore, *J. Am. Chem. Soc.* **1994**, *116*, 4537-4550.
[141] F. Morgenroth, E. Reuther, K. Müllen, *Angew. Chem. Int. Ed.* **1997**, *36*, 631-634.
[142] U.-M. Wiesler, K. Müllen, *Chem. Commun.* **1999**, 2293-2294.
[143] M. Müller, C. Kübel, K. Müllen, *Chem. Eur. J.* **1998**, *4*, 2099-2109.
[144] K. S. Novoselov, A. K. Geim, S. V. Morozov, D. Jiang, Y. Zhang, S. V. Dubonos, I. V. Grigorieva, A. A. Firsov, *Science* **2004**, *306*, 666.
[145] K. S. Novoselov, A. K. Geim, S. V. Morozov, D. Jiang, M. I. Katsnelson, I. V. Grigorieva, S. V. Dubonos, A. A. Firsov, *Nature* **2005**, *438*, 197-200.
[146] E. Gerstner, *Nat. Phys.* **2010**, *6*, 836-836.
[147] B. A. G. Hammer, R. Moritz, R. Stangenberg, M. Baumgarten, K. Müllen, *Chem. Soc. Rev.* **2015**, *44*, 4072-4090.
[148] W. Dilthey, W. Schommer, O. Trösken, *Ber. Dtsch. Chem. Ges. (A und B Serie)* **1933**, *66*, 1627-1628.
[149] W. Dilthey, W. Schommer, W. Höschen, H. Die-richs, *Ber. Dtsch. Chem. Ges. (A und B Serie)* **1935**, *68*, 1159-1162.
[150] T.-T.-T. Nguyen, M. Baumgarten, A. Rouhanipour, H. J. Räder, I. Lieberwirth, K. Müllen, *J. Am. Chem. Soc.* **2013**, *135*, 4183-4186.

[151] U. M. Wiesler, A. J. Berresheim, F. Morgenroth, G. Lieser, K. Müllen, *Macromolecules* **2001**, *34*, 187-199.
[152] J. Qu, N. G. Pschirer, D. Liu, A. Stefan, F. C. De Schryver, K. Müllen, *Chem. Eur. J.* **2004**, *10*, 528-537.
[153] S. Bernhardt, M. Kastler, V. Enkelmann, M. Baumgarten, K. Müllen, *Chem. Eur. J.* **2006**, *12*, 6117-6128.
[154] J. Qu, C. Kohl, M. Pottek, K. Müllen, *Angew. Chem. Int. Ed.* **2004**, *43*, 1528-1531.
[155] C. Kohl, T. Weil, J. Qu, K. Müllen, *Chem. Eur. J.* **2004**, *10*, 5297-5310.
[156] R. Stangenberg, Y. Wu, J. Hedrich, D. Kurzbach, D. Wehner, G. Weidinger, S. L. Kuan, M. I. Jansen, F. Jelezko, H. J. Luhmann, D. Hinderberger, T. Weil, K. Müllen, *Adv. Healthcare Mater.* **2015**, *4*, 377-384.
[157] T. Weil, U. M. Wiesler, A. Herrmann, R. Bauer, J. Hofkens, F. C. De Schryver, K. Müllen, *J. Am. Chem. Soc.* **2001**, *123*, 8101-8108.
[158] F. Morgenroth, A. J. Berresheim, M. Wagner, K. Müllen, *Chem. Commun.* **1998**, 1139-1140.
[159] C. Minard-Basquin, T. Weil, A. Hohner, J. O. Rädler, K. Müllen, *J. Am. Chem. Soc.* **2003**, *125*, 5832-5838.
[160] T. Weil, E. Reuther, C. Beer, K. Müllen, *Chem. Eur. J.* **2004**, *10*, 1398-1414.
[161] T. Weil, E. Reuther, K. Müllen, *Angew. Chem. Int. Ed.* **2002**, *41*, 1900-1904.
[162] H. John, R. Bauer, P. Espindola, P. Sonar, J. Heinze, K. Müllen, *Angew. Chem. Int. Ed.* **2005**, *44*, 2447-2451.
[163] S. Loi, U.-M. Wiesler, H.-J. Butt, K. Müllen, *Macromolecules* **2001**, *34*, 3661-3671.
[164] S. Loi, H.-J. Butt, C. Hampel, R. Bauer, U.-M. Wiesler, K. Müllen, *Langmuir* **2002**, *18*, 2398-2405.
[165] A. Herrmann, G. Mihov, G. W. M. Vandermeulen, H.-A. Klok, K. Müllen, *Tetrahedron* **2003**, *59*, 3925-3935.
[166] M. Yin, K. Ding, R. A. Gropeanu, J. Shen, R. Berger, T. Weil, K. Müllen, *Biomacromolecules* **2008**, *9*, 3231-3238.
[167] G. Mihov, D. Grebel-Koehler, A. Lübbert, G. W. M. Vandermeulen, A. Herrmann, H.-A. Klok, K. Müllen, *Bioconjugate Chem.* **2005**, *16*, 283-293.
[168] M. Mondeshki, G. Mihov, R. Graf, H. W. Spiess, K. Müllen, P. Papadopoulos, A. Gitsas, G. Floudas, *Macromolecules* **2006**, *39*, 9605-9613.
[169] M. Yin, J. Shen, G. O. Pflugfelder, K. Müllen, *J. Am. Chem. Soc.* **2008**, *130*, 7806-7807.
[170] M. Yin, C. R. W. Kuhlmann, K. Sorokina, C. Li, G. Mihov, E. Pietrowski, K. Koynov, M. Klapper, H. J. Luhmann, K. Müllen, T. Weil, *Biomacromolecules* **2008**, *9*, 1381-1389.
[171] C. S. Braun, J. A. Vetro, D. A. Tomalia, G. S. Koe, J. G. Koe, C. Russell Middaugh, *J. Pharm. Sci.* **2005**, *94*, 423-436.
[172] B. He, Y. Chu, M. Yin, K. Müllen, C. An, J. Shen, *Adv. Mater.* **2013**, *25*, 4580-4584.
[173] G. Meister, T. Tuschl, *Nature* **2004**, *431*, 343-349.
[174] Q. Zhu, Y. Arakane, R. W. Beeman, K. J. Kramer, S. Muthukrishnan, *Proc. Natl. Acad. Sci. U. S. A.* **2008**, *105*, 6650.
[175] G. D. Rose, A. R. Geselowitz, G. J. Lesser, R. H. Lee, M. H. Zehfus, *Science* **1985**, *229*, 834.
[176] L. Lins, A. Thomas, R. Brasseur, *Protein Sci.* **2003**, *12*, 1406-1417.
[177] S. Miller, J. Janin, A. M. Lesk, C. Chothia, *J. Mol. Biol.* **1987**, *196*, 641-656.
[178] A. Verma, O. Uzun, Y. Hu, Y. Hu, H.-S. Han, N. Watson, S. Chen, D. J. Irvine, F. Stellacci, *Nat. Mater.* **2008**, *7*, 588-595.
[179] M. Şologan, D. Marson, S. Polizzi, P. Pengo, S. Boccardo, S. Pricl, P. Posocco, L. Pasquato, *ACS Nano* **2016**, *10*, 9316-9325.

[180] D. M. Andala, S. H. R. Shin, H.-Y. Lee, K. J. M. Bishop, *ACS Nano* **2012**, *6*, 1044-1050.
[181] Y. Cesbron, C. P. Shaw, J. P. Birchall, P. Free, R. Lévy, *Small* **2012**, *8*, 3714-3719.
[182] M. Yu, F. Stellacci, *Small* **2012**, *8*, 3720-3726.
[183] J. Stirling, I. Lekkas, A. Sweetman, P. Djuranovic, Q. Guo, B. Pauw, J. Granwehr, R. Lévy, P. Moriarty, *PLoS One* **2014**, *9*, e108482.
[184] Q. K. Ong, F. Stellacci, *PLoS One* **2015**, *10*, e0135594.
[185] R. C. Van Lehn, A. Alexander-Katz, *Soft Matter* **2014**, *10*, 648-658.
[186] R. Stangenberg, I. Saeed, S. L. Kuan, M. Baumgarten, T. Weil, M. Klapper, K. Müllen, *Macromol. Rapid Commun.* **2014**, *35*, 152-160.
[187] M. Okuno, M. Mezger, R. Stangenberg, M. Baumgarten, K. Müllen, M. Bonn, E. H. G. Backus, *Langmuir* **2015**, *31*, 1980-1987.
[188] B. A. G. Hammer, Y. Wu, S. Fischer, W. Liu, T. Weil, K. Müllen, *ChemBioChem* **2017**, *18*, 960-964.
[189] D. A. Tomalia, J. B. Christensen, U. Boas, Cambridge University Press, New York, **2012**.
[190] A. E. Nel, L. Mädler, D. Velegol, T. Xia, E. M. V. Hoek, P. Somasundaran, F. Klaessig, V. Castranova, M. Thompson, *Nat. Mater.* **2009**, *8*, 543-557.
[191] S. E. McNeil, *Wiley Interdiscip. Rev.: Nanomed. Nanobiotechnol.* **2009**, *1*, 264-271.
[192] C. M. Goodman, C. D. McCusker, T. Yilmaz, V. M. Rotello, *Bioconjugate Chem.* **2004**, *15*, 897-900.
[193] N. Malik, R. Wiwattanapatapee, R. Klopsch, K. Lorenz, H. Frey, J. W. Weener, E. W. Meijer, W. Paulus, R. Duncan, *J. Controlled Release* **2000**, *65*, 133-148.
[194] H. Kobayashi, S. Kawamoto, S.-K. Jo, H. L. Bryant, M. W. Brechbiel, R. A. Star, *Bioconjugate Chem.* **2003**, *14*, 388-394.
[195] H. Kobayashi, S. Kawamoto, T. Saga, N. Sato, A. Hiraga, J. Konishi, K. Togashi, M. W. Brechbiel, *J. Magn. Reson. Imaging* **2001**, *14*, 705-713.
[196] C. Kojima, C. Regino, Y. Umeda, H. Kobayashi, K. Kono, *Int. J. Pharm.* **2010**, *383*, 293-296.
[197] S. J. Singer, G. L. Nicolson, *Science* **1972**, *175*, 720.
[198] J. C. Roberts, M. K. Bhalgat, R. T. Zera, *J. Biomed. Mater. Res.* **1996**, *30*, 53-65.
[199] L. Albertazzi, M. Serresi, A. Albanese, F. Beltram, *Mol. Pharmaceutics* **2010**, *7*, 680-688.
[200] C. D. Walkey, W. C. W. Chan, *Chem. Soc. Rev.* **2012**, *41*, 2780-2799.
[201] L. Vroman, *Nature* **1962**, *196*, 476-477.
[202] L. Vroman, A. Adams, G. Fischer, P. Munoz, *Blood* **1980**, *55*, 156-159.
[203] N. L. Anderson, M. Polanski, R. Pieper, T. Gatlin, R. S. Tirumalai, T. P. Conrads, T. D. Veenstra, J. N. Adkins, J. G. Pounds, R. Fagan, A. Lobley, *Mol. Cell. Proteomics* **2004**, *3*, 311.
[204] J. Lazarovits, Y. Y. Chen, E. A. Sykes, W. C. W. Chan, *Chem. Commun.* **2015**, *51*, 2756-2767.
[205] M. Lundqvist, J. Stigler, G. Elia, I. Lynch, T. Cedervall, K. A. Dawson, *Proc. Natl. Acad. Sci. U. S. A.* **2008**, *105*, 14265.
[206] J. Simon, T. Wolf, K. Klein, K. Landfester, F. R. Wurm, V. Mailänder, *Angew. Chem. Int. Ed.* **2018**, *57*, 5548-5553.
[207] S. Ritz, S. Schöttler, N. Kotman, G. Baier, A. Musyanovych, J. Kuharev, K. Landfester, H. Schild, O. Jahn, S. Tenzer, V. Mailänder, *Biomacromolecules* **2015**, *16*, 1311-1321.
[208] C. D. Walkey, J. B. Olsen, H. Guo, A. Emili, W. C. W. Chan, *J. Am. Chem. Soc.* **2012**, *134*, 2139-2147.

[209] S. Schöttler, G. Becker, S. Winzen, T. Steinbach, K. Mohr, K. Landfester, V. Mailänder, F. R. Wurm, *Nat. Nanotechnol.* **2016**, *11*, 372-377.
[210] M. Lundqvist, J. Stigler, T. Cedervall, T. Berggård, M. B. Flanagan, I. Lynch, G. Elia, K. Dawson, *ACS Nano* **2011**, *5*, 7503-7509.
[211] J. Simon, L. K. Müller, M. Kokkinopoulou, I. Lieberwirth, S. Morsbach, K. Landfester, V. Mailänder, *Nanoscale* **2018**, *10*, 10731-10739.
[212] L. K. Müller, J. Simon, C. Rosenauer, V. Mailänder, S. Morsbach, K. Landfester, *Biomacromolecules* **2018**, *19*, 374-385.
[213] G. Caracciolo, S. Palchetti, V. Colapicchioni, L. Digiacomo, D. Pozzi, A. L. Capriotti, G. La Barbera, A. Laganà, *Langmuir* **2015**, *31*, 10764-10773.
[214] D. Prozeller, J. Pereira, J. Simon, V. Mailänder, S. Morsbach, K. Landfester, *Adv. Sci.* **2019**, *6*, 1802199.
[215] S. Schöttler, K. Landfester, V. Mailänder, *Angew. Chem. Int. Ed.* **2016**, *55*, 8806-8815.
[216] R. van Furth, Z. Cohn, J. Hirsch, J. Humphrey, W. Spector, H. Langevoort, *Bull. W. H. O.* **1972**, *46*, 845.
[217] G. Caracciolo, F. Cardarelli, D. Pozzi, F. Salomone, G. Maccari, G. Bardi, A. L. Capriotti, C. Cavaliere, M. Papi, A. Laganà, *ACS Appl. Mater. Interfaces* **2013**, *5*, 13171-13179.
[218] P. Aggarwal, J. B. Hall, C. B. McLeland, M. A. Dobrovolskaia, S. E. McNeil, *Adv. Drug Deliver. Rev.* **2009**, *61*, 428-437.
[219] A. Gessner, A. Lieske, B.-R. Paulke, R. H. Müller, *J. Biomed. Mater. Res., Part A* **2003**, *65A*, 319-326.
[220] A. Åkesson, M. Cárdenas, G. Elia, M. P. Monopoli, K. A. Dawson, *RSC Adv.* **2012**, *2*, 11245-11248.
[221] G. Caracciolo, *Nanomedicine: NBM* **2015**, *11*, 543-557.
[222] A. R. Shaw, M. Suzuki, *Mol. Ther.- Methods Clin. Dev.* **2019**, *15*, 418-429.
[223] H. Liu, L. Jin, S. B. S. Koh, I. Atanasov, S. Schein, L. Wu, Z. H. Zhou, *Science* **2010**, *329*, 1038-1043.
[224] Y. S. Haviv, J. L. Blackwell, A. Kanerva, P. Nagi, V. Krasnykh, I. Dmitriev, M. Wang, S. Naito, X. Lei, A. Hemminki, D. Carey, D. T. Curiel, *Cancer Res.* **2002**, *62*, 4273.
[225] M. A. Barry, J. D. Rubin, S.-C. Lu, *FEBS Lett.* **2020**, doi:10.1002/1873-3468.13731.
[226] Z. Xu, Q. Qiu, J. Tian, J. S. Smith, G. M. Conenello, T. Morita, A. P. Byrnes, *Nat. Med.* **2013**, *19*, 452-457.
[227] R. Goswami, G. Subramanian, L. Silayeva, I. Newkirk, D. Doctor, K. Chawla, S. Chattopadhyay, D. Chandra, N. Chilukuri, V. Betapudi, *Front. Oncol.* **2019**, *9*.

2 Motivation and Conceptual Design

There have been considerable research activities in the design and application of dendrimers for nanomedicine in the last three decades. The remarkable features of dendrimers such as monodispersity, nano-size definition and precise multivalent surfaces are advantageous over those of polydisperse polymers regarding the reproducibility of the identical chemical structures, sizes and shapes. The structural composition of dendrimers has a substantial impact on their bioactivity in terms of biorecognition and -distribution as well as toxicity. Most notably, the dendrimer surface modification is relevant for the interaction with biological structures such as cells, viruses or nucleic acids. Hence, the chemical design of dendrimers can be adapted to therapeutic needs. However, most dendrimer types exhibit backfolding dependent on the physiological environment. This behavior impedes the investigation of interactions between a precisely defined multivalent periphery with biointerfaces to further understand the role of surface patterns in biorecognition. In contrast, the remarkable rigid scaffold of polyphenylene dendrimers (PPDs) imparts shape persistency preventing the dendritic branches from backfolding. Thus, the surface groups are distributed on the dendrimer surface with precise spatial arrangement. The employment of alternating sulfonic acid and *n*-propyl groups enables cellular internalization with low cytotoxicity both *in vitro* and *in vivo*. The so-called patchy, amphiphilic PPDs with well-defined globular structures are reminiscent to biological structures such as proteins due to their hydrophobic cavities, similar sizes and amphiphilic surface pattern. These first studies have paved the way towards the usage of PPDs in biomedical applications. Nevertheless, the performance of patchy dendrimers in biorecognition is still barely understood.

The objective of this work is the synthesis of PPDs with amphiphilic negatively charged surface pattern and their (bio-)conjugates in order to explore their interactions with biointerfaces. This includes the cellular uptake properties, interactions with proteins, peptides and protein-assemblies such as viruses. The aim is to improve the understanding of amphiphilic surface patterns in biorecognition. Moreover, the employment of the PPDs as an artificial protein corona on nanocarriers is envisioned. The intent is to tailor nanocarrier surfaces with amphiphilic pattern to control the adsorption of proteins (natural protein corona) in the blood stream which ultimately

influences their biodistribution. In addition, the engineering of the structural design of the PPD scaffold is a prerequisite to expand the scope of biomedical applicability for PPDs. Since patchy PPDs are globular structures, the implementation of a second biological function without the interruption of the surface pattern is hampered. Therefore, a major aim of this thesis is the desymmetrization of the dendritic structure to integrate an additional feature into the PPD scaffold. The synthesis of a dendron, which displays one quarter of the entire dendrimer, provides the advantage to retain the amphiphilic surface while enabling the attachment of a second group to the dendron core. By this strategy, the opportunity to combine the amphiphilic biorecognition motif with a biological function is envisioned. To further facilitate the attachment of several functions, the development of an amphiphilic PPD-protein-hybrid material is of great interest. This can be achieved by the approach of desymmetrization to a dendron scaffold with a functionality that allows the binding to proteins. The dendron-protein hybrid retains the biorecognition motif of the PPD while providing the ability to use the protein as a multifunctional core. The main objectives are summarized in Figure 2.1.

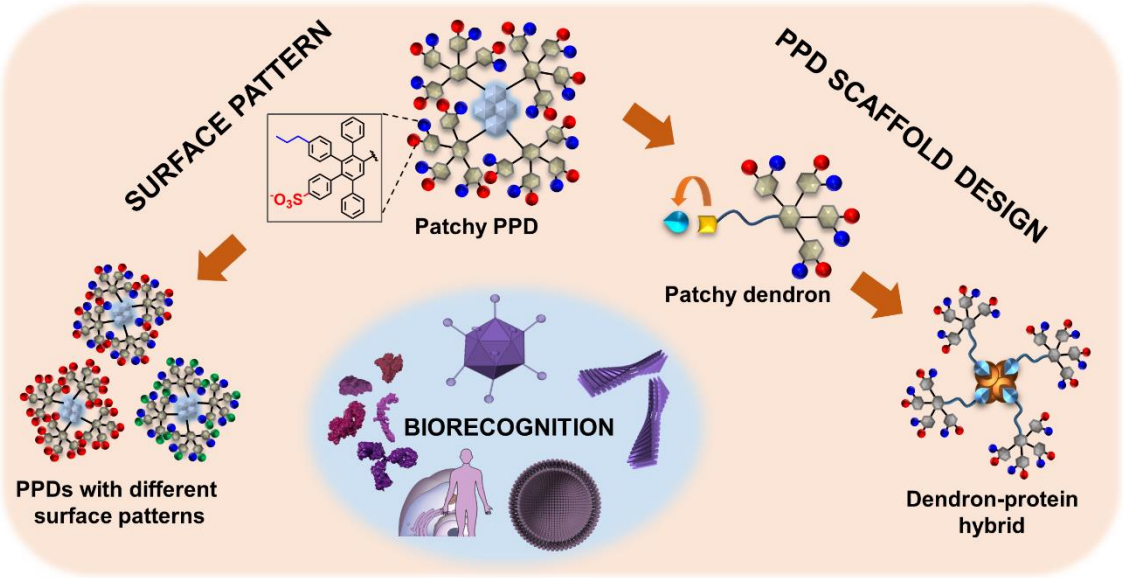

Figure 2.1. Conceptional design and aim of this work.

To explore the biorecognition properties and applicability of patchy PPDs as coating for gene delivery vectors, the interaction between patchy PPDs and the therapeutic gene-delivery vector Adenovirus 5 (Ad5) is investigated (chapter 3). The progression of Ad5-assisted gene therapy is highly demanded as the application of Ad5 is limited by critical factors. First, the cellular uptake of Ad5 is determined by the coxsackie-adenovirus receptor (CAR) on the cellular membrane, which is not present on every cell in the body.

Second, Ad5 is cleared by antibodies in the blood stream and mainly transported to the liver. Consequently, the aim of this project is the reprogramming of the cellular uptake of Ad5 to a CAR-independent way and the protection from antibody clearance by employing a dendrimer-coating on Ad5. In order to investigate the binding ability of patchy PPDs, amphiphilic PPDs with alternating sulfonic acid and *n*-propyl surface groups and a dendrimer with an exclusively sulfonic acid modified rim are employed. The dendrimer binding motif towards Ad5 as well as the performance of dendrimer-coated Ad5 concerning CAR-independent cellular uptake, gene transduction efficiency and shielding from antibody clearance are investigated. Since proteins in the blood stream play a critical role in the biodistribution and immune response, the impact of blood serum proteins is studied.

To deepen the understanding of the interactions of amphiphilic patterned nanoparticle surfaces with proteins in the blood stream, the second project (chapter 4) within this work focuses on the impact of patchy PPDs on the interactions with blood plasma proteins when applied to nanocarrier surfaces. PPDs with negatively charged amphiphilic, and exclusively anionic surface groups are synthesized and compared to PPDs with positively charged amphiphilic PPDs. Liposomes serve as a model system since they are similar to biological systems. The impact on the protein adsorption in human plasma by the dendrimer corona is assessed. The alteration of surface charges and hydrophobic groups provides an insight about the PPD parameters such as hydrophobicity and charges which eventually engineer the protein corona composition.

In order to advance the concept of PPD-based nanomedicine, by e.g. remodeling the Ad5 surface using amphiphilic PPDs, the implementation of a second feature to the PPD scaffold is a prerequisite. Therefore, the third project (chapter 5) focuses on the development of a desymmetrized patchy PPD structure with the possibility for post-modification. Maintaining a high density of amphiphilic surface pattern while attaching an additional feature to the dendritic scaffold presents the main challenge. These requirements are accomplished by the synthesis of a patchy dendron, which represents one dendritic branch of the entire PPD. The employment of a suitable bifunctional dendritic core with first, a moiety for dendron synthesis and second, a functionality which remains stable under the harsh conditions in PPD synthesis are essential. After dendron growth, the ligation of a “Click”-able linker to the dendron core for the attachment of bioactive groups such as a fluorophore for imaging or a different bio-orthogonal group is envisioned. The preservation of the biorecognition properties regarding cellular

internalization and Ad5-assisted gene delivery is investigated. Furthermore, the *in situ* post-modification of the dendron's focal point upon Ad5 complexation is studied as the accessibility of the biological function is essential for future applications in the field of targeting. Since the dendritic geometry is altered, the protein corona formation on dendron-coated liposomes is compared to the entire PPD to access the potential interactions of the dendrons in the blood stream, which is attractive for *in vivo* applications.

In addition to the synthesis of an amphiphilic dendron (chapter 5), the development of a dendron-streptavidin hybrid material is of great relevance to progress the applicability of PPDs in biomedicine (chapter 6). Previously, the use of streptavidin (SA) as an adapter for the attachment of PAMAM-dendrons has shown to enhance the ease of combining several functions on one biomolecule. Furthermore, a water-insoluble PPD with three peripheral perylene monoimide chromophores was bound to SA *via* a D-biotin moiety, which required the use of solubilization agents. By using a biotinylated patchy polyphenylene dendron the formation of a dendron-streptavidin hybrid without the need of solubilization agents is envisioned. Due to the fact, that the internalization of patchy PPDs into murine brain endothelial cells was demonstrated in previous studies, the potential of the patchy dendron and its respective SA-hybrid to cross the BBB are further investigated. Overcoming the BBB empowers the employment of dendron conjugates in the treatment of neurodegenerative diseases. Consequently, the impact of the dendron conjugates on Aβ-fibril formation is studied in order to explore their potential as a tool for the development of new therapeutic agents in the field of Alzheimer's disease.

3 Patchy Amphiphilic Dendrimers Bind Adenovirus and Control Its Host Interactions and In Vivo Distribution

[redacted]

Contribution

My contribution was the adjustment of the synthetic procedure and purification as well as performing the scale-up synthesis of the amphiphilic PPD3 for all *in vivo* and protein corona experiments. Furthermore, I performed the synthesis of the biotinylated dendrimer (dendron) for biolayer-interferometry measurements and contributed in scientific discussions. [redacted] synthesized and characterized the PPDs for *in vitro* studies. [redacted] conducted all animal experiments, performed some repeated TEM and cell experiments, measured the stability of the PPD3/Ad5 complex in serum, performed biolayer-interferometry measurements and kinetic binding analysis and designed the schematic overview. [redacted] performed and interpreted most *in vitro* cell experiments (flow cytometry measurements) of Ad5 in combination with the different dendrimers, factor X as well as the Ad5/F41 analysis, part of TEM analysis together with [redacted] and dynamic light scattering experiments. [redacted] performed part of the TEM experiments and interpreted the results. [redacted] coated PS-nanoparticles with PPD3 and conducted and interpreted the protein corona analysis (SDS-PAGE and LC-MS). [redacted] supervised experiments of [redacted], analyzed the results and wrote parts of the manuscript. [redacted] performed the PPD structure modeling. [redacted] conducted and interpreted PPD/Ad5 cell experiments. [redacted] performed and interpreted initial confocal imaging experiments. [redacted] performed the PPD structure modeling. [redacted] participated in the initial design of the project, supervised the synthesis of [redacted] and revised the manuscript. [redacted] designed the project, analyzed the results of [redacted] and wrote parts of the manuscript. [redacted] designed the project, provided funding support, analyzed the results, and wrote large parts of the manuscript.

Copyright

The following part is reproduced with permission from *ACS Nano* **2019**, *13*, 8749-8759, https://pubs.acs.org/doi/10.1021/acsnano.9b01484. Further permissions related to the material excerpted should be directed to the American Chemical Society (ACS).

Abstract

The surface of proteins is heterogeneous with sophisticated but precise hydrophobic and hydrophilic patches, which is essential for their diverse biological functions. To emulate such distinct surface patterns on macromolecules, we used rigid spherical synthetic dendrimers (polyphenylene dendrimers) to provide controlled amphiphilic surface patches with molecular precision. We identified an optimal spatial arrangement of these patches on certain dendrimers that enabled their interaction with human adenovirus 5 (Ad5). Patchy dendrimers bound to the surface of Ad5 formed a synthetic polymer corona that greatly altered various host interactions of Ad5 as well as *in vivo* distribution. The dendrimer corona (1) improved the ability of Ad5-derived gene transfer vectors to transduce cells deficient for the primary Ad5 cell membrane receptor and (2) modulated the binding of Ad5 to blood coagulation factor X, one of the most critical virus−host interactions in the bloodstream. It significantly enhanced the transduction efficiency of Ad5 while also protecting it from neutralization by natural antibodies and the complement system in human whole blood. Ad5 with a synthetic dendrimer corona revealed profoundly altered *in vivo* distribution, improved transduction of heart, and dampened vector sequestration by liver and spleen. We propose the design of bioactive polymers that bind protein surfaces solely based on their amphiphilic surface patches and protect against a naturally occurring protein corona, which is highly attractive to improve Ad5-based *in vivo* gene therapy applications.

3.1 Introduction

Only recently, it has been discovered that the protein corona largely determines the fate of nanoparticles in the bloodstream *in vivo*.[1-5] Unlike highly specific ligand−receptor recognition, protein corona formation on nanoparticle surfaces mainly depends on multiple weak molecular binding events.[4] Protein surfaces are not homogeneous but provide defined amphiphilic patterns. Although the role of such amphiphilic surface patches in cell biology is still barely understood, it has been found essential for their cellular distribution and various interactions with, for example, other proteins, membranes, and carbohydrates.[6] In consequence, molecular recognition concepts have been proposed such as the corona phase model based on folded heteropolymers constrained at a single-walled nanotube surface,[7] which indicate that slight polarity differences could induce large differences in molecular biorecognition. The importance of amphiphilic patches has been previously demonstrated in a synthetic model, where gold nanoparticles have been prepared with alternating hydrophobic and hydrophilic segments; these nanoparticles penetrated cellular membranes more efficiently than particles with the same functional groups homogeneously distributed on the surface.[8] Therefore, we hypothesized that by engineering specific amphiphilic patches, one could control biomolecule recognition and even engineer a protein-like corona by synthetic macromolecules.

In nature, viruses are among the most intelligent and efficient nanotransporters. Their enormous efficiency not only depends on their highly specific receptor binding, but they can also utilize blood plasma proteins as shielding corona to enhance their stability and evade the immune system.[9] Specific binding of blood plasma proteins is predetermined by the surface of the virus capsid. For instance, blood coagulation factor X (FX) binds to the surface of adenovirus type 5 (Ad5) forming a protein corona that shields the viruses from attack by natural antibodies and complement,[9] which also significantly enhances their liver transduction efficiency.[10, 11] In clinical trials, Ad5 is the most frequently used gene transfer vector to date[12] by providing high transduction efficiency in both dividing and nondividing cells and accommodating large transgene cassettes.[13] However, the clinical applicability of Ad5-based vectors is severely limited by this native protein corona formation[9, 10, 14] since the absorbed proteins dictate whether the vector can transduce certain cells *in vivo* and frequently lead to mistargeting and acute toxicity.[15] For example, the FX in the protein corona triggers highly efficient sequestration of Ad vector particles in the liver,[10, 11] which is a major limitation in Ad5-based gene therapy. In addition, while

Ad5 *in vitro* employs the coxsackie−adenovirus cell surface receptor (CAR) and α(v)β3/5 integrins to infect cells, the primary receptor CAR is often not available on target tissue *in vivo*,[16] and tumor cells are often refractory to transduction by Ad5.[17] Therefore, it would be a significant advancement for Ad-based gene therapy if one could engineer an artificial protein-like corona that replaces the natural protein corona, which should shield the vector from neutralizing antibodies and ultimately engineer virus tropism for therapeutic applications.

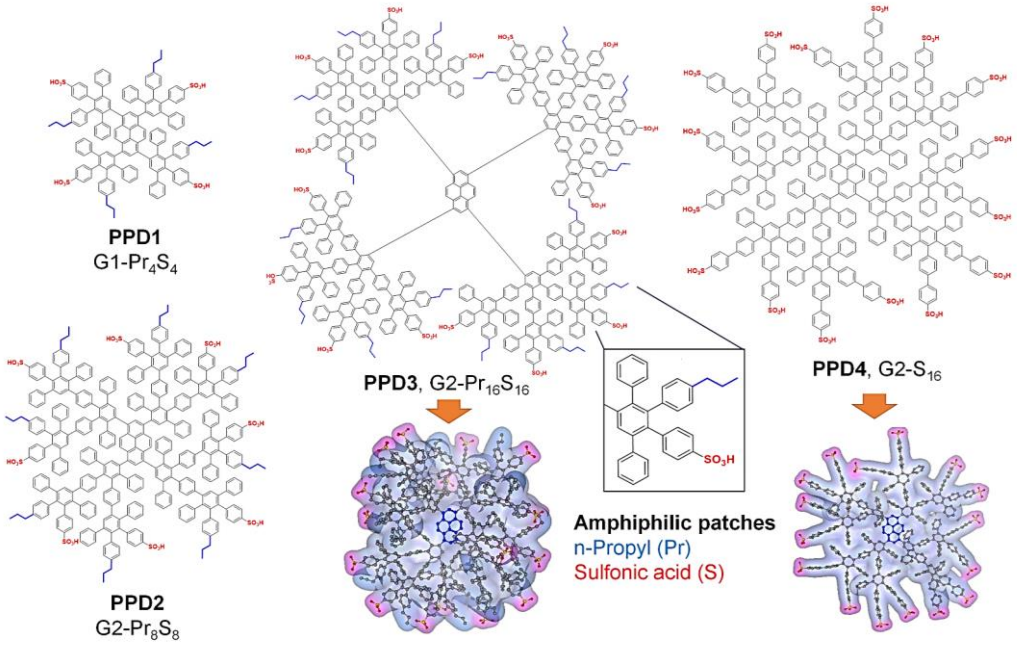

Scheme 3.1. Synthesized PPDs with Amphiphilic *n*-Propyl and Sulfonic Acid Surface Patches. Variation of the sizes (1st generation G1-Pr_4S_4, "PPD1" *vs* 2nd generation, e.g., G2-Pr_8S_8 or PPD2), negative charges as well as surface patches. Visualization of the 3D structure of patchy PPD3 and PPD4.

Our goal was to mimic the complex amphiphilic patterns like the surface topology of proteins by shape-persistent polyphenylene dendrimers (PPDs) to ultimately control biorecognition of Ad5. PPDs were prepared, providing alternating negatively charged sulfonic acid and hydrophobic *n*-propyl groups (e.g., amphiphilic groups) on their surfaces,[18, 19] and we have identified PPD3 (see Scheme 3.1) to provide an optimal amphiphilic surface texture for Ad5 vector binding. PPD3 forms a protein-like corona on Ad5 and alters Ad5 biorecognition and pathways for gene transduction. We could demonstrate enhanced vector transduction into low CAR cells, protecting Ad5 from FX binding and plasma neutralization, and alter the *in vivo* tissue distribution of Ad5. Our results are of great relevance to improve *in vivo* gene therapy by synthetic polymers, providing precise amphiphilic surface patterns. We further envision that our concept could be utilized to create nanoparticle therapeutics with tailored amphiphilic surface

patterns that serve as artificial protein corona to control the *in vivo* distribution of nanoparticles, which represents a holey grail in nanomedicine.

3.2 Results and Discussion

Dendrimers with Precise Amphiphilic Surface Patches. In cell biochemistry, sulfonic acid groups are only present in certain carbohydrates such as heparin. Inspired by heparin sulfate−glycosaminoglycans, which are observed in blood and undergo multiple protein−protein interactions, we have synthesized PPDs with surface-exposed sulfonic acid surface groups. In contrast to carboxylic acids, sulfonic acid groups are negatively charged independent of the pH (within the biologically relevant range). As lipophilic residues, propyl chains were selected due to their performance in a previous *in vitro* screening that analyzed the influence of various nonpolar substituents (i.e., phenyl, propyl, *iso*propyl, butyl, and hexyl chains) on the cell uptake and toxicity of PPDs.[20] 1,3,6,8-Tetraethynylpyrene served as the dendrimer core so that the blue emission of pyrene could be used as a fluorescence probe to enable monitoring of the macromolecules *via* fluorescence microscopy. PPDs with different but precisely established numbers and orientations of the sulfonic acid/*n*-propyl surface groups were synthesized by reacting the core with functionalized cyclopentadienone building blocks in Diels−Alder cycloadditions. Detailed characterization of each sample is also given in the Supporting Information Section 3.6.2 (Scheme 3.1).[21] We then considered the impact of the size (first *vs* second generation), surface-charge density (PPD2 *vs* PPD3), and significance of the *n*-propyl groups (PPD3 *vs* PPD4) on the interactions between the "patched" surface dendrimers and Ad5. In the following sections, we describe the formation of PPD3/ Ad5 complexes and their transduction pathways by a combination of biological and physicochemical methods. The key concern is to alter the surface topology of Ad5 by dendrimer binding to ultimately control and improve critical interactions with plasma proteins and cells.

PPD3/Ad5 Complexes with Improved Transduction Efficiency. PPD1 to PPD4 were mixed with Ad5 at a desired ratio in PBS buffer, and the gene transduction capabilities of Ad5 in the uncoated and complexed form were tested. Replication-defective Ad5-based vectors harboring a heterologous expression cassette for the enhanced green fluorescent protein (EGFP) were used as model system to study transduction of different cell lines (see SI for details, Ad5 mentioned in the experimental and results sections always refers to this vector). Vector particles and PPDs were incubated in PBS buffer at

a molar ratio of 1:10 000, and the complexes were subsequently used for transduction. After 24 h post transduction, EGFP was quantified by flow cytometry. CHO-K1 (a subclone of Hamster Chinese ovary noncancer cell line) and SKOV-3 (human ovarian cancer cell line) cells were selected, which are difficult to transduce by Ad5 due to low CAR receptor expression. The corresponding flow cytometry data are depicted in Figure 3.1c. From PPD1 to PPD3, with increasing numbers of alternating sulfonic acid/propyl groups, the transduction enhancement is increased accordingly with PPD3/Ad5 complexes exhibiting the highest transduction efficiencies, about 20-fold higher than Ad5 control alone. The presence of amphiphilic surface patches was crucial for bioactivity since PPD4 with similar size and the same number of acid groups as PPD3, but lacking the *n*-propyl chains, revealed almost no increase of transduction efficiency for SKOV3 cells. The trends seen for different dendrimers were also directly visualized by fluorescence microscopy (Figure 3.1b and Figure S3.3). With increasing virus concentrations (particle multiplicity of infection = physical particles per cell, pMOI) from 1000 pMOI to 5000 pMOI, the transduction enhancement with PPD3 became even more prominent (>30-fold, Figure 3.1d). Clearly, biorecognition of Ad5 could be altered after PPD3 binding to the virus surface, and both the ratio of the amphiphilic groups (sulfonic acid and *n*-propyl) and their surface density on PPDs are essential for their interactions with Ad5. This significant binding of PPD3 to Ad5 was therefore studied further by light scattering and electron microscopy (Figure 3.1e and Table S3.1). By increasing the ratio of PPD3 to Ad5, the particle sizes of formed complexes increased from 108 ± 11 nm (Ad5) up to about 729 ± 87 nm for PPD3/Ad5 (1000:1 ratio) (Table S3.1) but maintained low polydispersity index (PDI) below 0.2. In contrast, PPD4 with the same number of sulfonic acid groups as PPD3, but no *n*-propyl groups, did not form any complexes with Ad5 (Table S3.1) even at very high concentrations of the dendrimer (10 000:1). The PPD3/Ad5 complexes could be visualized by transmission electron microscopy (TEM) (Figure 3.1e), while, here again, no complexation of PPD4 with Ad5 was found. Obviously, PPD3 molecules formed a proteincorona-like structure on Ad5, and the result is in agreement with the transduction data and supported the assumption that defined patches of amphiphilic groups (sulfonic acid and *n*-propyl) are critical for promoting interactions with Ad5. The interaction between PPD3 and Ad5 was also detected by biolayer interferometry (BLI) (Figure S3.10, Figure S3.11, and Table S3.2). In the BLI experiment, Ad5 particles with high number of binding sites interact with a flat sensor surface densely coated with PPD3−dendrimer binding motifs. According to this method, the calculated K_D (equilibrium dissociation constant) is as low as 1.27 pM. Most likely, this very strong binding is a result from multivalent interactions of PPD3 and Ad5, and it

does not reflect the binding event of single PPD3 molecules with Ad5. However, we clearly show that strong interactions occur between this dendrimer and Ad5.

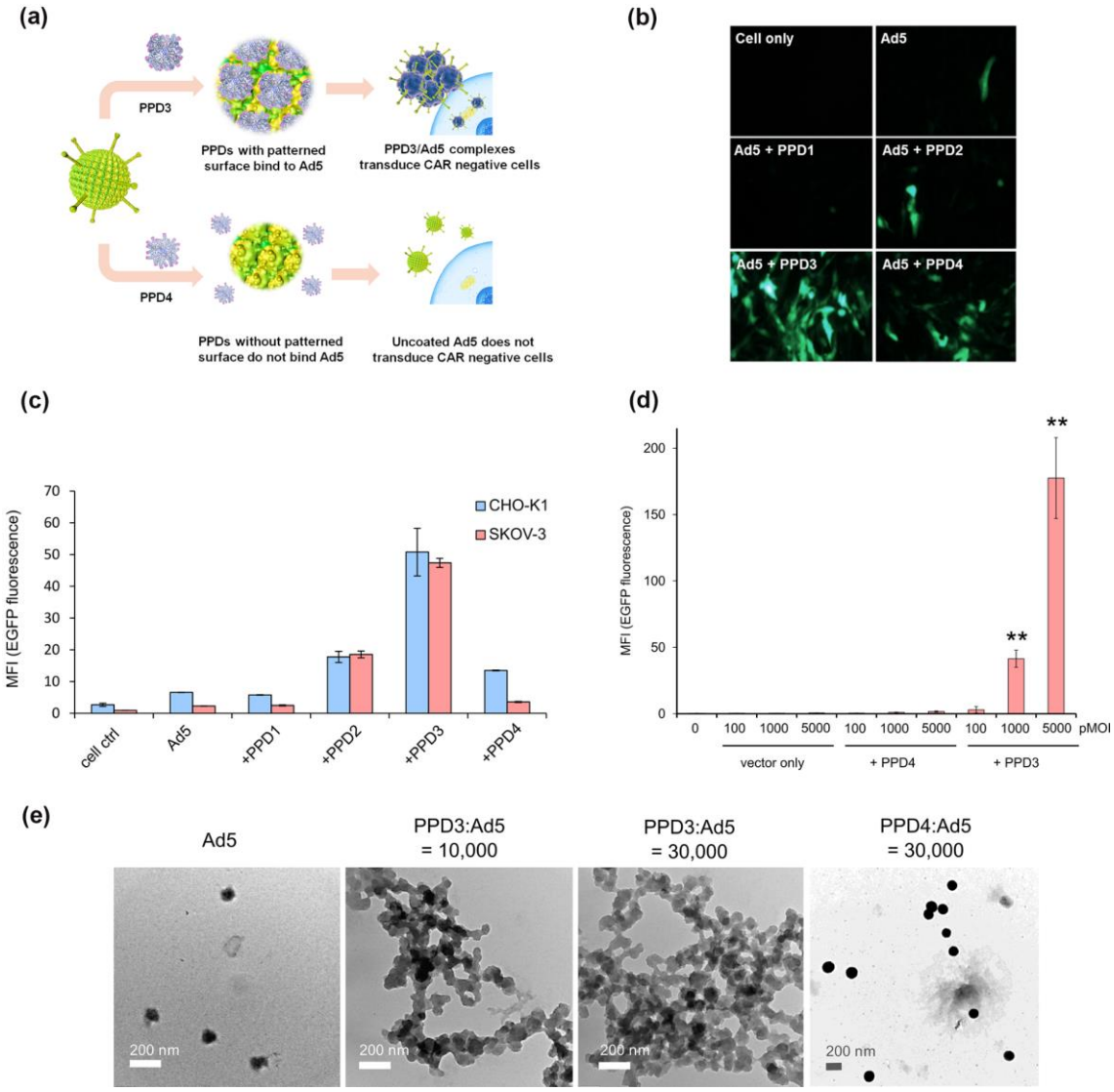

Figure 3.1. PPD3 and Ad5 formed complexes with increased transduction efficiency on CHO and SKOV-3 cells. (**a**) Illustration of PPD binding to Ad5 and transduction. (**b**) Fluorescence microscopy images of EGFP expression in CAR-negative CHO-K1 cells. PPD3 significantly enhanced Ad5 uptake and EGFP expression in comparison to other PPDs. (**c**) Flow cytometric quantification of Ad5-mediated EGFP expression in CAR-negative CHO-K1 and SKOV-3 cells after incubation with PPD1, PPD2, PPD3, and PPD4; MFI stands for mean fluorescence intensity as absolute values. Transduction was performed with 100 pMOI (particle multiplicity of infection). (**d**) Flow cytometric quantification of Ad5mediated EGFP expression in SKOV-3 cell with different pMOI of Ad5 (n = 3). (**e**) TEM images (scale 200 nm) of Ad5 before and after incubation with PPD3 and PPD4. Complex formation between dendrimer and Ad5 only occurred upon incubation with PPD3. ** represents p-value ≤ 0.01.

Enhanced Ad5 Transduction of Cells with Low CAR Expression. Coxsackie−adenovirus receptor (CAR) is the main receptor at the cellular membrane that recognizes and interacts with Ad5.[22] Consistently, cells that do not express CAR (e.g., most tumor cells) can hardly be transduced by Ad5. By increasing the ratio of PPD3 to Ad5, we observed

a saturable increase in the efficiency for Ad5 transduction of SKOV-3 cells with low CAR expression (Figure 3.2a). In contrast, transduction of A549 cells with high CAR levels was not influenced by increasing concentrations of PPD3 (Figure 3.2a). Similar observations were obtained with other high and low CAR cell lines (Figure S3.5). These results revealed that the formation of a PPD3 corona around Ad5 particles could promote an alternative, yet unknown pathway for Ad5 uptake that significantly improves Ad5 transduction into low CAR cells (Figure 3.2b).

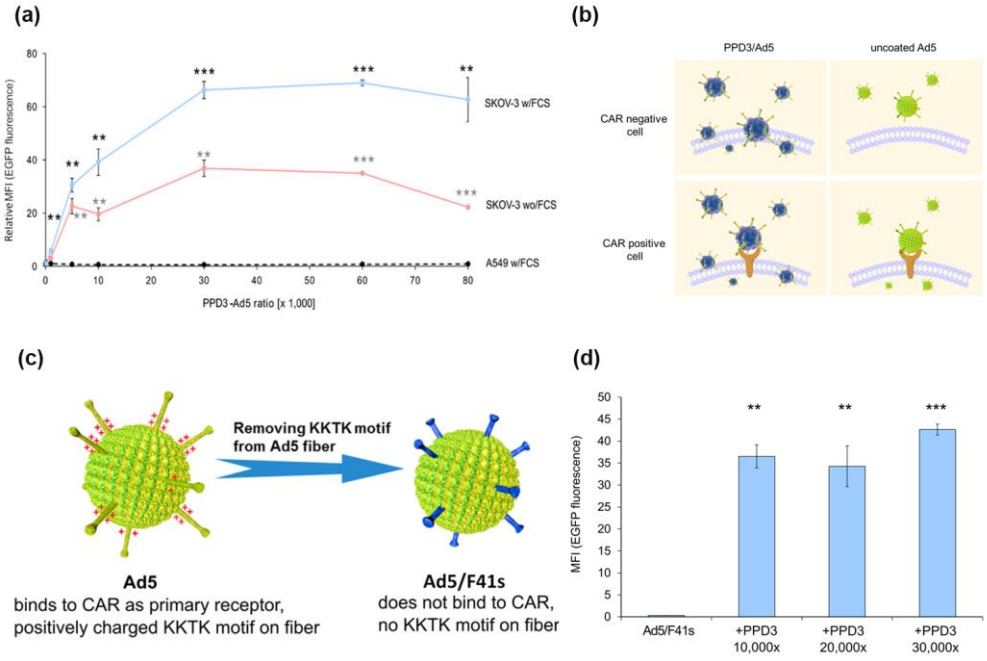

Figure 3.2. Transduction by PPD3/Ad5 complexes was independent of the primary Ad5 receptor CAR and the positively charged KKTK motif in the fiber capsomere. (**a**) In the presence of FCS, the transduction of SKOV-3 cells by PPD3/Ad5 complexes was increased (blue line) compared to the absence of FCS (red line) over a broad range of different PPD3/Ad5 ratios. Transduction of the human nonsmall cell lung carcinoma line A549 was not increased by PPD3/Ad5 complexes (dashed line). Transduction was performed with 1000 pMOI for all PPD3/Ad5 ratios. The relative MFI value calculated from transduction by Ad5 only is shown. (**b**) Illustration of the difference in cell uptake with PPD3/Ad5 and uncoated Ad5. PPD3/Ad5 uptake into CAR negative cells independent from CAR receptor, whereas uncoated Ad5 could not. For CAR positive cells, PPD3/Ad5 might still have utilized the CAR-binding pathway, thus resulting in the same transduction efficiency as uncoated Ad5. (**c**) Depiction of native Ad5 with positively charged KKTK motif in the fiber, binding CAR as primary receptor and recombinant Ad5/F41s without the positively charged KKTK motif in the fiber that does not bind CAR. (**d**) Transduction assay with Ad5/F41s and PPD3. Despite a lack of CAR binding, the KKTK motif PPD3/Ad5/F41s complexes revealed significantly enhanced transduction efficiency, which indicated the independence of both CAR and KKTK. ** represents p-value ≤ 0.01, *** represents p-value ≤ 0.001.

Enhanced Transduction in Serum. For *in vivo* applications, the impact of serum on the transduction efficacy of the PPD3/Ad5 complexes is crucial. As demonstrated in Figure 3.2a, the presence of fetal calf serum (FCS) did not reduce transduction efficiency of PPD3/Ad5 complexes; instead, we even observed a significantly increased Ad5 transduction efficiency. Increased transduction efficacy has been reported for DNA-containing lipoplexes[23] due to a protein corona coating of the lipoplexes, which induced

different cellular uptake pathways. In addition, it has also been shown that distinct corona proteins can enhance cellular binding and uptake.[24, 25] Therefore, to study the interaction between blood proteins and PPD3, the surface of a literature known model system, polystyrene nanoparticles (ø = 100 nm) were coated with PPD3, and the protein corona composition was compared to the uncoated nanoparticles. *Via* SDS-PAGE and proteomics (Figure S3.12 – Figure S3.14), we could demonstrate that the protein corona significantly changes after the nanoparticles were coated with PPD3. After incubation with blood serum, a significantly higher amount of vitronectin was bound the PPD3-coated nanoparticles in comparison to the uncoated ones. Vitronectin is one example of a corona protein that has been reported to mediate cellular interactions with cancer cells.[26] Further studies are required to analyze the interaction with serum proteins in greater detail. In these studies, we could clearly demonstrate that serum proteins stabilized the PPD3/Ad5 complexes in blood serum, which is attractive within *in vivo* applications.

Transduction Independent of Primary Ad5 Receptor CAR and Positively Charged KKTK Motif in Fiber Capsomere. Since PPD3 exhibits a net negative charge, we initially speculated that the interaction of Ad5 and PPD3 could be of electrostatic nature involving positively charged amino acids on Ad5. The most prominent positively charged motif at the Ad5 surface is the KKTK motif located at the fiber shaft.[27] Therefore, an Ad5 mutant Ad5/F41s lacking the KKTK and being unable to bind to CAR was investigated (Figure 3.2c). The structure of Ad5/F41s is almost identical to Ad5 with only a deletion of the KKTK motif on the fibers. PPD3/Ad5/F41s complexes demonstrated very high uptake into SKOV-3 cells, as indicated by high EGFP expression depicted in Figure 3.2d. This result, again, highlighted that compared to Ad5 alone, PPD3 enhanced vector transduction when the CAR pathway was not available. Also, PPD3 still interacted with Ad5/F41s efficiently despite the absence of the positively charged KKTK. Therefore, binding between PPD3 and Ad5 most likely occurred at a site distinct from the fiber and did not depend solely on electrostatic interactions between the negatively charged sulfonic acid groups of PPD3 and the positively charged KKTK sequence on Ad5. Instead, the main driving force for the dendrimer interaction with Ad5 could be the distinct alternating patches of hydrophilic negative charges and hydrophobic propyl groups of PPD3.

Dendrimer-Coated Ad5 Inhibits Transduction Pathway Mediated by Blood Coagulation Factor X (FX). Factor X is a Vitamin K-dependent zymogen of the coagulation cascade. It is a serine endopeptidase, which is synthesized in the liver.

Trimers of the Ad5 hexon protein bind with nanomolar affinity to FX, forming 240 FX binding sites per virion.[10] Following intravenous (i.v.) administration of Ad5, viral particles predominantly accumulate in and transduce the liver in rodent and nonhuman primate models.[28-30] This is a major limitation for Ad5-mediated gene therapy in humans. *In vitro*, FX functions as “bridge receptor” that facilitates attachment of Ad5 to cells. The γ-carboxyglutamic acid domain of FX binds Ad5, and the serine protease domain of FX binds cell-surface heparan sulfate proteoglycan (HSPG).[10] Therefore, in agreement with previously published work,[10] addition of FX to cell culture media could significantly enhance the transduction efficiency of Ad5 (Figure 3.3a). Surprisingly, after mixing of FX with PPD3/ Ad5 complexes, no transduction enhancement was observed (Figure 3.3a), which suggested that PPD3 either occupied a similar binding site on Ad5 as FX or that it was bound to a site that could affect FX binding. In both cases, FX would be unable to enhance transduction of PPD3/Ad5 complexes. The results were corroborated by using superphysiological levels of FX, which are also unable to improve Ad5 transduction (data not shown). There is a competition between the PPD3−Ad5 and FX−Ad5 binding, which indicates that the FX and PPD3 sites are overlapping. FX is known to interact with the hexon capsomer; thus, it is very likely that PPD3 also binds to the hexon proteins. Since FX leads to liver transduction of Ad5 *in vivo*, using the PPD3 corona that replaces the FX corona holds promise for reducing liver toxicity and also to redirect Ad5-based gene delivery systems to other organs.

PPD3 Corona Protects Ad5 from Plasma Neutralization. To solve the challenge of FX-mediated sequestration of Ad vectors by hepatocytes, a number of strategies have been proposed including genetic modifications of the virus capsid to ablate FX-binding.[31] However, Xu et al. have previously reported that elimination of FX binding enabled Ad neutralization by natural antibodies and complement. In this case, the vector was quickly neutralized due to the lack of the shielding by FX bound to the virus capsid.[9] To analyze if PPD3 could shield the viruses from neutralizing natural antibodies and complement, we incubated the PPD3/Ad5 complex with the plasma from an Ad naïve human donor prior to transduction. The efficiencies, analyzed on SKOV-3 cells, did not decrease after plasma incubation (Figure 3.3b). In addition, we formed complexes between Ad5 vectors ablated for FX-binding (Ad5ΔFX) and PPD3 to demonstrate that PPD3 can prevent plasma neutralization even without FX binding. These complexes were incubated with human plasma. In the absence of PPD3, the vectors were completely neutralized by plasma (Figure 3.3c), while in the presence of PPD3, infectivity was preserved to a very large degree: PPD3 not only binds to FX-binding ablated vectors but also protects them

from natural antibodies and complement (Figure 3.3d), which is essential for *in vivo* applications.

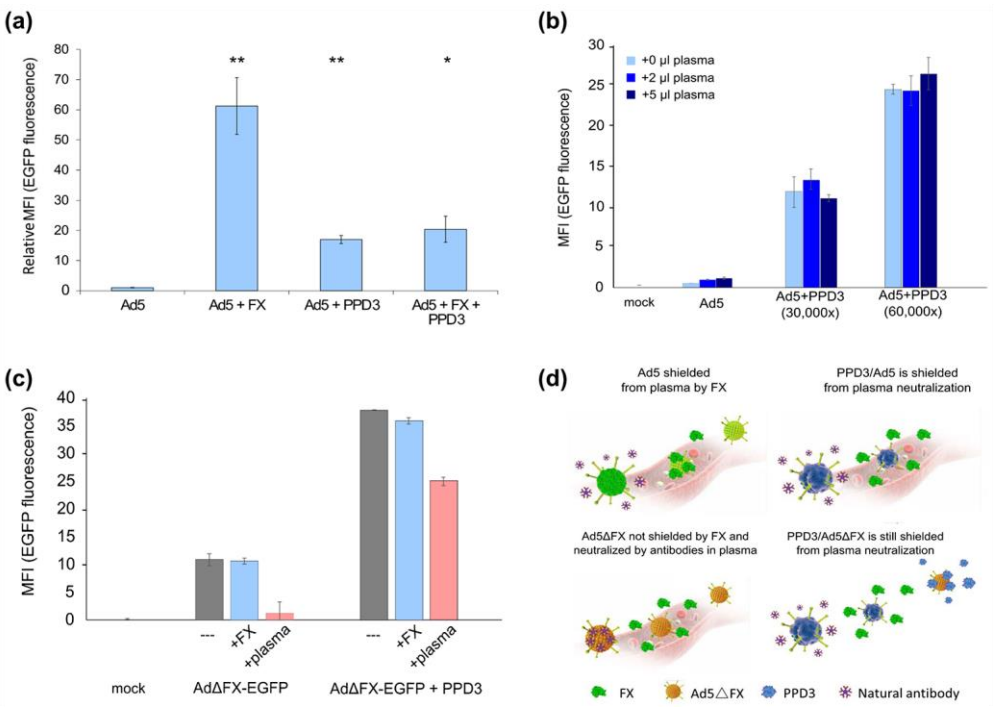

Figure 3.3. PPD3/Ad5 complexes exhibit increased transduction efficiency in human plasma and PPD3 protected FX-binding ablated capsids from neutralization by the IgM/complement pathway. (**a**) PPD3/Ad5 complexes were formed and SKOV-3 cells transduced (1000 pMOI) in the presence or absence of FX at its physiological concentration (8 µg/mL). While FX was expectedly able to significantly increase transduction of SKOV-3 cells, the transduction by PPD3/Ad5 complexes was not enhanced by FX, suggesting that PPD3/Ad5 complexes may not be able to bind FX. (**b**) PPD3/Ad5 complexes exhibited increased transduction of largely refractory SKOV-3 cells in the presence of human plasma of an Ad-naïve donor (1000 pMOI). (**c**) FX is known to shield Ad5 particles from attack by natural IgM antibodies and complement. A FX-binding ablated Ad5 vector, a preferable tool for gene transfer and oncolysis due to its significantly reduced hepatotropism, did not show enhanced transduction on SKOV-3 cells (1000 pMOI) but was expectedly neutralized after addition of 5 µL of plasma from an Ad-naïve donor. PPD3/Ad complexes at a molar excess of 30 000-times were largely resistant to neutralization, indicating that PPD3 can replace FX as a protective shield against IgM/complement. (**d**) Comparison of uncoated Ad5, PPD3/Ad5, Ad5ΔFX, and PPD3/Ad5ΔFX for their FX binding and subsequent neutralizing antibody binding. ∗ represents p-value ≤ 0.05, ∗∗ represents p-value ≤ 0.01.

PPD3 Corona Does Not Affect Wild Type Ad5 (wt Ad5) Activity and Ad5 Replication. The above experiments utilized a replication-defective adenoviral vector leaving it unclear whether PPDs would hamper the ability of the virus to replicate. Any negative impact on virus replication would disqualify PPD3/Ad5 complexes for oncolytic cancer treatment. Therefore, we analyzed the potential of PPD3/wt Ad5 complexes to lyse tumor cell lines. Since wt Ad5 lyses tumor cells, the cytotoxicity assay was used to evaluate the activity of wt Ad5 (Figure S3.6). The formation of complexes did, however, not inhibit virus replication, but increased lysis of SKOV-3 cells compared to wt Ad5 alone again made the PPD3/Ad5 complexes suitable tools for oncolytic virotherapy.

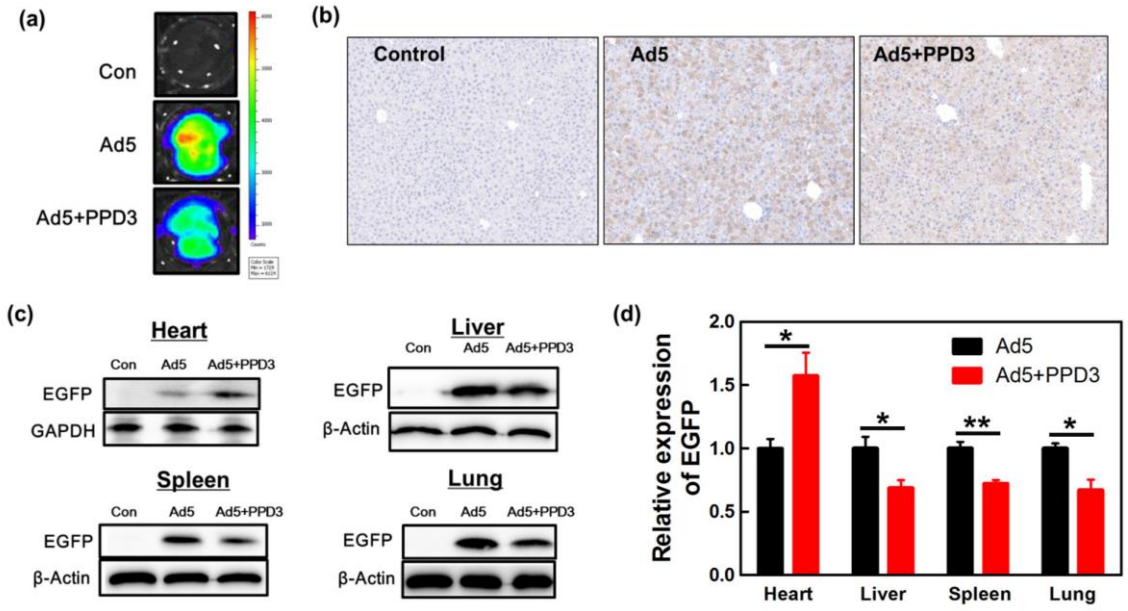

Figure 3.4. Decreased liver and improved heart transduction by PPD3/Ad5 complexes *in vivo*. (**a**) Fluorescence imaging of the whole mice liver. (**b**) Immunohistochemical analysis of liver tissue (10× magnification). The cell nucleus was stained by hematoxylin indicated in blue; EGFP was stained by antibodies and DAB (3,3′-diaminobenzidine) as depicted by yellow color. (**c**) Western blot of EGFP expression in heart, liver, spleen, and lung. (**d**) Quantification of relative EGFP expression in different organs based on Western blot. All data for PPD3/Ad5 are normalized to the corresponding EGFP expression with naked Ad5 (n = 3). ∗ represents p-value ≤ 0.05, ∗∗ represents p-value ≤ 0.01.

Decreased Liver Transduction and Improved Heart Transduction *in vivo*. PPD3/Ad5 complexes were injected into male C57BL/6J mice at the age of 9 weeks, and transduction was analyzed in different organs 14 days post injection. We speculated that PPD3/Ad5 complexes would exhibit reduced liver transduction compared to naked Ad5. Therefore, the EGFP expression level in liver was initially assessed by fluorescence imaging of the whole liver tissue (Figure 3.4a) to demonstrate Ad5-mediated transduction. In fact, EGFP expression in liver tissue was reduced by 40% as supported by immunohistochemical analysis of EGFP in hepatocytes (Figure 3.4b). Similar results were also seen by quantification of EGFP DNA in liver using real-time quantitative PCR (Figure S3.8). Noteworthy, the liver was found undamaged in both cases (Figure S3.9). In addition, EGFP expression was quantified in liver, heart, spleen, and lung by Western blot analysis (Figure 3.4c, d), which demonstrated decreased transduction of liver and spleen, and lung by about 40% compared to naked Ad5. Very surprisingly and importantly, PPD3/Ad5 complexes showed increased transduction of heart tissue by more than 40%.

Therapeutic Potential of Ad5 with Patchy Dendrimer Corona. PPDs with a defined surface patterning of amphiphilic groups was able to specifically bind to the Ad5 surface, altering the existing surface topology of Ad5 and imparting a synthetic dendrimer corona

providing different molecular recognition features (Figure 3.5a). In this way, the interaction of Ad5 with (a) its cellular CAR receptor, (b) plasma proteins, and (c) the coagulation factor X changes drastically. After PPD3 coating, the transduction mechanism of the PPD3 coated Ad5 becomes independent of naturally existing pathways such as CAR and FX, and it significantly prevents the immediate neutralization of the vector by the innate defense system composed of natural antibodies and complement. Firm evidence is provided that upon PPD3 binding, the conventional cellular uptake of Ad5 *via* CAR is changed, thus opening a different, still unknown pathway. This furnishes three significant advantages providing potential therapeutic opportunities. First, the complexes can traffic into CAR negative cells, which is not possible for Ad5 and Ad5/FX. This is highly attractive as many cancer or stem cells do not express CAR, and therefore, these cells cannot not be transduced by Ad5. Therefore, PPD3 holds great promise to widen the therapeutic options of Ad5 as depicted in Figure 3.5b.

Second, the interaction of Ad5 with serum proteins is altered. Intravenous delivery of adenovirus vectors requires that Ad5 is not inactivated in the bloodstream, and serum neutralizing activity is well documented for Ad5. In the case of Ad5 with PPD3 corona, serum proteins even boost gene transduction, which represents an essential feature for *in vivo* applications.

Third, PPD3 binding has a strong impact on Ad5 interactions with FX as both PPD3 and FX seem to compete for the same site at the surface of Ad5, and FX does not affect the transduction efficiency of preformed PPD3 coated Ad5.

Fourth, intravenous (i.v.) administration of Ad5 predominantly leads to accumulation of viral particles in the liver, and transduction occurs mainly in the liver. Therefore, several studies have been performed that document the role of blood coagulation FX in mediating liver gene transfer *in vivo* and the mechanism underlying Ad5 hepatocyte transduction[10, 14, 15, 32, 33] by FX binding to the hexon protein of Ad5 at high affinity (~2 nM), thus mediating hepatocyte transduction in mice and rats.[10] In this way, gene therapy to other organs has been greatly limited, which can be addressed and improved by Ad5 with PPD3 corona (Figure 3.5b). Our *in vivo* studies proved that the PPD3 corona significantly reduced the Ad5-mediated transduction indicated by EGFP expression in the liver by about 40% but increase the transduction in the heart by more than 40% in comparison to naked Ad5. There is, thus, evidence that the PPD3 corona imparts a different biorecognition profile for Ad5, which alters the Ad5 tropism *in vivo*.

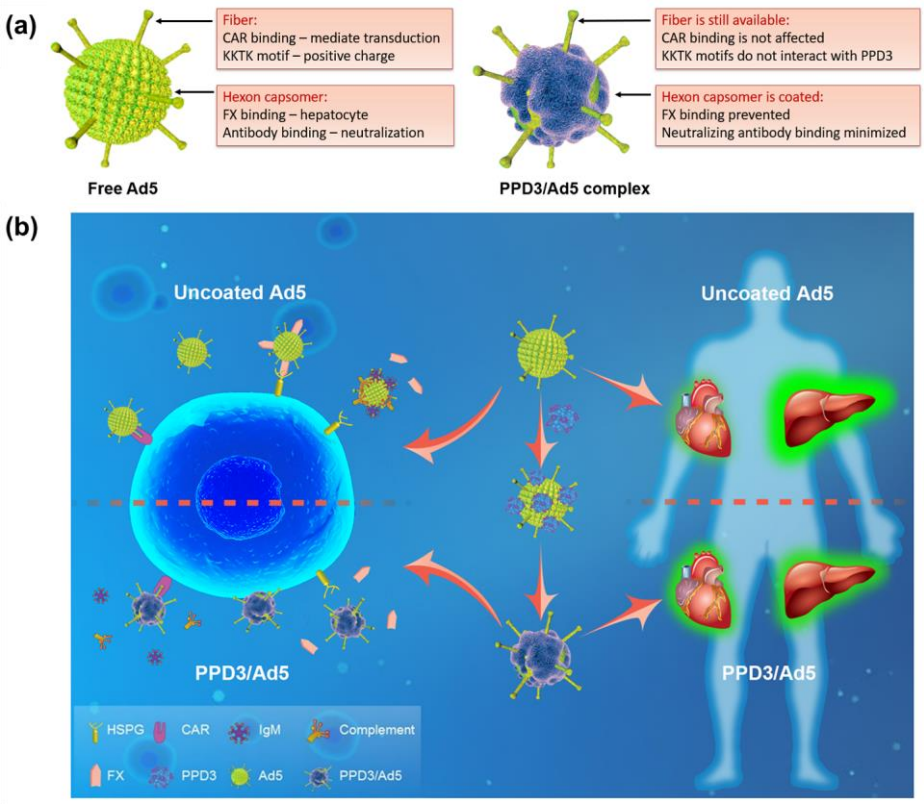

Figure 3.5. Schematic overview of the features of Ad5 with PPD3 corona. (**a**) Comparison of uncoated Ad5 and PPD3/Ad5 complex. CAR binding site and KKTK motif present on the fiber of naked Ad5, while FX and natural antibodies bind to the hexon. PPD3 forms a protein-mimicking corona on the virus capsid to prevent FX binding and vector neutralization. (**b**) Summary and visualization of PPD3 binding with Ad5, highlighting the impact of the PPD3 corona on cell Ad5 uptake processes and *in vivo* distribution (the figure is designed by the graphic designer Weihang Zhao and permission to use is granted).

3.3 Conclusions

Our results demonstrate that rationally synthesized amphiphilic surface patterns of three-dimensional macromolecules play a critical role for their biological recognition and interaction with Ad5. The opportunity to remodel the virus surface by precise molecular and supramolecular design provides control over virus−host interactions.

Redirecting Ad5 tropism has been achieved by genetic engineering of Ad5. However, PPDs with defined amphiphilic patches provide a versatile strategy to modify the Ad5 surface and to reengineer Ad5 biodistribution. On the basis of this, one could further advance Ad5-based gene therapy toward higher tissue/organ specificity. Although the reason why the PPD3 complexes target the heart is still unknown, it is envisioned that by synthesizing PPDs with different tissue targeting moieties, tissue distribution of PPD/Ad5 complexes will be controlled by rational design. Therefore, we shall attach further tissue specific targeting groups to PPD structures to redirect Ad5 transduction to

other organs. This will ultimately regulate the trafficking and cell uptake of viruses *in vivo*, one of the holey grails in gene therapy. Moreover, the concept of a bioactive protein-mimicking polymer corona could allow designing improved nanoparticle therapeutics to control their *in vivo* distribution, which is still one of the major challenges in nanomedicine.

3.4 Acknowledgements

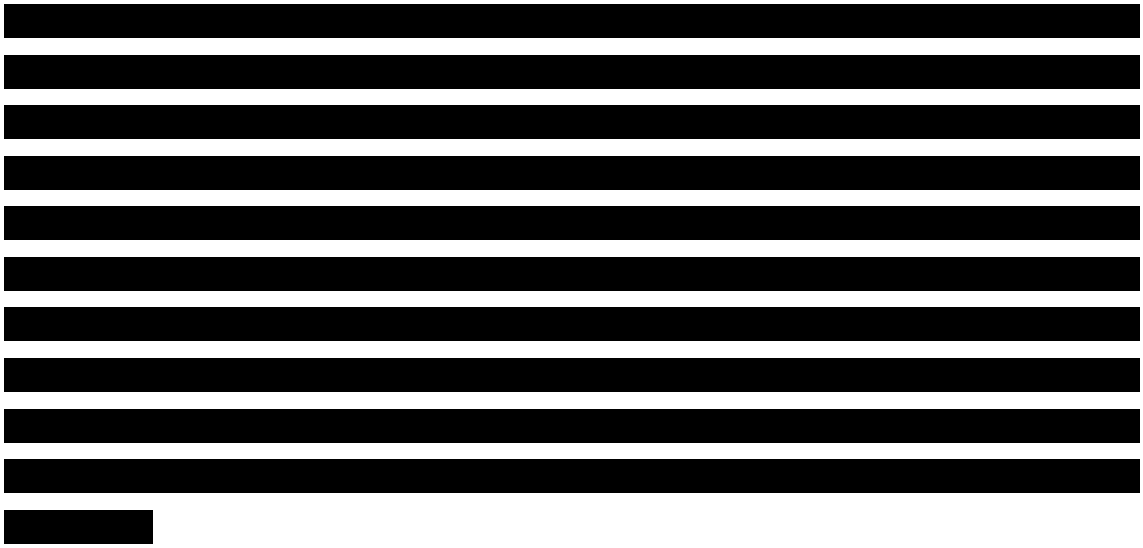

3.5 Methods

Complex Formation of Ad5 and PPD3. Complex formation of Ad5 and PPD3 was performed in 50 µL of phosphate buffered saline (PBS). This volume contained 5×10^9 Ad5 virus particles (VP) that resulted in a concentration of 10^8 Ad5 particles per µL (the concentration of Ad5 was quantified by measuring the absorbance at 260 nm and converted to number of particles with the equation: concentration (VP/mL) = $OD_{260} \times 1.1 \times 10^{12}$). PPD3 was added in defined ratios (if not otherwise mentioned, ratio of 1:10 000 was used in the experiments). The volume needed of the PPD3 stock solution (c = 1 mg/mL, solved in DMSO) was calculated according to the following formula (N, number of particles; r, ratio between PPD3 and Ad5; M, molecular weight of PPD3; V, volume; N_A, Avogadro constant; c, concentration):

$$\mathrm{V(PPD3)} = \frac{\mathrm{N\ (VP)} \times \mathrm{r} \times \mathrm{M(PPD3)}}{\mathrm{N_A} \times \mathrm{c(PPD3\ stock)}}$$

This is a calculation example for a PPD3/Ad5 ratio of 1:10 000:

$$\mathrm{V(PPD3)} = \frac{5 \times 10^9\ \mathrm{VP} \times 10{,}000 \times 9766\mathrm{g/mol}}{6.02 \times 10^{23} \times 1\ \mathrm{g/L}} = 0.8\ \mu\mathrm{L}$$

In this sample with a PPD3/Ad5 ratio of 1:10 000, 0.8 µL of the PPD3 stock solution was added to Ad5 particles and filled up with PBS to a volume of 50 µL. Before usage of PPD3, the stock solution was incubated in the sonicator for ~30 min to dissolve assembled molecules because after some storage time, PPD3 molecules tend to self-assemble. After mixing the solutions, they were incubated for 20 min at room temperature (RT) and were then used in experiments (Figure S3.1). Depending on the experiment settings, the procedure of complex formation was slightly adjusted as noted in the particular case.

The same procedure was performed with dendrimers PPD1, PPD2, and PPD3.

Experimental Protocol for Transduction Assay. For transduction assays, 96-well plates were used containing 2×10^4 cells per well, which were seeded the day before transduction. Cells were infected with pMOI 1000 unless otherwise specified and incubated for 24 h (CAR positive cell lines such as A549 cells, Hela cells, and MDCK2 cells) or 72 h (CAR negative cell lines such as SKOV-3 cells, CHO-K1 cells, and PTK1 cells) at 37 °C. EGFP positive cells and the overall mean fluorescence intensity (MFI) of EGFP expression was measured by flow cytometry.

PPD3/Ad5 Transduction of CAR Positive and CAR Negative Cells. Hela and MDCK-2 cells were maintained in MEM (minimum essential medium) (Gibco) supplemented with 10% heat inactivated FCS, 1% L-glutamine, and 1% penicillin/streptomycin. CHO-K1 cells were maintained in F-12 Nut Mix (HAM) 1X (Gibco) supplemented with 10% heat inactivated FCS and 1% penicillin/streptomycin. PTK1 cells were maintained in DMEM supplemented with 10% heat inactivated FCS, 1% glutamine, and 1% penicillin/streptomycin. All the cells were maintained at 37 °C under 5% CO_2. Then 50 µL of dendrimers and Ad5 solutions were left to equilibrate for 1 h at 37 °C and then added to 1 mL of medium in a 12-well flat bottom plate containing 10^5 cells (MOI = 10−100) for 24−48 h at 37 °C with medium supplemented with 2% of FCS. The same experimental conditions were used in other cell lines. The cells were harvested 24−48 h post-transduction, fixed in 1% paraformaldehyde, stored at 4 °C in PBS, and protected from light. The fraction of infected cells was quantified by flow cytometry, which measured GFP signal of infected cells. The sample acquisitions were performed with FACSCalibur

(BD Biosciences; USA), and 10 000 events were acquired for each sample. Untreated cells were set as negative control. Each experiment was performed in triplicate, and the data were analyzed from two independent experiments.

Animal Experiment and Bioluminescence Imaging. All animal studies were performed in compliance with protocols that had been approved by the Hubei Provincial Animal Care and Use Committee and the experimental guidelines of the Animal Experimentation Ethics Committee of Huazhong University of Science and Technology. Male C57BL/6J mice (purchased from China Three Gorges University) at the age of 9 weeks were used for *in vivo* experiments. All mice were housed in a specific pathogen-free facility. All mouse experiments were performed in compliance with institutional guidelines and according to the protocol approved by the Institutional Animal Care and Use Committee of Huazhong University of Science and Technology. The mice were divided into three groups: control group (3 mice), Ad5 group (6 mice), and Ad5+PPD3 group (6 mice). Ad5 (2×10^{10} VP) or Ad5 incubation with PPD3 (Ad5/PPD3 = 1:10 000, after 20 min) in 200 μL of PBS were administered *via* tail vein injection. After 2 weeks, all animals were killed. Then the hearts, livers, spleens, lungs, kidneys, and brains were harvested, and EGFP expression in the organs was visualized by bioluminescence imaging at 488 nm/507 nm (excitation/ emission). After that, half of the organs were cryopreserved at −80 °C, and half were fixed with fixative (4% formaldehyde, 50% ethyl alcohol, 2% acetic acid).

Western Blot Assay. All organs were ground, and whole proteins were extracted with lysis buffer (50 mM HEPES, pH 7.4, containing 150 mM NaCl, 1% Triton X-100, 0.4% SDS, protease inhibitor cocktail). Protein concentrations were determined by the bicinchoninic acid (BCA) protein assay kit. Samples were heated to 100 °C for 10 min in loading buffer with SDS and β-mercaptoethanol, run on 12% SDS-PAGE gels in electrophoresis buffer (25 mmol/L Tris, 250 mmol/L glycine, 0.1% SDS), and transferred to PVDF membranes. All blots were blocked in 5% skim milk in TBST (100 mM Tris−HCl pH 7.5, 150 mM NaCl, 0.1% Tween20) at room temperature for 1 h.

Membranes were probed with rabbit anti-EGFP, anti-GAPDH, or antiβ-actin (primary antibodies were used at a dilution of 1:4000 in 5% bovine serum albumin (BSA)−TBST). The HRP-linked secondary antibody was diluted 1:2000 in 5% milk−TBST and incubation at room temperature for 1 h. The blots were visualized using an ECL detection system.

Immunohistochemistry. Organs were fixed with formaldehyde and embedded in paraffin. For immunohistochemistry, thin sections of the embedded tissues were then

blocked with 5% BSA for 2 h at room temperature and incubated with anti-EGFP (1:200) at 4 °C overnight. After washing for 15 min, the sections were incubated with biotinconjugated secondary antibody for 30 min and further incubated with a solution of DAB. The sections were then dehydrated in ascending grades of ethyl alcohol, cleared with xylene, and covered with a coverslip.

Statistical Analysis. For statistical evaluation of the data, Microsoft Office Excel was used. The analysis included calculation of the mean value and the standard deviation. To compare, for example, different cell lines, relative values were computed. To analyze the data's statistical significance, p-values were calculated with the TTEST-function (student's t test) of Excel. P-values ≤ 0.05 were regarded as significant and labelled in graphs with one asterisk (∗). Data points with two asterisks indicated p-values ≤ 0.01 and three asterisks p-values ≤ 0.001. P-values of data points, which were regarded as significant, were also provided in brackets in the text where these data were analyzed and were marked with "p". Samples of all experiments were analyzed in triplicates. In the caption of the graphs, this is referred to as sample number (n).

3.6 Supporting Information

3.6.1 Materials, instruments, and animals

Chemicals were purchased from Sigma Aldrich unless otherwise stated. Cell lines were obtained from ATCC unless otherwise specified.

^{1}H and ^{13}C NMR spectra were recorded on Bruker AMX250, AC300, AMX500, and AMX700 NMR spectrometers using the residual proton or the carbon signal of the deuterated solvent as an internal standard. MALDI-TOF mass spectra were measured using a Bruker Reflex II, which was calibrated against poly(ethylene glycol) (3000 g/mol). Samples for MALDI-TOF MS were prepared by mixing the analyte with the matrix (dithranol) in THF in a ratio of 1:50. In some cases, cationization by mixing the matrix with potassium trifluoroacetate (K) or silver trifluoroacetate (Ag) was performed. All reported MALDI-TOF MS measurements were within the experimental error, characteristic for the applied technique. Flow cytometry was performed with a Beckman-Coulter Gallios 3L10C instrument.

For *in vivo* studies, C57BL/6J mice were purchased from China Three Gorges University. Bicinchoninic acid (BCA) protein assay kit was purchased from Suzhou Comin Biotechnology. The enhanced chemiluminescence (ECL) kit and PVDF membrane were purchased from Millipore. Antibodies against EGFP, *β*-Actin, GAPDH and secondary antibody were all obtained from Cell Signaling Technology. Western blots were scanned and bands quantified using Tanon-5500 Chemiluminescent Imaging System.

3.6.2 General procedure for the synthesis of polyphenylene dendrimers (PPDs)

All dendrimers were synthesized by previously reported procedures.[18, 19]

PPD 1 was recovered as a faint yellow solid in 71% yield. ^{1}H NMR (300 MHz, CD_2Cl_2, 298 K, *δ*): 0.75-0.90 (12H, t), 1.45-1.60 (8H, m), 2.35-2.40 (8H, t), 6.95-7.05 (8 H, m), 7.15-7.30 (32 H, m), 7.40-7.50 (32 H, m), and 7.70-7.85 (10H, m) ppm. ^{13}C NMR (75 MHz, CD_2Cl_2, 298 K, *δ*): 13.7, 16.2, 23.3, 25.2, 32.4, 38.3, 121.5-144.1, and 148.2 ppm. MALDI – MS found [M/Z] = 2210.91 g/mol with theoretical [M/Z] = 2210.45 g/mol.

PPD 2 was recovered as a faint yellow solid in 59% yield. ^{1}H NMR (300 MHz, CD_2Cl_2, 298 K, *δ*): 0.80-0.90 (24 H, t), 1.50-1.60 (16H, m), 2.40-2.45 (16H, t), and 7.05-7.75 (234

H, s) ppm. ^{13}C NMR (75 MHz, CD_2Cl_2, 298 K, *δ*): 13.7, 16.2, 24.1, 25.5, 36.5, 119.6-143.2, and 147.1 ppm. MALDI – MS found [M/Z] = 5745.12 g/mol with theoretical [M/Z] = 5744.14 g/mol.

PPD 3 was achieved in 63% yield as a yellow solid. ^{1}H NMR (300 MHz, CD_2Cl_2, 298 K, *δ*): 0.70-0.85 (48 H, m), 1.45-1.60 (32H, m), 2.35-2.50 (32H, m), and 7.10-7.80 (378 H, m) ppm. ^{13}C NMR (75 MHz, CD_2Cl_2, 298 K, *δ*): 13.7, 24.1, 37.6, 121.1-143.4, and 151.2 ppm. MALDI – MS found [M/Z] = 9767.15 g/mol. with theoretical [M/Z] = 9766.23 g/mol.

PPD 4 was recovered as a yellow solid in 69% yield. ^{1}H NMR (300 MHz, CD_2Cl_2, 298 K, *δ*): 7.15 - 7.90 (306 H, d) ppm. ^{13}C NMR (75 MHz, CD_2Cl_2, 298 K, *δ*): 121.1-145.2, 146.5, 148.2, 149.1, and 152.3 ppm. MALDI – MS found [M/Z] = 7265.03 g/mol with theoretical [M/Z] = 7264.32 g/mol.

3.6.3 Ad5-based vectors

Virus vectors were prepared according to standard protocols[34] and stored at –80 ℃. All vectors were purified by double CsCl banding and subsequent desalting by PD-10 columns (GE Healthcare). Vectors were stored in 50 mM HEPES, pH 7.5, 150 mM NaCl, 10% glycerol. Vector titers were determined by OD260.[34] Vector purity was confirmed by SDS-PAGE and silver staining.

3.6.4 Characterization of PPD/Ad5 interaction

Light scattering

Light scattering was used to determine interaction between Ad5 and PPD 3 by means of measuring the polydispersity index (PDI) and the hydrodynamic diameter of the particles in case of a monodisperse suspension. A monodisperse suspension was characterized by a PDI ≤ 0.2 and a polydisperse suspension by a PDI ≥ 0.2. Complex formation was performed in a volume of 1 mL PBS with 10^{11} Ad5 particles. PPD 3 was added in defined ratios to Ad5, then mixed and incubated for 10 min. After transfer to a cuvette, it was filled up with PBS to a total volume of 2 mL. All samples were tested for an appropriate scattering intensity before measurement (at least 5×10^4) and measured at an angle θ = 90°. For intensive cleaning of the cuvette, ethanol and acetone was used to avoid measurement errors by dust particles.

Table S3.1. Light scattering measurement of the complex formation with PPD and Ad5.

Sample		Only Ad5	PPD:Ad5 100:1	PPD:Ad5 200:1	PPD:Ad5 1000:1	PPD:Ad5 10,000:1
PPD(P16S16)	HD[1]	108 nm	205 nm	275 nm	729 nm	--
+ Ad5	PI[1]	0.03	0.12	0.01	0.17	--
PPD(P0S16)	HD[1]	--	108 nm	--	109 nm	110 nm
+ Ad5	PI[2]	--	0.10	--	0.09	0.03

[1]HD = Hydrodynamic Diameter.

[2]PDI = Polydispersity Index. When PDI < 0.2, the complex was considered as monodisperse.

Transmission electron microscopy (TEM)

For each sample, complex formation with different ratio of PPD 3 was prepared. The following procedure was performed similarly to Chen et al.[35] The incubation mixtures were incubated for 10 min and immediately one grid per sample was coated with 20 µL (2×10^9 Ad5 particles complexed with PPD 3) of the particular incubation mixture. Afterwards, samples were stained with 20 µL of 2% phosphotungstic acid (PTA) solution and incubated for 3 min. Grids were dried overnight and analyzed with Jeol JEM-1400 TEM after 24 h.

3.6.5 Investigation of PPD/Ad5 transfection with different cell lines

General experimental protocol for transduction assay

For transduction assays, 96 well plates were used containing 2×10^4 cells per well, which were seeded as before. Cells were infected with pMOI 1000 unless otherwise specified and incubated for 24 h (CAR positive cell lines such as A549 cells, Hela cells and MDCK-2 cells) or 72 h (CAR negative cell lines, such as SKOV-3 cells, CHO-K1 cells and PTK1 cells) at 37 °C. EGFP positive cells and the overall mean fluorescence intensity (MFI) of EGFP expression was measured with flow cytometry.

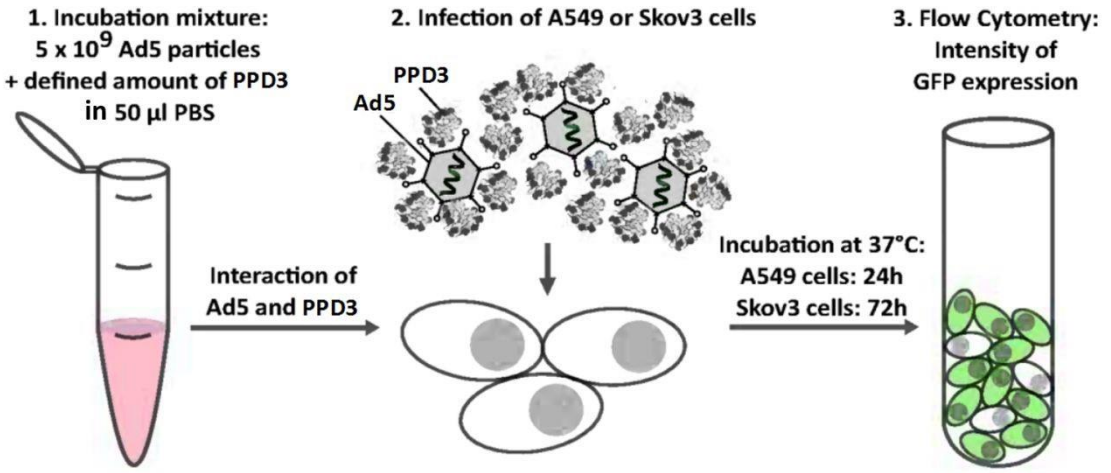

Figure S3.1. Infection Assay using Ad5 and defined concentrations of PPD3. Three steps are involved in the procedure. First, an incubation mixture was prepared with 5×10^9 Ad5 particles, a defined concentration of PPD3 and filled up to a volume of 50 μL with PBS. Second, cells were infected with Ad5 that had interacted with PPD3. And finally, after an incubation time according to the cell type the overall intensity of EGFP expression was measured with flow cytometry.

General gating strategy for flow cytometry

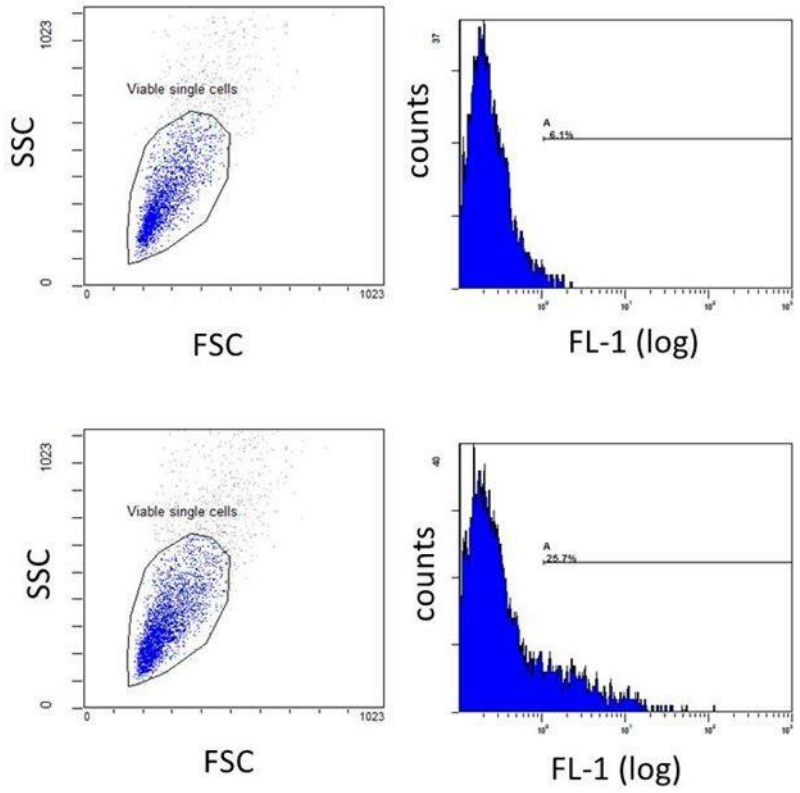

Figure S3.2. Example of gating strategy used for flow cytometry. The live single cells were gated according to their FSC/SSC profile (left panel), and the mean fluorescence intensity in channel FL-1 (FITC) was measured. The upper panel exemplarily shows the results after transduction of SKOV-3 cells with vector only, the lower panel after incubation of the vector with PPD-3.

Preformed PPD3/Ad5 complexes are essential for increased transduction.

The PPD3 and Ad5 was pre-incubated at different times and the transduction efficiencies were tested (Figure S3.3). Within 20 min, the transduction efficiency increased according to the increasing of PPD3/Ad5 pre-incubation time.

Prolonging the incubation time by more than 20 min resulted in no additional increase in transduction efficiency. Thus, the 20 min pre-incubation is optimal for sufficient complex formation, and this condition has also been applied in the following experiments. To further prove that the complex formation by preincubating PPD3 and Ad5 together is essential, PPD3 and Ad5 were added to SKOV-3 cells by various application procedures. Figure S3.3 depicts the efficiencies after three different treatment protocols. Pre-incubation of PPD3 and Ad5 for 20 min before addition of the complexes to cell culture yielded about an eight times higher transduction efficacy. When Ad5 was first added to SKOV3 cells and could interact with the cell membrane receptors, followed by the removal of excess Ad5 in solution by washing with PBS buffer and subsequent addition of PPD3, there was no increase in transduction efficiency compared with the Ad5 control experiment. This finding indicates the inability of the dendrimers to complex the virus once it is already attached to the cellular membrane (Figure S3.3). When PPD3 was first added to SKOV-3 cells, allowing to accumulate at the cellular membrane and removing excess PPD3 before Ad5 was added to the cells, again, no transduction enhancement was detected (Figure S3.3). This experiment suggests that only pre-formed the PPD3/Ad5 complexes are able to significantly enhance Ad5 uptake and transduction efficiency.

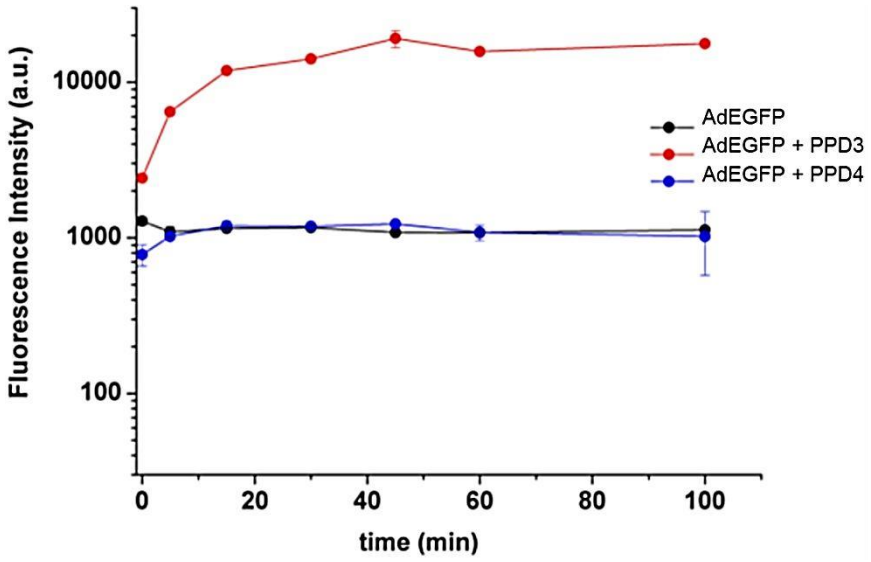

Figure S3.3. The influence of PPD and Ad5 pre-incubation time to the EGFP expression in CHO-K1 cells (n = 3). 500 pMOI Ad5 was used in the experiment.

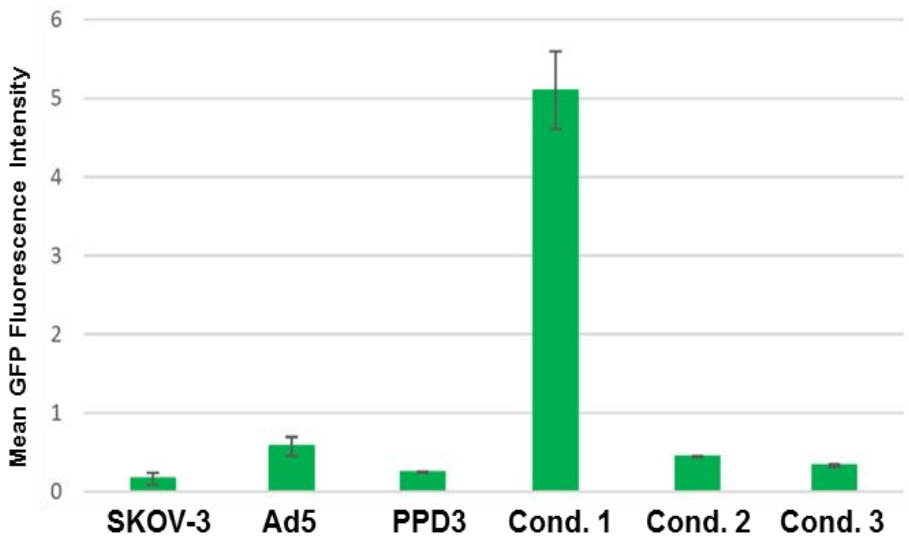

Figure S3.4. Ad5 transduction assay showed that PPD3/Ad5 complex formation is essential for enhancing transduction. Cond. 1: PPD3 pre-incubated with Ad5 for complex formation before adding to SKOV-3 cells. Cond. 2: Ad5 incubated with cells for 1 h and removed before adding PPD3. Cond. 3: PPD3 incubated with cells for 1 h and removed before adding Ad5. The cells were then incubated for 24 h for all three conditions and the EGFP expressing was analyzed by flow cytometer to evaluate the transfection efficiency.

PPD3/Ad5 transduction to different CAR positive and CAR negative cells

Hela and MDCK-2 cells were maintained in MEM (Minimum Essential Medium) (Gibco®) supplemented with 10% heat inactivated fetal calf serum (FCS), 1% L-glutamine and 1% Penicillin/Streptomycin. CHO-K1 cells were maintained in F-12 Nut Mix (HAM) 1X (Gibco®) supplemented with 10% heat inactivated FCS, 1% Penicillin/Streptomycin. PTK1 cells were maintained in DMEM supplemented with 10% heat inactivated FCS, 1%

glutamine, 1% Penicillin/Streptomycin. All the cells were maintained at 37 °C under 5% CO_2.

50 μL of dendrimers and Ad5 solutions were left equilibrate for 1 h at 37 °C and the added to 1 mL of medium in a 12-well flat bottom plate containing 10^5 cells (MOI = 10–100) for 24–48 h at 37 °C with medium supplemented with 2% of FCS. The same experimental conditions were used in other cell lines. The cells were harvested 24–48 h post-transduction, fixed in 1% paraformaldehyde, stored at 4 °C in PBS and protected from light. The fraction of infected cells was quantified by Fluorescence-Activated Cell Sorting (FACS), measuring GFP signal of infected cells. The sample acquisitions were performed with, FACSCalibur (BD Biosciences; USA) and 10^4 events were acquired for each sample. Untreated cells were set as negative control. Each experiment was performed in triplicate and the data were analyzed from two independent experiments.

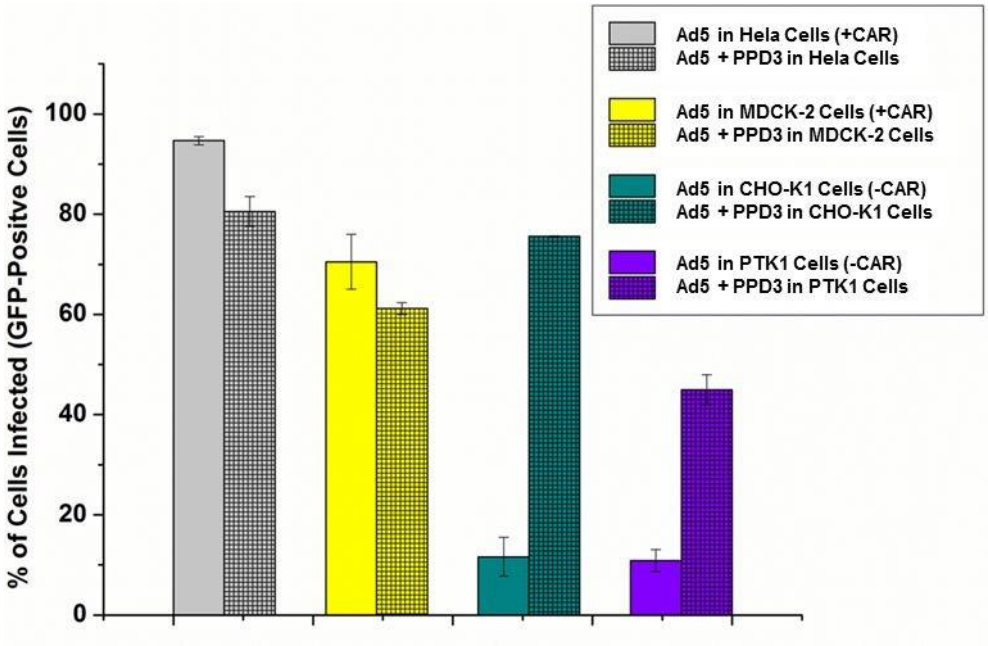

Figure S3.5. PPD3/Ad5 transduction efficiency in different (+)CAR and (-)CAR cell lines. Infectivity of Ad5 virus is expressed in % of infected cells (GFPPositive Cells). Different cell lines were tested with Ad5 with and without preincubation with PPD3 dendrimers at 10^{-7} M. Grey and yellow bars represent the % of infected cells in CAR receptor cell lines (+CAR). Cyan bars and violet bars represent the % of infected cells in a CAR negative receptor cell lines (-CAR). Grey bar represent the % of infected Hela cells (+CAR) after 48 h post-infection. Hela cells were infected with Ad5 (MOI = 10) with and without PPD3 at 10^{-7} M. Yellow bars represent the % of infected MDCK-2 (+CAR) cells after 48 h postinfection of Ad5 (MOI = 10) with and without PPD3 at 10^{-7} M. Cyan bars represent the % of infected CHO-K1 (-CAR) cells after 48 h post-infection of Ad5 (MOI = 100) with and without PPD3 at 10^{-7} M. Violet bars represent the % of infected PTK1 (-CAR) cells after 48 h post-infection of Ad5 (MOI = 10) with and without PPD3 at 10^{-7} M. Ad5 with/without PPD3 were pre-incubated 1 h at 37 °C 5% of CO_2. These experimental conditions were applied to all cell lines. The experiments were performed in duplicate. The error bars present the standard deviation.

3.6.6 Testing the wide type Ad5 (wtAd5) activity when complexed with PPD3

In this experiment we used replication-competent wild-type viruses instead of replication-defective vectors. Upon entry the viruses replicated in the cells, specific particles were formed and the cells were lysed. Therefore, to study cell viability after treatment with wtAd5, the CellTiter-Glo (Luminescent Cell Viability Assay by Promega) was applied. In brief, metabolic activity of the cells was measured *via* the ATP content according to the manufacturer's instructions. After cell lysis, the ATP amount measured decreased, indicating successful virus replication and release of progeny virions. As shown in the figure below, SKOV-3 cells were hardly lysed by Ad5 due to the fact that the virus did not efficiently enter the cells. After incubation with PPD3, however, more virus particles entered the cells and the cells could be lysed by replicating virus.

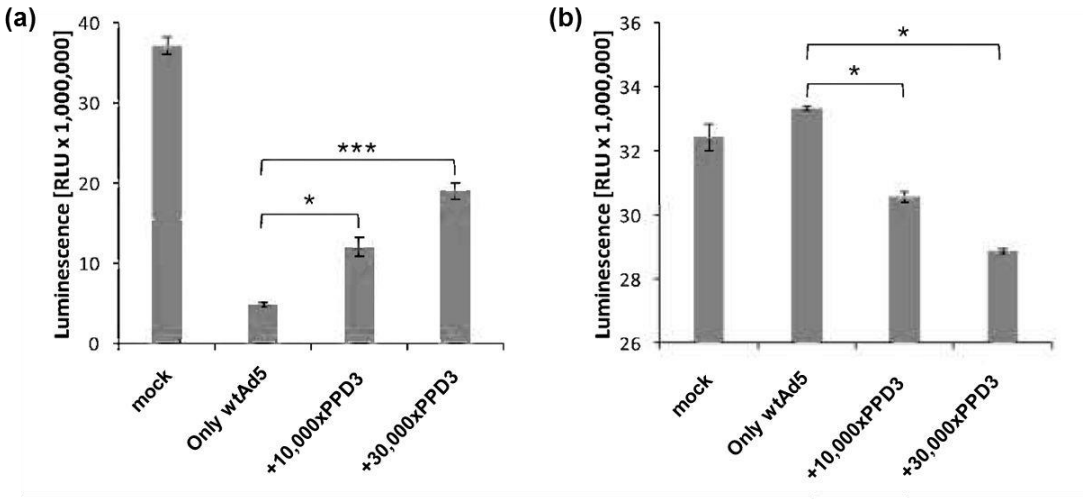

Figure S3.6. Wild type Ad5 activity when complexes with PPD3. (**a**) A549 cells were infected with MOI 1000 with and without PPD3 for 72 h. (**b**) SKOV-3 cells were infected with MOI 3000 with and without PPD3 for 72 h. The luminescence result (in relative light units (RLU)) represents cell viability (n = 3). * represents p-value ≤ 0.05, *** represents p-value ≤ 0.001.

3.6.7 Stability of PPD3/Ad5 complex in serum

CHO-K1 cells were used for these experiments. Firstly, Ad5 was pre-incubated with different concentrations of PPD3 for 20 min. Then, incubation was performed in FCS at 25 °C for 20 min (as a positive control), 4 °C for 48 h, 37 °C for 1hr or 37 °C for 48 h. Thereafter, Ad5 or PPD3/Ad5 were added into 24 well plates, which were seeded with CHO-K1 cells (the pMOI is 1000). All further steps were performed as described in section 5.1. After incubating of the PPD3/Ad5 complexes in FCS at 4 °C for 48 h or at

37 °C for 1 h, there was no significant reduction in their transduction efficiency. These results indicate that PPD3/Ad5 complexes remain stable in FCS.

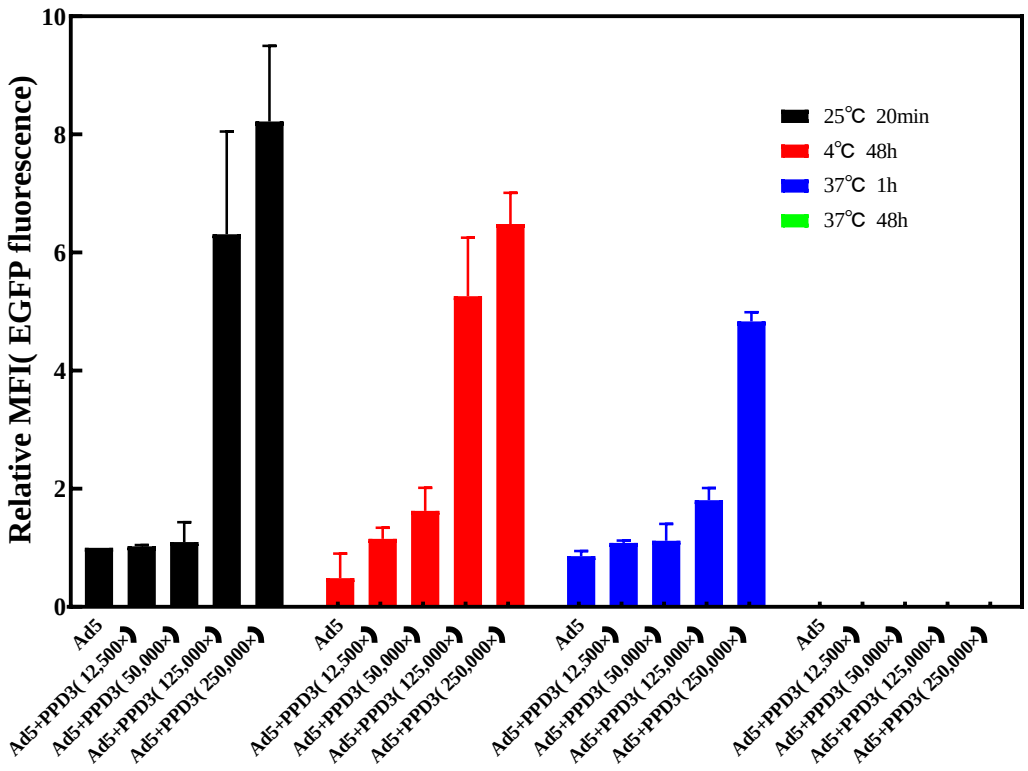

Figure S3.7. The stability of PPD3/Ad5 complex in FCS. Black columns represent the condition of 25 °C for 20 min, red columns represent 4 °C for 48 h and blue columns represent 37 °C for 1 h and green columns represent 37 °C for 48 h (the columns are so low that they do not appear in the diagram) (n = 3).

3.6.8 Real-time quantitative PCR (qPCR) analysis

We extracted the DNA of mice livers after 7 days and 14 days with TIANamp Genomic DNA Kit (DP304, Tiangen Biotech (Beijing), China). Then EGFP DNA level in livers was quantified by real-time quantitative PCR *via* StepOne Plus (Life Technologies, USA). 10 *μ*L of SYBR Green mixture (FastSYBR Mixture, CW2622M, CWBIO (Beijing), China), 0.4 *μ*L of 10 pmol/*μ*L primer forward and reverse (for EGFP: forward 5'-TTCAAGGACGACGGCAACTACAAG-3'; reverse 5'-GAACTCCAGCAGGACCATGTGATC-3'; for murine *β*-actin: forward 5'-ATCACTATTGGCAACGAGCGGTTC-3'; reverse 5'CAGCACTGTGTTGGCA TAGAGGTC-3'), 0.4 *μ*L 50×high Rox and 2 *μ*L sample were mixed in a final volume of 20 *μ*L. The results were consistent with western blot. We also observed significantly decrease of EGFP DNA in liver when mice were infected by PPD3/Ad5 complex instead of raw Ad5.

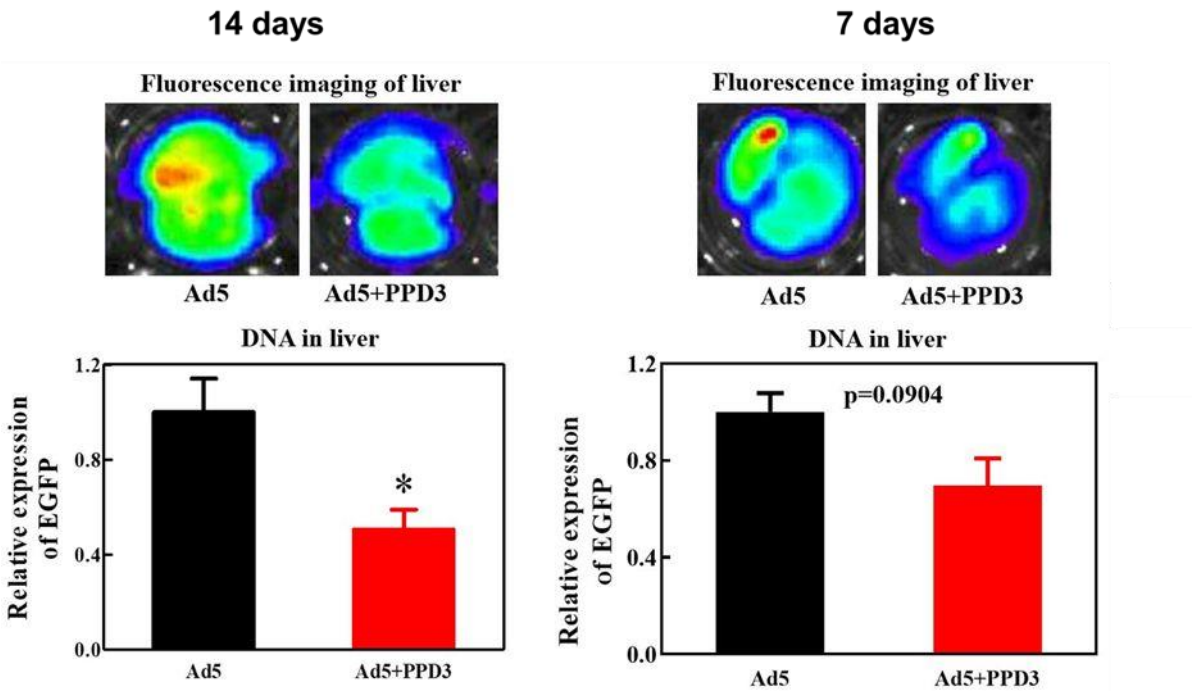

Figure S3.8. Quantification of EGFP DNA levels in the liver with qPCR (n = 3) after 7 days and 14 days. * represents p-value ≤ 0.05.

3.6.9 Hematoxylin and eosin staining:

For hematoxylin and eosin staining, thin sections of the embedded tissues were then stained with hematoxylin and eosin. After staining, the sections were dehydrated in ascending grades of ethyl alcohol, cleared with xylene, and covered with a coverslip.

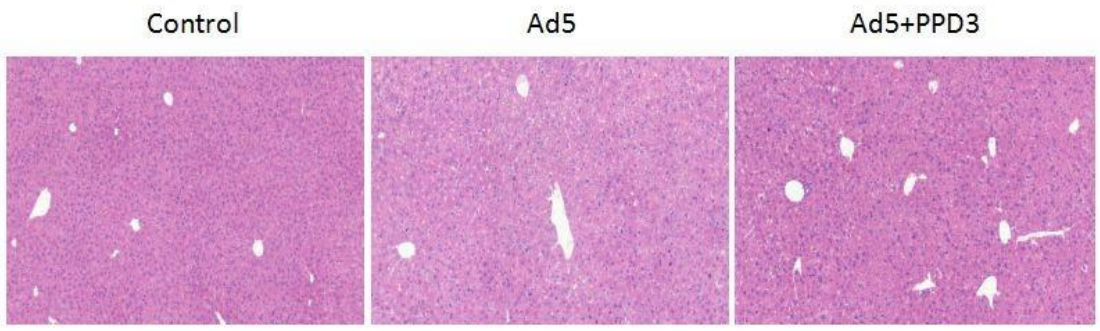

Figure S3.9. Hematoxylin and eosin (H&E) staining of liver tissues (10 time of magnification).

3.6.10 Kinetic binding analysis

The interaction between PPD3 and Ad5 was studied by Bio-Layer Interferometry assays (BLI) from Octet96 (Pall ForteBio, CA, USA). In order to receive a significant signal for this binding event, we immobilized PPD3 dendrons at the sensor surface and applied Ad5 as binding molecule. To immobilize PPD at the surface of streptavidin-coated biosensors, we used a biotinylated dendrimer branch of PPD3 with the same surface structure. The basic experiment contains four steps: Step 1: Hydration of the biosensor to record the baseline. Step 2: Immobilization of PPD3 dendrons on the streptavidin (SA) biosensor. Step 3: Washing and establishing the baseline. Step 4: Association of the Ad5. Step 5: Dissociation (Figure S3.10).

A significant interaction signal was seen even in the presence of only 2 pM Ad5. The K_D (equilibrium dissociation constant) determined by this method is 1.27×10^{-12} M. We believe that this very strong binding could be a result of multivalent interactions between the large virus particles providing large numbers of binding sites and the sensor surface densely coated with PPD3 dendrons. These results clearly support that there is a strong binding between PPD3 and Ad5 viruses.

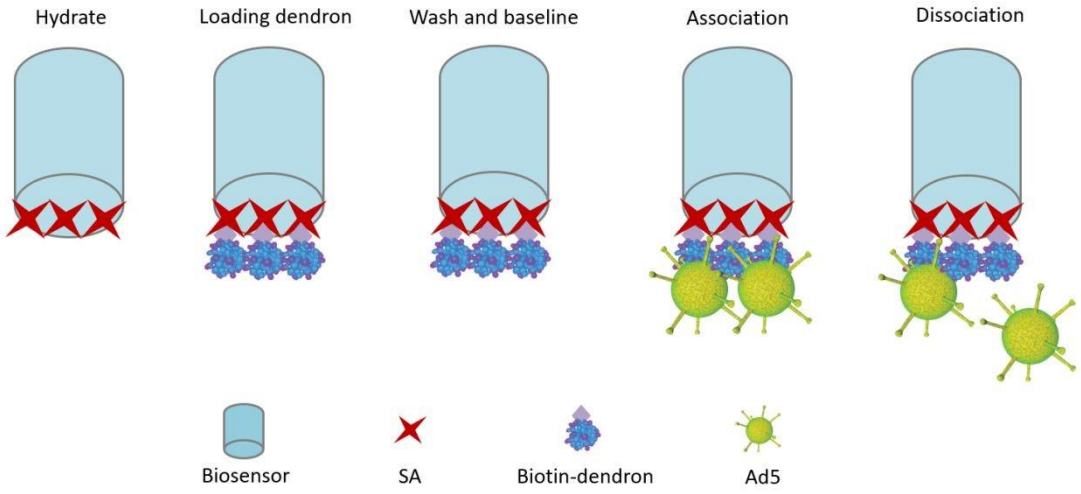

Figure S3.10. Workflow for dendron loading and dendron-Ad5 interaction assay.

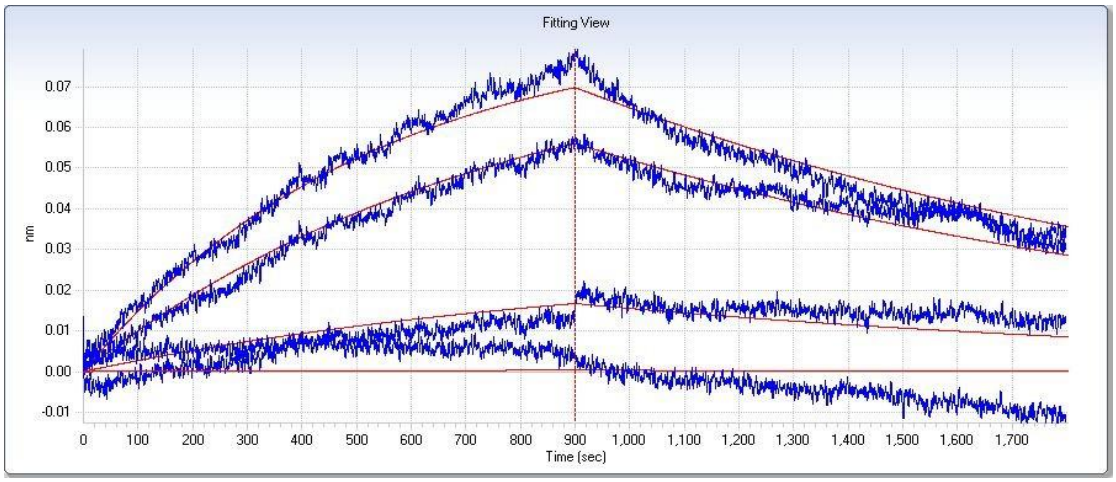

Figure S3.11. BLI analysis of Ad5 binding to biotinylated PPD3 dendrons immobilized on streptavidin-coated biosensors. Association and dissociation curves are shown at different concentrations. Red lines represent regression modelling.

Table S3.2. Kinetics analysis results.

Conc. (pM)	Response	KD (M)	kon(1/Ms)	kdis(1/s)	kobs(1/s)	Full R^2
2	0.076	1.27×10^{-12}	5.87×10^{8}	7.47×10^{-4}	1.92×10^{-3}	0.967526
1	0.0558	1.27×10^{-12}	5.87×10^{8}	7.47×10^{-4}	1.33×10^{-3}	0.967526
0.5	0.0129	1.27×10^{-12}	5.87×10^{8}	7.47×10^{-4}	1.04×10^{-3}	0.967526
0.25	0.0048	1.27×10^{-12}	5.87×10^{8}	7.47×10^{-4}	8.94×10^{-4}	0.967526

Conc. (nM): Molar concentration of the sample used in the association step. Response: Response calculated from the time window entered in the Steady State Analysis section. K_D (M): Equilibrium dissociation constant. k_{on} (1/Ms): Rate of association. k_{dis} (1/s): Rate of dissociation. k_{obs} (1/s): Observed binding rate. Full R^2: R^2 is the coefficient of determination, which is an estimate of the goodness of the curve fit.

3.6.11 Interaction of coated PPD3 with serum proteins

Coating of model nanoparticles with PPD3. Amino-functionalized nanoparticles[36] (PS-NP, concentration = 10 mg/mL, diameter 100 nm, zetapotential ~ + 40 mV) were incubated with dendrimers in a defined ratio (1 mg NP: 1 mg PPD3) for 1 h at room temperature. Afterwards the suspension was diluted with water (1 mL), centrifuged (20,000 g, 15 min) and resuspended in water.

Human serum and plasma. Blood serum and citrate plasma were collected from ten healthy donors at the Transfusion Center of the University Clinic of Mainz, Germany after obtaining informed consent. All serum and plasma samples were pooled and stored at –20 °C.

Protein corona analysis. The hard protein corona was analyzed as described in previous reports.[37, 38] A defined ratio of nanoparticles (0.05 m^2) and human blood plasma or serum (1 mL) was used. After 1 h of incubation at 37 °C, the nanoparticles were centrifuged and washed with PBS (three times, 1 mL, 20,000 g, 30 min, 4 °C) to remove unbound proteins. In the final step, the hard corona proteins were detached from the nanoparticles´ surface with 2% SDS with 62.5 mM TRIS hydrochloride and incubated for 5 min at 95 °C. The samples were further centrifuged (20,000 g, 30 min, 4 °C) and the resulting supernatant contained the hard corona proteins, which was analyzed by SDS-PAGE and LC-MS.

SDS PAGE for hard protein corona analysis. 1 μg of proteins (in 26 μL of samples volume) were diluted with sample buffer (10 μL) and reducing agent (4 μL), heated up to 70 °C for 10 min and applied on a 10% NuPAGE Bis-Tris Gel. The gel was run for 1 h at 120 V and proteins were further visualized *via* Pierce Silver Stain Kit according the manufacturers´ instructions.

Liquid chromatography coupled to mass spectrometry (LC-MS) analysis. Proteins were digested as previously described.[5, 39] Briefly, proteins were precipitated using ProteoExtract protein precipitation kit according to the manufactures´ instruction. The protein pellet was resuspended with RapiGest SF dissolved in 50 mM ammonium bicarbonate and further reduced with dithiothreitol (5 mM, 56 °C for 45 min) and alkylated with iodoacetamide (15 mM, 1 h). Proteins were digested with trypsin at 37 °C overnight. The reaction was terminated with 2 μL hydrochloric acid.

Resulting peptide samples were dilute with 0.1% formic acid and spiked with 50 fmol/µL Hi3 *E. Coli* Standard for absolute peptide quantification. LC-MS measurements were carried out on a Synapt G2- Si mass spectrometer coupled to a nanoACQUITY UPLC system. Data-independent acquisition (MS^E) experiments were performed, and peptides were ionized with a NanoLock Spray source in positive ion mode. MassLynx 4.1 and Progenesis QI for proteomics was used for data analysis and peptide identification. A reviewed human data base downloaded from Uniprot and additionally modified with the sequence information of Hi3 *E. coli* standard (chaperone protein ClpB) was used for absolute protein identification. A false discovery rate of 4% and a maximum protein mass of 600 kDa was chosen. Three assigned fragments were needed for peptide identification, for protein identification at least two assigned peptides and five assigned fragments were required. The absolute amount of protein in fmol was determined *via* TOP3/Hi3 approach.[40]

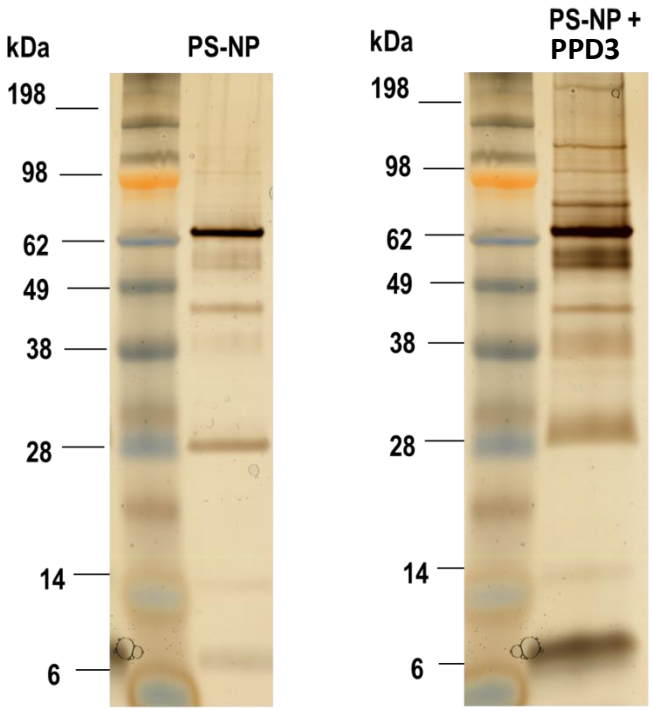

Figure S3.12. Hard protein corona analysis of polystyrene nanoparticles (PS-NP) and dendrimer (PPD3) coated nanoparticles after serum incubation. 1 µg of protein was applied to the SDS-PAGE (reducing conditions). One representative SDS-PAGE is shown. The experiment was repeated three times.

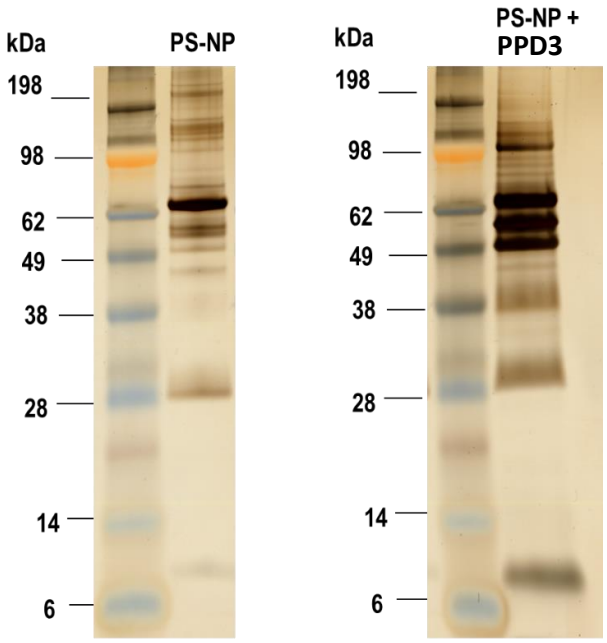

Figure S3.13. Hard protein corona analysis of polystyrene nanoparticles (PS-NP) and PPD3 coated nanoparticles after plasma incubation. 1 μg of protein was applied to the SDS-PAGE (reducing conditions). One representative SDSPAGE is shown. The experiment was repeated three times.

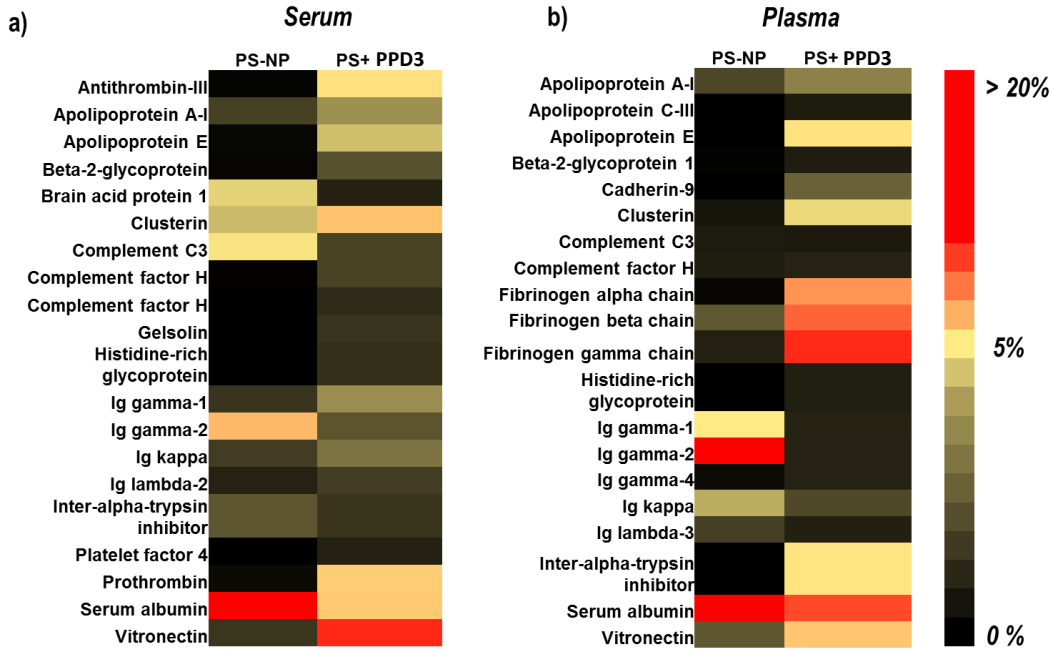

Figure S3.14. Proteomic analysis of the hard protein corona for polystyrene nanoparticles (PS-NP) coated with dendrimers (PPD3) after serum (**a**) and plasma (**b**) incubation. The top 20 most abundant corona proteins are visualized in the heat map. The amount of protein is given in % based on all identified proteins. The average of two technical replicates was calculated.

3.7 References

[1] M. Hadjidemetriou, K. Kostarelos, *Nat. Nanotechnol.* **2017**, *12*, 288-290.

[2] F. Chen, G. Wang, J. I. Griffin, B. Brenneman, N. K. Banda, V. M. Holers, D. S. Backos, L. Wu, S. M. Moghimi, D. Simberg, *Nat. Nanotechnol.* **2017**, *12*, 387-393.

[3] A. Salvati, A. S. Pitek, M. P. Monopoli, K. Prapainop, F. B. Bombelli, D. R. Hristov, P. M. Kelly, C. Åberg, E. Mahon, K. A. Dawson, *Nat. Nanotechnol.* **2013**, *8*, 137-143.

[4] S. Tenzer, D. Docter, J. Kuharev, A. Musyanovych, V. Fetz, R. Hecht, F. Schlenk, D. Fischer, K. Kiouptsi, C. Reinhardt, K. Landfester, H. Schild, M. Maskos, S. K. Knauer, R. H. Stauber, *Nat. Nanotechnol.* **2013**, *8*, 772-781.

[5] S. Schöttler, G. Becker, S. Winzen, T. Steinbach, K. Mohr, K. Landfester, V. Mailänder, F. R. Wurm, *Nat. Nanotechnol.* **2016**, *11*, 372-377.

[6] S. Fletcher, A. D. Hamilton, *Curr. Opin. Chem. Biol.* **2005**, *9*, 632-638.

[7] G. Bisker, J. Dong, H. D. Park, N. M. Iverson, J. Ahn, J. T. Nelson, M. P. Landry, S. Kruss, M. S. Strano, *Nat. Commun.* **2016**, *7*, 10241.

[8] A. Verma, O. Uzun, Y. Hu, Y. Hu, H.-S. Han, N. Watson, S. Chen, D. J. Irvine, F. Stellacci, *Nat. Mater.* **2008**, *7*, 588-595.

[9] Z. Xu, Q. Qiu, J. Tian, J. S. Smith, G. M. Conenello, T. Morita, A. P. Byrnes, *Nat. Med.* **2013**, *19*, 452-457.

[10] S. N. Waddington, J. H. McVey, D. Bhella, A. L. Parker, K. Barker, H. Atoda, R. Pink, S. M. K. Buckley, J. A. Greig, L. Denby, J. Custers, T. Morita, I. M. B. Francischetti, R. Q. Monteiro, D. H. Barouch, N. van Rooijen, C. Napoli, M. J. E. Havenga, S. A. Nicklin, A. H. Baker, *Cell* **2008**, *132*, 397-409.

[11] S. N. Waddington, A. L. Parker, M. Havenga, S. A. Nicklin, S. M. K. Buckley, J. H. McVey, A. H. Baker, *J. Virol.* **2007**, *81*, 9568.

[12] R. G. Crystal, *Hum. Gene Ther.* **2014**, *25*, 3-11.

[13] K. C. Samuel, A. B. Michael, *Curr. Gene Ther.* **2007**, *7*, 189-204.

[14] D. M. Shayakhmetov, A. Gaggar, S. Ni, Z.-Y. Li, A. Lieber, *J. Virol.* **2005**, *79*, 7478.

[15] R. Alba, A. C. Bradshaw, A. L. Parker, D. Bhella, S. N. Waddington, S. A. Nicklin, N. van Rooijen, J. Custers, J. Goudsmit, D. H. Barouch, J. H. McVey, A. H. Baker, *Blood* **2009**, *114*, 965-971.

[16] H. Mizuguchi, T. Hayakawa, *Hum. Gene Ther.* **2004**, *15*, 1034-1044.

[17] J. Fuxe, L. Liu, S. Malin, L. Philipson, V. P. Collins, R. F. Pettersson, *Int. J. Cancer* **2003**, *103*, 723-729.

[18] R. Stangenberg, Y. Wu, J. Hedrich, D. Kurzbach, D. Wehner, G. Weidinger, S. L. Kuan, M. I. Jansen, F. Jelezko, H. J. Luhmann, D. Hinderberger, T. Weil, K. Müllen, *Adv. Healthcare Mater.* **2015**, *4*, 377-384.

[19] R. Stangenberg, I. Saeed, S. L. Kuan, M. Baumgarten, T. Weil, M. Klapper, K. Müllen, *Macromol. Rapid Commun.* **2014**, *35*, 152-160.

[20] B. A. G. Hammer, Y. Wu, S. Fischer, W. Liu, T. Weil, K. Müllen, *ChemBioChem* **2017**, *18*, 960-964.

[21] U.-M. Wiesler, K. Müllen, *Chem. Commun.* **1999**, 2293-2294.

[22] J. M. Bergelson, J. A. Cunningham, G. Droguett, E. A. Kurt-Jones, A. Krithivas, J. S. Hong, M. S. Horwitz, R. L. Crowell, R. W. Finberg, *Science* **1997**, *275*, 1320.

[23] G. Caracciolo, L. Callipo, S. C. De Sanctis, C. Cavaliere, D. Pozzi, A. Laganà, *Biochim. Biophys. Acta, Biomembr.* **2010**, *1798*, 536-543.

[24] M. Kokkinopoulou, J. Simon, K. Landfester, V. Mailänder, I. Lieberwirth, *Nanoscale* **2017**, *9*, 8858-8870.

[25] L. Shen, S. Tenzer, W. Storck, D. Hobernik, V. K. Raker, K. Fischer, S. Decker, A. Dzionek, S. Krauthäuser, M. Diken, A. Nikolaev, J. Maxeiner, P. Schuster, C.

Kappel, A. Verschoor, H. Schild, S. Grabbe, M. Bros, *J. Allergy Clin. Immunol.* **2018**, *142*, 1558-1570.
[26] G. Caracciolo, F. Cardarelli, D. Pozzi, F. Salomone, G. Maccari, G. Bardi, A. L. Capriotti, C. Cavaliere, M. Papi, A. Laganà, *ACS Appl. Mater. Interfaces* **2013**, *5*, 13171-13179.
[27] N. C. Di Paolo, O. Kalyuzhniy, D. M. Shayakhmetov, *J. Virol.* **2007**, *81*, 12249-12259.
[28] H. A. Jaffe, C. Danel, G. Longenecker, M. Metzger, Y. Setoguchi, M. A. Rosenfeld, T. W. Gant, S. S. Thorgeirsson, L. D. Stratford-Perricaudet, M. Perricaudet, A. Pavirani, J. P. Lecocq, R. G. Crystal, *Nat. Genet.* **1992**, *1*, 372-378.
[29] M. A. Schnell, Y. Zhang, J. Tazelaar, G.-p. Gao, Q. C. Yu, R. Qian, S.-J. Chen, A. N. Varnavski, C. LeClair, S. E. Raper, J. M. Wilson, *Mol. Ther.* **2001**, *3*, 708-722.
[30] N. Tao, G.-P. Gao, M. Parr, J. Johnston, T. Baradet, J. M. Wilson, J. Barsoum, S. E. Fawell, *Mol. Ther.* **2001**, *3*, 28-35.
[31] R. Alba, A. C. Bradshaw, L. Coughlan, L. Denby, R. A. McDonald, S. N. Waddington, S. M. K. Buckley, J. A. Greig, A. L. Parker, A. M. Miller, H. Wang, A. Lieber, N. van Rooijen, J. H. McVey, S. A. Nicklin, A. H. Baker, *Blood* **2010**, *116*, 2656-2664.
[32] A. L. Parker, S. N. Waddington, C. G. Nicol, D. M. Shayakhmetov, S. M. Buckley, L. Denby, G. Kemball-Cook, S. Ni, A. Lieber, J. H. McVey, S. A. Nicklin, A. H. Baker, *Blood* **2006**, *108*, 2554-2561.
[33] F. Vigant, D. Descamps, B. Jullienne, S. Esselin, E. Connault, P. Opolon, T. Tordjmann, E. Vigne, M. Perricaudet, K. Benihoud, *Mol. Ther.* **2008**, *16*, 1474-1480.
[34] R. F. Kratzer, F. Kreppel, in *Functional Genomics: Methods and Protocols* (Eds.: M. Kaufmann, C. Klinger, A. Savelsbergh), Springer New York, New York, NY, **2017**, pp. 377-388.
[35] Z. Chen, Q. Wang, J. Sun, A. Gu, M. Jin, Z. Shen, Z. Qiu, J. Wang, X. Wang, Z. Zhan, J.-W. Li, *Tumor Biol.* **2013**, *34*, 17-24.
[36] A. Musyanovych, J. Dausend, M. Dass, P. Walther, V. Mailänder, K. Landfester, *Acta Biomater.* **2011**, *7*, 4160-4168.
[37] J. Simon, T. Wolf, K. Klein, K. Landfester, F. R. Wurm, V. Mailänder, *Angew. Chem. Int. Ed.* **2018**, *57*, 5548-5553.
[38] J. Simon, J. Müller, A. Ghazaryan, S. Morsbach, V. Mailänder, K. Landfester, *Nanoscale* **2018**, *10*, 21096-21105.
[39] D. Hofmann, S. Tenzer, M. B. Bannwarth, C. Messerschmidt, S.-F. Glaser, H. Schild, K. Landfester, V. Mailänder, *ACS Nano* **2014**, *8*, 10077-10088.
[40] J. C. Silva, M. V. Gorenstein, G.-Z. Li, J. P. C. Vissers, S. J. Geromanos, *Mol. Cell. Proteomics* **2006**, *5*, 144-156.

4 Amphiphilic Dendrimers Control Protein Binding and Corona Formation on Liposome Nanocarriers

[redacted]

Submitted to *Chemical Communications (in revision)*

Contributions

My contribution was the planning and conduct of the synthesis of the negatively charged PPD and the negatively charged amphiphilic PPD and their characterization, the summary, interpretation and statistics of the protein corona results, the design of the figures and the writing of large parts of the manuscript. [redacted] developed, synthesized and characterized the positively charged amphiphilic PPDs. [redacted] conducted all experiments regarding the protein corona on liposomes and PS-nanoparticles, analyzed the results and revised the manuscript. [redacted] conducted all protein corona experiments during the revision. [redacted] supervised the experiments of [redacted], interpreted the protein corona results and revised the manuscript. [redacted] was active in troubleshooting of negatively charged PPDs and revised the manuscript. [redacted] supervised the synthesis of [redacted] and revised the manuscript. [redacted] designed the project, discussed the experimental data, provided funding and revised the manuscript.

Abstract

Amphiphilic polyphenylene dendrimers (PPDs) with distinct lipophilic and postively or negatively charged surface groups were adsorbed onto liposomes and their impact on protein adsorption in the blood plasma was studied. The PPD corona reduced binding of specific opsonins and increased the adsorption of proteins controlling cellular uptake based on their surface patches.

4.1 Introduction

The formation of a protein corona on the surface of nanoparticles is a critical factor that determines their biodistribution, cellular uptake pathways and immune response. There are many parameters that influence protein adsorption on nanocarriers such as their size, surface charges, hydrogen bonds and van der Waals interactions.[1, 2] Liposomes are among the most applied nanocarriers, but their biological fate is hard to control.[3] A deeper understanding which surface groups facilitate binding of certain plasma proteins is still elusive. Polyethylene glycol surfaces usually reveal low protein adsorption and stealth-like properties.[1] However, instead of just limiting protein binding, it would be very attractive to design surface coatings that only adsorb certain proteins from blood plasma and thus, enhance cellular uptake or affect biodistribution. In order to understand and control protein corona formation, novel coatings mimicking features of proteins are designed providing amphiphilic patches with low nanometre dimensions due to hydrophilic, hydrophobic and charged surface groups at defined locations. Dendrimers are monodisperse macromolecules with customizable surface groups and nanometre dimensions.[4] However, many aliphatic dendrimers exhibit backfolding of their dendritic branches. Thus, surface groups are not exposed exclusively at the surface resulting in less defined peripheral patterns.[5] Widely used polycationic dendrimers such as poly(amidoamine) (PAMAM) dendrimers interact with blood plasma proteins but they also reveal high cellular toxicities and trigger immune responses.[6]

Herein, we apply polyphenylene dendrimers (PPDs) as coatings for liposomal nanocarriers to assess the impact of amphiphilic surface groups on plasma protein binding. The PPDs consist of a semi-rigid polyphenylene scaffold with no backfolding of dendritic branches.[7] We have shown that amphiphilic PPDs with alternating sulfonic acid and *n*-propyl groups provide cellular uptake as well as low cellular toxicity and mimic certain features of proteins.[8] In blood plasma, they form a novel PPD-corona at the surface of adenovirus 5 preventing the endogenous blood coagulation factor X from binding.[9] Liposomal nanocarriers coated with such similar PPDs reveal a considerably altered protein corona in blood serum.[10]

Herein, PPDs with either positively or negatively charged amphiphilic or exclusively anionic peripheral groups were prepared and the impact on protein corona formation was studied. We envision controlling the fate of liposomal nanocarriers by the PPD surface in biological fluids such as blood (Figure 4.1).

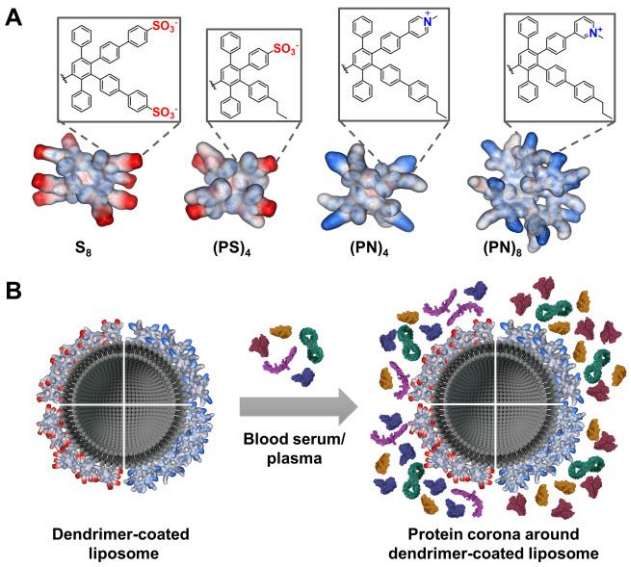

Figure 4.1. Protein corona on PPD-coated liposomes. (**A**) PPDs with various surface pattern consisting of sulfonic acid groups (S_8), alternating sulfonic acid and *n*-propyl groups ($(PS)_4$) or alternating pyridinium and *n*-propyl groups ($(PN)_4$ and $(PN)_8$), (P = *n*-propyl, S = sulfonate, N = pyridinium); (**B**) PPD-coating on liposomes alters the protein corona in blood serum and plasma.

4.2 Results and Discussion

The synthesis of charged PPDs was performed according to the divergent growth approach (Scheme 4.1, Figure S4.2 – Figure S4.5). Growth of the PPDs starts from an ethynylated core, which is reacted with tetraphenylcyclopentadienone (CP) building blocks in a [4+2] Diels–Alder cycloaddition. The CP determines the branching and the absolute surface pattern of the dendrimer.[11]

Building block **1a** with a sulfonate and *n*-propyl group was synthesized based on modified procedures from Stangenberg et al.[10, 12] and was directly used for the dendrimer growth whereas **1b** (Figure S4.3) and **1c** (Figure S4.4) were further modified with the desired surface functionalities by Suzuki coupling reactions (Scheme 4.1). For the anionic dendrimer with peripheral sulfonate groups, intermediate **3**[12] with two neopentyl-protected sulfonic acid moieties was synthesized by C-C coupling of the pinacol boronic ester **2** to di-bromo-modified compound **1b**. For cationic amphiphilic dendrimers, the unsymmetrical CP **1c** with an iodo- and bromo-substituent was synthesized based on modified protocols from Zhang et al. (Figure S4.4).[13] Terminal surface functionalities were attached to **1c** by Suzuki coupling of *n*-propyl functionalized phenyl derivative **4** and either *meta*- or *para*-substituted pyridine compounds **5** and **6** (Scheme 4.1). To achieve a positively charged pyridinium group on the dendrimer rim, the pyridine moieties were methylated. For the first-generation dendrimer, the methylation was performed prior to

dendrimer synthesis (*a priori*) to obtain pyridinium modified CP **7a**. When synthesizing a second-generation dendrimer, the pyridine group was methylated after dendrimer growth, due to incomplete dendrimer formation with already positively charged building blocks at higher generations. In addition, the *meta*-pyridinyl group of **7b** facilitated the methylation on the dendrimer surface. All PPDs are built around the core of 1,3,6,8-tetraethynylpyrene (**8**).[14] The cycloaddition to achieve both neopentyl-protected sulfonic acid-based dendrimers were performed at 145 °C in *o*-xylene for 48 h.[8, 12] After purification by silica gel column chromatography and *recycling*-gel permeation chromatography (GPC), the neopentyl protective groups of the sulfonic acids were thermally cleaved (180 °C in DMF) to obtain **10a** and **10b**.[8, 12] Deprotected dendrimers were further purified *via* GPC in DMF. The positively charged amphiphilic dendrimer **10c** was obtained by cycloaddition of pyrene core **8** and pyridinium-building block **7a** in DMSO at 140 °C for 3 d. The product was precipitated and purified by dialysis. The second-generation dendrimer was synthesized from a first-generation pyrene-based PPD **9,**[8] which was reacted with pyridine modified CP **7b** in *o*-xylene at 160 °C for 3 d. After purification by GPC, the product was methylated. Cationic amphiphilic dendrimer **10d** was obtained by precipitation in diethyl ether. NMR spectroscopy and MALDI-TOF or ESI mass spectroscopy confirmed the structure of **10a**-**10d**.

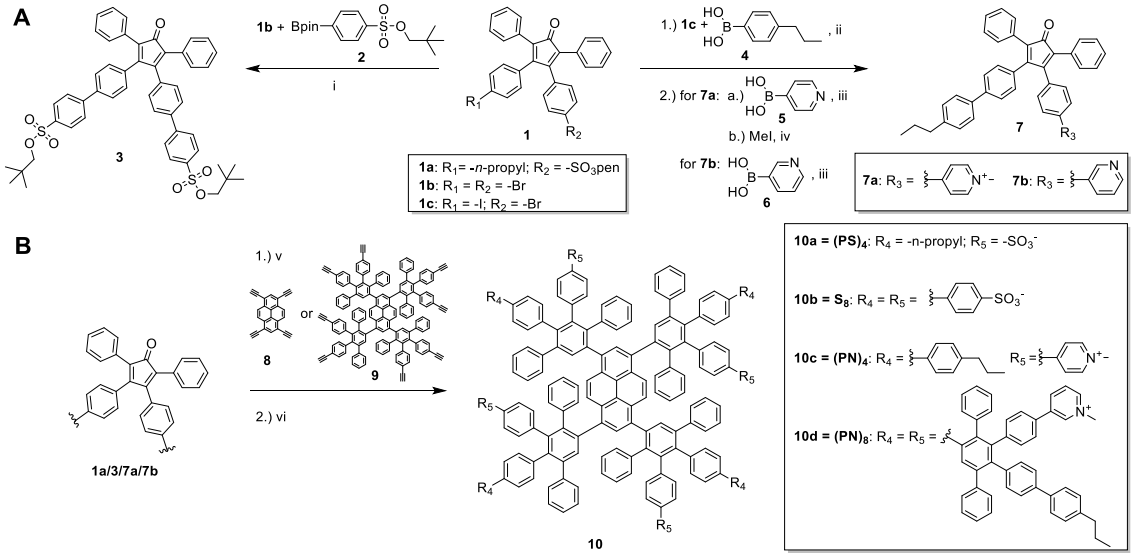

Scheme 4.1. Synthesis of polyphenylene dendrimers with different surface pattern. (**A**) Building block syntheses: i) $Pd(PPh_3)_4$, K_2CO_3 (aq), 1,4-dioxane, 90 °C, 15 h, 34%; ii) $Pd(PPh_3)_4$, K_2CO_3 (aq), 1,4-dioxane, 40 °C, 15 h; iii) $Pd(PPh_3)_4$, K_2CO_3 (aq), 1,4-dioxane, 80 °C, 48 h, 50-60%; iv) methanol, RT, 48 h, 70%; (**B**) dendrimer synthesis: v) **1a/3**: pyrene-core **8**, *o*-xylene, 145 °C, 48 h, 27%-45%; **7a**: pyrene-core **8**, DMSO, 140 °C, 3 d, 47%; **7b**: first-generation dendrimer core **9**, *o*-xylene, 160 °C, 3 d, 64%; vi) deprotection sulfonic acid groups to obtain **10a**, **10b**: DMF, 180 °C, 48 h, 85-88%; methylation to obtain **10d**: methyl iodide, methanol, RT, 24 h, 92%.

We coated liposomes and polystyrene nanoparticles with the PPDs and investigated protein corona formation in blood serum and plasma. To compare our results with our previous findings for highly branched amphiphilic PPDs,[10] we used the same liposome composition consisting of 2-dioleoyl-*sn*-glycero-3-phosphoethanolamine (DOPE), l-α-phosphatidylcholine (eggPC) and cholesterol (Chol) (PC:DOPE:Chol=1:1:1) as well as amino-functionalized polystyrene nanoparticles (PS-NH_2), which were prepared according to standard protocols.[15, 16] Liposomes or PS-NH_2 were mixed with the dendrimers **10a** $(PS)_4$, **10b** S_8, **10c** $(PN)_4$ or **10d** $(PN)_8$ (with P = *n*-propyl, S = sulfonate and N = pyridinium). Coating of both nanocarriers was verified by a shift of ζ-potential values (Figure S4.6). Interestingly, only for $(PS)_4$ and $(PN)_8$ liposome coating was observed (Figure S4.6B). It has been reported that amphiphilic dendrimers with alternating sulfonic acid (S) and *n*-propyl groups (P) are bound to a lipid monolayer by electrostatic interactions.[17] Since S_8 did not bind to liposomes efficiently (Figure S4.6B), we postulate that the hydrophobic interaction between *n*-propyl group and lipid tails is necessary to enhance binding to liposomes. In addition, second-generation dendrimer $(PN)_8$ coated liposomes to a higher extent than $(PN)_4$ resulting in a positive ζ-potential. Therefore, sufficient surface coverage of liposomes was only achieved for $(PS)_4$ and $(PN)_8$. To assess the impact of the *n*-propyl (P) group on the protein corona formation, we coated PS-NH_2 nanoparticles with $(PS)_4$ and S_8. Due to the positive ζ-potential of amino-functionalized PS particles, adsorption of negatively charged dendrimers is electrostatically driven. This was further supported by using positively charged $(PN)_4$ and $(PN)_8$, which did not show an efficient binding towards PS-NH_2 (Figure S4.6C). Thus, either blood serum or blood plasma was added to the dendrimer-coated liposomes (lipo-dendrimer) or PS-NH_2 nanoparticles. The protein adsorption was analyzed quantitatively by Pierce Assay (Figure S4.7) and LC-MS/MS (Figure 4.2, Figure S4.8 and Figure S4.9). For the blood serum preparation, fibrinogen and other blood clotting factors were removed by centrifugation, whereas blood plasma contained all proteins including clotting factors. For plasma, clotting was prevented by the addition of citrate as anticoagulant. Using the Pierce Assay, we could further confirm the binding efficiency of dendrimers to the particle surfaces by comparing the protein adsorption levels to uncoated nanocarriers (Figure S4.7B–E). The heatmaps depict an overview of all blood proteins bound onto lipo-dendrimers (lipo-$(PS)_4$ and lipo-$(PN)_8$; Figure 4.2A and Figure S4.8) as well as PS-dendrimers (PS-$(PS)_4$ and PS-S_8) (Figure S4.9) in blood plasma and serum. First, we observed a similar alteration in the adsorption of certain proteins from uncoated liposomes to lipo-dendrimers regardless of the difference between positively $(PN)_8$ and negatively $(PS)_4$ charged surface groups (Figure 4.2B).

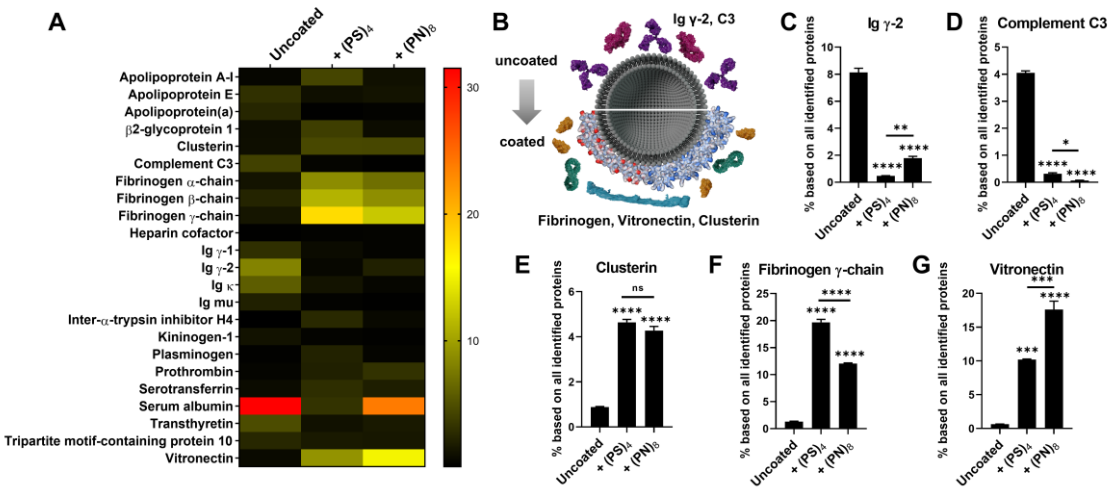

Figure 4.2. Comparison of adsorbed proteins between uncoated liposomes and lipo-dendrimers (lipo-$(PS)_4$ and lipo-$(PN)_8$). (**A**) Heatmap of adsorbed proteins to lipo-$(PS)_4$ and lipo-$(PN)_8$ in human plasma. Each protein amount is given in % relative to the total amount of all identified proteins. A list of all identified proteins is provided in Figure S4.12 and Figure S4.13. (**B**) Coating of liposomes lead to a different protein corona: Reduction of (**C**) Ig γ-2 adsorption and (**D**) Complement C3 and enhancement of (**E**) clusterin, (**F**) fibrinogen and (**G**) vitronectin (n = minimum 2; one-way ANOVA; not significant (ns) for $p > 0.05$, * for $p \leq 0.05$, ** for $p \leq 0.01$, *** for $p \leq 0.001$, **** for $p \leq 0.0001$).

Both dendrimer surfaces lead to a significant reduction of the opsonins immunoglobulin γ-2 (Ig γ-2) and complement C3 levels in comparison to uncoated liposomes (Figure 4.2C and D). Opsonins are recognized by immune cells, which are part of the mononuclear phagocytic system (MPS), and they mediate cellular uptake of nanocarriers into phagocytic cells.[1, 18] Thus, these opsonins enhance blood clearance and reduce the interaction with targeted cells.[19] In contrast, we observed an enhancement in clusterin binding from uncoated to covered liposomes (Figure 4.2E). Clusterin, also termed Apolipoprotein J, decreased unspecific cellular uptake of PEGylated nanocarriers *in vitro* and functioned as a dysopsonin for macrophages.[20] In general, apolipoproteins bind to a higher extent to hydrophobic nanocarriers.[21] Thus, we assume that the clusterin binding is related to the hydrophobic character of PPDs. Furthermore, fibrinogen was adsorbed on all lipo-dendrimers (Figure 4.2F). Previously, the pre-coating of PS nanoparticles with IgG-depleted plasma furnished a high enrichment of fibrinogen and a reduced cellular uptake in macrophages.[22] In addition, the dendrimer coating gave rise to accelerated vitronectin binding (Figure 4.2G). These findings were consistent with our previous studies for PPDs and dendrons with higher density of sulfonic acid and *n*-propyl groups (Figure S4.10).[10] Vitronectin was reported to mediate a selective uptake of lipoplexes into cancer cells with overexpressing $\alpha_v\beta_3$ vitronectin receptors.[23] We also found fibrinogen and vitronectin binding for PS-$(PS)_4$ and PS-S_8 (Figure S4.11C and D) emphasizing that the binding of these proteins is attributable to the hydrophobic PPD scaffold.

Second, we also observed remarkable differences in the protein corona that might be caused by the surface charges (Figure 4.3A). Binding of serum albumin (HSA) for lipo-$(PN)_8$ was enhanced whereas lipo-$(PS)_4$ only showed a very low HSA adsorption (Figure 4.3B). HSA is reported to serve as dysopsonin leading to higher blood circulation times.[24] PS-$(PS)_4$ and PS-S_8 also displayed a reduction of HSA in the protein corona compared to uncoated nanoparticles (Figure S4.11B). This suggests that the positively charged pyridinium group is involved in the interaction of lipo-$(PN)_8$ with HSA. In contrast, inter-α-trypsin inhibitor (IαI) H4 was increased for all negatively charged liposomes and nanoparticles (lipo-$(PS)_4$ (Figure 4.3C), PS-$(PS)_4$ and PS-S_8 (Figure S4.11E)) and IαI is known to interact with the highly negatively charged hyaluronic acid.[25] Additionally, lipo-$(PS)_4$ adsorbed β2-glycoprotein 1 also known as Apolipoprotein H (ApoH; Figure 4.3D), which is consistent with our previous findings.[10] ApoH binds to negatively charged phospholipids and mediates cellular uptake into mesenchymal stem cells.[26, 27] For PS-S_8, we observed an even higher ApoH adsorption, suggesting that this interaction is favoured by the peripheral sulfonates (Figure S4.11F).

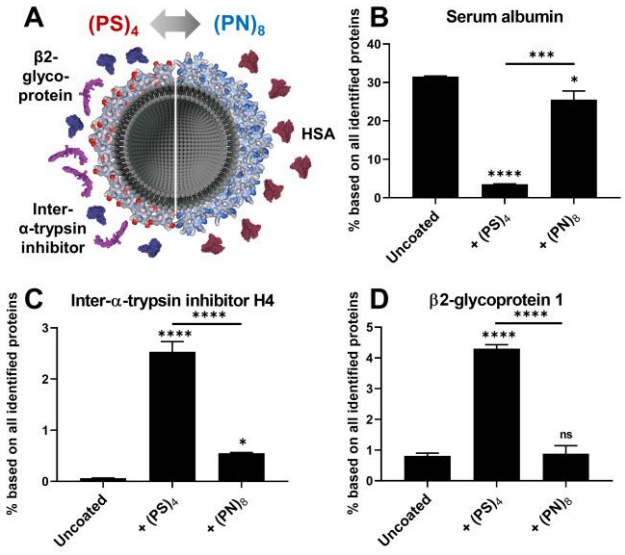

Figure 4.3. Comparison of adsorbed proteins between lipo-$(PS)_4$ and lipo-$(PN)_8$). (**A**) Differences in the protein corona of lipo-$(PS)_4$ and lipo-$(PN)_8$) concerning an enhancement of (**B**) HSA for lipo-$(PN)_8$, and (**C**) inter-α-trypsin-inhibitor as well as (**D**) β2-glycoprotein 1 for lipo-$(PS)_4$ (n = minimum 2; one-way ANOVA; ns for $p > 0.05$, * for $p \leq 0.05$, *** for $p \leq 0.001$, **** for $p \leq 0.0001$).

4.3 Conclusion

In conclusion, we synthesized PPDs with different surface patterns in terms of amphiphilicity and charges with the advantage of shape persistence leading to surface structures with nano-site perfection. We could show that surface charges and hydrophobicity of PPDs alter the protein corona on liposomes. For all PPDs, a reduction of opsonization proteins and enhancement of proteins, which might control selective cellular uptake, were observed. Thus, we demonstrated that the protein corona of nanoparticles is modulated through PPD coating, which opens new avenues to control their biodistribution *in vivo*.

4.4 Acknowledgements

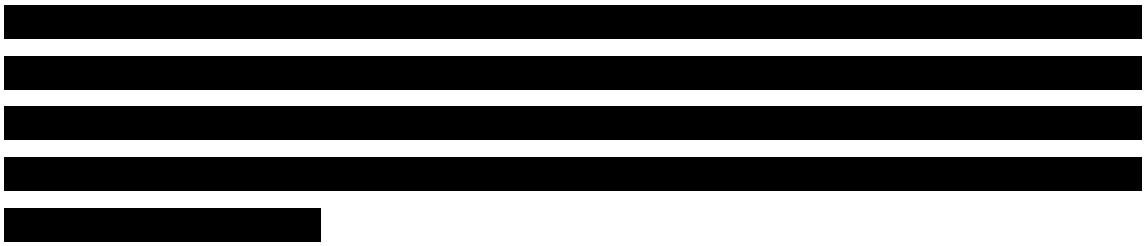

4.5 Supporting Information

4.5.1 Synthesis of dendrimers with different surface patterns

Materials and Instruments

Chemicals and Solvents. All chemicals were obtained from commercial suppliers such as Sigma Aldrich, TCI, Acros Organics, Fisher Scientific, etc., and were utilized without further purification. The solvents (HPLC grade) were purchased from Fisher Scientific or Acros Organics. Chloroform (Rotisolv®, HPLC grade) for the *recycling*-gel permeation chromatography (GPC) system was purchased from Carl Roth. The deuterated solvents were purchased from Sigma Aldrich. Argon (Westfalen AG) was used for reactions under inert gas.

Silica Gel Chromatography. For thin-layer chromatography (TLC) Alugram Sil G/UV254 plates from Macherey-Nagel were used and the detection of substances was performed under UV light at 254 nm or 366 nm. Macherey-Nagel silica gel with particle size of 0.04–0.063 mm or 0.063–0.2 mm was used for preparative silica gel chromatography.

Gel Permeation Chromatography (GPC). Dendrimers with peripheral neopentyl-protected sulfonic acid groups were purified on a *recycling*-GPC purification system from Shimadzu. Dendrimers with deprotected peripheral sulfonic acid groups were purified by size exclusion chromatography using Sephadex® LH-20 in DMF.

Nuclear Magnetic Resonance Spectroscopy (NMR). All ^{1}H NMR and ^{13}C NMR spectra were recorded on a Bruker Avance III 300 MHz, Avance III 500 MHz, Avance III 700 MHz or Bruker Avance III 850 MHz spectrometer in deuterated solvents such as CD_2Cl_2, THF-d_8 and DMSO-d_6 at 298 K. ^{13}C NMR were recorded in j-modulated spin-echo (JMOD) mode. Spectra were analyzed by applying the software MestReNova.

Matrix-assisted Laser Desorption/Ionization–Time of Flight (MALDI-TOF) Mass Spectrometry. MALDI-TOF mass spectra were measured on a Waters MALDI Synapt G2-SI or Bruker rapifleX MALDI-TOF/TOF. Precursors and uncharged dendrimers were dissolved in THF and measured by applying *trans*-2-[3-(4-*tert*-butylphenyl)-2-methyl-2-

propenylidene]malononitrile (DCTB) or dithranol as matrix. Deprotected sulfonic acid based dendrimers were solvated in DMF and diluted in a saturated α-cyano-4-hydroxycinnamic acid (CHCA) solution in water:acetonitrile (1:1) + 0.1% TFA. All dendrimers with peripheral pyridine groups were measured in tetrahydrofuran (THF) with tetracyanoquinodimethane (TCNQ) as matrix. Processing of data was performed in mMass.

Electrospray Ionization (ESI) Spectrometry. ESI spectra were measured on a Waters Synapt G2-SI. The samples were dissolved in methanol.

Atmospheric Pressure Chemical Ionization Mass Spectrometry (APCI-MS). APCI mass spectra of building blocks and intermediates were measured on an Advion expression-L Compact Mass Spectrometer (CMS) (Advion Inc. 61 Brown Rd, Suite 100, Ithaca, NY 14850, USA) by either applying the sample (solid) as an atmospheric solid analysis probe (ASAP) or measuring directly from TLC plates by an automated TLC plate reader (Plate express).

Field Desorption Mass Spectrometry (FD-MS). FD mass spectra of intermediates were measured on a VG Instruments ZAB 2-SE-FPD using an 8 kV accelerating voltage.

Nomenclature for Polyphenylene Dendrimers.

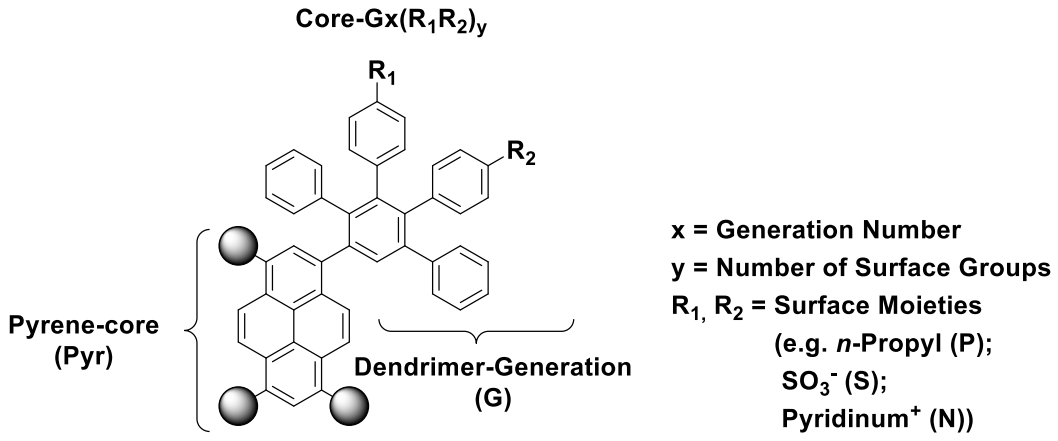

Figure S4.1. Systematic designation of polyphenylene dendrimers (PPDs).

Synthesis of a first-generation negatively charged amphiphilic polyphenylene dendrimer – $(PS)_4$

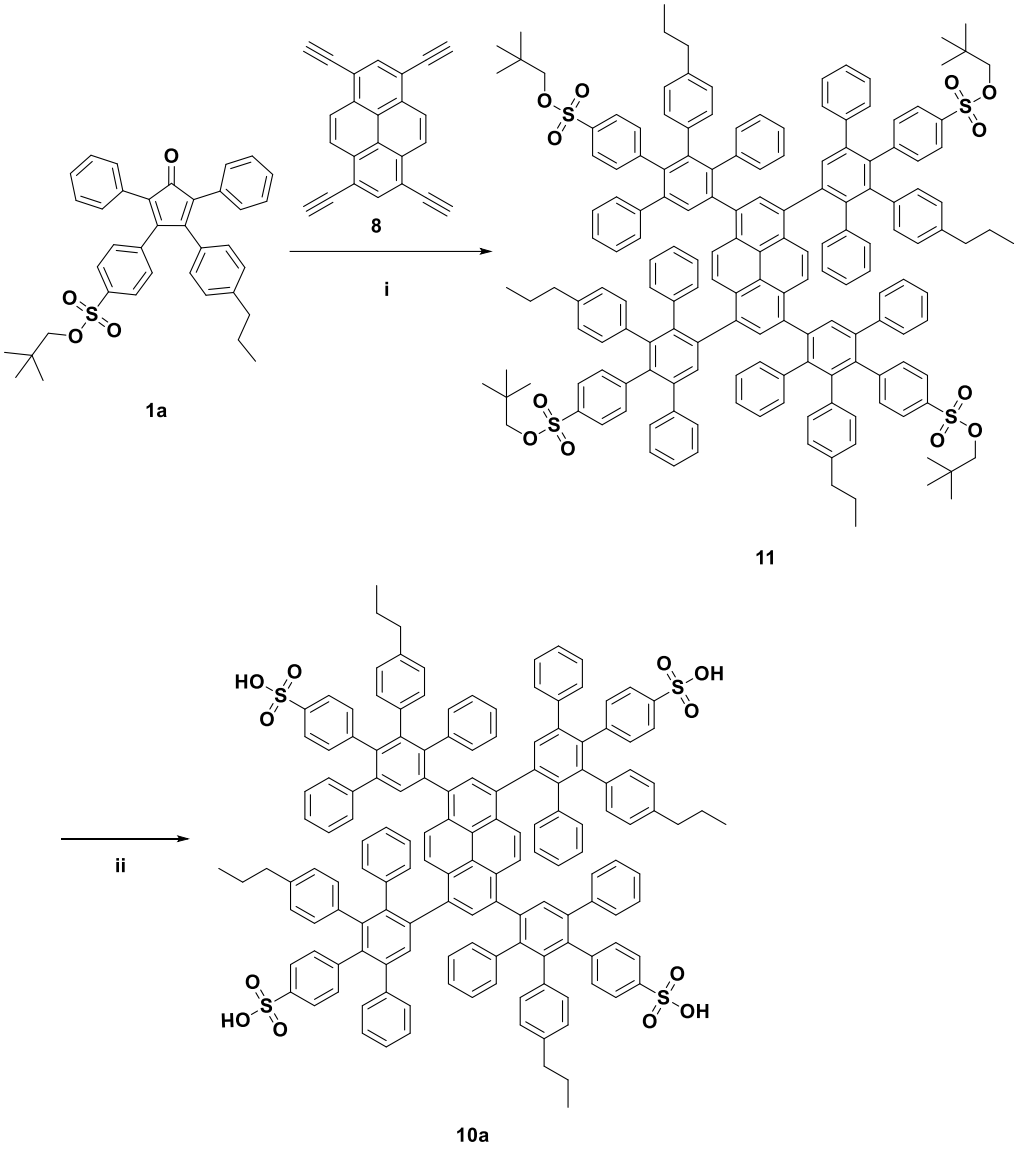

Figure S4.2. Synthesis of first-generation amphiphilic dendrimer **10a** with alternating sulfonic acid and *n*-propyl groups according to Stangenberg et al.[8] i) o-xylene, 145 °C, 48 h, 45% yield; ii) DMF, 180 °C, 48 h, 85% yield.

*Neopentyl 4-(3-oxo-2,4-diphenyl-5-(4-propylphenyl)cyclopenta-1,4-dien-1-yl)benzenesulfonate (**1a**)*

Surface building block **1a** was synthesized according to the literature in a four-step synthesis.[10, 12] All spectral data were in agreement with the literature.[10, 12]
^{1}H NMR (300 MHz, CD_2Cl_2): δ(ppm) = 7.70 (d, *J* = 8.5 Hz, 2H), 7.31–7.22 (m, 8H), 7.20–7.12 (m, 4H), 7.01 (d, *J* = 8.3 Hz, 2H), 6.83 (d, *J* = 8.2 Hz, 2H), 3.64 (s, 2H), 2.54 (t, *J* = 7.8, 7.2 Hz, 2H), 1.61 (dt, *J* = 13.7, 7.4 Hz, 2H), 0.92 (t, *J* = 7.3 Hz, 3H), 0.87 (s, 9H).

^{13}C NMR (75 MHz, CD_2Cl_2): δ(ppm) = 200.22, 155.08, 152.76, 144.50, 139.78, 135.83, 131.36, 130.72, 130.66, 130.32, 129.56, 128.84, 128.74, 128.56, 128.09, 127.61, 125.62, 80.56, 38.26, 32.05, 26.27, 24.77, 14.02.
FD-MS: *m/z* calcd. for $C_{37}H_{36}O_4S$: 576.7, found 576.8 $[M]^{\bullet+}$.

*1,3,6,8-Tetraethynylpyrene (**8**)*

Pyrene core **8** was synthesized in three steps according to the literature.[14]

*Pyr-G1-(PSpen)$_4$ **11***

The synthesis of neopentyl-protected dendrimer **11** was modified from the previously reported method.[8] 1,3,6,8-Tetraethynylpyrene (**8**) (10 mg, 33.5 µmol) and building block **1a** (116 mg, 201 µmol, 6 equiv) were dissolved in 3 mL *o*-xylene. The mixture was degassed with argon and stirred at 145 °C for 48 h in a sealed microwave tube. The product was precipitated in methanol, filtered off and purified by silica gel chromatography using a mixture of cyclohexane and THF (3:1). The product was further purified by *recycling*-GPC in chloroform to obtain dendrimer **11** as a yellow solid (38 mg, 45%).

^{1}H NMR (700 MHz, CD_2Cl_2): δ (ppm) = 7.98–7.73 (m, 5H), 7.60–7.31 (m, 11H), 7.26–6.23 (m, 66H), 3.54–3.30 (m, 8H), 2.50–2.27 (m, 8H), 1.52–1.38 (m, 8H), 0.88–0.66 (m, 48H).

^{13}C NMR (176 MHz, CD_2Cl_2): δ(ppm) = 147.44, 147.16, 142.17, 141.36, 141.06, 140.65, 140.53, 140.10, 139.77, 138.10, 137.26, 137.01, 136.65, 136.32, 132.99, 132.81, 131.67, 130.37, 130.28, 128.20, 128.15, 127.92, 127.79, 127.45, 126.99, 126.72, 80.04, 37.68, 26.10, 24.67, 13.49.

MALDI-TOF: *m/z* calcd. for $C_{168}H_{154}O_{12}S_4$ 2491.03, found 2492.98 $[M+H]^+$.

Pyr-G1-(PS)$_4$ ***10a***

Negatively charged amphiphilic dendrimer **10a** was synthesized according to the literature[8] with a modified purification protocol. Briefly, neopentyl-protected dendrimer **11** (12.0 mg, 4.81 µmol) was dissolved in 2 mL dry DMF, the resulting solution was degassed with argon and stirred at 180 °C for 48 h in a sealed microwave tube. Subsequently, DMF was removed *in vacuo*. The residue was dissolved in methanol and precipitated in diethyl ether. The resulting product was further purified by gel permeation chromatography (GPC) applying Sephadex LH-20 in DMF to obtain Pyr-G1-(PS)$_4$ **10a** as a light yellow solid (9 mg, 85%).

^{1}H NMR (700 MHz, DMSO): δ (ppm) = 8.02–6.20 (m, 82H), 2.44–2.28 (m, 8H), 1.52–1.31 (m, 8H), 0.79–0.58 (m, 12H).

^{13}C NMR (176 MHz, DMSO): δ (ppm) = 145.51, 145.41, 141.11, 141.02, 139.64, 139.27, 137.01, 130.93, 130.36, 129.61, 129.54, 127.74, 127.70, 127.46, 127.43, 127.12, 126.72, 125.09, 124.18, 123.89, 36.54, 23.50, 13.12.

MALDI-TOF: *m/z* calcd. for $C_{148}H_{114}O_{12}S_4$ 2210.72, found 2210.73 $[M]^{\bullet+}$.

Synthesis of a first-generation negatively charged polyphenylene dendrimer – S_8

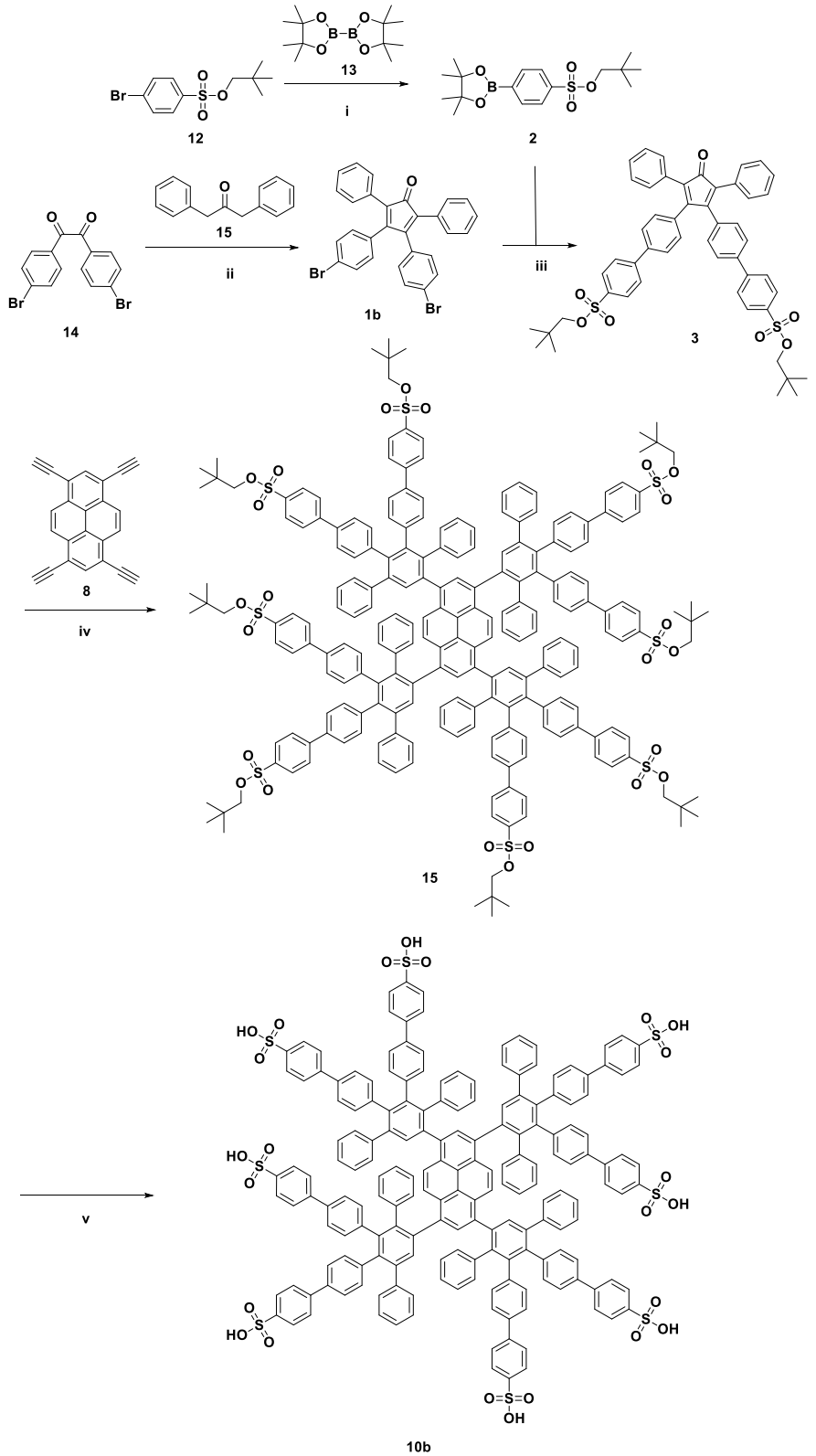

Figure S4.3. Synthesis of first-generation negatively charged dendrimer **10b**. i) KOAc, $Pd(dppf)Cl_2$, 1,4-dioxane, 90 °C, 6 h, 99% yield; ii) TBAH, ethanol, 85 °C, 0.5 h, 85% yield; iii) $Pd(PPh_3)_4$, K_2CO_3 (aq), 1,4-dioxane, 90 °C, 15 h, 34% yield; iv) o-xylene, 145 °C, 36 h, 27% yield; v) DMF, 180 °C, 48 h, 88% yield.

*Neopentyl 4-bromobenzenesulfonate (**12**)*

Compound **17** was synthesized according to the literature.[10, 12] All spectral data were in agreement with the literature.[12]

^{1}H NMR (300 MHz, CD_2Cl_2): δ(ppm) = 7.79–7.70 (m, 4H), 3.67 (s, 2H), 0.89 (s, 9H).

^{13}C NMR (75 MHz, CD_2Cl_2): δ(ppm) = 135.64, 133.12, 129.95, 129.27, 80.63, 32.08, 26.22.

FD-MS: *m/z* calcd. for $C_{11}H_{15}BrO_3S$: 307.2, found 308.7 $[M+H]^+$.

*Neopentyl 4-(4,4,5,5-tetramethyl-1,3,2-dioxaborolan-2-yl)benzenesulfonate (**2**)*

In a dry Schlenk flask neopentyl 4-bromobenzenesulfonate (**12**) (1.00 g, 3.26 mmol), bis(pinacolato)diboron (**13**) (1.24 g, 4.88 mmol, 1.5 equiv) and potassium acetate (703 mg, 7.16 mmol, 2.2 equiv) were dissolved in 15 mL dry 1,4-dioxane. After degassing with argon [1,1′-bis(diphenylphosphino)ferrocene]dichloropalladium(II) ($Pd(dppf)Cl_2$) (53.2 mg, 65.1 µmol, 0.02 equiv) was added under argon atmosphere. The reaction mixture was stirred at 90 °C for 6 h under argon atmosphere. Subsequently, ethyl acetate was added and the organic layer was washed with water. The organic layer was dried over magnesium sulphate. After removing the solvent *in vacuo* the crude product was purified by silica gel column chromatography using a mixture of cyclohexane and ethyl acetate (10:1) to obtain compound **2** as a colourless solid (1.14 g, 99%).

^{1}H NMR (300 MHz, CD_2Cl_2): δ (ppm) = 7.95 (d, *J* = 8.1 Hz, 2H), 7.86 (d, *J* = 8.1 Hz, 2H), 3.65 (s, 2H), 1.35 (s, 12H), 0.88 (s, 9H).

^{13}C NMR (75 MHz, CD_2Cl_2): δ (ppm) = 138.47, 135.62, 127.23, 122.32, 84.95, 83.63, 79.89, 31.89, 26.50, 25.26, 25.06.

APCI-MS: *m/z* calcd. for $C_{17}H_{27}BO_5S$: 354.2, found 371.7 $[M+NH_4]^+$.

*3,4-Bis(4-bromophenyl)-2,5-diphenylcyclopenta-2,4-dien-1-one (**1b**)*

1,2-Bis(4-bromophenyl)ethane-1,2-dione (**14**) (1.5 g, 4.08 mmol) and 1,3-diphenylacetone (**15**) (857 mg, 4.08 mmol) were dissolved in 150 mL ethanol and heated up to 85 °C. Subsequently, 1 M methanolic tetrabutylammonium hydroxide (TBAH) solution (1.06g, 4.08 mL, 4.08 mmol) was added. After stirring at 85 °C for 0.5 h, the reaction mixture was diluted in ethyl acetate. The organic layer was washed with water,

dried over sodium sulphate and concentrated *in vacuo*. The product was precipitated in an ethanol water mixture to afford building block **1b** as a dark red solid (1.89 g, 85%).

^{1}H NMR (300 MHz, CD_2Cl_2): δ (ppm) = 7.41–7.32 (m, 4H), 7.32–7.25 (m, 6H), 7.24–7.15 (m, 4H), 6.90–6.77 (m, 4H).

^{13}C NMR (75 MHz, CD_2Cl_2): δ (ppm) = 153.28, 132.24, 131.81, 131.38, 130.85, 130.49, 128.54, 128.18, 126.38, 123.35.

APCI-MS: *m/z* calcd. for $C_{29}H_{18}Br_2O$ 539.97, found 540.7 $[M+H]^+$.

*Dineopentyl 4',4'''-(4-oxo-3,5-diphenylcyclopenta-2,5-diene-1,2-diyl)bis-([1,1'-biphenyl]-4-sulfonate) (**3**)*

Building block **1b** (700mg, 1.29 mmol) and neopentyl 4-(4,4,5,5-tetramethyl-1,3,2-dioxaborolan-2-yl)benzenesulfonate (**2**) were dissolved in 40 mL 1,4-dioxane. Then, an aqueous 2 M potassium carbonate solution (2.68 g, 9.68 mL, 19.4 mmol) was added and the mixture was degassed with argon. Tetrakis(triphenylphosphine)palladium(0) ($Pd(PPh_3)_4$) was added and the reaction mixture was stirred at 90 °C overnight under argon atmosphere. The crude mixture was diluted with dichloromethane and the organic layer was washed with water and dried over sodium sulfate. After removing the solvent *in vacuo* the crude product was purified by silica gel column chromatography using a mixture of cyclohexane and THF (5:1) to obtain building block **3** as a red solid (340 mg, 34%).

^{1}H NMR (300 MHz, CD_2Cl_2): δ (ppm) = 7.85 (dd, J = 48.4, 8.3 Hz, 8H), 7.52 (d, J = 8.1 Hz, 4H), 7.33–7.22 (m, 10H), 7.12 (d, J = 8.2 Hz, 4H), 0.89 (s, 18H).

^{13}C NMR (75 MHz, CD_2Cl_2): δ = 200.21, 153.98, 145.80, 139.36, 135.30, 133.95, 131.15, 130.58, 128.84, 128.52, 128.11, 127.98, 127.30, 126.54, 80.23, 31.92, 26.10.

MALDI-TOF: *m/z* calcd. for $C_{51}H_{48}O_7S_2$ 3531.24, found 836.39 $[M]^{\bullet+}$.

*Pyr-G1-(Spen)$_8$ (**15**)*

1,3,6,8-Tetraethynylpyrene (**8**) (6 mg, 20.1 µmol) and building block **3** (101 mg, 121 µmol, 6 equiv) were dissolved in 3 mL *o*-xylene, degassed with argon and stirred at 145 °C for 36 h in a sealed microwave tube. The solvent was removed *in vacuo* and the crude product was purified by silica gel chromatography using a mixture of cyclohexane and THF (2:1). The product was further purified by *recycling*-GPC in chloroform to obtain dendrimer **15** as a yellow solid (19 mg, 27%).

^{1}H NMR (700 MHz, CD_2Cl_2): δ (ppm) = 8.03 – 7.80 (m, 21H), 7.71 – 7.48 (m, 19H), 7.38 – 6.38 (m, 75H), 3.71 – 3.57 (m, 16H), 0.93 – 0.81 (m, 72H).

^{13}C NMR (176 MHz, CD_2Cl_2): δ(ppm) = 146.12, 141.80, 141.54, 141.24, 140.17, 138.98, 136.90, 136.54, 136.19, 134.78, 132.82, 130.42, 130.33, 128.72, 128.68, 128.12, 128.07, 127.70, 127.61, 126.88, 126.28, 125.94, 80.12, 31.89, 26.09.

MALDI-TOF: *m/z* calcd. for $C_{224}H_{202}O_{24}S_8$ 3531.24, found 3532.72 $[M+H]^+$.

*Pyr-G1-S$_8$ (**10b**)*

Pyr-G1-(Spen)$_8$ **15** (7.00 mg, 1.98 µmol) was dissolved in 2 mL dry DMF, the resulting solution was degassed with argon and stirred at 180 °C in a sealed microwave tube for 48 h. The solvent was evaporated *in vacuo* and the product was precipitated in diethyl ether. The product was further purified by gel permeation chromatography (Sephadex LH-20) in DMF. Dendrimer **10b** was obtained as a slight yellow solid (5.2 mg, 88%).

^{1}H NMR (700 MHz, DMSO): δ (ppm) = 7.98–7.86 (m, 2H), 7.85–7.75 (m, 2H), 7.65–6.31 (m, 110H).

^{13}C NMR (176 MHz, DMSO): δ (ppm) = 147.06, 146.43, 141.53, 140.92, 139.74, 139.06, 138.45, 136.59, 136.14, 131.79, 129.62, 127.63, 126.61, 125.99, 125.94, 125.43, 125.35, 125.01, 124.96, 124.51.

MALDI-TOF: *m/z* calcd. for $C_{184}H_{122}O_{24}S_8$ 2970.61, found 2971.59 $[M+H]^+$, 2994.56 $[M+Na]^+$, 3009.56 $[M+K]^+$.

Synthesis of a first-generation positively charged amphiphilic polyphenylene dendrimer –$(PN)_4$

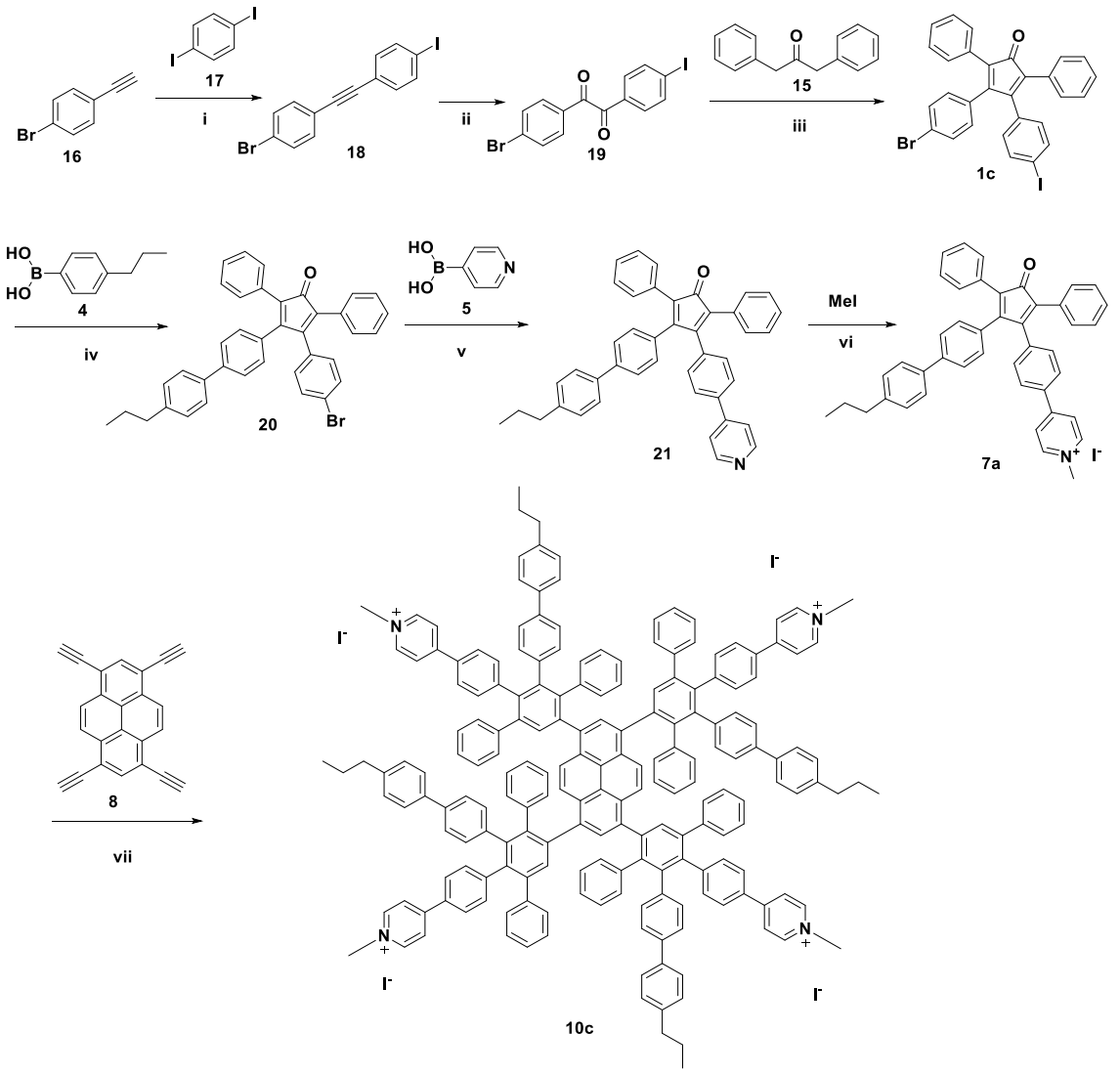

Figure S4.4. Synthesis of positively charged first-generation dendrimer **10c** with alternating pyridinium and n-propyl groups. i) CuI, PPh_3, $PdCl_2(Ph_3P)_2$, 1,4-dioxane, 40 °C, 15 h, 60% yield; ii) I_2, $[Ru(p\text{-cymene})Cl_2]_2$, tert-butyl hydroperoxide (70% in H_2O), 1,4-dioxane, 50 °C, 15 h, 86% yield; iii) TBAH, ethanol, 85 °C, 20 min, 60% yield; iv) $Pd(PPh_3)_4$, K_2CO_3 (aq), 1,4-dioxane, 40 °C, 15 h; v) $Pd(PPh_3)_4$, K_2CO_3 (aq), 1,4-dioxane, 80 °C, 15 h, 60 % yield; vi) methanol, RT, 48 h, 70% yield; vii) DMSO, 140 °C, 3 d, 47% yield.

*1-Bromo-4-((4-iodophenyl)ethynyl)benzene (**18**)*

4-Bromophenylacetylene (2.0 g, 11.05 mmol) (**16**), 1,4-diiodobenzene (**17**) (7.29 g, 22.10 mmol, 2 equiv), copper(I) iodide (210 mg, 1.1 mmol, 0.1 equiv) and triphenylphosphine (579 mg, 2.21 mmol, 0.2 equiv) were dissolved in 200 mL 1,4-dioxane in a 500 mL flask. To this mixture 50 mL triethylamine was added and the solution was degassed with argon. Bis(triphenylphosphine)palladium(II) dichloride ($PdCl_2(Ph_3P)_2$) (338 mg, 0.552 mmol) was added and the solution was stirred at 40 °C under argon atmosphere overnight. Then, the solution was filtered and the solvent was removed *in vacuo* followed by an extraction with dichloromethane. The organic layer was dried over magnesium sulphate and purified by silica gel flash chromatography using hexane as eluent to obtain compound **18** as a bright yellow solid (2.54 g, 60%).

^{1}H NMR (300 MHz, THF-d_8): δ (ppm) = 7.75 (d, J = 7.9 Hz, 2 H), 7.55 (d, J = 8.0 Hz, 2 H), 7.42 (d, J = 8.1 Hz, 2 H), 7.27 (d, J = 8.0 Hz, 2 H).

^{13}C NMR (75 MHz, THF-d_8): δ (ppm) = 138.44, 134.62, 133.71, 133.62, 132.64, 132.43, 123.31, 123.17, 122.81, 95.06, 90.08.

APCI-MS: *m/z* calcd. for $C_{14}H_8BrI$: 381.9, found 383.9 $[M+2H]^+$.

*1-(4-Bromophenyl)-2-(4-iodophenyl)ethane-1,2-dione (**19**)*

Tolane **18** (1.0 g, 2.61 mmol), iodine (132 mg, 0.522 mmol, 0.2 equiv) and dichloro(*p*-cymene)ruthenium(II) dimer (16 mg, 0.026 mmol, 0.01 equiv) were added to a 50 mL flask and dissolved in as little 1,4-dioxane as possible. 1.5 mL (10.44 mmol, 4 equiv) of a 70 % *tert*-butyl hydroperoxide solution was slowly added to the solution. The mixture was stirred at 50 °C overnight. After evaporation of the solvent and purification *via* silica gel flash column chromatography using hexane as eluent followed by THF benzil **19** was obtained as a yellow solid (931 mg, 86%).

^{1}H NMR (300 MHz, THF-d_8): δ (ppm) = 7.97 (d, J = 8.5 Hz, 2H), 7.88 (d, J = 8.6 Hz, 2H), 7.75 (d, J = 8.5 Hz, 2H), 7.70 (d, J = 8.5 Hz, 2H).

^{13}C NMR (75 MHz, THF-d_8): δ (ppm) = 193.57, 193.21, 139.43, 138.19, 133.33, 132.99, 132.27, 131.86, 130.91, 128.89, 125.95, 121.07, 104.30.

*3-(4-Bromophenyl)-4-(4-iodophenyl)-2,5-diphenylcyclopenta-2,4-dien-1-one (**1c**)*

Benzil **19** (500 mg, 1.2 mmol) and 1,3-diphenylacetone **3** (279 mg, 1.33 mmol, 1.1 equiv) were dissolved in 15 mL ethanol in a 50 mL flask. The solution was heated under reflux and 0.24 mL tetrabutylammonium hydroxide (1M in THF) were added. After 20 min the reaction was stopped by cooling in an ice bad. After cooling at −20 °C for a few hours the product was filtered off. Building block **1c** was received as a purple solid (424 mg, 60%).

^{1}H NMR (300 MHz, CD_2Cl_2): δ (ppm) = 7.56 (d, J = 8.3 Hz, 2 H), 7.35 (d, J = 8.5 Hz, 2 H), 7.31–7.24 (m, 6 H), 7.24–7.17 (m, 4 H), 6.82 (d, J = 8.5 Hz, 2 H), 6.68 (d, J = 8.5 Hz, 2 H).

^{13}C NMR (75 MHz, CD_2Cl_2): δ (ppm) = 200.17, 153.53, 153.42, 137.91, 132.92, 132.38, 131.96, 131.59, 131.53, 131.02, 131.01, 130.64, 128.70, 128.33, 126.57, 126.50, 123.50, 95.41.

APCI-MS: *m/z* calcd. for $C_{29}H_{18}BrIO$: 588.0, found 589.1 $[M+H]^+$.

*3-(4-Bromophenyl)-2,5-diphenyl-4-(4'-propyl-[1,1'-biphenyl]-4-yl)cyclopenta-2,4-dien-1-one (**20**)*

Building block **1c** (230 mg, 0.390 mmol) and 4-propylbenzeneboronic acid (**4**) (83 mg, 0.507 mmol, 1.3 equiv) were added to a 50 mL flask and were dissolved in 25 mL 1,4-dioxane. To this solution 0.97 mL of a 2 M potassium carbonate solution were added and degassed with argon. Then, $Pd(PPh_3)_4$ (27 mg, 0.023 mmol, 0.06 equiv) was added and the reaction mixture was stirred at 40 °C overnight. The reaction mixture was filtered and extracted with DCM followed by a filtration over a silica gel flash column using a mixture of THF and hexane (1:19). Product **20** was used without further purification.

APCI-MS: *m/z* calcd. for $C_{38}H_{29}BrO$: 580.1, found 581.5 $[M+H]^+$.

*2,5-Diphenyl-3-(4'-propyl-[1,1'-biphenyl]-4-yl)-4-(4-(pyridin-4-yl)phenyl)cyclopenta-2,4-dien-1-one (**21**)*

Building block **20** (380 mg, 0.653 mmol) and 4-pyridineboronic acid (**5**) (321 mg, 2.61 mmol, 4 equiv) were dissolved in 25 mL 1,4-dioxane in a 50 mL flask. 3.27 mL of a 2M

potassium carbonate solution were added and the mixture was degassed. After adding $Pd(PPh_3)_4$ (45 mg, 0.038 mmol, 0.06 equiv) the mixture was stirred at 80 °C for two days under argon atmosphere. The solvent was removed followed by an extraction with DCM. The purification was performed by silica gel flash chromatography using a mixture of THF and hexane (1:2). Building block **21** was received as a violet solid (236 mg, 60%).

^{1}H NMR (300 MHz, CD_2Cl_2): δ (ppm) = 8.64–8.57 (m, 2 H), 7.58–7.43 (m, 8 H), 7.32–7.20 (m, 12 H), 7.12 (d, J = 8.4 Hz, 2 H), 7.03 (d, J = 8.4 Hz, 2 H), 2.66–2.55 (m, 2 H), 1.70–1.56 (m, 2 H), 0.94 (t, J = 7.3 Hz, 3 H).

^{13}C NMR (75 MHz, CD_2Cl_2): δ (ppm) = 200.53, 154.81, 154.22, 152.06, 150.89, 150.83, 148.64, 147.60, 143.18, 141.65, 138.71, 138.51, 137.80, 136.47, 134.64, 132.17, 131.58, 131.44, 130.83, 130.78, 130.50, 129.66, 129.60, 129.58, 129.17, 128.87, 128.68, 128.65, 128.21, 128.12, 127.53, 127.15, 127.03, 126.80, 126.70, 126.13, 125.99, 122.09, 121.78, 38.16, 25.15, 14.17.

APCI-MS: *m/z* calcd. for $C_{43}H_{33}NO$: 579.3, found 580.4 $[M+H]^+$.

*1-Methyl-4-(4-(3-oxo-2,4-diphenyl-5-(4'-propyl-[1,1'-biphenyl]-4-yl)cyclopenta-1,4-dien-1-yl)phenyl)pyridin-1-ium (**7a**)*

Building block **21** (220 mg, 0.38 mmol) was dissolved in 1 mL methyl iodide in a 10 mL Schlenk tube followed by the addition of 1 mL methanol. After two days, the product was precipitated by the addition of diethyl ether. After filtration, compound **7a** was obtained as a red-brown solid (192 mg, 70%).

^{1}H NMR (300 MHz, DMSO-d_6): δ (ppm) = 8.96 (d, J = 6.6 Hz, 2 H), 8.46 (d, J = 7.1 Hz, 2 H), 8.00 (d, J = 8.5 Hz, 2 H), 7.59 (d, J = 2.7 Hz, 2 H), 7.56 (d, J = 2.5 Hz, 2 H), 7.35–7.16 (m, 14 H), 7.08 (d, J = 8.4 Hz, 2 H), 4.29 (s, 3 H), 2.56 (t, J = 7.5 Hz, 2 H), 1.58 (h, J = 7.4 Hz, 2 H), 0.87 (t, J = 7.3 Hz, 3 H).

^{13}C NMR (75 MHz, DMSO-d_6): δ (ppm) = 199.29, 154.27, 153.12, 153.03, 145.53, 141.99, 139.93, 136.65, 136.13, 133.09, 131.26, 130.43, 130.31, 130.20, 129.86, 129.59, 128.16, 128.11, 127.79, 127.60, 126.29, 126.11, 125.82, 124.93, 123.88, 47.04, 36.74, 23.91, 13.52.

ESI-MS: *m/z* calcd. for $C_{44}H_{36}NO^+$: 594.28, found 592.22 $[M+H]^+$.

*Pyr-G1(PN)$_4$ (**10c**)*

Building block **7a** (100 mg, 0.17 mmol) and 1,3,6,8-tetraethynylpyrene (**8**) (6.9 mg, 0.023 mmol, 0.14 equiv) were dissolved in 5 mL DMSO in a 10 mL Schlenk tube. After degassing with argon, the mixture was heated up to 140 °C for three days. After the addition of diethyl ether product **10c** precipitated and was filtered off. Purification was performed applying dialyses (1000 MWCO) in methanol. Dendrimer **10c** was received as yellow crystals (33.3 mg, 47%).

^{1}H NMR (300 MHz, DMSO-d_6): δ (ppm) = 8.90 (d, J = 6.7 Hz, 8 H), 8.47–6.04 (m, 106 H), 4.25 (s, 12 H), 1.65–1.42 (m, 8 H), 0.86 (t, J = 6.5 Hz, 12 H).

^{13}C-NMR (126 MHz, DMSO-d_6): δ (ppm) = 153.09, 145.46, 141.13, 140.68, 136.32, 132.60, 131.58, 130.31, 129.66, 128.88, 127.88, 126.60, 125.91, 124.83, 123.33, 46.88, 36.71, 24.64, 13.53.

ESI-MS: *m/z* calcd. for $(C_{196}H_{154}N_4)^{4+}$: 641.31, found 641.14; *m/z* calcd. for $(C_{196}H_{154}N_4)^{3+}$: 897.38, found 897.31; *m/z* calcd. for $(C_{196}H_{154}N_4)^{2+}$: 1409.52, found 1409.44.

Synthesis of a second-generation positively charged amphiphilic polyphenylene dendrimer – $(PN)_8$

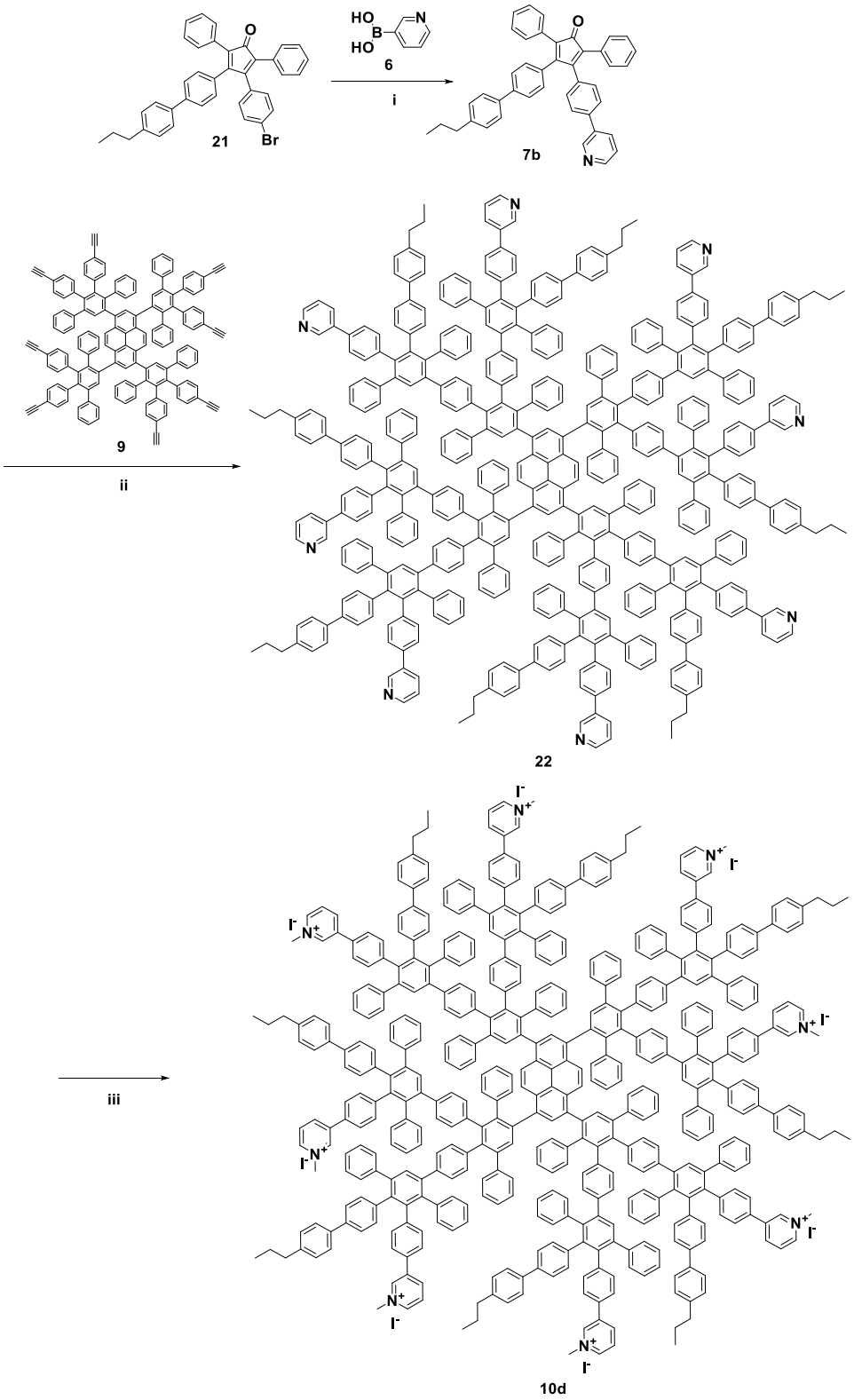

Figure S4.5. Synthesis of second-generation dendrimer **15d** with alternating pyridinum and *n*-propyl groups. i) $Pd(PPh_3)_4$, K_2CO_3 (aq), 1,4-dioxane, 80 °C, 15 h, 50 % yield; ii) *o*-xylene, 160 °C, 3 d, 64% yield; iii) methanol, RT, 15 h, 92% yield.

*2,5-Diphenyl-3-(4'-propyl-[1,1'-biphenyl]-4-yl)-4-(4-(pyridin-3-yl)phenyl)cyclopenta-2,4-dien-1-one (**7b**)*

Compound **21** (380 mg, 0.653 mmol) and 4-pyridineboronic acid (**6**) (321 mg, 2.61 mmol, 4 equiv) were dissolved in 25 mL 1,4-dioxane in a 50 mL flask. 3.27 mL of a 2M potassium carbonate solution were added and the mixture was degassed with argon. After adding $Pd(PPh_3)_4$ (45 mg, 0.038 mmol, 0.06 equiv) the mixture was stirred at 80 °C for two days under argon atmosphere. The solvent was removed *in vacuo* followed by an extraction with dichloromethane (DCM). The purification was performed by silica gel flash chromatography using a mixture of THF and hexane (1:2). Building block **7b** was received as a violet solid (112 mg, 50%).

^{1}H NMR (300 MHz, CD_2Cl_2): δ (ppm) = 8.82 (d, J = 2.4 Hz, 1 H), 8.55 (dd, J = 4.9, 1.6 Hz, 1 H), 7.88 (dt, J = 8.1, 2.1 Hz, 1 H), 7.55–7.43 (m, 5 H), 7.27 (d, J = 9.3 Hz, 14 H), 7.11 (d, J = 8.2 Hz, 2 H), 7.04 (d, J = 8.3 Hz, 2 H), 2.61 (t, J = 7.6 Hz, 2 H), 1.74–1.54 (m, 2 H), 0.94 (t, J = 7.3 Hz, 3 H).

^{13}C NMR (75 MHz, CD_2Cl_2): δ (ppm) = 200.61, 154.85, 154.44, 149.31, 148.66, 143.16, 141.61, 138.41, 137.82, 136.12, 134.58, 133.56, 132.22, 131.62, 131.52, 130.79, 130.76, 130.50, 129.55, 128.63, 128.61, 128.14, 128.07, 127.14, 127.06, 126.76, 126.53, 126.13, 125.97, 124.08, 38.14, 25.12, 14.12.

APCI-MS: *m/z* calcd. for $C_{43}H_{33}NO$: 579.3, found 580.4 $[M+H]^+$.

*Pyr-G1-(ethynyl)$_8$ **9***

First generation dendrimer **9** was synthesized according to the literature.[8]

^{1}H NMR (300 MHz, THF-d_8): δ (ppm) = 8.05–7.31 (m, 8 H), 7.29–7.02 (m, 28 H), 7.02–6.71 (m, 34 H), 6.71–6.43 (m, 12 H), 3.47–3.32 (m, 8 H).

^{13}C NMR (126 MHz, THF-d_8): δ (ppm) = 142.00, 141.69, 132.76, 131.84, 131.49, 131.42, 130.98, 130.85, 128.69, 128.61, 121.22, 120.89, 78.90.

MALDI-TOF: m/z calcd. for $C_{152}H_{90}$: = 1914.70, found 1914.62 $[M]^{\bullet+}$.

*Pyr-G2-(PN)$_8$ uncharged **22***

First generation dendrimer core **9** (50 mg, 0.0261 mmol) and building block **7b** (242 mg, 0.418 mmol, 16 equiv) were dissolved in 1 mL *o*-xylene in a 10 mL Schlenk tube. After degassing, the reaction mixture was heated up to 160 °C for three days. Subsequently, dendrimer **22** was precipitated in methanol and purified by GPC in THF. Dendrimer **22** was obtained as a yellow solid (106 mg, 64%).

^{1}H NMR (500 MHz, THF-d_8): δ (ppm) = 8.67 (d, *J* = 12.4 Hz, 8H), 8.40 (s, 8H), 7.80–7.72 (m, 8H), 7.56–6.30 (m, 274H), 1.60 (h, *J* = 6.1, 5.7 Hz, 16H), 0.90 (t, *J* = 7.3 Hz, 24H).

^{13}C NMR (126 MHz, THF-d_8): δ (ppm) = 149.21, 148.92, 142.99, 142.59, 142.41, 142.35, 142.33, 142.17, 142.10, 141.75, 141.66, 141.39, 141.25, 141.17, 140.37, 140.27, 139.97, 139.81, 139.74, 139.42, 139.05, 138.89, 138.85, 138.77, 136.66, 136.63, 135.99, 135.71, 134.19, 134.16, 133.43, 133.09, 130.88, 129.61, 129.59, 128.58, 127.95, 127.26, 127.24, 126.68, 126.27, 125.99, 125.72, 124.10, 68.07, 67.92, 67.75, 67.57, 38.53, 25.94, 25.79, 25.64, 25.48, 14.15.

MALDI-TOF: *m/z* calcd. for $C_{488}H_{354}N_8$ 6324.79, found 6325.89 $[M+H]^+$.

*Pyr-G2-(PN)$_8$ **10d***

Dendrimer **22** (106 mg, 0.017 mmol) was dissolved in 1 mL methyl iodide in a 10 mL Schlenk tube followed by the addition of 1 mL methanol. After 24 h diethyl ether was added leading to precipitation of the product which was filtered off to obtain dendrimer **10d** as a yellow-brown solid (116 mg, 92 %).

^{1}H NMR (300 MHz, DMSO-d_6): δ (ppm) = 9.22 (s, 8 H), 8.81 (s, 8 H), 8.68 (s, 8 H), 8.03 (s, 8 H), 7.63–6.38 (m, 266 H), 4.27 (s, 24 H), 1.60–1.44 (m, 16 H), 0.83 (t, J = 7.0 Hz, 24 H).

^{13}C NMR (126 MHz, DMSO-d_6): δ (ppm) = 153.21, 143.25, 140.89, 140.25, 137.99, 136.30, 132.30, 131.63, 130.83, 129.95, 129.48, 128.87, 127.78, 127.57, 125.88, 125.53, 124.62, 124.23, 47.95, 40.02, 39.86, 39.69, 39.52, 39.35, 39.19, 39.02, 36.69, 23.99, 13.52.

ESI-MS: *m/z* calcd. for $(C_{496}H_{378}N_8)^{8+}$: 806.37, found 806.24; *m/z* calcd. for $(C_{496}H_{378}N_8I)^{7+}$: 939.56, found 939.55; *m/z* calcd. for $(C_{496}H_{378}N_8I_2)^{6+}$: 1117.30, found

1117.29; *m/z* calcd. for $(C_{496}H_{378}N_8I_3)^{5+}$: 1366.14, found 1366.15; *m/z* calcd. for $(C_{496}H_{378}N_8I_4)^{4+}$: 1739.40, found 1739.39.

4.5.2 Protein corona on dendrimer-coated liposomes and polystyrene nanoparticles

Material and methods

Liposome synthesis. Based on previous reports,[15] amine functionalized liposomes were synthesized using 1,2-dioleoyl-*sn*-glycero-3-phosphoethanolamine (DOPE), L-*α*-phosphatidylcholine (egg PC) and cholesterol (Chol) with a molar ratio of egg PC:DOPE:Chol = 1:1:1 by film hydration followed by extrusion. Cholesterol and the lipids were dissolved in chloroform at a concentration of 10 mg mL^{-1}. All components (Egg PC = 835 µL, DOPE = 767 µL and Cholesterol = 398 µL) were mixed with 2 mL of chloroform containing 1 vol% EtOH in a 50 mL round-bottomed flask. The mixture was dried using a rotary evaporator at room temperature (30 min, 450 mbar) and further at 42°C (30 min, 3 mbar). To remove organic solvent residuals the flask was placed into a vacuum oven for 1 hour. (Diameter Ø: 242 ± 6 nm, ζ – Potential: - 52 ± 6 mV)

Polystyrene nanoparticle synthesis. According to previous reports,[28, 29] amine functionalised polystyrene nanoparticles were prepared *via* direct miniemulsion. For colloidal stability, the ionic surfactant cetyl trimethyl ammonium chloride was used. To generate amino groups, 2-aminoethyl methacrylate hydrochloride (2 wt% to styrene) was copolymerized with styrene. Excessive surfactant was removed *via* dialysis. A detailed protocol is given in previous reports.[18] (Diameter Ø: 98 ± 10 nm, ζ – Potential: + 34 ± 12 mV)

Coating of nanoparticles and liposomes with dendrimers. All dendrimers were dissolved in DMSO at a concentration of 10 mg mL^{-1}. PS-NH_2 nanoparticles (10 mg mL^{-1}, 100 µL) and liposomes-NH_2 (3 mg mL^{-1}, 333 µL) were mixed with the dendrimers (10 mg mL^{-1}, 100 µL) and incubated at room temperature for 1 h. To remove unbound dendrimers, the liposome dispersion was diluted with 1 mL of PBS and the PS-nanoparticle dispersion with 1 mL of water. Afterwards, the mixture was centrifuged (20 000 g, 15 min, 4°C). Finally, polystyrene nanoparticles were resuspended in 100 µL of water and liposomes were resuspended in 100 µL of PBS.

Zeta Potential. Measurements were performed using a Nano Z Zetasizer (Malvern Instruments GmbH, Herrenberg, Germany). Uncoated and coated liposomes/PS-nanoparticles (20 µL) were diluted with 1 mL of a 1 mM KCl solution and measured instantly at 25 °C. Each measurement was repeated in technical triplicate.

Human serum/plasma. Human blood serum and plasma was obtained from healthy donors from the Transfusion Center of the University Clinic of Mainz, Germany. For plasma preparation, citrate was used as an anticoagulant. Six serum batches and ten plasma batches were pooled together and stored at −20 °C.

Protein corona analysis. Uncoated and coated liposomes or polystyrene nanoparticles (10 mg mL^{-1}, 100 µL) were incubated with 1 mL of human serum or human plasma at 37 °C for 1 h. The protein corona coated liposomes and nanoparticles were centrifuged (20 000 g, 15 min, 4 °C) and washed with 1 mL PBS solution to remove unbound and loosely bound proteins. Overall, this step was repeated three times. The adsorbed corona proteins were detached from the surface by resuspending the liposome/nanoparticle pellet in 100 µL of an aqueous solution containing 2% SDS supplemented with 62.5 mM Tris-HCL (Sigma Aldrich, Germany). Afterwards, the dispersion was incubated for 5 min at 95 °C and centrifuged as described above. The supernatant contained the detached corona proteins.

Protein Assay. The protein concentration was determined by Pierce 660 nm Protein Assay (Thermo Fisher, Germany) according to manufacturer's instructions.

In solution digestion. Prior to LC-MS analysis, proteins were digested according to former protocols.[16, 18, 30] Briefly, SDS was removed *via* Pierce detergent removal columns (Thermo Fisher, Germany) according to the manufacture's instruction. Afterwards, proteins were precipitated using ProteoExtract protein precipitation kit (Merck Millipore, Germany) overnight and the protein pellet was isolated *via* centrifugation (14 000 g, 10 min). Precipitated proteins were resuspended in RapiGest SF (Waters, USA) dissolved in 50 mM ammonium bicarbonate (Sigma Aldrich, Germany) and incubated at 80 °C for 15 min. Further, proteins were reduced with dithithreitol at 56 °C for 45 min (5 mM, Sigma Aldrich, Germany) and alkylated with idoacetoamide at room temperature in the dark for 1 h (15 mM, Sigma Aldrich, Germany). Digestion was carried out using a protein:trypsin ratio of 50:1 for 14–18 h at 37 °C and stopped by adding 2 µL

hydrochloric acid (Sigma Aldrich, Germany). To remove degradation products of RapiGest SF, the peptide sample was centrifuged (14 000 g, 15 min, 4 °C).

Liquid chromatography-high resolution mass spectrometry (LC-MS). The peptide samples were spiked with 50 fmol of Hi3 EColi Standard (Waters, USA) for absolute protein quantification. Peptides were separated using a nanoACQUITY UPLC system equipped with a C18 nanoACQUITY Trap Column (5 µm, 180 µm x 20 mm, Waters, USA) and C18 analytic reversed phase column (1.7 µm, 75 µm x 150 mm, Waters, USA). The UPLC system was coupled to a Synapt G2-Si mass spectrometer (Waters, USA) and electrospray ionization (ESI) was carried in positive ion with a nanoLockSpray source. The high-resolution mass spectrometer was operated in resolution mode performing data-independent experiments (MS^E). Data was processed with MassLynx 4.1 and all proteins were identified with Progenesis QI. A reviewed human data base downloaded from Uniprot and the peptide sequence of Hi3 Ecoli standard (Chaperone protein CLpB, Water, USA) was added for absolute protein quantification. Based on the TOP3/Hi3 approach[31] all proteins were quantified and the absolute amount in fmol is calculated.

Statistical Analysis. GraphPad Prism 8.4.2 Software was used for statistical analysis applying a one-way ANOVA followed by Tukey's post-hoc multiple comparisons test for all protein corona results. For zeta-potential and Pierce Assay a one-way ANOVA followed by Dunnett's post-hoc multiple comparisons test was used. Significance was considered at *p*-values such as not significant (ns) for $p > 0.05$, and significant * for $p \leq 0.05$, ** for $p \leq 0.01$, *** for $p \leq 0.001$, **** for $p \leq 0.0001$.

Supplementary figures: Coating of liposomes and polystyrene nanoparticles and their respective protein corona

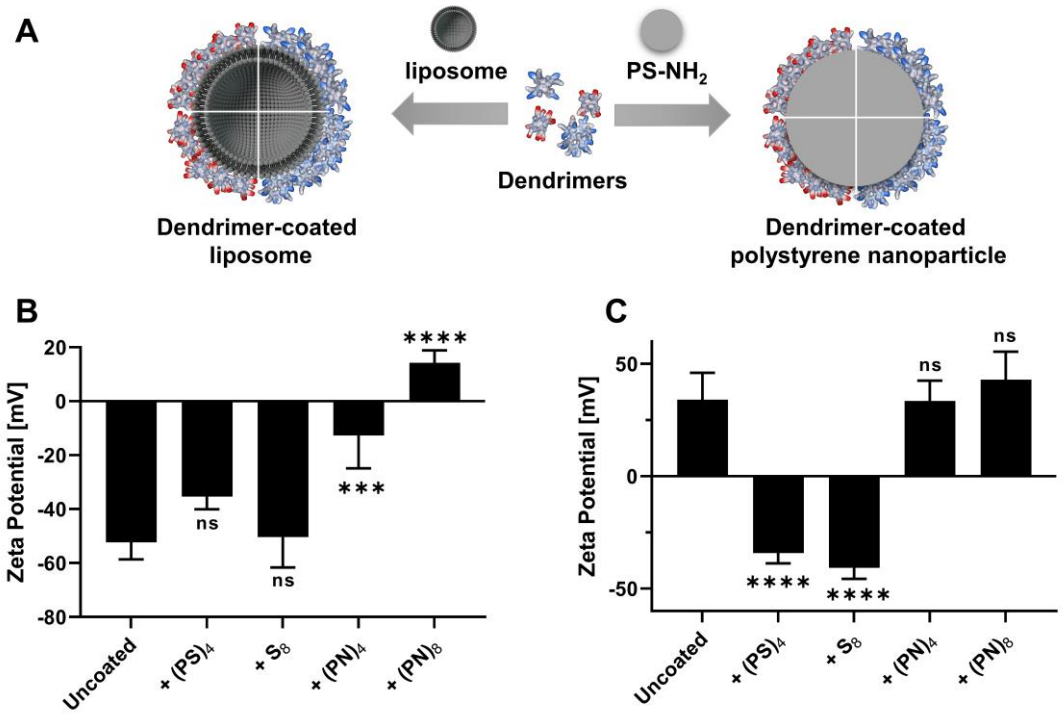

Figure S4.6. Verification of dendrimer-coating on liposomes and polystyrene nanoparticles (PS-NH_2). (**A**) Dendrimers were mixed with liposomes and ζ-potentials of (**B**) lipo-dendrimers and (**C**) PS-dendrimers were measured. $(PN)_4$ and S_8 did not show a clear change in ζ-potential values when mixed with liposomes indicating an insufficient coating. The same was observed for $(PN)_4$ and $(PN)_8$ when mixed with PS nanoparticles (n = minimum 2; one-way ANOVA; ns for $p > 0.05$, *** for $p \leq 0.001$, **** for $p \leq 0.0001$).

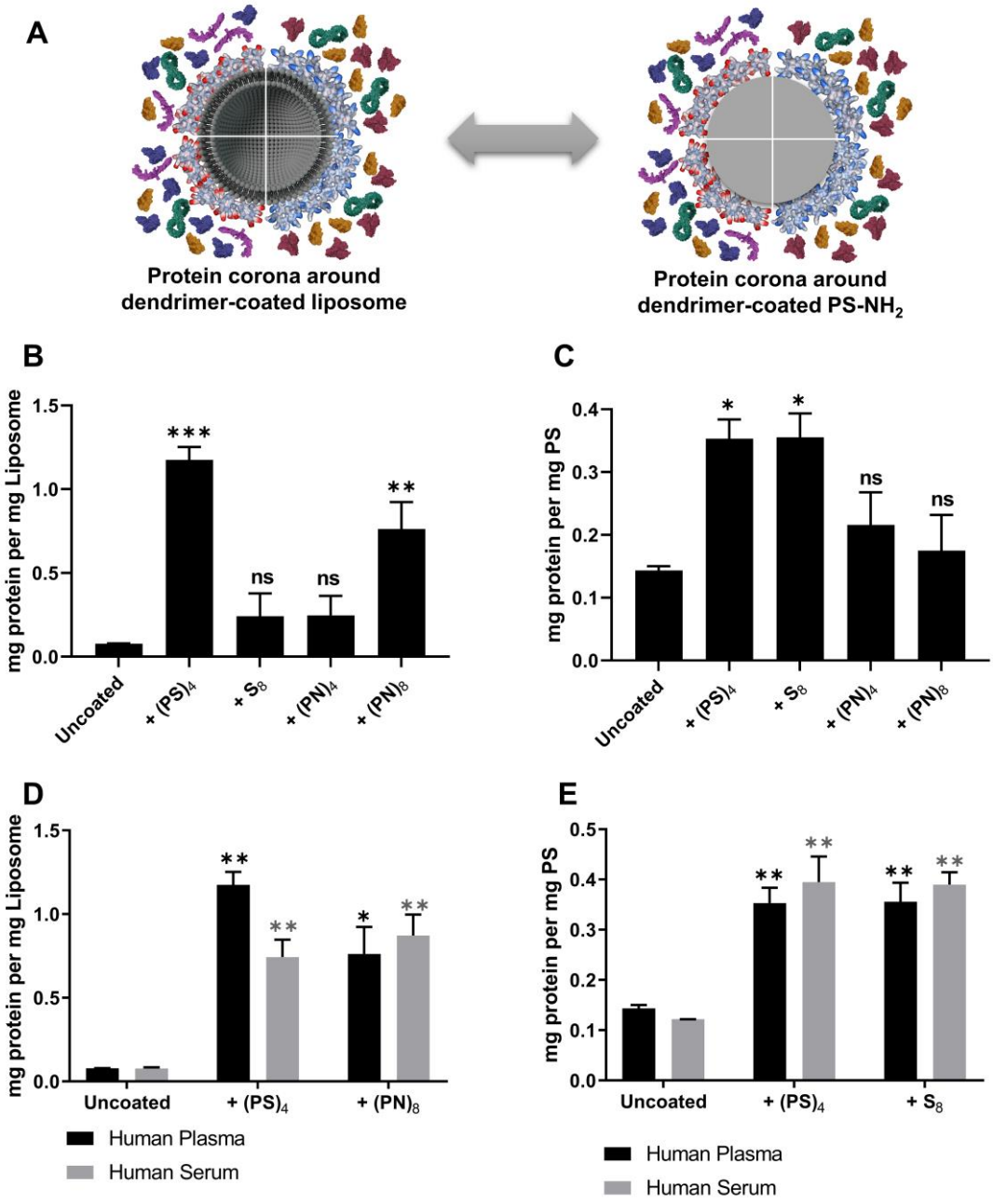

Figure S4.7. Verification of protein adsorption on lipo-dendrimers and PS-dendrimers: (**A**) Comparison of protein adsorption on lipo-dendrimers and PS-dendrimers. Quantification of protein adsorption by Pierce Assay for (**B**) lipo-dendrimers and (**C**) PS-dendrimers in blood plasma. Liposomes and PS nanoparticles with insufficient dendrimer binding did not show significant differences in protein quantities. Protein quantification by Pierce Assay for efficient dendrimer-coatings in human plasma and serum for (**D**) lipo-$(PS)_4$ and lipo-$(PN)_8$ as well as (**E**) PS-$(PS)_4$ and PS-S_8 (n = minimum 2; one-way ANOVA; ns for $p > 0.05$, * for $p \leq 0.05$, ** for $p \leq 0.01$, *** for $p \leq 0.001$).

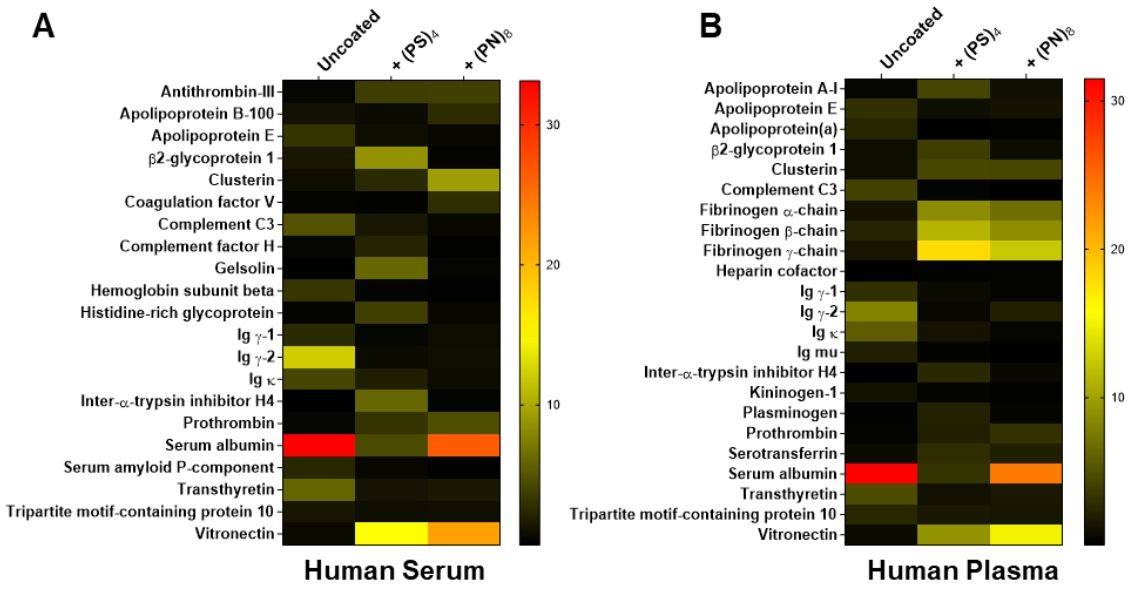

Figure S4.8. Heatmaps of adsorbed proteins to dendrimer-coated liposomes lipo-$(PS)_4$ and lipo-$(PN)_8$ in (**A**) blood serum and (**B**) blood plasma.

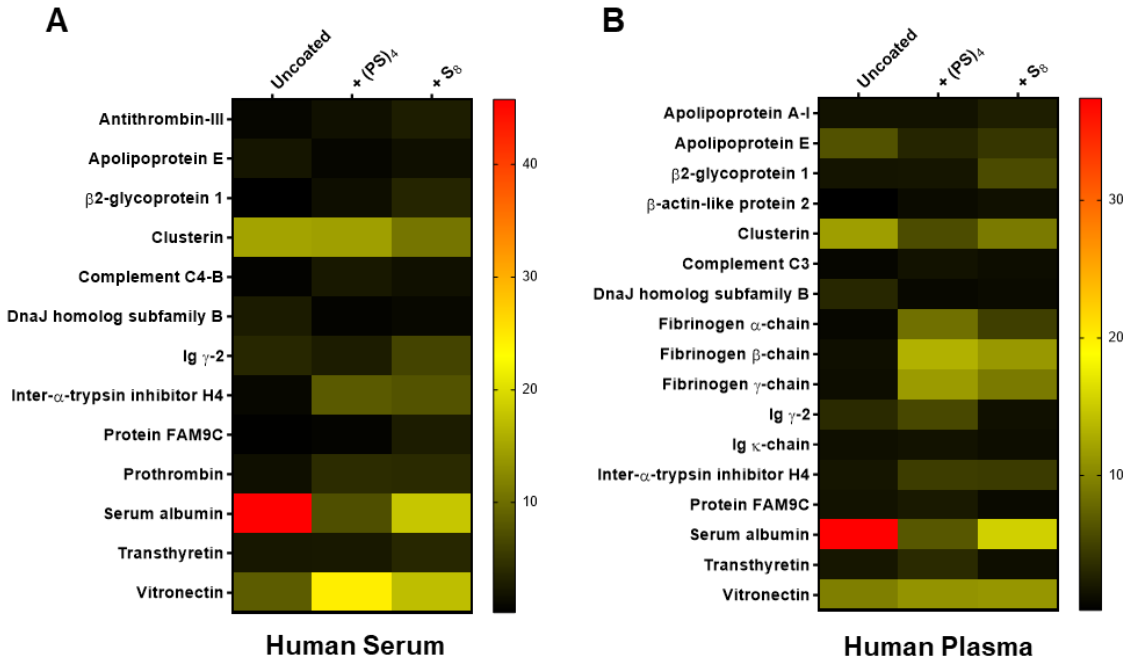

Figure S4.9. Heatmaps of adsorbed proteins to dendrimer-coated polystyrene nanoparticles PS-$(PS)_4$ and PS-S_8 in (**A**) blood serum and (**B**) blood plasma.

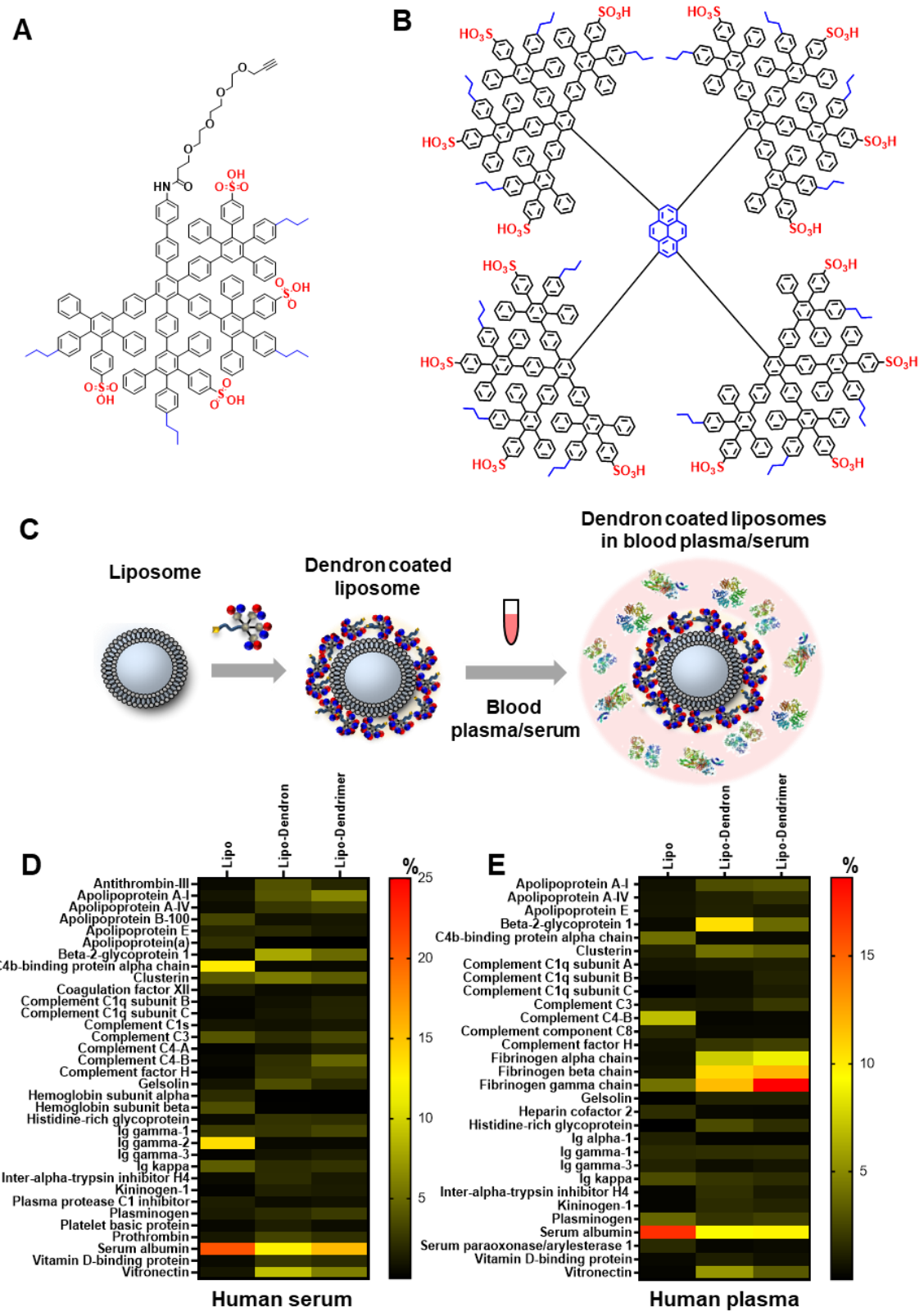

Figure S4.10. Protein corona on dendron- and dendrimer-coated liposomes. (**A**) Amphiphilic polyphenylene dendron[10] and (**B**) amphiphilic polyphenylene dendrimer[8] with high density of surface pattern. (**C**) Coating of liposomes and addition of human serum and plasma. Heat map of adsorbed proteins on lipo-dendron and lipo-dendrimer in (**D**) human serum and (**E**) human plasma. (**C**-**E**). Reproduced from Wagner et al.[10] (https://doi.org/10.1002/anie.201913708). Licensed under a Creative Commons Attribution (CC BY) license (http://creativecommons.org/licenses/by/4.0/).

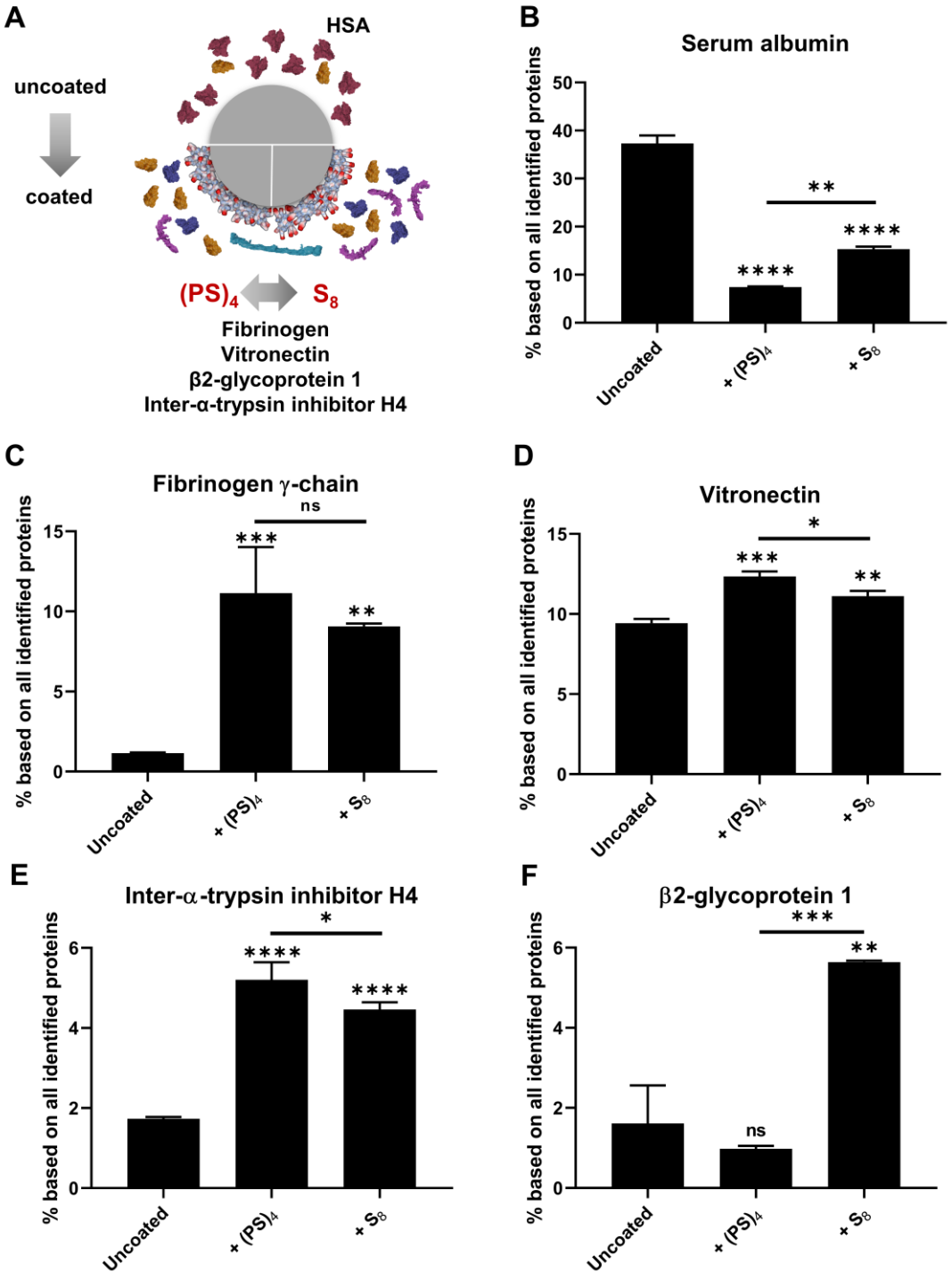

Figure S4.11. Comparison of adsorbed proteins between uncoated polystyrene nanoparticles (PS-NH_2) and PS-dendrimers (PS-$(PS)_4$ and PS-S_8). (**A**) Coating of PS-NH_2 lead to a different protein corona: Reduction of (**B**) serum albumin adsorption and enhancement of (**C**) fibrinogen, (**D**) vitronectin, (**E**) inter-α-trypsin inhibitor H4 and (**F**) β-2 glycoprotein 1 (n = minimum 2; one-way ANOVA; ns for $p > 0.05$, * for $p \leq 0.05$, ** for $p \leq 0.01$, *** for $p \leq 0.001$, **** for $p \leq 0.0001$).

				Average in %						Standard deviation					
				Plasma			Serum			Plasma			Serum		
Accession	Peptide count	Unique peptides	Description	Uncoated	(PS)4	(PN)8	Uncoated	(PS)4	(PN)8	Uncoated	(PS)4	(PN)8	Uncoated	(PS)4	(PN)8
\63267;P68032	6	3	Actin_ aortic smooth muscle OS=Homo sapiens GN=ACTA2 PE=1 SV=1	0.42	0.01	0.01	0.13	0.07	0.24	0.00	0.01	0.00	0.01	0.05	0.20
63261;Q562R1	9	3	Actin_ cytoplasmic 1 OS=Homo sapiens GN=ACTB PE=1 SV=1	0.58	0.08	0.12	1.85	0.48	0.32	0.01	0.03	0.00	0.06	0.36	0.11
P02763	3	3	Alpha-1-acid glycoprotein 1 OS=Homo sapiens GN=ORM1 PE=1 SV=1	0.28	0.01	0.00	0.35	0.10	0.03	0.01	0.00	0.00	0.01	0.14	0.02
P01011	2	2	Alpha-1-antichymotrypsin OS=Homo sapiens GN=SERPINA3 PE=1 SV=2	0.04	0.00	0.01	0.03	0.07	0.01	0.00	0.01	0.00	0.01	0.08	0.01
P01009	14	12	Alpha-1-antitrypsin OS=Homo sapiens GN=SERPINA1 PE=1 SV=3	0.67	0.11	0.16	0.54	0.24	0.27	0.04	0.01	0.00	0.01	0.17	0.16
P04217	4	4	Alpha-1B-glycoprotein OS=Homo sapiens GN=A1BG PE=1 SV=4	0.01	0.20	0.05	0.02	0.06	0.37	0.01	0.02	0.01	0.00	0.04	0.51
P08697	10	10	Alpha-2-antiplasmin OS=Homo sapiens GN=SERPINF2 PE=1 SV=3	0.09	0.26	0.14	0.54	0.25	0.37	0.01	0.00	0.01	0.01	0.24	0.34
P02765	11	11	Alpha-2-HS-glycoprotein OS=Homo sapiens GN=AHSG PE=1 SV=1	0.04	0.46	0.04	0.02	0.90	0.09	0.00	0.04	0.01	0.00	0.70	0.05
P01023	11	9	Alpha-2-macroglobulin OS=Homo sapiens GN=A2M PE=1 SV=3	0.21	0.02	0.01	0.11	0.04	0.05	0.00	0.00	0.00	0.01	0.04	0.03
P01019	8	7	Angiotensinogen OS=Homo sapiens GN=AGT PE=1 SV=1	0.00	0.02	0.00	0.15	0.21	0.05	0.00	0.00	0.00	0.01	0.22	0.04
P16157	4	2	Ankyrin-1 OS=Homo sapiens GN=ANK1 PE=1 SV=3	0.22	0.00	0.01	0.10	0.01	0.02	0.01	0.00	0.00	0.01	0.00	0.01
P01008	38	37	Antithrombin-III OS=Homo sapiens GN=SERPINC1 PE=1 SV=1	0.80	0.90	0.82	0.38	5.23	4.84	0.03	0.07	0.04	0.01	5.66	5.16
P02647	32	32	Apolipoprotein A-I OS=Homo sapiens GN=APOA1 PE=1 SV=1	0.42	4.65	1.02	0.21	1.16	2.05	0.02	0.12	0.02	0.00	0.94	1.75
P02652	8	8	Apolipoprotein A-II OS=Homo sapiens GN=APOA2 PE=1 SV=1	0.04	0.17	0.13	0.03	0.21	0.19	0.01	0.07	0.00	0.00	0.17	0.23
P06727	41	41	Apolipoprotein A-IV OS=Homo sapiens GN=APOA4 PE=1 SV=3	0.15	0.63	0.91	0.12	1.07	0.86	0.03	0.15	0.07	0.01	0.38	0.72
P04114	155	131	Apolipoprotein B-100 OS=Homo sapiens GN=APOB PE=1 SV=2	1.43	0.14	0.25	1.12	0.73	6.38	0.02	0.01	0.02	0.03	0.33	10.38
P02656	2	2	Apolipoprotein C-III OS=Homo sapiens GN=APOC3 PE=1 SV=1	0.08	0.26	0.15	0.05	1.50	1.14	0.01	0.01	0.00	0.01	1.93	1.53
P05090	8	7	Apolipoprotein D OS=Homo sapiens GN=APOD PE=1 SV=1	0.49	0.13	0.16	0.05	0.16	0.43	0.53	0.02	0.00	0.00	0.03	0.17
P02649	28	27	Apolipoprotein E OS=Homo sapiens GN=APOE PE=1 SV=1	2.96	0.84	1.08	3.01	0.88	0.41	0.05	0.06	0.04	0.02	0.32	0.06
P08519	12	10	Apolipoprotein(a) OS=Homo sapiens GN=LPA PE=1 SV=1	2.40	0.11	0.21	0.80	0.49	0.08	0.04	0.00	0.00	0.01	0.00	0.44	0.07
P02730	14	11	Band 3 anion transport protein OS=Homo sapiens GN=SLC4A1 PE=1 SV=3	1.63	0.02	0.02	1.11	0.06	0.20	0.15	0.01	0.00	0.16	0.04	0.32
P02749	21	20	Beta-2-glycoprotein 1 OS=Homo sapiens GN=APOH PE=1 SV=3	0.81	4.30	0.88	1.48	6.86	0.40	0.09	0.13	0.26	0.01	5.69	0.57
P04003	19	17	C4b-binding protein alpha chain OS=Homo sapiens GN=C4BPA PE=1 SV=2	0.58	0.07	0.12	1.09	0.35	0.93	0.03	0.01	0.00	0.04	0.42	0.83
Q96IY4	3	3	Carboxypeptidase B2 OS=Homo sapiens GN=CPB2 PE=1 SV=2	0.03	0.02	0.00	0.02	0.11	0.10	0.01	0.01	0.00	0.01	0.06	0.09
P15169	3	3	Carboxypeptidase N catalytic chain OS=Homo sapiens GN=CPN1 PE=1 SV=1	0.10	0.02	0.00	0.07	0.09	0.02	0.00	0.00	0.00	0.00	0.13	0.03
Q5VT06	5	5	Centrosome-associated protein 350 OS=Homo sapiens GN=CEP350 PE=1 SV=1	0.00	0.01	0.00	0.00	0.30	0.00	0.00	0.00	0.00	0.00	0.51	0.00
P10909	29	29	Clusterin OS=Homo sapiens GN=CLU PE=1 SV=1	0.88	4.64	4.27	0.72	2.14	4.28	0.03	0.13	0.19	0.03	1.67	6.58
P00740	20	20	Coagulation factor IX OS=Homo sapiens GN=F9 PE=1 SV=2	0.07	0.92	0.68	0.01	0.31	1.80	0.00	0.02	0.01	0.00	0.28	2.92
P12259	42	34	Coagulation factor V OS=Homo sapiens GN=F5 PE=1 SV=4	0.16	0.19	0.06	0.23	0.21	7.11	0.01	0.02	0.01	0.00	0.14	11.55
P08709	6	5	Coagulation factor VII OS=Homo sapiens GN=F7 PE=1 SV=1	0.05	0.44	0.26	0.00	0.14	0.01	0.01	0.03	0.03	0.00	0.19	0.01
P00742	5	4	Coagulation factor X OS=Homo sapiens GN=F10 PE=1 SV=2	0.01	0.01	0.06	0.00	0.04	0.05	0.00	0.00	0.01	0.00	0.02	0.03
P03951	17	16	Coagulation factor XI OS=Homo sapiens GN=F11 PE=1 SV=1	0.03	0.26	0.21	0.02	0.34	0.19	0.01	0.04	0.02	0.00	0.14	0.06
P00748	12	11	Coagulation factor XII OS=Homo sapiens GN=F12 PE=1 SV=3	0.02	0.03	0.02	0.02	0.71	0.20	0.00	0.00	0.00	0.01	0.59	0.14
P00736	12	12	Complement C1r subcomponent OS=Homo sapiens GN=C1R PE=1 SV=2	0.03	0.09	0.04	0.01	0.58	3.09	0.00	0.07	0.01	0.00	0.42	4.64
P09871	5	4	Complement C1s subcomponent OS=Homo sapiens GN=C1S PE=1 SV=1	0.00	0.09	0.07	0.00	0.13	3.29	0.00	0.02	0.01	0.00	0.10	5.55
P06681	7	6	Complement C2 OS=Homo sapiens GN=C2 PE=1 SV=2	0.00	0.03	0.01	0.00	0.38	0.01	0.00	0.02	0.00	0.00	0.47	0.01
P01024	106	100	Complement C3 OS=Homo sapiens GN=C3 PE=1 SV=2	4.05	0.32	0.07	4.82	1.37	0.31	0.07	0.03	0.00	0.02	0.87	0.22
P0C0L4	65	3	Complement C4-A OS=Homo sapiens GN=C4A PE=1 SV=2	1.25	0.06	0.12	0.88	0.22	0.23	0.08	0.00	0.01	0.05	0.17	0.21
P0C0L5	66	3	Complement C4-B OS=Homo sapiens GN=C4B PE=1 SV=2	1.07	0.05	0.11	0.75	0.19	0.20	0.06	0.00	0.01	0.03	0.15	0.18
P13671	17	13	Complement component C6 OS=Homo sapiens GN=C6 PE=1 SV=3	0.06	0.01	0.00	0.01	0.18	0.02	0.00	0.01	0.00	0.00	0.17	0.03
P10643	10	9	Complement component C7 OS=Homo sapiens GN=C7 PE=1 SV=2	0.28	0.16	0.03	0.05	0.25	0.52	0.01	0.03	0.00	0.01	0.08	0.51
P07358	11	11	Complement component C8 beta chain OS=Homo sapiens GN=C8B PE=1 SV=3	0.03	0.13	0.05	0.03	0.16	0.06	0.00	0.01	0.00	0.00	0.18	0.06
P02748	14	11	Complement component C9 OS=Homo sapiens GN=C9 PE=1 SV=2	0.81	0.05	0.02	0.76	0.27	0.41	0.01	0.00	0.00	0.00	0.15	0.27
P00751	22	19	Complement factor B OS=Homo sapiens GN=CFB PE=1 SV=2	0.04	0.07	0.02	0.05	1.18	0.16	0.00	0.01	0.00	0.01	1.15	0.12
P00746	5	5	Complement factor D OS=Homo sapiens GN=CFD PE=1 SV=5	0.01	0.02	0.01	0.00	0.22	0.01	0.01	0.00	0.00	0.00	0.20	0.01
\08603;Q0298	65	59	Complement factor H OS=Homo sapiens GN=CFH PE=1 SV=4	0.22	0.10	0.05	0.33	3.42	0.21	0.01	0.01	0.01	0.01	3.77	0.17
Q03591	15	3	Complement factor H-related protein 1 OS=Homo sapiens GN=CFHR1 PE=1 SV=2	0.12	0.59	0.06	0.10	1.91	0.33	0.01	0.02	0.00	0.01	1.96	0.30
P36980	8	2	Complement factor H-related protein 2 OS=Homo sapiens GN=CFHR2 PE=1 SV=1	0.01	0.04	0.00	0.00	0.14	0.03	0.00	0.00	0.00	0.00	0.16	0.04
Q9BXR6	16	12	Complement factor H-related protein 5 OS=Homo sapiens GN=CFHR5 PE=1 SV=1	0.26	0.35	0.33	0.30	0.14	1.10	0.01	0.01	0.01	0.01	0.12	1.65
P02671	47	46	Fibrinogen alpha chain OS=Homo sapiens GN=FGA PE=1 SV=2	1.19	9.63	5.90	0.47	0.64	0.69	0.04	0.10	0.38	0.01	0.05	0.41
P02675	53	50	Fibrinogen beta chain OS=Homo sapiens GN=FGB PE=1 SV=2	2.23	12.22	7.74	0.72	1.48	0.73	0.01	0.45	0.01	0.02	1.57	0.51
P02679	40	38	Fibrinogen gamma chain OS=Homo sapiens GN=FGG PE=1 SV=3	1.32	19.69	12.06	0.14	0.59	0.49	0.06	0.53	0.10	0.00	0.08	0.20
P02751	30	24	Fibronectin OS=Homo sapiens GN=FN1 PE=1 SV=4	0.15	0.11	0.06	0.04	0.23	0.63	0.01	0.00	0.00	0.01	0.07	0.99
P06396	44	42	Gelsolin OS=Homo sapiens GN=GSN PE=1 SV=1	0.13	0.91	0.20	0.06	5.21	0.40	0.00	0.08	0.00	0.02	4.47	0.13
P14136	6	3	Glial fibrillary acidic protein OS=Homo sapiens GN=GFAP PE=1 SV=1	0.19	0.01	0.04	0.11	0.20	0.36	0.04	0.01	0.00	0.04	0.24	0.33
P22352	2	2	Glutathione peroxidase 3 OS=Homo sapiens GN=GPX3 PE=1 SV=2	0.00	0.01	0.00	0.00	0.20	0.03	0.00	0.01	0.00	0.00	0.33	0.06
P00738	13	8	Haptoglobin OS=Homo sapiens GN=HP PE=1 SV=1	0.46	0.09	0.24	0.39	0.07	0.64	0.10	0.02	0.01	0.10	0.04	0.92
P00739	7	4	Haptoglobin-related protein OS=Homo sapiens GN=HPR PE=2 SV=2	0.04	0.02	0.06	0.03	0.05	0.02	0.00	0.00	0.00	0.00	0.04	0.02
P69905	2	2	Hemoglobin subunit alpha OS=Homo sapiens GN=HBA1 PE=1 SV=2	0.15	0.06	0.03	1.53	0.24	0.07	0.01	0.02	0.00	0.09	0.15	0.05
42;P02100;P6	4	4	Hemoglobin subunit beta OS=Homo sapiens GN=HBB PE=1 SV=2	0.39	0.03	0.00	3.10	0.32	0.13	0.00	0.00	0.00	0.04	0.22	0.05
P02790	15	12	Hemopexin OS=Homo sapiens GN=HPX PE=1 SV=2	0.54	0.35	0.30	0.44	1.42	0.69	0.00	0.04	0.05	0.04	1.30	0.33
P05546	18	16	Heparin cofactor 2 OS=Homo sapiens GN=SERPIND1 PE=1 SV=3	0.10	0.14	0.27	0.08	0.55	0.93	0.00	0.01	0.01	0.00	0.55	0.87
Q04756	6	6	Hepatocyte growth factor activator OS=Homo sapiens GN=HGFAC PE=1 SV=1	0.00	0.04	0.00	0.00	0.41	0.02	0.00	0.00	0.00	0.00	0.49	0.03
P04196	24	22	Histidine-rich glycoprotein OS=Homo sapiens GN=HRG PE=1 SV=1	0.24	1.45	0.13	0.22	3.14	1.16	0.02	0.57	0.02	0.02	2.60	1.06
Q14520	17	17	Hyaluronan-binding protein 2 OS=Homo sapiens GN=HABP2 PE=1 SV=1	0.21	0.39	1.27	0.07	0.93	0.81	0.00	0.04	0.11	0.01	0.75	0.34
\01876;P0187	10	9	Ig alpha-1 chain C region OS=Homo sapiens GN=IGHA1 PE=1 SV=2	0.63	0.13	0.08	0.40	0.26	0.12	0.02	0.02	0.00	0.00	0.14	0.01
P01857	13	7	Ig gamma-1 chain C region OS=Homo sapiens GN=IGHG1 PE=1 SV=1	2.92	0.78	0.27	2.50	0.29	1.00	0.01	0.04	0.02	0.09	0.20	0.57
P01859	7	4	Ig gamma-2 chain C region OS=Homo sapiens GN=IGHG2 PE=1 SV=2	8.13	0.47	1.79	12.17	0.46	0.69	0.31	0.02	0.13	0.21	0.42	0.36
P01860	12	5	Ig gamma-3 chain C region OS=Homo sapiens GN=IGHG3 PE=1 SV=2	0.30	0.18	0.01	0.10	0.22	0.09	0.04	0.07	0.00	0.01	0.05	0.06
P01861	5	2	Ig gamma-4 chain C region OS=Homo sapiens GN=IGHG4 PE=1 SV=1	0.06	0.05	0.03	0.04	0.08	0.03	0.00	0.00	0.00	0.01	0.06	0.03
P01834	7	6	Ig kappa chain C region OS=Homo sapiens GN=IGKC PE=1 SV=1	5.75	1.08	0.32	4.10	1.54	1.32	0.28	0.01	0.02	0.35	1.18	1.53
9A064;P0CF74	5	5	Ig lambda-2 chain C regions OS=Homo sapiens GN=IGLC2 PE=1 SV=1	0.97	0.32	0.06	0.43	0.78	0.28	0.12	0.09	0.01	0.08	0.68	0.20
\01871;P0422(	15	12	Ig mu chain C region OS=Homo sapiens GN=IGHM PE=1 SV=3	2.04	0.16	0.09	1.23	0.28	0.43	0.06	0.02	0.01	0.04	0.21	0.43
A0A075B6Q5	2	2	Immunoglobulin heavy variable 3-64 OS=Homo sapiens GN=IGHV3-64 PE=3 SV=1	0.43	0.04	0.06	0.52	0.19	0.30	0.04	0.02	0.00	0.01	0.25	0.30
P17936	6	6	Insulin-like growth factor-binding protein 3 OS=Homo sapiens GN=IGFBP3 PE=1 SV=2	0.02	0.00	0.00	0.00	0.28	0.01	0.00	0.00	0.00	0.00	0.30	0.01
P35858	2	2	Insulin-like growth factor-binding protein complex acid labile subunit OS=Homo sapiens GN=IGFALS PE=1 SV=1	0.03	0.42	0.39	0.00	0.23	0.22	0.02	0.42	0.01	0.00	0.33	0.11
P19827	7	6	Inter-alpha-trypsin inhibitor heavy chain H1 OS=Homo sapiens GN=ITIH1 PE=1 SV=3	0.00	0.04	0.01	0.00	0.04	0.01	0.00	0.00	0.00	0.00	0.05	0.01
P19823	21	19	Inter-alpha-trypsin inhibitor heavy chain H2 OS=Homo sapiens GN=ITIH2 PE=1 SV=2	0.14	0.43	0.33	0.12	0.40	0.23	0.01	0.02	0.01	0.01	0.34	0.26
Q14624	50	50	Inter-alpha-trypsin inhibitor heavy chain H4 OS=Homo sapiens GN=ITIH4 PE=1 SV=4	0.06	2.53	0.55	0.01	5.40	0.47	0.00	0.20	0.01	0.01	5.48	0.56
P01042	29	27	Kininogen-1 OS=Homo sapiens GN=KNG1 PE=1 SV=2	1.12	0.10	0.12	0.79	2.21	1.02	0.01	0.02	0.00	0.03	1.98	1.49
P18428	10	9	Lipopolysaccharide-binding protein OS=Homo sapiens GN=LBP PE=1 SV=3	0.16	0.17	0.00	0.10	0.73	0.23	0.00	0.04	0.00	0.02	0.74	0.35
O75145	5	3	Liprin-alpha-3 OS=Homo sapiens GN=PPFIA3 PE=1 SV=3	1.25	0.11	0.32	0.66	0.33	0.38	0.06	0.00	0.02	0.04	0.14	0.41
P51884	17	15	Lumican OS=Homo sapiens GN=LUM PE=1 SV=2	0.08	0.09	0.36	0.21	0.12	0.56	0.01	0.00	0.05	0.01	0.06	0.22
P36955	14	13	Pigment epithelium-derived factor OS=Homo sapiens GN=SERPINF1 PE=1 SV=4	0.05	0.02	0.01	0.02	1.26	0.14	0.00	0.01	0.00	0.00	1.32	0.12
P03952	19	17	Plasma kallikrein OS=Homo sapiens GN=KLKB1 PE=1 SV=1	0.00	0.03	0.01	0.00	1.35	0.30	0.00	0.01	0.00	0.00	1.13	0.44
P05155	14	11	Plasma protease C1 inhibitor OS=Homo sapiens GN=SERPING1 PE=1 SV=2	0.04	0.12	0.06	0.04	0.26	0.16	0.01	0.01	0.00	0.00	0.18	0.12
P05154	14	12	Plasma serine protease inhibitor OS=Homo sapiens GN=SERPINA5 PE=1 SV=3	0.19	0.09	0.13	0.04	0.43	0.27	0.00	0.01	0.02	0.00	0.39	0.28
47;Q02325;Q1	53	51	Plasminogen OS=Homo sapiens GN=PLG PE=1 SV=2	0.14	2.01	0.31	0.07	0.92	1.02	0.00	0.19	0.00	0.01	0.54	1.02
P02775	5	5	Platelet basic protein OS=Homo sapiens GN=PPBP PE=1 SV=3	0.04	0.15	0.07	0.03	1.35	0.42	0.00	0.01	0.00	0.00	0.69	0.33
\02776;P1072(	5	5	Platelet factor 4 OS=Homo sapiens GN=PF4 PE=1 SV=2	0.09	0.06	0.00	0.06	2.19	0.42	0.01	0.05	0.00	0.00	3.10	0.61
Q15113	9	6	Procollagen C-endopeptidase enhancer 1 OS=Homo sapiens GN=PCOLCE PE=1 SV=2	0.00	0.48	0.77	0.00	0.39	0.41	0.00	0.01	0.07	0.00	0.41	0.29
P27918	9	9	Properdin OS=Homo sapiens GN=CFP PE=1 SV=2	0.91	0.08	0.05	1.13	0.81	0.13	0.04	0.00	0.01	0.05	1.24	0.12
P02760	7	6	Protein AMBP OS=Homo sapiens GN=AMBP PE=1 SV=1	0.03	0.04	0.03	0.01	0.09	0.05	0.01	0.03	0.00	0.01	0.09	0.03
Q9UKS5	2	2	Protein Z-dependent protease inhibitor OS=Homo sapiens GN=SERPINA10 PE=1 SV=1	0.00	0.03	0.00	0.00	0.04	0.00	0.00	0.00	0.00	0.00	0.03	0.00
Q92954	14	11	Proteoglycan 4 OS=Homo sapiens GN=PRG4 PE=1 SV=2	0.06	0.05	0.01	0.02	0.29	0.03	0.01	0.01	0.00	0.00	0.33	0.03
P00734	46	43	Prothrombin OS=Homo sapiens GN=F2 PE=1 SV=2	0.31	2.26	3.56	0.32	2.05	2.25	0.03	0.10	0.24	0.00	2.80	3.15
P49908	5	4	Selenoprotein P OS=Homo sapiens GN=SELENOP PE=1 SV=3	0.01	0.03	0.02	0.00	0.97	0.07	0.02	0.01	0.00	0.00	0.64	0.06
P02787	22	19	Serotransferrin OS=Homo sapiens GN=TF PE=1 SV=3	0.71	3.04	1.61	0.52	1.22	1.85	0.03	0.35	0.08	0.01	0.65	2.68
P02768	67	66	Serum albumin OS=Homo sapiens GN=ALB PE=1 SV=2	31.51	3.50	25.53	33.12	3.15	13.66	0.16	0.13	2.27	0.81	3.56	17.17
P02743	8	7	Serum amyloid P-component OS=Homo sapiens GN=APCS PE=1 SV=2	0.21	0.05	0.04	2.24	0.72	0.17	0.34	0.02	0.01	0.24	1.13	0.19
P27169	9	9	Serum paraoxonase/arylesterase 1 OS=Homo sapiens GN=PON1 PE=1 SV=3	1.02	0.19	0.41	0.19	0.39	0.61	0.01	0.04	0.05	0.01	0.50	0.47
P11277	6	5	Spectrin beta chain_ erythrocytic OS=Homo sapiens GN=SPTB PE=1 SV=5	0.99	0.10	0.33	0.67	0.04	0.11	0.04	0.06	0.09	0.04	0.03	0.08
Q9H2K2	2	2	Tankyrase-2 OS=Homo sapiens GN=TNKS2 PE=1 SV=1	0.10	0.03	0.00	0.10	0.06	0.01	0.00	0.02	0.00	0.01	0.09	0.01
P05452	5	3	Tetranectin OS=Homo sapiens GN=CLEC3B PE=1 SV=3	0.02	0.04	0.02	0.00	0.12	0.68	0.00	0.00	0.00	0.00	0.09	1.08
P07996	9	5	Thrombospondin-1 OS=Homo sapiens GN=THBS1 PE=1 SV=2	0.01	0.00	0.00	0.00	0.13	0.01	0.00	0.00	0.00	0.00	0.05	0.01
P02766	10	10	Transthyretin OS=Homo sapiens GN=TTR PE=1 SV=1	4.70	0.64	1.39	5.93	1.25	2.39	0.17	0.02	0.09	0.11	0.70	2.26
Q9UDY6	2	2	Tripartite motif-containing protein 10 OS=Homo sapiens GN=TRIM10 PE=1 SV=3	2.40	1.34	1.27	1.34	0.82	2.37	0.59	0.20	0.04	0.05	0.77	1.96
P02774	36	36	Vitamin D-binding protein OS=Homo sapiens GN=GC PE=1 SV=1	0.35	0.52	0.14	0.28	1.11	1.05	0.03	0.02	0.01	0.00	0.76	0.95
P04070	9	8	Vitamin K-dependent protein C OS=Homo sapiens GN=PROC PE=1 SV=1	0.03	0.09	0.24	0.01	2.19	0.26	0.00	0.05	0.03	0.00	3.61	0.30
P07225	13	12	Vitamin K-dependent protein S OS=Homo sapiens GN=PROS1 PE=1 SV=1	0.04	0.45	0.32	0.03	0.30	0.08	0.00	0.04	0.01	0.01	0.15	0.04
P22891	8	8	Vitamin K-dependent protein Z OS=Homo sapiens GN=PROZ PE=1 SV=2	0.00	0.01	0.09	0.00	0.04	0.03	0.00	0.00	0.01	0.00	0.05	0.01
\04004;Q9954	29	28	Vitronectin OS=Homo sapiens GN=VTN PE=1 SV=1	0.64	10.20	17.61	0.64	10.26	12.36	0.02	0.08	1.23	0.00	14.31	12.27

Figure S4.12. List of all identified corona proteins on lipo-dendrimers lipo-$(PS)_4$ and lipo-$(PN)_8$ in human serum and plasma.

				Average in %						Standard deviation					
				Plasma			Serum			Plasma			Serum		
Accession	Peptide count	nique peptide	Description	Uncoated	(PS)4	S8	Uncoated	(PS)4	S8	Uncoated	(PS)4	S8	Uncoated	(PS)4	S8
6;P68032;P63267;P	9	4	Actin_ aortic smooth muscle OS=Homo sapiens GN=ACTA2 PE=1 SV=1	0.91	0.11	0.36	0.24	0.14	0.26	0.16	0.01	0.03	0.06	0.01	0.00
i0709;P63261;Q658	13	5	Actin_ cytoplasmic 1 OS=Homo sapiens GN=ACTB PE=1 SV=1	0.95	1.47	0.57	0.33	0.80	1.08	0.02	0.08	0.01	0.02	0.06	0.74
P02763;P19652	4	4	Alpha-1-acid glycoprotein 1 OS=Homo sapiens GN=ORM1 PE=1 SV=1	0.02	0.05	0.01	0.02	0.03	0.03	0.00	0.01	0.00	0.00	0.00	0.00
;Q5TYW2;Q5VUR7;	3	3	Ankyrin repeat domain-containing protein 20A2 OS=Homo sapiens GN=ANKRD20A2 PE=4 SV=1	0.08	0.08	0.05	0.06	0.08	0.09	0.00	0.01	0.00	0.00	0.01	0.07
P01008	32	31	Antithrombin-III OS=Homo sapiens GN=SERPINC1 PE=1 SV=1	0.02	0.05	0.02	0.70	1.58	2.72	0.00	0.02	0.00	0.07	0.03	1.54
P02647	25	25	Apolipoprotein A-I OS=Homo sapiens GN=APOA1 PE=1 SV=1	1.49	1.47	2.33	0.44	1.84	0.41	0.03	0.16	0.01	0.02	0.02	0.36
P02652	2	2	Apolipoprotein A-II OS=Homo sapiens GN=APOA2 PE=1 SV=1	0.16	0.02	0.09	0.04	0.03	0.03	0.03	0.00	0.03	0.04	0.00	0.01
P06727	28	25	Apolipoprotein A-IV OS=Homo sapiens GN=APOA4 PE=1 SV=3	1.39	0.69	0.67	0.93	1.43	0.57	0.04	0.12	0.03	0.16	0.07	0.46
P04114	40	34	Apolipoprotein B-100 OS=Homo sapiens GN=APOB PE=1 SV=2	0.12	0.12	0.09	0.08	0.10	0.18	0.01	0.01	0.00	0.01	0.00	0.10
P02649	26	25	Apolipoprotein E OS=Homo sapiens GN=APOE PE=1 SV=1	6.19	3.34	4.11	2.05	0.71	1.52	0.39	0.28	0.06	0.07	0.01	0.31
Q96P47	3	3	Arf-GAP with GTPase_ ANK repeat and PH domain-containing protein 3 OS=Homo sapiens GN=AGAP3 PE=1 SV=2	0.14	0.29	0.10	0.11	0.13	0.18	0.01	0.06	0.01	0.08	0.01	0.11
O95817	2	2	BAG family molecular chaperone regulator 3 OS=Homo sapiens GN=BAG3 PE=1 SV=3	0.00	0.00	0.00	0.00	0.00	0.00	0.00	0.00	0.00	0.00	0.00	0.00
P02730	8	8	Band 3 anion transport protein OS=Homo sapiens GN=SLC4A1 PE=1 SV=3	0.00	0.03	0.04	0.02	0.10	0.05	0.00	0.02	0.00	0.00	0.00	0.00
P02749	15	15	Beta-2-glycoprotein 1 OS=Homo sapiens GN=APOH PE=1 SV=3	1.61	0.98	5.64	0.21	1.41	3.49	0.95	0.07	0.04	0.00	0.03	0.42
Q562R1	8	3	Beta-actin-like protein 2 OS=Homo sapiens GN=ACTBL2 PE=1 SV=2	0.22	1.04	1.34	0.07	0.06	0.04	0.05	0.01	0.04	0.05	0.02	0.03
Q9Y2P5	3	2	Bile acyl-CoA synthetase OS=Homo sapiens GN=SLC27A5 PE=1 SV=1	0.03	0.09	0.05	0.03	0.31	0.10	0.01	0.00	0.02	0.01	0.02	0.08
P80723	2	2	Brain acid soluble protein 1 OS=Homo sapiens GN=BASP1 PE=1 SV=2	1.35	0.22	0.60	0.69	0.18	0.40	0.05	0.01	0.02	0.41	0.03	0.27
P04003	18	16	C4b-binding protein alpha chain OS=Homo sapiens GN=C4BPA PE=1 SV=2	0.38	1.20	0.52	0.20	0.19	0.08	0.03	0.10	0.02	0.01	0.03	0.06
Q96IY4	3	3	Carboxypeptidase B2 OS=Homo sapiens GN=CPB2 PE=1 SV=2	0.00	0.00	0.00	0.02	0.11	0.05	0.00	0.00	0.00	0.00	0.01	0.02
P10909	28	25	Clusterin OS=Homo sapiens GN=CLU PE=1 SV=1	11.74	5.90	9.09	14.63	14.37	10.69	0.23	0.26	0.09	0.84	0.18	2.05
P00740	7	7	Coagulation factor IX OS=Homo sapiens GN=F9 PE=1 SV=2	0.19	0.18	0.05	0.09	0.14	0.11	0.01	0.02	0.00	0.00	0.00	0.00
P12259	28	23	Coagulation factor V OS=Homo sapiens GN=F5 PE=1 SV=4	0.15	0.35	0.33	0.16	0.34	0.35	0.01	0.03	0.01	0.02	0.02	0.18
P03951	10	10	Coagulation factor XI OS=Homo sapiens GN=F11 PE=1 SV=1	0.14	0.31	0.16	0.13	0.19	0.17	0.00	0.01	0.00	0.01	0.00	0.12
P02747	4	4	Complement C1q subcomponent subunit C OS=Homo sapiens GN=C1QC PE=1 SV=3	0.05	0.04	0.04	0.07	0.17	0.05	0.00	0.01	0.01	0.01	0.01	0.04
P00736	16	14	Complement C1r subcomponent OS=Homo sapiens GN=C1R PE=1 SV=2	0.02	0.04	0.06	0.06	0.29	0.11	0.00	0.00	0.00	0.00	0.01	0.01
P09871	14	13	Complement C1s subcomponent OS=Homo sapiens GN=C1S PE=1 SV=1	0.05	0.14	0.12	0.07	0.17	0.08	0.00	0.02	0.00	0.01	0.01	0.00
P01024	107	100	Complement C3 OS=Homo sapiens GN=C3 PE=1 SV=2	0.63	1.09	1.13	0.76	0.41	0.82	0.03	0.18	0.04	0.06	0.07	0.45
P0C0L4	45	2	Complement C4-A OS=Homo sapiens GN=C4A PE=1 SV=2	0.01	0.02	0.01	0.14	0.18	0.11	0.00	0.00	0.00	0.00	0.04	0.04
P0C0L5	46	3	Complement C4-B OS=Homo sapiens GN=C4B PE=1 SV=2	0.07	1.03	0.66	0.39	2.26	1.58	0.02	0.06	0.02	0.04	0.25	0.46
P13671	8	6	Complement component C6 OS=Homo sapiens GN=C6 PE=1 SV=3	0.08	0.15	0.20	0.08	0.53	0.22	0.02	0.00	0.03	0.02	0.03	0.06
P10643	5	3	Complement component C7 OS=Homo sapiens GN=C7 PE=1 SV=2	0.00	0.01	0.02	0.00	0.08	0.03	0.00	0.00	0.00	0.00	0.01	0.02
P02748	11	11	Complement component C9 OS=Homo sapiens GN=C9 PE=1 SV=2	0.10	0.07	0.12	0.17	0.38	0.22	0.01	0.00	0.01	0.00	0.02	0.10
P00751	2	2	Complement factor B OS=Homo sapiens GN=CFB PE=1 SV=2	0.00	0.01	0.02	0.01	0.11	0.03	0.00	0.01	0.00	0.00	0.01	0.00
P08603;Q02985	47	42	Complement factor H OS=Homo sapiens GN=CFH PE=1 SV=4	0.06	0.35	0.13	0.10	0.92	0.19	0.01	0.05	0.00	0.01	0.02	0.12
Q03591;P36980	11	6	Complement factor H-related protein 1 OS=Homo sapiens GN=CFHR1 PE=1 SV=2	0.01	0.28	0.73	0.05	0.78	0.58	0.00	0.04	0.07	0.03	0.03	0.03
Q9BXR6	13	12	Complement factor H-related protein 5 OS=Homo sapiens GN=CFHR5 PE=1 SV=1	0.13	0.11	0.15	0.06	0.29	0.19	0.01	0.00	0.00	0.00	0.02	0.05
Q16555	3	3	Dihydropyrimidinase-related protein 2 OS=Homo sapiens GN=DPYSL2 PE=1 SV=1	0.24	0.11	0.16	0.12	0.24	0.15	0.01	0.00	0.00	0.01	0.01	0.02
Q726W7	2	2	DnaJ homolog subfamily B member 7 OS=Homo sapiens GN=DNAJB7 PE=2 SV=2	3.06	0.55	0.97	2.89	0.55	0.93	0.10	0.02	0.02	2.13	0.04	0.76
Q8TE02	2	2	Elongator complex protein 5 OS=Homo sapiens GN=ELP5 PE=1 SV=2	0.37	0.46	0.20	0.32	0.36	0.49	0.01	0.02	0.01	0.02	0.01	0.42
P02671	43	42	Fibrinogen alpha chain OS=Homo sapiens GN=FGA PE=1 SV=2	0.72	7.17	4.80	0.22	0.16	0.21	0.04	0.77	0.15	0.13	0.03	0.15
P02675	48	48	Fibrinogen beta chain OS=Homo sapiens GN=FGB PE=1 SV=2	1.25	15.17	11.27	0.08	0.10	0.07	0.09	0.21	0.13	0.00	0.01	0.04
P02679	37	35	Fibrinogen gamma chain OS=Homo sapiens GN=FGG PE=1 SV=3	1.15	11.15	9.06	0.06	0.21	0.07	0.04	2.87	0.18	0.00	0.02	0.02
P47929	2	2	Galectin-7 OS=Homo sapiens GN=LGALS7 PE=1 SV=2	0.00	0.00	0.00	0.08	0.00	0.00	0.00	0.00	0.00	0.00	0.00	0.00
P06396	27	27	Gelsolin OS=Homo sapiens GN=GSN PE=1 SV=1	0.23	0.28	0.27	0.21	0.58	0.20	0.08	0.07	0.00	0.13	0.02	0.16
P14136	8	5	Glial fibrillary acidic protein OS=Homo sapiens GN=GFAP PE=1 SV=1	0.23	0.14	0.12	0.22	0.09	0.23	0.01	0.01	0.00	0.13	0.00	0.01
P22352	4	3	Glutathione peroxidase 3 OS=Homo sapiens GN=GPX3 PE=1 SV=2	0.01	0.04	0.07	0.02	0.18	0.05	0.00	0.01	0.00	0.00	0.00	0.01
P04406	4	4	Glyceraldehyde-3-phosphate dehydrogenase OS=Homo sapiens GN=GAPDH PE=1 SV=3	0.01	0.05	0.02	0.04	0.09	0.05	0.00	0.00	0.00	0.00	0.01	0.04
P00738	6	2	Haptoglobin OS=Homo sapiens GN=HP PE=1 SV=1	0.07	0.09	0.04	0.13	0.08	0.09	0.01	0.00	0.00	0.01	0.02	0.01
P00739	4	2	Haptoglobin-related protein OS=Homo sapiens GN=HPR PE=2 SV=2	0.05	0.04	0.02	0.05	0.04	0.03	0.00	0.00	0.00	0.00	0.00	0.02
P69905	4	4	Hemoglobin subunit alpha OS=Homo sapiens GN=HBA1 PE=1 SV=2	0.00	0.01	0.01	0.13	0.15	0.06	0.00	0.00	0.00	0.02	0.00	0.04
1;P02100;P68871;P	5	3	Hemoglobin subunit beta OS=Homo sapiens GN=HBB PE=1 SV=2	0.00	0.10	0.01	0.17	0.18	0.08	0.00	0.00	0.00	0.01	0.01	0.05
P02790	7	6	Hemopexin OS=Homo sapiens GN=HPX PE=1 SV=2	0.04	0.16	0.20	0.04	0.14	0.16	0.00	0.04	0.01	0.00	0.02	0.02
Q04756	2	2	Hepatocyte growth factor activator OS=Homo sapiens GN=HGFAC PE=1 SV=1	0.00	0.04	0.03	0.00	0.08	0.00	0.00	0.00	0.00	0.00	0.00	0.00
P04196	11	11	Histidine-rich glycoprotein OS=Homo sapiens GN=HRG PE=1 SV=1	0.00	0.16	0.25	0.03	0.67	0.33	0.00	0.01	0.02	0.02	0.04	0.08
P01876	7	3	Ig alpha-1 chain C region OS=Homo sapiens GN=IGHA1 PE=1 SV=2	0.17	0.18	0.14	0.17	0.17	0.08	0.01	0.03	0.00	0.02	0.01	0.05
P01857	15	5	Ig gamma-1 chain C region OS=Homo sapiens GN=IGHG1 PE=1 SV=1	0.49	0.77	0.48	0.94	1.50	0.84	0.02	0.03	0.01	0.06	0.01	0.67
P01859	11	3	Ig gamma-2 chain C region OS=Homo sapiens GN=IGHG2 PE=1 SV=2	3.27	3.84	1.38	3.65	2.68	6.16	0.22	0.07	0.04	0.18	0.22	1.31
P01860	14	4	Ig gamma-3 chain C region OS=Homo sapiens GN=IGHG3 PE=1 SV=2	0.02	0.06	0.05	0.06	0.13	0.04	0.00	0.00	0.00	0.00	0.01	0.03
P01834	7	7	Ig kappa chain C region OS=Homo sapiens GN=IGKC PE=1 SV=1	1.29	1.32	1.14	1.05	1.72	1.20	0.04	0.08	0.06	0.21	0.06	0.05
l;P0CF74;P0CG04;Pl	5	3	Ig lambda-2 chain C regions OS=Homo sapiens GN=IGLC2 PE=1 SV=1	0.09	0.18	0.25	0.15	0.44	0.32	0.02	0.01	0.02	0.04	0.07	0.02
P01871	16	7	Ig mu chain C region OS=Homo sapiens GN=IGHM PE=1 SV=3	0.37	0.29	0.22	0.49	0.56	0.30	0.01	0.01	0.01	0.03	0.03	0.10
P04220	11	2	Ig mu heavy chain disease protein OS=Homo sapiens PE=1 SV=1	0.04	0.06	0.09	0.05	0.11	0.10	0.01	0.04	0.01	0.00	0.00	0.01
5;A0A0C4DH42;P01	2	2	Immunoglobulin heavy variable 3-23 OS=Homo sapiens GN=IGHV3-23 PE=1 SV=2	0.02	0.03	0.02	0.07	0.07	0.04	0.00	0.00	0.00	0.00	0.00	0.03
Q6UXK2	4	4	Immunoglobulin superfamily containing leucine-rich repeat protein 2 OS=Homo sapiens GN=ISLR2 PE=2 SV=1	0.07	0.49	0.39	0.03	0.04	0.21	0.01	0.00	0.01	0.00	0.00	0.05
P19823	7	7	Inter-alpha-trypsin inhibitor heavy chain H2 OS=Homo sapiens GN=ITIH2 PE=1 SV=2	0.16	0.18	0.14	0.13	0.18	0.07	0.01	0.02	0.01	0.00	0.00	0.05
Q14624	59	58	Inter-alpha-trypsin inhibitor heavy chain H4 OS=Homo sapiens GN=ITIH4 PE=1 SV=4	1.73	5.20	4.46	0.77	8.28	7.51	0.04	0.44	0.18	0.08	0.54	1.54
P01042	21	20	Kininogen-1 OS=Homo sapiens GN=KNG1 PE=1 SV=2	0.22	0.16	0.22	0.42	1.61	0.77	0.01	0.00	0.01	0.01	0.06	0.17
Q6PIL6	2	2	Kv channel-interacting protein 4 OS=Homo sapiens GN=KCNIP4 PE=1 SV=1	0.23	0.14	0.33	0.21	0.39	0.26	0.01	0.00	0.00	0.00	0.02	0.03
P18428	12	12	Lipopolysaccharide-binding protein OS=Homo sapiens GN=LBP PE=1 SV=3	0.02	0.18	0.04	0.02	0.48	0.36	0.00	0.01	0.00	0.00	0.02	0.23
P51884	9	8	Lumican OS=Homo sapiens GN=LUM PE=1 SV=2	0.12	0.03	0.04	0.12	0.01	0.01	0.00	0.00	0.00	0.01	0.00	0.00
Q13201	7	7	Multimerin-1 OS=Homo sapiens GN=MMRN1 PE=1 SV=3	0.75	0.20	0.40	0.72	0.62	0.49	0.04	0.02	0.04	0.06	0.07	0.07
Q86VZ4	5	4	NACHT_ LRR and PYD domains-containing protein 14 OS=Homo sapiens GN=NLRP14 PE=1 SV=1	1.09	1.28	0.48	1.38	1.05	1.61	0.24	0.05	0.08	0.21	0.02	0.23
Q96NY8	4	4	Nectin-4 OS=Homo sapiens GN=NECTIN4 PE=1 SV=1	0.03	0.09	0.04	0.02	0.05	0.00	0.00	0.00	0.00	0.00	0.00	0.00
P03952	14	14	Plasma kallikrein OS=Homo sapiens GN=KLKB1 PE=1 SV=1	0.03	0.13	0.82	0.02	0.35	0.40	0.00	0.01	0.00	0.01	0.03	0.27
P05155	8	8	Plasma protease C1 inhibitor OS=Homo sapiens GN=SERPING1 PE=1 SV=2	0.05	0.09	0.08	0.12	0.47	0.18	0.01	0.01	0.01	0.01	0.01	0.06
P05154	7	7	Plasma serine protease inhibitor OS=Homo sapiens GN=SERPINA5 PE=1 SV=3	0.00	0.03	0.01	0.02	0.17	0.08	0.00	0.00	0.01	0.00	0.01	0.00
P00747	14	14	Plasminogen OS=Homo sapiens GN=PLG PE=1 SV=2	0.00	0.04	0.03	0.01	0.30	0.06	0.00	0.00	0.00	0.00	0.00	0.03
P02775	5	4	Platelet basic protein OS=Homo sapiens GN=PPBP PE=1 SV=3	0.00	0.00	0.00	0.00	0.07	0.03	0.00	0.00	0.00	0.00	0.00	0.01
P02776;P10720	4	4	Platelet factor 4 OS=Homo sapiens GN=PF4 PE=1 SV=2	0.00	0.07	0.11	0.01	1.16	0.27	0.00	0.01	0.01	0.00	0.04	0.24
A5A3E0	6	2	POTE ankyrin domain family member F OS=Homo sapiens GN=POTEF PE=1 SV=2	1.66	0.52	0.62	1.27	0.61	0.72	0.04	0.02	0.02	0.05	0.05	0.58
P07737	2	2	Profilin-1 OS=Homo sapiens GN=PFN1 PE=1 SV=2	0.00	0.02	0.01	0.02	0.13	0.06	0.00	0.00	0.00	0.00	0.00	0.01
P27918	7	6	Properdin OS=Homo sapiens GN=CFP PE=1 SV=2	0.04	0.05	0.10	0.11	0.52	0.23	0.00	0.04	0.01	0.02	0.04	0.19
Q8IZP9	2	2	Protein FAM9C OS=Homo sapiens GN=FAM9C PE=1 SV=1	1.48	2.34	0.90	0.27	0.56	2.71	0.06	0.16	0.03	0.02	0.03	0.08
P05109	2	2	Protein S100-A8 OS=Homo sapiens GN=S100A8 PE=1 SV=1	0.03	0.16	0.14	0.20	0.07	0.01	0.00	0.00	0.00	0.01	0.01	0.01
P06702	3	3	Protein S100-A9 OS=Homo sapiens GN=S100A9 PE=1 SV=1	0.05	0.29	0.36	0.29	0.35	0.15	0.03	0.09	0.04	0.05	0.30	0.08
Q92954	10	10	Proteoglycan 4 OS=Homo sapiens GN=PRG4 PE=1 SV=2	0.94	0.82	0.24	0.76	0.78	1.23	0.05	0.08	0.01	0.05	0.02	0.87
P00734	37	35	Prothrombin OS=Homo sapiens GN=F2 PE=1 SV=2	0.06	0.14	0.12	1.49	4.14	3.96	0.00	0.00	0.01	0.12	0.19	0.02
P0C7K3	2	2	Putative cyclin-Y-like protein 3 OS=Homo sapiens GN=CCNY13 PE=3 SV=1	0.02	0.10	0.03	0.02	0.01	0.03	0.01	0.01	0.00	0.00	0.00	0.00
Q99969	3	2	Retinoic acid receptor responder protein 2 OS=Homo sapiens GN=RARRES2 PE=1 SV=1	0.00	0.03	0.06	0.00	0.03	0.01	0.00	0.01	0.01	0.00	0.00	0.01
Q8IZV5	2	2	Retinol dehydrogenase 10 OS=Homo sapiens GN=RDH10 PE=1 SV=1	0.02	0.08	0.06	0.03	0.20	0.14	0.00	0.00	0.00	0.00	0.02	0.01
Q13103	3	3	Secreted phosphoprotein 24 OS=Homo sapiens GN=SPP2 PE=1 SV=1	0.11	0.02	0.03	0.04	0.04	0.01	0.02	0.00	0.00	0.00	0.01	0.00
P49908	2	2	Selenoprotein P OS=Homo sapiens GN=SELENOP PE=1 SV=3	0.00	0.03	0.04	0.01	0.12	0.03	0.00	0.00	0.00	0.01	0.01	0.02
P02787	9	8	Serotransferrin OS=Homo sapiens GN=TF PE=1 SV=3	0.11	0.56	0.56	0.09	0.15	0.10	0.01	0.04	0.01	0.00	0.01	0.02
P02768	67	67	Serum albumin OS=Homo sapiens GN=ALB PE=1 SV=2	37.31	7.44	15.33	45.57	7.18	17.88	1.65	0.14	0.52	1.78	0.37	1.09
P02743	7	6	Serum amyloid P-component OS=Homo sapiens GN=APCS PE=1 SV=2	0.00	0.02	0.02	0.00	0.23	0.17	0.00	0.00	0.00	0.00	0.02	0.08
P27169	6	4	Serum paraoxonase/arylesterase 1 OS=Homo sapiens GN=PON1 PE=1 SV=3	0.18	0.02	0.04	0.01	0.02	0.01	0.02	0.00	0.00	0.00	0.00	0.01
Q96DN5	2	2	TBC1 domain family member 31 OS=Homo sapiens GN=TBC1D31 PE=1 SV=2	0.13	0.07	0.07	0.14	0.07	0.15	0.01	0.00	0.01	0.01	0.00	0.03
P07996	8	8	Thrombospondin-1 OS=Homo sapiens GN=THBS1 PE=1 SV=2	0.12	0.27	0.18	0.18	0.53	0.27	0.01	0.00	0.01	0.02	0.06	0.21
P02766	11	10	Transthyretin OS=Homo sapiens GN=TTR PE=1 SV=1	1.78	2.37	1.20	2.17	2.28	3.61	0.05	0.21	0.05	0.20	0.10	0.85
P02774	20	20	Vitamin D-binding protein OS=Homo sapiens GN=GC PE=1 SV=1	0.30	0.24	0.26	0.31	0.39	0.16	0.02	0.00	0.01	0.00	0.14	0.11
P04004	28	28	Vitronectin OS=Homo sapiens GN=VTN PE=1 SV=1	9.43	12.34	11.12	8.30	24.29	16.98	0.26	0.31	0.32	0.92	1.61	3.97

Figure S4.13. List of all identified corona proteins on PS nanoparticles coated with $(PS)_4$ and S_8.

4.6 References

[1] S. Schöttler, K. Landfester, V. Mailänder, *Angew. Chem. Int. Ed.* **2016**, *55*, 8806-8815.

[2] A. E. Nel, L. Mädler, D. Velegol, T. Xia, E. M. V. Hoek, P. Somasundaran, F. Klaessig, V. Castranova, M. Thompson, *Nat. Mater.* **2009**, *8*, 543-557.

[3] G. Caracciolo, *Nanomedicine: NBM* **2015**, *11*, 543-557.

[4] R. M. Kannan, E. Nance, S. Kannan, D. A. Tomalia, *J. Intern. Med.* **2014**, *276*, 579-617.

[5] P. K. Maiti, T. Çağın, S.-T. Lin, W. A. Goddard, *Macromolecules* **2005**, *38*, 979-991.

[6] A. Åkesson, M. Cárdenas, G. Elia, M. P. Monopoli, K. A. Dawson, *RSC Adv.* **2012**, *2*, 11245-11248.

[7] P. Carbone, F. Negri, F. Müller-Plathe, *Macromolecules* **2007**, *40*, 7044-7055.

[8] R. Stangenberg, Y. Wu, J. Hedrich, D. Kurzbach, D. Wehner, G. Weidinger, S. L. Kuan, M. I. Jansen, F. Jelezko, H. J. Luhmann, D. Hinderberger, T. Weil, K. Müllen, *Adv. Healthcare Mater.* **2015**, *4*, 377-384.

[9] Y. Wu, L. Li, L. Frank, J. Wagner, P. Andreozzi, B. Hammer, M. D'Alicarnasso, M. Pelliccia, W. Liu, S. Chakrabortty, S. Krol, J. Simon, K. Landfester, S. L. Kuan, F. Stellacci, K. Müllen, F. Kreppel, T. Weil, *ACS Nano* **2019**, *13*, 8749-8759.

[10] J. Wagner, L. Li, J. Simon, L. Krutzke, K. Landfester, V. Mailänder, K. Müllen, D. Y. W. Ng, Y. Wu, T. Weil, *Angew. Chem. Int. Ed.* **2020**, *59*, 5712-5720.

[11] U. M. Wiesler, A. J. Berresheim, F. Morgenroth, G. Lieser, K. Müllen, *Macromolecules* **2001**, *34*, 187-199.

[12] R. Stangenberg, I. Saeed, S. L. Kuan, M. Baumgarten, T. Weil, M. Klapper, K. Müllen, *Macromol. Rapid Commun.* **2014**, *35*, 152-160.

[13] G. Zhang, M. Auer-Berger, D. W. Gehrig, P. W. M. Blom, M. Baumgarten, D. Schollmeyer, E. J. W. List-Kratochvil, K. Müllen, *Molecules* **2016**, *21*, 1400.

[14] S. Bernhardt, M. Kastler, V. Enkelmann, M. Baumgarten, K. Müllen, *Chem. Eur. J.* **2006**, *12*, 6117-6128.

[15] M. Gai, J. Simon, I. Lieberwirth, V. Mailänder, S. Morsbach, K. Landfester, *Polym. Chem.* **2020**, *11*, 527-540.

[16] M. Kokkinopoulou, J. Simon, K. Landfester, V. Mailänder, I. Lieberwirth, *Nanoscale* **2017**, *9*, 8858-8870.

[17] M. Okuno, M. Mezger, R. Stangenberg, M. Baumgarten, K. Müllen, M. Bonn, E. H. G. Backus, *Langmuir* **2015**, *31*, 1980-1987.

[18] J. Simon, T. Wolf, K. Klein, K. Landfester, F. R. Wurm, V. Mailänder, *Angew. Chem. Int. Ed.* **2018**, *57*, 5548-5553.

[19] D. E. Owens, N. A. Peppas, *Int. J. Pharm.* **2006**, *307*, 93-102.

[20] S. Schöttler, G. Becker, S. Winzen, T. Steinbach, K. Mohr, K. Landfester, V. Mailänder, F. R. Wurm, *Nat. Nanotechnol.* **2016**, *11*, 372-377.

[21] A. Gessner, R. Waicz, A. Lieske, B. R. Paulke, K. Mäder, R. H. Müller, *Int. J. Pharm.* **2000**, *196*, 245-249.

[22] J. Simon, L. K. Müller, M. Kokkinopoulou, I. Lieberwirth, S. Morsbach, K. Landfester, V. Mailänder, *Nanoscale* **2018**, *10*, 10731-10739.

[23] G. Caracciolo, F. Cardarelli, D. Pozzi, F. Salomone, G. Maccari, G. Bardi, A. L. Capriotti, C. Cavaliere, M. Papi, A. Laganà, *ACS Appl. Mater. Interfaces* **2013**, *5*, 13171-13179.

[24] G. Caracciolo, S. Palchetti, V. Colapicchioni, L. Digiacomo, D. Pozzi, A. L. Capriotti, G. La Barbera, A. Laganà, *Langmuir* **2015**, *31*, 10764-10773.

[25] L. Chen, S. J. Mao, L. R. McLean, R. W. Powers, W. J. Larsen, *J. Biol. Chem.* **1994**, *269*, 28282-28287.

[26] Y. Sheng, A. Sali, H. Herzog, J. Lahnstein, S. A. Krilis, *J. Immunol.* **1996**, *157*, 3744.
[27] S. Ritz, S. Schöttler, N. Kotman, G. Baier, A. Musyanovych, J. Kuharev, K. Landfester, H. Schild, O. Jahn, S. Tenzer, V. Mailänder, *Biomacromolecules* **2015**, *16*, 1311-1321.
[28] S. Lerch, M. Dass, A. Musyanovych, K. Landfester, V. Mailänder, *Eur. J. Pharm. Biopharm.* **2013**, *84*, 265-274.
[29] D. Baumann, D. Hofmann, S. Nullmeier, P. Panther, C. Dietze, A. Musyanovych, S. Ritz, K. Landfester, V. Mailänder, *Nanomedicine* **2013**, *8*, 699-713.
[30] S. Schöttler, G. Becker, S. Winzen, T. Steinbach, K. Mohr, K. Landfester, V. Mailänder, F. R. Wurm, *Nat. Nanotechnol.* **2016**, *11*, 372-377.
[31] J. C. Silva, M. V. Gorenstein, G.-Z. Li, J. P. C. Vissers, S. J. Geromanos, *Mol. Cell. Proteomics* **2006**, *5*, 144-156.

5 Amphiphilic Polyphenylene Dendron Conjugates for Surface Remodeling of Adenovirus 5

[redacted]

Contributions

My contribution was the development, the planning and performance of the multi-step dendron synthesis as well as the purification and characterization of all intermediates and final dendrons. I performed the cell culture, cellular uptake experiments including confocal microscopy and cytotoxicity experiments. In addition, I developed the protocol for Click reaction on the virus surface and accomplished a part of the DLS and zeta potential measurements of Ad5/dendron complexes (high ratios) together with [redacted]. I interpreted the virus experiments, wrote large parts of the manuscript and designed the figures. [redacted] conducted the virus experiments including TEM, fluorescence microscopy, FACS, DLS and zeta potential. [redacted] performed the Click reaction on the virus surface largely based on the protocol provided by me as well as biolayer-interferometry measurements and kinetic binding analysis (refer to chapter 3). [redacted] conducted all experiments regarding the protein corona on liposomes and PS-nanoparticles analyzed the results and contributed in writing parts of the manuscript. [redacted] supervised the experiments of [redacted], interpreted the results and revised the manuscript. [redacted] contributed in the design of the project and revised the manuscript. [redacted] supervised the synthesis and biological studies and revised the manuscript. [redacted] supervised all experiments of [redacted] and revised the manuscript. [redacted] designed the project, discussed the experimental data, provided funding, and revised the manuscript.

Copyright

The following part is reproduced from *Angewandte Chemie, International Edition* **2020**, *59*, 5712-5720. DOI: 10.1002/anie.201913708; Copyright (2020) The Authors. Published by Wiley-VCH Verlag GmbH & Co. KGaA and licensed under a Creative Commons Attribution (CC BY) license (https://creativecommons.org/licenses/by/4.0/).

Abstract

Amphiphilic surface groups play an important role in many biological processes. The synthesis of amphiphilic polyphenylene dendrimer branches (dendrons), providing alternating hydrophilic and lipophilic surface groups and one reactive ethynyl group at the core is reported. The amphiphilic surface groups serve as biorecognition units that bind to the surface of adenovirus 5 (Ad5), which is a common vector in gene therapy. The Ad5/dendron complexes showed high gene transduction efficiencies in coxsackie-adenovirus receptor (CAR)-negative cells. Moreover, the dendrons offer incorporation of new functions at the dendron core by *in situ* post-modifications, even when bound to the Ad5 surface. Surfaces coated with these dendrons were analyzed for their blood-protein binding capacity, which is essential to predict their performance in the blood stream. A new platform for introducing bioactive groups to the Ad5 surface without chemically modifying the virus particles is provided.

5.1 Introduction

Amphiphilicity plays an important role in the formation of biological architectures such as the structure of proteins, the self-assembly of peptides, or the build-up of biological membranes.[1-3] Because of the characteristics of amphiphiles to organize into higher ordered structures,[4] their interactions with other biomolecules is a complex process of high biological relevance, which is still not fully understood. For example, the exposure of nanomaterials like polymers, liposomes, or nanoparticles to biological fluids, such as human blood plasma, gives rise to a protein corona around nanoparticles that also directs their transport *in vivo*.[5, 6] It has been demonstrated that either the variation of surface charges[7, 8] or coating of nanoparticles, for example, with polymers like polyethylene glycol,[9] has an impact on the protein corona and often controls their aggregation[10] and biodistribution,[11] as well as cellular uptake properties.[9] By employing amphiphilic surface patterns on nanoparticles, their influence on biological systems was studied.[12, 13] It is still very challenging to control the surface contour of nanoparticles[13] and to impart distinct amphiphilic surface patterns with molecular precision that maintains their perfect nanosize definition in various biological environments.[14] Therefore, highly branched macromolecules with precise structures and molecular weights, such as dendrimers, have emerged as a monodisperse platform providing characteristic features of proteins.[15] Hence, they are often referred to as “artificial proteins”[16, 17] and their applications in biomedicine range from drug delivery of serum albumin mimicking polyphenylene dendrimers[18] to multivalent dendrimers as antiviral drugs[19] and gene delivery agents.[20] For example, it has been demonstrated that dendrons bind to a virus capsid by supramolecular interactions, leading to an electrostatically driven self-assembly into dendron-virus complexes. These complexes could be disassembled by an optical trigger to release the virus.[21, 22]

Amphiphilic polyphenylene dendrimers (PPDs) are macromolecules with given surface patterns consisting of, for example, alternating sulfonic acid and *n*-propyl groups.[23] These dendrimers are internalized into cells while showing low toxicity both *in vitro* and *in vivo* and they possess the ability to transport lipophilic drugs within their nonpolar inner cavities.[18] PPDs are unique because of the rigidity of their sterically demanding and space-filling pentaphenylbenzene scaffold, and therefore provide persistent three-dimensional structures.[24] This class of dendrimer has the advantage that surface patterns can be exactly positioned since no backfolding of single dendritic arms (dendrons) can occur.[25] Furthermore, we have shown previously that out of a set of

amphiphilic PPDs, only one type of PPD, with high density of amphiphilic surface patterns, was able to bind to adenovirus 5 (Ad5).[26] Less-branched amphiphilic PPDs showed a significantly lower binding to Ad5 and a negatively charged PPD surface did not lead to any binding. These findings indicated that the dense amphiphilic surface motif is required for Ad5 binding.[26]

Adenovirus (Ad) is a non-enveloped double-stranded DNA virus with an icosahedral capsid infecting respiratory epithelial cells.[27, 28] Ads are the most common vectors in gene therapy because of their significant advantages, such as genetic stability, well-characterized biology, and high transduction efficiency in cells.[27, 29] They enter cells by specific interaction with the coxsackie-adenovirus receptor (CAR) and integrins, limiting applications to such cell types.[30] Moreover, the three major capsid proteins – hexon protein, penton base, and fiber – bind to antibodies, which lead to immunogenic responses or neutralization, which needs to be reduced for *in vivo* applications.[27] One strategy focuses on shielding the Ad surface from antibody binding by covalent attachment of polymers like polyethylene glycol.[31, 32]

We discovered recently that the formation of an amphiphilic PPD corona promotes cellular internalization into CAR-negative cells, which cannot be intrinsically targeted by Ad5.[26] In human blood serum, neutralization by antibodies and binding of coagulation factor X (FX), the primary transport mechanism of Ad5 to the liver, were altered significantly after PPD adsorption. We show that there are no electrostatic interactions between the positively charged fibers of Ad5 and negatively charged sulfonic acids of the PPD. In addition, FX could not bind to Ad5 when shielded with the dendrimer, indicating that the PPD blocks the binding site for FX. As the amphiphilic PPDs bind to the virus capsid proteins, they also impart a novel surface pattern onto Ad5, controlling their various interactions with other blood serum proteins.[26] As a consequence, reduced gene transduction in liver tissue and an enhanced transduction in heart tissue were observed *in vivo*.[26] Thus, amphiphilic PPDs provide a novel platform for virus redirection into different cells and tissues because of their ability to coat and protect Ad5 from FX binding, which influences cellular uptake and biodistribution of Ad5 *in vivo*. Enhanced structural variability of the dendrimer scaffold is a prerequisite to further advance the applicability of amphiphilic PPDs in biomedicine. Therefore, a dendritic structure that enables the incorporation of additional functionalities is required (Figure 5.1).

Consequently, we combine the defined amphiphilic pattern of PPD3 for biorecognition with a novel synthetic handle to enable post-modifications (Figure 5.1). Since PPDs are

symmetric macromolecules, the incorporation of an additional feature is challenging while retaining the desired amphiphilic surface structures. Therefore, we desymmetrized the PPD3 structure and synthesized the first amphiphilic polyphenylene dendron having one dendrimer branch, that is, one quarter of the entire PPD3, which combines Ad5 binding features with the potential for post-modification. We demonstrate a novel multistep synthesis of an amphiphilic polyphenylene dendron with a propargyl-modified triethylene glycol linker at the core. By applying this linker, high water solubility as well as the possibility to introduce functional units like either a fluorophore for imaging or a bio-orthogonal group by copper(I)-catalyzed azide–alkyne cycloaddition (CuAAC) are envisioned. Additionally, upon complexation with Ad5, the alkyne group can act as a functional handle for *in situ* CuAAC to serve as a versatile platform for introducing chemical modifications on the viral surface. Furthermore, we analyzed the binding of blood proteins to understand the influence of amphiphilic dendron-coated surfaces in the blood stream.

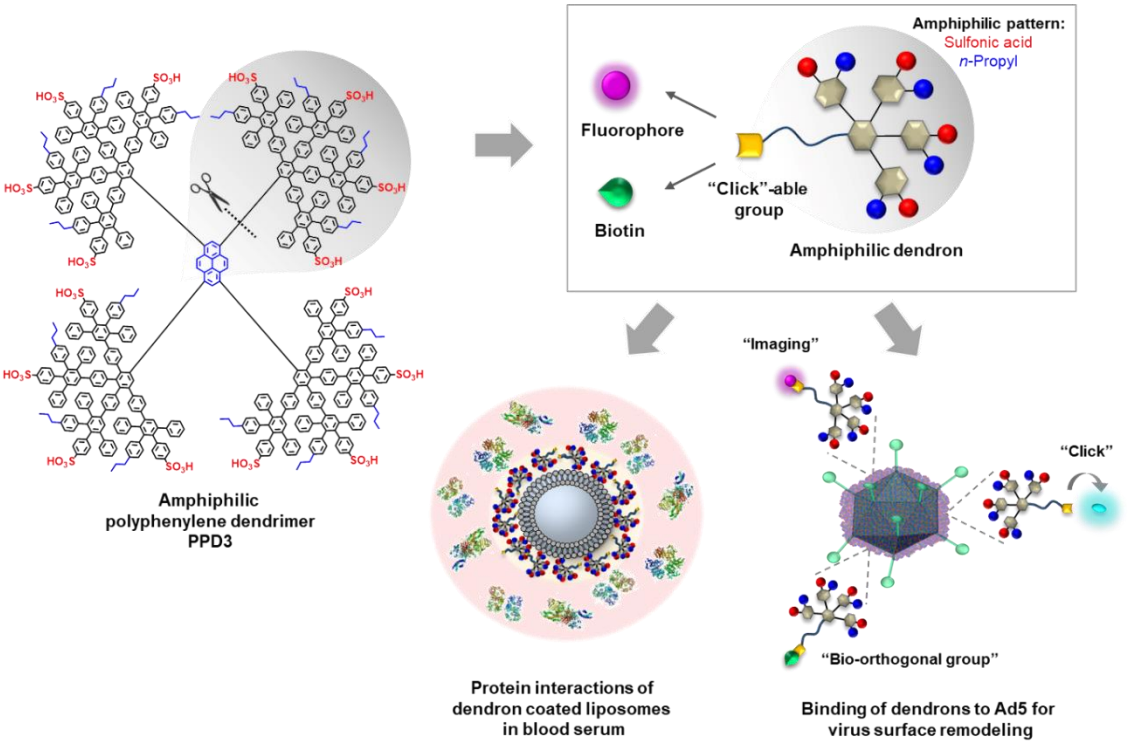

Figure 5.1. Structural design of an amphiphilic polyphenylene dendron by desymmetrization of amphiphilic dendrimer PPD3. By the employment of a clickable ethynyl group, the introduction of a second function by post-modification was achieved. The amphiphilic pattern of these dendron-conjugates interacts with biological structures like proteins and was verified by interactions of dendron-coated liposomes with blood serum proteins (protein structures: PDB-files 4NHH,[33] 1FZC,[34] 5Z0B[35]) as well as binding to Ad5 for re-direction into CAR-negative cells.

5.2 Results and Discussion

The divergent synthesis of a second-generation amphiphilic dendron (Scheme 5.1) is based on iterative [4+2] Diels–Alder cycloadditions of an ethynylated core with tetraphenylcyclopentadienones (CPs). The CP either determines the branching or serves as an end-capping unit introducing the surface patterns.[36] As previously reported, a high density of amphiphilic surface groups resulting from a highly branched dendrimer scaffold leads to Ad5 binding.[26] To integrate this dense surface pattern into a dendron scaffold, we synthesized a dendritic branch with similar amphiphilic surface groups, representing one quarter of the entire dendrimer. Therefore, the AB4 building block **1**, with four branching points was used, and was synthesized based on modified protocols from Morgenroth et al.[37] The synthesis scheme of **1**, as well as all reaction conditions are summarized in Figure S5.1A (see the Supporting Information). The bifunctionalized CP **2**, with an *n*-propyl group and neopentyl-protected sulfonic acid group, was applied as an end-capping unit and was synthesized based on modified protocols from Stangenberg et al.[23] The syntheses and reaction conditions are summarized in Figure S5.1B.

In this study, the neopentyl-protected amphiphilic polyphenylene dendron **7** was synthesized and post-modified with a propargyl-TEG-linker followed by attachment of either a D-biotin or Cyanine 5 (Cy5) moiety by a CuAAC (Scheme 5.1). Cy5 was introduced for cellular uptake experiments and co-visualization of dendron uptake and Ad5 gene delivery. D-Biotin was attached as an example of a bio-orthogonal group to study the influence of a functional group on Ad5 binding.

The detailed structure of the dendron core is crucial since its accessibility, as well as peripheral functionality after dendron growth are required. The dendron **7** was synthesized from a bifunctional biphenyl dendron core (**3**), which allowed minimization of the steric hindrance for the post-modification step. The iodo group of **3** enabled the coupling with an ethynyl group that is required for dendron growth, while the aniline group offered the possibility for post-modification at the focal point after dendron synthesis. In a condensation reaction, the aniline group was protected with benzophenone, resulting in an imine to prevent side reactions of the amine group during the harsh reaction conditions of PPD synthesis. In the next step, the tri*iso*propylsilyl (TIPS) protected ethynyl group was introduced by Sonogashira–Hagihara coupling followed by removal of the silyl groups to afford the dendron core **4** in good yields (75% over three steps). Further dendron growth was conducted by utilizing the branching unit **1** (AB4[37]) in a

[4+2] Diels–Alder cycloaddition under standard reaction conditions. Since **4** only features one dienophile (ethynyl group), the reaction time was reduced from 48[18] to 24 hours.

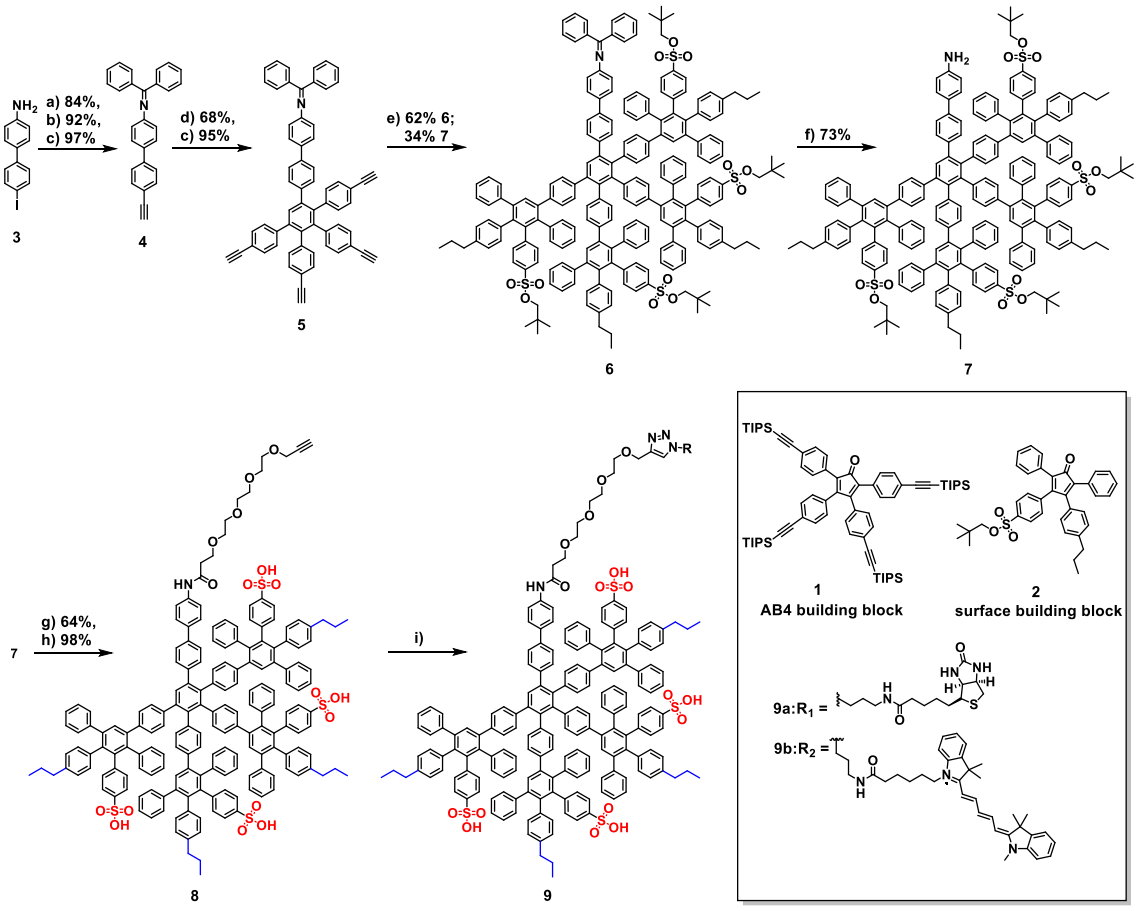

Scheme 5.1. Synthesis of amphiphilic polyphenylene dendron conjugates. a) Benzophenone, toluene, and molecular sieves 4Å, 15 h; b) TIPS-acetylene, CuI, $Pd(Ph_3P)_2Cl_2$, THF/ NEt_3 (5:1), RT, 15 h; c) TBAF, THF, 0 °C, 0.5 h; d) AB4 building block, *o*-xylene, 160 °C, 24 h; c) TBAF, THF, 0 °C, 0.5 h; e) Surface building block, *o*-xylene, 145 °C, 48 h; f) HCl, THF, 20 min; g) propargyl-TEG-COOH, EDC·HCl, DMAP, DMF, RT, 24 h; h) DMF, 180 °C, 36 h; i) RN_3, $CuSO_4$, sodium ascorbate, TBTA, DMF/H_2O (7:2 for **9a**; 7:1 for **9b**), RT, 24 h.

After deprotection of the ethynyl groups, the first generation dendron **5** was obtained in 65% yield over two steps. Subsequently, the next [4+2] Diels–Alder reaction with **2** was performed for 48 hours at reduced temperatures of 145 °C to avoid deprotection of the sulfonic acid groups.[23] Under these reaction conditions, the imine protective group was partially cleaved so that imine-dendron **6** (62%) as well as amine-dendron **7** (34%) were isolated by column chromatography. The remaining imine protective group of **6** was removed by acidic treatment to afford **7**. After ligation of **7** to a triethylene glycol (TEG) derivative (propargyl-TEG-linker) by amide coupling, the sulfonic acid groups were deprotected thermally to obtain the propargyl-TEG-dendron **8**. The removal of the neopentyl group requires high temperatures so that the heat-sensitive bioactive groups were attached after deprotecting the sulfonic acid groups. D-Biotin and Cy5 derivatives

were ligated by ligand-accelerated CuAAC, applying tris((1-benzyl-4-triazolyl)methyl)amine (TBTA) as the ligand. The crude products were purified by gel permeation chromatography (GPC) in *N,N'*-dimethylformamide to remove CuAAC reagents and unreacted starting materials to afford the biotinylated dendron **9a** and Cy5-dendron **9b**. A detailed reaction scheme is provided in Figure S5.2.

Because of the asymmetry of **2**, second-generation dendrons were obtained as constitutional isomers, as reported previously.[23, 38] The constitutional isomers were confirmed by ^{1}H NMR spectroscopy, where they are most notably visible in the spectra of the neopentyl-protected dendrons (see Figure S5.5). NMR spectroscopy and MALDI-TOF spectrometry demonstrate the successful synthesis of the propargyl-modified dendron **8** (see Figure S5.6, Figure S5.7 and Figure S5.13) and post-modification by CuAAC to achieve **9a** and **9b** (see Figure S5.8, Figure S5.12, Figure S5.14, and Figure S5.15). The signals in the ^{1}H NMR spectrum can be assigned to **8**, **9a**, and **9b**. The detailed synthesis description, as well as characterization of dendron intermediates and final products are summarized in the Supporting Information.

It is well known that Ads are involved in several protein interactions in the blood stream.[39] However, after PPD3 complexation, blood coagulation factor X (FX) could not bind to Ad5.[26] To shed light on the potential interaction partners of amphiphilic dendrons in the blood stream, we analyzed proteins binding to surfaces coated with **8**. The virus capsid was simplified by applying nanocarriers as already validated model systems with less complexity.[40, 41] Thus, liposomes[40] prepared from 1,2-dioleoyl-*sn*-glycero-3-phosphoethanolamine (DOPE), L-α-phosphatidylcholine (egg PC) and cholesterol (Chol) (PC:DOPE:Chol=1:1:1, Ø=242±6 nm), as well as polystyrene particles (PS-NH_2, 98±10nm)[41] with comparable sizes to Ad5 were coated with the amphiphilic dendrimer PPD3 and **8** (for details see the Supporting Information). Then, the protein adsorption in blood plasma as well as in blood serum was analyzed. As mentioned above, changes of surface charges as well as polymer coatings can influence the protein corona of nanoparticles.[8] As previously reported, amphiphilic patterned PPDs seem to bind to a lipid monolayer by electrostatic interactions between negatively charged sulfonic acid groups and positively charged headgroups of the lipid (see Figure S5.22).[42] Here, the dendron/dendrimer-coated liposomes and polystyrene (PS) particles were prepared following a standard protocol.[9, 41] Briefly, either liposomes or nanoparticles were incubated with excess dendron or PPD3 and purified by centrifugation. The coating was verified by DLS and zeta potential (see Table S5.1). Then, either blood serum or plasma was added (Figure 5.2A). After centrifugation, washing steps, and desorption of corona

proteins, the isolated proteins were analyzed qualitatively by SDS-PAGE (see Figure S5.17 – Figure S5.20) and quantitatively by a Pierce Assay (see Figure S5.21) and LC-MS/MS (Figure 5.2B,C; see Figure S5.16).

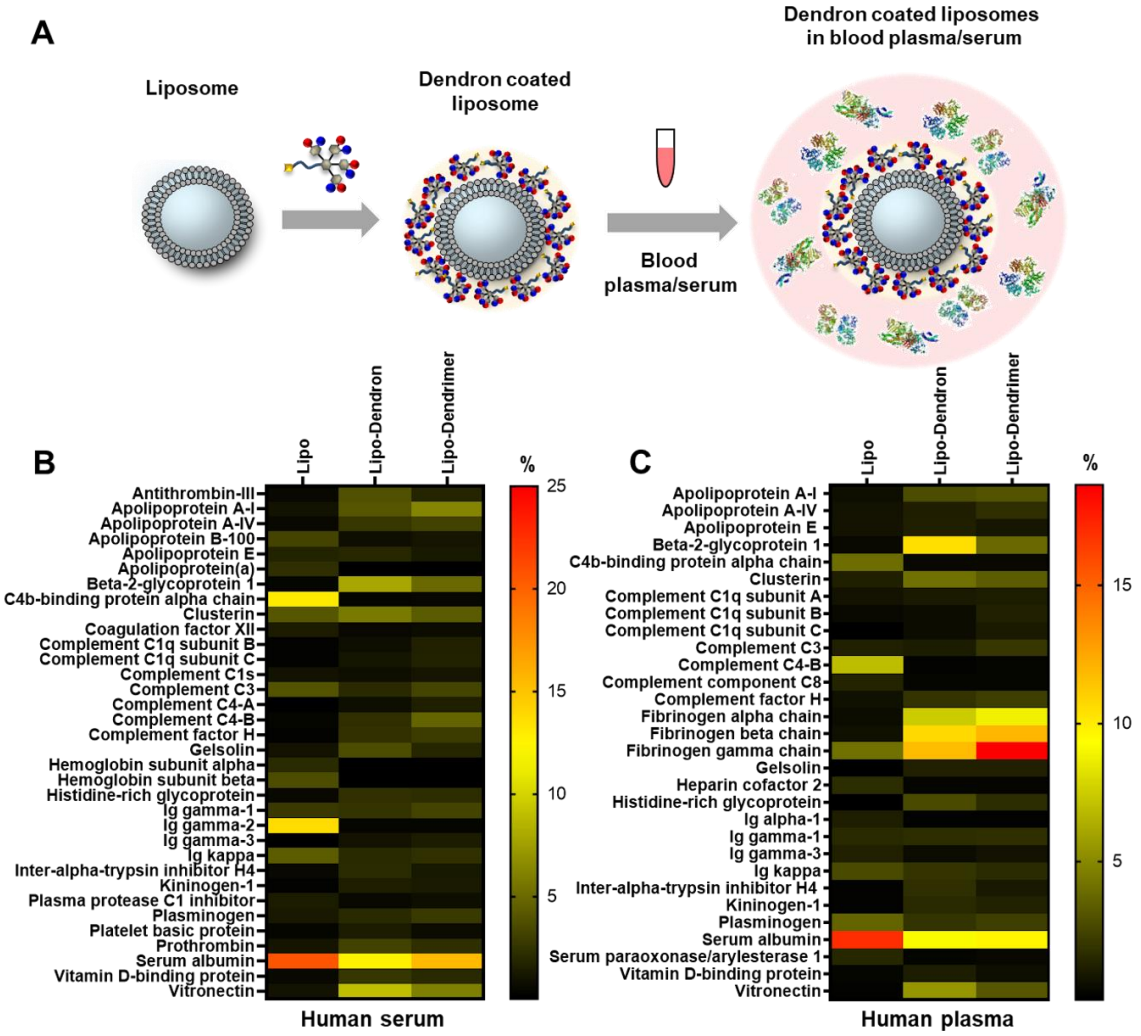

Figure 5.2. Dendron-coated liposomes form a protein corona in blood serum/plasma. (**A**) Coating of liposomes with dendron **8** and incubation with blood serum or blood plasma leading to protein corona (protein structures: PDB-files 4NHH[33], 1FZC[34], 5Z0B[35]). Heat map of adsorbed proteins to **8** and dendrimer PPD3-coated liposomes in blood serum (**B**) and blood plasma (**C**). The amount of each protein is given in % based on all identified corona proteins. A list of all identified proteins is provided in Figure S5.34 – Figure S5.37.

Coating with either **8** or PPD3 had a major impact on protein corona formation of liposomes (Figure 5.2) and PS nanoparticles (see Figure S5.16). For unfunctionalized liposomes and PS nanoparticles, we detected high amounts of albumin (ca. 26 ± 3%) and immunoglobulins (e.g. Ig kappa, 6 ± 1%) in the protein corona after serum incubation. However, after coverage with **8** (lipo-dendron) the amount of Ig kappa is significantly lower (ca. 2 ± 0.2%) Immunoglobulins belong to the protein class of opsonins and can mediate the interaction with phagocytic cells.[43] The adsorption of IgG can dramatically reduce the blood circulation time, and thereby also reduce the interaction with targeted

cells.[44] As reported in the literature, the protein source additionally shapes the protein corona formation.[45, 46] This observation is in line with our findings as we have observed differences in the protein corona composition after serum and plasma incubation (Figure 5.2B *versus* C).

For serum preparation, blood was clotted and then centrifuged to remove the clot. The resulting supernatant no longer contained all proteins. Because of this preparation, fibrinogen and other clotting factors were removed. In contrast, for plasma preparation, an anticoagulant was added to prevent blood clotting and therefore the plasma contained all blood proteins including the clotting factors. For **8**- and PPD3-covered liposomes, the amount of fibrinogen was higher than for the unfunctionalized ones after plasma incubation. Comparable results were obtained for **8**- and PPD3-coated PS (see Figure S5.16 – Figure S5.18), indicating that the protein interactions are governed by the **8** and PPD3 coating and not by the underlying base material. In addition, minor differences were observed for the protein corona composition of lipo-dendron and lipo-dendrimer after serum and plasma incubation. This effect was most prominent for β-2 glycoprotein 1, also known as Apolipoprotein H (ApoH).[8] The corona of lipo-dendron was enriched with ApoH (8 ± 0.5% serum, 11 ± 1.5% plasma), whereas lower amounts were detected for both lipo-dendrimer (5 ± 0.3% serum, 4 ± 0.3% plasma) and unfunctionalized liposomes (0.5 ± 0.2% serum, 0.3 ± 0.5% plasma). It has been previously shown that the coating of PS nanoparticles with ApoH leads to favorable interaction with human mesenchymal stem cells.[8] A similar trend was observed for the adsorption of vitronectin, which increased in case of the lipo-dendron compared to either PPD3-coated or unfunctionalized liposomes. Here, we found that the protein corona of the lipo-dendron was enriched with vitronectin (9 ± 0.8% serum, 6 ± 0.5% plasma), whereas lower amounts were adsorbed on either the lipo-dendrimer (6 ± 0.5% serum, 3 ± 0.2% plasma) or unfunctionalized liposomes (1 ± 0.7% serum, 0.2 ± 0.3% plasma). Interestingly, vitronectin was also detected in the protein corona of DOTAP/DNA lipoplexes and it was demonstrated that vitronectin could mediate a selective uptake of the lipoplexes towards MDA-MB-435S cancer cells, which have a high expression level of the vitronectin $\alpha_v\beta_3$ integrin receptor.[47] Taken together, these results indicate that coating with **8** favors the interactions with specific blood proteins, which eventually also determine the interactions with cells and cellular uptake behavior.

Since amphiphilic dendrimers with alternating sulfonic acid and *n*-propyl groups are internalized into cells and transported by vesicles,[18] we tested the cellular uptake of the dendron to assess whether the surface pattern of a desymmetrized dendron is similar to

the symmetric PPD3 dendrimer. The Chinese Hamster ovary cell line CHO-K1 was selected, since it possesses low CAR-expression, rendering it also suitable for gene transduction experiments within this study. The cells were incubated with 1 µM **9b** for 24 hours, washed with phosphate buffered saline (PBS), and the nucleus was stained with Hoechst 33258. The cellular internalization was followed by confocal laser scanning microscopy. As depicted in Figure 5.3A, **9b** was internalized into CHO-K1 cells. We observed that **9b** was located in vesicles in a similar way reported for amphiphilic PPDs.[18] The comparison with the blank control is provided in Figure S5.23.

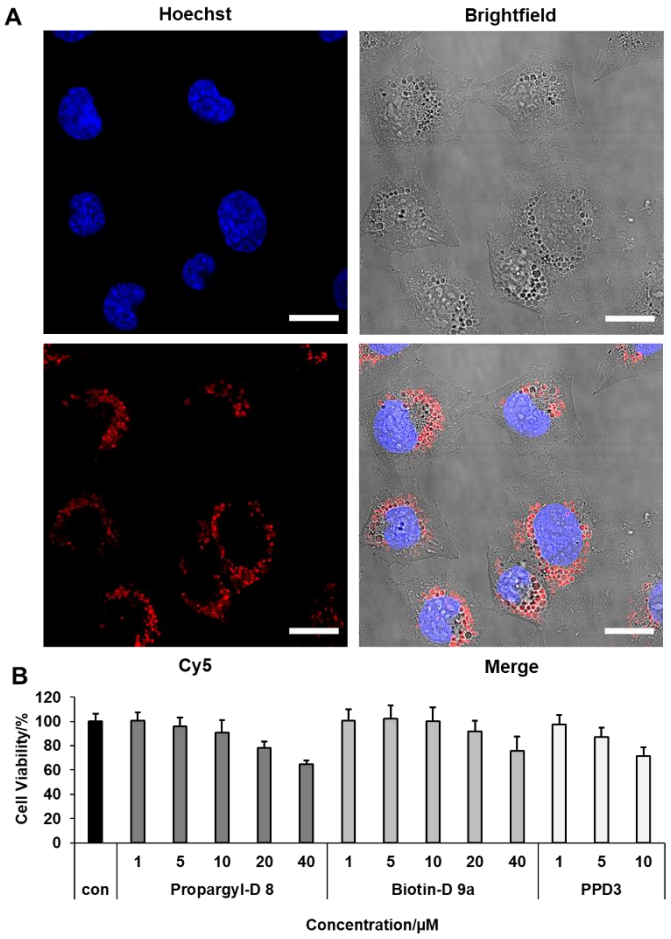

Figure 5.3. Cellular internalization of amphiphilic dendrons and cell viability on CHO-K1 (**A**) Confocal image of CHO-K1 cells incubated with 1 µM Cy5-Dendron **9b** for 24 h and nucleus staining with Hoechst 33258 (scale = 20 µM) (**B**) Cell viability of **8** and **9a** compared to PPD3 by applying four times higher dendron concentration to achieve approximate same quantities of surface patterns. Cell viability was tested with CellTiter-Glo®-Assay. Data from three independent experiments with quadruplicates (total n = 12) is shown.

Cell compatibility of **8** and **9a** was compared to PPD3 in CHO-K1 cells by a cell viability assay. Cells were treated with 1–40 µM **8** and **9a** as well as 1–10 µM PPD3 for 24 hours. We used four equivalents of dendron conjugates compared to PPD3 to adjust the numbers of surface patterns to approximately similar quantities. The cell viability was determined by quantification of the ATP levels by applying the CellTiterGlo®-Assay. Both

dendron conjugates and PPD3 displayed no significant cytotoxicity up to 20 and 5 µM, respectively.

Next, we studied the performance of the dendron conjugates in Ad5-assisted gene transduction (Figure 5.4A). The formation of a dendron corona was studied by transmission electron microscopy (TEM), dynamic light scattering (DLS), and zeta potential, and we performed a functional assay to assess its capability to transport Ad5 into CAR-negative cells as monitored by fluorescence microscopy. The influence of surface patterns on gene transduction was compared with PPD3 using flow cytometry. Consequently, **8**, **9a**, and **9b**, as well as PPD3, were mixed with Ad5 at the ratios of 1:20k to 1:500k (Ad5/dendron) and 1:5k to 1:125k (Ad5/PPD3), respectively, in PBS and complex formation as well as gene transduction of Ad5 in low CAR expressing cell line CHO-K1 were tested. For all experiments, four equivalents of dendron related to PPD3 were used to compare their properties while maintaining approximately the same surface pattern. Here we used an eGFP-expressing Ad5 and analyzed its interaction with the dendrons. TEM analysis of vector particles incubated with the dendron for 40 minutes at a molar ratio of 1:100k was performed. Results clearly confirmed that **8**, **9a**, and **9b** bound to and formed complexes with Ad5 (Figure 5.4B; see Figure S5.24). To further analyze this interaction, DLS measurements were conducted. Our data shows that dendrons alone self-assemble in solution because of their intrinsic amphiphilicity (see Table S5.5 and Figure S5.26B). Nevertheless, in the presence of Ad5, all dendrons demonstrably bound to the vector particles, which was clearly indicated by an increase of the vector particle size (see Table S5.3 and Table S5.4, and Figure S5.25 and Figure S5.26A). To further confirm this interaction, we measured the surface charge of dendrons alone, Ad5 alone, and dendron-coated Ad5 by zeta potential analysis. Dendron-coated vector particles showed a ratio-dependent increase of the negative surface charge compared to dendrons alone or Ad5 particles alone (see Table S5.3 – Table S5.5), confirming the binding of Ad5 and analyzed dendrons. Additionally, we could show that at ratios beyond 1:1000k for Ad5/**8** and 1:200k for Ad5/**9a**, saturation of Ad5 particles is reached, which results in free, unbound dendron molecules in solution (see Table S5.4 and Figure S5.26).

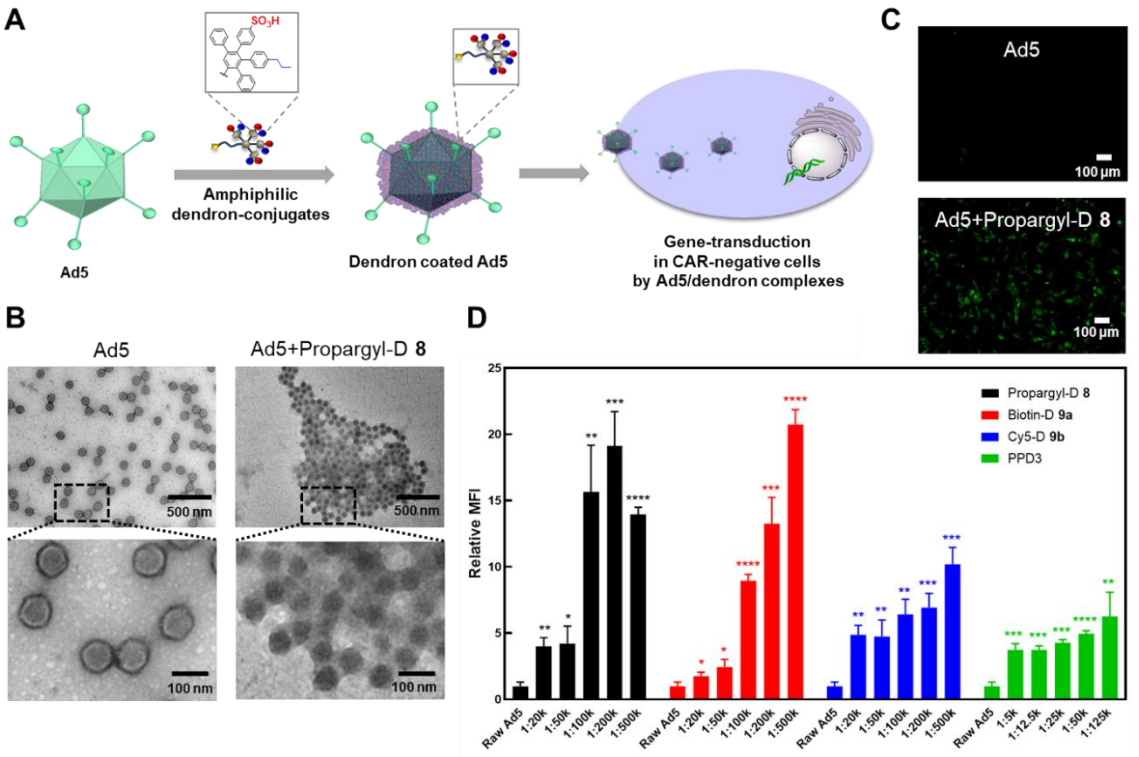

Figure 5.4. Dendron-Ad5 complex formation leads to EGFP-transduction in CAR-negative cells. (**A**) Coating of Ad5 by dendrons and the potential for cellular uptake into CAR-negative cells resulting in gene transduction; (**B**) TEM images show binding of dendrons to Ad5 (Ad5: Dendron = 1: 100k); (**C**) Fluorescent microscopy image of EGFP-transduction in CAR-negative CHO-K1 cells (Ad5: Dendron = 1: 500k); (**D**) Flow cytometry of CHO-K1 cells incubated with Ad5-dendron complexes with ratios of Ad5: Dendron = 1:20k–1:500k and Ad5: PPD3 = 1:5k–1:125k, respectively (n = 3, * represents p-value <0.05, ** represents p-value <0.01, *** represents p-value <0.001, **** represents p-value <0.0001).

We previously used biolayer interferometry (BLI) to study the binding strength of an amphiphilic dendrimer binding motif to Ad5.[26] This method required the immobilization of the dendrimer on a streptavidin-coated surface (see Figure S5.32). Thus, we used **9a** and an equilibrium dissociation constant value of K_D =1.27 pM was determined (see Figure S5.33 and Table S5.6). Since the dendron binds to Ad5 in a multivalent way, this value does not present a single binding event of the dendron to Ad5, but point towards strong interactions between Ad5 and dendron.[26] We observed green fluorescence by fluorescence microscopy for all cells treated with Ad5/dendron complexes whereas Ad5 alone led to low gene transduction (Figure 5.4C; see Figure S5.27). Therefore, all dendron conjugates as well as the control dendrimer PPD3 bound to Ad5, and they transported Ad5 into cells by a CAR-independent pathway, leading to EGFP-expression. We quantified the gene transduction of Ad5 in low CAR cell line CHO-K1 by flow cytometry by measuring the fluorescence intensity of EGFP. We found that gene transduction was enhanced when increasing the molar ratio of the dendron to Ad5 (Figure 5.4D, see Figure S5.28). A double-positive signal of EGFP and Cy5 was observed when infecting the cell with Ad5/**9b** (see Figure S5.29). We found a significantly

higher gene transduction of Ad5 when coated with four molar equivalents of **8** and **9a** compared to coating with one molar equivalent of the sterically more demanding PPD3. The dendron **9b** showed lower gene transduction efficiency than **8** and **9a**, and it could be due to the attachment of the fluorophore that might also influence Ad5 binding and its cellular uptake. These results indicate that four molar equivalents of **8** and **9a** increase Ad5 transport into these CAR-negative cells compared to one molar equivalent of PPD3. As reported for amphiphilic PPDs,[26] distinct amphiphilic surface patterns of the dendrons are crucial for biorecognition of Ad5. Even though the amphiphilic dendrons only represent one quarter of the full dendrimer PPD3, they retain both Ad5 binding capacity and gene transduction into CAR-negative cells, while providing a second functionality for post-modifications (Figure 5.4A and Figure 5.5A).

In the next step, we studied whether the functionality at the focal point of the dendron was still accessible after complexation with Ad5. Consequently, we covalently modified the dendrons *in situ* by CuAAC on the Ad5 surface. The reaction was performed using **8** with 3-azido-7-hydroxycoumarin, which is known to become highly fluorescent when forming a 1,2,3-triazole product (Figure 5.5A).[48] As negative control, we used **9a** attached to Ad5, which cannot undergo a CuAAC. We first investigated if the CuAAC proceeded in the micromolar range as well as the necessity of a ligand like TBTA to stabilize the copper(I) species.[49] After 1 hour of incubation of **8** and 3-azido-7-hydroxycoumarin with click reagents at a concentration of 10 µM dendron, we only found high fluorescence for the TBTA-treated sample. This observation indicates the importance of adding a ligand like TBTA to the reaction mixture (see Figure S5.30). Additionally, it is reported that this class of ligands protect biomolecules from reactive oxygen species (ROS) during the ligation.[50]

For CuAAC on the Ad5 surface, we used the water-soluble (4-{[bis-(1-*tert*-butyl-1*H*-[1,2,3]triazol-4-ylmethyl)-amino]-methyl}-[1,2,3]triazol-1-yl)-acetic acid (BTTAA), which is even more efficient in aqueous solutions than TBTA.[51, 52] Briefly, **8** was incubated with Ad5 for 1 hour, and unbound dendrons were removed by ultrafiltration. Subsequently, the CuAAC reagents were added. The negative control, **9a**-coated Ad5, was treated under the same reaction conditions. In addition, ultrafiltered **8** without Ad5 was prepared and click reagents were added to the supernatant to demonstrate that free dendrons could be removed by ultrafiltration. After incubation for 1 hour, fluorescence spectra were recorded (Figure 5.5B). Since free 3-azido-7-hydroxycoumarin is slightly fluorescent, we subtracted it as background. We observed a 21-fold increase in relative fluorescence intensity at 477 nm compared to the biotin-dendron coated Ad5 that served as negative

control (Figure 5.5C). These results indicate successful CuAAC at the focal points of **8** after formation of Ad5/ dendron complexes. Therefore, we demonstrate that the functionalities of the dendron core are still accessible for post-modifications even after complexation with Ad5. This model reaction proves that our structural dendron concept represents a promising tool for future applications in terms of *in situ* attachment of cell targeting groups or drug molecules.

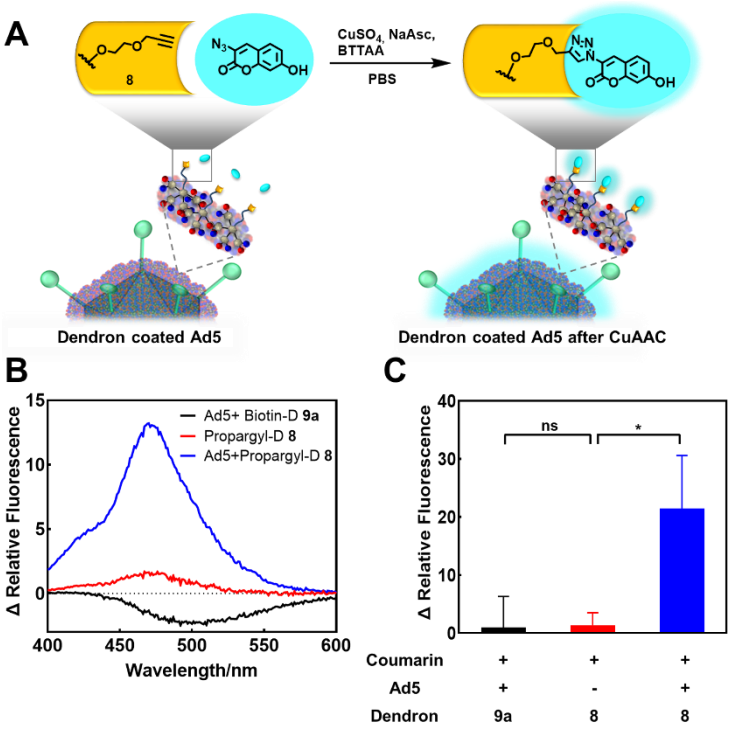

Figure 5.5. CuAAC on dendrons bound to Ad5. (**A**) CuAAC of **8** with 3-azido-7-hydroxycoumarin on the Ad5 surface leads to fluorescence of the dendron-fluorophore conjugate (λ_{abs}= 404 nm, λ_{em}= 477 nm after click reaction). (**B**) Fluorescence spectra of dendron conjugates after treatment with CuAAC reagents. Ad5 was mixed with either **8** or **9a** (negative control). After incubation for 40 min, unbound dendron was removed by ultrafiltration. The dendron **8** alone was treated under the same reaction conditions. Then, CuAAC reagents were added and fluorescence spectra were recorded after incubation for 1 h. 3-azido-7-hydroxycoumarin was subtracted as background. (**C**) The change in relative fluorescence of Ad5+Biotin-D **9a** group, Propargyl-D **8** group (with ultrafiltration), and Ad5+Biotin-D **9a** group at 477nm (emission) after treatment are described in (**B**). 3-Azido-7-hydroxycoumarin was subtracted as background and the change in relative fluorescence of Ad5/propargyl-dendron after CuAAC (blue column) is relative to the Ad5+Biotin-D **9a** group (black column) that serves as negative control (n=3, * represents $p<0.05$, ns means not significant).

5.3 Conclusion

Ad5 is a common vector in gene therapy but its clinical usage has limitations because of the mistargeting of plasma-protein-coated Ad5 and acute toxicity. We present the synthesis of amphiphilic polyphenylene dendrons that bind to the surface of Ad5 through their polar and nonpolar surface groups and facilitate transport of the Ad5/dendron complexes into CAR-negative cells. In this way, these dendrons maintained the crucial

biorecognition features of the full dendrimer PPD3. As the dendrons form a new outer layer at the Ad5 surface, their interaction with blood plasma proteins might be crucial for future applications. Dendron-coated liposomes were found to interact with specific proteins of the blood serum and plasma proteins such as vitronectin and ApoH, which could promote uptake into cancer and mesenchymal stem cells. In contrast to dendrimer PPD3, the dendrons provide an additional functionality for post-modifications such as introducing either a fluorophore for imaging or D-biotin as a bio-orthogonal group. By desymmetrization of the dendrimer structure, we accessed a new platform for introducing bioactive groups to the Ad5 surface without the needing to covalently modify the virus particles. These reactive groups were accessible at the Ad5 surface as shown by CuAAC reactions. Moreover, this new concept of forming a supramolecular dendron corona at virus surfaces presents exciting opportunities for attaching, for example, cell targeting groups or drug molecules, and paves the way to rational control of Ad5 biodistribution to ultimately improve its capacity in virus-assisted gene therapy.

5.4 Acknowledgements

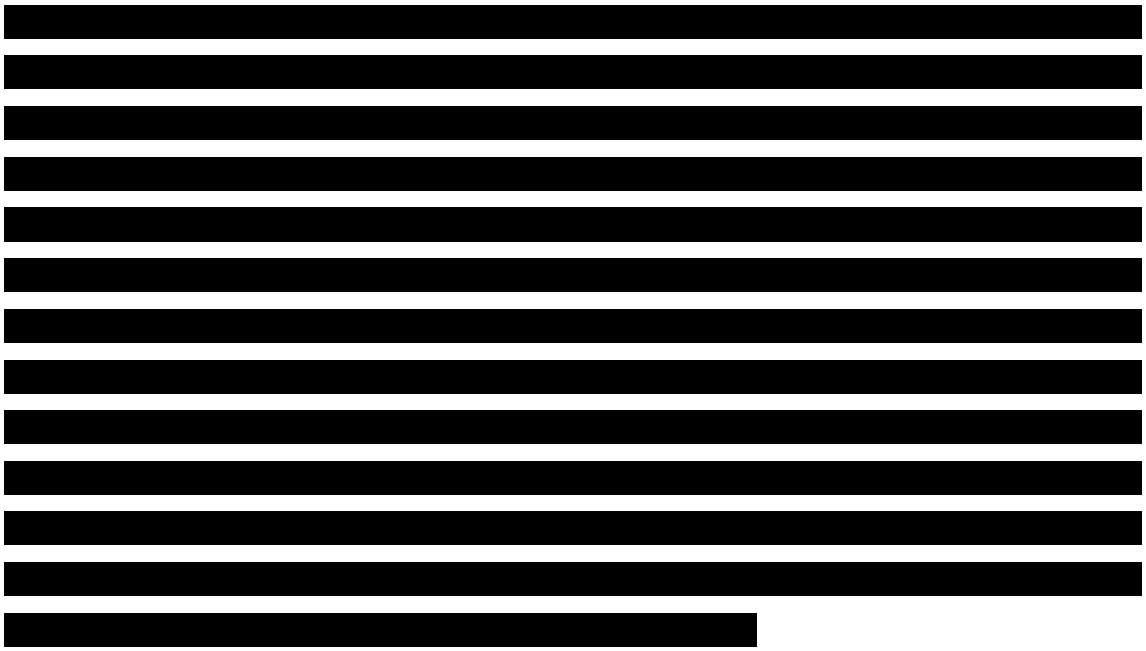

5.5 Supporting Information

5.5.1 Syntheses

Materials

All chemicals were purchased from commercial sources (Sigma Aldrich, Acros Organics, Fisher Scientific, Thermo Scientific, TCI, Chempur, PurePEG etc.) and were used without any further purification. The organic solvents (ethyl acetate, dichloromethane (DCM), cyclohexane, *o*-xylene, dimethylformamide (DMF), dimethylsulfoxide (DMSO), 1,4-dioxane, methanol, tetrahydrofuran (THF), toluene) were obtained from Fisher Scientific or Acros Organics and used without further purification (HPLC grade). H_2O for reactions and purification was purified by a Merck Millipore purification system. Thin-layer chromatography (TLC) was performed on Alugram Sil G/UV254 plates from Macherey-Nagel and substances were detected under UV light at 254 nm or 366 nm. Column chromatography was performed applying Macherey Nagel silica gel with particle size of 0.04-0.063 mm or 0.063-0.2 mm. Size-exclusion chromatography was carried out using Sephadex® LH-20 in DMF.

Instruments

Nuclear Magnetic Resonance Spectroscopy (NMR). ^{1}H-NMR and ^{13}C-NMR were recorded on a Bruker Avance III 300 MHz, Avance III 500 MHz or Avance III 700 MHz spectrometer in deuterated solvents like CD_2Cl_2, MeOD and DMSO-d_6. ^{13}C-NMR were recorded in j-modulated spin-echo (JMOD) mode. Spectra were analyzed in either MestReNova or Topspin.

Matrix-assisted Laser Desorption/Ionization–Time of Flight Mass Spectrometry (MALDI-TOF). MALDI-TOF mass spectra were measured on a Bruker rapifleX MALDI-TOF/TOF and a Waters MALDI Synapt G2-SI. Dendron intermediates (before sulfonic acid deprotection) were dissolved in THF and measured by applying *trans*-2-[3-(4-*tert*-butylphenyl)-2-methyl-2-propenylidene]malononitrile (DCTB) as matrix. Deprotected dendrons were solvated in DMF and diluted in a saturated α-cyano-4-hydroxycinnamic acid (CHCA) solution in water/acetonitrile (1:1) + 0.1% TFA. Processing of data was performed in mMass.

Atmospheric Pressure Chemical Ionization Mass Spectrometry (APCI-MS). APCI mass spectra of precursors were recorded on an Advion expression-L Compact Mass

Spectrometer (CMS) (Advion Inc. 61 Brown Rd, Suite 100, Ithaca, NY 14850, USA) by either measuring the sample with an atmospheric solid analysis probe (ASAP) or directly from TLC plates by an automated TLC plate reader (Plate express).

Field Desorption Mass Spectrometry (FD-MS). FD mass spectra of precursors were recorded on a VG Instruments ZAB 2-SE-FPD using an 8 kV accelerating voltage.

Synthesis of building blocks

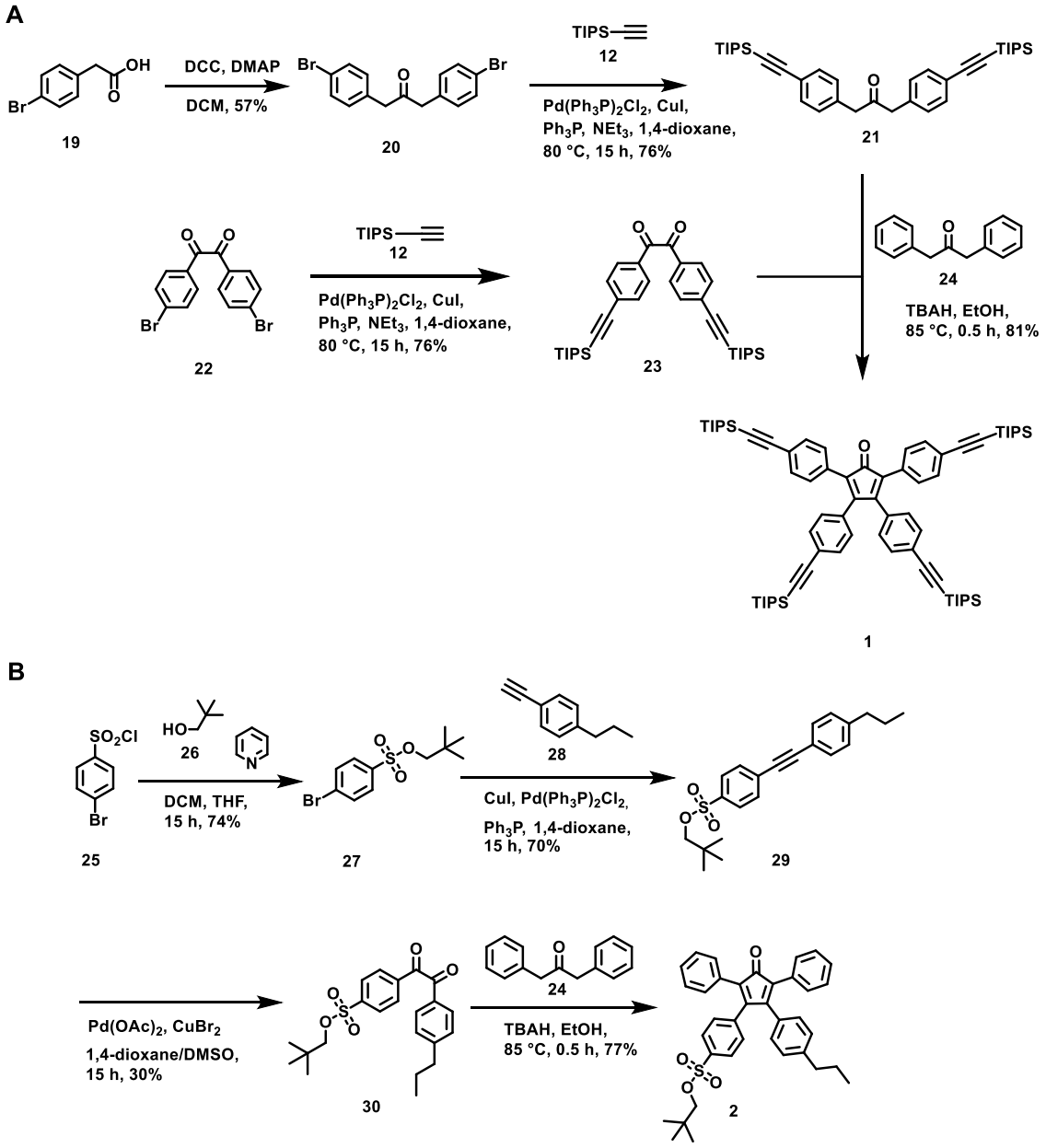

Figure S5.1. Reaction scheme of building blocks. (**A**) AB4 building block **1**, synthesized based on modified protocols from Morgenroth et al.[37] and (**B**) synthesis of surface building block **2** based on modified protocols from Stangenberg et al.[23]

*1,3-Bis(4-bromophenyl)propan-2-one (**20**)*

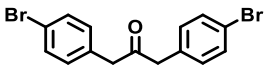

20

1,3-Bis(4-bromophenyl)propan-2-one (**20**) was synthesized according to the literature with modified protocol for purification.[53] Briefly, in a dry two neck round-bottom flask equipped with a dropping funnel dicyclohexylcarbodiimide (DCC) (9.6 g, 46.5 mmol) and 4-(dimethylamino)pyridine (DMAP) (1.42 g, 11.6 mmol) were dissolved in 100 mL dry dichloromethane. After degassing with argon for 30 min, *p*-bromophenylacetic acid (10.0 g, 46.5 mmol) in 100 mL dry dichloromethane was added dropwise and the reaction mixture was stirred for 24 h at room temperature. Then, the resulting *N,N'*-dicyclohexylurea was filtered off and the organic layer was washed with 10% hydrochloric acid and water. The crude product was purified by column chromatography using a mixture of cyclohexane and dichloromethane (1:2) to afford **20** as a white solid (4.85 g, 57%). All spectral data was in agreement with the literature.[53]

^{1}H NMR (300 MHz, CD_2Cl_2): δ(ppm) = 7.52–7.47 (m, 4H), 7.10–7.05 (m, 4H), 3.75 (s, 4H).

^{13}C NMR (75 MHz, CD_2Cl_2): δ(ppm) = 204.60, 133.62, 132.18, 131.90, 121.47, 48.95.

FD-MS: *m/z* calcd. for $C_{15}H_{12}Br_2O$ 368.1, found 369.6 $[M+H]^+$.

General procedure P1 for Sonogashira-Hagihara coupling:

The synthesis of ethynylated aryl compounds was modified from previously reported methods.[23, 36] Aromatic bromo compound (1 equiv), ethynyl derivative (1.1 equiv per bromine on the bromo compound) and triphenylphosphine (0.1 equiv) were dissolved in a mixture of 1,4-dioxane and triethylamine (2:1, 40 mL per gram bromo compound). After degassing with argon for 30 min, bis(triphenylphosphine)palladium(II)chloride ($Pd(Ph_3)P)_2Cl_2$) (0.05 equiv) and copper iodide (0.1 equiv) were added. The reaction mixture was stirred under reflux at 85 °C and argon atmosphere for 15 h. The reaction mixture was cooled to room temperature, the palladium catalyst was filtered off and the fitration residue was washed with dichloromethane. The solvents were removed *in vacuo* and the residue was dissolved in dichloromethane. The organic layer was washed with water, dried over sodium sulfate and the solvent was evaporated. The crude product was purified by column chromatography.

*1,3-bis(4-((triisopropylsilyl)ethynyl)phenyl)propan-2-one (**21**)*

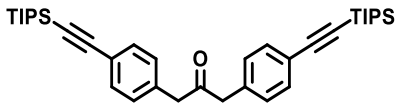

21

4,4‘-Bromodiphenylacetone (**20**) (2.0 g, 5.4 mmol) was reacted with tri*iso*propylsilylacetylene (**12**) (2.48 g, 3.1 mL, 13.6 mmol) according to general procedure **P1**. The crude product was purified by silica gel column chromatography using a mixture of cyclohexane and dichloromethane (2:1) and compound **21** was recovered as a yellow solid (2.36 g, 76%). All spectral data was in agreement with the literature.[36]

^{1}H NMR (300 MHz, CD_2Cl_2): δ(ppm) = 7.44 (d, *J* = 8.4 Hz, 4H), 7.10 (d, *J* = 8.2 Hz, 4H), 3.74 (s, 4H), 1.14 (s, 42H).

^{13}C NMR (75 MHz, CD_2Cl_2): δ(ppm) = 204.84, 135.05, 132.66, 130.10, 122.79, 107.29, 91.32, 49.53, 18.99, 11.89.

FD-MS: *m/z* calcd. for $C_{37}H_{54}OSi_2$ 571.0, found 571.3 $[M]^{\bullet+}$.

*1,2-bis(4-((triisopropylsilyl)ethynyl)phenyl)ethane-1,2-dione (**23**)*

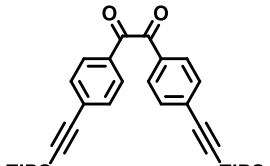

23

1,2-Bis(4-bromophenyl)ethane-1,2-dione (**22**) (10 g, 27.2 mmol) was reacted with tri*iso*propylsilylacetylene (**12**) (10.9 g, 13.4 mL, 59.8 mmol) according to general procedure **P1**. The crude product was purified by silica gel column chromatography using a mixture of cyclohexane and dichloromethane (7:3) to obtain compound **23** as a yellow solid (2.36 g, 76%).

^{1}H NMR (300 MHz, CD_2Cl_2): δ(ppm) = 7.95–7.84 (m, 4H), 7.64–7.55 (m, 4H), 1.14 (d, *J* = 2.6 Hz, 42H).

^{13}C NMR (75 MHz, CD_2Cl_2): δ(ppm) = 193.83, 132.96, 132.57, 130.74, 130.22, 106.27, 97.24, 18.94, 11.82.

FD-MS: *m/z* calcd. for $C_{36}H_{50}O_2Si_2$ 571.0, found 570.1 $[M-H]^{-}$.

*Neopentyl-4-((4-propylphenyl)ethynyl)benzenesulfonate (**29**)*

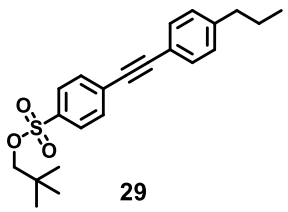

29

Neopentyl-4-bromobenzenesulfonate (**27**) (5 g, 16.3 mmol) was reacted with 1-ethynyl-4-propylbenzene (**28**) (2.58 g, 2.84 mL, 17.9 mmol) according to general procedure **P1**. The crude product was purified by silica gel column chromatography using a mixture of cyclohexane and dichloromethane (3:1) to obtain compound **29** as a white solid (4.21 g, 70%). All spectral data was in agreement with the literature.[23]

^{1}H NMR (300 MHz, CD_2Cl_2): δ(ppm) = 7.86 (d, J = 8.5 Hz, 2H), 7.69 (d, J = 8.5 Hz, 2H), 7.48 (d, J = 8.2 Hz, 2H), 7.21 (d, J = 8.2 Hz, 2H), 3.68 (s, 2H), 2.62 (t, J = 7.3 Hz, 2H), 1.65 (h, J = 7.3 Hz, 2H), 0.96 (t, J = 7.3 Hz, 3H), 0.89 (s, 9H).

^{13}C NMR (75 MHz, CD_2Cl_2): δ(ppm) = 145.01, 135.44, 132.57, 132.23, 129.81, 129.29, 128.46, 119.88, 94.15, 87.54, 80.51, 38.49, 32.09, 26.25, 24.93, 14.09.

FD-MS: *m/z* calcd. for $C_{22}H_{26}O_3S$ 370.5, found 370.7 $[M]^{\bullet+}$.

*Neopentyl-4-bromobenzenesulfonate (**27**)*

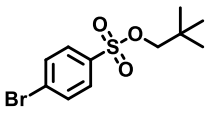

27

The synthesis of neopentyl-4-bromobenzenesulfonate (**27**) was modified from previously reported methods.[23] Briefly, in a dry two-neck flask neopentyl alcohol (**26**) (15.5 g, 176 mmol) was dissolved in dry dichloromethane and pyridine (7.66 g, 7.8 mL, 96.9 mmol) was added. The solution was cooled down to 0 °C and 4-bromobenzenesulfonyl chloride (**25**) dissolved in dry tetrahydrofuran (THF) (25 mL) was added dropwise. The resulting suspension was stirred at room temperature under argon atmosphere for 15 h. Pyridinium chloride was filtered off and the filtrate was reduced *in vacuo*. The crude product was purified by silica gel column chromatography using a mixture of cyclohexane and dichloromethane (1:2) to afford **27** as a white solid (19.9 g, 74%). All spectral data was in agreement with the literature.[23]

^{1}H NMR (300 MHz, CD_2Cl_2): δ(ppm) = 7.79–7.70 (m, 4H), 3.67 (s, 2H), 0.89 (s, 9H).

^{13}C NMR (75 MHz, CD_2Cl_2): δ(ppm) = 135.64, 133.12, 129.95, 129.27, 80.63, 32.08,

26.22.

FD-MS: *m/z* calcd. for $C_{11}H_{15}BrO_3S$: 307.2, found 308.7 $[M+H]^+$.

*Neopentyl-4-((2-oxo-2(-4-propylphenyl)acetyl)benzenesulfonate (**30**)*

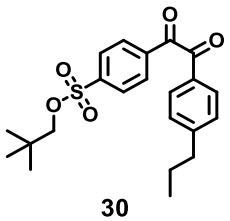

30

Neopentyl-4-((4-propylphenyl)ethynyl)benzenesulfonate (**29**) (2 g, 5.40 mmol) was solvated in 2 mL 1,4-dioxane and 15 mL dimethylsulfoxide were added. Subsequently, copper(II) bromide (121 mg, 0.54 mmol) and palladium(II) acetate (121 mg, 0.54 mmol) were added and the reaction mixture was stirred at 90 °C under argon atmosphere for 8 h. Then, water was added followed by extraction with ethyl acetate. The organic layer was dried over sodium sulfate and concentrated *in vacuo*. The crude product was purified by silica gel column chromatography using a mixture of cyclohexane and DCM (3:4) to afford **30** as a yellow oil (642 mg, 30%). All spectral data was in agreement with the literature.[23]

^{1}H NMR (300 MHz, CD_2Cl_2): δ(ppm) = 8.18–8.12 (m, 2H), 8.06–8.01 (m, 2H), 7.92–7.86 (m, 2H), 7.39–7.34 (m, 2H), 2.69 (t, J = 7.5 Hz, 2H), 1.75–1.58 (m, 2H), 0.95 (t, J = 7.3 Hz, 3H), 0.90 (s, 9H).

^{13}C-NMR (75 MHz, CD_2Cl_2): δ(ppm) 193.50, 152.23, 141.75, 137.34, 131.05, 130.79, 130.62, 129.90, 128.98, 81.04, 38.75, 32.15, 26.21, 24.71, 14.05.

FD-MS: *m/z* calcd. for $C_{22}H_{26}O_5S$: 402.5, found 403.2 $[M+H]^+$.

General procedure P2 for Knoevenagel reaction:

1,3-Diphenylacetone derivative (1 equiv) and benzil derivative (1 equiv) were dissolved in ethanol (~15 mL per 500 mg benzil) and heated up to 85 °C. Subsequently, 1 M methanolic tetrabutylammonium hydroxide (TBAH) solution (0.25 equiv) was added. After stirring at 85 °C for 0.5 h, the reaction mixture was diluted in dichloromethane. The organic layer was washed with water, dried over sodium sulfate and concentrated *in vacuo*. The crude product was purified by silica gel column chromatography.

*2,3,4,5-tetrakis(4-((triisopropylsilyl)ethynyl)phenyl)cyclopenta-2,4-dien-1-one (AB4 building block, **1**)*

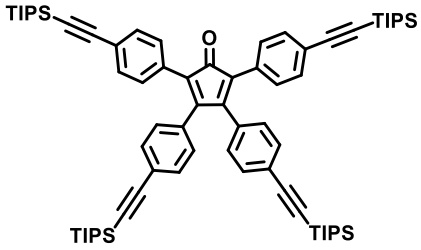

1

1,3-bis(4-((tri*iso*propylsilyl)ethynyl)phenyl)propan-2-one (**21**) (4 g, 7.01 mmol) was reacted with 1,2-bis(4-((tri*iso*propylsilyl)ethynyl)phenyl)ethane-1,2-dione (**23**) (4 g, 7.01 mmol) in 120 mL ethanol according to general procedure **P2**. The crude product was purified by silica gel column chromatography using a mixture of cyclohexane and THF (20:1) to afford **1** as a dark red solid (6.3 g, 81%). All spectral data was in agreement with the literature.

^{1}H NMR (300 MHz, CD_2Cl_2): δ(ppm) = 7.38–7.32 (m, 4H), 7.32–7.27 (m, 4H), 7.19–7.13 (m, 4H), 6.91–6.85 (m, 4H), 1.12 (d, J = 1.4 Hz, 84H).

^{13}C NMR (75 MHz, CD_2Cl_2): δ(ppm) = 199.52, 154.57, 132.31, 132.19, 131.15, 130.53, 129.85, 125.95, 124.52, 107.46, 107.02, 93.17, 92.51, 18.99, 11.87.

FD-MS: *m/z* calcd. for $C_{73}H_{100}OSi_4$ 1106, found 1108 $[M+2H]^{2+}$.

*Neopentyl 4-(3-oxo-2,4-diphenyl-5-(4-propylphenyl)cyclopenta-1,4-dien-1-yl)benzene-sulfonate (surface building block, **2**)*

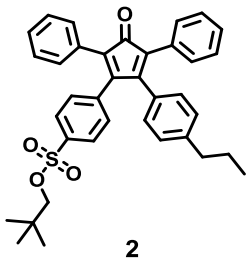

2

1,3-Diphenylacetone (**24**) (308 mg, 1.47 mmol) was reacted with neopentyl-4-((2-oxo-2(-4-propylphenyl)acetyl)benzenesulfonate (**30**) (590 mg, 1.47 mmol) in 10 mL ethanol according to general procedure **P2**. The crude product was purified by silica gel column chromatography using a mixture of cyclohexane and THF (4:1) to afford **2** as a dark purple solid (653 mg, 77%). All spectral data was in agreement with the literature.[23]

^{1}H NMR (300 MHz, CD_2Cl_2): δ(ppm) = 7.70 (d, *J* = 8.5 Hz, 2H), 7.31–7.22 (m, 8H), 7.20–

7.12 (m, 4H), 7.01 (d, *J* = 8.3 Hz, 2H), 6.83 (d, *J* = 8.2 Hz, 2H), 3.64 (s, 2H), 2.54 (t, *J* = 7.8, 7.2 Hz, 2H), 1.61 (dt, *J* = 13.7, 7.4 Hz, 2H), 0.92 (t, *J* = 7.3 Hz, 3H), 0.87 (s, 9H).

^{13}C NMR (75 MHz, CD_2Cl_2): δ(ppm) = 200.22, 155.08, 152.76, 144.50, 139.78, 135.83, 131.36, 130.72, 130.66, 130.32, 129.56, 128.84, 128.74, 128.56, 128.09, 127.61, 125.62, 80.56, 38.26, 32.05, 26.27, 24.77, 14.02.

FD-MS: *m/z* calcd. for $C_{37}H_{36}O_4S$: 576.7, found 576.8 $[M]^{\bullet+}$.

Synthesis of PPD3

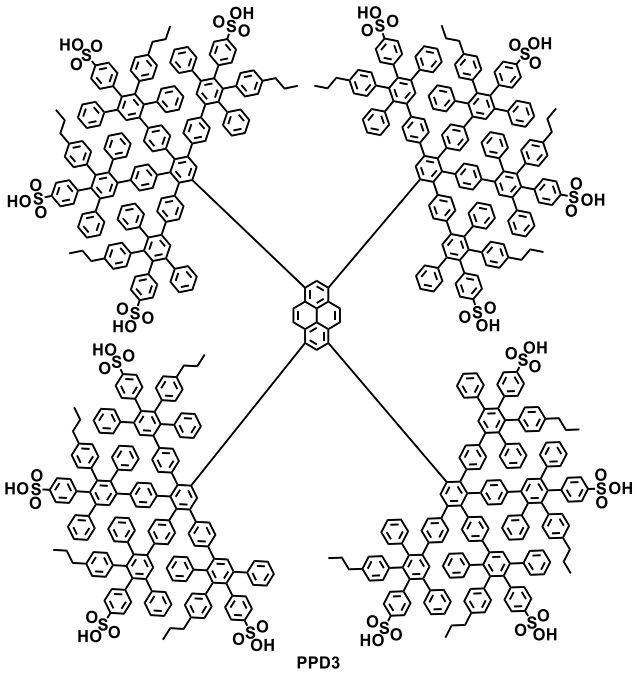

PPD3

PPD3 was synthesized in a divergent way as previously reported. All spectral data was in agreement with the literature.[18, 23]

^{1}H NMR (700 MHz, DMSO): δ(ppm) = 7.50 – 6.06 (m, 378H), 2.44 – 2.16 (m, 32H), 1.56 – 1.20 (m, 32H), 0.79 – 0.46 (m, 48H).

^{13}C NMR (176 MHz, DMSO): δ(ppm) = 162.80, 145.06–124.19, 120.10, 34.37, 23.53, 13.14.

MALDI-TOF: *m/z* calcd. for $C_{664}H_{506}O_{48}S_{16}$ 9766.26, found 9766.10 $[M]^{\bullet+}$.

Synthesis of dendron conjugates

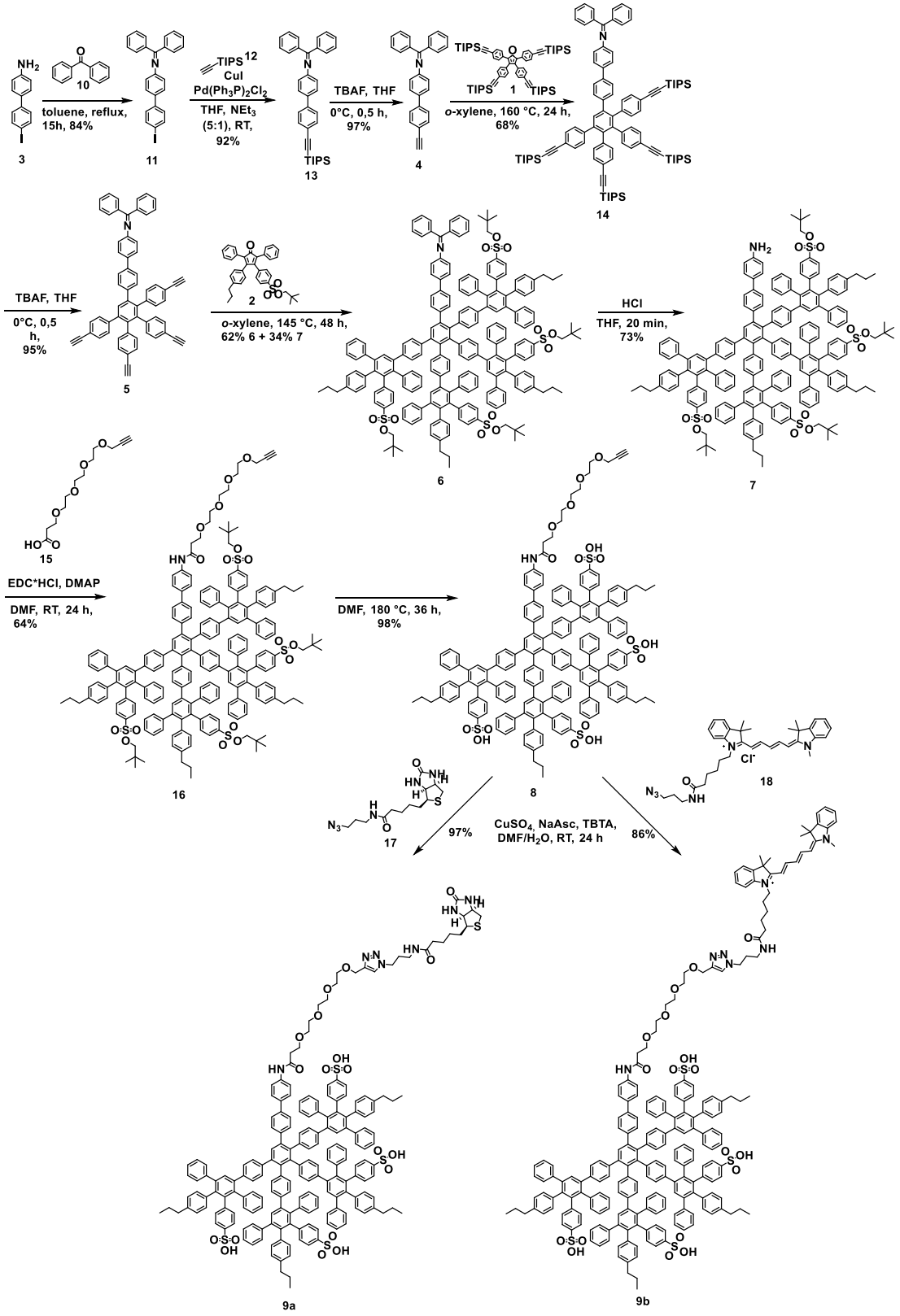

Figure S5.2. Detailed reaction scheme of dendron synthesis

*N-(4'-iodo-[1,1'-biphenyl]-4-yl)-1,1-diphenylmethanimine (**11**)*

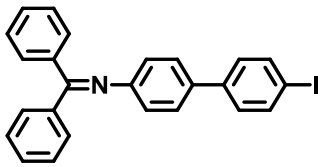

11

In a dry 25 mL Schlenk tube benzophenone (**10**) (100 mg, 549 µmol) and 4'-iodo-[1,1'-biphenyl]-4-amine (**3**) (178 mg, 604 µmol) were dissolved in 2 mL dry toluene and a 4 Å molecular sieve was added. The reaction mixture was heated under reflux for 24 h. Then, the molecular sieve was filtered off and washed with diethyl ether. Product **11** precipitated as a yellow solid (212 mg, 84%).

^{1}H NMR (500 MHz, CD_2Cl_2): δ(ppm) = 7.79–7.68 (m, 4H), 7.52–7.47 (m, 1H), 7.47–7.35 (m, 4H), 7.34–7.26 (m, 5H), 7.21–7.11 (m, 2H), 6.84–6.73 (m, 2H).

^{13}C NMR (126 MHz, CD_2Cl_2): δ(ppm) = 168.77, 151.76, 140.68, 140.06, 138.32, 136.78, 134.91, 131.36, 129.93, 129.88, 129.81, 129.16, 128.97, 128.71, 128.55, 127.34, 121.91, 92.77.

APCI-MS: *m/z* calcd. for $C_{25}H_{18}IN$ 459.1, found 459.5 $[M]^{\bullet+}$.

*N-(4'-((triisopropylsilyl)ethynyl)-[1,1'-biphenyl]-4-yl)1,1-diphenylmethanimine (**13**)*

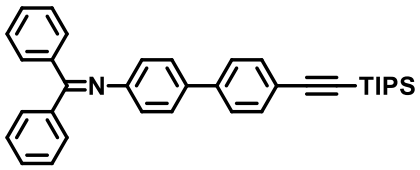

13

Imine **11** (300 mg, 0.65 mmol) and TIPS-acetylene (**12**) (137 mg, 169 µL, 0.75 mmol, 1.15 equiv) were dissolved in 10 mL THF and 2 mL triethylamine. After degassing, $Pd(Ph_3)P)_2Cl_2$ (45.8 mg, 65.3 µmol, 0.1 equiv) and copper iodide (24.9 mg, 131 µmol, 0.2 equiv) were added. The reaction mixture was stirred at room temperature under argon atmosphere for 15 h. Then, it was filtered and the filtrate was diluted with dichloromethane. The organic layer was washed with water, dried over sodium sulfate and purified by column chromatography using a mixture of cyclohexane and dichloromethane (1:2) to obtain **13** as a yellow solid (309 mg, 92%).

^{1}H NMR (500 MHz, CD_2Cl_2): δ (ppm) = 7.78–7.71 (m, 2H), 7.53–7.46 (m, 5H), 7.46–7.38 (m, 4H), 7.31 (m, 3H), 7.20–7.12 (m, 2H), 6.79 (d, J = 8.1 Hz, 2H), 1.14 (s, 21H).

^{13}C NMR (126 MHz, CD_2Cl_2): δ (ppm) = 168.19, 151.14, 140.43, 139.50, 136.23, 134.63,

132.28, 130.77, 129.36, 129.23, 128.59, 128.13, 127.98, 126.22, 121.85, 121.33, 107.00, 91.10, 18.42, 11.34.

APCI: m/z calcd. for $C_{36}H_{39}N_{Si}$ 513.3, found 513.8 $[M]^{\bullet+}$.

*N-(4'-ethynyl-[1,1'-biphenyl]-4-yl)-1,1-diphenylmethanimine (**4**)*

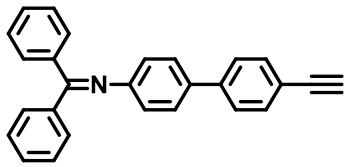

4

To an ice-cooled solution of **13** (155 mg, 302 µmol) in 24 mL dry THF 453 µL of a 1 M tetrabutylammonium fluoride (TBAF) solution in THF (118 mg, 453 µmol, 1.5 equiv) were added. The reaction mixture was stirred at 0 °C under argon atmosphere for 0.5 h. The reaction was quenched by water addition, extracted with dichloromethane and dried over sodium sulfate. After evaporation of the solvents compound **4** was obtained as a yellow solid (105 mg, 97%).

^{1}H-NMR (500 MHz, CD_2Cl_2) δ(ppm) = 7.78–7.70 (m, 2H), 7.56–7.46 (m, 5H), 7.45–7.38 (m, 4H), 7.35–7.26 (m, 3H), 7.19–7.14 (m, 2H), 6.84–6.75 (m, 2H), 3.17 (s, 1H).

^{13}C-NMR (126 MHz, CD_2Cl_2) δ(ppm) = 168.80, 151.83, 141.54, 140.05, 136.78, 135.06, 133.01, 131.36, 129.94, 129.82, 129.17, 128.71, 128.55, 127.52, 126.93, 121.91, 120.95, 84.00, 78.07.

MALDI-TOF: *m/z* calcd. for $C_{27}H_{19}N$ 357.15, found 357.22 $[M]^{\bullet+}$.

Terms for following dendron nomenclature

R-Core-Gx-$(abcd)_y$

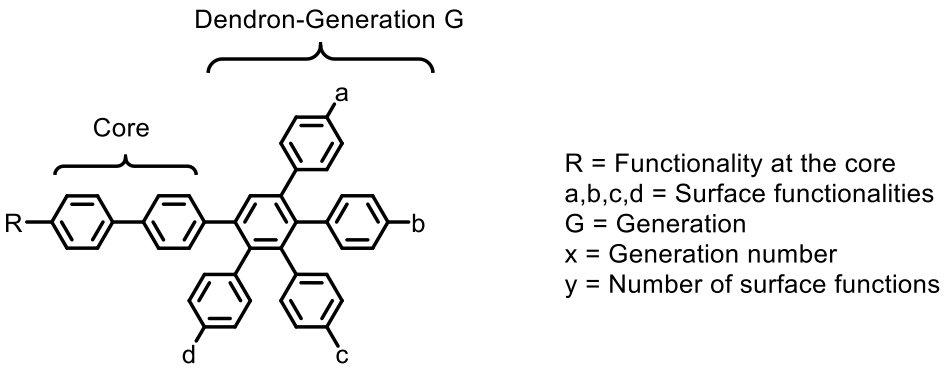

Imine-biphenyl-G1-(ethinyl-TIPS)$_4$ ***14***

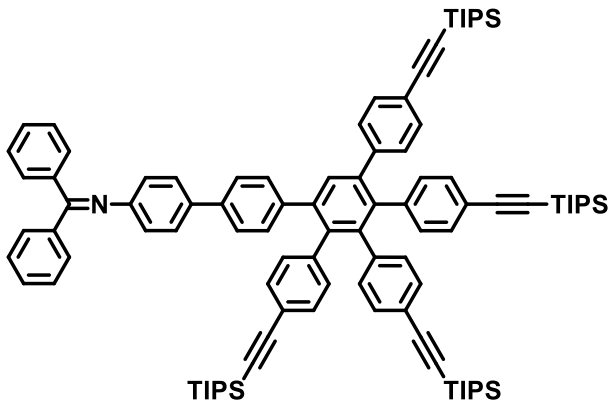

14

Dendron core **4** (30.0 mg, 83.9 µmol) and AB4-building block **1** (139 mg, 126 µmol, 1,5 equiv) were dissolved in 3 mL *o*-xylene and stirred at 160 °C in a sealed microwave tube under argon atmosphere for 24 h. After concentration *in vacuo* the crude product was purified by column chromatography using a mixture of cyclohexane and DCM (3:2) to obtain compound **14** as a yellow solid (82.4 mg, 68%).

^{1}H NMR (500 MHz, CD_2Cl_2): δ (ppm) = 7.77–7.70 (m, 2H), 7.52–7.45 (m, 2H), 7.44–7.36 (m, 6H), 7.34–7.25 (m, 5H), 7.18–7.03 (m, 12H), 6.84 (m, J = 8.2, 1.8 Hz, 4H), 6.79–6.73 (m, 4H), 1.15–1.04 (m, 84H).

^{13}C NMR (126 MHz, CD_2Cl_2): δ (ppm) = 168.66, 151.43, 142.10, 141.47, 141.40, 140.98, 140.83, 140.64, 140.48, 140.36, 140.13, 139.33, 139.13, 138.96, 136.83, 135.33, 132.23, 131.93, 131.84, 131.44, 131.40, 131.29, 131.19, 130.78, 130.34, 129.95, 129.80, 129.12, 128.69, 128.52, 127.32, 126.31, 122.24, 121.85, 121.69, 121.59, 121.46, 107.47, 107.40, 107.36, 91.66, 91.36, 91.24, 91.22, 18.97, 11.89.

MALDI-TOF: *m/z* calcd. for $C_{27}H_{19}N$ 1433.84, found 1433.73 $[M]^{\bullet+}$, 1456.72 $[M+Na]^+$, 1472.69 $[M+K]^+$.

Imine-biphenyl-G1-(ethinyl)$_4$ ***5***

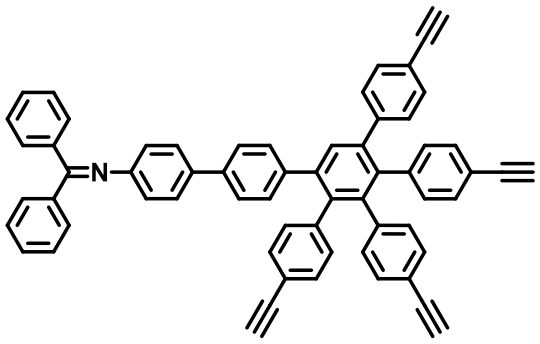

5

To an ice-cooled solution of dendron **14** (130 mg, 90.6 µmol) in 20 mL dry THF, 543 µL of a 1 M TBAF solution in THF (142 mg, 543 µmol, 6 equiv) were added. The reaction mixture was stirred at 0 °C under argon atmosphere for 0.5 h. The reaction was quenched by water addition, extracted with dichloromethane and dried over sodium sulfate. After evaporation of the solvents compound **5** was obtained as a yellow solid (69.6 mg, 95%).

^{1}H NMR (500 MHz, CD_2Cl_2): δ (ppm) = 7.77–7.71 (m, 2H), 7.56 (s, 1H), 7.48 (d, J = 7.4 Hz, 1H), 7.45–7.36 (m, 5H), 7.34–7.26 (m, 6H), 7.18–7.13 (m, 4H), 7.11 (dd, J = 8.3, 2.7 Hz, 6H), 7.07–7.03 (m, 2H), 6.88–6.80 (m, 4H), 6.78–6.73 (m, 4H), 3.15–2.99 (m, 4H).
^{13}C NMR (126 MHz, CD_2Cl_2): δ (ppm) = 168.68, 151.45, 142.39, 141.42, 141.39, 141.21, 141.04, 140.88, 140.84, 140.10, 139.28, 139.23, 138.89, 136.83, 135.31, 132.08, 132.01, 132.00, 131.91, 131.55, 131.53, 131.28, 130.79, 130.44, 129.95, 129.79, 129.13, 128.69, 128.53, 127.32, 126.33, 125.97, 121.85, 120.86, 120.28, 120.20, 120.02, 83.96, 83.90, 83.88, 83.80, 78.03, 77.77, 77.70, 77.66.
MALDI-TOF: *m/z* calcd. for $C_{63}H_{39}N$ 809.31, found 809.37 $[M]^{\bullet+}$.

Imine-biphenyl-G2-(PSpen)$_4$ ***6***

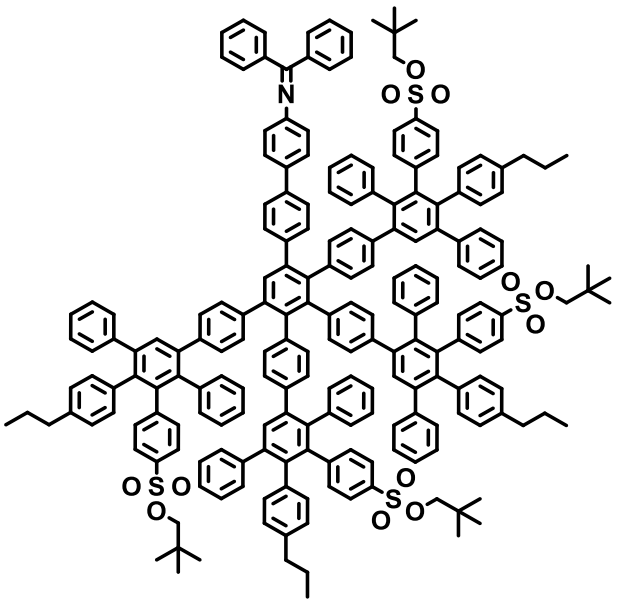

6

Imine-biphenyl-G1-(ethinyl)$_4$ dendron **5** (110 mg, 136 µmol) and surface building block **2** (627 mg, 1.09 mmol, 8 equiv) were dissolved in 10 mL *o*-xylene and stirred at 145 °C in a sealed Ace pressure tube under argon atmosphere for 48 h. After concentration *in vacuo* the crude product was purified by column chromatography using a mixture of cyclohexane and THF (3:1) to obtain imine-protected dendron **6** as a light brown solid (237 mg, 62 %) and amine dendron **7** as a brown solid (130 mg, 34%).

^{1}H NMR (700 MHz, CD_2Cl_2): δ (ppm) = 7.75 (d, J = 7.7 Hz, 2H), 7.56–7.31 (m, 21H), 7.28–7.22 (m, 4H), 7.20–7.02 (m, 30H), 7.01–6.95 (m, 6H), 6.91–6.63 (m, 42H), 6.58–6.52 (m, 2H), 6.50–6.40 (m, 4H), 3.44–3.31 (m, 8H), 2.43–2.31 (m, 8H), 1.51–1.45 (m, 8H), 0.85–0.72 (m, 48H).

^{13}C NMR (176 MHz, CD_2Cl_2): δ (ppm) = 151.37–125.82, 121.71, 80.25, 80.03, 79.96, 37.15, 25.73, 24.65, 13.56.

MALDI-TOF: *m/z* calcd. for $C_{207}H_{183}NO_{12}S_4$ 3002.26, found 3001.97 $[M]^{\bullet+}$, 3024.95 $[M+Na]^+$, 3040.95 $[M+K]^+$.

Amine-biphenyl-G2-(PSpen)$_4$ ***7***

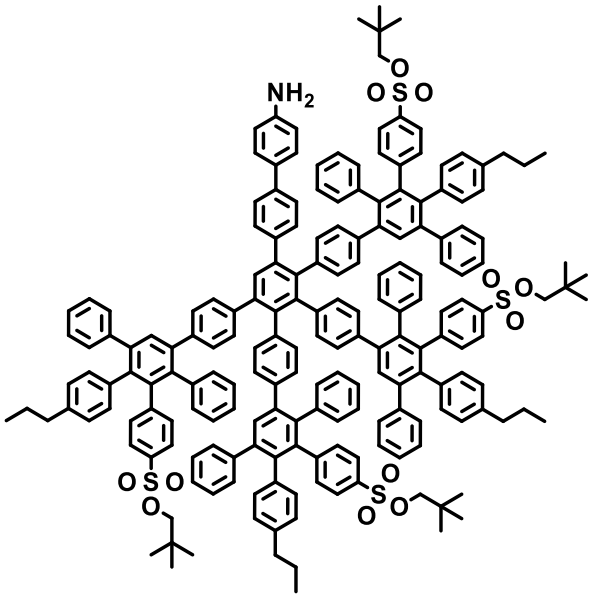

7

Imine-biphenyl-G2-(PSpen)$_4$ **6** (110 mg, 36.6 µmol) was dissolved in 3 mL THF and 1 mL 2 N hydrochloric acid were added. After stirring at room temperature under argon atmosphere for 5 min, 0.5 mL of concentrated hydrochloric acid were added and stirred for further 20 min. Then, ethyl acetate and water were added. The organic layer was separated, washed twice with water and dried over sodium sulfate. After concentration *in vacuo* the crude mixture was purified by column chromatography using a mixture of cyclohexane and THF (3:1) to afford compound **7** as a light brown solid (76 mg, 73%).

^{1}H NMR (700 MHz, CD_2Cl_2): δ (ppm) = 7.58–7.31 (m, 17H), 7.20–6.97 (m, 32H), 6.91–6.81 (m, 14H), 6.79–6.62 (m, 32H), 6.59–6.54 (m, 2H), 6.45 (dd, J = 13.1, 4.1 Hz, 4H), 3.46–3.31 (m, 8H), 2.43–2.28 (m, 8H), 1.52–1.44 (m, 8H), 0.85–0.71 (m, 48H).

^{13}C NMR (176 MHz, CD_2Cl_2): δ(ppm) = 151.99–125.64, 115.10, 80.04, 79.98, 37.67, 26.18, 24.63, 13.42.

MALDI-TOF: *m/z* calcd. for $C_{194}H_{175}NO_{12}S_4$ 2838.20, found 2838.01 $[M]^{\bullet+}$, 2860.97 $[M+Na]^+$, 2876.9625 $[M+2Na]^{2+}$.

Propargyl-TEG-amide-biphenyl-G2-(PSpen)$_4$ ***16***

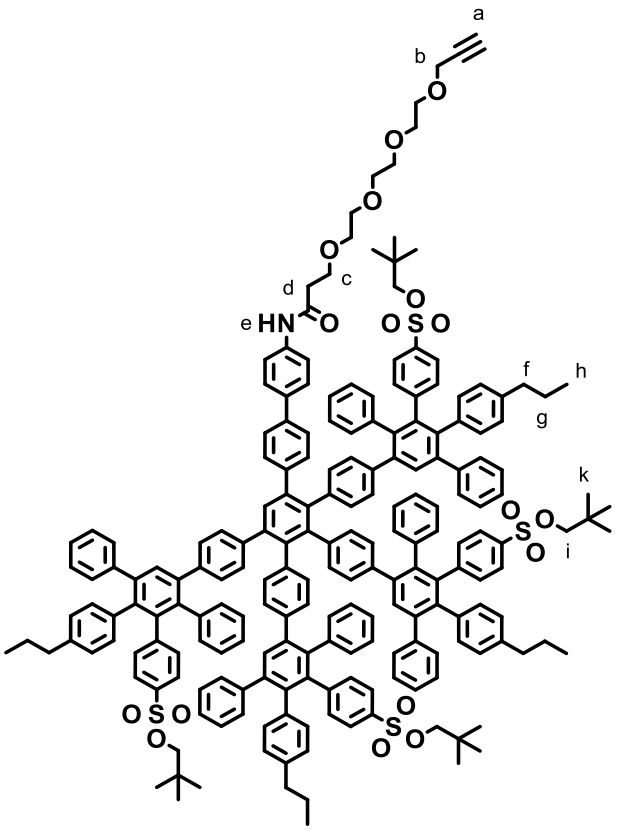

16

Amine-biphenyl-G2-(PSpen)$_4$ **7** (57.0 mg, 20.0 µmol) was dissolved in 3 mL DMF and propyne-*O*-(2-carboxyethyl)-*O′*-propargyl-triethylene glycol (**15**) (26.1 mg, 100 µmol, 5 equiv) in 0.5 mL DMF was added. Then, *N*-(3-dimethylaminopropyl)-*N′*-ethylcarbodiimide hydrochloride (EDC*HCl) (19.23 mg, 100 µmol) and 4-dimethylaminopyridine (DMAP) (7.35 mg, 60.2 µmol) were added. The reaction mixture was stirred at room temperature under argon atmosphere for 24 h. DMF was evaporated and the crude product was purified by silica gel chromatography using a mixture of DCM and methanol (20:1) to obtain Propargyl-TEG-amide-biphenyl-G2-(PSpen)$_4$ **16** as a light brown solid (40.1 mg, 64%).

^{1}H NMR (700 MHz, CD_2Cl_2): δ (ppm) = 8.60 (s, 1H,H_e), 7.64 (d, J = 8.3 Hz, 2H, H_{arom}), 7.58–7.30 (m, 17H, H_{arom}), 7.20–6.93 (m, 32H, H_{arom}), 6.92–6.79 (m, 14H, H_{arom}), 6.79–6.60 (m, 30H, H_{arom}), 6.57 (d, J = 7.0 Hz, 2H, H_{arom}), 6.45 (d, J = 17.4 Hz, 4H, H_{arom}), 4.15–4.08 (m, 2H, H_f), 3.82 (t, J = 5.6 Hz, 2H, H_c), 3.72–3.55 (m, 12H, H_{TEG}), 3.44–3.28 (m, 8H, H_i), 2.64 (t, J = 5.6 Hz, 2H, - H_d), 2.48–2.28 (m, 9H, H_a, H_f), 1.51–1.37 (m, 8H, H_g), 0.86–0.69 (m, 48H, H_h, H_k).

^{13}C NMR (176 MHz, CD_2Cl_2): δ (ppm) = 162.57, 147.74–120.66, 80.19, 80.12, 74.75,

74.41, 71.08, 70.97, 70.90, 70.88, 69.74, 67.65, 58.78, 38.61, 37.83, 26.29, 24.81, 13.64.

MALDI-TOF: *m/z* calcd. for $C_{206}H_{193}NO_{17}S_4$ 3080.32, found 3080.60 $[M]^{\bullet+}$, 3103.58 $[M+Na]^+$, 3119.41 $[M+2Na]^{2+}$.

Propargyl-TEG-amide-biphenyl-G2-(PS)$_4$ ***8***

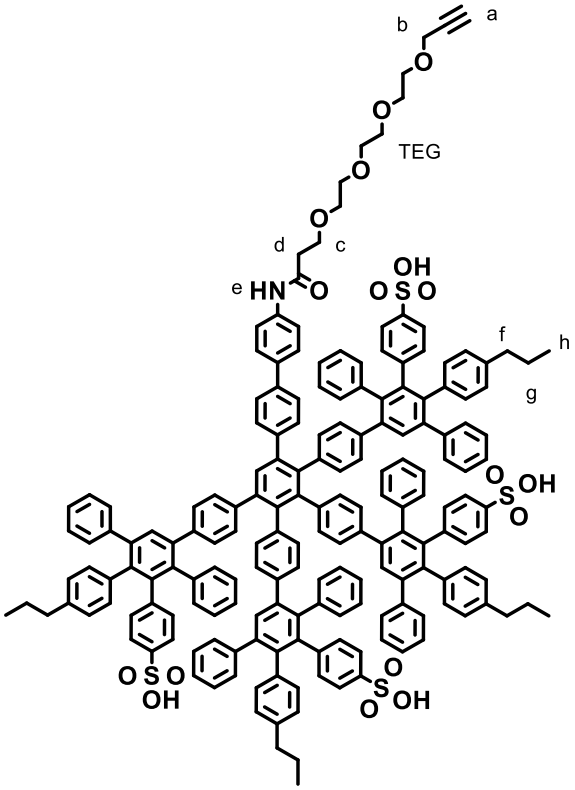

8

Propargyl-TEG-amide-biphenyl-G2-(PSpen)$_4$ (180 mg, 58.4 µmol) **16** was dissolved in 20 mL dry DMF, degassed with argon and stirred in a sealed Ace pressure tube at 180 °C for 36 h. Then, DMF was evaporated *in vacuo*, the residue was dissolved in methanol and precipitated in diethyl ether. After filtration propargyl-TEG-amide-biphenyl-G2-(PS)$_4$ **8** was obtained as a light brown solid (160 mg, 98%).

^{1}H NMR (500 MHz, DMSO-d_6): δ(ppm) = 10.03 (s, 1H, H_e), 7.75–7.56 (m, 4H, H_{arom}), 7.50–7.23 (m, 7H, H_{arom}), 7.22–6.54 (m, 84H, H_{arom}), 6.52–6.30 (m, 6H, H_{arom}), 4.11 (m, 2H, H_f), 3.71 (t, J = 5.6 Hz, 2H, H_c), 3.55–3.44 (m, 12H, H_{TEG}), 2.57 (t, J = 4.9 Hz, 2H, H_d), 2.44–2.23 (m, 9H, $H_{a,}$ H_f), 1.47–1.31 (m, 8H, H_g), 0.74–0.61 (m, 12H, H_h).

^{13}C NMR (126 MHz, DMSO): δ (ppm) = 145.54–119.32, 77.08, 69.75, 69.69, 69.47, 68.50, 66.67, 57.47, 36.44, 23.52, 13.11.

MALDI-TOF: *m/z* calcd. for $C_{186}H_{153}NO_{17}S_4$ 2800.00, found 2801.28 $[M+H]^+$, 2824.35 $[M+Na]^+$, 2840.31 $[M+K]^+$, 2862.25 $[M+NaK]^{2+}$, 2878.33 $[M+2K]^{2+}$.

Biotin-triazole-TEG-amide-biphenyl-G2-(PS)$_4$ ***9a***

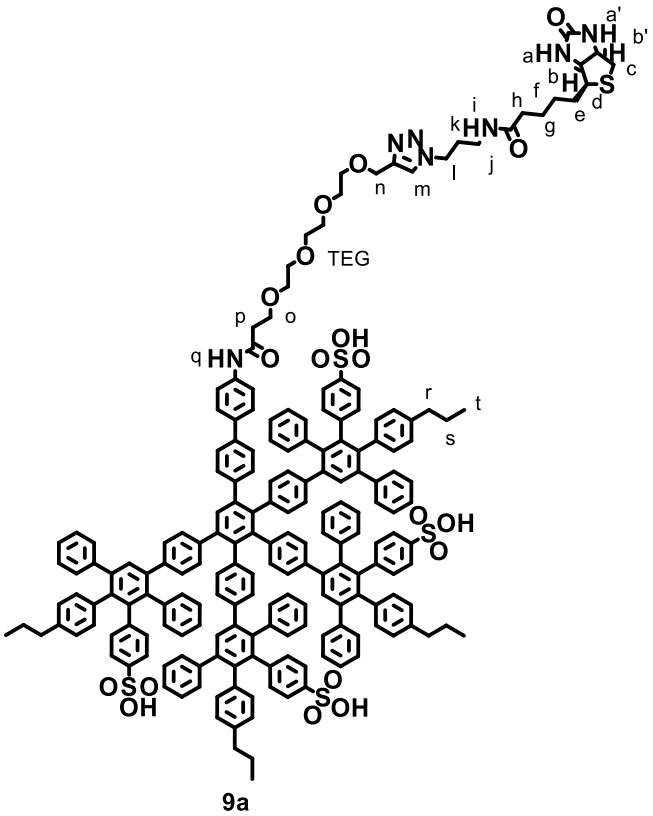

Propargyl-TEG-amide-biphenyl-G2-$(PS)_4$ **8** (10 mg, 3.57 µmol) and azido-biotin derivative **17** (6.99 mg, 21.4 µmol) dissolved in each 0.5 mL DMF were combined and 1-(1-benzyltriazol-4-yl)-*N*,*N*-bis[(1-benzyltriazol-4-yl)methyl]methanamine (TBTA) (1.89 mg; 3.57 µmol) in 290 µL DMF was added. After degassing with argon, copper sulfate (0.57 mg, 3.57 µmol) in 136 µL ultrapure water and sodium ascorbate (1.41 mg, 7.14 µmol) in 224 µL ultrapure water were added. The reaction mixture was shaken at room temperature for 48 h under exclusion of light. The reaction mixture was purified *via* gel permeation chromatography (GPC) applying Sephadex LH-20 in DMF to obtain Biotin-triazole-TEG-amide-biphenyl-G2-$(PS)_4$ **9a** as a light brown solid (10.8 mg, 97%).
^{1}H NMR (700 MHz, DMSO-d_6) δ(ppm) = 10.03 (s, 1H, H_q), 8.08 (d, J = 3.0 Hz, 1H, H_{arom}), 7.88 (t, J = 4.5 Hz, 1H, H_i), 7.73–7.66 (m, 2H, H_{arom}), 7.60 (s, 2H, H_{arom}), 7.48–6.27 (m, 100H, H_{arom}, H_a, $H_{a'}$, H_m), 4.49 (s, 2H, H_n), 4.32 (t, J = 7.0 Hz, 2H, H_l), 4.28 (t, J = 6.5 Hz, 1H, $H_{b'}$), 4.13–4.09 (m, 1H, H_b), 3.71 (t, J = 6.2 Hz, 2H, H_o), 3.58–3.44 (m, 12H, H_{PEG}),

3.11–3.06 (m, 1H, H_d), 3.02 (q, J = 6.4 Hz, 2H, H_j), 2.79 (dd, J = 12.5, 5.1 Hz, 1H,H_c), 2.64–2.53 (m, 3H, $H_{c'}$, H_p), 2.45–2.22 (m, 8H, H_r), 2.06 (t, J = 7.5 Hz, 2H, H_h), 1.92 (p, J = 6.7 Hz, 2H, H_k), 1.68–1.23 (m, 14H, H_e, H_f, H_g, H_s), 0.74–0.62 (m, 12H, H_t).

^{13}C NMR (176 MHz, DMSO) δ(ppm) = 172.19, 162.68, 145.51-119.31, 69.76, 69.66, 68.95, 66.64, 63.53, 61.02, 59.19, 55.39, 47.15, 40.02,37.23, 36.44, 35.64, 35.17, 33.90, 33.60, 29.95, 28.19, 28.02, 25.23, 23.52, 13.12.

MALDI-TOF: *m/z* calcd. for $C_{199}H_{175}N_7O_{19}S_5$ 3126.15, found 3149.65 $[M+Na]^+$, 3171.62 $[M+2Na]^{2+}$, 3187.58 $[M+K]^+$, 3193.61 $[M+3Na]^{3+}$.

Cyanine 5-triazole-TEG-amide-biphenyl-G2-(PS)$_4$ ***9b***

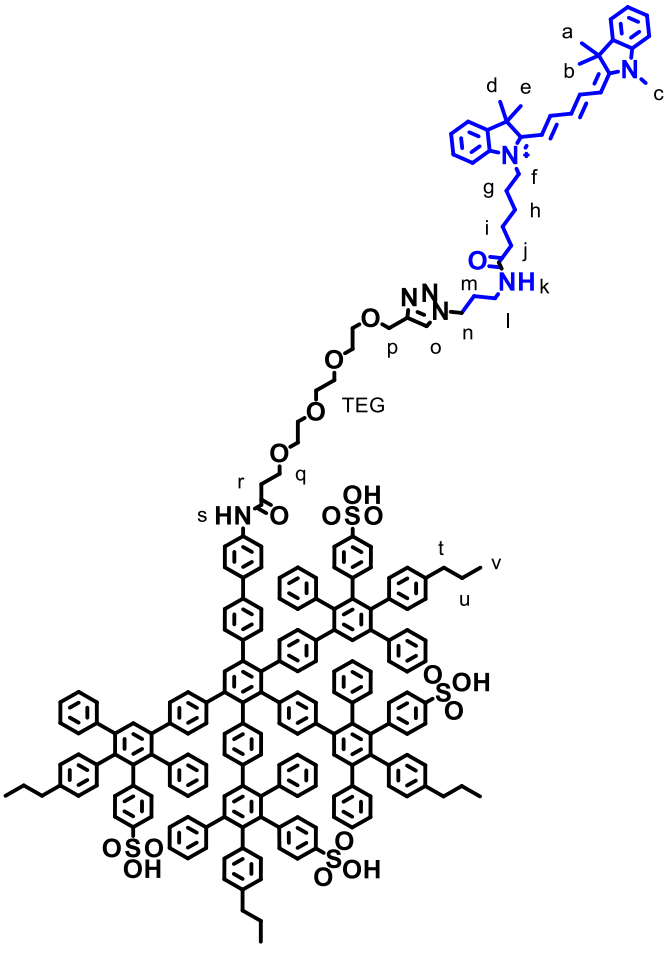

9b

Propargyl-TEG-amide-biphenyl-G2-$(PS)_4$ **8** (6.00 mg, 2.14 µmol) and Cy5-azide derivative **18** (3.86 mg, 6.42 µmol) dissolved in each 0.3 mL DMF were combined and TBTA (1.14 mg; 2.14 µmol) in 100 µL DMF was added. After degassing with argon, copper sulfate (0.34 mg, 2.14 µmol) in 46 µL ultrapure water and sodium ascorbate (0.85 mg, 4.28 µmol) in 54 µL ultrapure water were added. The reaction mixture was shaken

at room temperature for 48 h under exclusion of light. The reaction mixture was purified *via* GPC applying Sephadex LH-20 in DMF to obtain Cyanine 5-triazole-TEG-amide-biphenyl-G2-$(PS)_4$ **9b** as a blue solid (6.2 mg, 86%).

^{1}H NMR (700 MHz, DMSO-d_6) δ(ppm) = 10.00 (s, 1H, H_s), 8.35–8.23 (m, 2H, H_{arom}), 7.89–7.81 (m, 1H, H_k), 7.65 (d, J = 7.4 Hz, 2H, H_{arom}), 7.53 (dd, J = 14.7, 7.4 Hz, 2H, H_{arom}), 7.43–6.15 (m, 117H, H_{arom}), 4.45 (s, 2H, H_p), 4.26 (t, J = 7.0 Hz, 2H, H_n), 4.05–3.96 (m, 2H, H_f), 3.70–3.64 (m, 2H, H_r), 3.54–3.40 (m, 15H, $H_{TEG,}$ H_c), 2.98–2.93 (m, 2H, H_l), 2.35–2.22 (m, 8H, H_t), 2.00 (t, J = 7.1 Hz, 2H, H_j), 1.84 (q, J = 7.0 Hz, 2H, H_m), 1.64–1.54 (m, 12H, $H_{a,}$ $H_{b,}$ $H_{d,}$ H_e), 1.52–1.44 (m, 2H, H_i), 1.43–1.16 (m, 12H, $H_{g,}$ $H_{h,}$ H_u), 0.72–0.54 (m, 12H, H_v).

^{13}C NMR (176 MHz, DMSO) δ(ppm) = 154.33, 145.52–124.18, 123.88, 122.29, 118.68, 111.00, 69.80, 69.72, 68.50, 65.75, 63.57, 48.85, 47.15, 36.55, 36.45, 35.64, 34.40, 29.93, 27.11, 26.94, 24.84, 23.54, 13.14, 12.88.

MALDI-TOF: *m/z* calcd. for $C_{221}H_{198}N_7O_{18}S_4^+$ 3365.37, found 3365.28 $[M]^{\bullet+}$, 3387.26 $[M+Na]^+$, 3410.25 $[M+2Na]^{2+}$.

NMR-Spectra of key derivatives and final dendrons

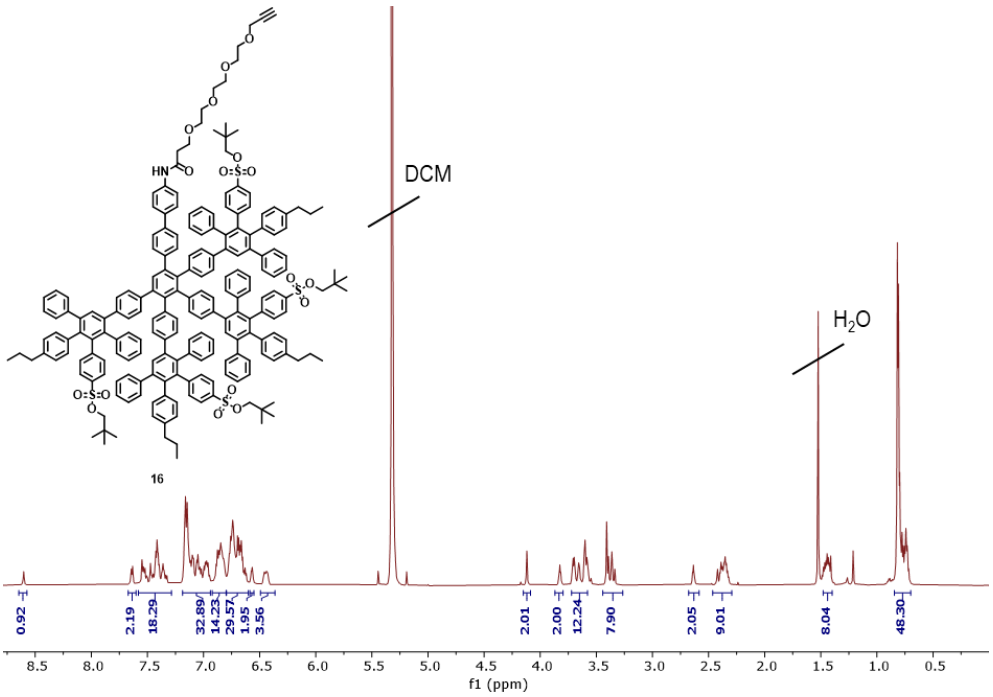

Figure S5.3. ^{1}H NMR spectrum (700 MHz) of protected dendron **16** recorded in deuterated dichloromethane.

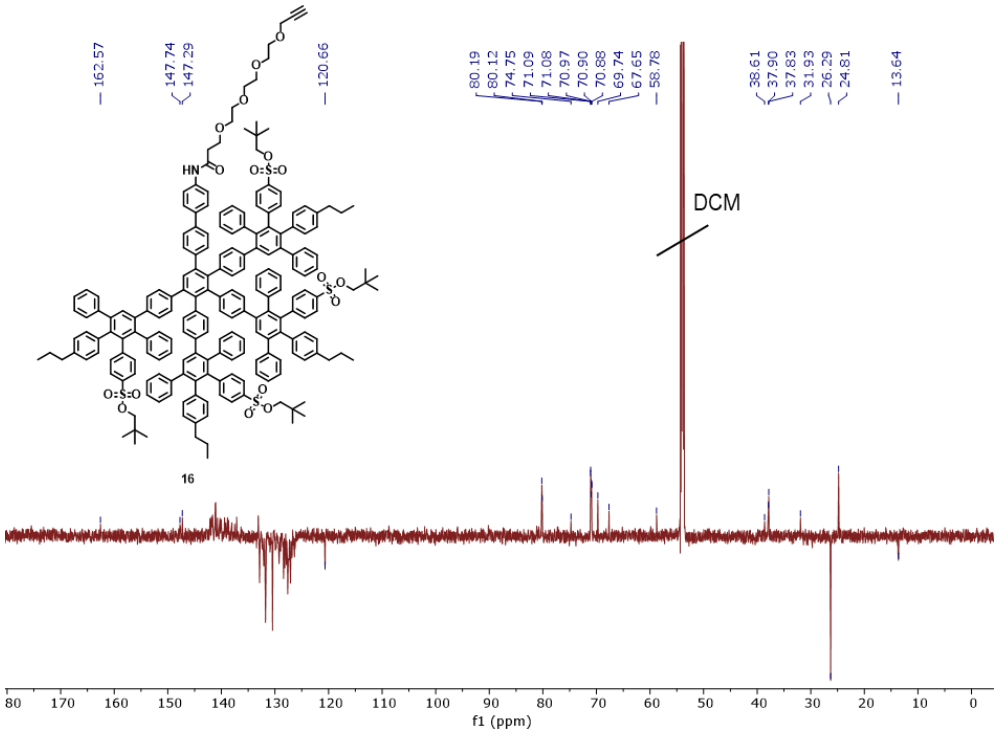

Figure S5.4. ^{13}C NMR spectrum (176 MHz) of protected dendron **16** recorded in deuterated dichloromethane.

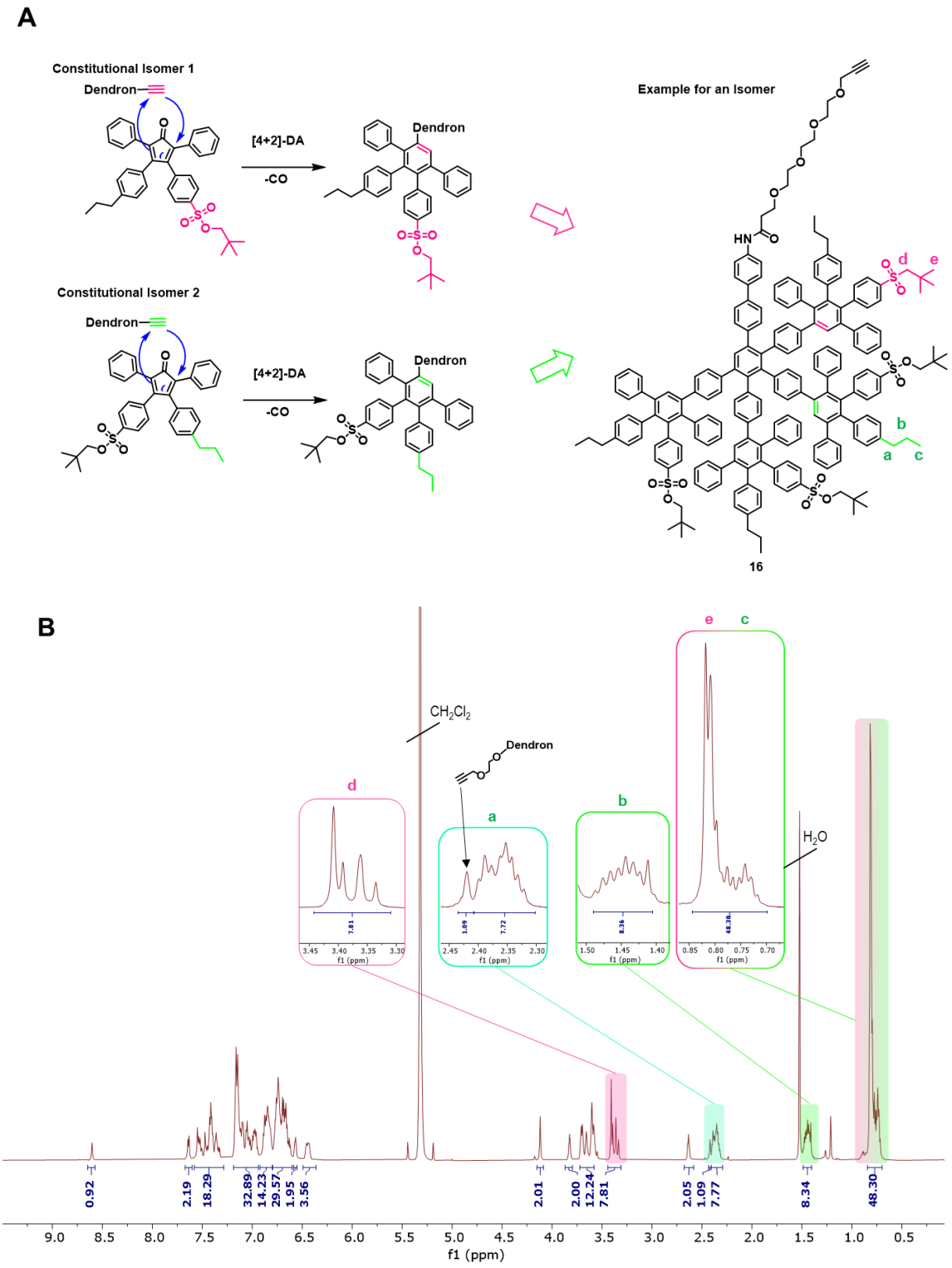

Figure S5.5. Constitutional isomers of deprotected dendron **16**. (**A**) shows the possibility to form two different constitutional isomers in each [4+2]-Diels-Alder reaction. (**B**) Constitutional isomers can be followed by ^{1}H NMR spectroscopy. The signal of the neopentyl-CH_2 group splits from a singlet to 4 signals with differences in intensity.

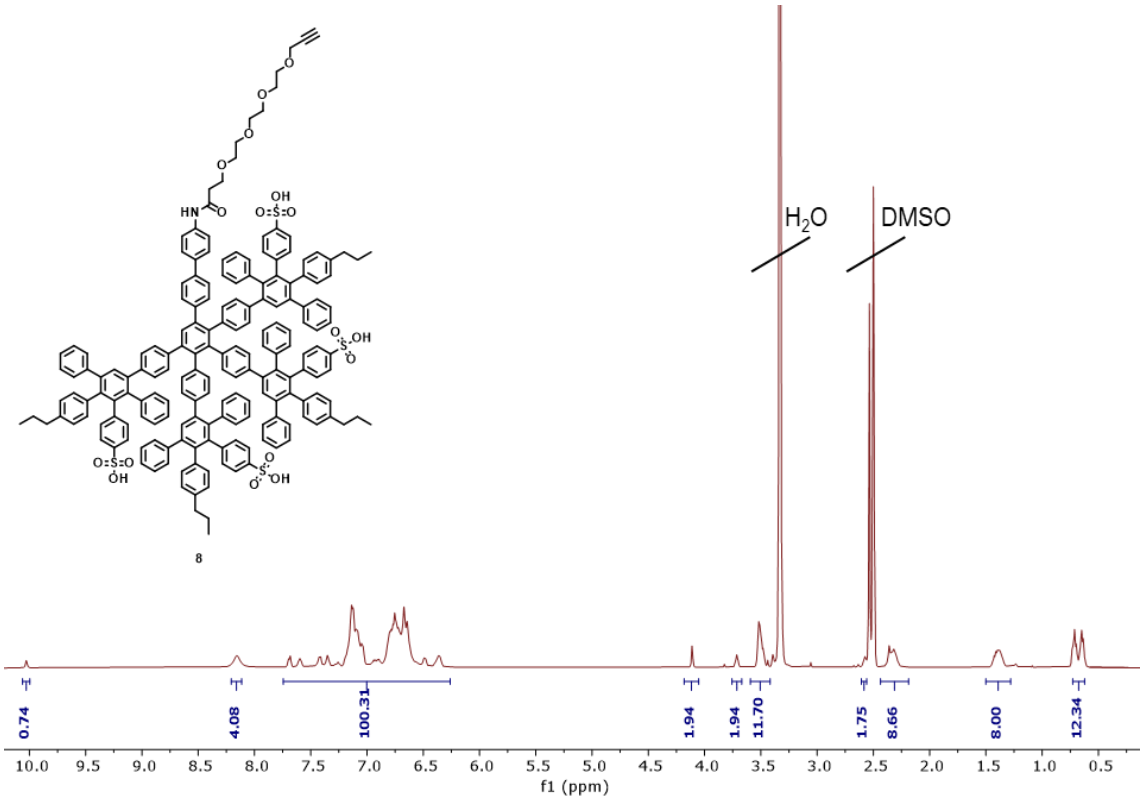

Figure S5.6. ^{1}H NMR spectrum (500 MHz) of deprotected dendron **8** recorded in deuterated dimethyl sulfoxide

.

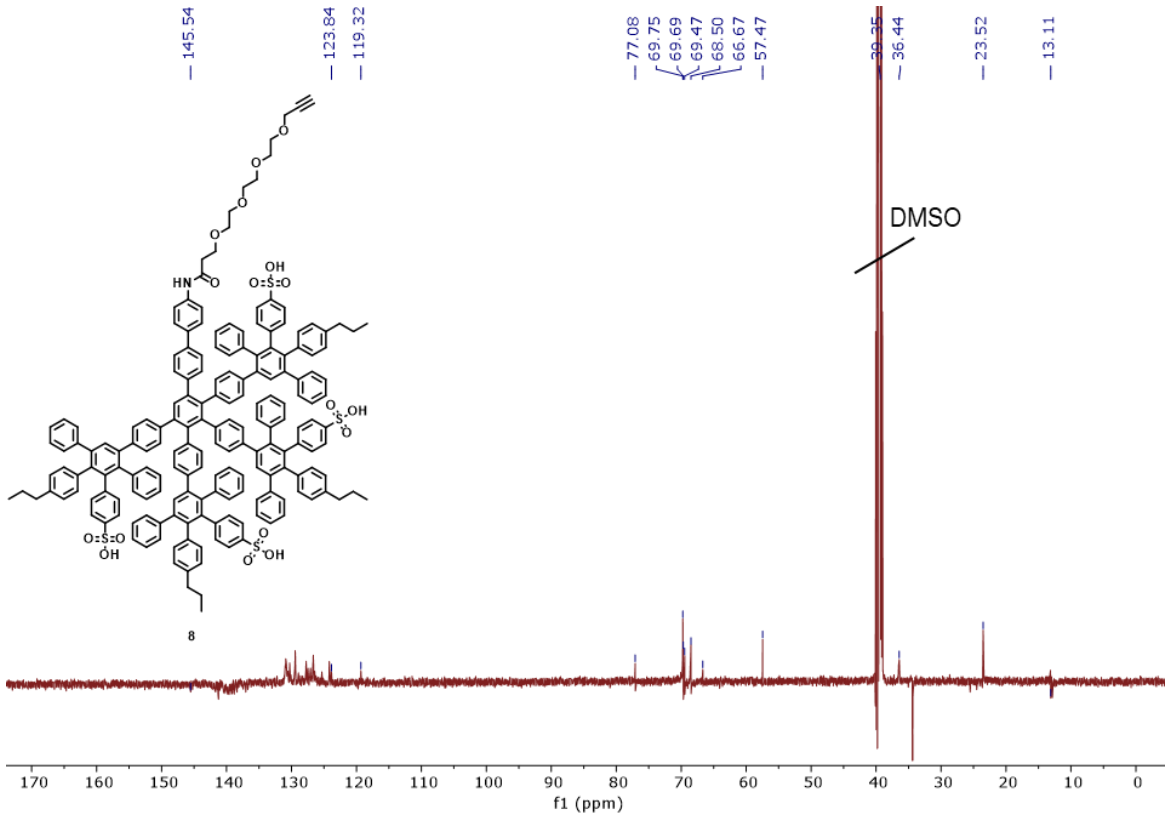

Figure S5.7. ^{13}C NMR spectrum (126 MHz) of protected dendron **8** recorded in deuterated dimethyl sulfoxide.

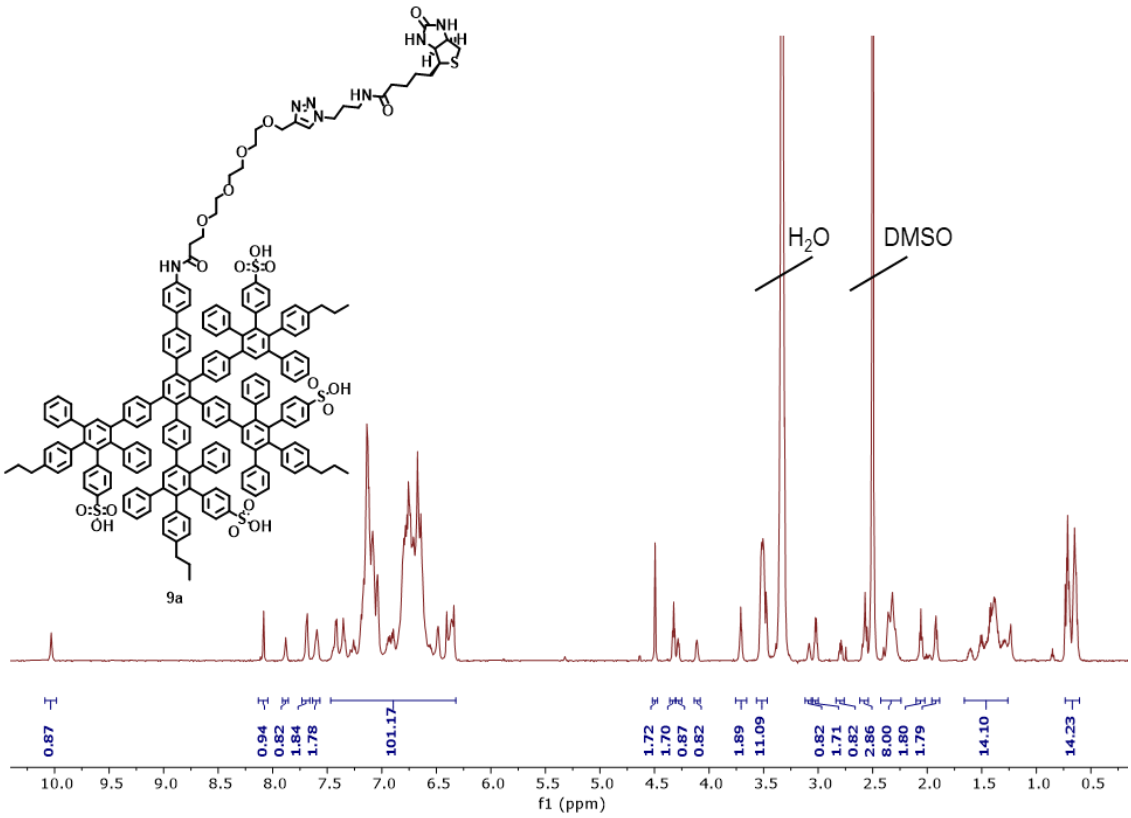

Figure S5.8. [1]H NMR spectrum (700 MHz) of biotin-dendron **9a** recorded in deuterated dimethyl sulfoxide.

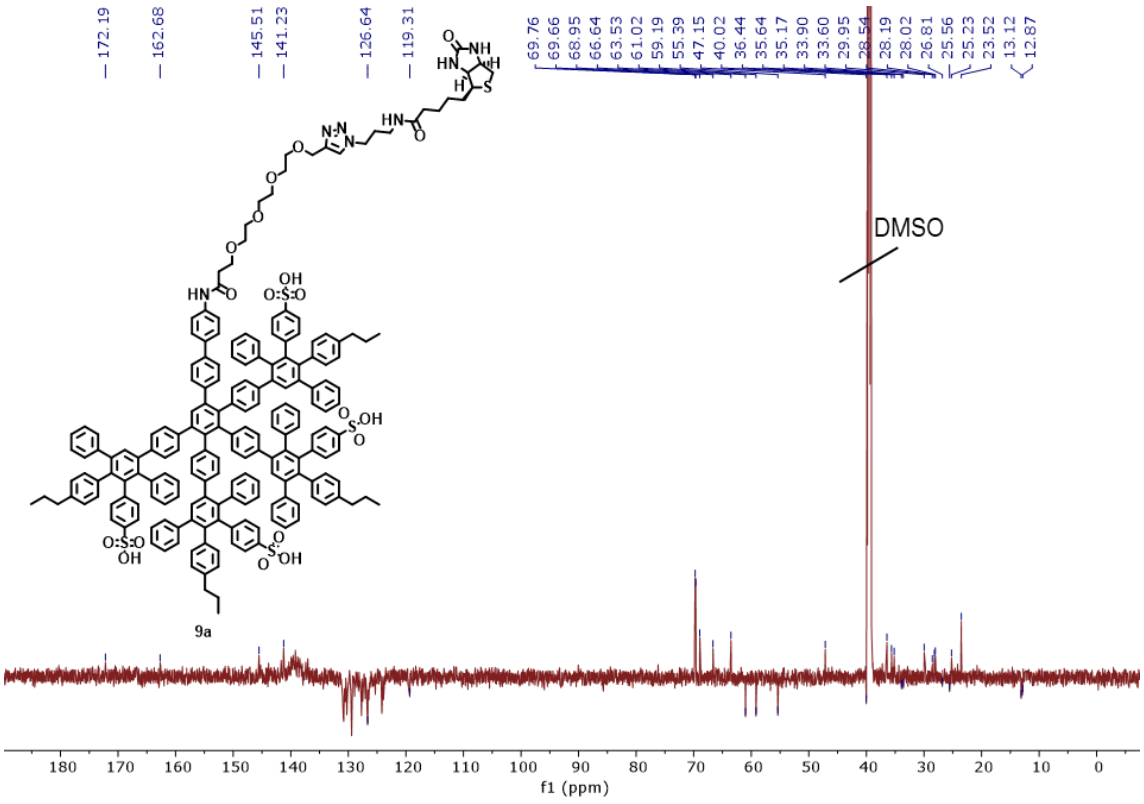

Figure S5.9. [13]C NMR spectrum (176 MHz) of biotin-dendron **9a** recorded in deuterated dimethyl sulfoxide.

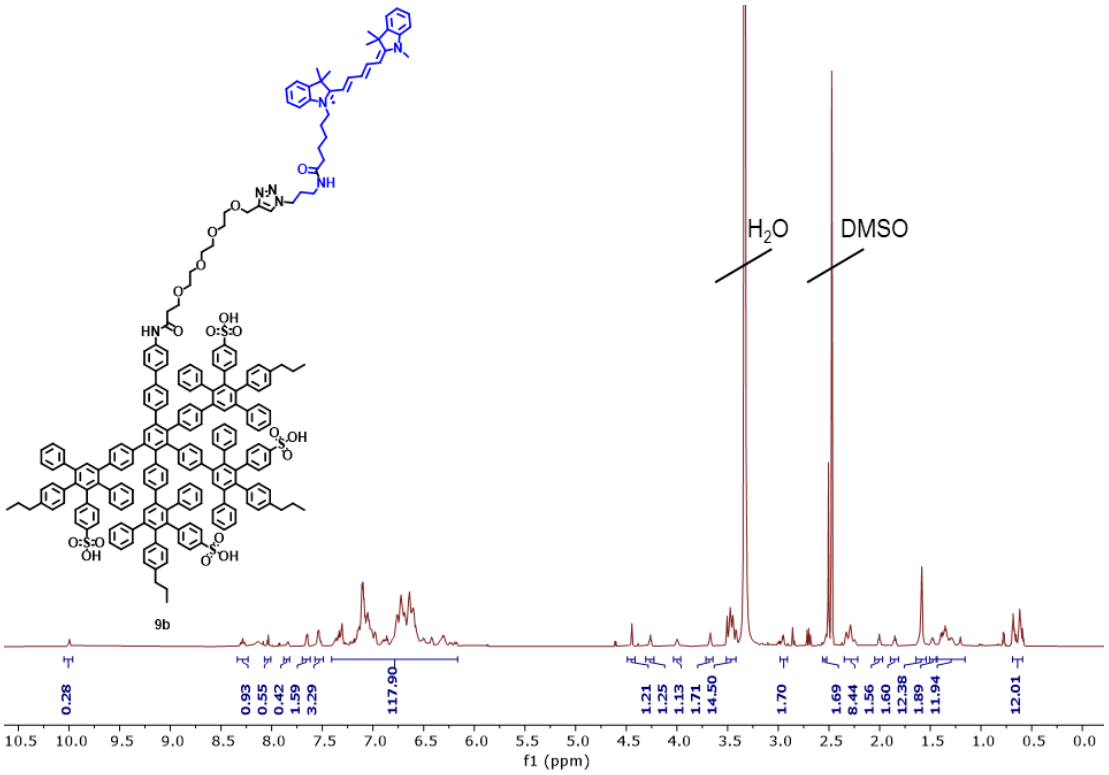

Figure S5.10. ^{1}H NMR spectrum (700 MHz) of Cy5-dendron **9b** recorded in deuterated dimethyl sulfoxide.

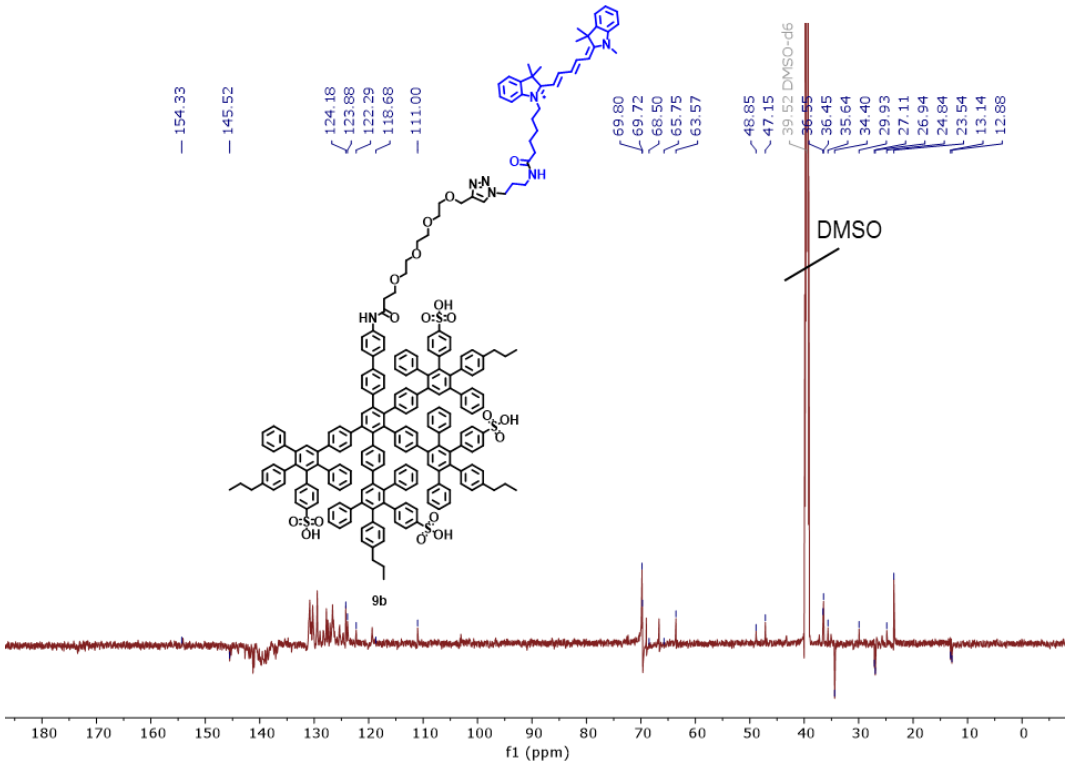

Figure S5.11. ^{13}C NMR spectrum (176 MHz) of Cy5-dendron **9b** recorded in deuterated dimethyl sulfoxide.

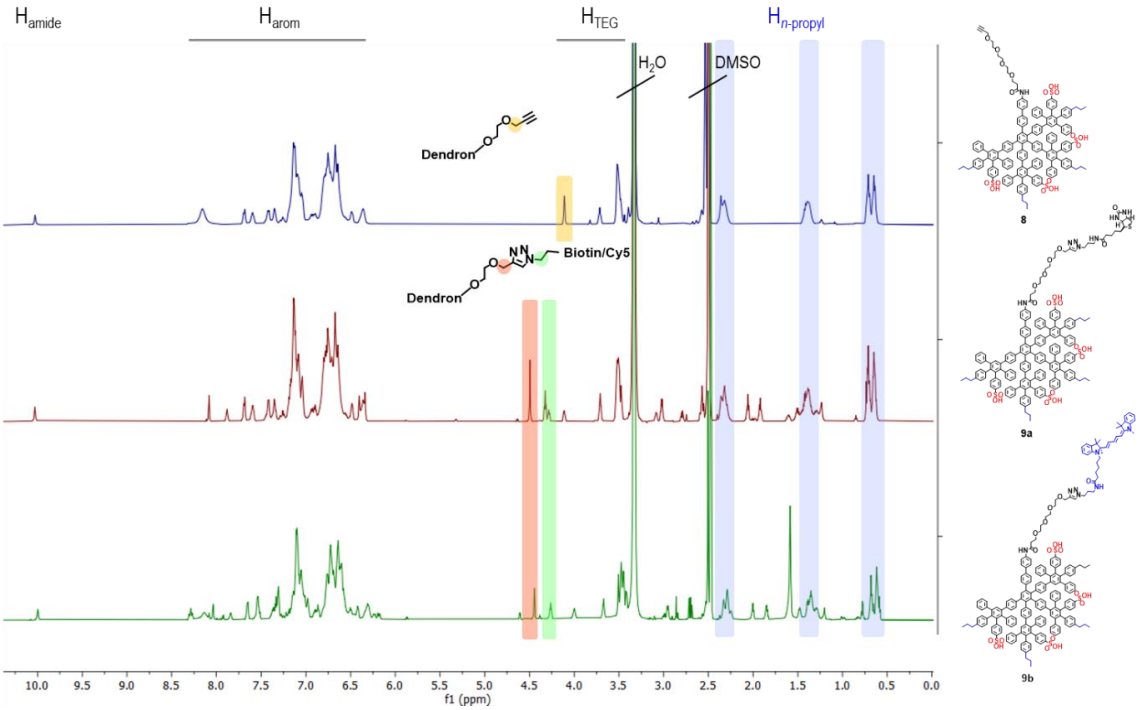

Figure S5.12. Summarized ^{1}H NMR spectra of final dendrons (**8**, **9a** and **9b**) showing significant shifts of signals (compare yellow and red highlighted signals) and appearance of a characteristic signal (green) after successful CuAAC.

MALDI-TOF mass spectra of final dendrons

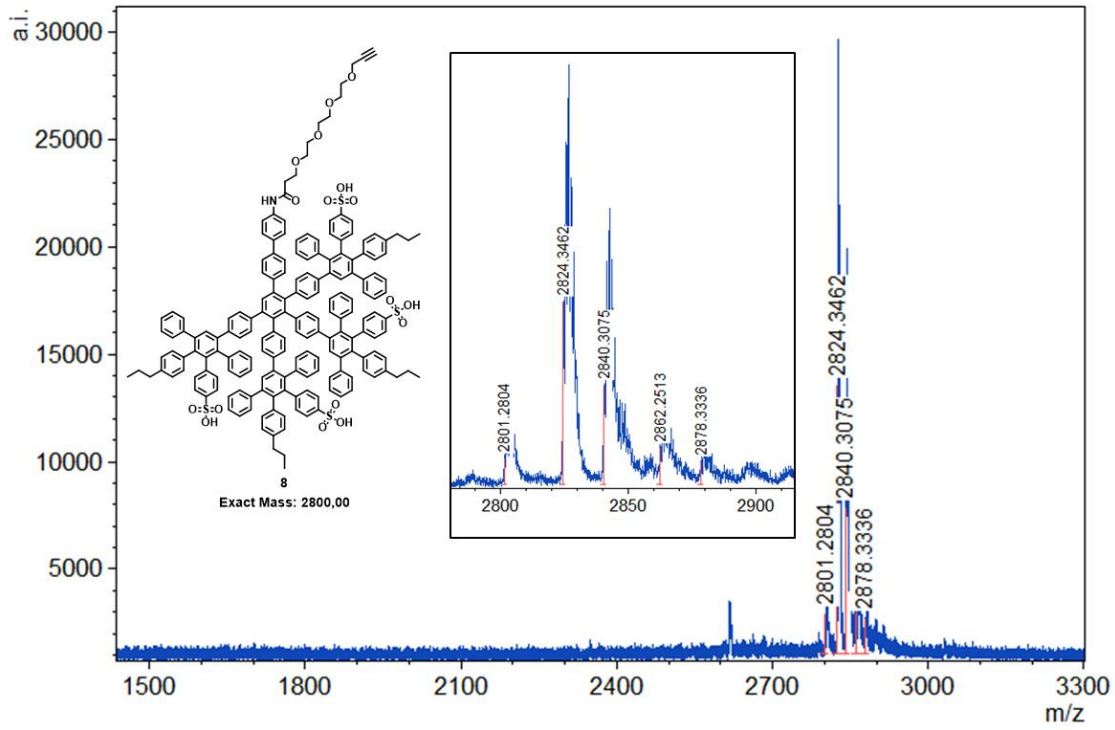

Figure S5.13. MALDI-TOF mass spectrum of dendron **8**.

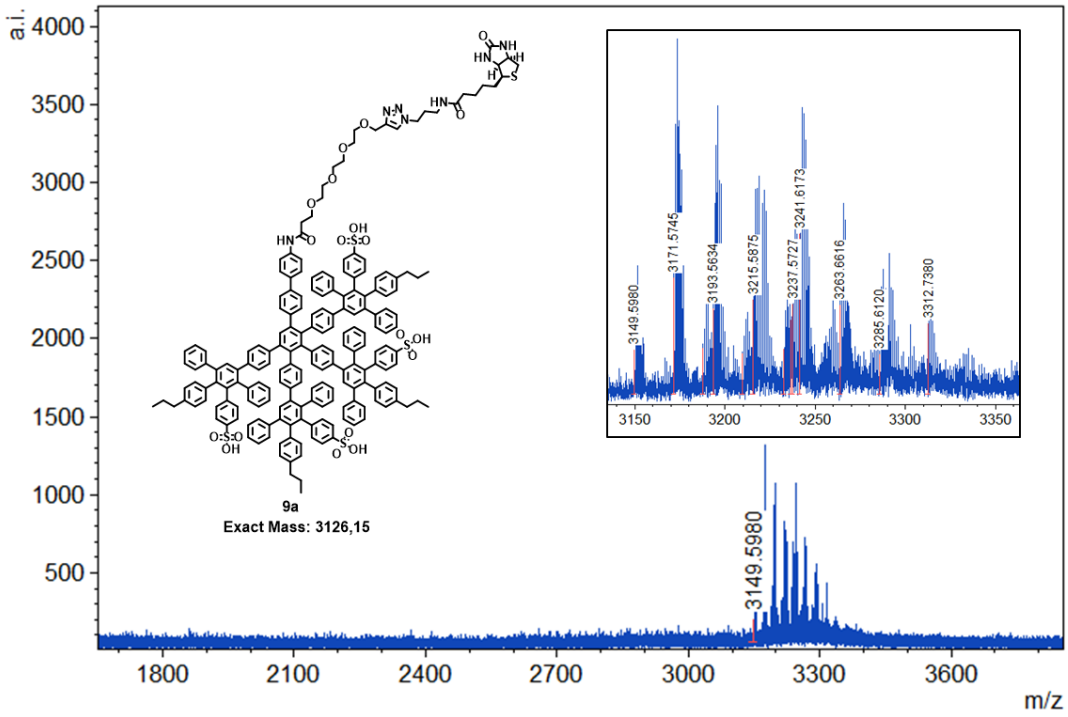

Figure S5.14. MALDI-TOF mass spectrum of biotin-dendron **9a**

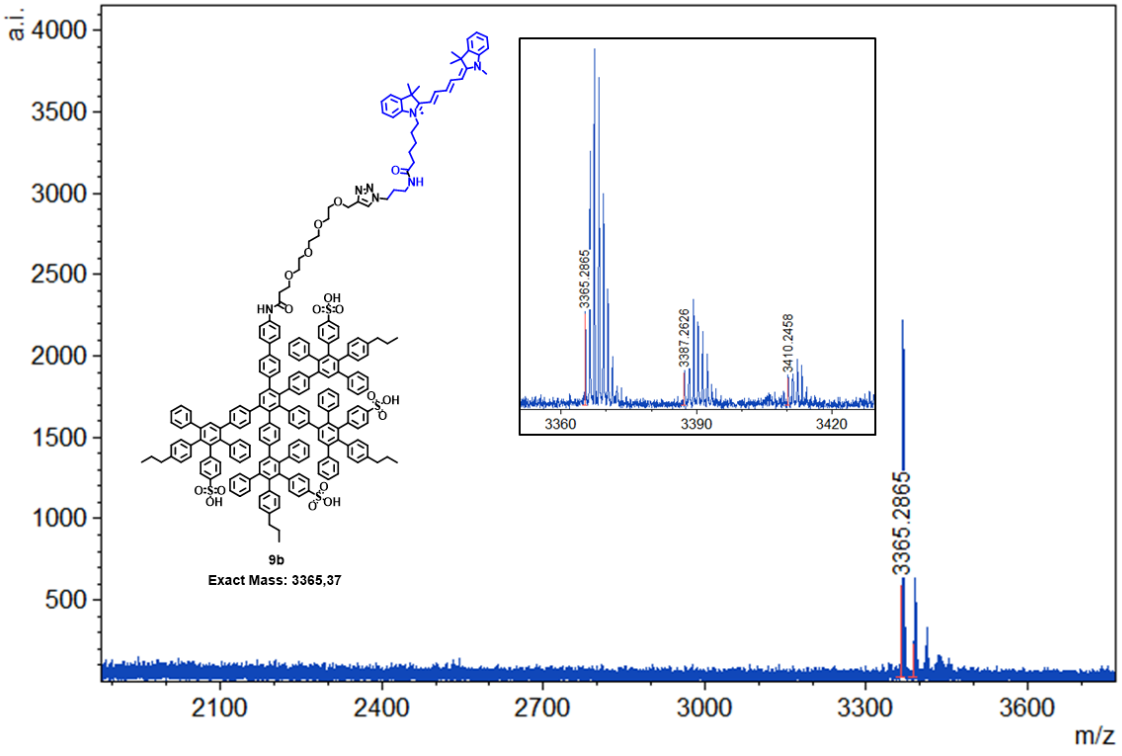

Figure S5.15. MALDI-TOF mass spectrum of Cy5-dendron **9b**

5.5.2 Interaction of dendrons with serum proteins

Synthesis of liposomes

Amine functionalized liposomes were prepared from 1,2-dioleoyl-*sn*-glycero-3-phosphoethanolamine (DOPE), L-*α*-phosphatidylcholine (egg PC) and cholesterol (Chol) with a molar ratio of egg PC:DOPE:Chol = 1:1:1 by film hydration followed by extrusion. All lipids and cholesterol stock solutions were prepared in chloroform at a concentration of 10 mg mL^{-1}. Afterwards, egg PC (835 µL), DOPE (767 µL) and Chol solutions (398 µL) were added into a 50 mL round-bottomed flask with 2 mL of chloroform containing 1 vol% EtOH. First, the mixture was dried with a rotary evaporator for 30 min at 450 mbar and then for an additional 30 min at 3 mbar and 42 °C. To remove organic solvent residues, the mixture was placed in a vacuum oven for 1 h. (Diameter Ø: 242 ± 6 nm, ζ–Potential: –49 mV ± 7.5 mV)

Synthesis of polystyrene nanoparticles

Amine functionalized polystyrene nanoparticles were synthesized *via* the previously reported direct miniemulsion protocol[54, 55]. Cetyl trimethyl ammonium chloride was used a cationic surfactant to stabilize the dispersion and 2-aminoethyl methacrylate hydrochloride (2 wt% to styrene) was copolymerized with styrene. The dispersion was purified *via* centrifugation and dialysis. A detailed protocol is described in previous reports.[43] (Diameter Ø: 98 ± 10 nm, ζ–Potential: + 49 mV)

Coating of liposomes and nanoparticles with dendron 8 or dendrimer

Dendron **8** or the amphiphilic dendrimer was dissolved in DMSO at a concentration of 20 mg mL^{-1}. Liposomes-NH_2 (3 mg mL^{-1}, 333 µL) or PS-NH_2 nanoparticles (10 mg mL^{-1}, 100 µL) were incubated with dendron **8** or the dendrimer (20 mg mL^{-1}, 50 µL) for 1 h at room temperature. The mixture was centrifuged (20 000 g, 1 h, 4 °C). Liposomes were resuspended in 100 µL of PBS and polystyrene nanoparticles in 100 µL of water.

Table S5.1. Zeta Potential measurements of liposomes (20 µL) uncoated or coated with dendron/dendrimer in 1 mM KCl solution (1 mL). Dynamic light scattering measurements at an angle of 90°C of liposomes (20 µL) uncoated or coated with dendron/dendrimer in PBS (1 mL).

	Zeta Potential (mV)	**Size (nm)**
Liposome	−49 ± 7.5 mV	242 nm ± 6 nm
Liposome+Dendron	−32 ± 3.4 mV	863 nm ± 181 nm
Liposome+Dendrimer	−27 ± 3.7 mV	963 nm ± 60 nm

Human plasma/serum

Human blood serum and plasma was obtained from six (serum) or ten (plasma) healthy donors at the Transfusion Center of the University Clinic of Mainz, Germany, pooled and stored at −20 °C. Citrate was used as an anticoagulant for plasma preparation.

Protein corona preparation

Liposomes coated with dendron **8** and dendrimer as well as nanoparticles (1 mg) were incubated with human serum and plasma (1 mL) for 1 h at 37°C. Subsequently the dispersion was centrifuged (20 000 g, 1 h, 4 °C) and washed with PBS (3 times, 1 mL) to remove loosely and unbound proteins. To desorb the attached corona proteins, the liposome/nanoparticle pellet was resuspended in 100 µL of 2% SDS supplemented with 62.5 mM Tris hydrochloride solution and incubated for 5 min at 95 °C. Afterwards, the dispersion was centrifuged and the supernatant containing the desorbed corona proteins was analyzed by Pierce Assay, SDS PAGE and LC-MS.

Pierce assay

The Pierce 660 nm Protein Assay was used to determine the protein concentration. The assay was performed according to the manufacturer's instruction. The absorbance was measured with a Tecan infinite plate reader.

SDS PAGE

Proteins (2-3 µg in 26 µL) were loaded on a NuPage 10% Bis-Tris protein gels. Samples were mixed with 4 µL of NuPage Sample Reducing Agent and 10 µL of NuPage LDS Sample Buffer. Electrophoresis was carried out for 1 h at 120 V and gels were stained with Pierce Silver Staining Kit according to the manufacturer's instruction. All components were obtained from Thermo Fisher.

In solution digestion

Digestion of corona proteins was performed according to former instruction.[56],[57] Briefly, SDS was removed from the protein samples with Pierce detergent removal columns (Thermo Fisher). Afterwards, the proteins were precipitated overnight using ProteoExtract protein precipitation kit (CalBioChem) according to the manufacturer's instructions. The resulting proteins pellet was re-suspended in RapiGest SF (Waters Cooperation) dissolved in ammonium bicarbonate (50 mM) buffer. Proteins were reduced with dithiothreitol (Sigma, 5 mM, 45 min at 56 °C) and alkylated with idoacetoamide (Sigma, 15 mM, 60 min at room temperature). A ratio between protein:trypsin (50:1) was used and the digestion was carried out over 16 h at 37 °C. The reaction was quenched with 2 µL hydrochloric acid (Sigma).

Liquid chromatography coupled to mass spectrometry (LC-MS analysis)

Peptide samples were diluted with 0.1% formic acid and 50 fmol μL^{-1} Hi3 Ecoli (Waters Cooperation) was added for absolute protein quantification.[58] LC-MS measurements were performed with a Synapt G2- Si mass spectrometer coupled to a nanoACQUITY UPLC. A NanoLockSpray source was used in positive ion mode for electrospray ionization (ESI). Data-independent acquisition (MS^E) experiments were carried out and the Synapt G2-Si was operated in resolution mode. For data acquisition and processing MassLynx 4.1 and peptides/proteins were identified with Progenesis QI (2.0). The human database was downloaded from Uniprot modified with the sequence information of Hi3 Ecoli standard for absolute quantification. Processing parameters for peptide and protein identification were applied as described in detail in previous reports.[9, 59] The absolute amount of each protein was determined in fmol based on the TOP3/Hi3.[60] Each measurement was performed in technical duplicates or triplicates.

Protein Corona: Supplementary figures

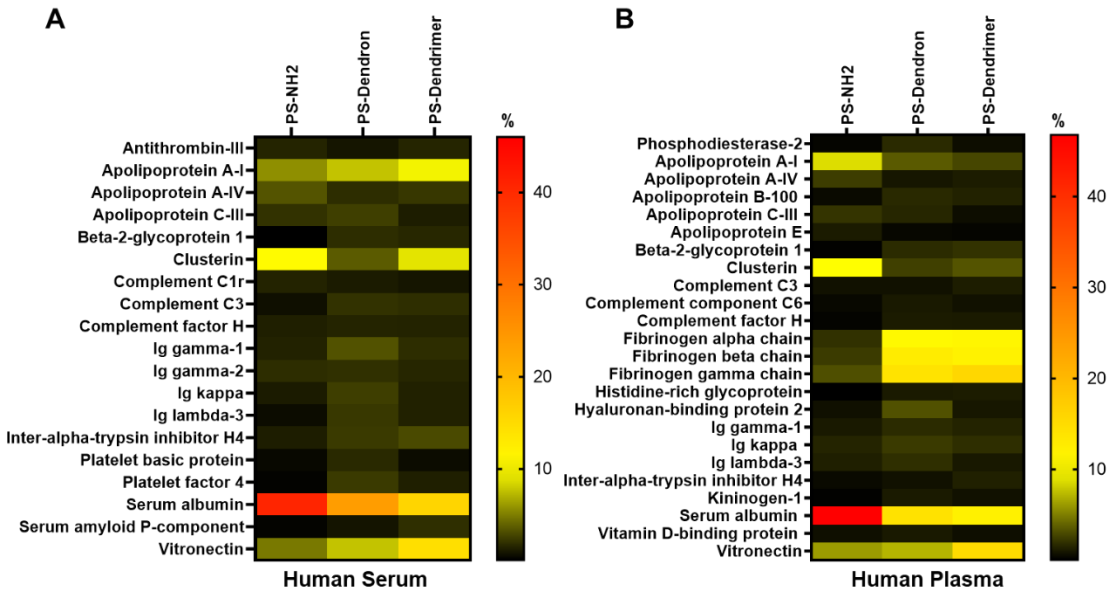

Figure S5.16. Heat map of adsorbed proteins to dendron **8** and dendrimer coated polystyrene nanoparticles in (**A**) blood serum and (**B**) blood plasma. The amount of each protein is given in % based on all identified corona proteins. A list of all identified proteins is supplemented at the end of the SI (Fig. S34-S37).

Table S5.2. Average amount in % and the standard deviation of identified proteins adsorbed to lipo-dendron and lipo-dendrimer mentioned in the main manuscript. A list of all identified proteins can be found at the end of this document (Fig. S34-S37).

	Liposome	Liposome + Dendron	Liposome + Dendrimer
Vitronectin	1 ± 0.7% serum	9 ± 0.8% serum	6 ± 0.5% serum
	0.2 ± 0.3% plasma	6 ± 0.5% plasma	3 ± 0.2% plasma
ApoH	0.5 ± 0.2% serum	8 ± 0.5% serum	5 ± 0.3% serum
	0.3 ± 0.5% plasma	11 ± 1.5% plasma	4 ± 0.3% plasma
IgG kappa	6 ± 1% serum	2 ± 0.2% serum	2 ± 0.1% serum

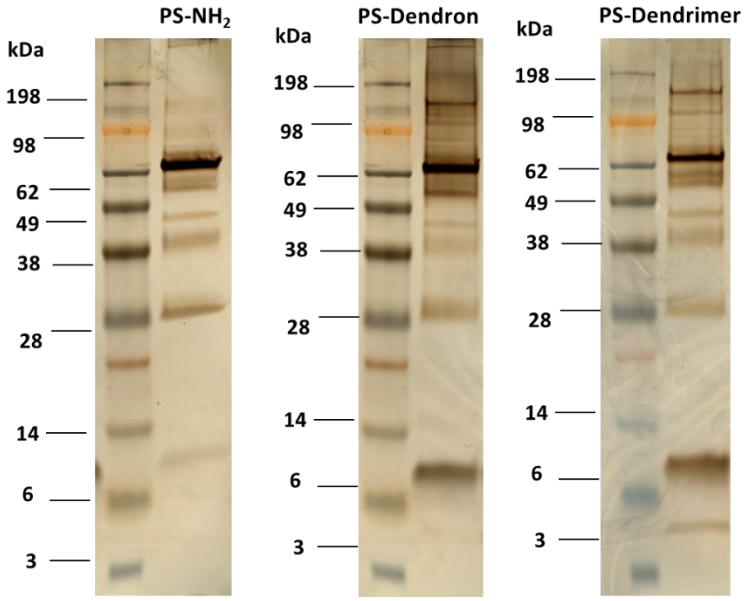

Figure S5.17. Hard protein corona analysis of polystyrene nanoparticles (PS-NH_2) coated with dendron **8** or dendrimer PPD3 after serum incubation. 2–3 µg of protein was applied to the SDS-PAGE (reducing conditions).

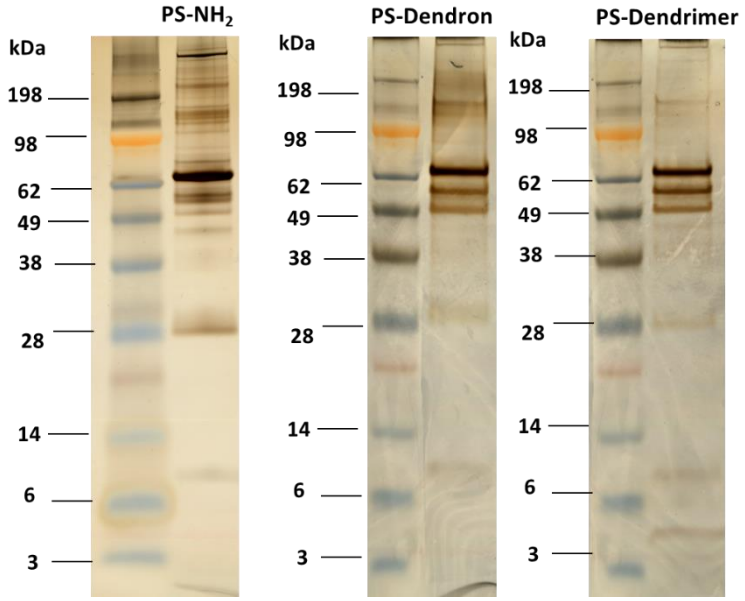

Figure S5.18. Hard protein corona analysis of polystyrene nanoparticles (PS-NH_2) coated with dendron **8** or dendrimer PPD3 after plasma incubation. 2–3 µg of protein was applied to the SDS-PAGE (reducing conditions).

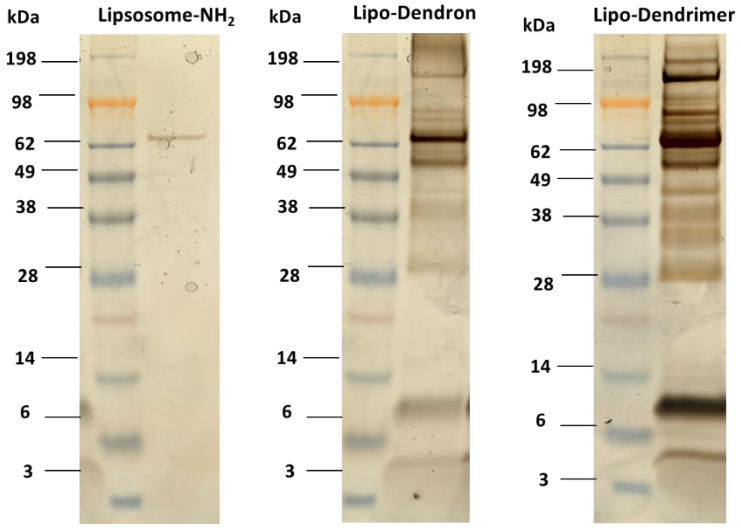

Figure S5.19. Hard protein corona analysis of liposomes (Lipo-NH_2) coated with dendron **8** or dendrimer PPD3 after serum incubation. 2–3 µg of protein was applied to the SDS-PAGE (reducing conditions).

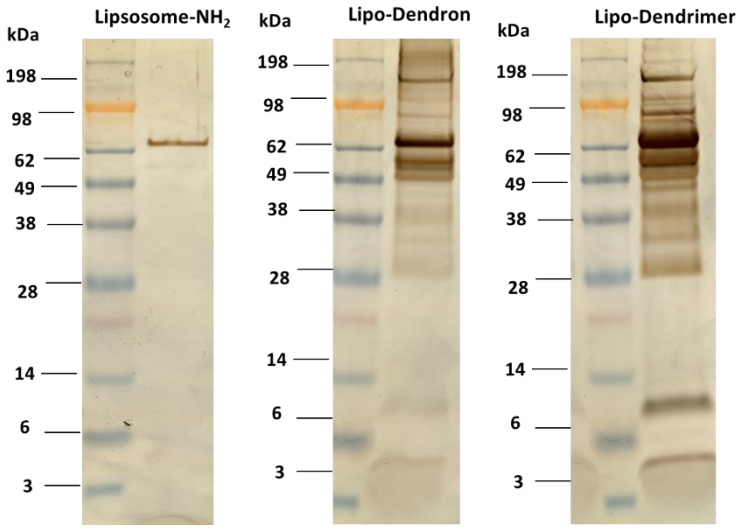

Figure S5.20. Hard protein corona analysis of liposomes (Lipo-NH_2) coated with dendron **8** or and dendrimer after plasma incubation. 2–3 µg of protein was applied to the SDS-PAGE (reducing conditions).

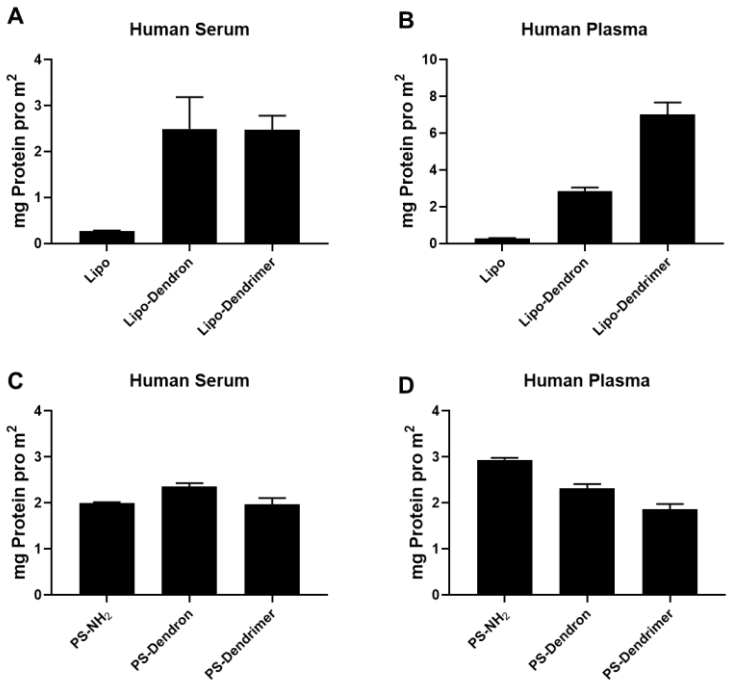

Figure S5.21. The absolute amount of adsorbed corona proteins (in mg) per surface area (m^2) of the liposomes (**A**,**B**) and polystyrene nanoparticles (**C**,**D**) was determined *via* Pierce Assay.

Interaction of Amphiphilic PPDs with lipid monolayer

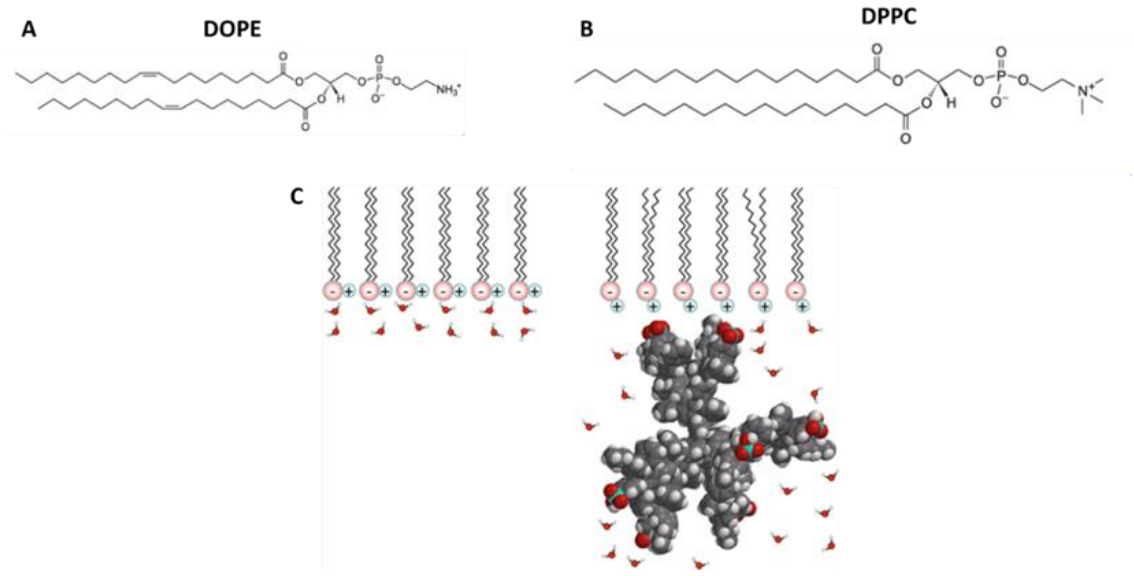

Figure S5.22. Assumption how the amphiphilic PPD surface motif might interact with the liposomes. (**A**)**,** (**B**) Molecular structure of the lipids DOPE and DPPC. (**C**) Illustration of the molecular configuration of DPPC, water, and the dendrimer molecules before (left) and after (right) dendrimer injection. Figure adapted from Okuno et al.[42] (Langmuir **2015**, 31, 1980-1987; https://pubs.acs.org/doi/10.1021/la504252s) with permission from Copyright (2015) American Chemical Society. The interactions between an amphiphilic PPD and a lipid monolayer consisting of zwitterionic lipids (DPPC, (**B**)) were studied. By X-ray reflectivity measurements it was found that the interaction between the amphiphilic dendrimers and the zwitterionic lipids is mainly electrostatic. They proved that upon adsorption of the dendrimer towards the lipid surface, the monolayer remains intact.[42] As DOPE is also a zwitterionic lipid with a similar structure, we assume that the interaction between the amphiphilic dendron or dendrimer and the DOPE liposomes are also electrostatically driven. An incorporation of the lipophilic n-propyl group was not observed.

5.5.3 Cellular uptake and cytotoxicity studies

Materials and Instruments

Confocal laser scanning microscopy was performed using Leica TCS SP5. CellTiter-Glo® Cell Viability Assay was purchased from Promega and luminescence intensities were measured on a Glomax Multi 96-well plate reader from Promega.

3.2 Methods

Cell culture

CHO-K1 (Chinese hamster ovary cell line) cells were obtained from DSMZ-German Collection of Microorganisms and Cell Cultures GmbH and cultured in DMEM/F12 medium (Gibco®) supplemented with 10% fetal bovine serum (FBS), 1% penicillin/streptomycin and 1x MEM (Minimum Essential Medium) non-essential amino acids at 37 °C in a humidified 5% CO_2-Incubator.

Cellular uptake of Cy5-dendron 9b

CHO-K1 cells at a density of 15 000 cells/well were seeded in a 8 well chambered µ-Slide coverslip (ibidi GmbH, Germany) in 200 µL medium and were incubated for 24 h to allow adhesion. Then, Cy5-dendron **9b** was predissolved in DMSO and diluted in ultrapure water to achieve a final concentration of 3 mg mL^{-1} (0.1% DMSO). The Cy5-dendron stock solution was diluted in medium to obtain a concentration of 1 µM.

200 µL of dendron solution were added to the well. As blank control, cells were incubated with fresh media. After incubation for 24 h at 37 °C and 5% CO_2 the medium containing the dendron was removed. Cell nuclei were stained with Hoechst 33258 for 15 min in medium and cells were washed for three times with PBS. After adding of fresh medium cells were imaged using a confocal laser scanning microscope (TCS SP5) equipped with a 63x oil immersion objective. The emission of Cy5 labelled dendron **9b** was recorded using a 633 HeNe laser for excitation with a detection bandwidth of 645-745 nm and Hoechst nucleus staining was recorded using a 405 Diode with a detection bandwidth of 415-500 nm. Acquired images were processed with ImageJ.

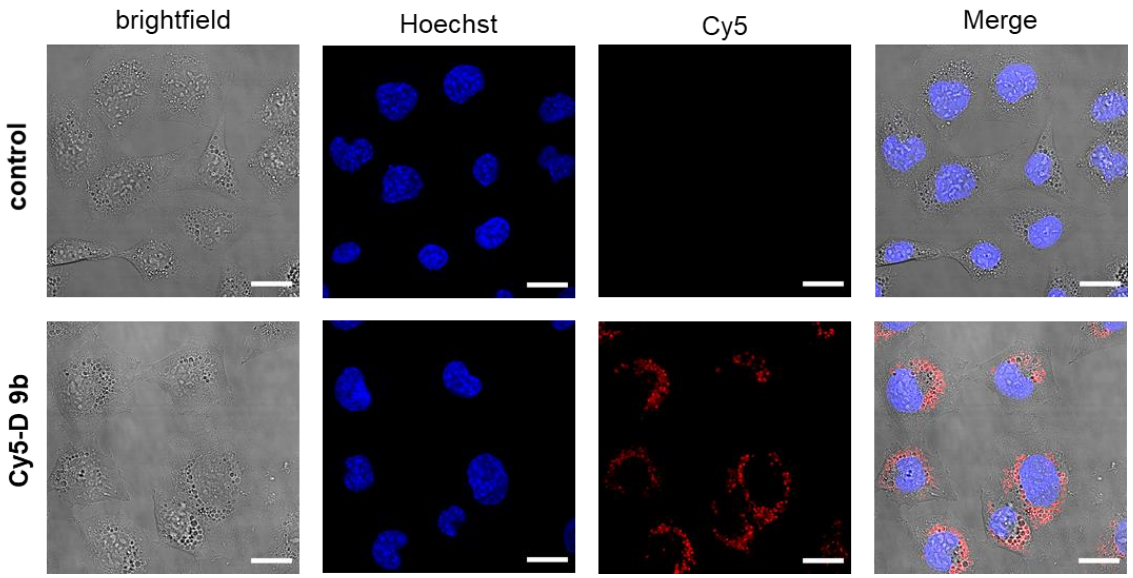

Figure S5.23. Cellular uptake of Cy5-dendron **9b** in CHO-K1 cells. Cells were treated with 1 µM dendron solution in medium for 24 h. As blank control cells were incubated with fresh medium for 24 h. After staining the nuclei with Hoechst 33258, cells were imaged by confocal laser scanning microscopy (scale bar = 20 µm).

Cell viability/cytotoxicity–CellTiter-Glo® luminescent cell viability assay

CHO-K1 cells at a density of 6000 cells/well were seeded in a white 96-well plate and incubated for 24 h to allow attachment. Propargyl-dendron **8**, biotin-dendron **9** as well as PPD3 were predissolved in DMSO at concentrations of 20 mg mL^{-1} and diluted in ultrapure water to achieve stock solutions with a final concentration of 1 mM for dendron conjugates **8** and **9a** as well as 100 µM for PPD3. The medium was removed, various concentrations (1-40 µM) dendron-conjugates **8** and **9a** as well as PPD3 in medium were added and the cells were incubated for further 24 h. As blank control cells were incubated with fresh media. After incubation, cell viability of CHO-K1 cells treated with dendron conjugates was determined applying CellTiter-Glo®-Assay from Promega (G7570) according to manufacturer's instructions.

5.5.4 Adenovirus 5 studies

Materials

Human adenovirus type 5 (Ad5, pAV[Exp]-CMV>EGFP) was purchased from Hanbio (China) and Cyagen Biosciences (China). CHO-K1 cell line was purchased from China Center for Type Culture Collection (Wuhan University). DME/F12 medium, fetal bovine serum (FBS) and phosphate buffered saline (PBS) were purchased from Hyclone (USA). Penicillin/streptomycin, (4-{[bis-(1-*tert*-butyl-1H-[1,2,3]triazol-4-ylmethyl)-amino]-methyl}-[1,2,3]triazol-1-yl)-acetic acid (BTTAA), $CuSO_4$ and sodium ascorbate were purchased from Sigma Aldrich (USA).

Instruments

Fluorescent imaging was carried out by a fluorescent microscope MF52 (Guangzhou Micro-shot Technology Co., Ltd., China). Transmission electron microscopy (TEM) was carried out by HT7700 (Hitachi, Japan). Flow cytometry was performed with FC500 (Beckman, USA). Fluorescence of coumarin was measured by microplate reader Varioskan LUX (Thermo Fisher Scientific, USA). Fluorescence spectra and intensities were measured on a SPARK 20M microplate reader from TECAN Group Ltd or Varioskan LUX (Thermo Fisher Scientific, USA). Dynamic light scattering and Zeta potential were measured by Zetasizer nano ZS90 (Malvern, UK).

Methods

Complex formation and characterization of dendron/Ad5 interaction

Complex formation of Ad5 and dendron conjugates or dendrimer PPD3 was performed in 5 µL of phosphate buffered saline (PBS). This volume contained 4×10^8 Ad5 virus particles (VP) (the concentration of Ad5 was quantified by measuring the absorbance at 260 nm and converted to number of particles with the equation: concentration (VP/mL) = $OD_{260} \times 1.1 \times 10^{12}$). Dendron-conjugates were dissolved in DMSO to obtain a stock solution of 1 mM and further diluted in 5 mM phosphate buffer, pH 7.4 to achieve a concentration of 50 µM. Dendron or dendrimer was added in defined ratios (for TEM, ratio of Ad5 to dendron is 1:100,000). After incubation of Ad5 and dendron for 40 min, 5 µL of Ad5 or Ad5/dendron was added on a copper grid for 5 min, followed by staining with uranyl acetate (3%) for 45 s. Copper grid was blot dry by filter paper and dried for 2 h before imaging in TEM.

This is the calculation for the Dendron/Ad5 ratio of 1:100,000 (N, number of particles; r, ratio between Dendron and Ad5; V, volume; N_A , Avogadro constant; c, concentration):

$$V = \frac{n}{c} = \frac{N/N_A}{c} = \frac{N \times r/N_A}{c} = \frac{4 \times 10^8 VP \times 1 \times 10^5/(6.02 \times 10^{23} mol^{-1})}{50 \times 10^{-6} mol/L} = 1.33 \times 10^{-6} L$$

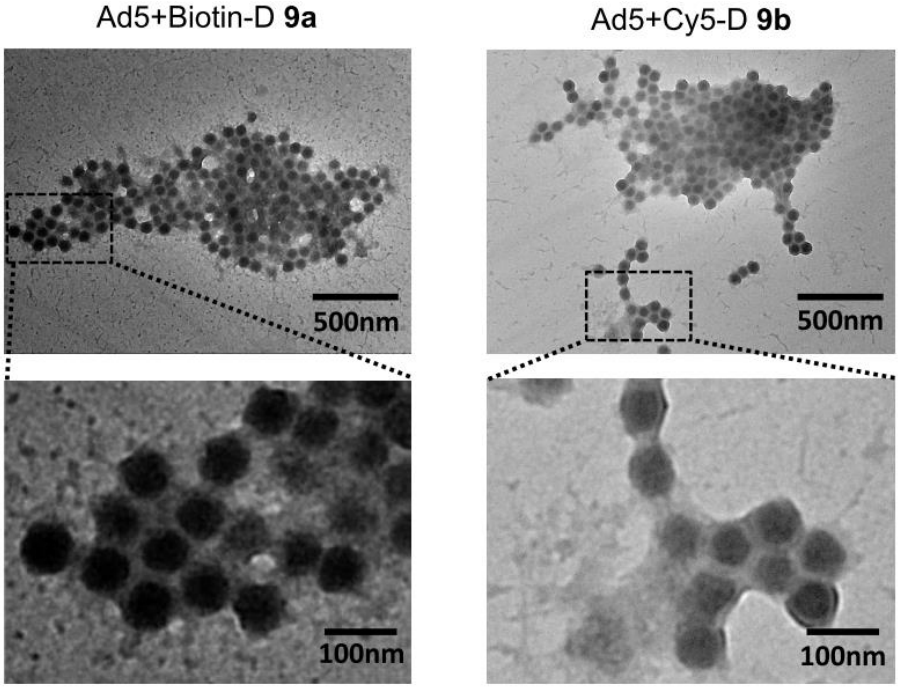

Figure S5.24. TEM images show binding of dendron-conjugates (Biotin-D **9a** and Cy5-D **9b**) to Ad5.

Dynamic light scattering (DLS) and zeta potential

DLS and zeta potential at diluted conditions

Dynamic light scattering was used to determine interaction between Ad5 and dendrons by means of measuring the polydispersity index (PDI) and the hydrodynamic diameter of the particles. Complex formation was performed in a volume of 30 µL phosphate buffer (5mM, pH7.4) with 5×10^8 Ad5 particles. Dendron was added in defined ratios to Ad5, then mixed and incubated for 40 min. After transfer to a cuvette, it was filled up with PB to a total volume of 0.9 mL. All samples were measured at 25 °C and an angle θ = 90°. For intensive cleaning of the cuvette, ethanol and acetone was used to avoid measurement errors by dust particles.

Zeta potential was used to determine the charge on the surface of Ad5 or complexes of Ad5 and dendrons. All samples were prepared the same as DLS and measured at 25 °C.

Table S5.3. Size and zeta potential of Ad5/dendron complexes with an Ad5-concentration of 4.5 x 10^8 vp/mL in 5 mM phosphate buffer after incubation for 40 min.

Sample	Size(nm)	PDI	Zeta potential (mV)
Only Ad5	109.4 ± 1.0	0.149	–18.1 ± 2.0
Ad5+Propargyl-D (1:1k)	113.8 ± 3.6	0.103	–19.6 ± 1.4
Ad5+Propargyl-D (1:20k)	159.2 ± 11.7	0.186	–29.0 ± 1.0
Ad5+Propargyl-D (1:100k)	684.5 ± 25.8	0.610	–37.5 ± 0.9
Ad5+Biotin-D (1:100k)	639.0 ± 31.3	0.608	–30.3 ± 1.6

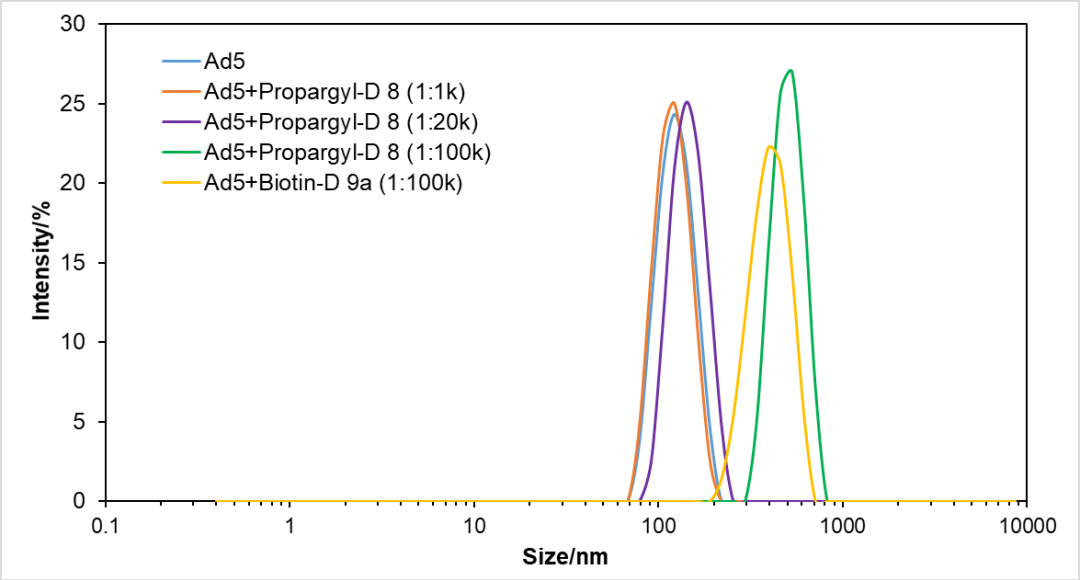

Figure S5.25. Size distribution by intensity. Ad5 vector with a concentration of 4.5x10^8 vp/mL in 5 mM phosphate buffer, pH 7.4 was incubated for 40 min with propargyl-dendron **8** at the ratios 1:1k–1:100k (Ad5:Dendron) as well as biotin-dendron **9a** at the ratio of 1:100k.

4.3.2.2 DLS and zeta potential at high Ad5 concentration and high ratios

The surface charge of vector particles was measured using a ZetaSizer Nano-ZS (Malvern, Worcestershire, UK) and analyzed with ZetaSizer 7.12 software. For the analysis an *E1*-deleted replication-incompetent human adenovirus type 5 vector (GenBank ID: AY339865.1, sequence from nt 1 to 440 and from nt 3523 to 35935) was used. The vector carried a CMV promoter-driven enhanced GFP expression cassette, subcloned from a pEGFP-N1 plasmid (Clontech 6085-1) that was inserted in reverse orientation in the deleted E1 region.

Dendron-conjugates (propargyl-dendron **8** and biotin-dendron **9a**) were dissolved in DMSO to achieve 20 mg mL^{-1} stock solutions. Then, 1×10^{11} Ad5 particles were dispersed in 1 mL 50 mM HEPES buffer, pH 7.4 and dendron was added at the ratio 1:200k (Ad5: Dendron) and 1:1000k respectively according to the calculation described in chapter 4.3.1. In order to determine the saturation of the Ad5 vector by dendrons DLS and zeta potential of propargyl-dendron **8** and biotin-dendron **9a** without Ad5 were measured as negative controls. A higher Ad5 concentration compared to the DLS measurements in 4.3.2.1 was applied to compare the size of Ad5/dendron complexes with the size of free dendron (free dendron is smaller and cannot be detected at lower concentrations). In addition the saturation of Ad5 at a certain ratio was studied.

Table S5.4. Size and zeta potential of Ad5/dendron complexes. Ad5 vector with a concentration of $1x10^{11}$ vp/mL was incubated with propargyl-dendron **8** at the ratios 1:200k (Ad5:Dendron) and 1:1000k as well as biotin-dendron **9a** at the ratio 1:200k in 50 mM HEPES buffer pH 7.4 for 15 min. We observed an increase in size when mixing dendron with Ad5 and for Ad5 + propargyl-dendron **8** at the ratio of 1:1000k and biotin-dendron **9a** at a ratio 1:200k a second peak was observed (Fig. S26).

Sample	Size (nm)			PDI	Zeta potential (mV)
	Z-average	Intensity Peak 1	Intensity Peak 2		
Only Ad5	116.6 ± 0.5	120.6 ± 0.5	-	0.01	–18.3 ± 1.5
Ad5+Propargyl-D **8** (1:200k)	202.4 ± 2.7	263.6 ± 4.5	-	0.23	–41.2 ± 1.9
Ad5+Propargyl-D **8** (1:1000k)	179.2 ± 1.2	473.9 ± 13.8	61.5 ± 1.78	0.48	–43.8 ± 2.8
Ad5+Biotin-D **9a** (1:200k)	241.6 ± 2.7	500.3 ± 40.5	80.7 ± 5.3	0.48	–38.2 ± 2.2

Table S5.5. Size and zeta potential of free dendrons as control. Propargyl-dendron **8** and biotin-dendron **9a** were incubated in 50 mM HEPES buffer pH 7.4 for 15 min (200k = 33.4 µM, 1000k = 167 µM).

Sample	Size (nm)			PDI	Zeta potential (mV)
	Z-average	Intensity Peak 1	Intensity Peak 2		
Propargyl-D **8** (200k)	76.0 ± 1.9	111 ± 4.4	-	0.31	–22.6 ± 3.0
Propargyl-D **8** (1000k)	88.4 ± 1.5	127 ± 1.0	-	0.32	–39.7 ± 3.0
Biotin-D **9a** (200k)	64.9 ± 1.4	81.0 ± 2.4	-	0.28	–28.2 ± 2.6

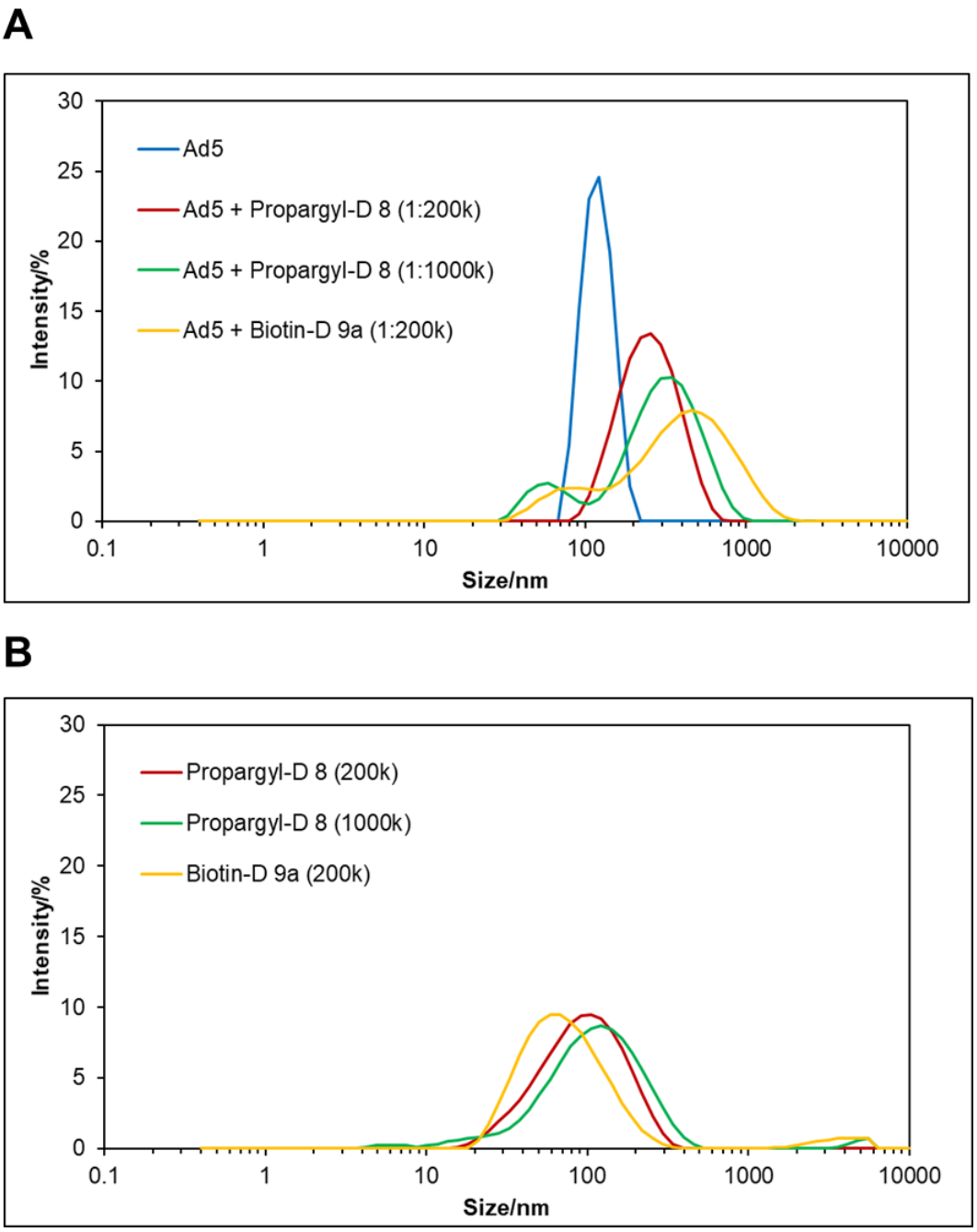

Figure S5.26. Size distribution by intensity. (**A**) Ad5 vector with a concentration of $1x10^{11}$ vp/mL was incubated with propargyl-dendron **8** at the ratios 1:200k (Ad5:Dendron) and 1:1000k as well as biotin-dendron **9a** at the ratio 1:200k in 50 mM HEPES buffer pH 7.4 for 15 min. Then, DLS was measured and the saturation of Ad5 by the dendrons was verified. We observed an increase in size when mixing dendron with Ad5 and for Ad5 + propargyl-dendron **8** at the ratio of 1:1000k and biotin-dendron **9a** at a ratio 1:200k a second peak was observed. To assess whether this peak is related to unbound dendron in the mixture, free dendron was measured at same concentrations, which is shown in (**B**). For free dendron-conjugates we observed a size of about 100 nm which can be explained by assembly processes of the dendron in buffer solution due to its amphiphilic nature. Thus, we assume that the second peak (for Ad5 + propargyl-dendron **8** at the ratio of 1:1000k and biotin-dendron **9a** at a ratio 1:200k) is related to unbound dendron which means that the Ad5 vector is saturated at these ratios.

Transduction in CAR-negative cell line CHO-K1

For transduction assays, 24-well plates were used containing 5×10^4 cells per well, which were seeded the day before transduction. Cells were cultured in DMEM/F12 medium with 10% FBS and 1% penicillin/streptomycin (PS, 10 000 IU penicillin and 10 000 µg/mL streptomycin) at 37 ºC in a humidified atmosphere containing 5% CO_2. Dendron conjugates were added to Ad5 in defined ratios (1:20k (1:20 × 10^3), 1:50k, 1:100k, 1:200k, 1:500k) and then incubated for 40 min. Cells were infected by Ad5 or Ad5/dendron with pMOI (particle multiplicity of infection) 200 unless otherwise specified and incubated for 4 h at 37 °C. Then, Ad5 or Ad5/dendron was removed, and cells were continued to culture for 24 h. EGFP positive cells and the overall mean fluorescence intensity (MFI) of EGFP expression was measured by fluorescent microscope (EGFP, excitation: 488nm, emission: 510nm) and flow cytometry (For EGFP, excitation: 488 nm, emission: 510 nm; for Cy5: excitation: 630 nm, emission: 670 nm).

This is a calculation example for a Dendron/Ad5 ratio of 1:500,000 (N, number of particles; N_{cell}, number of cells; pMOI, particle multiplicity of infection; r, ratio between Dendron and Ad5; V, volume; N_A , Avogadro constant; c, concentration):

$$V = \frac{n}{c} = \frac{N/N_A}{c} = \frac{N_{cell} \times pMOI \times r/N_A}{c}$$

$$= \frac{5 \times 10^4 \times 200\ VP \times 5 \times 10^5/(6.02 \times 10^{23} mol^{-1})}{5 \times 10^{-6} mol/L} = 1.66 \times 10^{-6} L$$

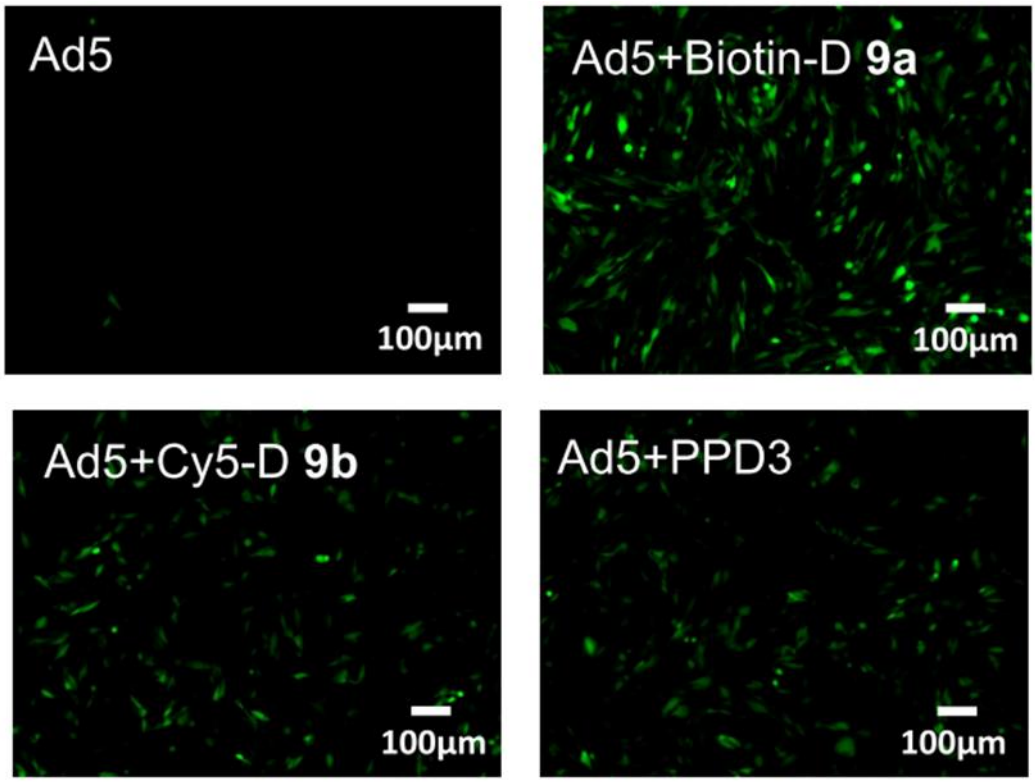

Figure S5.27. Fluorescent microscopy image of EGFP-transduction in CAR-negative CHO-K1 cells with infection by Ad5 (control), Ad5/dendron (Ad5: dendron=1: 500k) or Ad5/dendrimer (Ad5: dendrimer=1: 125k).

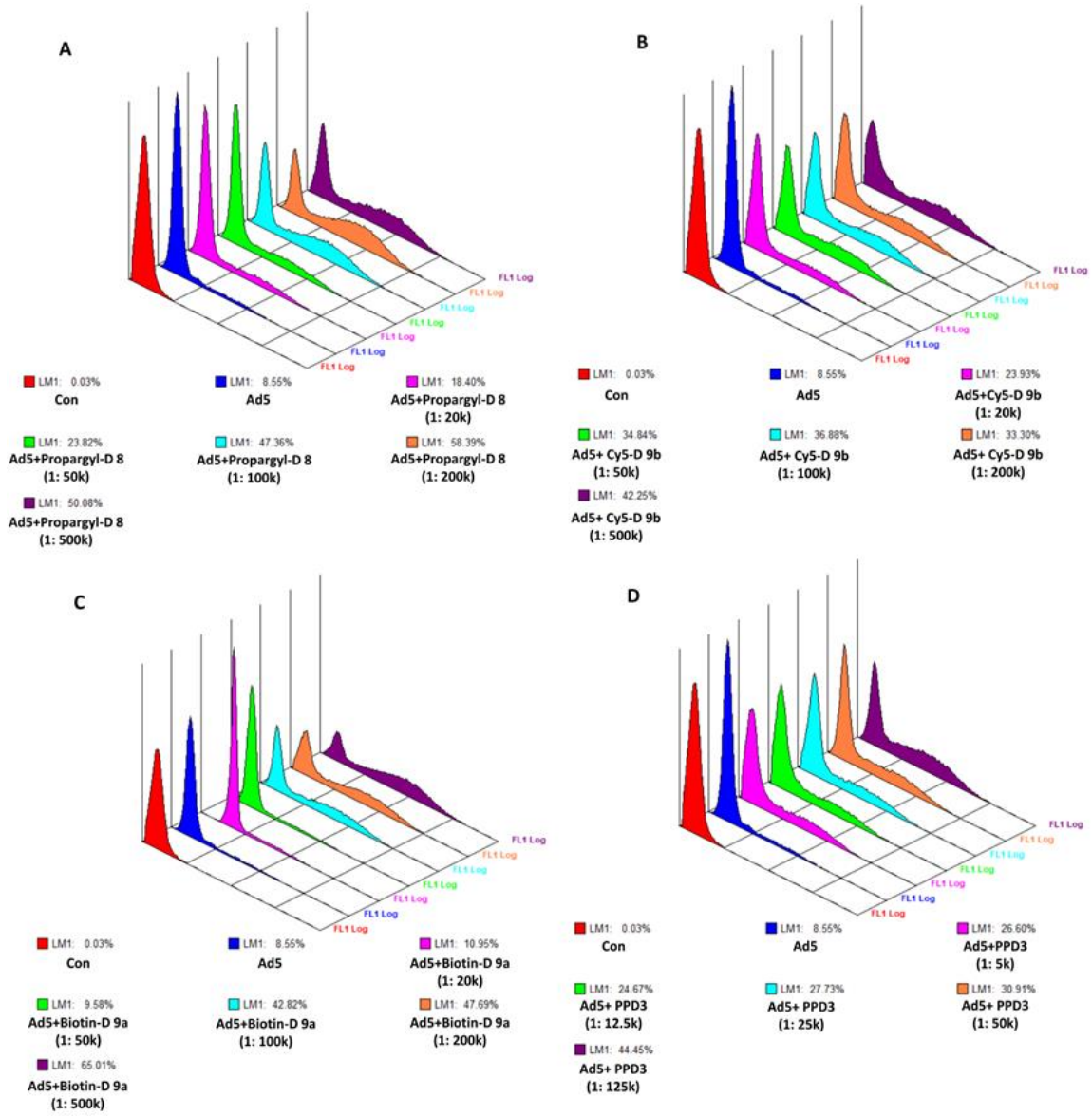

Figure S5.28. Flow cytometric quantification for CHO-K1 infected by Ad5 or Ad5/dendron. (**A**), (**B**), (**C**), (**D**) represent the results of Ad5/propargyl-D **8**, Ad5/Cy5-D **9b**, Ad5/biotin-D **9a** and Ad5/PPD3, respectively.

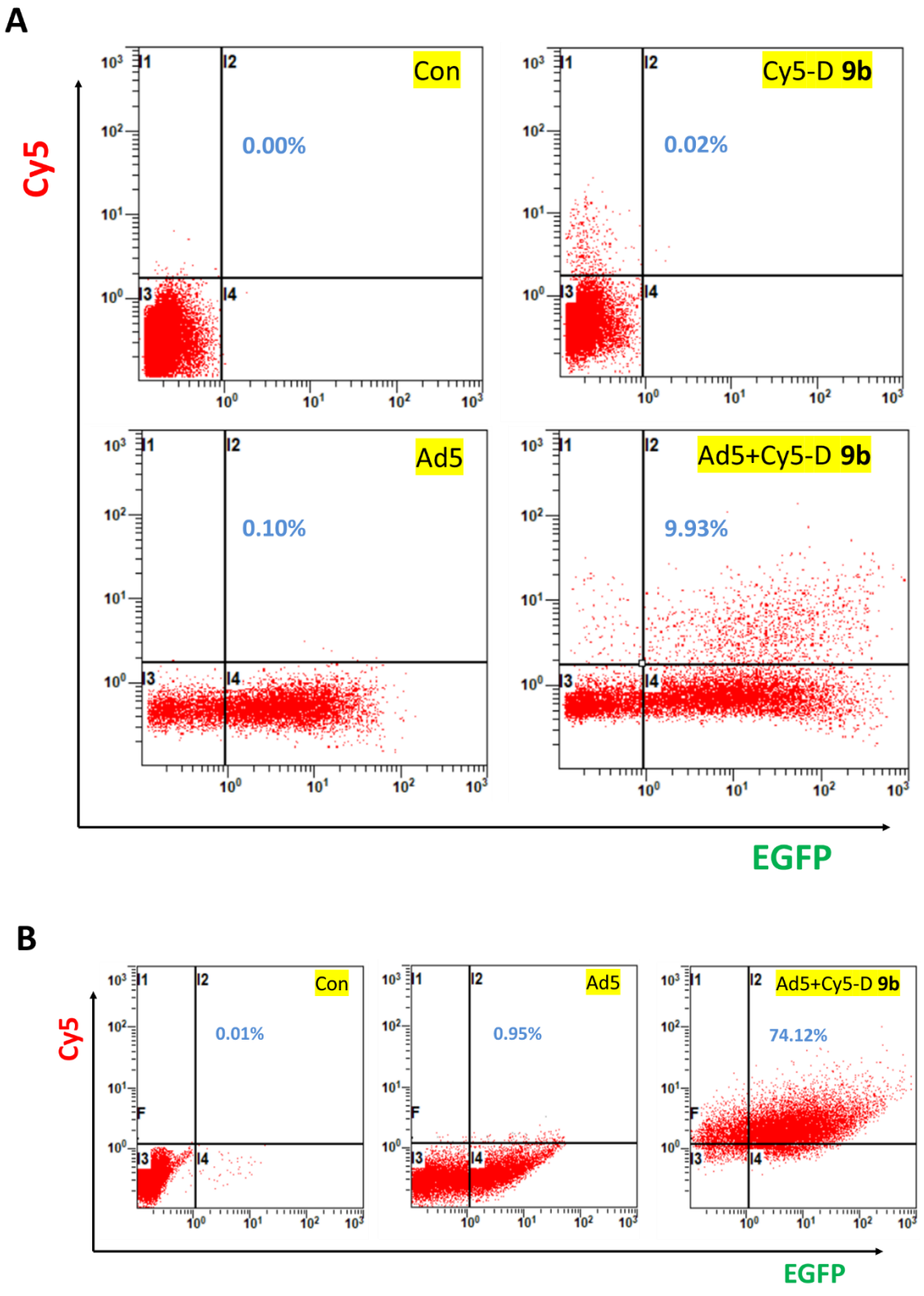

Figure S5.29. Flow cytometric quantification for CHO-K1 infected by Ad5 or Ad5/Cy5-D **9b**. (**A**) The pMOI is 500 and the ratio of Ad5 to Cy5-D **9b** is 1000k. (**B**) The pMOI is 2000 and the ratio of Ad5 to Cy5-D **9b** is 1000k. The difference between (**A**) and (**B**) is the Ad5 batch. Ad5 used for (**A**) was purchased from Hanbio, while (**B**) from Cyagen Biosciences. All Ad5 used for main text is the same with (**A**).

Copper(I)-catalyzed azide-alkyne cycloaddition (CuAAC) on dendron coated Ad5

Investigating the importance of a ligand in CuAAC

Stock solutions of propargyl-dendron **8** (1 mM in water, 10% DMSO), 7-hydroxy-3-azido-coumarin (6 mM in DMSO), $CuSO_4$ (1 mM in water), sodium ascorbate (NaAsc, 2 mM in water) and TBTA (1 mM in DMSO) were prepared. 10 µL of each propargyl-dendron **8**, 7-hydroxy-3-azido-coumarin and TBTA were added to 950 µL PBS. Then, $CuSO_4$ (10 µL) and NaAsc (10 µL) were added to obtain a 10 µM concentration of dendron. The reaction mixture was shaken for 1 h under protection from light. For the CuAAC without TBTA, 10 µL of PBS was added instead of the ligand. 6 µM coumarin in PBS was used as a control. The fluorescence spectra of coumarin (λ_{exc} = 375 nm; λ_{em} = 420-600 nm) was measured on a SPARK 20M microplate reader from TECAN Group Ltd.

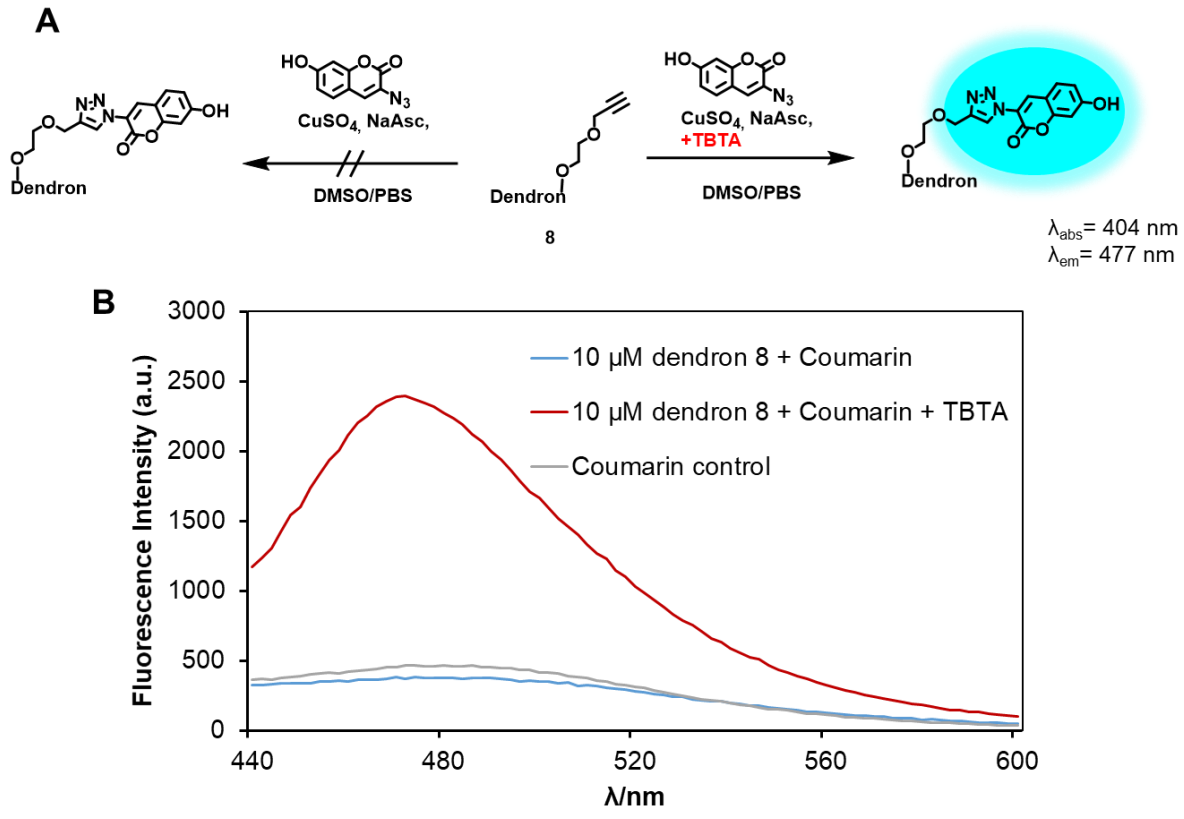

Figure S5.30. Investigation of ligand dependency of CuAAC. (**A**) Reaction scheme of CuAAC with and without TBTA (**B**) Fluorescence spectra of 10 µM dendron **8** incubated with 7-hydroxy-3-azido-coumarin and click reagents with and without addition of TBTA as well as 7-hydroxy-3-azido-coumarin as a control after incubation for 1 h. Only when adding TBTA, the fluorescence intensity at 477 nm was increased significantly indicating a successful CuAAC between dendron **8** and coumarin.

CuAAC on Ad5/dendron complexes

Stock solutions of dendrons **8** and **9a** (1 mM in DMSO), 7-hydroxy-3-azido-coumarin (6 mM in DMSO), $CuSO_4$ (1 mM in water), sodium ascorbate (NaAsc, 2 mM in water) and BTTAA (1mM in DMSO) were prepared. For CuAAC without Ad5, propargyl-dendron **8**, coumarin-azide and BTTAA were first added into PBS (final volume is 55 µL), then $CuSO_4$ and NaAsc were added, and shaked for 1 h (protect from light). 2.2 µL of every reagent were used that results in a concentration of 240 µM coumarin (the concentration of dendron is 40 µM). As negative control, coumarin alone was used as well as biotin-dendron **9a** that was treated under same CuAAC conditions.

For CuAAC on the Ad5 surface, Ad5 and propargyl-dendron **8** with an Ad5 concentration of 1.3×10^{11} vp/mL and an Ad5 to propargyl-dendron **8** ratio of 1:500k were first incubated for 1 h (the volume of Ad5 is 20.3 µL and the volume of propargyl-dendron **8** is 2.2 µL). Then, unbound dendron was removed by ultrafiltration (100 kDa) for 3 times (25 °C, 6000 rpm, 10 min). Subsequently, Ad5 or Ad5/dendron was incubated with CuAAC reagents for 1 h. As negative controls, biotin-dendron **9a** was treated under same conditions and propargyl-D **8** (without Ad5) was ultrafiltered for 3 times before incubated with other reagents in order to prove that free dendrons can be removed by ultrafiltration. The fluorescence intensity of coumarin was measured on a Varioskan LUX microplate reader (Thermo Fisher Scientific, USA).

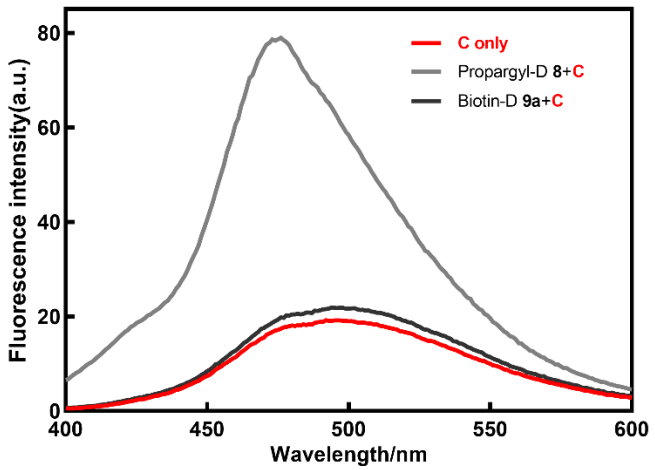

Figure S5.31. CuAAC with BTTAA. Propargyl-dendron **8** and biotin-dendron **9a** (negative control) were incubated with CuAAC reagents and BTTAA. 7-Hydroxy-3-azido-coumarin (C only) was used as control. Only for propargyl-dendron **8** treated with coumarin and CuAAC reagents a significant increase in fluorescence intensity at 477 nm was observed.

4.3.5 Kinetic binding analysis[26]

The following chapter is reproduced with permission from *ACS Nano* **2019**, *13*, 8749-8759, https://pubs.acs.org/doi/10.1021/acsnano.9b01484. Further permissions related to the material within this chapter excerpted should be directed to the ACS journal.

The interaction between biotin-dendron **9a** and Ad5 was studied by Bio-Layer Interferometry assays (BLI) from Octet96 (Pall ForteBio, CA, USA). In order to receive a significant signal for this binding event, we have immobilized biotin-dendron **9a** at the sensor surface and applied Ad5 as binding molecule. To immobilize the dendron at the surface of streptavidin-coated biosensors, we used biotin-dendron **9a**. The basic experiment contains four steps: Step 1 included hydration of the biosensor to record the baseline. Step 2: Immobilization of biotin-dendron **9a** on the streptavidin (SA) biosensor. Step 3: Washing and establishing the baseline. Step 4: Association of the Ad5. Step 5: dissociation (Fig. S32).

A significant interaction signal could be seen even in the presence of only 2 pM Ad5. The K_D (equilibrium dissociation constant) determined by this method is 1.27×10^{-12} M. We believe that this very strong binding could be a result of multivalent interactions between the large virus particles providing large numbers of binding sites and the sensor surface densely coated with dendrons. These results clearly support that there is a strong binding between biotin-dendron **9a** and Ad5 viruses.

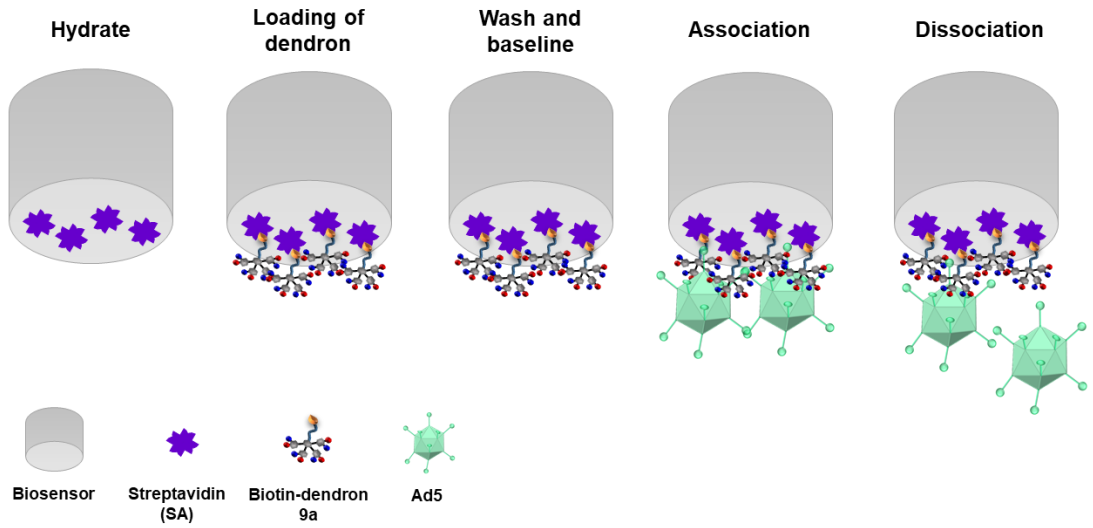

Figure S5.32. Workflow for dendron loading and dendron-Ad5 interaction assay[26] (adapted with permission from ACS Nano **2019**, 13, 8749-8759, https://pubs.acs.org/doi/10.1021/acsnano.9b01484).

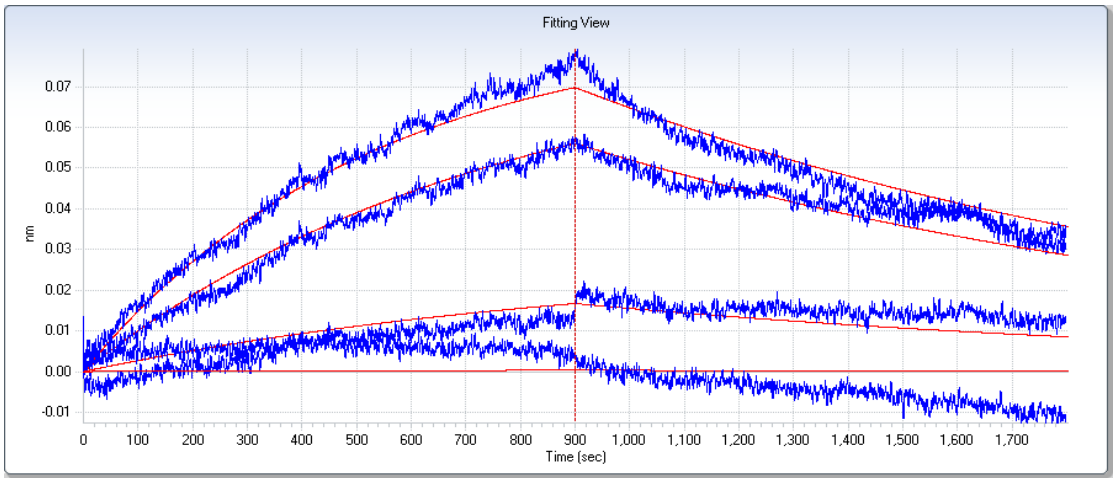

Figure S5.33: BLI analysis of Ad5 binding to biotin-dendron **9a** immobilized on streptavidin-coated biosensors. Association and dissociation curves are shown at different concentrations. Red lines represent regression modelling[26] (reprinted with permission from ACS Nano **2019**, 13, 8749-8759, https://pubs.acs.org/doi/10.1021/acsnano.9b01484).

Table S5.6: Kinetic analysis results.[26] (reproduced with permission from ACS Nano **2019**, 13, 8749-8759, https://pubs.acs.org/doi/10.1021/acsnano.9b01484).

Conc. (pM)	Response	K_D (M)	k_{on} (1/Ms)	k_{diss} (1/s)	k_{obs} (1/s)	Full R^2
2	0.076	$1.27 \cdot 10^{-12}$	$5.87 \cdot 10^{8}$	$7.47 \cdot 10^{-4}$	$1.92 \cdot 10^{-3}$	0.967526
1	0.0558	$1.27 \cdot 10^{-12}$	$5.87 \cdot 10^{8}$	$7.47 \cdot 10^{-4}$	$1.33 \cdot 10^{-3}$	0.967526
0.5	0.0129	$1.27 \cdot 10^{-12}$	$5.87 \cdot 10^{8}$	$7.47 \cdot 10^{-4}$	$1.04 \cdot 10^{-3}$	0.967526
0.25	0.0048	$1.27 \cdot 10^{-12}$	$5.87 \cdot 10^{8}$	$7.47 \cdot 10^{-4}$	$8.94 \cdot 10^{-4}$	0.967526

Conc.(nM): The molar concentration of the sample used in the association step. Response: Response calculated from the time window entered in the Steady State Analysis section. K_D (M): Equilibrium dissociation constant. k_{on} (1/Ms): Rate of association. k_{dis} (1/s): Rate of dissociation. k_{obs} (1/s): Observed binding rate. Full R^2: R^2 is the coefficient of determination which is an estimate of the goodness of the curve fit.

Protein structure images used within this article were taken from rcsb.org:

PDB ID: 4NHH

Y. Wu, Anthony P. West, Helen J. Kim, Matthew E. Thornton, Andrew B. Ward, Pamela J. Bjorkman, Cell Reports 2013, 5, 1443-1455.

PDB ID: 1FZC

S. J. Everse, G. Spraggon, L. Veerapandian, M. Riley, R. F. Doolittle, Biochemistry 1998, 37, 8637-8642.

PDB ID: 5Z0B

J. Park, M. S. Kim, D. H. Shin (2018), Crystal structure of plasma-derived human serum albumin, doi: 10.2210/pdb5Z0B/pdb

Appendix: All identified Corona proteins

				Average (%), technical duplicates				Std, technical duplicates		
Accession	**Peptide count**	**Unique peptides**	**Description**	**Liposome**	**Liposome-Dendron**	**Liposome-Dendrimer**		**Liposome**	**Liposome-Dendron**	**Liposome-Dendrimer**
P04217	5	5	Alpha-1B-glycoprotein OS=Homo sapiens GN=A1BG PE=1 SV=4	0.10	0.11	0.27		0.07	0.01	0.02
P08697	7	7	Alpha-2-antiplasmin OS=Homo sapiens GN=SERPINF2 PE=1 SV=3	0.38	0.24	0.29		0.44	0.05	0.04
P02765	7	7	Alpha-2-HS-glycoprotein OS=Homo sapiens GN=AHSG PE=1 SV=1	0.66	0.72	0.28		0.07	0.14	0.00
P01019	3	3	Angiotensinogen OS=Homo sapiens GN=AGT PE=1 SV=1	0.00	0.14	0.13		0.00	0.01	0.01
P01008	37	37	Antithrombin-III OS=Homo sapiens GN=SERPINC1 PE=1 SV=1	0.69	3.82	1.76		0.17	0.25	0.39
P02647	32	30	Apolipoprotein A-I OS=Homo sapiens GN=APOA1 PE=1 SV=1	0.41	4.05	6.24		0.02	0.84	2.19
P02652	2	2	Apolipoprotein A-II OS=Homo sapiens GN=APOA2 PE=1 SV=1	0.00	0.17	0.22		0.00	0.06	0.01
P06727	33	31	Apolipoprotein A-IV OS=Homo sapiens GN=APOA4 PE=1 SV=3	0.54	2.55	3.14		0.02	0.41	0.10
P04114	66	64	Apolipoprotein B-100 OS=Homo sapiens GN=APOB PE=1 SV=2	2.21	0.79	1.01		0.27	0.14	0.14
P02649	19	19	Apolipoprotein E OS=Homo sapiens GN=APOE PE=1 SV=1	2.32	1.90	1.18		0.15	0.31	0.03
O14791	2	2	Apolipoprotein L1 OS=Homo sapiens GN=APOL1 PE=1 SV=5	0.08	0.06	0.10		0.05	0.01	0.00
P08519	4	3	Apolipoprotein(a) OS=Homo sapiens GN=LPA PE=1 SV=1	3.31	0.03	0.01		2.59	0.01	0.01
P02749	18	18	Beta-2-glycoprotein 1 OS=Homo sapiens GN=APOH PE=1 SV=3	0.52	7.83	4.95		0.18	0.54	0.34
P04003	16	14	C4b-binding protein alpha chain OS=Homo sapiens GN=C4BPA PE=1 SV=2	14.53	0.43	0.46		0.72	0.10	0.01
P10909	20	20	Clusterin OS=Homo sapiens GN=CLU PE=1 SV=1	6.14	5.71	4.28		2.06	0.59	0.19
P00740	7	6	Coagulation factor IX OS=Homo sapiens GN=F9 PE=1 SV=2	0.47	0.20	0.31		0.05	0.14	0.27
P00742	3	3	Coagulation factor X OS=Homo sapiens GN=F10 PE=1 SV=2	0.00	0.11	0.18		0.00	0.01	0.01
P00748	12	11	Coagulation factor XII OS=Homo sapiens GN=F12 PE=1 SV=3	2.02	0.52	0.67		0.00	0.07	0.02
P02745	3	3	Complement C1q subcomponent subunit A OS=Homo sapiens GN=C1QA PE=1 SV=2	0.22	0.50	0.47		0.02	0.10	0.01
P02746	8	8	Complement C1q subcomponent subunit B OS=Homo sapiens GN=C1QB PE=1 SV=3	0.01	0.81	1.58		0.00	0.08	0.10
P02747	5	4	Complement C1q subcomponent subunit C OS=Homo sapiens GN=C1QC PE=1 SV=3	0.02	1.03	1.62		0.01	0.20	0.38
P00736	21	19	Complement C1r subcomponent OS=Homo sapiens GN=C1R PE=1 SV=2	0.01	0.29	0.96		0.00	0.02	0.05
P09871	13	12	Complement C1s subcomponent OS=Homo sapiens GN=C1S PE=1 SV=1	0.01	0.80	1.10		0.00	0.34	0.18
P01024;Q95568	109	106	Complement C3 OS=Homo sapiens GN=C3 PE=1 SV=2	5.93	1.99	3.22		2.66	0.15	0.31
P0C0L4	78	2	Complement C4-A OS=Homo sapiens GN=C4A PE=1 SV=2	0.14	0.73	1.56		0.03	0.06	0.10
P0C0L5	81	5	Complement C4-B OS=Homo sapiens GN=C4B PE=1 SV=2	0.43	2.21	4.71		0.08	0.19	0.31
P01031	26	26	Complement C5 OS=Homo sapiens GN=C5 PE=1 SV=4	0.03	0.14	0.49		0.00	0.01	0.05
P13671	26	26	Complement component C6 OS=Homo sapiens GN=C6 PE=1 SV=3	0.48	0.48	0.77		0.07	0.02	0.03
P10643	14	14	Complement component C7 OS=Homo sapiens GN=C7 PE=1 SV=2	0.11	0.49	0.80		0.08	0.06	0.04
P07357	2	2	Complement component C8 alpha chain OS=Homo sapiens GN=C8A PE=1 SV=2	0.02	0.03	0.09		0.02	0.01	0.01
P07358	6	6	Complement component C8 beta chain OS=Homo sapiens GN=C8B PE=1 SV=3	0.10	0.17	0.31		0.01	0.01	0.02
P02748	18	16	Complement component C9 OS=Homo sapiens GN=C9 PE=1 SV=2	0.24	0.55	0.69		0.03	0.05	0.11
P00751	12	11	Complement factor B OS=Homo sapiens GN=CFB PE=1 SV=2	0.46	0.49	0.44		0.13	0.02	0.13
P08603	68	58	Complement factor H OS=Homo sapiens GN=CFH PE=1 SV=4	0.09	2.32	2.79		0.02	0.26	0.21
Q03591	13	3	Complement factor H-related protein 1 OS=Homo sapiens GN=CFHR1 PE=1 SV=2	0.27	0.89	0.56		0.12	0.21	0.04
P36980	6	2	Complement factor H-related protein 2 OS=Homo sapiens GN=CFHR2 PE=1 SV=1	0.09	0.24	0.19		0.04	0.05	0.01
Q02985	5	2	Complement factor H-related protein 3 OS=Homo sapiens GN=CFHR3 PE=1 SV=2	0.00	0.05	0.05		0.00	0.01	0.01
Q98XR6	3	2	Complement factor H-related protein 5 OS=Homo sapiens GN=CFHR5 PE=1 SV=1	0.04	0.04	0.01		0.05	0.02	0.01
P27105	4	3	Erythrocyte band 7 integral membrane protein OS=Homo sapiens GN=STOM PE=1 SV=3	0.76	0.01	0.00		0.04	0.00	0.00
P06396	38	37	Gelsolin OS=Homo sapiens GN=GSN PE=1 SV=1	0.79	3.60	1.84		0.05	0.45	0.19
P69905	3	3	Hemoglobin subunit alpha OS=Homo sapiens GN=HBA1 PE=1 SV=2	1.82	0.06	0.05		0.05	0.00	0.01
P68871	5	4	Hemoglobin subunit beta OS=Homo sapiens GN=HBB PE=1 SV=2	5.33	0.08	0.04		0.99	0.00	0.01
P02790	7	7	Hemopexin OS=Homo sapiens GN=HPX PE=1 SV=2	0.49	0.42	0.22		0.44	0.02	0.02
P04196	22	21	Histidine-rich glycoprotein OS=Homo sapiens GN=HRG PE=1 SV=1	0.70	2.34	2.15		0.03	0.14	0.20
Q14520	8	8	Hyaluronan-binding protein 2 OS=Homo sapiens GN=HABP2 PE=1 SV=1	0.17	0.71	0.55		0.05	0.11	0.06
P01876;P01877	8	7	Ig alpha-1 chain C region OS=Homo sapiens GN=IGHA1 PE=1 SV=2	0.41	0.25	0.40		0.05	0.02	0.00
P01857	11	4	Ig gamma-1 chain C region OS=Homo sapiens GN=IGHG1 PE=1 SV=1	2.49	2.49	3.17		0.12	0.07	0.19
P01859	9	3	Ig gamma-2 chain C region OS=Homo sapiens GN=IGHG2 PE=1 SV=2	1.15	0.44	0.43		0.09	0.03	0.04
P01860	14	6	Ig gamma-3 chain C region OS=Homo sapiens GN=IGHG3 PE=1 SV=2	0.12	0.93	1.36		0.09	0.45	0.49
P01861	8	2	Ig gamma-4 chain C region OS=Homo sapiens GN=IGHG4 PE=1 SV=1	0.01	0.01	0.01		0.01	0.00	0.00
P01834	7	7	Ig kappa chain C region OS=Homo sapiens GN=IGKC PE=1 SV=1	6.33	2.00	2.35		1.00	0.20	0.14
8Q6;P0CF74;P0(	6	4	Ig lambda-2 chain C regions OS=Homo sapiens GN=IGLC2 PE=1 SV=1	0.70	0.61	0.64		0.01	0.04	0.13
P01871	10	3	Ig mu chain C region OS=Homo sapiens GN=IGHM PE=1 SV=3	0.46	0.11	0.21		0.57	0.02	0.00
P17936	2	2	Insulin-like growth factor-binding protein 3 OS=Homo sapiens GN=IGFBP3 PE=1 SV=2	0.00	0.05	0.07		0.00	0.02	0.02
P35858	11	11	Insulin-like growth factor-binding protein complex acid labile subunit OS=Homo sapiens GN=IGFALS PE=1 SV=1	0.21	0.16	0.50		0.24	0.04	0.06
P08514	4	3	Integrin alpha-IIb OS=Homo sapiens GN=ITGA2B PE=1 SV=3	0.64	0.01	0.01		0.36	0.00	0.00
P05106	2	2	Integrin beta-3 OS=Homo sapiens GN=ITGB3 PE=1 SV=2	0.00	0.00	0.00		0.00	0.00	0.00
P19827	9	9	Inter-alpha-trypsin inhibitor heavy chain H1 OS=Homo sapiens GN=ITIH1 PE=1 SV=3	0.28	0.25	0.38		0.04	0.02	0.04
P19823	21	20	Inter-alpha-trypsin inhibitor heavy chain H2 OS=Homo sapiens GN=ITIH2 PE=1 SV=2	0.01	0.47	0.65		0.00	0.02	0.09
Q14624	44	44	Inter-alpha-trypsin inhibitor heavy chain H4 OS=Homo sapiens GN=ITIH4 PE=1 SV=4	0.40	2.06	1.17		0.03	0.17	0.18
P29622	5	5	Kallistatin OS=Homo sapiens GN=SERPINA4 PE=1 SV=3	0.11	0.14	0.20		0.04	0.03	0.00
P01042	23	22	Kininogen-1 OS=Homo sapiens GN=KNG1 PE=1 SV=2	0.21	1.48	1.26		0.00	0.07	0.07
P18428	7	6	Lipopolysaccharide-binding protein OS=Homo sapiens GN=LBP PE=1 SV=3	0.10	0.46	0.24		0.15	0.02	0.04
P51884	4	4	Lumican OS=Homo sapiens GN=LUM PE=1 SV=2	0.20	0.37	0.47		0.04	0.05	0.03
Q96PD5	2	2	N-acetylmuramoyl-L-alanine amidase OS=Homo sapiens GN=PGLYRP2 PE=1 SV=1	0.00	0.01	0.05		0.00	0.01	0.01
P36955	14	13	Pigment epithelium-derived factor OS=Homo sapiens GN=SERPINF1 PE=1 SV=4	1.56	0.46	0.44		0.54	0.03	0.02
P03952	19	18	Plasma kallikrein OS=Homo sapiens GN=KLKB1 PE=1 SV=1	0.64	0.45	0.56		0.03	0.05	0.01
P05155	14	13	Plasma protease C1 inhibitor OS=Homo sapiens GN=SERPING1 PE=1 SV=2	0.91	0.55	0.80		0.33	0.05	0.02
P05154	7	6	Plasma serine protease inhibitor OS=Homo sapiens GN=SERPINA5 PE=1 SV=3	0.11	0.29	0.20		0.08	0.01	0.03
P00747	47	43	Plasminogen OS=Homo sapiens GN=PLG PE=1 SV=2	0.07	2.02	2.69		0.03	0.06	0.47
P02775	4	4	Platelet basic protein OS=Homo sapiens GN=PPBP PE=1 SV=3	0.31	1.37	0.59		0.06	0.05	0.07
P02776;P10720	4	4	Platelet factor 4 OS=Homo sapiens GN=PF4 PE=1 SV=2	0.23	0.64	0.53		0.01	0.09	0.07
P02760	8	8	Protein AMBP OS=Homo sapiens GN=AMBP PE=1 SV=1	0.09	0.37	0.48		0.00	0.18	0.09
Q9UKS5	3	3	Protein Z-dependent protease inhibitor OS=Homo sapiens GN=SERPINA10 PE=1 SV=1	0.00	0.13	0.21		0.00	0.01	0.02
P00734	31	29	Prothrombin OS=Homo sapiens GN=F2 PE=1 SV=2	1.00	3.15	2.18		0.27	0.16	0.11
P49908	5	5	Selenoprotein P OS=Homo sapiens GN=SELENOP PE=1 SV=3	0.03	0.61	0.73		0.03	0.06	0.07
P02787	12	12	Serotransferrin OS=Homo sapiens GN=TF PE=1 SV=3	0.23	0.24	0.13		0.15	0.04	0.02
P02768	67	63	Serum albumin OS=Homo sapiens GN=ALB PE=1 SV=2	25.98	12.72	15.44		3.39	0.67	0.99
P02743	9	9	Serum amyloid P-component OS=Homo sapiens GN=APCS PE=1 SV=2	0.34	1.90	0.35		0.05	0.17	0.04
P27169	6	6	Serum paraoxonase/arylesterase 1 OS=Homo sapiens GN=PON1 PE=1 SV=3	0.06	0.11	0.19		0.04	0.02	0.02
P02766	4	4	Transthyretin OS=Homo sapiens GN=TTR PE=1 SV=1	0.02	0.25	0.19		0.01	0.03	0.00
P02774	32	31	Vitamin D-binding protein OS=Homo sapiens GN=GC PE=1 SV=1	0.38	2.57	2.02		0.14	0.36	0.21
P04004	19	17	Vitronectin OS=Homo sapiens GN=VTN PE=1 SV=1	1.11	9.04	5.94		0.70	0.82	0.47
				100.00	100.00	100.00				

Figure S5.34. Average amount in % and the standard deviation of all identified proteins adsorbed to lipo-dendron and lipo-dendrimer in blood serum

				Average (%), technical triplicates			Std,technical triplicates		
Accession	Peptide count	Unique peptides	Description	PS-NH2	PS-Dendron	PS-Dendrimer	PS-NH2	PS-Dendron	PS-Dendrimer
;P63267;P68032;:	9	2	Actin, aortic smooth muscle OS=Homo sapiens GN=ACTA2 PE=1 SV=1	0.25	0.30	0.34	0.04	0.04	0.09
I261;P60709;Q9B:	15	6	Actin, cytoplasmic 2 OS=Homo sapiens GN=ACTG1 PE=1 SV=1	0.47	0.28	0.39	0.15	0.07	0.10
P61204	1	1	ADP-ribosylation factor 3 OS=Homo sapiens GN=ARF3 PE=1 SV=2	0.00	0.00	0.00	0.00	0.00	0.01
P01009	4	3	Alpha-1-antitrypsin OS=Homo sapiens GN=SERPINA1 PE=1 SV=3	0.14	0.25	0.13	0.05	0.02	0.06
P02765	6	5	Alpha-2-HS-glycoprotein OS=Homo sapiens GN=AHSG PE=1 SV=1	0.04	0.32	0.16	0.03	0.04	0.07
P01008	21	20	Antithrombin-III OS=Homo sapiens GN=SERPINC1 PE=1 SV=1	1.46	0.89	1.50	0.75	0.27	0.24
P02647	34	33	Apolipoprotein A-I OS=Homo sapiens GN=APOA1 PE=1 SV=1	5.65	7.66	9.51	0.58	0.69	1.12
P02652	4	4	Apolipoprotein A-II OS=Homo sapiens GN=APOA2 PE=1 SV=1	0.05	0.18	0.07	0.04	0.09	0.05
P06727	33	30	Apolipoprotein A-IV OS=Homo sapiens GN=APOA4 PE=1 SV=3	3.36	1.83	2.21	0.42	0.39	0.47
P04114	83	78	Apolipoprotein B-100 OS=Homo sapiens GN=APOB PE=1 SV=2	0.24	0.31	0.49	0.01	0.15	0.21
P02656	2	2	Apolipoprotein C-III OS=Homo sapiens GN=APOC3 PE=1 SV=1	2.04	2.51	1.22	1.34	0.92	0.36
P02649	20	20	Apolipoprotein E OS=Homo sapiens GN=APOE PE=1 SV=1	0.92	0.95	0.73	0.26	0.26	0.19
P02749	18	17	Beta-2-glycoprotein 1 OS=Homo sapiens GN=APOH PE=1 SV=3	0.10	1.84	1.61	0.05	0.32	0.28
Q562R1	6	3	Beta-actin-like protein 2 OS=Homo sapiens GN=ACTBL2 PE=1 SV=2	0.03	0.04	0.05	0.02	0.01	0.01
P04003	13	10	C4b-binding protein alpha chain OS=Homo sapiens GN=C4BPA PE=1 SV=2	0.41	0.44	0.46	0.02	0.07	0.07
Q9NP86	1	1	Calcium-binding protein 5 OS=Homo sapiens GN=CABP5 PE=1 SV=1	0.02	0.06	0.11	0.02	0.02	0.02
P10909	21	21	Clusterin OS=Homo sapiens GN=CLU PE=1 SV=1	10.56	3.60	8.92	2.82	0.34	1.34
P00740	6	5	Coagulation factor IX OS=Homo sapiens GN=F9 PE=1 SV=2	0.07	0.08	0.13	0.05	0.03	0.01
P12259	14	13	Coagulation factor V OS=Homo sapiens GN=F5 PE=1 SV=4	0.11	0.18	0.27	0.02	0.03	0.06
P00748	2	1	Coagulation factor XII OS=Homo sapiens GN=F12 PE=1 SV=3	0.11	0.13	0.10	0.04	0.06	0.05
P02745	1	1	Complement C1q subcomponent subunit A OS=Homo sapiens GN=C1QA PE=1 SV=2	0.00	0.05	0.04	0.00	0.05	0.04
P02746	7	7	Complement C1q subcomponent subunit B OS=Homo sapiens GN=C1QB PE=1 SV=3	0.10	0.62	0.57	0.05	0.12	0.08
P02747	5	4	Complement C1q subcomponent subunit C OS=Homo sapiens GN=C1QC PE=1 SV=3	0.39	0.75	0.70	0.14	0.18	0.18
P00736	19	19	Complement C1r subcomponent OS=Homo sapiens GN=C1R PE=1 SV=2	1.45	1.13	0.89	0.20	0.20	0.16
P09871	12	10	Complement C1s subcomponent OS=Homo sapiens GN=C1S PE=1 SV=1	0.14	0.27	0.34	0.04	0.04	0.04
P01024	103	99	Complement C3 OS=Homo sapiens GN=C3 PE=1 SV=2	0.65	2.02	1.86	0.02	0.14	0.18
P0C0L4	57	2	Complement C4-A OS=Homo sapiens GN=C4A PE=1 SV=2	0.28	0.34	0.38	0.14	0.07	0.22
P0C0L5	56	1	Complement C4-B OS=Homo sapiens GN=C4B PE=1 SV=2	0.41	0.50	0.56	0.21	0.10	0.33
P01031	13	13	Complement C5 OS=Homo sapiens GN=C5 PE=1 SV=4	0.02	0.07	0.10	0.02	0.02	0.03
P13671	11	11	Complement component C6 OS=Homo sapiens GN=C6 PE=1 SV=3	0.02	0.17	0.21	0.00	0.00	0.01
P10643	9	9	Complement component C7 OS=Homo sapiens GN=C7 PE=1 SV=2	0.03	0.11	0.19	0.02	0.03	0.05
P02748	17	16	Complement component C9 OS=Homo sapiens GN=C9 PE=1 SV=2	0.25	0.41	0.65	0.08	0.06	0.04
P00751	9	9	Complement factor B OS=Homo sapiens GN=CFB PE=1 SV=2	0.26	0.28	0.15	0.18	0.13	0.07
P08603;Q02985	53	47	Complement factor H OS=Homo sapiens GN=CFH PE=1 SV=4	1.27	1.48	1.44	0.38	0.24	0.36
Q03591	14	3	Complement factor H-related protein 1 OS=Homo sapiens GN=CFHR1 PE=1 SV=2	0.20	0.80	0.80	0.02	0.08	0.07
P36980	6	1	Complement factor H-related protein 2 OS=Homo sapiens GN=CFHR2 PE=1 SV=1	0.02	0.11	0.10	0.01	0.02	0.02
Q9BXR6	5	4	Complement factor H-related protein 5 OS=Homo sapiens GN=CFHR5 PE=1 SV=1	0.15	0.10	0.11	0.05	0.04	0.06
P02671	4	4	Fibrinogen alpha chain OS=Homo sapiens GN=FGA PE=1 SV=2	0.02	0.11	0.08	0.00	0.05	0.05
Q13643	1	1	Four and a half LIM domains protein 3 OS=Homo sapiens GN=FHL3 PE=1 SV=4	0.07	0.00	0.00	0.12	0.00	0.00
P06396	30	29	Gelsolin OS=Homo sapiens GN=GSN PE=1 SV=1	0.37	0.85	0.67	0.16	0.14	0.16
Q96EK6	1	1	Glucosamine 6-phosphate N-acetyltransferase OS=Homo sapiens GN=GNPNAT1 PE=1 SV=1	0.01	0.02	0.02	0.02	0.01	0.01
P22352	4	4	Glutathione peroxidase 3 OS=Homo sapiens GN=GPX3 PE=1 SV=2	0.37	0.38	0.53	0.33	0.23	0.44
P00738	7	7	Haptoglobin OS=Homo sapiens GN=HP PE=1 SV=1	0.12	0.30	0.13	0.01	0.03	0.02
P69905	2	2	Hemoglobin subunit alpha OS=Homo sapiens GN=HBA1 PE=1 SV=2	0.09	0.11	0.14	0.02	0.01	0.04
P68871	8	5	Hemoglobin subunit beta OS=Homo sapiens GN=HBB PE=1 SV=2	0.66	0.58	0.45	0.01	0.02	0.05
P02042	6	1	Hemoglobin subunit delta OS=Homo sapiens GN=HBD PE=1 SV=2	0.02	0.02	0.02	0.01	0.00	0.01
P69892;P69891	2	1	Hemoglobin subunit gamma-2 OS=Homo sapiens GN=HBG2 PE=1 SV=2	0.02	0.02	0.04	0.01	0.01	0.03
Q6ZVN8	1	1	Hemojuvelin OS=Homo sapiens GN=HFE2 PE=1 SV=1	0.21	0.10	0.24	0.05	0.02	0.02
P02790	9	8	Hemopexin OS=Homo sapiens GN=HPX PE=1 SV=2	0.11	0.51	0.19	0.04	0.03	0.01
P04196	12	10	Histidine-rich glycoprotein OS=Homo sapiens GN=HRG PE=1 SV=1	0.05	0.89	0.48	0.02	0.23	0.11
Q14520	3	2	Hyaluronan-binding protein 2 OS=Homo sapiens GN=HABP2 PE=1 SV=1	0.10	0.10	0.08	0.04	0.00	0.01
P01876;P01877	12	12	Ig alpha-1 chain C region OS=Homo sapiens GN=IGHA1 PE=1 SV=2	0.37	0.55	0.30	0.08	0.10	0.11
P01857	10	4	Ig gamma-1 chain C region OS=Homo sapiens GN=IGHG1 PE=1 SV=1	1.42	3.28	1.81	0.11	0.24	0.10
P01859	11	6	Ig gamma-2 chain C region OS=Homo sapiens GN=IGHG2 PE=1 SV=2	1.82	1.93	1.56	0.22	0.29	0.34
P01860	13	6	Ig gamma-3 chain C region OS=Homo sapiens GN=IGHG3 PE=1 SV=2	0.15	0.62	0.45	0.09	0.16	0.08
P01861	7	1	Ig gamma-4 chain C region OS=Homo sapiens GN=IGHG4 PE=1 SV=1	0.03	0.12	0.04	0.00	0.07	0.01
P01834	6	5	Ig kappa chain C region OS=Homo sapiens GN=IGKC PE=1 SV=1	1.13	2.47	1.36	0.20	1.22	0.66
;B9A064;P0CF74	5	5	Ig lambda-3 chain C regions OS=Homo sapiens GN=IGLC3 PE=1 SV=1	0.54	2.26	1.35	0.35	0.84	0.07
P01871	17	5	Ig mu chain C region OS=Homo sapiens GN=IGHM PE=1 SV=3	0.91	0.80	0.90	0.14	0.05	0.10
P04220	12	1	Ig mu heavy chain disease protein OS=Homo sapiens PE=1 SV=1	0.04	0.04	0.04	0.01	0.00	0.00
)B4J1X5;A0A0C4	3	3	Immunoglobulin heavy variable 3-74 OS=Homo sapiens GN=IGHV3-74 PE=3 SV=1	0.14	0.11	0.10	0.03	0.03	0.06
A0A075B652	2	2	Immunoglobulin kappa variable 2D-29 OS=Homo sapiens GN=IGKV2D-29 PE=3 SV=1	0.49	0.46	0.44	0.02	0.04	0.10
P08514	6	6	Integrin alpha-IIb OS=Homo sapiens GN=ITGA2B PE=1 SV=3	0.04	0.04	0.04	0.03	0.01	0.01
Q14624	42	41	Inter-alpha-trypsin inhibitor heavy chain H4 OS=Homo sapiens GN=ITIH4 PE=1 SV=4	1.20	2.34	2.94	0.23	0.41	0.73
P13645	9	8	Keratin, type I cytoskeletal 10 OS=Homo sapiens GN=KRT10 PE=1 SV=6	0.11	0.07	0.09	0.04	0.03	0.04
P35527	15	12	Keratin, type I cytoskeletal 9 OS=Homo sapiens GN=KRT9 PE=1 SV=3	0.66	0.20	0.16	0.25	0.08	0.06
P04264	16	14	Keratin, type II cytoskeletal 1 OS=Homo sapiens GN=KRT1 PE=1 SV=6	0.54	0.26	0.28	0.04	0.02	0.01
Q7Z794	2	1	Keratin, type II cytoskeletal 1b OS=Homo sapiens GN=KRT77 PE=2 SV=3	0.94	0.66	0.49	0.43	0.36	0.41
P35908	5	4	Keratin, type II cytoskeletal 2 epidermal OS=Homo sapiens GN=KRT2 PE=1 SV=2	0.13	0.07	0.08	0.03	0.02	0.02
P04259	4	3	Keratin, type II cytoskeletal 6B OS=Homo sapiens GN=KRT6B PE=1 SV=5	0.11	0.08	0.08	0.02	0.04	0.04
P01042	21	20	Kininogen-1 OS=Homo sapiens GN=KNG1 PE=1 SV=2	0.40	1.26	0.82	0.13	0.15	0.05
P18428	8	8	Lipopolysaccharide-binding protein OS=Homo sapiens GN=LBP PE=1 SV=3	0.07	0.44	0.76	0.05	0.05	0.03
Q96A32	1	0	Myosin regulatory light chain 2, skeletal muscle isoform OS=Homo sapiens GN=MYLPF PE=2 SV=1	0.00	0.00	0.00			
Q9NRC9	1	1	Otoraplin OS=Homo sapiens GN=OTOR PE=1 SV=1	0.00	0.01	0.02	0.00	0.02	0.04
Q8NEN9	1	1	PDZ domain-containing protein 8 OS=Homo sapiens GN=PDZD8 PE=1 SV=1	0.06	0.03	0.07	0.05	0.01	0.01
P42336	1	1	Phosphatidylinositol 4,5-bisphosphate 3-kinase catalytic subunit alpha isoform OS=Homo sapiens GN=PIK3CA PE=1 SV=2	0.02	0.02	0.02	0.01	0.00	0.01
P05155	7	7	Plasma protease C1 inhibitor OS=Homo sapiens GN=SERPING1 PE=1 SV=2	0.10	0.39	0.43	0.04	0.01	0.06
P00747	22	21	Plasminogen OS=Homo sapiens GN=PLG PE=1 SV=2	0.52	0.92	0.65	0.32	0.34	0.38
P02775	5	5	Platelet basic protein OS=Homo sapiens GN=PPBP PE=1 SV=3	0.41	1.68	0.56	0.15	0.21	0.13
P02776	5	3	Platelet factor 4 OS=Homo sapiens GN=PF4 PE=1 SV=2	0.21	2.34	1.27	0.10	0.23	0.17
P10720	3	1	Platelet factor 4 variant OS=Homo sapiens GN=PF4V1 PE=1 SV=1	0.10	1.08	0.60	0.05	0.23	0.15
Q6S8J3;A5A3E0	9	4	POTE ankyrin domain family member E OS=Homo sapiens GN=POTEE PE=2 SV=3	0.14	0.07	0.17	0.11	0.04	0.08
P27918	7	6	Properdin OS=Homo sapiens GN=CFP PE=1 SV=2	0.23	0.36	0.39	0.03	0.08	0.03
Q92954	6	6	Proteoglycan 4 OS=Homo sapiens GN=PRG4 PE=1 SV=2	0.01	0.11	0.14	0.01	0.03	0.05
P00734	17	16	Prothrombin OS=Homo sapiens GN=F2 PE=1 SV=2	0.67	0.41	0.73	0.08	0.06	0.09
A6NIZ1	1	1	Ras-related protein Rap-1b-like protein OS=Homo sapiens PE=2 SV=1	0.01	0.02	0.04	0.01	0.01	0.01
Q99969	2	2	Retinoic acid receptor responder protein 2 OS=Homo sapiens GN=RARRES2 PE=1 SV=1	0.01	0.03	0.04	0.01	0.00	0.02
Q9H2S5	2	2	RING finger protein 39 OS=Homo sapiens GN=RNF39 PE=2 SV=2	0.22	0.04	0.30	0.25	0.03	0.26
P02787	30	29	Serotransferrin OS=Homo sapiens GN=TF PE=1 SV=3	0.42	0.35	0.38	0.19	0.09	0.22
P02768	65	63	Serum albumin OS=Homo sapiens GN=ALB PE=1 SV=2	40.66	23.77	15.79	5.46	0.42	1.02
P0DJI8	6	3	Serum amyloid A-1 protein OS=Homo sapiens GN=SAA1 PE=1 SV=1	0.14	0.75	0.69	0.02	0.06	0.01
P0DJI9	4	1	Serum amyloid A-2 protein OS=Homo sapiens GN=SAA2 PE=1 SV=1	0.13	0.53	0.48	0.07	0.01	0.17
P02743	9	8	Serum amyloid P-component OS=Homo sapiens GN=APCS PE=1 SV=2	0.24	0.85	1.92	0.05	0.05	0.13
Q15527	2	2	Surfeit locus protein 2 OS=Homo sapiens GN=SURF2 PE=1 SV=3	0.77	0.18	0.24	0.24	0.11	0.09
P03986	1	0	T-cell receptor gamma-2 chain C region OS=Homo sapiens GN=TRGC2 PE=1 SV=1	0.00	0.00	0.00			
P07996	8	6	Thrombospondin-1 OS=Homo sapiens GN=THBS1 PE=1 SV=2	0.01	0.05	0.08	0.00	0.01	0.02
P02766	7	7	Transthyretin OS=Homo sapiens GN=TTR PE=1 SV=1	0.18	0.39	0.48	0.03	0.09	0.10
P62256	1	1	Ubiquitin-conjugating enzyme E2 H OS=Homo sapiens GN=UBE2H PE=1 SV=1	1.67	2.44	2.77	0.62	0.39	0.45
Q8WVN8	1	1	Ubiquitin-conjugating enzyme E2 Q2 OS=Homo sapiens GN=UBE2Q2 PE=1 SV=1	0.00	0.02	0.02	0.00	0.03	0.03
P02774	25	23	Vitamin D-binding protein OS=Homo sapiens GN=GC PE=1 SV=1	0.54	0.75	0.80	0.15	0.13	0.13
P04004	24	24	Vitronectin OS=Homo sapiens GN=VTN PE=1 SV=1	4.79	7.65	14.41	0.36	0.79	3.01
Q6ZN30	1	1	Zinc finger protein basonuclin-2 OS=Homo sapiens GN=BNC2 PE=1 SV=1	2.61	1.44	1.76	0.69	0.78	1.39
Q49AA0	1	1	Zinc finger protein ZFP69 OS=Homo sapiens GN=ZFP69 PE=2 SV=2	0.01	0.23	0.10	0.02	0.24	0.13
				100.00	100.00	100.00			

Figure S5.35. Average amount in % and the standard deviation of all identified proteins adsorbed to PS-dendron and PS-dendrimer in blood serum

				Average (%), technical duplicates				Std, technical duplicates		
Accession	Peptide count	Unique peptides	Description	Liposome	Liposome-Dendron	Liposome-Dendrimer		Liposome	Liposome- Dendron	Liposome-Dendrimer
P04217	6	5	Alpha-1B-glycoprotein OS=Homo sapiens GN=A1BG PE=1 SV=4	0.05	0.06	0.13		0.08	0.01	0.01
P02765	10	10	Alpha-2-HS-glycoprotein OS=Homo sapiens GN=AHSG PE=1 SV=1	0.19	0.87	0.24		0.23	0.21	0.01
P01008	8	8	Antithrombin-III OS=Homo sapiens GN=SERPINC1 PE=1 SV=1	0.06	0.55	0.39		0.09	0.08	0.01
P02647	27	27	Apolipoprotein A-I OS=Homo sapiens GN=APOA1 PE=1 SV=1	0.59	2.79	3.05		0.29	1.24	0.17
P06727	32	31	Apolipoprotein A-IV OS=Homo sapiens GN=APOA4 PE=1 SV=3	0.70	1.16	1.69		0.63	0.69	0.00
P02656	2	2	Apolipoprotein C-III OS=Homo sapiens GN=APOC3 PE=1 SV=1	0.35	0.85	0.15		0.47	0.15	0.00
P02649	20	20	Apolipoprotein E OS=Homo sapiens GN=APOE PE=1 SV=1	0.75	1.20	0.85		1.07	0.28	0.02
P02749	20	20	Beta-2-glycoprotein 1 OS=Homo sapiens GN=APOH PE=1 SV=3	0.34	10.46	3.83		0.48	1.49	0.26
P04003	11	9	C4b-binding protein alpha chain OS=Homo sapiens GN=C4BPA PE=1 SV=2	4.00	0.34	0.36		5.66	0.05	0.03
Q9HA72	1	1	Calcium homeostasis modulator protein 2 OS=Homo sapiens GN=CALHM2 PE=2 SV=1	11.38	0.35	0.21		16.10	0.31	0.02
P49747	3	3	Cartilage oligomeric matrix protein OS=Homo sapiens GN=COMP PE=1 SV=2	0.00	0.81	0.16		0.00	0.62	0.04
O43866	3	3	CD5 antigen-like OS=Homo sapiens GN=CD5L PE=1 SV=1	0.00	0.02	0.05		0.00	0.01	0.01
P10909	20	19	Clusterin OS=Homo sapiens GN=CLU PE=1 SV=1	1.19	4.13	3.35		1.68	0.26	0.02
P00740	5	5	Coagulation factor IX OS=Homo sapiens GN=F9 PE=1 SV=2	0.00	0.06	0.10		0.00	0.01	0.00
P00748	14	13	Coagulation factor XII OS=Homo sapiens GN=F12 PE=1 SV=3	0.21	0.51	0.59		0.29	0.05	0.01
P02745	5	5	Complement C1q subcomponent subunit A OS=Homo sapiens GN=C1QA PE=1 SV=2	0.74	0.99	1.09		1.05	0.06	0.00
P02746	8	8	Complement C1q subcomponent subunit B OS=Homo sapiens GN=C1QB PE=1 SV=3	0.43	0.48	1.22		0.60	0.06	0.08
P02747	5	5	Complement C1q subcomponent subunit C OS=Homo sapiens GN=C1QC PE=1 SV=3	0.04	0.48	1.02		0.05	0.13	0.02
P00736	18	17	Complement C1r subcomponent OS=Homo sapiens GN=C1R PE=1 SV=2	0.40	0.20	0.45		0.08	0.12	0.04
P09871	17	17	Complement C1s subcomponent OS=Homo sapiens GN=C1S PE=1 SV=1	0.00	0.82	0.44		0.00	0.32	0.01
P01024	99	97	Complement C3 OS=Homo sapiens GN=C3 PE=1 SV=2	1.21	1.05	2.00		1.58	0.13	0.08
P0C0L4	59	1	Complement C4-A OS=Homo sapiens GN=C4A PE=1 SV=2	11.97	0.33	0.51		16.90	0.02	0.02
P0C0L5	60	2	Complement C4-B OS=Homo sapiens GN=C4B PE=1 SV=2	6.94	0.19	0.30		9.80	0.01	0.01
P13671	27	26	Complement component C6 OS=Homo sapiens GN=C6 PE=1 SV=3	0.00	0.30	0.34		0.00	0.09	0.01
P10643	11	10	Complement component C7 OS=Homo sapiens GN=C7 PE=1 SV=2	0.29	0.12	0.18		0.41	0.02	0.01
P07358	14	12	Complement component C8 beta chain OS=Homo sapiens GN=C8B PE=1 SV=3	1.35	0.33	0.32		1.57	0.09	0.00
P07360	4	4	Complement component C8 gamma chain OS=Homo sapiens GN=C8G PE=1 SV=3	0.00	0.03	0.13		0.00	0.01	0.00
P02748	5	5	Complement component C9 OS=Homo sapiens GN=C9 PE=1 SV=2	0.00	0.11	0.14		0.00	0.02	0.00
P00751	15	14	Complement factor B OS=Homo sapiens GN=CFB PE=1 SV=2	3.93	0.26	0.27		5.45	0.17	0.05
P08603;Q02985	66	59	Complement factor H OS=Homo sapiens GN=CFH PE=1 SV=4	0.64	1.92	2.32		0.75	0.62	0.07
Q03591	11	1	Complement factor H-related protein 1 OS=Homo sapiens GN=CFHR1 PE=1 SV=2	0.24	0.53	0.32		0.08	0.08	0.02
P36980	7	2	Complement factor H-related protein 2 OS=Homo sapiens GN=CFHR2 PE=1 SV=1	0.01	0.21	0.19		0.02	0.04	0.02
Q9BXR6	6	4	Complement factor H-related protein 5 OS=Homo sapiens GN=CFHR5 PE=1 SV=1	0.01	0.04	0.02		0.02	0.02	0.00
Q9NYJ30	2	1	Endothelial cell-specific molecule 1 OS=Homo sapiens GN=ESM1 PE=1 SV=2	0.00	0.02	0.03		0.00	0.01	0.00
P02671	54	53	Fibrinogen alpha chain OS=Homo sapiens GN=FGA PE=1 SV=2	0.52	7.43	8.74		0.15	1.40	0.38
P02675	54	53	Fibrinogen beta chain OS=Homo sapiens GN=FGB PE=1 SV=2	0.67	10.68	11.93		0.95	1.08	0.24
P02679	38	33	Fibrinogen gamma chain OS=Homo sapiens GN=FGG PE=1 SV=3	4.12	11.74	18.63		0.67	1.62	0.13
P06396	33	33	Gelsolin OS=Homo sapiens GN=GSN PE=1 SV=1	0.04	1.24	1.24		0.06	0.20	0.00
P02790	19	18	Hemopexin OS=Homo sapiens GN=HPX PE=1 SV=2	0.00	0.70	0.95		0.00	0.09	0.05
P05546	8	8	Heparin cofactor 2 OS=Homo sapiens GN=SERPIND1 PE=1 SV=3	1.65	0.28	0.25		1.43	0.09	0.01
P04196	20	20	Histidine-rich glycoprotein OS=Homo sapiens GN=HRG PE=1 SV=1	0.00	2.71	1.62		0.01	0.11	0.26
Q14520	8	7	Hyaluronan-binding protein 2 OS=Homo sapiens GN=HABP2 PE=1 SV=1	0.00	0.41	0.43		0.00	0.04	0.00
P01876;P01877	9	8	Ig alpha-1 chain C region OS=Homo sapiens GN=IGHA1 PE=1 SV=2	1.14	0.17	0.18		0.28	0.06	0.02
P01857	10	5	Ig gamma-1 chain C region OS=Homo sapiens GN=IGHG1 PE=1 SV=1	1.56	1.68	1.75		1.33	0.67	0.20
P01859	7	3	Ig gamma-2 chain C region OS=Homo sapiens GN=IGHG2 PE=1 SV=2	0.33	0.25	0.23		0.40	0.05	0.01
P01860	12	5	Ig gamma-3 chain C region OS=Homo sapiens GN=IGHG3 PE=1 SV=2	1.22	0.51	0.76		0.77	0.21	0.09
P01861	7	1	Ig gamma-4 chain C region OS=Homo sapiens GN=IGHG4 PE=1 SV=1	0.15	0.09	0.09		0.17	0.03	0.00
P01834	5	5	Ig kappa chain C region OS=Homo sapiens GN=IGKC PE=1 SV=1	2.72	1.91	1.60		3.49	0.05	0.15
;A0M8Q6;B9A064;P0CG04;	6	3	Ig lambda-2 chain C regions OS=Homo sapiens GN=IGLC2 PE=1 SV=1	0.61	0.67	0.69		0.62	0.06	0.01
P0CF74	4	1	Ig lambda-6 chain C region OS=Homo sapiens GN=IGLC6 PE=4 SV=1	0.29	0.19	0.15		0.05	0.08	0.01
P01871;P04220	9	9	Ig mu chain C region OS=Homo sapiens GN=IGHM PE=1 SV=3	0.66	0.79	0.95		0.67	0.26	0.01
P17936	4	4	Insulin-like growth factor-binding protein 3 OS=Homo sapiens GN=IGFBP3 PE=1 SV=2	0.03	0.09	0.13		0.04	0.02	0.00
P35858	9	9	Insulin-like growth factor-binding protein complex acid labile subunit OS=Homo sapiens GN=IGFALS PE=1 SV=1	0.09	0.19	0.17		0.06	0.05	0.01
P19823	21	20	Inter-alpha-trypsin inhibitor heavy chain H2 OS=Homo sapiens GN=ITIH2 PE=1 SV=2	0.00	0.18	0.36		0.00	0.02	0.02
Q14624	42	42	Inter-alpha-trypsin inhibitor heavy chain H4 OS=Homo sapiens GN=ITIH4 PE=1 SV=4	0.15	1.71	0.95		0.21	0.78	0.04
P13645	14	14	Keratin, type I cytoskeletal 10 OS=Homo sapiens GN=KRT10 PE=1 SV=6	8.96	0.11	0.05		10.63	0.04	0.00
P19012	2	2	Keratin, type I cytoskeletal 15 OS=Homo sapiens GN=KRT15 PE=1 SV=3	1.52	0.07	0.05		2.15	0.01	0.01
P08779	1	1	Keratin, type I cytoskeletal 16 OS=Homo sapiens GN=KRT16 PE=1 SV=4	0.00	0.02	0.00		0.00	0.01	0.00
Q04695	2	2	Keratin, type I cytoskeletal 17 OS=Homo sapiens GN=KRT17 PE=1 SV=2	0.00	0.06	0.04		0.00	0.02	0.00
P35527	13	12	Keratin, type I cytoskeletal 9 OS=Homo sapiens GN=KRT9 PE=1 SV=3	0.40	0.19	0.04		0.57	0.01	0.00
P04264;P35908	20	18	Keratin, type II cytoskeletal 1 OS=Homo sapiens GN=KRT1 PE=1 SV=6	1.39	0.95	0.83		1.97	0.58	0.00
P01042	25	24	Kininogen-1 OS=Homo sapiens GN=KNG1 PE=1 SV=2	0.16	1.57	1.28		0.23	0.17	0.07
P18428	7	7	Lipopolysaccharide-binding protein OS=Homo sapiens GN=LBP PE=1 SV=3	0.00	0.31	0.18		0.00	0.12	0.01
P36955	13	13	Pigment epithelium-derived factor OS=Homo sapiens GN=SERPINF1 PE=1 SV=4	0.27	0.39	0.29		0.38	0.22	0.01
P03952	25	23	Plasma kallikrein OS=Homo sapiens GN=KLKB1 PE=1 SV=1	0.09	0.50	0.38		0.12	0.09	0.00
P05155	10	10	Plasma protease C1 inhibitor OS=Homo sapiens GN=SERPING1 PE=1 SV=2	0.32	0.46	0.54		0.45	0.35	0.02
P05154	5	5	Plasma serine protease inhibitor OS=Homo sapiens GN=SERPINA5 PE=1 SV=3	0.00	0.15	0.11		0.00	0.01	0.00
P00747;Q02325;Q15195	56	54	Plasminogen OS=Homo sapiens GN=PLG PE=1 SV=2	3.69	1.88	2.29		5.11	0.11	0.11
P02760	5	5	Protein AMBP OS=Homo sapiens GN=AMBP PE=1 SV=1	0.37	0.11	0.22		0.52	0.02	0.02
Q9HD43	1	0	Receptor-type tyrosine-protein phosphatase H OS=Homo sapiens GN=PTPRH PE=1 SV=3	0.00	0.00	0.00		0.00	0.00	0.00
P49908	4	4	Selenoprotein P OS=Homo sapiens GN=SELENOP PE=1 SV=3	0.00	0.26	0.23		0.00	0.07	0.00
P02768	55	54	Serum albumin OS=Homo sapiens GN=ALB PE=1 SV=2	16.92	9.14	9.66		20.95	0.78	0.49
P27169	10	10	Serum paraoxonase/arylesterase 1 OS=Homo sapiens GN=PON1 PE=1 SV=3	1.48	0.25	0.39		2.10	0.04	0.06
Q9H1Z9	1	1	Tetraspanin-10 OS=Homo sapiens GN=TSPAN10 PE=2 SV=1	0.00	0.43	1.04		0.00	0.20	0.22
Q9H0R3	3	2	Transmembrane protein 222 OS=Homo sapiens GN=TMEM222 PE=1 SV=2	0.00	0.40	0.36		0.00	0.03	0.03
P02774	29	28	Vitamin D-binding protein OS=Homo sapiens GN=GC PE=1 SV=1	0.29	1.07	0.58		0.13	0.05	0.02
P04004	20	19	Vitronectin OS=Homo sapiens GN=VTN PE=1 SV=1	0.17	5.48	3.21		0.25	0.53	0.19
				100.00	100.00	100.00				

Figure S5.36. Average amount in % and the standard deviation of all identified proteins adsorbed to lipo-dendron and lipo-dendrimer in blood plasma

				Average (%), technical triplicates				Std,technical triplicates		
Accession	Peptide count	Unique peptides	Description	PS-NH2	PS-Dendron	PS-Dendrimer		PS-NH2	PS-Dendron	PS-Dendrimer
P16885	6	6	1-phosphatidylinositol 4,5-bisphosphate phosphodiesterase gamma-2 OS=Homo sapiens GN=PLCG2 PE=1 SV=4	0.23	1.67	0.64		0.03	0.23	0.45
P43652	2	2	Afamin OS=Homo sapiens GN=AFM PE=1 SV=1	0.03	0.05	0.02		0.00	0.01	0.01
P01009	6	6	Alpha-1-antitrypsin OS=Homo sapiens GN=SERPINA1 PE=1 SV=3	0.06	0.11	0.06		0.01	0.01	0.05
P02765	9	9	Alpha-2-HS-glycoprotein OS=Homo sapiens GN=AHSG PE=1 SV=1	0.18	0.91	0.28		0.01	0.02	0.03
P03950	2	2	Angiogenin OS=Homo sapiens GN=ANG PE=1 SV=1	0.01	0.07	0.09		0.00	0.01	0.04
P02647	35	30	Apolipoprotein A-I OS=Homo sapiens GN=APOA1 PE=1 SV=1	8.66	3.55	3.02		0.92	0.06	1.11
P02652	5	5	Apolipoprotein A-II OS=Homo sapiens GN=APOA2 PE=1 SV=1	0.19	0.10	0.05		0.03	0.01	0.00
P06727	35	35	Apolipoprotein A-IV OS=Homo sapiens GN=APOA4 PE=1 SV=3	2.41	0.89	1.22		0.05	0.04	0.47
P04114	135	129	Apolipoprotein B-100 OS=Homo sapiens GN=APOB PE=1 SV=2	0.42	1.62	1.35		0.03	0.09	0.06
P02656	2	2	Apolipoprotein C-III OS=Homo sapiens GN=APOC3 PE=1 SV=1	2.04	1.52	0.68		0.28	0.11	0.54
P02649	22	22	Apolipoprotein E OS=Homo sapiens GN=APOE PE=1 SV=1	1.07	0.31	0.25		0.15	0.04	0.14
P02730	12	12	Band 3 anion transport protein OS=Homo sapiens GN=SLC4A1 PE=1 SV=3	0.13	0.15	0.22		0.01	0.01	0.04
P02749	16	15	Beta-2-glycoprotein 1 OS=Homo sapiens GN=APOH PE=1 SV=3	0.11	1.71	1.93		0.01	0.03	0.20
P04003	12	9	C4b-binding protein alpha chain OS=Homo sapiens GN=C4BPA PE=1 SV=2	0.28	0.21	0.14		0.03	0.01	0.04
P15169	3	3	Carboxypeptidase N catalytic chain OS=Homo sapiens GN=CPN1 PE=1 SV=1	0.40	0.26	0.23		0.05	0.04	0.14
O43866	5	5	CD5 antigen-like OS=Homo sapiens GN=CD5L PE=1 SV=1	0.05	0.04	0.04		0.00	0.00	0.01
P10909	24	23	Clusterin OS=Homo sapiens GN=CLU PE=1 SV=1	10.01	2.51	3.43		0.25	0.07	0.49
P00740	11	10	Coagulation factor IX OS=Homo sapiens GN=F9 PE=1 SV=2	0.20	0.36	0.19		0.03	0.02	0.08
P03951	15	15	Coagulation factor XI OS=Homo sapiens GN=F11 PE=1 SV=1	0.02	0.22	0.23		0.00	0.00	0.01
P05160	4	4	Coagulation factor XIII B chain OS=Homo sapiens GN=F13B PE=1 SV=3	0.00	0.04	0.02		0.00	0.00	0.01
P00736	6	6	Complement C1r subcomponent OS=Homo sapiens GN=C1R PE=1 SV=2	0.01	0.04	0.06		0.00	0.00	0.02
P06681	5	4	Complement C2 OS=Homo sapiens GN=C2 PE=1 SV=2	0.02	0.09	0.16		0.00	0.01	0.04
P01024	84	82	Complement C3 OS=Homo sapiens GN=C3 PE=1 SV=2	0.69	0.69	1.21		0.03	0.04	0.24
P0C0L5	45	7	Complement C4-B OS=Homo sapiens GN=C4B PE=1 SV=2	0.30	0.27	0.37		0.03	0.03	0.07
P13671	14	13	Complement component C6 OS=Homo sapiens GN=C6 PE=1 SV=3	0.35	1.01	0.76		0.04	0.08	0.31
P02748	12	12	Complement component C9 OS=Homo sapiens GN=C9 PE=1 SV=2	0.10	0.15	0.15		0.00	0.00	0.01
P00751	5	5	Complement factor B OS=Homo sapiens GN=CFB PE=1 SV=2	0.01	0.06	0.03		0.00	0.01	0.00
P08603;Q02985	45	40	Complement factor H OS=Homo sapiens GN=CFH PE=1 SV=4	0.02	0.54	0.74		0.00	0.05	0.14
Q03591;P36980	13	7	Complement factor H-related protein 1 OS=Homo sapiens GN=CFHR1 PE=1 SV=2	0.16	1.09	1.10		0.01	0.09	0.27
Q7Z5Q1	3	3	Cytoplasmic polyadenylation element-binding protein 2 OS=Homo sapiens GN=CPEB2 PE=2 SV=3	0.00	0.05	0.03		0.00	0.01	0.01
Q5TAQ9	4	2	DDB1- and CUL4-associated factor 8 OS=Homo sapiens GN=DCAF8 PE=1 SV=1	0.10	0.14	0.08		0.01	0.05	0.03
Q3B726	3	3	DNA-directed RNA polymerase I subunit RPA43 OS=Homo sapiens GN=TWISTNB PE=1 SV=1	0.02	0.05	0.01		0.01	0.01	0.01
P02671	52	49	Fibrinogen alpha chain OS=Homo sapiens GN=FGA PE=1 SV=2	1.96	10.78	10.82		0.03	0.41	1.69
P02675	55	55	Fibrinogen beta chain OS=Homo sapiens GN=FGB PE=1 SV=2	2.31	12.63	12.03		0.05	0.21	0.73
P02679	34	30	Fibrinogen gamma chain OS=Homo sapiens GN=FGG PE=1 SV=3	3.10	13.94	15.11		0.13	0.54	2.12
P02751	16	15	Fibronectin OS=Homo sapiens GN=FN1 PE=1 SV=4	0.08	0.37	0.13		0.01	0.02	0.09
P06396	26	26	Gelsolin OS=Homo sapiens GN=GSN PE=1 SV=1	0.11	0.47	0.60		0.01	0.03	0.07
Q9H0R5	4	3	Guanylate-binding protein 3 OS=Homo sapiens GN=GBP3 PE=1 SV=3	0.09	0.05	0.03		0.03	0.01	0.02
P00738;P00739	3	3	Haptoglobin OS=Homo sapiens GN=HP PE=1 SV=1	0.06	0.09	0.07		0.00	0.00	0.03
Q96MM6	2	2	Heat shock 70 kDa protein 12B OS=Homo sapiens GN=HSPA12B PE=1 SV=2	0.06	0.27	0.07		0.04	0.21	0.08
P02790	11	11	Hemopexin OS=Homo sapiens GN=HPX PE=1 SV=2	0.09	0.40	0.40		0.02	0.01	0.08
Q04756	4	4	Hepatocyte growth factor activator OS=Homo sapiens GN=HGFAC PE=1 SV=1	0.01	0.07	0.10		0.00	0.01	0.01
P04196	14	14	Histidine-rich glycoprotein OS=Homo sapiens GN=HRG PE=1 SV=1	0.04	1.04	1.06		0.01	0.01	0.18
Q14520	10	10	Hyaluronan-binding protein 2 OS=Homo sapiens GN=HABP2 PE=1 SV=1	0.63	3.19	1.06		0.04	0.16	0.48
P01876	12	5	Ig alpha-1 chain C region OS=Homo sapiens GN=IGHA1 PE=1 SV=2	0.40	0.48	0.44		0.02	0.01	0.03
P01877	9	2	Ig alpha-2 chain C region OS=Homo sapiens GN=IGHA2 PE=1 SV=3	0.04	0.06	0.04		0.00	0.00	0.01
P01857	11	4	Ig gamma-1 chain C region OS=Homo sapiens GN=IGHG1 PE=1 SV=1	0.98	1.70	1.42		0.04	0.08	0.13
P01859	11	5	Ig gamma-2 chain C region OS=Homo sapiens GN=IGHG2 PE=1 SV=2	0.77	0.67	0.66		0.03	0.01	0.04
P01860	13	4	Ig gamma-3 chain C region OS=Homo sapiens GN=IGHG3 PE=1 SV=2	0.15	0.30	0.39		0.01	0.02	0.08
P01861	11	2	Ig gamma-4 chain C region OS=Homo sapiens GN=IGHG4 PE=1 SV=1	0.02	0.05	0.04		0.00	0.00	0.01
P01834	6	6	Ig kappa chain C region OS=Homo sapiens GN=IGKC PE=1 SV=1	1.44	2.29	1.83		0.06	0.15	0.12
V8Q6;P0CF74;P0C	7	2	Ig lambda-3 chain C regions OS=Homo sapiens GN=IGLC3 PE=1 SV=1	1.22	1.86	1.00		0.23	0.06	0.09
P01871	14	5	Ig mu chain C region OS=Homo sapiens GN=IGHM PE=1 SV=3	0.70	0.41	0.50		0.02	0.01	0.02
P04220	11	2	Ig mu heavy chain disease protein OS=Homo sapiens PE=1 SV=1	0.22	0.31	0.24		0.00	0.04	0.10
P17936	2	2	Insulin-like growth factor-binding protein 3 OS=Homo sapiens GN=IGFBP3 PE=1 SV=2	0.01	0.05	0.05		0.01	0.00	0.04
P19823	4	2	Inter-alpha-trypsin inhibitor heavy chain H2 OS=Homo sapiens GN=ITIH2 PE=1 SV=2	0.07	0.10	0.06		0.02	0.00	0.01
Q14624	41	40	Inter-alpha-trypsin inhibitor heavy chain H4 OS=Homo sapiens GN=ITIH4 PE=1 SV=4	0.40	0.67	1.21		0.07	0.02	0.24
P01042	22	22	Kininogen-1 OS=Homo sapiens GN=KNG1 PE=1 SV=2	0.11	1.04	0.70		0.01	0.03	0.05
P18428	10	10	Lipopolysaccharide-binding protein OS=Homo sapiens GN=LBP PE=1 SV=3	0.05	0.26	0.53		0.01	0.01	0.10
P51884	6	6	Lumican OS=Homo sapiens GN=LUM PE=1 SV=2	0.17	0.06	0.08		0.02	0.01	0.02
Q14934	2	2	Nuclear factor of activated T-cells, cytoplasmic 4 OS=Homo sapiens GN=NFATC4 PE=1 SV=2	0.09	0.03	0.02		0.00	0.01	0.01
Q9UG56	2	2	Phosphatidylserine decarboxylase proenzyme, mitochondrial OS=Homo sapiens GN=PISD PE=2 SV=4	0.15	0.35	0.25		0.02	0.01	0.05
P03952	13	12	Plasma kallikrein OS=Homo sapiens GN=KLKB1 PE=1 SV=1	0.02	0.12	0.10		0.00	0.00	0.06
P00747	26	26	Plasminogen OS=Homo sapiens GN=PLG PE=1 SV=2	0.02	0.34	0.25		0.00	0.01	0.07
Q6S8J3	5	2	POTE ankyrin domain family member E OS=Homo sapiens GN=POTEE PE=2 SV=3	0.08	0.04	0.02		0.01	0.00	0.01
Q6S5H5	3	2	POTE ankyrin domain family member G OS=Homo sapiens GN=POTEG PE=2 SV=5	0.04	0.07	0.03		0.07	0.06	0.03
P27918	5	5	Properdin OS=Homo sapiens GN=CFP PE=1 SV=2	0.06	0.12	0.07		0.01	0.01	0.03
P02760	3	3	Protein AMBP OS=Homo sapiens GN=AMBP PE=1 SV=1	0.01	0.03	0.02		0.00	0.00	0.00
Q92954	15	12	Proteoglycan 4 OS=Homo sapiens GN=PRG4 PE=1 SV=2	0.60	0.34	0.36		0.25	0.02	0.00
P00734	3	2	Prothrombin OS=Homo sapiens GN=F2 PE=1 SV=2	0.04	0.05	0.04		0.01	0.00	0.01
Q99969	3	3	Retinoic acid receptor responder protein 2 OS=Homo sapiens GN=RARRES2 PE=1 SV=1	0.01	0.08	0.08		0.00	0.01	0.02
Q13103	5	4	Secreted phosphoprotein 24 OS=Homo sapiens GN=SPP2 PE=1 SV=1	0.15	0.03	0.02		0.02	0.01	0.01
P49908	4	3	Selenoprotein P OS=Homo sapiens GN=SELENOP PE=1 SV=3	0.01	0.09	0.03		0.00	0.01	0.02
P02787	22	20	Serotransferrin OS=Homo sapiens GN=TF PE=1 SV=3	0.05	0.29	0.14		0.00	0.01	0.07
P02768;Q92985	65	58	Serum albumin OS=Homo sapiens GN=ALB PE=1 SV=2	46.77	14.04	11.69		1.29	0.56	0.91
P0DJI8	6	2	Serum amyloid A-1 protein OS=Homo sapiens GN=SAA1 PE=1 SV=1	0.02	0.05	0.05		0.00	0.00	0.02
P0DJI9	5	2	Serum amyloid A-2 protein OS=Homo sapiens GN=SAA2 PE=1 SV=1	0.04	0.13	0.09		0.00	0.02	0.02
P27169	11	11	Serum paraoxonase/arylesterase 1 OS=Homo sapiens GN=PON1 PE=1 SV=3	0.19	0.08	0.08		0.00	0.00	0.01
Q92563	4	4	Testican-2 OS=Homo sapiens GN=SPOCK2 PE=1 SV=1	0.23	0.59	0.66		0.03	0.04	0.12
P02766	8	8	Transthyretin OS=Homo sapiens GN=TTR PE=1 SV=1	0.18	0.38	0.59		0.01	0.02	0.00
P02774	30	29	Vitamin D-binding protein OS=Homo sapiens GN=GC PE=1 SV=1	0.61	1.01	0.56		0.04	0.08	0.04
P04070	4	3	Vitamin K-dependent protein C OS=Homo sapiens GN=PROC PE=1 SV=1	0.05	0.00	0.00		0.01	0.00	0.00
P04004	26	25	Vitronectin OS=Homo sapiens GN=VTN PE=1 SV=1	6.07	7.08	14.96		0.06	0.17	0.56
Q8N9V3	3	2	WD repeat, SAM and U-box domain-containing protein 1 OS=Homo sapiens GN=WDSUB1 PE=1 SV=3	0.10	0.04	0.02		0.01	0.02	0.01
Q6ZN30	3	3	Zinc finger protein basonuclin-2 OS=Homo sapiens GN=BNC2 PE=1 SV=1	0.82	0.57	0.39		0.42	0.05	0.20
				100.00	100.00	100.00	0.00	5.27	4.35	13.96

Figure S5.37. Average amount in % and the standard deviation of all identified proteins adsorbed to PS-dendron and PS-dendrimer in blood plasma.

5.6 References

[1] R. Lipowsky, *Nature* **1991**, *349*, 475-481.
[2] D. Eisenberg, W. Wilcox, A. D. McLachlan, *J. Cell. Biochem.* **1986**, *31*, 11-17.
[3] A. Dehsorkhi, V. Castelletto, I. W. Hamley, *J. Pept. Sci.* **2014**, *20*, 453-467.
[4] S. Zhang, *Biotechnol. Adv.* **2002**, *20*, 321-339.
[5] T. Cedervall, I. Lynch, S. Lindman, T. Berggård, E. Thulin, H. Nilsson, K. A. Dawson, S. Linse, *Proc. Natl. Acad. Sci. U. S. A.* **2007**, *104*, 2050-2055.
[6] J. Müller, K. N. Bauer, D. Prozeller, J. Simon, V. Mailänder, F. R. Wurm, S. Winzen, K. Landfester, *Biomaterials* **2017**, *115*, 1-8.
[7] S. Tenzer, D. Docter, J. Kuharev, A. Musyanovych, V. Fetz, R. Hecht, F. Schlenk, D. Fischer, K. Kiouptsi, C. Reinhardt, K. Landfester, H. Schild, M. Maskos, S. K. Knauer, R. H. Stauber, *Nat. Nanotechnol.* **2013**, *8*, 772-781.
[8] S. Ritz, S. Schöttler, N. Kotman, G. Baier, A. Musyanovych, J. Kuharev, K. Landfester, H. Schild, O. Jahn, S. Tenzer, V. Mailänder, *Biomacromolecules* **2015**, *16*, 1311-1321.
[9] S. Schöttler, G. Becker, S. Winzen, T. Steinbach, K. Mohr, K. Landfester, V. Mailänder, F. R. Wurm, *Nat. Nanotechnol.* **2016**, *11*, 372-377.
[10] Y. T. Ho, N. A. Azman, F. W. Y. Loh, G. K. T. Ong, G. Engudar, S. A. Kriz, J. C. Y. Kah, *Bioconjugate Chem.* **2018**, *29*, 3923-3934.
[11] M. P. Monopoli, C. Åberg, A. Salvati, K. A. Dawson, *Nat. Nanotechnol.* **2012**, *7*, 779-786.
[12] O. Uzun, Y. Hu, A. Verma, S. Chen, A. Centrone, F. Stellacci, *Chem. Commun.* **2008**, 196-198.
[13] A. Verma, O. Uzun, Y. Hu, Y. Hu, H.-S. Han, N. Watson, S. Chen, D. J. Irvine, F. Stellacci, *Nat. Mater.* **2008**, *7*, 588-595.
[14] L. Guerrini, A. R. Alvarez-Puebla, N. Pazos-Perez, *Materials* **2018**, *11*.
[15] B. K. Nanjwade, H. M. Bechra, G. K. Derkar, F. V. Manvi, V. K. Nanjwade, *Eur. J. Pharm. Sci.* **2009**, *38*, 185-196.
[16] R. Esfand, D. A. Tomalia, *Drug Discov. Today* **2001**, *6*, 427-436.
[17] S. Svenson, D. A. Tomalia, *Adv. Drug Deliver. Rev.* **2012**, *64, Supplement*, 102-115.
[18] R. Stangenberg, Y. Wu, J. Hedrich, D. Kurzbach, D. Wehner, G. Weidinger, S. L. Kuan, M. I. Jansen, F. Jelezko, H. J. Luhmann, D. Hinderberger, T. Weil, K. Müllen, *Adv. Healthcare Mater.* **2015**, *4*, 377-384.
[19] Z. Mhlwatika, B. A. Aderibigbe, *Molecules* **2018**, *23*, 2205.
[20] J. Yang, Q. Zhang, H. Chang, Y. Cheng, *Chem. Rev.* **2015**, *115*, 5274-5300.
[21] M. A. Kostiainen, O. Kasyutich, J. J. L. M. Cornelissen, R. J. M. Nolte, *Nat. Chem.* **2010**, *2*, 394-399.
[22] G. Doni, M. A. Kostiainen, A. Danani, G. M. Pavan, *Nano Lett.* **2011**, *11*, 723-728.
[23] R. Stangenberg, I. Saeed, S. L. Kuan, M. Baumgarten, T. Weil, M. Klapper, K. Müllen, *Macromol. Rapid Commun.* **2014**, *35*, 152-160.
[24] B. A. G. Hammer, K. Müllen, *J. Nanopart. Res.* **2018**, *20*, 262.
[25] P. Carbone, F. Negri, F. Müller-Plathe, *Macromolecules* **2007**, *40*, 7044-7055.
[26] Y. Wu, L. Li, L. Frank, J. Wagner, P. Andreozzi, B. Hammer, M. D'Alicarnasso, M. Pelliccia, W. Liu, S. Chakrabortty, S. Krol, J. Simon, K. Landfester, S. L. Kuan, F. Stellacci, K. Müllen, F. Kreppel, T. Weil, *ACS Nano* **2019**, *13*, 8749-8759.
[27] W. S. M. Wold, K. Toth, *Curr. Gene Ther.* **2013**, *13*, 421-433.
[28] R. G. Crystal, *Hum. Gene Ther.* **2014**, *25*, 3-11.
[29] C. S. Lee, E. S. Bishop, R. Zhang, X. Yu, E. M. Farina, S. Yan, C. Zhao, Z. Zheng, Y. Shu, X. Wu, J. Lei, Y. Li, W. Zhang, C. Yang, K. Wu, Y. Wu, S. Ho, A.

Athiviraham, M. J. Lee, J. M. Wolf, R. R. Reid, T.-C. He, *Genes Dis.* **2017**, *4*, 43-63.
[30] J. N. Glasgow, M. Everts, D. T. Curiel, *Cancer Gene Ther.* **2006**, *13*, 830-844.
[31] C. R. O'Riordan, A. Lachapelle, C. Delgado, V. Parkes, S. C. Wadsworth, A. E. Smith, G. E. Francis, *Hum. Gene Ther.* **1999**, *10*, 1349-1358.
[32] M. A. Croyle, Q.-C. Yu, J. M. Wilson, *Hum. Gene Ther.* **2000**, *11*, 1713-1722.
[33] Y. Wu, Anthony P. West, Helen J. Kim, Matthew E. Thornton, Andrew B. Ward, Pamela J. Bjorkman, *Cell Rep.* **2013**, *5*, 1443-1455.
[34] S. J. Everse, G. Spraggon, L. Veerapandian, M. Riley, R. F. Doolittle, *Biochemistry* **1998**, *37*, 8637-8642.
[35] J. Park, M. S. Kim, D. H. Shin, DOI: 10.2210/pdb5z0b/pdb, **2018**.
[36] U. M. Wiesler, A. J. Berresheim, F. Morgenroth, G. Lieser, K. Müllen, *Macromolecules* **2001**, *34*, 187-199.
[37] F. Morgenroth, A. J. Berresheim, M. Wagner, K. Müllen, *Chem. Commun.* **1998**, 1139-1140.
[38] G. Mihov, I. Scheppelmann, K. Müllen, *J. Org. Chem.* **2004**, *69*, 8029-8037.
[39] A. H. Baker, J. H. McVey, S. N. Waddington, N. C. Di Paolo, D. M. Shayakhmetov, *Mol. Ther.* **2007**, *15*, 1410-1416.
[40] C. Weber, M. Voigt, J. Simon, A.-K. Danner, H. Frey, V. Mailänder, M. Helm, S. Morsbach, K. Landfester, *Biomacromolecules* **2019**, *20*, 2989-2999.
[41] M. Kokkinopoulou, J. Simon, K. Landfester, V. Mailänder, I. Lieberwirth, *Nanoscale* **2017**, *9*, 8858-8870.
[42] M. Okuno, M. Mezger, R. Stangenberg, M. Baumgarten, K. Müllen, M. Bonn, E. H. G. Backus, *Langmuir* **2015**, *31*, 1980-1987.
[43] J. Simon, T. Wolf, K. Klein, K. Landfester, F. R. Wurm, V. Mailänder, *Angew. Chem. Int. Ed.* **2018**, *57*, 5548-5553.
[44] D. E. Owens, N. A. Peppas, *Int. J. Pharm.* **2006**, *307*, 93-102.
[45] S. Schöttler, K. Klein, K. Landfester, V. Mailänder, *Nanoscale* **2016**, *8*, 5526-5536.
[46] V. Mirshafiee, R. Kim, M. Mahmoudi, M. L. Kraft, *Int. J. Biochem. Cell Biol.* **2016**, *75*, 188-195.
[47] G. Caracciolo, F. Cardarelli, D. Pozzi, F. Salomone, G. Maccari, G. Bardi, A. L. Capriotti, C. Cavaliere, M. Papi, A. Laganà, *ACS Appl. Mater. Interfaces* **2013**, *5*, 13171-13179.
[48] K. Sivakumar, F. Xie, B. M. Cash, S. Long, H. N. Barnhill, Q. Wang, *Org. Lett.* **2004**, *6*, 4603-4606.
[49] V. O. Rodionov, S. I. Presolski, S. Gardinier, Y.-H. Lim, M. G. Finn, *J. Am. Chem. Soc.* **2007**, *129*, 12696-12704.
[50] V. Hong, S. I. Presolski, C. Ma, M. G. Finn, *Angew. Chem. Int. Ed.* **2009**, *48*, 9879-9883.
[51] C. Besanceney-Webler, H. Jiang, T. Zheng, L. Feng, D. Soriano del Amo, W. Wang, L. M. Klivansky, F. L. Marlow, Y. Liu, P. Wu, *Angew. Chem. Int. Ed.* **2011**, *50*, 8051-8056.
[52] C. Uttamapinant, A. Tangpeerachaikul, S. Grecian, S. Clarke, U. Singh, P. Slade, K. R. Gee, A. Y. Ting, *Angew. Chem. Int. Ed.* **2012**, *51*, 5852-5856.
[53] M. L. Keshtov, E. I. Mal'tsev, D. V. Marochkin, A. V. Muranov, A. R. Khokhlov, *J. Polym. Sci. Part B Polym. Phys.* **2012**, *54*, 289-296.
[54] D. Baumann, D. Hofmann, S. Nullmeier, P. Panther, C. Dietze, A. Musyanovych, S. Ritz, K. Landfester, V. Mailänder, *Nanomedicine* **2012**, *8*, 699-713.
[55] S. Lerch, M. Dass, A. Musyanovych, K. Landfester, V. Mailänder, *Eur. J. Pharm. Biopharm.* **2013**, *84*, 265-274.
[56] D. Hofmann, S. Tenzer, M. B. Bannwarth, C. Messerschmidt, S.-F. Glaser, H. Schild, K. Landfester, V. Mailänder, *ACS Nano* **2014**, *8*, 10077-10088.
[57] S. Tenzer, *ACS Nano* **2011**, *5*, 7155-7167.

[58] R. A. Bradshaw, A. L. Burlingame, S. Carr, R. Aebersold, *Mol. Cell. Proteomics* **2006**, *5*, 787.
[59] M. Kokkinopoulou, J. Simon, K. Landfester, V. Mailander, I. Lieberwirth, *Nanoscale* **2017**, *9*, 8858-8870.
[60] J. C. Silva, M. V. Gorenstein, G. Z. Li, J. P. C. Vissers, S. J. Geromanos, *Mol. Cell. Proteomics* **2006**, *5*, 144-156.

6 Amphiphilic Polyphenylene Dendrimer Conjugates Crossing the Blood-Brain Barrier and Inhibiting Aβ Fibrillation

[redacted]

To be submitted

Author Contributions

My contribution was the design, planning and performance of the synthesis of all dendron conjugates as well as the dendronized streptavidin (SA-D) both unlabelled and labelled; the characterization of SA-D including concentration determination, SDS-PAGE, HABA-Assay, agarose gel electrophoresis and analysis of AFM images as well as co-writing of the manuscript. [redacted] performed the Aβ-studies including characterization by TEM, kinetics, CD, and bio-application including cytotoxicity test, TEER test for BBB, cell uptake (*in vivo* together with [redacted], and *in vitro*), cell culture of endothelial cells and neurons including primary cells preparation, contributed in co-writing of the manuscript and draw the scheme. [redacted] measured and optimized conditions for AFM. [redacted] designed the project. [redacted] supervised the project, performed experiments (cell experiments, *in vivo* experiments, staining, and imaging), analyzed data, wrote and corrected the manuscript. [redacted] interpreted some experimental results, aquired funding for the project and revised the manuscript.

Abstract

Drug delivery to the brain for the treatment of neurological disorders is challenging due to restrictive mechanisms at the blood-brain barrier (BBB). Polyphenylene dendrons provide alternating negatively charged sulfonic acid and hydrophobic *n*-propyl amphiphilic surface groups. These amphiphilic groups facilitate interactions with membranes of endothelial cells, blood proteins and might interact with amyloid-beta (Aβ) peptides, which are essential in Alzheimer´s plaque formation. We synthesized dendrimer branches (dendrons) with amphiphilic surface groups that were assembled by the protein streptavidin to form the respective streptavidin-dendron conjugates (**SA-D**). For the first time, we could demonstrate that amphiphilic polyphenylene dendrons and **SA-D** conjugates are transported into the brain after systemic application in mice. We observed vesicular cell uptake in endosomes and good cell compatibility for endothelial and neuronal cells *in vitro*. With a combination of thioflavin T aggregation kinetics, transmission electron microscopy, and circular dichroism spectroscopy we found a direct interaction of the polyphenylene dendron with Aβ peptides leading to inhibition of fibril formation and disassembly of formed Aβ fibrils by the interaction with the secondary structure of the peptide. In consequence, *in vitro* Aβ cytotoxicity for primary murine neurons was significantly inhibited by the amphiphilic dendrons. Our data suggest that amphiphilic polyphenylene dendrons have a high potential to inhibit Aβ fibrillation *in vivo* after passage of the BBB, which is of high relevance for future applications in Alzheimer´s disease.

6.1 Introduction

Alzheimer's disease (AD) is the most common form of dementia associated with plaques and tangles in the brain. This disease accounts for 60-70% of dementia cases and the numbers are rising worldwide. The disease impact for patients, families, and the economy is dramatic, yet, efficient drugs to reverse or stop the pathology of AD are still lacking. Therefore, the investigation of AD pathology and new therapeutic interventions is highly relevant.[1] Following the amyloid hypothesis[2, 3], the appearance of the amyloid-beta-peptide (Aβ) in high brain parenchymal concentrations is an early toxic event in the pathogenesis of AD. In AD, the amyloid precursor protein (APP) is cleaved by proteases. The processing of the transmembrane protein APP releases small Aβ-peptide monomers that accumulate in the brain generating oligomers, protofibrils and finally senile plaques.[2] It has been shown that the amyloid accumulation is followed by neuroinflammation, tau accumulation, metabolism and synaptic dysfunction, neuronal death and cognitive decline.[2, 4] Therefore, drugs inhibiting the early step of oligomer formation would offer high potential to stop AD progression, before the cascade of multiple pathological effects occurs.[4] Another challenge in AD treatment is the development of drugs, which show adequate blood-brain barrier (BBB) permeability, which is essential for treating chronic diseases.[5] Furthermore, to reduce side effects, a noninvasive passage though the BBB is crucial. Consequently, AD therapeutics should combine anti-amyloid properties as well as efficient BBB transport.

Preclinical anti-amyloid strategies have been investigated as Aβ fibrils occur even before the first clinical symptoms appear and neurons are irreversibly damaged. However, the amount of amyloid plaques does not correlate with the disease severity, suggesting that the oligomeric and protofibrillary structures trigger a neurotoxic cascade.[2, 4] Therefore, recent discussions indicate that anti-amyloid strategies targeting toxic oligomeric Aβ aggregation would be most beneficial in the early stages of AD. Several therapeutic approaches reached preclinical development stages, which focus on the reduction of amyloid oligomer levels or the breaking of formed β-sheet fibrils.[4] Current strategies include antibodies for the neutralization of oligomeric species, overexpression of Aβ-degrading enzymes, catalytic antibodies, small molecule inhibitors, and β-sheet blockers.[4, 6] In addition, several concepts on AD treatment based on dendrimers functioning as β-sheet blockers were developed.[7] Dendrimers are macromolecules consisting of a central core, a shell and periphery. Each segment starting from the core is called dendron and each layer of the dendrimer is termed generation. With increasing

generations the dendrimer size and branching is enhanced leading to more functional groups on its periphery.[8] For example, dendrimers consisting of a poly(propylene)imine (PPI), poly(amidoamine) (PAMAM), phosphorus or poly(lysine) scaffold and positively charged terminal groups interact with Aβ fibrils, which affected aggregation and toxicity of Aβ.[9] Cationic dendrimers have several limitations as they are quickly eliminated by both kidney and liver and they reveal cytotoxicity at high concentrations and increasing dendrimer generations due to electrostatic interactions with cellular membranes resulting in nanopores in the membrane. To enhance blood-circulation times and to lower the toxicity, anionic and neutral dendrimers are generally favored.[10]

To address these challenges, negatively charged amphiphilic (also denoted as patchy) polyphenylene dendrimers (PPDs) consisting of alternating sulfonic acid and *n*-propyl groups have been designed and synthesized.[11, 12] Previously, the internalization of amphiphilic PPDs into brain endothelial cells was presented hereby showing their potential for brain delivery.[12] A particular amphiphilic PPD has been shown to bind to the protein-based capsid of adenovirus 5 (Ad5) thus forming a new dendrimer corona. The new PPD corona re-directed the Ad5 biodistribution both *in vitro* and *in vivo* and facilitated uptake into cancer cells, which offers the potential for virus-assisted gene therapy.[13] We have shown previously that the respective amphiphilic dendron (Figure 6.2A) possesses the same cellular uptake and virus binding features as the full PPD. Thus, polyphenylene dendrons could be considered as minimal fragments of a globular PPD revealing similarly high cell viability, interactions with blood serum proteins and virus binding as the full dendrimer. However, dendrons have the advantage that they can be modified easily so that they could be in principal attached to different surfaces.[14]

In this study, we generated an amphiphilic polyphenylene dendron with terminal D-biotin[14] and we assembled four of these dendrons onto the protein streptavidin (**SA-D**). For the dendron (**D**) and the **SA-D** we observed good cell uptake and cell compatibility in a brain endothelial cell line and primary neuronal cells. *In vivo* we could demonstrate brain delivery of amphiphilic polyphenylene dendrons and the corresponding **SA-D** conjugate in a mouse model. Amphiphilic dendrons and the **SA-D** conjugates inhibited Aβ fibril formation as well as induced the disassembly of already formed fibrils *in vitro* and the dendrons even reduced Aβ toxicity in primary murine neuronal cultures. By using the dendron (bio)-conjugates we envision a high potential for treatment of Aβ aggregation in Alzheimer's disease and for **SA-D** a use as drug delivery platform in brain diseases in the future.

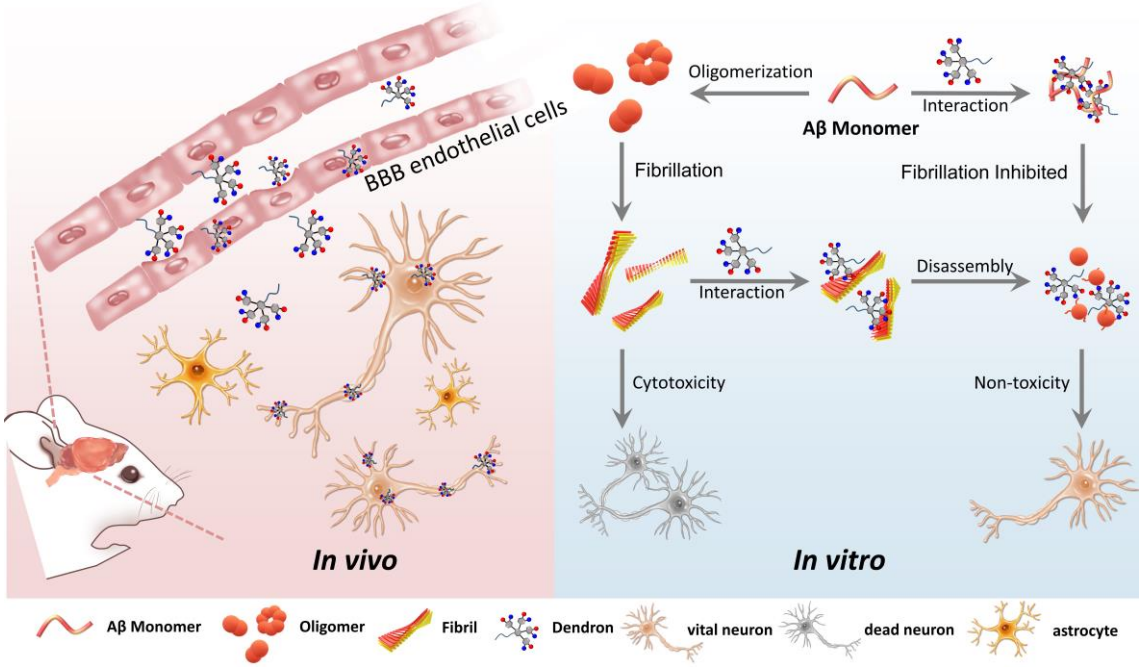

Figure 6.1. Schematic overview of the study. *In vivo* uptake of amphiphilic dendron (**D**) and the streptavidin-dendron conjugate (**SA-D**) was found mainly for endothelial cells and neurons. *In vitro* anti-amyloidogenic activity of **D** and **SA-D** was studied by incubating with $A\beta_{1-42}$ peptide. Inhibition of fiber formation as well as disassembly of formed Aβ fibrils was observed. These Aβ amphiphilic dendron interactions inhibited cytotoxicity of Aβ fibrils in primary murine neuronal cells.

6.2 Results and Discussion

Synthesis and Characterization of Amphiphilic Dendron and SA-D. The synthesis of an amphiphilic polyphenylene dendron with a propargyl-moiety (dendron **1**, **D**), a D-biotin (**biotin-D**, **2**) or a Cy5 chromophore (**Cy5-D**, **3**) at the terminus was published previously (Figure 6.2A).[14] The chemical structures and comprehensive characterization of all dendron conjugates applied herein are summarized in the Supporting Information (SI, Figure S6.1). Four **biotin-D** (**2**) were then assembled on the protein streptavidin (SA) (Figure 6.2A). SA is a homotetrameric protein with four biotin-binding sites and the binding affinity of D-biotin to streptavidin is among the strongest interactions ($K_d \sim 10^{-14}$ M) in nature.[15] The assembly of four biotin-dendrons on streptavidin (Figure 6.2A) affords a hybrid macromolecule with a SA protein core and an amphiphilic dendron shell. In this way, important features such as shape and the number of amphiphilic surface groups could be varied. Moreover, SA is often used as platform in drug delivery as it allows easy preparation of nanocarriers with drugs and targeting or imaging molecules by simple self-assembly in solution.[16] Therefore, **SA-D** could be easily equipped with other substituents. **SA-D** was prepared by the addition of **biotin-D** in

DMSO to a solution of SA (or Cy5-labelled SA (**Cy5-SA-D**) for imaging experiments) (SI, Figure S6.2–Figure S6.4) in phosphate buffer at pH 7.4. After incubation of the **SA-D** mixture for 2 h, **SA-D** was purified by size exclusion chromatography (SEC) to remove excessive amounts of dendron. **Cy5-SA-D** (SI, Figure S6.2 – Figure S6.4) was prepared and purified following the same procedure. SA complexed with free D-biotin (**SA-B**) served as a reference (SI, Figure S6.5). The occupation of D-biotin binding sites of SA by the **biotin-Ds** was verified by the addition of 2-[(4-hydroxyphenyl)-diazenyl]benzoic acid (HABA). HABA binds to free D-biotin binding-sites resulting in an absorption band at 500 nm (orange color).[17] When adding HABA to **SA-D** this absorption band was absent as also observed for **SA-B** (yellow color) (Figure 6.2B and Figure S6.6). Moreover, an increase in absorption in the UV region (~250-350 nm) alludes the presence of the aromatic polyphenylene dendrons (Figure 6.2B). These findings indicate the successful occupation of the biotin-binding sites by **biotin-D**. In addition, sodium dodecyl sulfate polyacrylamide gel electrophoresis (SDS-PAGE) analysis of **SA-D** without and with heating and addition of the denaturation agent 1,4-dithio-D-threitol (DTT) confirm the binding of dendrons to SA (Figure 6.2C). The **SA-D** tetrameric complex mainly remained in the loading pockets without the employment of heat. This finding can be explained by aggregation of the **SA-D** conjugate in the MES running buffer. As also observed for **SA-B**, the SA monomer and tetramer of **SA-D** are only separated after heating, which denatures SA so that it disassembles into monomers. The disassembly was reduced for **SA-B** and **SA-D** compared to SA alone as the tetramers coexist with the monomers in the gel. This observation can be attributed to the fact that the biotin-binding increases the thermal stability and resistance of SA against denaturing agents.[18] The successful attachment of the biotin-dendrons was also verified by agarose gel electrophoresis (Figure S6.7). In contrast to SA and **SA-B**, the **SA-D** conjugate did not show any migration in the gel during electrophoresis, as also observed for the SDS-PAGE. In addition, in atomic force microscopy (AFM) and dynamic light scattering (DLS) experiments (Figure 6.2E and Table S6.1) **SA-D** revealed larger sizes compared to the reference **SA-B** (Figure 6.2D and Table S6.1). In 25 mM phosphate buffer at pH 7.4, a hydrodynamic radius (R_h) of 3.3 nm for **SA-B** and 25.1 nm for **SA-D** (Table S6.1) were measured. The ionic strength of the solution also had a significant effect on the hydrodynamic radius (R_h) of the **SA-D** bioconjugate. The application of 50 mM phosphate buffer (PB) at pH 7.4 further decreased the R_h of **SA-D** to 23.8 nm, whereas ultrapure water or 100 mM PB resulted in larger R_h values of 37.3 nm and 32.8 nm respectively. However, the height topographic images by AFM showed an expected size increase from ~3 nm for **SA-B (**Figure 6.2D) to ~5-6 nm for **SA-D** (Figure 6.2E). Previously,

polyphenylene dendrimer protein conjugates always required the addition of detergents to solubilize the hydrophobic polyphenylene scaffold.[19] In contrast, **SA-D** and **Cy5-SA-D** were achieved in aqueous solution after SEC without any auxilaries such as detergents with concentrations up to 17 µM and 30 µM respectively.

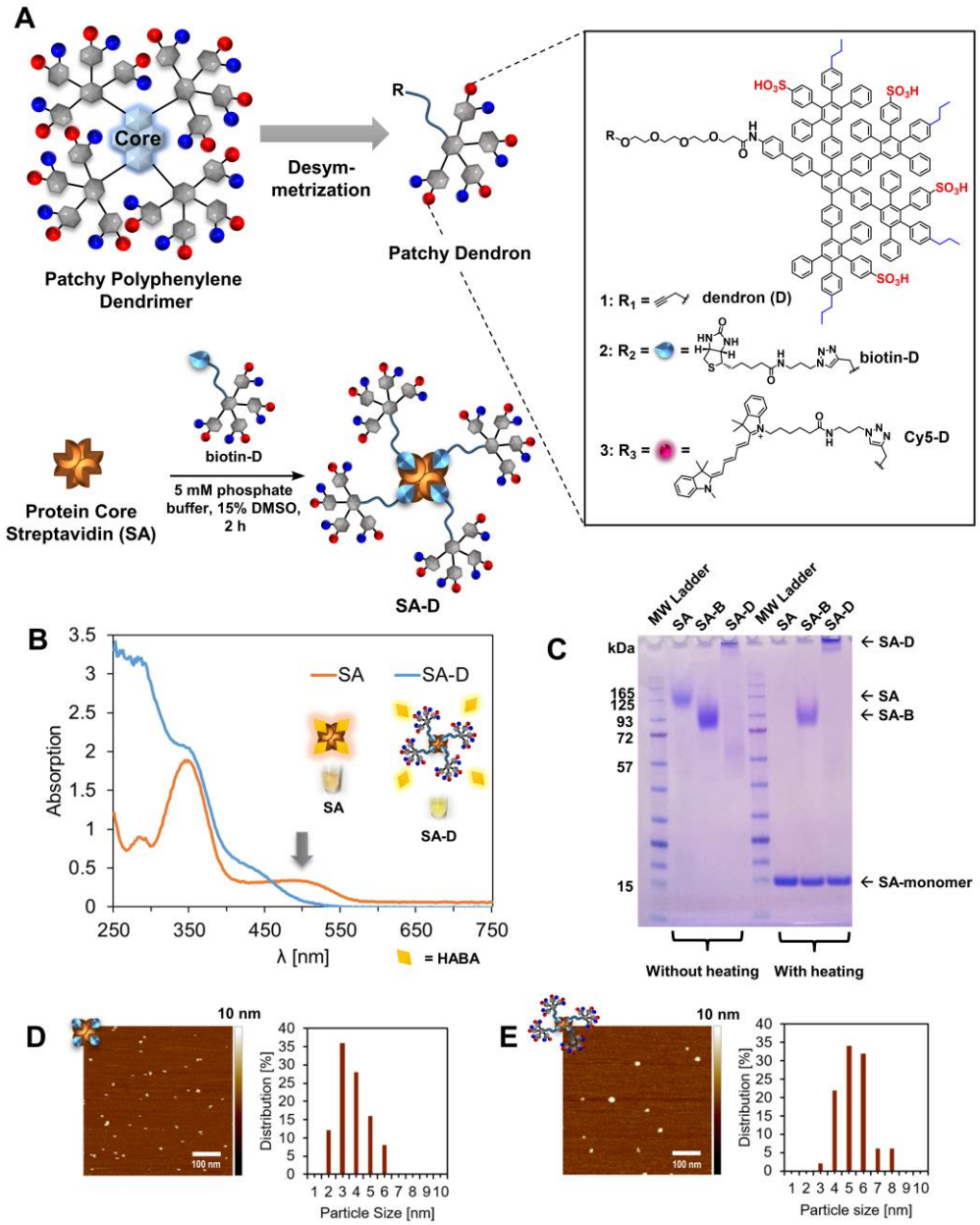

Figure 6.2. Preparation and characterization of **SA-D**. (**A**) Schematic overview of a patchy PPD and patchy dendrons which correspond to one dendritic branch of the entire dendrimer. The focal point of dendron **1** can be functionalized to achieve **biotin-D** (**2**) and **Cy5-D** (**3**).[14] Four equivalents of **biotin-D** (**2**) are supramolecularely bound to SA. (**B**) HABA-Assay shows a distinct absorption band at 500 nm for SA, which is reduced for **SA-D** indicating that all four binding sites have been occupied by dendron **2**. (**C**) SDS-PAGE under heating and non-heating conditions shows the formation of **SA-D** and **SA-B**, respectively. (**D**, **E**) AFM topographic images reveal an increase in height after dendrons bound to SA (**E**) in comparison to free D-biotin complexed to SA (**D**).

Cellular uptake of Dendron and SA-D. For a successful brain delivery across an intact BBB, ideally a transcytotic pathway is addressed.[5] To investigate the molecule´s potential for transcytotic brain delivery an endosomal uptake and trafficking in brain endothelial cells needs to be investigated. Therefore, cellular uptake was first investigated *in vitro* for murine brain endothelial cells in a bEnd.3 cell line (ATCC® CRL-2299™, Manassas, VA, USA). bEnd.3 cells were stained with an endothelial cell marker CD105 (green) and a strong, distinct uptake for **Cy5-D** and **Cy5-SA-D** (both in red) in cellular vesicles could be observed, as shown in Figure 6.3.

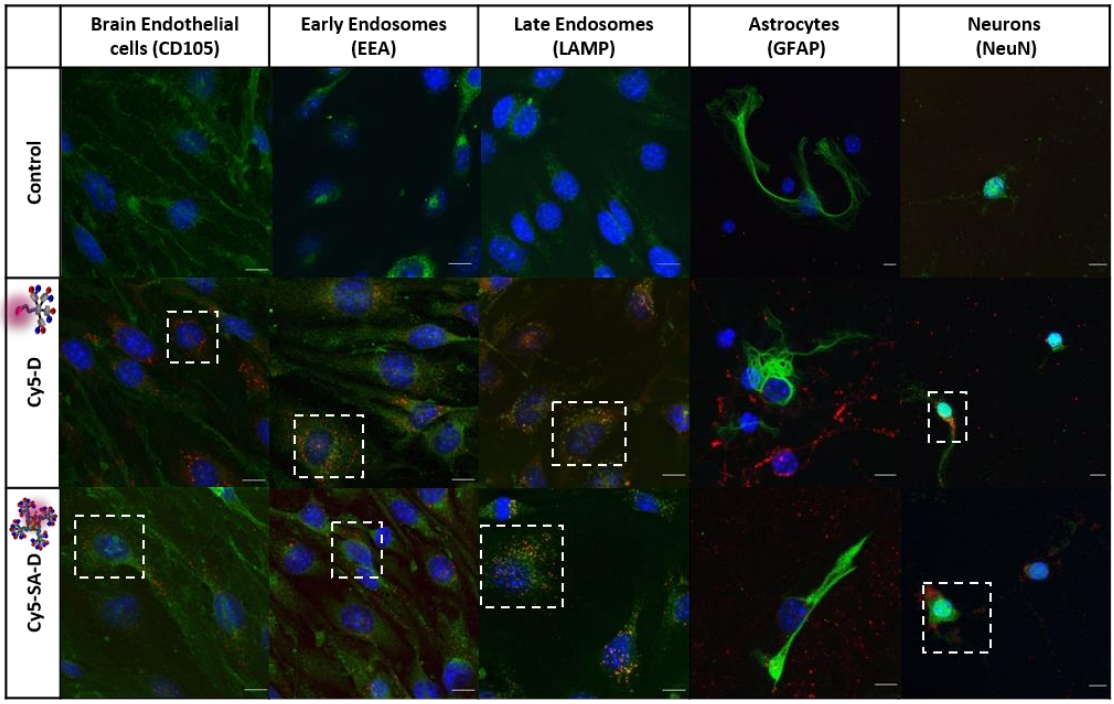

Figure 6.3. Cy5-D and Cy5-SA-D uptake in brain endothelial and neuronal cells *in vitro*. Brain endothelial cells (bEnd.3) and primary murine neuronal cells were incubated with **Cy5-D** (red), **Cy5-SA-D** (red) or PBS for 24 h. Cells were fixed, stained with cell-specific antibody markers for endothelial cells (CD105), astrocytes (GFAP) and neurons (NeuN). Nuclei were stained with DAPI and visualized in blue. Examples of **Cy5-D** and **Cy5-SA-D** positive cells are highlighted in boxes with dashed lines. The scale is 10 µm.

Co-staining for early endosomes (EEA) or for late endosomes (LAMP) revealed that after 24 h **Cy5-D** and **Cy5-SA-D** were mainly localized in late endosomes. From late endosomes, either a release into the cytosol, trafficking to lysosome, or trafficking for endosomal release could occur. Co-localization with early and late endosomes proved the uptake of **Cy5-D** and **Cy5-SA-D** by the endosomal pathway, which would enable a transcytotis for successful brain delivery. After a successful brain delivery, a potential uptake in target cells is interesting in regard to future drug delivery. To address this question, uptake in murine primary glia cells positive for GFAP and NeuN positive primary murine neurons was tested. Confocal imaging revealed a very low uptake in GFAP

positive astrocytes compared to a strong uptake in NeuN positive neurons, which showed a strong uptake into the cytosol as well as into the dendrites and axons (Figure 6.3). If the observed specific uptake for neurons could be confirmed *in vivo*, such observed cell type-specific uptake could be crucial to reduce side effects in other, i.e. non-diseased cells in future clinical applications.

Effects on cell viability and BBB integrity. Before *in vivo* studies can be addressed, the toxicity of the investigated molecules was assessed. Cell compatibility of the unlabelled dendron **1** and **SA-D** was analyzed in cell viability assays (CellTiterGlo) for endothelial cells as well as a murine primary neuronal cell culture. In order to test the cell compatibility of dendron **1** and **SA-D**, bEnd.3 endothelial cells and primary murine neuronal cells were treated for 24 h. Cell vitality was assessed by quantification of ATP levels with CellTiterGlo-Assay. For bEnd.3 cells, the treatment with high dendron **1** concentrations (20 µM, 40 µM) resulted in 93.7 ± 1.3 % and 86.6 ± 4.2 % cell vitality (Figure 6.4A). The incubation of **SA-D** (2.5 µM (binding 10 µM dendron **2**), 5 µM (binding 20 µM dendron **2**)) resulted in a cell vitality of 91.1 ± 3.1 % and 96.3 ± 2.4 %, respectively (Figure 6.4A). Neuronal cells showed a cell vitality of 91 ± 1.4 % and 80 ± 2.8 %, respectively, after dendron **1** incubation (20 µM, 40 µM). For **SA-D**, a vitality of 97.3 ± 2.7 % and 77.8 ± 2.2 % was observed (Figure 6.4B). Cell vitality reduction up to 25 % is usually considered as low toxicity. Hence, the cell compatibility of dendron **1** and **SA-D** is very high, even towards very sensitive primary neurons.

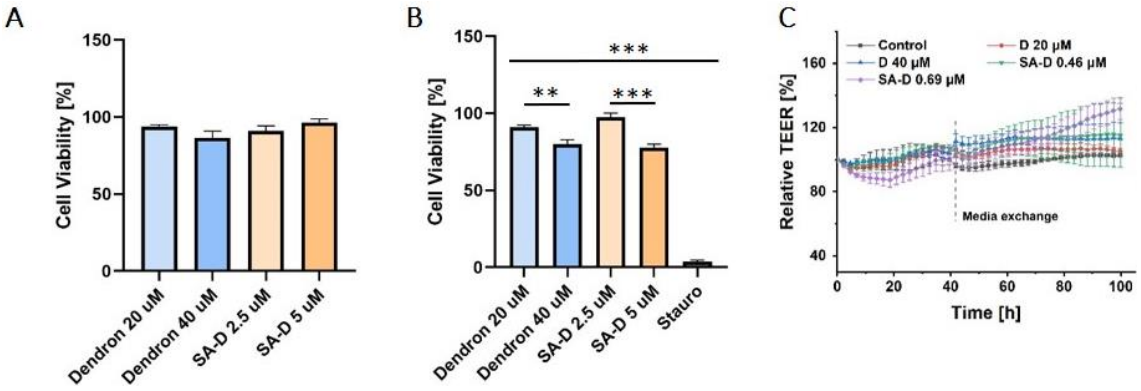

Figure 6.4. Dendron and SA-D toxicity for brain endothelial cells and primary neuronal cells. Cells were incubated with dendron **1**, **SA-D**, PBS or staurosporine (cell toxin for dead cell control) for 24 h. Cell vitality was assessed by CellTiterGlo Assay and is presented in %. Data are presented as mean with SEM (standard error of the mean). n = minimum 6; one-way ANOVA; ns > 0.05, * p ≤ 0.05, ** p ≤ 0.01, *** p ≤ 0.001. (**A**) Brain endothelial cells (bEnd.3), 95 % Confidence Interval (CI) was 90.3 – 97.0 % (**D** 20 µM), 75.9 – 97.3 % (**D** 40 µM), 83.1 – 99.1 % (**SA-D** 2.5 µM) and 90.0 – 103 % (**SA-D** 5 µM). (**B**) Primary murine neuronal cells. 95 % CI was 87.5 – 94.4 % (**D** 20 µM), 72.9 – 87.2 % (**D** 40 µM), 90.3 – 104 % (**SA-D** 2.5 µM) and 72.1 – 83.4 (**SA-D** 5 µM) (**C**) The effects of dendron **1** and **SA-D** on BBB integrity were measured by cell impedance measurements. TEER at 0 h was set to 100 %.

For brain delivery, not only the cell viability of endothelial cells is important, but also the impact on the barrier integrity. BBB integrity was tested in a BBB *in vitro* model measuring transendothelial electrical resistance (TEER) with the cellZscope system (nanoAnalytics). After 24 h, the TEER was 99.63 ± 1.10 % and 101.67 ± 1.41 % for dendron **1** (20 µM and 40 µM) and 102.71 ± 4.72 % and 90.61 ± 4.91 % for **SA-D** (0.46 µM, 0.69 µM). At 40 h, a recovery to 106.99 ± 2.28 % for 0.46 µM **SA-D** could be observed (Figure 6.4C). A long-term observation with media exchange at 42 h clearly indicates a stable barrier up to 100 h. Data of the BBB integrity analysis prove that the dendron had nearly no effect on *in vitro* barrier function and only minor effects and recovery were observed for **SA-D.** For **SA-D** with higher concentration (0.69 µM) the TEER dropped to 89.21 ± 4.81 % after 20 h but recovered to 102.33 ± 5.70 % at 40 h and after media exchange showed an increase to 131.69 ± 6.86 % at 100 h. Non- or minimal changes in TEER values indicated dendron and **SA-D** transport across the BBB by transcytosis without disrupting the tight junctions. Such transcytosis mediated transport, across an intact barrier of the herein investigated dendron and **SA-D** conjugates during drug delivery would be crucial to reduce side effects in future clinical treatment.

In vivo brain uptake of polyphenylene dendron and SA-D conjugates. Next, we have studied the ability of the polyphenylene dendron and its bioconjugate to cross the BBB and reach the brain *in vivo* in mice after systemic application (i.v. injection in the tail vein). We have used the Cy5-labelled dendron **3** (**Cy5-D**) and Cy5-labelled **SA-D** (**Cy5-SA-D**) in order to follow brain delivery (Figure 6.5) and biodistribution (Figure S6.8) by fluorescence microscopy. Mice were injected with **Cy5-D** and **Cy5-SA-D** and 24 h after injection perfused with 4% paraformaldehyde (PFA). Brains were sliced and co-stained for cell-specific markers with commercial antibodies. Anti-endoglin (Anti-CD105) was used for brain endothelial cells, glial fibrillary acidic protein (GFAP) was used for astrocytes and neuronal nuclei (NeuN) was used for neurons. Co-staining for endothelial cells revealed a diffuse uptake of **Cy5-D** or **Cy5-SA-D** (both in red) into the endothelial cells in the mouse brain (Figure 6.5). Distinct strong, vesicular signals for cellular uptake were obtained in neurons positive for NeuN. Very interestingly, very low or no uptake was observed for GFAP positive astrocytes (Figure 6.5 arrows). These data proved the successful delivery of the polyphenylene dendron and its bioconjugate into endothelial and neuronal cells with remarkable selectivity over astrocytes, comparable to the *in vitro* cell uptake data. The differences in cellular uptake could be explained by different uptake mechanisms for these different cell types. Transport into astrocytes often proceeds *via*

phagocytosis, pinocytosis as well as endocytosis. Neurons are not considered phagocytic cells, but they reveal a high synaptic uptake and also endocytosis occurs. Since Aβ possesses not only intracellular but also extracellular cytotoxicity, a strong uptake of the dendron or the SA-dendron conjugate into neurons could likely inhibit toxic effects of intracellular Aβ[20], and would reduce dendron and **SA-D** off-target uptake by the surrounding astrocytes.

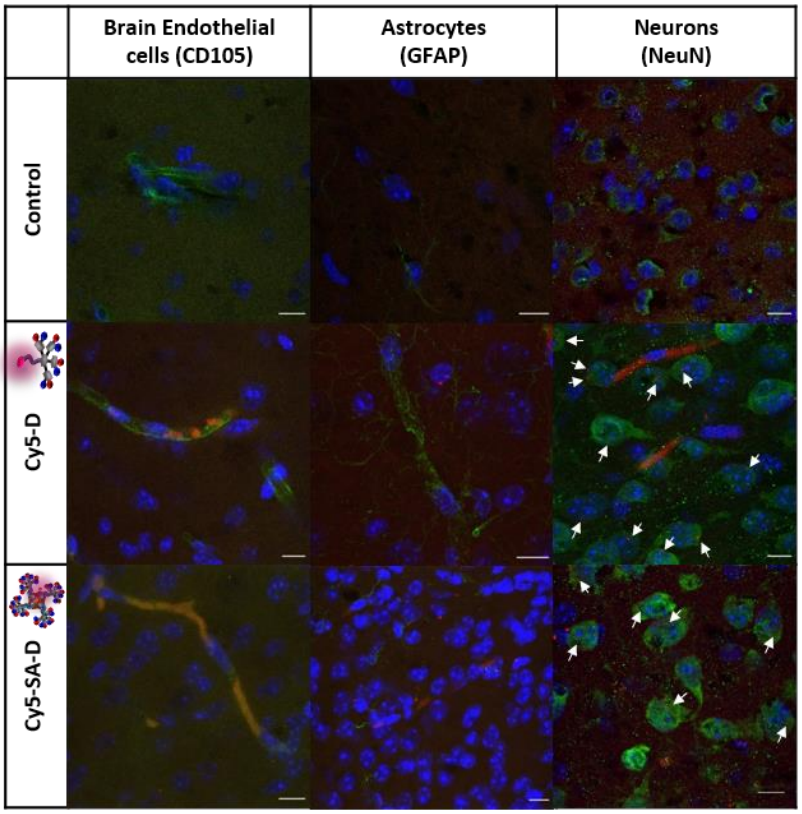

Figure 6.5. Cy5-dendron and Cy5-SA-D delivery to the mouse brain. Mice were injected with **Cy5-D** (red), **Cy5-SA-D** (red) or PBS for control. After 24 h, mice were perfused, brains were sliced and stained with markers: CD105 for brain endothelial cells, GFAP for astrocytes and NeuN for neurons. **Cy5-D** and **Cy5-SA-D** positive cells are highlighted with arrows. Nuclei were stained with DAPI (blue). The scale is 10 µm.

Inhibition of Aβ fibrillation. After showing the successful brain delivery and specific neurons uptake of polyphenylene dendron and **SA-D** both *in vitro* and *in vivo*, we next investigate their anti-amyloid activities to $A\beta_{1\text{-}42}$. Thioflavin T (ThT) was selected as the fluorescent probe to monitor Aβ fibrillation process. ThT could bind specifically to the β-sheets during the fibrillation and show a significant fluorescence enhancement. Such fluorescence intensity increase occurs due to the rotational immobilization of the central C-C bond connecting the benzothiazole and aniline rings[21, 22] during ThT binding to the side chain channels along the axis of the fibrils.[23] The fibrillation process of $A\beta_{1\text{-}42}$ was studied by kinetics experiment, as shown in Figure S6.9A. Aβ monomers of different concentrations were incubated with ThT at 37˚C for 16 h. After 1 h lag phase, exponential

increase of the fluorescence intensity started, indicating that for the supramolecular polymerization reaction of Aβ, the nucleation process ended after 1 h and nuclei (Aβ oligomers) as well as monomers started to form the β-sheet containing fibrils in the elongation phase (exponential phase of the sigmoid curve).[24, 25] After 4-5 h, the fluorescence intensity reached a plateau, which was maintained until 16 h indicating that the fibrillation process was complete after 5 h (Figure S6.9A). The morphology of the Aβ oligomers and fibrils was monitored by TEM imaging. The peptide monomers could not be imaged in TEM due to their small sizes (Figure S6.9B), while the Aβ oligomers showed particle-like and amorphous structures (Figure S6.9C). After 16 h, long fibrils could be observed in the TEM images (Figure S6.9D). These data indicated the time scale for Aβ fibrillation *in vitro* and proved the formation of the Aβ fibrils received by the used fibrillation protocol.

The impact of dendron **1** (**D**) and **SA-D** at different ratios on Aβ fibrillation is presented in Figure 6.6A and B, respectively. For the dendron **1** at 1:1 (**D**:Aβ) molar ratio, a clear decrease of the slope in the exponential phase is observed indicating a slowdown of the elongation process of the fibrillation and less β-sheet formation. Further increasing the amount of Aβ to **D**:Aβ 1:5 and 1:8, the elongation phase and the final amount of Aβ fibrils were still inhibited, for 1:8 the final plateau showed a decrease to 491.8 % compared to 739.8 % for Aβ alone (Figure 6.6A, green and dark magenta line). Since one molecule **SA-D** binds four dendrons, at an equimolar **SA-D**:Aβ ratio fibril formation is completely inhibited (Figure 6.6B, red line). With higher ratio of Aβ, 1:5 and 1:8 (**SA-D**:Aβ), the fibril elongation phase was still reduced leading in the case of **SA-D**:Aβ 1:8 to a decrease in the final fibril concentration to 490.6 %, compared to 739.8 % for Aβ alone (Figure 6.6B, dark magenta and grey line). TEM imaging results were also consistent with these kinetics experiments. At equimolar ratios fibrillation was inhibited, while with a further increase of Aβ, fibrils were formed again, which was imaged in TEM (Figure 6.6).

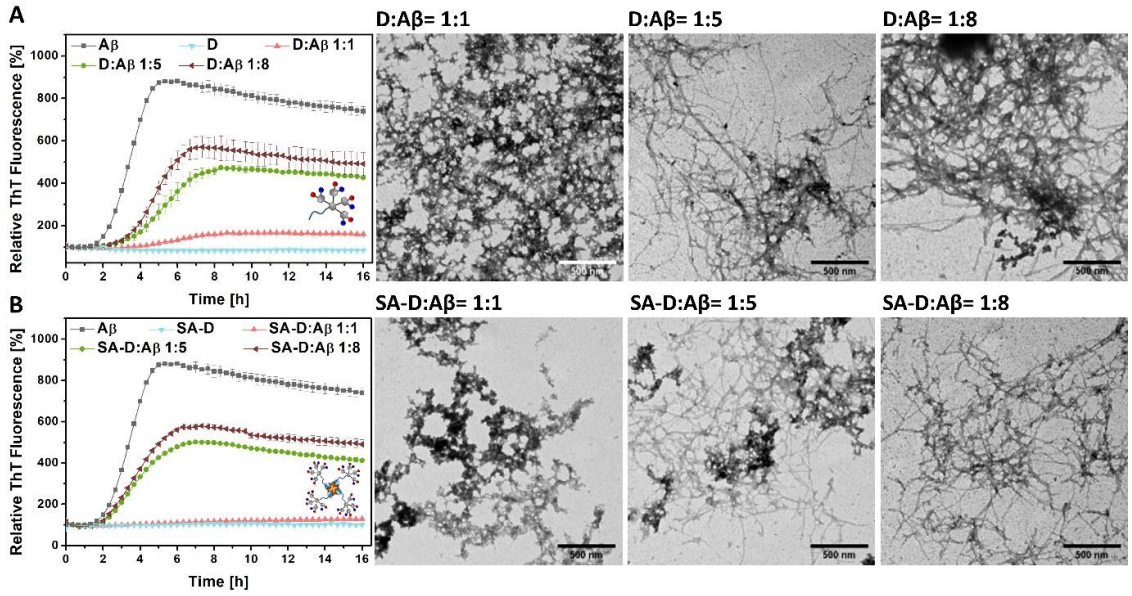

Figure 6.6. Aβ fibrillation with dendron **1** and **SA-D** with increasing Aβ concentrations. ThT kinetics of Aβ with dendron **1** (**A**), **SA-D** (**B**) in different molar ratios (Aβ alone, 1:1, 1:5, 1:8 **D**:Aβ or **SA-D**:Aβ, the concentration of dendron **1** and **SA-D** is 1.6 µM), and the corresponding TEM images of the mixtures. The scale bar is 500 nm.

In the next experiment, we kept the same molar ratios of dendron **1** or **SA-D** to Aβ. To contribute to the fact that four dendrons are attached to SA, we used four molar equivalents of dendron **1** compared to **SA-D**. After 2 h, the fluorescence intensity of Aβ alone started to increase and reached a plateau at around 5-6 h. While incubating dendron **1** and Aβ at the molar ratio 4:1 (**D:**Aβ), there was no obvious increase in fluorescence intensity even after incubation for 16 h (Figure 6.7A, red line). Using equimolar concentrations of **SA-D** with Aβ (**SA-D**: Aβ 1:1, each **SA-D** carried 4 dendrons), also no fluorescence intensity increase was observed during the 16 h incubation time (Figure 6.7B, red line). These data suggested that the fibrillation of Aβ was inhibited by both the dendron and **SA-D** at a ratio of dendron and Aβ 4:1. Increasing the amount of Aβ to 4:3 (**D**:Aβ) or 1:3 (**SA-D**:Aβ, each **SA-D** carried 4 dendrons), the slope of the elongation phase was still decreased, contrasting to Aβ alone, accordingly the formed plateau was reduced to 181.7 % and 176 % compared to Aβ alone (349.3 %). For both free and bound dendron, a similar inhibition effect on the Aβ fibrillation was observed. TEM images of the mixture also proved the kinetics results. As shown in Figure 6.7, after the experiments no ordered fibrils but some amorphous structures could be seen in **D**:Aβ (4:1) for free dendron and with **SA-D**:Aβ (1:1) for bound dendron, and some fibrils were observed in the **D**:Aβ (4:3) and **SA-D**:Aβ (1:3) solutions. These results indicate that the free dendron and **SA-D** bound dendron effectively inhibited or retarded Aβ fibrillation.

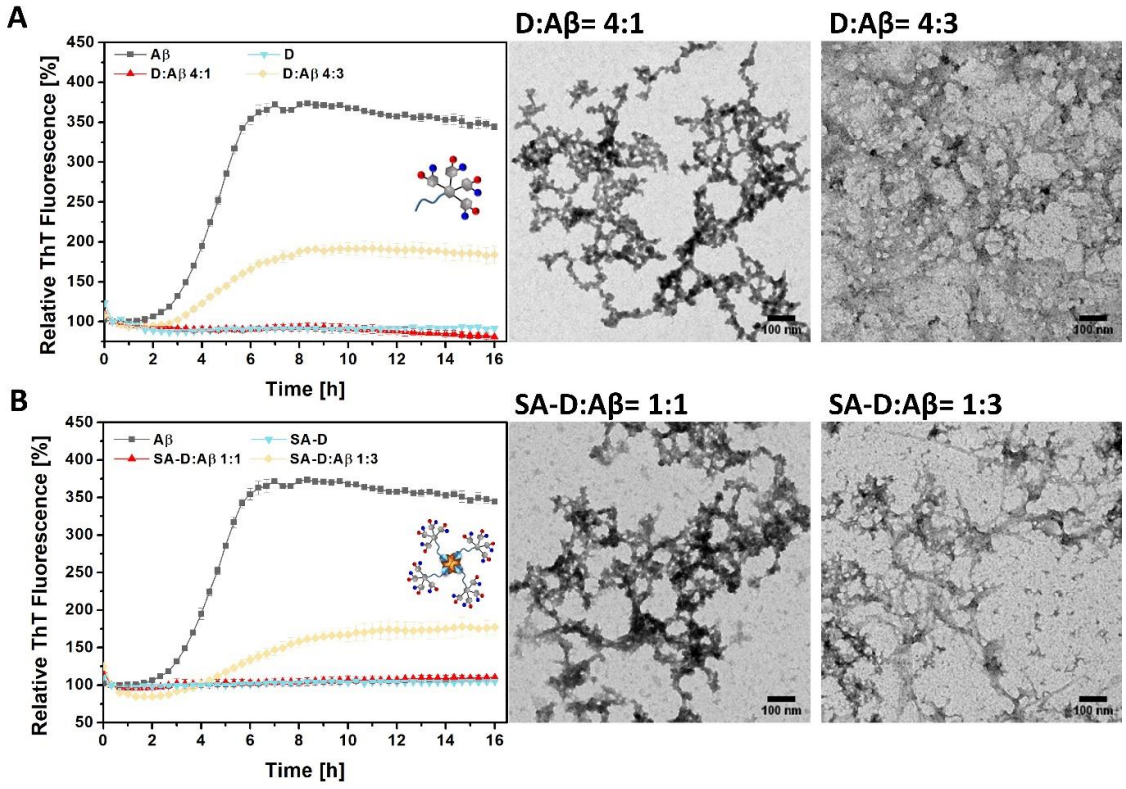

Figure 6.7. Aβ fibrillation with dendron **1** and **SA-D** at equimolar dendron concentrations. ThT kinetics of Aβ with dendron **1** (**A**), **SA-D** (**B**) in different molar ratios (in all ratios, the Aβ concentration is 5 µM), and the corresponding TEM images of the mixture. The scale bar is 100 nm.

As a control experiment, **SA-B** was also incubated with Aβ and kinetics behavior was assessed (Figure S6.10). After 16 h of incubation, **SA-B**:Aβ solutions displayed a similar kinetics of fibril formation as for Aβ alone with an even higher relative intensity of the plateau. The increase of the fluorescence intensity indicates that **SA-B** alone did not inhibit Aβ fibrillation, but it may rather contribute to the fibrillation process. Amyloid fibrils were observed in TEM images of both 1:1 and 1:3 (**SA-B**:Aβ) ratios, proving that **SA-B** has no inhibition effect on Aβ fibrillation. Thus, inhibition was caused by the attached dendrons. We also compared the inhibition effect of the amphiphilic dendron to the polycationic poly(amido)amine (PAMAM) dendrimers of the third generation (G3), which was reported to modulate the amyloid formation.[26] As shown in Figure 6.8, ratios of 1:1 and 5:1 (PAMAM:Aβ) affected the nucleation and elongation phase of Aβ fibrillation but there was nearly no effect on the final plateau of Aβ fibrils formed. Even a high PAMAM amount of 5:1 (PAMAM:Aβ) did not inhibit the fibrillation process. TEM images clearly visualized the formation of Aβ fibril structures. Klajnert et al. reported an inhibition of PAMAM dendrimers (G3) for $A\beta_{1-28}$ peptide at pH 5,5.[26] They described a reduction of the elongation rate and the final fibrillation for PAMAM. In our study for the full length $A\beta_{1-42}$ peptide at a physiological pH of 7, we could also observe the effect on the slope of the

elongation phase, but no reduction of the final amount of fibrils. These differences might be explained by the different peptides and pH conditions used. In addition, PAMAM dendrimer with peripheral positively charged amino groups are cytotoxic for primary neuronal cells (Figure S6.11) as well as for intestinal cell line Caco-2.[27] At physiological pH conditions and for the full length Aβ, the herein presented polyphenylene dendrons exhibited a significant inhibition of Aβ fibrillation (Figure 6.6 and Figure 6.7) compared to PAMAM G3 (Figure 6.8).

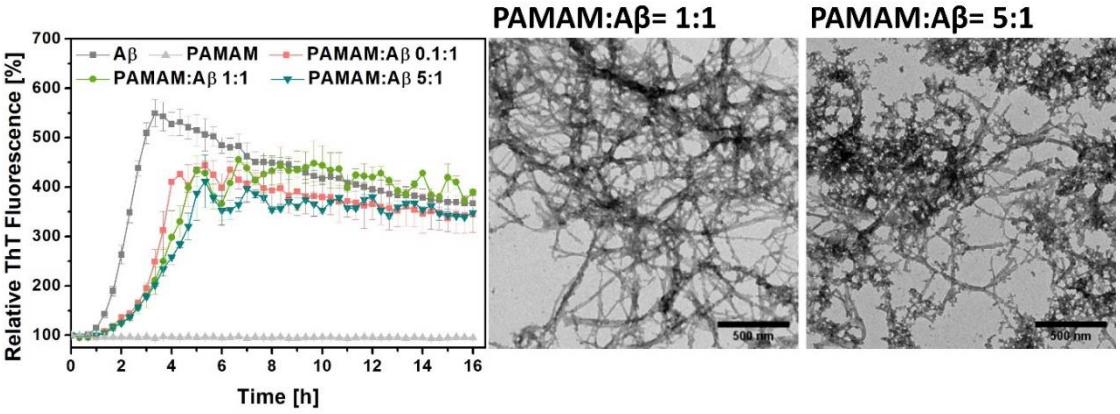

Figure 6.8. ThT kinetics of Aβ with PAMAM (G3). PAMAM: Aβ 1:1 and 5:1 molar ratio (in all ratios, Aβ concentration is 5 µM), and the corresponding TEM images of the mixture. The scale bar is 500 nm.

To elucidate the inhibition mechanism of the polyphenylene dendron on Aβ fibrillation, we characterized its interaction with circular dichroism (CD) spectroscopy. As displayed in Figure 6.9, the Aβ monomers exhibited a negative peak around 198 nm, indicating the random coil structure.[28] For Aβ fibrils alone, the negative peak disappeared and a pair of new peaks (a positive peak at around 198 nm and a negative peak at 216 nm) were observed, proving that the random structure of the peptide was converted to β-sheets. When incubating the dendron **1** with Aβ monomers at a 4:3 (**D**:Aβ) ratio, a positive peak at 198 nm could still be observed, but with lower intensity compared to Aβ, suggesting that Aβ still partially formed the β-sheets (Figure 6.9, yellow line). Increasing the amount of dendron from 2:1 to 4:1 (**D**:Aβ), no β-sheet bands could be observed. These results indicate that the fibrillation inhibition mechanism is based on a direct interaction of the dendron with the secondary structure of the fibrils. The observed loss of β-sheets was consistent with the kinetics results (Figure 6.7A). With low dendron to Aβ concentrations (e.g. **D**:Aβ 4:3), the fibrillation process of Aβ monomer could not be totally inhibited so that β-sheets were still formed. This resulted in the observation of a ThT fluorescence increase and the CD signals of β-sheets. When increasing the ratio of **D**:Aß (e.g. 4:1),

Aß fibrillation was fully inhibited, and no fluorescence increase and CD signal of β-sheet could be seen (Figure 6.9, purple line).

We propose that hydrophobic patches of the polyphenylene dendron interact with hydrophobic domains of Aβ (amino acids LVFFA, IIGLM) and upon binding the repulsion between negatively charged sulfonate groups of the dendron and anionic peptide residues might induce the unfolding of the peptide.[28] Furthermore, it could be expected that the aromatic amino acids of Aβ interact with the aromatic groups of the polyphenylene dendron and that due to this π-stacking the fibrillation and β-sheet formation of Aβ is inhibited.[29]

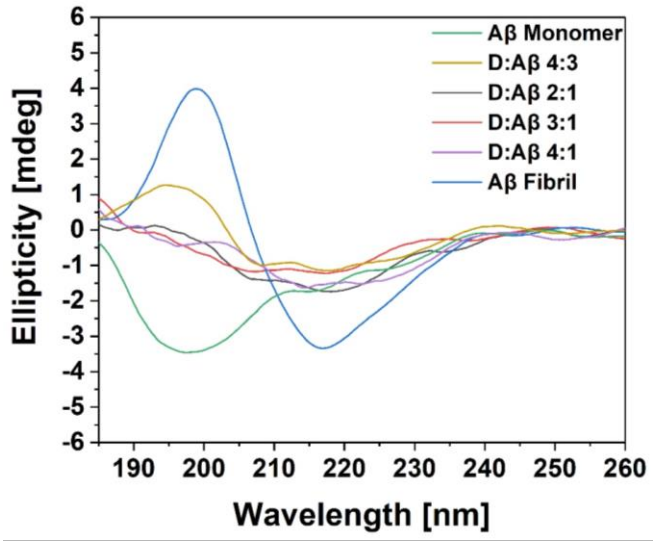

Figure 6.9. Circular dichroism spectrum of Aβ and dendron **1** with Aβ peptide. Aβ fibrils or Aβ monomers incubated with in different **D**:Aβ (monomer) molar ratios and circular dichroism spectrums were measured.

Disassembly of Aβ fibrils. In most cases when AD is diagnosed, amyloid plaques already exist and generate toxicity to neurons. Therefore, eliminating the already formed plaques is a very important property for therapeutic candidates. However, few molecules have been reported to successfully disrupt the preformed Aβ aggregates.[29] To investigate, whether an amphiphilic polyphenylene dendron can reverse fibrillation, Aβ fibrils were generated and incubated with dendron **1** or **SA-D**. The effect was characterized by TEM, as presented in Figure 6.10A, Aβ fibril structure could be seen. When incubating Aβ fibrils with dendron **1** 1:1 (**D**:Aβ fibril), there was still some fibril structure observed in the TEM (Figure 6.10B), indicating that not all the fibrils could be disassembled at an equimolar ratio. Increasing the amount of dendron **1**, the fibrils could hardly be seen (Figure 6.10B, 2:1 **D**:Aβ fibril). As for **SA-D**, after incubating with Aβ fibril at 1:1 and 2:1 (**SA-D**:Aβ fibril), the fiber structure disappeared (Figure 6.10C), and thus only amorphous structures could be observed. As a comparison, PAMAM dendrimers

G3 were also applied to check the disassembly of preformed fibrils. As obvious from Figure S6.12, after incubating for 16 h, lots of fibrils could still be observed on TEM images, indicating that PAMAM could not effectively disassemble the fibril even with concentration ratios of 7.9:1 (PAMAM:Aβ). These results provide firm evidence that polyphenylene dendron and **SA-D** not only lead to Aβ fibrillation inhibition, but also contribute to the disassembling of preformed fibrils. Binding of a polyphenylene dendron to preformed Aβ fibrils could lead to an intercalation of the dendron with fibrils which could lead to β-sheet breaking. Due to the observed β-sheet inhibition and breaking power of the polyphenylene dendron, it might be a promising amyloid disorder therapeutic candidate.

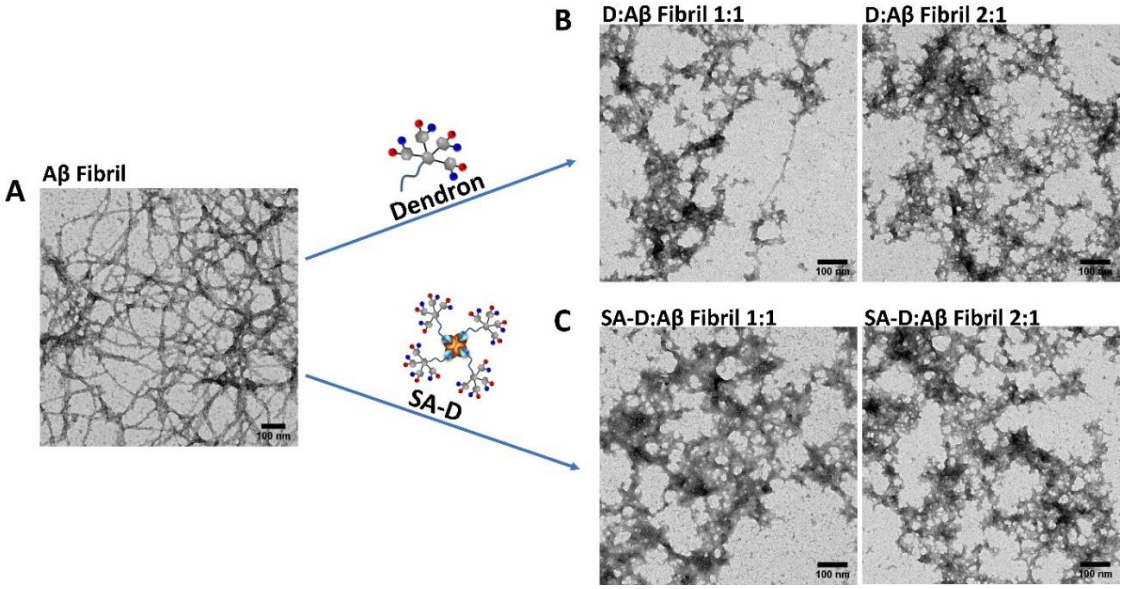

Figure 6.10. Dendron **1** and **SA-D** Aβ fibril disassembly. TEM images of (**A**) the pre-formed Aβ fibrils, (**B**) Aβ fibril mixed with dendron **1** in **D**:Aβ Fibril molar ratio of 1:1 and 2:1 and (**C**) Aβ fibril mixed with **SA-D** in **SA-D**:Aβ fibril molar ratio of 1:1 and 2:1. The scale bar is 100 nm.

Inhibition of Aβ toxicity. To verify the potential of dendron and **SA-D** to reduce the toxicity of Aβ fibrils on the cell vitality of primary murine neuronal cells, cell vitality was assessed by the CellTiter-Glo® Assay. Aβ fibrils were formed at 37°C for 16 h on an orbital shaker prior to the cell application. 24 h after the treatment with Aβ fibrils, with Aβ alone (10, 5 µM) or in the presence of dendron **1** (10, 20, 40 µM) or **SA-D** (2.5 or 5 µM) cell vitality was assessed. Aβ fibrils 10 µM or 5 µM reduced the cell vitality to 63.67 ± 2.24 % and 69.1 ± 2.3 %, respectively (Figure 6.11). Treatment with **D**:Aβ 10 or 5 µM (1:1) significantly rescued the toxicity, showing a vitality of 89.6 ± 3.7 % or 95.4 ± 2.48 % and **D**:Aβ 5 µM 4:1 showed a cell vitality of 78.8 ± 4.42 %, with **SA-D**:Aβ 5 µM the cell vitality reached 60 ± 4.34 %. Cell viability for cells treated with the cell toxin staurosporine (dead cell control) was 22.2 ± 5.17 %.

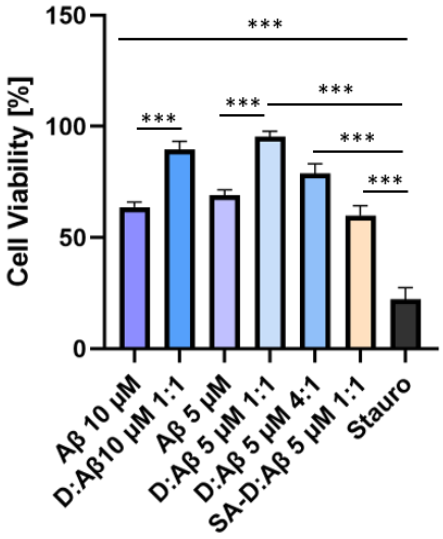

Figure 6.11. Dendron **1** and **SA-D** inhibition of Aβ toxicity on murine primary neurons. Primary murine neurons were incubated with Aβ, **D**:Aβ, **SA-D**:Aβ, staurosporine (Stauro, cell toxin, dead cell control) and respective controls to assess the toxic effect of Aβ and the dendron **1**-Aβ complexes. Cell vitality was quantified after 24 h of incubation with CellTiterGlo-Assay. Vitality is presented in % to controls and mean with SEM. n = minimum 6; one-way ANOVA; * $p \leq 0.05$, ** $p \leq 0.01$, *** $p \leq 0.001$. 95 % CI was 58.5 – 68.9 % (Aβ 10 µM), 95 % CI 63.8 – 74.4 95 % (Aβ 5 µM), 95 % CI 9.59 -34.9 (Stauro), Aβ 10 µM vs. **D**:Aβ 10 µM 1:1; p = < 0.001, Aβ 5 µM vs. **D**:Aβ 5 µM 1:1; p = < 0.001, Aβ 5 µM vs. **D**:Aβ 5 µM 4:1; p = 0.451, Aβ 5 µM vs **SA-D**:Aβ 5 µM 1:1; p = 0.561.

These data proved that binding of the dendron with equimolar concentrations inhibited the cell toxic effect of both Aβ concentrations. Due to the Aβ-dendron interaction, the Aβ peptides lost most of their β-sheet formation (Figure 6.9). This is one of the possible mechanism in reducing the cell toxicity because β-sheet rich Aβ forms fibrils and interact with the cell membrane, leading to disruption of the Ca^{2+} homeostasis of neurons.[30-32] The second relevant mechanism we consider is, that dendron-bound-Aβ might not bind to NGF-, NMDA- or insulin receptors, which trigger the pathologic cascade of Aβ.[33]

6.3 Conclusion

For the first time, brain delivery of an amphiphilic polyphenylene dendron and its bioconjugate with dominant uptake in neurons *in vivo* and *in vitro* was presented. The dendron was bound to streptavidin *via* a D-biotin moiety attached to its focal point. The polyphenylene dendron could be bound to streptavidin without the help of detergents to solubilize the dendron scaffold. Dendron and **SA-D** demonstrated high biocompatibility to both endothelial cells and primary neurons, and successfully passed the BBB layer by a transcytotic pathway. Specific uptake in neurons compared to astrocytes was observed. Such property would be very beneficial for future medical applications and

dramatically reduce side effects in non-diseased cells. Furthermore, the dendron and its bioconjugates induced anti-amyloid fibrillation behavior for full length $A\beta_{1-42}$ peptide in physiological conditions, and showed a significant reduction of the Aβ toxicity on primary murine neurons. These results not only provide possibilities for the therapy of toxic Aβ oligomerization and fibrillation in early stage of protein-misfolding induced neurodegenerative disorders, such as Alzheimer´s disease, but also afford a platform as functional delivery system to the brain for intracerebral diseases.

6.4 Acknowledgements

[redacted]

6.5 Materials and Methods

Ethics*:* The experimental procedures were authorized by the ethical committee and the authority "Landesuntersuchungsamt Rheinland-Pfalz" the protocol number is "Aktenzeichen "23 177-07/G 16-1-024". Investigations were performed according to the principles of laboratory animal care (European, national and international laws).

Materials: Reagents were of analytical grade and used as received and purchased from Sigma-Aldrich (Seelze or Hamburg, Germany), unless otherwise stated. PAMAM dendrimer, generation 3.0 with amino surface group was purchased from Sigma-Aldrich (412422). Amyloid $beta_{1-42}$ ($A\beta_{1-42}$, DAEFRHDSGYEVHHQKLVFFAEDVGSNKGAIIGLMVGGVVIA) was purchased from Anaspec Incorporated (purity ≥ 95%). Water was purified by a Milli-Q filter system.

Instruments for Measurements: Fluorescence spectra were measured on TECAN. Transmission electron microscopy (TEM) images were recorded on JEOL JEM1400 Transmission electron microscope. The absorbance of Aβ solution was measured by Nanodrop 2000 (Thermo Scientific™). CD spectra were measured on JASCO J-1500 Circular Dichroism Spectrophotometer.

Systemic delivery of dendron and bioconjugates: Cy5-D (11,2 µM final concentration in blood) or **Cy5-SA-D** (2,8 µM final concentration in the blood) were injected *via* the tail vein in mice. For control, mice got a PBS injection. Perfusion, with PBS supplemented with heparin-natrium (Ratiopharm, 5000 E.I.) followed by paraformaldehyde (PFA) 4%, of the mice was performed 24 h after particles injection. The organs (brain, liver, kidney, spleen, lung, and heart) were collected and stored in PBS at 4°C.

Immunhistochemistry: For immunohistochemisty organs were incubated with 30 % sucrose for 24 h and frozen in -80 ˚C freezer to obtain 30 µm slices using a freezing microtome (Leica CM 1325). Slices were washed 3 times with PBS 0.01 M, unmasked with 1% sodium dodecyl sulfate for 5 minutes at room temperature, blocked and permeabilized with 7 % normal donkey serum (017-000-121, Dianova, Hamburg) and 0.8 % Triton in PBS 0.01 M. First antibody was incubated with 2 % bovine serum albumin (001-000-161, Dianova, Hamburg) and 0.3 % Triton in PBS 0.01 M overnight at room temperature. After 3 times washing with PBS 0.01 M the secondary antibody was incubated for 2 h at room temperature in 2 % bovine serum albumin in PBS 0.01 M. DAPI solution (0.5 µg/ml) was incubated for 10 minutes. Before mounting with Fluoromount-G®(SouthernBiotech, USA) slices were washed 3 times with PBS 0.01 M and one time with Milli-Q water.

Imaging and Image preparation: Images were taken by a TCS SP5 confocal (Leica) using the LAS AF software. Projections of Z-stacks were visualized using ImageJ.

Cell culture bEnd.3 cells: A murine cell line, bEnd.3, from brain endothelioma (American Type Culture Collection, Manassas, VA, USA) was cultured as recommended by the manufacturer at a humidified atmosphere with 37°C and 5 % CO_2.[33] DMEM (Glutamax, gibco by life technology, Darmstadt, Germany) supplemented with 10 % fetal calf serum and 2 % penicillin/streptomycin was the used media. For experiments, passages 10–30 were used with 80.000 cells/transwell insert, or 100.000 cells/IBIDI-8-well-chamber.

Generation and culture of primary murine cortical neuronal cells: Primary murine neuronal dissociated cell culture were performed as previously described by Kaech and Banker[34] with changes according to Beaudoin and colleagues[35]. Forebrains of new born mice (postnatal day 1) were isolated. Following meninges depletion the tissue was washed three times with ice-cold HBSS -/- and incubated in 0.05% trypsin/EDTA (gibco by life technology, Darmstadt, Germany) for 20 min, followed by incubation with DNase I (Roche, 11284932001) (2000U in 5 ml) for 5 min. Brain tissue was homogenized in

Neuronal Plating Medium (MEM, 10% horse serum, 0.6% glucose) and vital cells were counted (Countess FL cell counter). Primary neurons were seeded in plating medium with cell numbers of 200,000 cells per well of 24-well plate. The medium was replaced with Neuronal Maintenance Medium [Neurobasal Medium (gibco by life technology, Darmstadt, Germany) with 2 mM glutamine (gibco by life technology, 25030024) and supplemented with B27 Supplement (gibco, 17504044)] after 30 min. Cells were treated with ARAC (5 µM) on day 2 *in vitro*. Once a week one-third of the medium was replaced with fresh Neuronal Maintenance Medium and ARAC treatment was repeated.

Cell uptake study and Immunocytochemistry: Cy5-D or **Cy5-SA-D** were applied in a final concentration of 0.45 µM and 1.8 µM to bEnd.3 cells or primary murine neurons for 24 h. Cells were finally fixed with PFA 4%. For immuncytochemisty cells were washed 3 times with PBS 0.01 M, blocked and permeablized with 7 % normal donkey serum (017-000-121, Dianova, Hamburg) and 0.8 % Triton in PBS 0.01 M. First antibody was incubated with 2 % bovine serum albumin (001-000-161, Dianova, Hamburg) and 0.3 % Triton in PBS 0.01 M overnight at room temperature. After 3 times washing with PBS 0.01 M the secondary antibody was incubated for 2 h at room temperature in 2 % bovine serum albumin in PBS 0.01 M. DAPI solution (0.5 µg/ml) was incubated for 10 minutes. Before mounting with Fluoromount-G®(SouthernBiotech, USA) slices were washed 3 times with PBS 0.01 M and one time with Milli-Q water.

Preparation of $A\beta_{1-42}$ stock film: $A\beta_{1-42}$ stock solution was prepared according to the technical data sheet from the company. $A\beta_{1-42}$ powder (1 mg) was firstly dissolved in 440 µL HFIP and sonicate for 10 min. Then the stock solution will be aliquot to 0.1 mg/tube and HFIP was removed by rotational vacuum concentrator (RVC 2-18 CDplus, Martin Christ Gefriertrocknungsanlagen GmbH). The stock films were then stored under -20 ˚C.

Aβ fibrillation: $A\beta_{1-42}$ stock film (0.1 mg) was dissolved in 2.5 µL DMSO and diluted with 100 µL DPBS solution. The solution was sonicated with ice for 8 min to fully dissolve $A\beta_{1-42}$. The concentration of $A\beta_{1-42}$ monomer solution was confirmed by nanodrop. To obtain Aβ oligomer, $A\beta_{1-42}$ monomer solution was incubated undisturbed at room temperature for 24 h. For fibrils, the monomer solution was β incubated at 37 ˚C with vigorously shaking for 16 h. Pre-formed fibrils (5 µM) were incubated with dendron **1**, **SA-D** or PAMAM for 16 h in PBS for further investigations.

Cell viability assay including Aβ toxicity: Viability for bEnd.3 cells (80,000 cells/well, 50 µL media) and primary neuronal cells (200,000 cells/well, 500 µL media) was investigated using the cell viability assay CellTiter-Glo® Assay (Promega, G7570). Cells

were treated for 24 h after reaching 100 % confluence with dendron **1** (20 or 40 µM), **SA-D** (2.5 or 5 µM), Aβ (5 µM) or a combination of **D**:Aβ and **SA-D**:Aβ and staurosporine (1 µM) as a control for dead cells. Aβ stock film (0.1 mg) was dissolved in 2.5 µL DMSO and diluted with 100 µL DPBS solution. The solution was sonicated with ice for 8 min to fully dissolve Aβ. The concentration of the Aβ monomer solution was confirmed by nanodrop. 250 µL of dendron **1** or **SA-D** mixed with Aβ (10 µM) with different ratios (**D**:Aβ = 4:1 and 1:1, **SA-D**:Aβ = 1:1) were prepared in neuron media. The mixture was then incubated at 37 ˚C for 16 h in advance to the toxicity assay Aβ alone was also incubate at the same condition to obtain fibrils. Afterwards, the Aβ (5 µM), **D**:Aβ = 4:1 and 1:1, **SA-D**:Aβ = 1:1 was incubated with primary neurons with 5 µM Aβ for 24 h. The CellTiter-Glo® Assay was performed according to the manufacturer's instructions. Luminescence was detected using a GloMaxMulti 96-well plate reader (Promega). Cell Viability in % was related to untreated control cells (100 %). All the experiments were run at least two times in triplicates.

Membrane impedance measurement: The measurement of Transendothelial Electrical Resistance (TEER) and capacitance of the cell layer (*Ccl*) in the *in vitro* BBB model of a bEnd.3 monolayer on a transwell insert was measured by a CellZscope system (NanoAnalytics, Münster, Germany).

Fibrillation kinetics: Thioflavin T (ThT) was chosen as the indicator for $A\beta_{1-42}$ aggregation behavior characterization. ThT was dissolved in PBS buffer with a concentration of 2 mM as a stock solution and stored at 4 ˚C. For measurement of ThT fluorescence during the fibrillation process, $A\beta_{1-42}$ was diluted with DPBS into different concentrations and mixed with ThT solution, the final concentration of ThT was 10 µM. The kinetics were then conducted in 96 well plates (Greiner µClear®, black with clear bottom) with a 16 h period of fibrillation time at 37 ˚C. The fluorescence intensity was tested every 10 min, and with excitation of 450 nm and emission of 490 nm.

For $A\beta_{1-42}$ fibrillation kinetics, HFIP-treated stock film was dissolved in 2.5 µL DMSO and further diluted with 100 µL PBS. The solution was sonicated for 8 min and vortex for 10 s. The concentration of the solution was calculated by its UV-vis absorbance tested *via* Nanodrop.

Transmission Electron Microscopy: 10 µL of the sample was added onto the carbon coated-copper grid for 10 min and the redundant sample was removed with filter paper. The sample was then stained with 4 % (w/v) uranyl acetate for 60 s and dried with filter

paper. The copper grids were washed with MiliQ for three times to remove the excess uranyl acetate and dried under room temperature.

Circular dichroism (CD) spectroscopy: 200 µL of the sample was added to a 0.1 cm quartz for far-UV (180-260 nm) measurements. The bandwidth was 0.2 nm. The scanning speed was 100 nm/min with a response time of 4 seconds. Each spectrum was tested for 3 scans.

Statistics: Data are presented as mean ± standard error of the mean (SEM). All statistical tests were performed using Prism8.3 (GraphPad Prism, La Jolla, CA). The effects of the different treatments were analyzed by one-way analysis of variance (ANOVA) followed by Tukey´s multiple comparisons test for post hoc test. Significance was considered at p values of * $p \leq 0.05$, ** $p \leq 0.01$, *** $p \leq 0.001$.

6.6 Supporting Information

6.6.1 Synthesis

Materials. Organic solvents for reactions and purification were purchased from Fisher Scientific or Acros Organics and used without any further purification (HPLC grade). Ultrapure water for reactions and purifications were obtained from a Merck MilliQ water purification system. All chemicals were purchased from commercial suppliers like Sigma Aldrich, Fisher Scientific, Acros Organics, Thermo Scientific etc. if not stated otherwise and were used without any further purification. For size-exclusion chromatography Sephadex® G25 or G50 in ultrapure water were used.

Instruments. ^{1}H-NMR and ^{13}C-NMR spectra were measured on an Avance III 700 MHz spectrometer in DMSO-d_6 at 298 K. ^{13}C-NMR spectra were recorded in j-modulated spin-echo (JMOD) mode. MestReNova was used to analyze the spectra. MALDI-TOF measurements were performed on a Bruker rapifleX MALDI-TOF/TOF and a Waters MALDI Synapt G2-SI. mMass was used for data processing. Absorption spectra and intensities were measured on a SPARK 20M microplate reader from TECAN Group Ltd. The samples were measured in a Greiner 384 flat transparent well plate.

6.6.2 Dendron Synthesis

Dendron-conjugates **1**, **2** and **3** were synthesized as previously reported.[14]

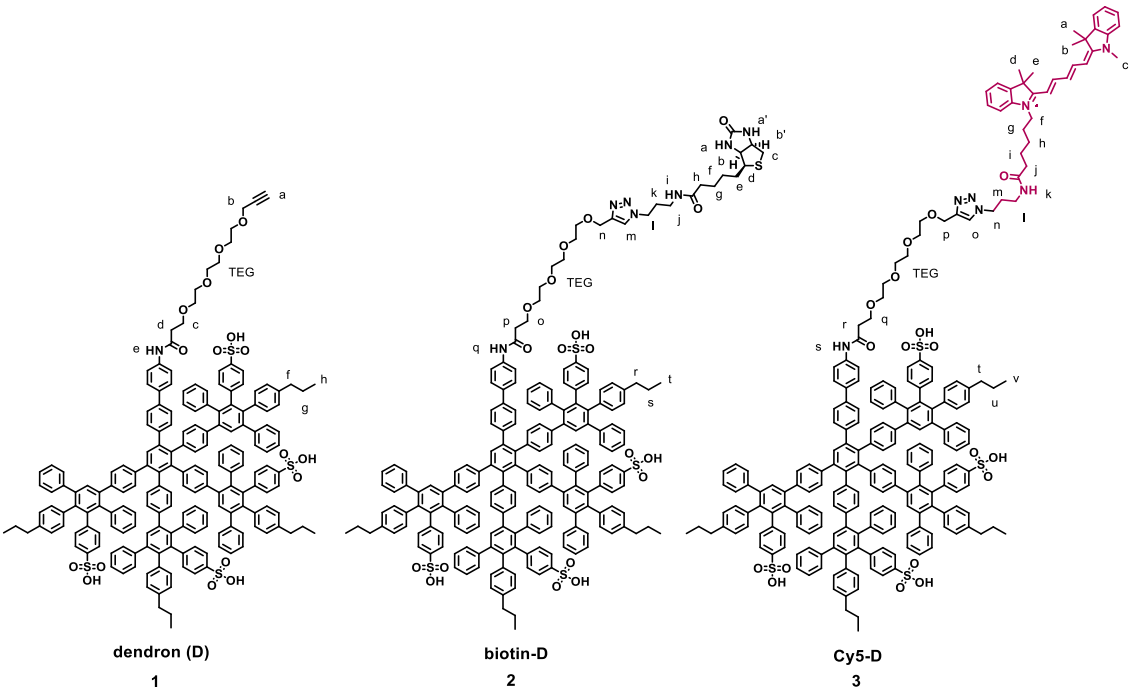

Figure S6.1. Synthesized dendron-conjugates: unfunctionalized dendron (**D**, **1**), **biotin-D** (**2**) and **Cy5-D** (**3**).

Dendron (**D, 1**) was obtained in 98% yield. All spectral data is in agreement with the literature.[14]

^{1}H NMR (500 MHz, DMSO-d_6): δ(ppm) = 10.03 (s, 1H, H_e), 7.75–7.56 (m, 4H, H_{arom}), 7.50–7.23 (m, 7H, H_{arom}), 7.22–6.54 (m, 84H, H_{arom}), 6.52–6.30 (m, 6H, H_{arom}), 4.11 (m, 2H, H_f), 3.71 (t, J = 5.6 Hz, 2H, H_c), 3.55–3.44 (m, 12H, H_{TEG}), 2.57 (t, J = 4.9 Hz, 2H, H_d), 2.44–2.23 (m, 9H, H_a, H_f), 1.47–1.31 (m, 8H, H_g), 0.74–0.61 (m, 12H, H_h).

^{13}C NMR (126 MHz, DMSO): δ (ppm) = 145.54–119.32, 77.08, 69.75, 69.69, 69.47, 68.50, 66.67, 57.47, 36.44, 23.52, 13.11.

MALDI-TOF: *m/z* calcd. for $C_{186}H_{153}NO_{17}S_4$ 2800.00, found 2801.28 $[M+H]^+$, 2824.35 $[M+Na]^+$, 2840.31 $[M+K]^+$, 2862.25 $[M+NaK]^{2+}$, 2878.33 $[M+2K]^{2+}$.

Biotin-D (**2**) was obtained in 97% yield. All spectral data is in agreement with literature.[14]

^{1}H NMR (700 MHz, DMSO-d_6) δ(ppm) = 10.03 (s, 1H, H_q), 8.08 (d, J = 3.0 Hz, 1H, H_{arom}), 7.88 (t, J = 4.5 Hz, 1H, H_i), 7.73–7.66 (m, 2H, H_{arom}), 7.60 (s, 2H, H_{arom}), 7.48–6.27 (m, 100H, H_{arom}, H_a, $H_{a'}$, H_m), 4.49 (s, 2H, H_n), 4.32 (t, J = 7.0 Hz, 2H, H_l), 4.28 (t, J = 6.5 Hz,

1H, $H_{b'}$), 4.13–4.09 (m, 1H, H_b), 3.71 (t, J = 6.2 Hz, 2H, H_o), 3.58–3.44 (m, 12H, H_{PEG}), 3.11–3.06 (m, 1H, H_d), 3.02 (q, J = 6.4 Hz, 2H, H_j), 2.79 (dd, J = 12.5, 5.1 Hz, 1H,H_c), 2.64–2.53 (m, 3H, $H_{c'}$, H_p), 2.45–2.22 (m, 8H, H_r), 2.06 (t, J = 7.5 Hz, 2H, H_h), 1.92 (p, J = 6.7 Hz, 2H, H_k), 1.68–1.23 (m, 14H, H_e, H_f, H_g, H_s), 0.74–0.62 (m, 12H, H_t).

^{13}C NMR (176 MHz, DMSO) δ(ppm) = 172.19, 162.68, 145.51-119.31, 69.76, 69.66, 68.95, 66.64, 63.53, 61.02, 59.19, 55.39, 47.15, 40.02,37.23, 36.44, 35.64, 35.17, 33.90, 33.60, 29.95, 28.19, 28.02, 25.23, 23.52, 13.12.

MALDI-TOF: *m/z* calcd. for $C_{199}H_{175}N_7O_{19}S_5$ 3126.15, found 3149.65 $[M+Na]^+$, 3171.62 $[M+2Na]^{2+}$, 3187.58 $[M+K]^+$, 3193.61 $[M+3Na]^{3+}$.

Cy5-D (**3**) was obtained in 86% yield. All spectral data is in agreement with literature.[14]

^{1}H NMR (700 MHz, DMSO-d_6) δ(ppm) = 10.00 (s, 1H, H_s), 8.35–8.23 (m, 2H, H_{arom}), 7.89–7.81 (m, 1H, H_k), 7.65 (d, *J* = 7.4 Hz, 2H, H_{arom}), 7.53 (dd, *J* = 14.7, 7.4 Hz, 2H, H_{arom}), 7.43–6.15 (m, 117H, H_{arom}), 4.45 (s, 2H, H_p), 4.26 (t, *J* = 7.0 Hz, 2H, H_n), 4.05–3.96 (m, 2H, H_f), 3.70–3.64 (m, 2H, H_r), 3.54–3.40 (m, 15H, $H_{TEG,}$ H_c), 2.98–2.93 (m, 2H, H_l), 2.35–2.22 (m, 8H, H_t), 2.00 (t, *J* = 7.1 Hz, 2H, H_j), 1.84 (q, *J* = 7.0 Hz, 2H, H_m), 1.64–1.54 (m, 12H, $H_{a,}$ $H_{b,}$ $H_{d,}$ H_e), 1.52–1.44 (m, 2H, H_i), 1.43–1.16 (m, 12H, $H_{g,}$ $H_{h,}$ H_u), 0.72–0.54 (m, 12H, H_v).

^{13}C NMR (176 MHz, DMSO) δ(ppm) = 154.33, 145.52–124.18, 123.88, 122.29, 118.68, 111.00, 69.80, 69.72, 68.50, 65.75, 63.57, 48.85, 47.15, 36.55, 36.45, 35.64, 34.40, 29.93, 27.11, 26.94, 24.84, 23.54, 13.14, 12.88.

MALDI-TOF: *m/z* calcd. for $C_{221}H_{198}N_7O_{18}S_4^+$ 3365.37, found 3365.28 $[M]^{\bullet+}$, 3387.26 $[M+Na]^+$, 3410.25 $[M+2Na]^{2+}$.

6.6.3 Preparation of Streptavidin (SA)-Conjugates

Cy5-labelled SA (Cy5-SA)

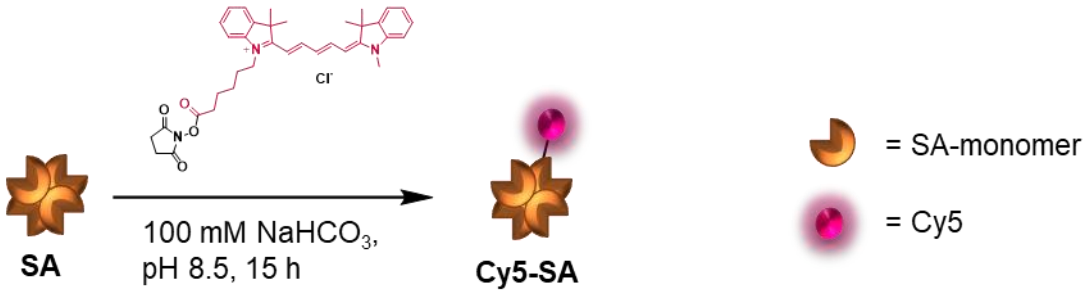

Figure S6.2. Modification of SA with the fluorophore Cy5. 1 molar equivalent of SA-tetramer was labelled with 1 molar equivalent of Cy5 resulting in 3 unlabelled SA-monomers and 1 labelled SA-monomer statistically.

SA (8 mg, 0.15 µmol) was dissolved in 1 mL 100 mM $NaHCO_3$ buffer, pH 8.5 and Cy5-NHS ester (93 µg, 0.15 µmol) dissolved in 15 µL DMSO was added. The reaction mixture was shaken at room temperature for 15 h with the exclusion of light. To remove unreacted Cy5, the reaction mixture was purified using Sephadex G-50 in ultrapure water. After lyophilization Cy5-labelled SA was obtained as a blue solid (7.8 mg, 99%).

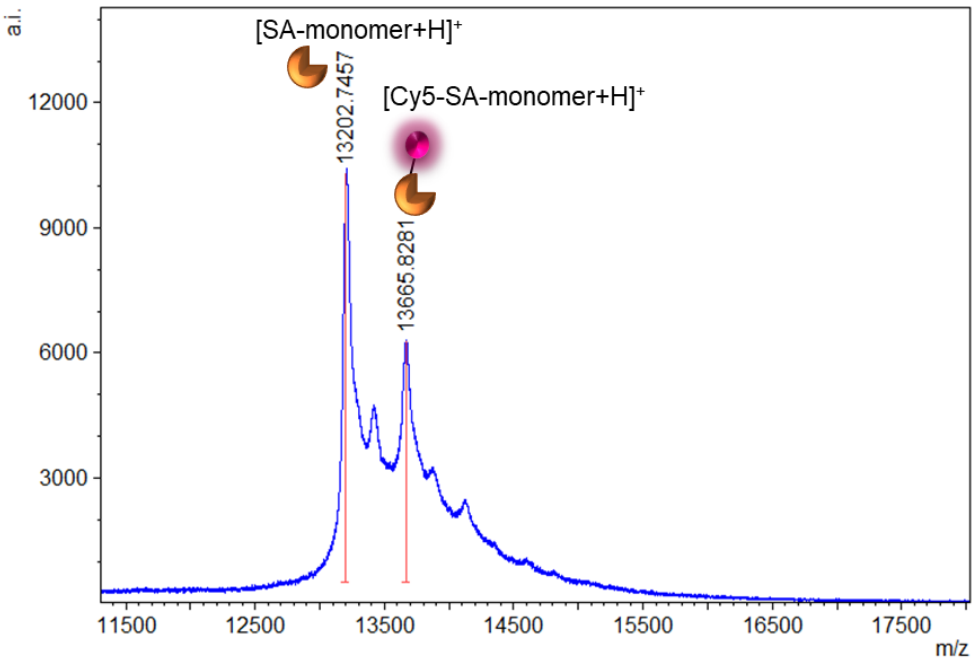

Figure S6.3. MALDI-TOF mass spectrum of Cy5-labelled SA. Both unlabelled (m/z = 13202.75 [SA-monomer+H]$^+$) and Cy5-labelled SA monomer (m/z = 13665.83 [Cy5-SA-monomer+H]$^+$) were observed due to the statistic labeling with 1 equivalent Cy5 to 1 equivalent of SA-tetramer.

Preparation of SA-D

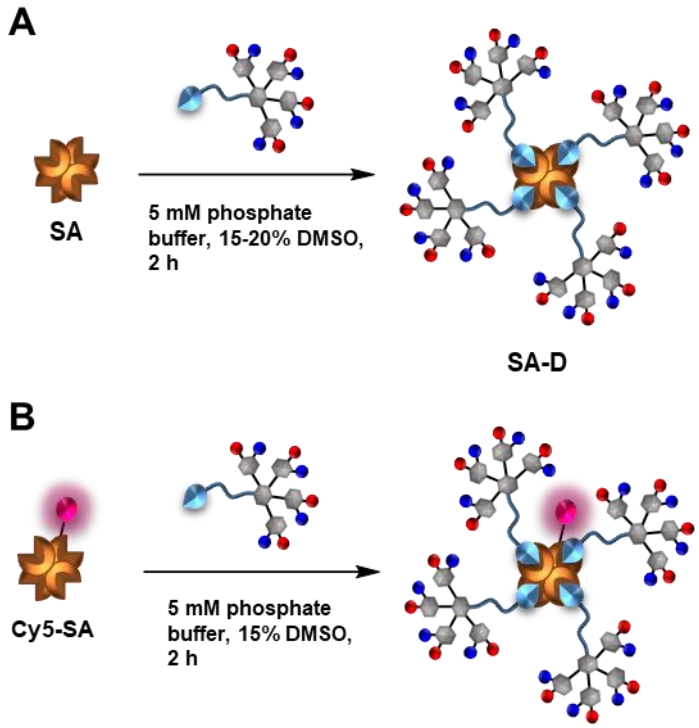

Figure S6.4. Preparation of (**A**) dendronized SA (**SA-D**) and (**B**) dendronized Cy5-SA (**Cy5-SA-D**)

A) Unlabelled **SA-D**:

1.) 2 mg scale: **Biotin-D** (**2**) (522 µg, 167 nmol, 4.5 equiv) was dissolved in 200 µL DMSO and 200 µL autoclaved ultrapure water was added. After vigorous shaking, dendron **2** was added to a solution of SA (2.00 mg, 37.9 nmol) in 600 µL ultrapure water. 10 mg mL^{-1} SA contained 20 mM phosphate buffer pH 6.5 resulting in a ~4 mM phosphate buffer concentration in the mixture. The mixture was slightly shaken for 2 h at room temperature and purified by size exclusion chromatography using autoclaved Sephadex G-50 in ultrapure water. The purification was performed under sterile conditions. The concentration was determined by BCA-Assay.

2.) 1 mg scale: For smaller scales, the complex formation was performed at lower concentrations as described for the Cy5-labelled **SA-D** in procedure B.

B) Cy5-labelled SA-D (**Cy5-SA-D**): **Biotin-D** (**2**) (267 µg, 85.1 nmol, 4.5 equiv) was dissolved in 125 µL DMSO and 200 µL 5 mM phosphate buffer was added. After vigorous shaking, dendron **2** was added to a solution of SA (1.00 mg, 1.89 nmol) in 500 µL 5 mM phosphate buffer, pH 7.4. The mixture was slightly shaken for 2 h at room temperature and purified by size exclusion chromatography using autoclaved Sephadex G-50 in

ultrapure water. The purification was performed under sterile conditions. The concentration was determined by linear calibration against **Cy5-SA** at a wavelength of λ_{Abs}= 650 nm.

Preparation of SA-B as reference

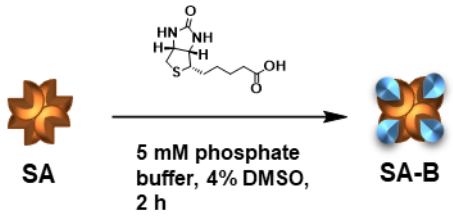

Figure S6.5. Preparation of SA complexed with free D-biotin (**SA-B**) as reference

10.4 µL of a 1 mg mL^{-1} solution of D-Biotin in DMSO (10.4 µg, 42.5 nmol, 4.5 equiv) were added to a solution of SA (0.5 mg, 9.46 nmol) in 250 µL 5 mM phosphate buffer, pH 7.4. Afterwards, the mixture was treated the same as described for **SA-D** (see above).

6.6.4 Characterization of the SA-D conjugates

Determination of the SA concentration

BCA-Assay for unlabelled samples. The concentration of **SA-D** and **SA-B** was determined by the bicinchoninic acid assay (BCA-Assay) with bovine serum albumin (BSA) as standard for the calibration curve. For this purpose, Pierce™ BCA Protein Assay Kit from Thermo Scientific™ was used and the concentration was determined following the supplier's instructions. BSA standards were used at the concentrations of 0.5, 1, 2.5, 5, 10, 20, 40 and 200 µg/ml. **SA-D** and **SA-B** conjugates were diluted to 1:100 (v/v) in order to achieve a concentration that fits to the range of the calibration curve. Both samples and standard were incubated for 30 min at 37 °C with the BCA Assay reagents. Then, the absorption intensity was measured at 562 nm in a 384 flat transparent well plate in triplicates.

Absorbance intensity of Cy5 for labelled samples. The concentration of Cy5-labelled SA was determined using a standard calibration curve with **Cy5-SA** as standard at the concentrations of 1, 5, 10, 50 and 100 µM in MilliQ water. 30 µL of each standard (**Cy5-SA**) and purified **Cy5-SA-D** were transferred in triplicates to a Greiner 384 flat transparent well plate. The absorption intensity was measured at 650 nm.

HABA-Assay

Native SA, purified **SA-B** or **SA-D** solutions were diluted in ultrapure water to afford 1 mg mL^{-1} SA solutions. 25 µL SA solutions were mixed with 0.5 µL 2-(4'hydroxyazobenzene)-benzoic acid (HABA) solution (1 mg mL^{-1} in DMSO) and absorbance spectra (250 nm–750 nm) were measured in a UV-star flat bottom 384-well plate.

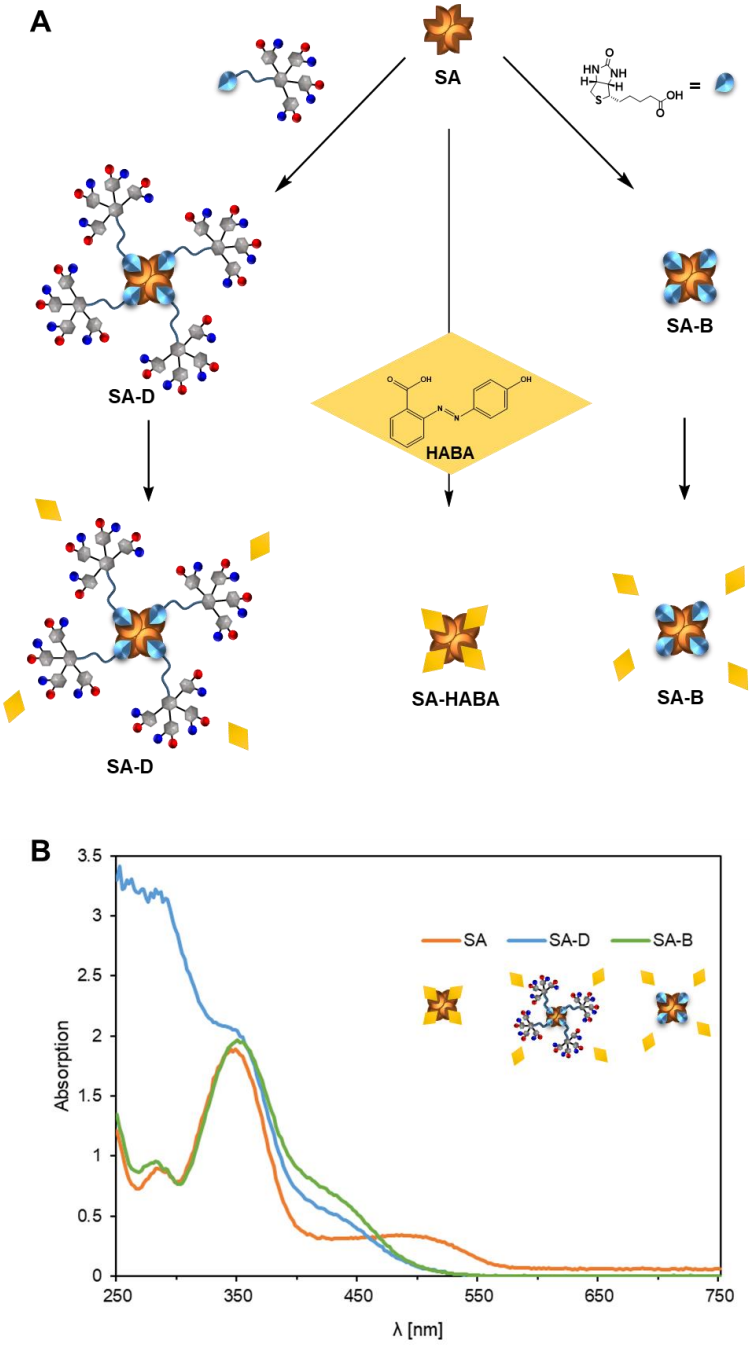

Figure S6.6. HABA-Assay. (**A**) Illustration of experimental procedure. (**B**) Absorbance spectra of SA, **SA-B** and **SA-D** treated with HABA. **Biotin-D** (**2**) binds to SA and thus occupies the biotin-binding sites. HABA binds to the same binding site as D-biotin resulting in an absorption band at 500 nm. Upon binding of D-biotin and biotin-dendron, HABA cannot bind which does not result in an absorption maximum at 500 nm.

SDS-PAGE

SDS-PAGE was performed using a NuPAGE Bis-Tris Gel (4-12%) from Invitrogen. Proteins were applied under (a) denaturing conditions (with heating and DTT) as well as (b) non-denaturing conditions (without heating, no DTT). (a) For denaturing conditions 16 µL of a 0.4 mg mL^{-1} protein solution were mixed with 6 µL sample buffer (NuPAGE, Invitrogen) and 2 µL of 1 M DTT solution and incubated at 95 °C for 10 min. The mixture (20 µL) was loaded on the SDS gel. (b) For non-denaturing conditions 16 µL of a 0.4 mg mL^{-1} protein solution were mixed with 6 µL sample buffer (NuPAGE, Invitrogen) and 2 µL of ultrapure water and the resulting 20 µL solution was loaded to the SDS-Gel. As a reference, 2 µL of Protein Marker VI (10-245) was used. The gel was run in 1x 2-(N-morpholino)ethanesulfonic acid (MES) SDS running buffer with constant voltage of 150 V for 45 min. The gel was washed for three times with ultrapure water and stained with Imperial™ Protein Stain from Thermo Scientific for 1 h under gentle orbital shaking. The gel was destained overnight in ultrapure water.

Agarose Gel Electrophoresis

Agarose gel electrophoresis was conducted applying 1% agarose gels based on tris-acetate-EDTA (TAE) buffer. 500 mg agarose was heated up in 50 mL 1x tris-acetate-EDTA (TAE) buffer until complete dissolving of the agarose. The agarose was let set in an agarose gel-mold for 30 min, transferred to an electrophoresis tank and was covered with 1x TAE buffer. 15 µL of each SA (0.4 mg mL^{-1}), **SA-B** (0.4 mg mL^{-1}) and **SA-D** (0.3 mg mL^{-1}) were mixed with 15 µL glycerol and 25 µL of each sample was loaded to the agarose gel loading wells. The electrophoresis was performed in a Mini-Sub® Cell GT from Bio-Rad at 150 V for 45 min on ice. The gel was washed for three times with ultrapure water and stained with Imperial™ Protein Stain from Thermo Scientific for 1 h under gentle orbital shaking. The gel was destained overnight in ultrapure water.

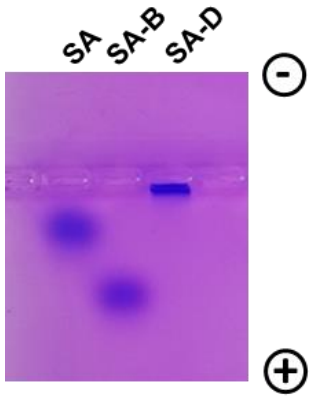

Figure S6.7. Agarose gel of SA conjugates. SA, **SA-B** and **SA-D** were applied to an agarose gel and the electrophoresis was run at 150 V for 45 min.

Atomic Force Microscopy (AFM)

AFM measurements were conducted on a Dimension FastScan Bio atomic force microscope from Bruker, which was operated in the PeakForce mode. AFM probes with a nominal spring constant of 0.25 Nm^{-1} were employed (FastScan-D, Bruker) for measurement in liquid. A circular mica disc (15 mm) was used as the substrate. Measurements were performed at scan rates between 0.8 and 2 Hz. Different areas of the mica substrate were scanned in order to ensure the integrity of the shown images. The images were finally processed by the software NanoScope Analysis 1.8. For sample preparation, the initial **SA-B** and **SA-D** solutions (25 µM in ultrapure water (MilliQ)) were diluted to 600 nM with MilliQ water and subsequently applied onto the freshly cleaved mica substrate. The solution was left to incubate for 15 minutes in order to deposit the desired species on the mica substrate. After successful adsorption, the supernatant was removed and fresh MilliQ water (250 µL) was added for the measurement. Images were processed using NanoScope Analysis 1.8.

Dynamic Light Scattering

SA-D samples were purified *via* size exclusion chromatography as described in chapter 1.4.2. After determination of the protein concentration by BCA-Assay (chapter 1.5.1.1) the sample was diluted with the respective buffer concentrations to achieve an **SA-D** concentration of 0.5 mg mL^{-1} in ultrapure water as well as 25, 50 and 100 mM phosphate buffer, pH 7.4. Samples were filtered through a 0.2 µm filter prior to the measurement to remove dust particles.

Light scattering measurements were performed on an ALV spectrometer consisting of a goniometer and an ALV-5004 multiple-tau full-digital correlator (320 channels) which

allows measurements over an angular range from 30° to 150°. A He-Ne Laser (wavelength of 632.8 nm) is used as light source. For temperature-controlled measurements the light scattering instrument is equipped with a thermostat from Julabo.

Measurements were performed at 20°C at 9 angles ranging from 30° to 150°.

Table S6.1. Hydrodynamic Radius (R_h) and PDI of **SA-D** in ultrapure water (MilliQ) and 25 mM, 50 mM and 100 mM phosphate buffer. A significant size increase of **SA-D** compared to the control **SA-B** was observed at all buffer concentrations. *A bimodal distribution was observed due to a second process at about 300 nm.

	R_h/nm	**PDI**
SA-D in MilliQ	37.3	0.181
SA-D in 25 mM PB	25.1	0.351
SA-D in 50 mM PB	23.8	0.208
SA-D in 100 mM PB	32.8	0.178
SA-B in MilliQ	-	-
SA-B in 25 mM PB	3.3*	0.570*

6.6.5 Biological Characterization

In Vivo Biodistribution

Mice were injected with **Cy5-D** (**3**) and **Cy5-SA-D** systemically *via* tail vein. 24 h after injection mice were perfused and organs were sliced and counterstained with nuclei dye DAPI. Imaging of the organs revealed a high uptake of dendron and **SA-D** in liver and spleen and low uptake in kidney, lung and heart.

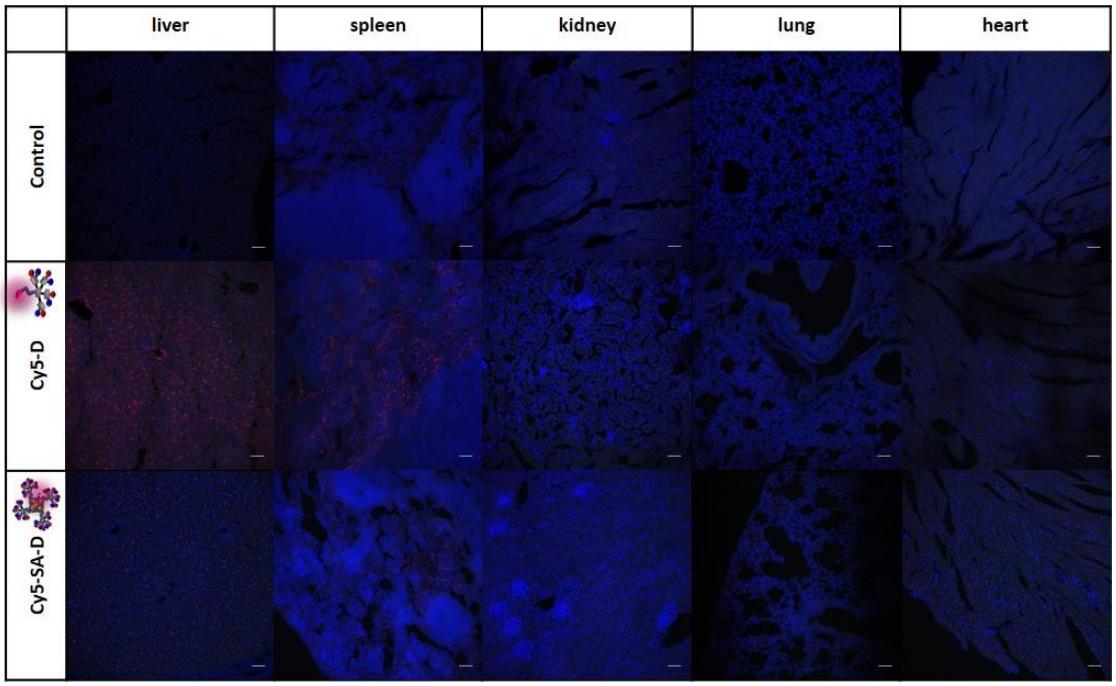

Figure S6.8. Biodistribution of **Cy5-D** and **Cy5-SA-D**. Mice were injected **Cy5-D** (red), **Cy5-SA-D** (red) or PBS for control. After 24 h mice were perfused and organs sliced, fixed and imaged. The scale is 50 µm.

6.6.6 Anti-amyloid fibrillation behavior

Kinetics of Aβ fibrillation

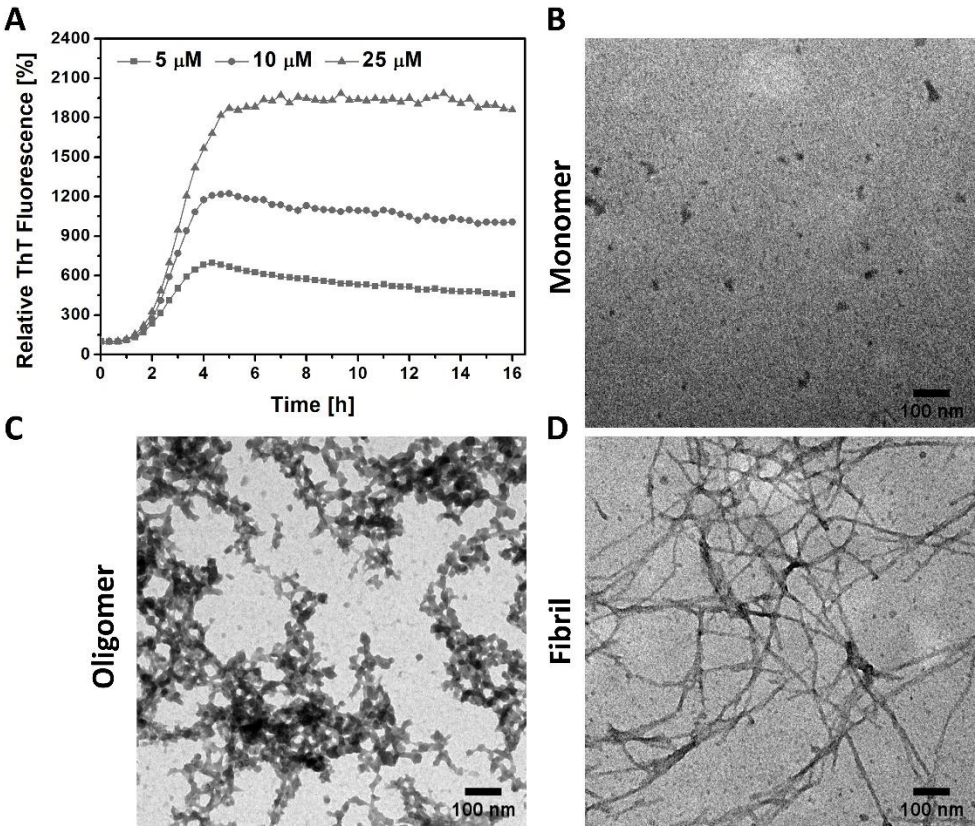

Figure S6.9. Aβ fibrillation. (**A**) ThT kinetics of Aβ at a concentration of 5 μM, 10 μM, and 25 μM. Increasing fluorescence indicates the fibrillation of Aβ. (**B**, **C** and **D**) TEM images of Aβ monomers, oligomers, and fibrils. The scale bar is 100 nm.

Kinetics of Aβ fibrillation with SA-B

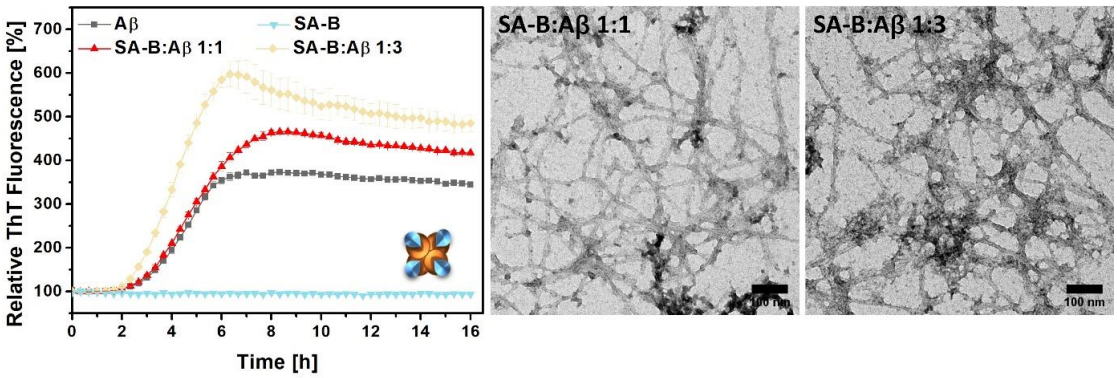

Figure S6.10. ThT kinetics of Aβ with **SA-B** in 1:1 and 1:3 molar ratio (in all ratios, the Aβ concentration is 5 μM), and the corresponding TEM images of the mixture. The scale bar is 100 nm.

6.6.7 Cytotoxicity of PAMAM dendrimer on primary murine neuronal cells

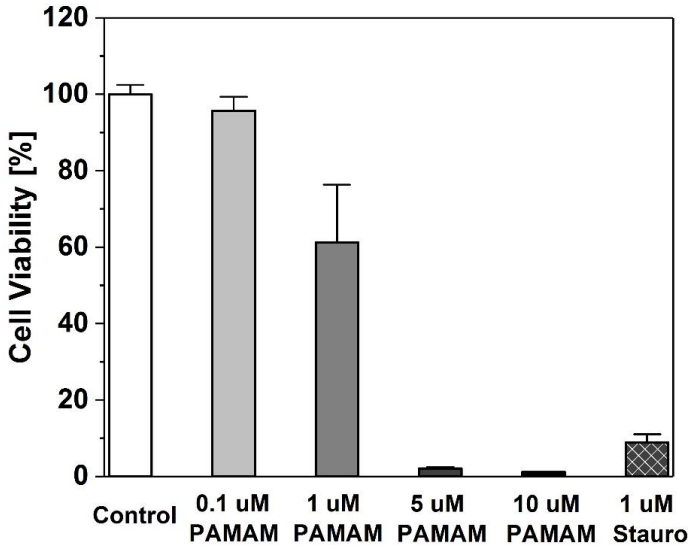

Figure S6.11. PAMAM dendrimer with different concentration were incubated with primary murine neuronal cells for 24 h. Cell vitality was assessed by CellTiterGlo Assay and is presented in %.

6.6.8 Disassembly behavior of PAMAM dendrimer on Aβ fibril

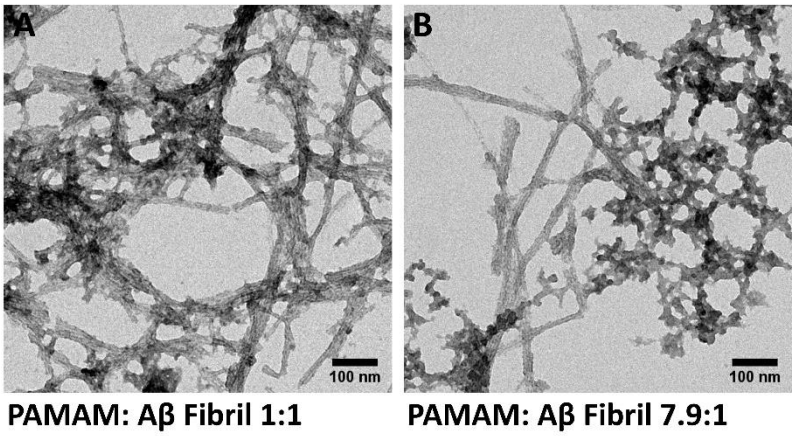

Figure S6.12. TEM images of (**A**) PAMAM: Aβ fibril 1:1 and (**B**) PAMAM: Aβ fibril 7.9:1 molar ratio. Scale bar is 100 nm.

6.7 References

[1] *Alzheimers Dement.* **2020**, *16*, 391-460.
[2] D. J. Selkoe, J. Hardy, *EMBO Mol. Med.* **2016**, *8*, 595-608.
[3] P. Carrillo-Mora, R. Luna, L. Colín-Barenque, *Oxid. Med. Cell. Longev.* **2014**, *2014*, 795375.
[4] L. K. Huang, S. P. Chao, C. J. Hu, *J. Biomed. Sci.* **2020**, *27*, 18.
[5] D. Furtado, M. Björnmalm, S. Ayton, A. I. Bush, K. Kempe, F. Caruso, *Adv. Mater.* **2018**, *30*, 1801362.
[6] G.-f. Chen, T.-h. Xu, Y. Yan, Y.-r. Zhou, Y. Jiang, K. Melcher, H. E. Xu, *Acta Pharmacol. Sin.* **2017**, *38*, 1205-1235.
[7] G. Aliev, G. M. Ashraf, V. V. Tarasov, V. N. Chubarev, J. Leszek, K. Gasiorowski, A. Makhmutova, S. S. Baeesa, M. Avila-Rodriguez, A. A. Ustyugov, S. O. Bachurin, *Curr. Neuropharmacol.* **2019**, *17*, 288-294.
[8] F. Vögtle, G. Richardt, N. Werner, in *Dendrimer Chemistry*, WILEY-VCH, Weinheim, **2009**, pp. 1-24.
[9] V. Leiro, S. Duque Santos, C. D. F. Lopes, A. Paula Pêgo, *Adv. Funct. Mater.* **2018**, *28*, 1700313.
[10] R. M. Kannan, E. Nance, S. Kannan, D. A. Tomalia, *J. Intern. Med.* **2014**, *276*, 579-617.
[11] R. Stangenberg, I. Saeed, S. L. Kuan, M. Baumgarten, T. Weil, M. Klapper, K. Müllen, *Macromol. Rapid Commun.* **2014**, *35*, 152-160.
[12] R. Stangenberg, Y. Wu, J. Hedrich, D. Kurzbach, D. Wehner, G. Weidinger, S. L. Kuan, M. I. Jansen, F. Jelezko, H. J. Luhmann, D. Hinderberger, T. Weil, K. Müllen, *Adv. Healthcare Mater.* **2015**, *4*, 377-384.
[13] Y. Wu, L. Li, L. Frank, J. Wagner, P. Andreozzi, B. Hammer, M. D'Alicarnasso, M. Pelliccia, W. Liu, S. Chakrabortty, S. Krol, J. Simon, K. Landfester, S. L. Kuan, F. Stellacci, K. Müllen, F. Kreppel, T. Weil, *ACS Nano* **2019**, *13*, 8749-8759.
[14] J. Wagner, L. Li, J. Simon, L. Krutzke, K. Landfester, V. Mailänder, K. Müllen, D. Y. W. Ng, Y. Wu, T. Weil, *Angew. Chem. Int. Ed.* **2020**, *59*, 5712-5720.
[15] C. M. Dundas, D. Demonte, S. Park, *Appl. Microbiol. Biotechnol.* **2013**, *97*, 9343-9353.
[16] S. L. Kuan, C. Förtsch, D. Y. W. Ng, S. Fischer, Y. Tokura, W. Liu, Y. Wu, K. Koynov, H. Barth, T. Weil, *Macromol. Biosci.* **2016**, *16*, 803-810.
[17] G. T. Hermanson, *Bioconjugate techniques*, Third edition ed., Elsevier/AP, London ; Waltham, MA, **2013**.
[18] M. n. González, C. E. Argaraña, G. D. Fidelio, *Biomol. Eng.* **1999**, *16*, 67-72.
[19] C. Minard-Basquin, T. Weil, A. Hohner, J. O. Rädler, K. Müllen, *J. Am. Chem. Soc.* **2003**, *125*, 5832-5838.
[20] A. Y. Lai, J. McLaurin, *Int. J. of Alzheimers Dis.* **2011**, *2011*, 548380.
[21] A. Srivastava, P. K. Singh, M. Kumbhakar, T. Mukherjee, S. Chattopadyay, H. Pal, S. Nath, *Chem. Eur. J.* **2010**, *16*, 9257-9263.
[22] V. I. Stsiapura, A. A. Maskevich, V. A. Kuzmitsky, K. K. Turoverov, I. M. Kuznetsova, *J. Phys. Chem. A* **2007**, *111*, 4829-4835.
[23] M. R. H. Krebs, E. H. C. Bromley, A. M. Donald, *J. Struct. Biol.* **2005**, *149*, 30-37.
[24] J. Masel, V. A. A. Jansen, *Biophys. Chem.* **2000**, *88*, 47-59.
[25] R. Sabaté, M. Gallardo, J. Estelrich, *Peptide Science* **2003**, *71*, 190-195.
[26] B. Klajnert, M. Cortijo-Arellano, J. Cladera, M. Bryszewska, *Biochem. Biophys. Res. Commun.* **2006**, *345*, 21-28.
[27] M. El-Sayed, M. Ginski, C. Rhodes, H. Ghandehari, *J. Controlled Release* **2002**, *81*, 355-365.
[28] Z. Wang, X. Dong, Y. Sun, *Langmuir* **2019**, *35*, 14681-14687.

[29] H. Sun, J. Liu, S. Li, L. Zhou, J. Wang, L. Liu, F. Lv, Q. Gu, B. Hu, Y. Ma, S. Wang, *Angew. Chem. Int. Ed.* **2019**, *58*, 5988-5993.
[30] M. Kawahara, I. Ohtsuka, S. Yokoyama, M. Kato-Negishi, Y. Sadakane, *Int. J. of Alzheimers Dis.* **2011**, *2011*, 304583.
[31] L. K. Simmons, P. C. May, K. J. Tomaselli, R. E. Rydel, K. S. Fuson, E. F. Brigham, S. Wright, I. Lieberburg, G. W. Becker, D. N. Brems, *Mol. Pharmacol.* **1994**, *45*, 373.
[32] M. Sakono, T. Zako, *FEBS J.* **2010**, *277*, 1348-1358.
[33] Y. Omidi, L. Campbell, J. Barar, D. Connell, S. Akhtar, M. Gumbleton, *Brain Res.* **2003**, *990*, 95-112.
[34] S. Kaech, G. Banker, *Nat. Protoc.* **2006**, *1*, 2406-2415.
[35] G. M. J. Beaudoin, S.-H. Lee, D. Singh, Y. Yuan, Y.-G. Ng, L. F. Reichardt, J. Arikkath, *Nat. Protoc.* **2012**, *7*, 1741-1754.

7 Summary and Outlook

This work aimed to shed light on the role of amphiphilic surface patterns in biorecognition. This included the coating of nanocarriers such as the gene delivery vector Ad5 and liposomes with the amphiphilic PPDs to study the impact of a patchy dendrimer corona on the protein adsorption. Consequently, the remodeling of the biological fate of the nanocarriers was evaluated in biological fluids, i.e. blood serum/plasma, and *in vivo.* A main goal was the advancement of the PPD scaffold to integrate an additional function extending the versatility of PPDs in biomedical applications. Hence, patchy poly-phenylene dendrimers, dendron-conjugates and a dendron-protein hybrid material were synthesized. Most of the application-related parts of this work were elaborated in collaborations as stated in the respective chapters. The achievements are summarized in Figure 7.1.

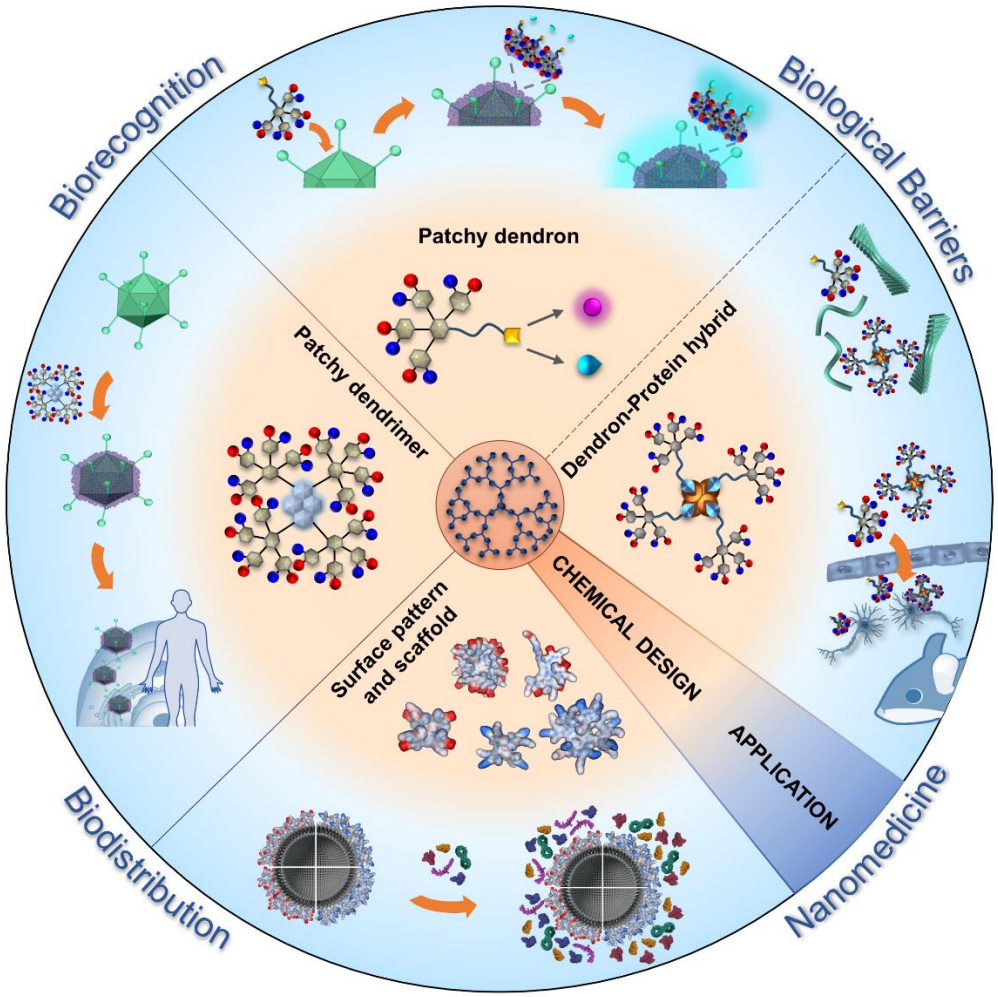

Figure 7.1. Summary of all projects: From Chemical Design to Application.

Surface Patterns of PPDs Determine their Biorecognition and Control the Biological Fate of Adenovirus 5 and Liposome Nanocarriers (chapter 3 and chapter 4)

In the first project, the ability of patchy PPDs to bind Ad5 was studied. The second-generation dendrimer with high density amphiphilic surface pattern (PPD3) resulted in an efficient binding to Ad5. PPD3 facilitated the transport of Ad5 into cells with low CAR expression, whereas the anionic dendrimer showed no binding capacity. Thus, this finding indicates that the *n*-propyl group participates in the binding event. Furthermore, the binding did not seem to be electrostatically driven since the removal of positive charges from Ad5-fibers did not hamper binding of the amphiphilic PPD. Instead, the interaction of the dendrimer occurred on the virus capsid as it modulated the binding of coagulation factor X, which is binding to the main capsid protein, the hexon protein. In addition, the dendrimer coating shielded from antibody and complement binding. *In vivo* studies revealed a reprogramming of Ad5-distribution by the dendrimer corona. The gene transduction was increased in the heart and diminished in liver and spleen. In conclusion, this initial study demonstrated the interaction of amphiphilic surface patches with protein interfaces, i.e. Ad5. Moreover, the dendrimer-coating could modulate the natural protein corona of Ad5 which in consequence, most likely caused the alteration of the *in vivo* distribution. Preliminary studies by employing dendrimer-coated polystyrene nanoparticles as model system disclosed the adsorption of specific blood serum proteins. The ability to control the protein adsorption on Ad5 by a PPD-coating opened up a way to the employment of PPD coatings with distinct amphiphilic surface patterns for nanocarrier systems in order to shape and potentially customize their protein corona.

Based on this, PPDs with an amphiphilic anionic rim (sulfonate and *n*-propyl groups) and an exclusive anionic periphery (sulfonate groups) were synthesized and compared to PPDs with a positively charged amphiphilic surface (methyl-pyridinium and *n*-propyl groups). The latter were synthesized by [redacted]. To assess the impact of amphiphilic patterned PPDs on the biological fate of nanocarriers, liposomes (and polystyrene nanoparticles) were coated with the dendrimers. First, both negatively and positively charged dendrimer coronas demonstrated the reduction of specific opsonization proteins (Ig γ-2, C3) and the enhancement of proteins that diminish unspecific cellular uptake (clusterin, fibrinogen, vitronectin) in human plasma. The adsorption behavior of these proteins appeared to be based on hydrophobic interactions. Second, differences in the protein corona which were attributable to surface charges were observed. This included the adsorption of HSA for cationic PPD-coated liposomes and the adsorption of ApoH and inter-α-trypsin inhibitor H4 for anionic PPD covered

nanocarriers. These findings indicated that it might be possible to modulate the protein adsorption in the blood stream based on a PPD corona by both hydrophobic and electrostatic interactions. In conclusion, the protein corona of nanocarriers can be tailored using dendrimers with different distinct surface pattern in order to remodel their biorecognition and -distribution.

In the future, the biodistribution of PPD-coated nanocarriers could be further investigated *in vivo*. In addition, the impact of the surface groups which impart the amphiphilic surface pattern could be studied. For example, the sulfonic acid group can be exchanged to a carboxylic acid or phosphonic acid group, which was already described by Hammer et al. (refer to chapter 1.3.3). These groups did not affect the cellular uptake but may change protein adsorption and consequently, biodistribution. Furthermore, the chain length of the aliphatic hydrophobic group (*n*-propyl) could be altered. Apart from amphiphilicity, PPDs with various surface patterns such as polymers, sugars or peptides could be synthesized and coated to nanocarriers to deepen the understanding of the hydrophobic PPD scaffold and the periphery on protein corona formation. Although the interaction of PPDs with liposomes seemed to be mainly electrostatically driven, the presence of hydrophobic *n*-propyl groups enhanced the coating. Thus, a versatile nanocarrier system is required to study PPD-coatings with various surface patterns. The screening of diverse PPDs providing surface structures with precise spatial arrangement would further contribute to the understanding of the interaction of distinct recognition motifs with biological structures.

Development of Amphiphilic Polyphenylene Dendron Conjugates for Biomedical Applications (chapter 5 and chapter 6)

As described in chapter 5, the synthetic pathway of an amphiphilic bifunctional polyphenylene dendron was developed to advance the PPD structure for biomedical purposes. The critical factors of dendron synthesis are summarized in Scheme 7.1. The employment of a suitable bifunctional dendritic core proved to be the decisive factor in dendron synthesis. First, a functionality that enables dendron growth and second, a moiety which is thermally stable during PPD synthesis were achieved by the synthesis of a biphenyl-core with an ethynyl group for dendron growth and a protected aniline group. After dendron growth, the aniline group at the focal point of the dendron was deprotected and successfully post-modified with an ethynylated linker which served as an “Click”-able handle for the attachment of bioactive groups. The second critical step was the required thermal deprotection step of the sulfonic acids. Due to the sensitivity of

many bioactive groups, this step was performed prior to the ligation of the biological function. In this way, Cy5, which served as fluorophore for imaging, and the bio-orthogonal molecule D-biotin were successfully attached. The biorecognition properties given by the amphiphilic surface patches was retained. The adsorption of blood serum and plasma proteins remained similar to highly branched PPD3 when coated to liposomes. As also demonstrated in chapter 4, the binding of opsonization proteins was diminished whereas the adsorption of proteins furnishing selective cellular uptake was observed. Most notably, the adsorption of vitronectin and ApoH, reported to mediate selective cellular uptake, was even higher for the dendron compared to PPD3. The dendron preserved its cellular uptake behavior and a high cell viability up to 20 µM was maintained. In addition, the interaction with Ad5 and the CAR-independent gene transduction was retained while the reactive handle of the focal point was available for post-modifications which was successfully shown by a CuAAC with 3-azido-7-hydroxycoumarin. This model-reaction also indicated the accessibility of the focal point of the dendron which would be attractive for further investigations in the field of targeting and drug delivery.

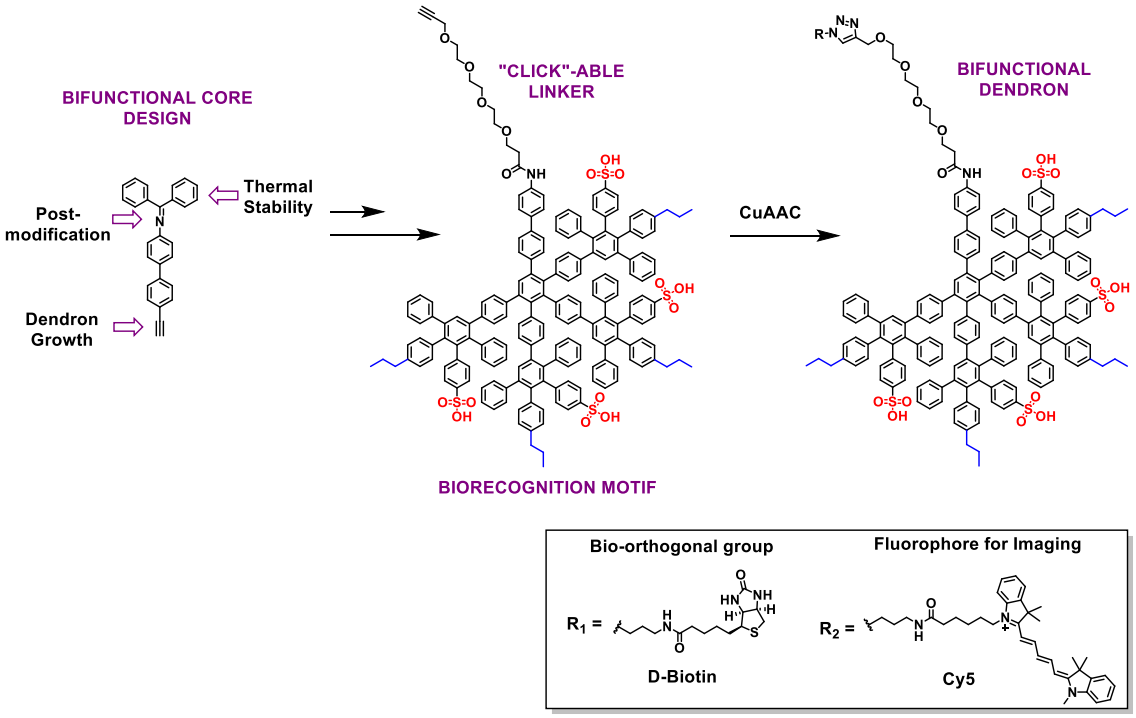

Scheme 7.1. Critical steps in dendron synthesis – from the design of a bifunctional core towards the attachment of an additional biological function by a “Click”-able linker.

Furthermore, the amphiphilic dendron was used for the construction of a polyphenylene dendron-protein hybrid material, which is described in chapter 6. The patchy dendron was bound to streptavidin *via* a D-biotin moiety. Both dendron and SA-dendron hybrid

(SA-D) were internalized into murine brain endothelial cells and neurons *in vitro*. In addition, the delivery to the brain was observed *in vivo*. Consequently, the dendron-conjugates gave promise towards the use in neurodegenerative diseases such as Alzheimer's disease. The fibrillation process of the Aβ-peptide was altered. The dendron conjugates both inhibited fibril formation and disassembled pre-existing fibrils. The degeneration of neurons caused by Aβ-fibrils was prevented by the addition of the dendron conjugates. These studies demonstrated, that the dendron is sufficient for an antiamyloidogenic effect. The SA-D did not show any improvement, but it introduces the opportunity to combine several functions within one biomolecule which is highly attractive in combination therapies. In conclusion, the structural design of both dendron and SA-D allowed the utilization in biomedical applications due to the preservation of the biorecognition motif and the advantage to attach an additional function.

For future applications, the attachment of targeting groups such as antibodies is of great relevance. The target-oriented transport of Ad5 to a certain cell in the body would advance Ad5-assisted gene therapy. Furthermore, the attachment of targeting groups such as angiopep-2 or transferrin could enhance the delivery to the brain, which is attractive for the treatment of neurodegenerative diseases. The covalent attachment of drugs or MRI contrast agents by a trigger-responsive linker (e.g. pH or reductive/ enzymes) to the dendron's focal point could allow the use of the dendron in drug delivery, combination therapy and theranostics respectively. Moreover, the use of SA as an adapter enables the combination of even multiple functionalities in one biomolecule. Dendrimers are also applied in biosensors to enhance the binding by their multivalent surface. The biotinylated dendron could be attached to a SA-coated surface and serve as a recognition motif for e.g. Ad5. Another possibility towards PPD-protein hybrid materials would be the covalent attachment to a protein. The ethynyl-group of the dendron's focal point could be, for example, either used for the ligation by CuAAC or thiol-yne reaction. In addition, the reactive group of the linker could be exchanged to reactive groups such as a tetrazole/tetrazine or cyclooctyne that can be reacted without the need of potentially toxic catalysts. The main challenge of the integration of another reactive handle would be the thermal stability which is required during the deprotection of the sulfonic acids. In consequence, the thermal stability of the Click-able group needs to be assessed or the attachment of the linker after the heating step needs to be considered. Apart from the amphiphilic surface pattern, the biorecognition motif could be changed to e.g. peptides, PEG or polymer chaines (as described above) in order to

further explore the role of distinct surface pattern in biorecognition in combination with a second feature linked to the dendron scaffold.

In summary, the engineering of the protein adsorption of nanocarriers by a dendrimer corona and the development of a desymmetrized PPD structure opened an avenue towards PPD-based nanotherapeutics and further deepend the understanding of precisely positioned amphiphilic surface patterns in biorecognition.

List of Abbreviations

AD	Alzheimer's disease
Ad5	Adenovirus 5
AFM	Atomic force microscopy
AICD	Amyloid precursor protein intracellular domain
APCI-MS	Atmospheric pressure chemical ionization mass spectrometry
ApoH	Apolipoprotein H
APP	Amyloid precursor protein
ASAP	Atmospheric solid analysis probe
ATRP	Atom transfer radical polymerization
Aβ	Amyloid-beta
BACE	Beta-site amyloid precursor protein cleaving enzyme (beta-secretase)
BBB	Blood-brain barrier
BCA	Bicinchoninic acid
BLI	Biolayer interferometry
BTTAA	4-{[bis-(1-*tert*-butyl-1H-[1,2,3]triazol-4-ylmethyl)-amino]-methyl}-[1,2,3]triazol-1-yl)-acetic acid
C3	Complement C3
CAR	Coxsackie-adenovirus receptor
CD	Circular dichroism
CHO-K1	Chinese hamster ovary cell line
CO	Carbon monoxide
CP	Cyclopentadienone
CuAAC	Copper(I)-catalyzed azide alkyne cycloaddition
Cy5	Cyanine 5
D	Dendron
DCM	Dichloromethane
DLS	Dynamic light scattering
DMEM	Dulbecco's Minimum Essential Medium
DMF	*N,N*-Dimethylformamide
DMSO	Dimethyl sulfoxide

DNA	Deoxyribonucleic acid
DOX	Doxorubicin
dsDNA	Double-stranded deoxyribonucleic acid
DTT	Dithiothreitol
ECM	Extracellular matrix
EGFP	Enhanced green fluorescent protein
EPR	Enhanced permeability and retention effect
ESI	Electrospray ionization
FACS	Fluorescence-activated cell sorting
FBS	Fetal bovine serum
FCS	Fetal calf serum
FDA	Food and Drug Administration
FD-MS	Field desorption mass spectrometry
FX	Blood-coagulation factor X
G	Generation
GPC	Gel permeation chromatography
HA	Hemagglutinin
HABA	2-[(4-Hydroxyphenyl)-diazenyl]benzoic acid
HIV	Human immunodeficiency virus
HPV	human papillomavirus
HSA	Human serum albumin
HSPG	Heparane sulfate proteoglycan
HSV	Herpes simplex virus
i.v.	Intravenous
Ig	Immunoglobulin
IαI	inter-alpha-trypsin inhibitor
Lipo	Liposome
LPR1	Low density lipoprotein receptor-related protein 1
MALDI-TOF MS	Matrix-assisted laser desorption/ionization–time of flight mass spectrometry
MES	2-(*N*-morpholino)ethanesulfonic acid
MFI	Mean fluorescence intensity
MPS	Mononuclear phagocyte system

MRI	Magnetic resonance imaging
mRNA	Messenger ribonucleic acid
N	Pyridinium
NaAsc	Sodium ascorbate
NHS	*N*-Hydroxysuccinimidyl
NMR	Nuclear magnetic resonance
NVU	Neurovascular unit
P	*n*-propyl
PAH	Polyaromatic hydrocarbons
PAMAM	Poly(amido)amine
PB	Phosphate buffer
PBS	Phosphate buffered saline
PDI	Polydispersity index
PEG	Polyethylene glycol
pMOI	Particle multiplicity of infection
POPAM	Poly(propyleneamine)
PPD	Polyphenylene dendrimer
PS	Polystyrene
RES	Reticuloendothelial system
RNA	Ribonucleic acid
S	Sulfonic acid
SA	Streptavidin
SA-D	Dendronized streptavidin
SANS	Small-angle neutron scattering
SDS-PAGE	Sodium dodecyl sulfate–polyacrylamide gel electrophoresis
SEC	Size exclusion chromatography
SEM	Standard error of the mean
SPAAC	Strain-promoted azide-alkyne cycloaddition
TBAF	Tetra-*n*-butyl-ammonium fluoride
TBTA	Tris((1-benzyl-4-triazolyl)methyl)amine
TEER	Transendothelial electrical resistance
TEG	Triethylene glycol
TEM	Transmission electron microscopy

THF	Tetrahydrofurane
ThT	Thioflavin T
TIPS	Tri*iso*propylsilyl
TLC	Thin-layer chromatography
VP	Virus particle

List of Figures

Figure 1.1. Dendritic polymers. Synthetic dendritic structures are divided in monodisperse dendrimers and polydisperse polymers. 2
Figure 1.2. Dendrimer scaffold....3
Figure 1.3. Dendrimers as “artificial proteins”. 4
Figure 1.4. Relevance of surface and interior chemistry of dendrimers for pharmaceutical applications. 9
Figure 1.5. Mechanism of amyloid-β (Aβ) aggregation starting from cleavage by the γ-secretase and β-secretase (BACE) into Aβ, the soluble amyloid precursor protein (sAPPβ) and the amyloid precursor protein intracellular domain (AICD). The Aβ monomer aggregate into oligomers, followed by fibril formation and consquently amyloid plaques leading to degeneration of neurons. Dendrimers can alter the aggregation process. 12
Figure 1.6. Selective chemical protein modifications....14
Figure 1.7. Dendrimer-protein hybrid materials. 16
Figure 1.8. Rigid dendrimers with multiple phenylene units. 17
Figure 1.9. Examples of dendrimer cores with different geometries influencing the branching and spatial orientation of dendritic branches. 20
Figure 1.10. Building blocks for PPD synthesis....20
Figure 1.11. PPD as fluorescent probe for bioassays. 21
Figure 1.12. Comparison of amphiphilic Au-nanoparticle surfaces with the surface of amphiphilic PPDs and proteins....25
Figure 1.13. Dependency of size (generation G) and surface chemistry of dendrimers on the biodistribution, toxicity, biopermeability and immunogenicity. 28
Figure 1.14. Parameters influencing the protein corona formation and biological fate of nanocarriers. 29
Figure 1.15. Adenovirus-assisted gene therapy. 31
Figure 2.1. Conceptional design and aim of this work. 42
Figure 3.1. PPD3 and Ad5 formed complexes with increased transduction efficiency on CHO and SKOV-3 cells. 51
Figure 3.2. Transduction by PPD3/Ad5 complexes was independent of the primary Ad5 receptor CAR and the positively charged KKTK motif in the fiber capsomere. 52

Figure 3.3. PPD3/Ad5 complexes exhibit increased transduction efficiency in human plasma and PPD3 protected FX-binding ablated capsids from neutralization by the IgM/complement pathway.. 55
Figure 3.4. Decreased liver and improved heart transduction by PPD3/Ad5 complexes in vivo. 56
Figure 3.5. Schematic overview of the features of Ad5 with PPD3 corona. 58
Figure 4.1. Protein corona on PPD-coated liposomes. 83
Figure 4.2. Comparison of adsorbed proteins between uncoated liposomes and lipo-dendrimers (lipo-$(PS)_4$ and lipo-$(PN)_8$). 86
Figure 4.3. Comparison of adsorbed proteins between lipo-$(PS)_4$ and lipo-$(PN)_8$). 87
Figure 5.1. Structural design of an amphiphilic polyphenylene dendron by desymmetrization of amphiphilic dendrimer PPD3. 123
Figure 5.2. Dendron-coated liposomes form a protein corona in blood serum/plasma. 127
Figure 5.3. Cellular internalization of amphiphilic dendrons and cell viability on CHO-K1. 129
Figure 5.4. Dendron-Ad5 complex formation leads to EGFP-transduction in CAR-negative cells. 131
Figure 5.5. CuAAC on dendrons bound to Ad5. 133
Figure 6.1. Schematic overview of the study. 197
Figure 6.2. Preparation and characterization of **SA-D**. 199
Figure 6.3. Cy5-D and Cy5-SA-D uptake in brain endothelial and neuronal cells *in vitro*. 200
Figure 6.4. Dendron and SA-D toxicity for brain endothelial cells and primary neuronal cells. 201
Figure 6.5. Cy5-dendron and Cy5-SA-D delivery to the mouse brain. 203
Figure 6.6. Aβ fibrillation with dendron **1** and **SA-D** with increasing Aβ concentrations. 205
Figure 6.7. Aβ fibrillation with dendron **1** and **SA-D** at equimolar dendron concentrations. 206
Figure 6.8. ThT kinetics of Aβ with PAMAM (G3). 207
Figure 6.9. Circular dichroism spectrum of Aβ and dendron **1** with Aβ peptide. 208
Figure 6.10. Dendron **1** and **SA-D** Aβ fibril disassembly. 209
Figure 6.11. Dendron **1** and **SA-D** inhibition of Aβ toxicity on murine primary neurons. 210
Figure 7.1. Summary of all projects: From Chemical Design to Application. 231

List of Schemes

Scheme 1.1. Divergent approach. 6
Scheme 1.2. Convergent approach. 7
Scheme 1.3. Cyclodehydrogenation of PPD **1-16** to PAH **1-17**. 17
Scheme 1.4. Divergent PPD synthesis. 19
Scheme 1.5. *A posteriori* surface modifications for biological applications. 22
Scheme 3.1. Synthesized PPDs with Amphiphilic *n*-Propyl and Sulfonic Acid Surface Patches. 48
Scheme 4.1. Synthesis of polyphenylene dendrimers with different surface pattern. 84
Scheme 5.1. Synthesis of amphiphilic polyphenylene dendron conjugates. 125
Scheme 7.1. Critical steps in dendron synthesis – from the design of a bifunctional core towards the attachment of an additional biological function by a "Click"-able linker. 234

List of Supporting Figures

Figure S3.1. Infection Assay using Ad5 and defined concentrations of PPD3. 66
Figure S3.2. Example of gating strategy used for flow cytometry. 66
Figure S3.3. The influence of PPD and Ad5 pre-incubation time to the EGFP expression in CHO-K1 cells (n = 3). 68
Figure S3.4. Ad5 transduction assay showed that PPD3/Ad5 complex formation is essential for enhancing transduction. 68
Figure S3.5. PPD3/Ad5 transduction efficiency in different (+)CAR and (-)CAR cell lines. 69
Figure S3.6. Wild type Ad5 activity when complexes with PPD3. 70
Figure S3.7. The stability of PPD3/Ad5 complex in FCS. 71
Figure S3.8. Quantification of EGFP DNA levels in the liver with qPCR (n = 3) after 7 days and 14 days. 72
Figure S3.9. Hematoxylin and eosin (H&E) staining of liver tissues (10 time of magnification). 72
Figure S3.10. Workflow for dendron loading and dendron-Ad5 interaction assay. 73
Figure S3.11. BLI analysis of Ad5 binding to biotinylated PPD3 dendrons immobilized on streptavidin-coated biosensors. 74
Figure S3.12. Hard protein corona analysis of polystyrene nanoparticles (PS-NP) and dendrimer (PPD3) coated nanoparticles after serum incubation. 76
Figure S3.13. Hard protein corona analysis of polystyrene nanoparticles (PS-NP) and PPD3 coated nanoparticles after plasma incubation. 77
Figure S3.14. Proteomic analysis of the hard protein corona for polystyrene nanoparticles (PS-NP) coated with dendrimers (PPD3) after serum (**a**) and plasma (**b**) incubation. 77
Figure S4.1. Systematic designation of polyphenylene dendrimers (PPDs). 90
Figure S4.2. Synthesis of first-generation amphiphilic dendrimer **10a** with alternating sulfonic acid and *n*-propyl groups according to Stangenberg et al. 91
Figure S4.3. Synthesis of first-generation negatively charged dendrimer **10b**. 94
Figure S4.4. Synthesis of positively charged first-generation dendrimer **10c** with alternating pyridinium and n-propyl groups. 98
Figure S4.5. Synthesis of second-generation dendrimer **15d** with alternating pyridinum and *n*-propyl groups. 103

Figure S4.6. Verification of dendrimer-coating on liposomes and polystyrene nanoparticles (PS-NH_2). 109
Figure S4.7. Verification of protein adsorption on lipo-dendrimers and PS-dendrimers. 110
Figure S4.8. Heatmaps of adsorbed proteins to dendrimer-coated liposomes lipo-$(PS)_4$ and lipo-$(PN)_8$ in (**A**) blood serum and (**B**) blood plasma. 111
Figure S4.9. Heatmaps of adsorbed proteins to dendrimer-coated polystyrene nanoparticles PS-$(PS)_4$ and PS-S_8 in (**A**) blood serum and (**B**) blood plasma. 111
Figure S4.10. Protein corona on dendron- and dendrimer-coated liposomes....112
Figure S4.11. Comparison of adsorbed proteins between uncoated polystyrene nanoparticles (PS-NH_2) and PS-dendrimers (PS-$(PS)_4$ and PS-S_8). 113
Figure S4.12. List of all identified corona proteins on lipo-dendrimers lipo-$(PS)_4$ and lipo-$(PN)_8$ in human serum and plasma. 114
Figure S4.13. List of all identified corona proteins on PS nanoparticles coated with $(PS)_4$ and S_8. 115
Figure S5.1. Reaction scheme of building blocks. 136
Figure S5.2. Detailed reaction scheme of dendron synthesis 143
Figure S5.3. ^{1}H NMR spectrum (700 MHz) of protected dendron **16** recorded in deuterated dichloromethane. 155
Figure S5.4. ^{13}C NMR spectrum (176 MHz) of protected dendron **16** recorded in deuterated dichloromethane. 155
Figure S5.5. Constitutional isomers of deprotected dendron **16**. 156
Figure S5.6. ^{1}H NMR spectrum (500 MHz) of deprotected dendron **8** recorded in deuterated dimethyl sulfoxide 157
Figure S5.7. ^{13}C NMR spectrum (126 MHz) of protected dendron **8** recorded in deuterated dimethyl sulfoxide. 157
Figure S5.8. ^{1}H NMR spectrum (700 MHz) of biotin-dendron **9a** recorded in deuterated dimethyl sulfoxide. 158
Figure S5.9. ^{13}C NMR spectrum (176 MHz) of biotin-dendron **9a** recorded in deuterated dimethyl sulfoxide. 158
Figure S5.10. ^{1}H NMR spectrum (700 MHz) of Cy5-dendron **9b** recorded in deuterated dimethyl sulfoxide. 159
Figure S5.11. ^{13}C NMR spectrum (176 MHz) of Cy5-dendron **9b** recorded in deuterated dimethyl sulfoxide. 159
Figure S5.12. Summarized ^{1}H NMR spectra of final dendrons (**8**, **9a** and **9b**). 160

Figure S5.13. MALDI-TOF mass spectrum of dendron **8**. 160
Figure S5.14. MALDI-TOF mass spectrum of biotin-dendron **9a**..... 161
Figure S5.15. MALDI-TOF mass spectrum of Cy5-dendron **9b**..... 161
Figure S5.16. Heat map of adsorbed proteins to dendron **8** and dendrimer coated polystyrene nanoparticles in (**A**) blood serum and (**B**) blood plasma. 165
Figure S5.17. Hard protein corona analysis of polystyrene nanoparticles (PS-NH_2) coated with dendron **8** or dendrimer PPD3 after serum incubation. 166
Figure S5.18. Hard protein corona analysis of polystyrene nanoparticles (PS-NH_2) coated with dendron **8** or dendrimer PPD3 after plasma incubation. 166
Figure S5.19. Hard protein corona analysis of liposomes (Lipo-NH_2) coated with dendron **8** or dendrimer PPD3 after serum incubation. 167
Figure S5.20. Hard protein corona analysis of liposomes (Lipo-NH_2) coated with dendron **8** or and dendrimer after plasma incubation..... 167
Figure S5.21. The absolute amount of adsorbed corona proteins (in mg) per surface area (m^2) of the liposomes (**A**,**B**) and polystyrene nanoparticles (**C**,**D**) was determined *via* Pierce Assay. 168
Figure S5.22. Assumption how the amphiphilic PPD surface motif might interact with the liposomes. 168
Figure S5.23. Cellular uptake of Cy5-dendron **9b** in CHO-K1 cells. 170
Figure S5.24. TEM images show binding of dendron-conjugates (Biotin-D **9a** and Cy5-D **9b**) to Ad5..... 172
Figure S5.25. Size distribution by intensity. 173
Figure S5.26. Size distribution by intensity. 176
Figure S5.27. Fluorescent microscopy image of EGFP-transduction in CAR-negative CHO-K1 cells with infection by Ad5 (control), Ad5/dendron (Ad5: dendron=1: 500k) or Ad5/dendrimer (Ad5: dendrimer=1: 125k). 178
Figure S5.28. Flow cytometric quantification for CHO-K1 infected by Ad5 or Ad5/dendron..... 179
Figure S5.29. Flow cytometric quantification for CHO-K1 infected by Ad5 or Ad5/Cy5-D **9b**..... 180
Figure S5.30. Investigation of ligand dependency of CuAAC. 181
Figure S5.31. CuAAC with BTTAA..... 182
Figure S5.32. Workflow for dendron loading and dendron-Ad5 interaction assay 183
Figure S5.33: BLI analysis of Ad5 binding to biotin-dendron **9a** immobilized on streptavidin-coated biosensors. 184

Figure S5.34. Average amount in % and the standard deviation of all identified proteins adsorbed to lipo-dendron and lipo-dendrimer in blood serum.....186
Figure S5.35. Average amount in % and the standard deviation of all identified proteins adsorbed to PS-dendron and PS-dendrimer in blood serum 187
Figure S5.36. Average amount in % and the standard deviation of all identified proteins adsorbed to lipo-dendron and lipo-dendrimer in blood plasma 188
Figure S5.37. Average amount in % and the standard deviation of all identified proteins adsorbed to PS-dendron and PS-dendrimer in blood plasma.....189
Figure S6.1. Synthesized dendron-conjugates. 217
Figure S6.2. Modification of SA with the fluorophore Cy5. 219
Figure S6.3. MALDI-TOF mass spectrum of Cy5-labelled SA.....219
Figure S6.4. Preparation of (**A**) dendronized SA (**SA-D**) and (**B**) dendronized Cy5-SA (**Cy5-SA-D**).....220
Figure S6.5. Preparation of SA complexed with free D-biotin (**SA-B**) as reference ...221
Figure S6.6. HABA-Assay. 222
Figure S6.7. Agarose gel of SA conjugates. 224
Figure S6.8. Biodistribution of **Cy5-D** and **Cy5-SA-D**. 226
Figure S6.9. Aβ fibrillation.....227
Figure S6.10. ThT kinetics of Aβ with **SA-B** in 1:1 and 1:3 molar ratio (in all ratios, the Aβ concentration is 5 µM), and the corresponding TEM images of the mixture. 227
Figure S6.11. PAMAM dendrimer with different concentration were incubated with primary murine neuronal cells for 24 h. 228
Figure S6.12. TEM images of (**A**) PAMAM: Aβ fibril 1:1 and (**B**) PAMAM: Aβ fibril 7.9:1 molar ratio.....228

List of Supporting Tables

Table S3.1. Light scattering measurement of the complex formation with PPD and Ad5. 65
Table S3.2. Kinetics analysis results. 74
Table S5.1. Zeta Potential measurements of liposomes (20 µL) uncoated or coated with dendron/dendrimer in 1 mM KCl solution (1 mL). Dynamic light scattering measurements at an angle of 90°C of liposomes (20 µL) uncoated or coated with dendron/dendrimer in PBS (1 mL). 163
Table S5.2. Average amount in % and the standard deviation of identified proteins adsorbed to lipo-dendron and lipo-dendrimer mentioned in the main manuscript. 165
Table S5.3. Size and zeta potential of Ad5/dendron complexes with an Ad5-concentration of 4.5 x 10^8 vp/mL in 5 mM phosphate buffer after incubation for 40 min. 173
Table S5.4. Size and zeta potential of Ad5/dendron complexes. 175
Table S5.5. Size and zeta potential of free dendrons as control. 175
Table S5.6: Kinetic analysis results 184
Table S6.1. Hydrodynamic Radius (R_h) and PDI of **SA-D** in ultrapure water (MilliQ) and 25 mM, 50 mM and 100 mM phosphate buffer. 225

Appendix

List of Publications

- Patchy Amphiphilic Dendrimers Bind Adenovirus and Control Its Host Interactions and In Vivo Distribution.
  [redacted] *ACS Nano*, **2019**, 13, 8, 8749-8759. (+ shared first)

- Amphiphilic Polyphenylene Dendron Conjugates for Surface Remodeling of Adenovirus 5.
  [redacted]
  Angewandte Chemie, International Edition **2020**, *59*, 5712-5720.

- Amphiphilic Dendrimers Control Protein Binding and Corona Formation on Liposome Nanocarriers.
  [redacted]
  submitted to Chemical Communications. (+ shared first, in revision)

- Amphiphilic Polyphenylene Dendrimer Conjugates Crossing the Blood-Brain Barrier and Inhibiting Aβ Fibrillation.
  [redacted] *to be submitted*. (+ shared first)

Conferences and Summer Schools

- Control of Adenovirus Host Interactions by Amphiphilic Polyphenylene Dendron Bioconjugates.

  [redacted]

  Twente/Mainz Mini-Symposium, MPIP Mainz, Germany, May 2019 (Poster)

- Control of Adenovirus Host Interactions by Amphiphilic Polyphenylene Dendrimers.

  [redacted]

  Proteins @ Interfaces School, MPIP Mainz, Germany, November 2018 (Poster)

- Synthesis of Bioactive Amphiphilic Polyphenylene Dendrimers.

  [redacted]

  The World Polymer Congress MACRO18, Cairns, Australia, July 2018 (Poster)

- Synthesis of Bioactive Amphiphilic Polyphenylene Dendrimers.

  [redacted]

  "A Corbella" International Summer School on Organic Synthesis (ISOS 2018), Gargnano (Brescia), Italy, June 2018 (Poster)

Curriculum Vitae